Development and Applications of Techniques in Laser Femtochemistry

Thesis by

Søren Pedersen

In Partial Fulfillment of the Requirements

for the Degree of

Doctor of Philosophy

California Institute of Technology

Pasadena, California

1996

(Submitted February 5, 1996)

Acknowledgments

Many people deserve to be acknowledged for their help during my graduate studies. To all of those not mentioned here specifically, you have my deepest gratitude for your efforts. Several individuals deserve a special mentioning and I wish to take this opportunity to express my appreciation.

I wish to thank my research advisor, Ahmed Zewail, for giving me the opportunity to be involved in a number of exciting projects and for numerous fruitful scientific discussions. His incredible enthusiasm for ultrafast chemical dynamics has been inspiring and contagious. Funding for these projects by the US Air Force Office of Scientific Research and the National Science Foundation was greatly appreciated.

I owe my gratitude to all the graduate students and postdocs with whom I have worked through the years on different projects. The close collaborations with Luis Bañares, Thomas Baumert, Jennifer Herek, Sang Kyu Kim and Marcus Motzkus were both stimulating and enjoyable.

I would also like to thank Qianli Liu and Earl Potter for the successful work together during the brief period they spent in our laboratory. I am thankful to Bob Bowman for teaching me the ins and outs of the CPM laser.

In addition, I wish to thank Hans Frey, Ahmed Heikal, Dan Kennefick, Hakno Lee, Rob Navin, Marcel Widmer and Chuck Williamson for interactions on and off the soccer field.

I greatly appreciated the efficiency and helpfulness of the Caltech staff, especially those in the Chemistry and Physics departments. In particular, I wish to acknowledge the help of Guy Duremburg and Tom Dunn.

Finally, I want to thank my family for their help and support during my time at Caltech.

Abstract

Femtosecond laser pulses provide the necessary time resolution to study fundamental dynamics of chemical reactions at the temporal scale of atomic resolution. New experimental techniques are introduced to the field of laser femtochemistry to generalize the range of accessible systems and further the understanding of molecular dynamics. In addition, theoretical models are developed that complement the experimental results and form the required basis for the interpretation of ultrafast measurements. The combination of multiphoton ionization with mass spectrometry and femtosecond lasers is introduced to isolate the elementary steps of reactions, differentiating parent and intermediate species and establishing the time scale for their dynamics. In two examples, using this approach, the direct real-time detection of diradical intermediates was made, and in another study the stepwise nature of a process initiated by the Norrish Type-I alfa-cleavage of acetone was revealed. This technique was also employed in the direct observation of vibrational motion in the transition state of a reaction (stilbene isomerization). The kinetic-energy time-of-flight (KETOF) method is developed to describe anisotropy and rotational alignment in the transition-state region and is applied to the dissociation of HgI_2. An extension of the pump-probe scheme is made using the non-linear optical technique of femtosecond degenerate four-wave-mixing (DFWM) and application is made to the study of gas phase reaction dynamics of uni- (NaI) and bi-molecular (NaH_2) systems. A detailed theoretical description of femtosecond transition-state dynamics is provided and illustrated via numerous examples. A kinetic model is developed, describing molecular response functions for ionization, fluorescence, depletion and absorption measurements. Effects of pulse width and saturation are discussed and comparison is made to classical and quantum mechanical models.

Table of Contents

Chapter 1

Introduction to Femtochemistry

The nature of a chemical reaction is governed by the evolution of the molecular system through a transition-state region from the initial reactant to the final products. In this region it is determined how the chemical bonds are broken or formed and the time scale for this to occur lies in the picosecond (10^{-12} s) to femtosecond (10^{-15} s) regime. Using femtosecond (fs) laser pulses it is possible to achieve the necessary temporal resolution to directly observe, in real-time, the motion of the atoms in a molecule. The introduction of such laser pulses to the study of ultrafast dynamics of chemical reactions has led to the exciting field of femtochemistry pioneered by Zewail.[1]

Typically, a fs pump laser pulse initiates the reaction and a second fs pulse is introduced at a time delay later to probe or, in other words, take a picture of the system at this certain time. By repeatedly performing this so-called pump-probe experiment at discrete time delays, a complete motion picture of the reaction is obtained with detailed information about the whole evolution of the system. Such femtosecond transition-state spectroscopy (FTS) experiments have led to a wide range of applications since their first introduction and development by the Zewail group, and have already provided answers to many fundamental questions. The scope of this established, yet rapidly expanding field of femtochemistry is reviewed in recent books by Zewail[2] and by Manz and Wöste,[3] and is illustrated by the recent exciting conferences in Lausanne[4] and Berlin.[5]

In the first example of a pump-probe experiment, the dissociation of ICN along a repulsive potential energy surface was directly observed and the reaction was seen to be complete in less than 1 ps.[6] The method of detection was by means of laser-induced fluorescence (LIF) emitted as a result of probing. These methods have since been extended to enable the observation of dynamics in more complex molecular systems[2] and even to control a chemical reaction.[7] Recent technological advances have formed the basis for a very promising technique, fs-

resolved electron diffraction.[8, 9] The probe in this case is an ultrafast electron pulse which scatters off the transition-state species, revealing the internuclear separations from an analysis of the resulting diffraction pattern. As such it is a very direct means of investigating the dynamics and promises to yield significant results in the future.

In order to characterize a reaction, it is important to acquire detailed knowledge about the translational, vibrational and rotational dynamics involved. The aim of different experimental techniques, each with a unique combination of the arrangement of the laser pulses, the molecular system and the detection scheme, is to gain an understanding of the influence on the dynamics of one or more of these three types of degrees of freedom. In so doing, key information is provided towards a complete picture of the reaction. For example, using a fs pump-probe arrangement and probing to ionization, it was possible to see vibrational motion in the transition state reached in the isomerization of the stilbene molecule.[10, 11] Upon the absorption of a photon, this molecule twists to its isomer and this behavior is similar to that of rhodopsin, a molecule that plays a vital role in vision. In addition to being able to apply such ultrafast experimental approaches, it is equally important to possess the necessary theoretical tools to interpret the experimental data.

The goal of this thesis is therefore not only to develop new experimental techniques but also to provide the complete theoretical basis required in the analysis of the experiments. These techniques enhance the ability to gain information about and link the different significant aspects of the molecular dynamics of a chemical system. The approaches developed and applied here are summarized below, and some of these methods have already led to further investigations in different unique systems.

Chapter two presents a description of the fs laser system[12, 13] used in the study of ultrafast dynamics. The idea of a pump-probe experiment is presented and is followed by discussions of different conditions for a molecular system and the detection arrangements. A description is provided of the molecular beam machine equipped with time-of-flight (TOF) mass spectrometry in different modes of operation. Fluorescence detection with a monochromator and the use of a quartz cell with a gas phase sample is also detailed.

In chapter three, a necessary theoretical description of fs transition-state dynamics is developed and illustrated via numerous examples.[14] A kinetic model is used to describe the signal observed in many typical pump-probe experiments and examples are given to illustrate the effects that influence transients, signal *vs.* time delay. The response of the molecular system is derived for various types of dynamics with one or more rate determining processes. Furthermore, the influence on the signal of the finite temporal width and shape of the laser pulses is quantitatively presented. Effects are discussed both in the unsaturated and the saturated regime of transition probabilities. The results of the kinetic model approach are compared with the predictions of classical and quantum mechanical models.

Chapter four illustrates experimental and theoretical aspects of the detection of ultrafast dynamics via multi-photon ionization (MPI). The idea of mass selectivity used as a tool to separate parent, intermediate and product dynamics is developed. This approach has been applied to directly observe the fast (150fs) birth and slower (700fs) decay of diradical intermediates,[15] produced by the ultrafast decarbonylation of (certain) cycloketones. In addition, the technique was employed to establish the stepwise nature of the fragmentation of excited acetone, $(CH_3)_2CO$, via the acetyl radical, CH_3CO, to $2CH_3 + CO$. The initial process, Norrish Type-I α-cleavage, as well as the build-up and decay of the

intermediate could be clearly separated and the lifetimes were measured.[16] In a separate study,[17] the femtochemistry of organometallics was investigated by separating the dynamics of metal-metal and metal-ligand bond cleavage in $M_2(CO)_{10}$. Chapter four also includes a discussion of laser-induced fluorescence detection and the concept of fluorescence depletion.[18] A comparison to measurements with ionization is made and experimental results are fitted using the relevant kinetic model developed in chapter three.

Chapter five gives a thorough account and further development of the kinetic-energy time-of-flight (KETOF) method first introduced in refs. 19, 20. Knowledge of the anisotropic distribution of the velocity of the emerging fragments from a reaction provides key insight into the translational, vibrational and rotational motion in the transition state. By carefully choosing the orientation of the polarization of the fs pump and probe laser pulses and by tuning the probe to the transition-state region, as opposed to the nascent fragments, it is possible to directly observe the spatial alignment of the atoms in the molecule in the transition state. A discussion of existing theory is given to explain results obtained by detecting free fragments. A new theory is developed to describe the anisotropic spatial distributions and velocity profiles obtained by probing the transition state. The theory matches the experimental observations[19] made using the molecular beam apparatus with the TOF tube operated in a mode to see the velocity distribution at each mass peak. Since its introduction, KETOF has been applied in other studies in our group including the velocity gating in complex systems with applications to the caging problem in a pure solvent cluster of iodobenzenes.[21]

In chapter six are the results of recent work using non-linear optical techniques with femtosecond laser pulses to study molecular dynamics.[22] Degenerate four-wave-mixing (DFWM), using fs laser pulses, is introduced to

study transition-state dynamics of chemical reactions in the gas phase. The ultrafast techniques are applied to a range of systems: atomic, unimolecular and bimolecular. It is shown how fs DFWM can be incorporated in different temporal pulse schemes to extract the dynamics. The DFWM beams are configured in a folded-boxcar geometry, producing a spatially separated, background-free, coherent fs signal pulse. Aspects of the technique, such as absorption, are investigated. Advantage is taken of the relatively broad spectral width of the fs pulses, extending the techniques to two-color grating experiments in the gas phase. The unimolecular system, NaI, provided a means of testing this new approach. The experimental observations of the wave packet motion are in excellent agreement with results obtained using laser-induced fluorescence (LIF).[23, 24] A control experiment was also performed on this system, demonstrating the advantages of the non-linear technique. Atomic sodium was investigated with fs DFWM and the oscillatory wave packet behavior (2 ps period) was observed, corresponding to the fine structure splitting of the 3p level ($17.2cm^{-1}$). In addition, fs DFWM was applied to the reactive and nonreactive collisions of the $Na+H_2$ system which serves as a good model for studying dynamics of non-adiabatic quenching processes and collision complexes, important to the understanding of bimolecular systems.

Chapter seven includes an appendix A devoted to the derivations of some general formulae and specific cases pertaining to the kinetic model of chapter three. Selected papers, relevant to the approaches presented in the preceding chapters, are given in appendices B through G.

Because of the versatility of the different techniques, developed and applied as detailed in this thesis, it is possible to study more chemical systems in even greater depth, revealing new exciting aspects of their ultrafast dynamics.

1.1 References

1. A. H. Zewail, Laser Selective Chemistry - Is it Possible?*Phys. Today* **1980**, *33*, 27.
2. A. H. Zewail, *Femtochemistry - ultrafast dynamics of the chemical bond* (World Scientific, Singapore, 1994), vol. I & II.
3. J. Manz, L. Wöste, Eds.; *Femtosecond Chemistry* (VCH Verlagsgesellschaft mbH, Weinheim (Germany), ed. 1, 1995).
4. M. Chergui, Ed.; Femtosecond Chemistry, the Lausanne Conference (World Scientific, Singapore, 1995).
5. *J. Phys. Chem* **97**, no. 48 (Femtosecond Chemistry: The Berlin Conference 1993).
6. (a) N. F. Scherer, J. L. Knee, D. D. Smith, A. H. Zewail, *J. Phys. Chem.* **89**, 5141 (1985); (b) M. Dantus, M. J. Rosker, A. H. Zewail, *J. Chem. Phys.* **87**, 2395 (1987).
7. E. D. Potter, J. L. Herek, S. Pedersen, Q. Liu, A. H. Zewail, *Nature* **355**, 66 (1991).
8. J. C. Williamson, A. H. Zewail, *J. Phys. Chem.* **98**, 2766 (1994).
9. M. Dantus, S. B. Kim, J. C. Williamson, A. H. Zewail, *J. Phys. Chem.* **98**, 2782 (1994).
10. S. Pedersen, L. Bañares, A. H. Zewail, *J. Chem. Phys.* **97**, 8801 (1992).
11. J. S. Baskin, L. Bañares, S. Pedersen, A. H. Zewail (to be submitted).
12. M. J. Rosker, M. Dantus, A. H. Zewail, *J. Chem. Phys.* **89**, 6113 (1988).
13. M. Dantus, *"Femtosecond Transition-state Spectroscopy of Chemical Reaction," Ph.D. Thesis, California Institute of Technology* (1991).
14. S. Pedersen, A. H. Zewail (to be submitted).
15. S. Pedersen, J. L. Herek, A. H. Zewail, *Science* **266**, 1359 (1994).

16. S. K. Kim, S. Pedersen, A. H. Zewail, *J. Chem. Phys.* **103**, 477 (1995).

17. S. K. Kim, S. Pedersen, A. H. Zewail, *Chem. Phys. Lett.* **233**, 500 (1995).

18. J. L. Herek, S. Pedersen, L. Bañares, A. H. Zewail, *J. Chem. Phys.* **97**, 9046 (1992).

19. T. Baumert, S. Pedersen, A. H. Zewail, *J. Phys. Chem.* **97**, 12447 (1993).

20. S. Pedersen, T. Baumert, A. H. Zewail, *J. Phys. Chem.* **97**, 12460 (1993).

21. P. Y. Cheng, D. Zhong, A. H. Zewail, *J. Phys. Chem.* **99**, 15733 (1995).

22. M. Motzkus, S. Pedersen, A. H. Zewail (to be submitted).

23. T. S. Rose, M. J. Rosker, A. H. Zewail, *J. Chem. Phys.* **88**, 6672 (1988).

24. T. S. Rose, M. J. Rosker, A. H. Zewail, *J. Chem. Phys.* **91**, 7415 (1988).

Chapter 2

Experimental Apparatus for Studies of Femtosecond Dynamics

2.1 Femtosecond Laser System and Pump-Probe Scheme

The femtosecond laser pulses were generated from a colliding pulse mode-locked ring dye laser (CPM) similar to that developed by a research team led by C.V. Shank at Bell Laboratories.[1] A complete description of the femtosecond laser system used in our laboratory is provided in the thesis of Marcos Dantus.[2] Here, an outline of the key features is presented.

The CPM laser, as shown schematically in Fig. 2.1, was pumped by a 514.5 nm continuous Ar^+ laser (Coherent, Innova 100), typically operated at 2-3 W. The output pulses, emerging from the cavity at a repetition rate of 83 MHz, had a wavelength near 620 nm and temporal widths as short as 60 fs (measured with real-time auto-correlation and fit assuming hyperbolic secant squared pulse shape). Due to the low energy in each pulse (maximum energy of ~240 pJ), it was necessary to amplify the CPM output by a factor of a million to 0.2-0.3 mJ. This was achieved using a four-stage pulsed dye amplifier (PDA) pumped by a (ns) Q-switched Nd:YAG laser (Spectra Physics, Quanta Ray DCR3) with a 20 Hz repetition rate (see Fig. 2.2). Therefore, only about one in every four million pulses is amplified. For the same reason that two prism pairs were placed within the CPM cavity, four prisms are positioned after the PDA. These serve to recompress the pulses which have suffered positive group velocity dispersion. The PDA output pulses are thus shortened by a factor of ten, back to ~60fs.

Tunability of the wavelength of the ultrafast pulses was accomplished in several ways. For example, by focusing part of the PDA output into a D_2O cell, a white light continuum could be generated[3] from which frequency selection was possible using an interference filter (Corion, 10 nm bandwidth). This was typically followed by amplification in a flowing dye cell using residual 532 nm YAG laser light (with optimized synchronization). Frequency doubling of the

PDA output or of a chosen wavelength was achieved using a 0.2 or 0.5 mm Type-I KD*P crystal of appropriate phase-matching angle.[4] Sum-frequency mixing of the 532 nm YAG laser with 620 nm was used[5] in generating 286 nm pulses with duration almost as short as the incident fs pulse. Other frequency mixing schemes are also possible with the system, e.g., sum frequency mixing of residual infrared from the YAG (1064 nm) with 620 nm to give 391.7 nm.

Fig. 2.3 shows the arrangement for a typical pump-probe experiment. Using a beam splitter, pulses are diverted into the two arms of a Michelson interferometer. By directing the probe pulse (λ_{Pr}) to a retroreflecting mirror on a computer-controlled actuator, the delay of the probe with respect to the pump could be varied before collinearly recombining the beams using a dichroic mirror. The choice of wavelength (e.g., using frequency doubling as indicated in Fig. 2.3) could be made in each arm before recombination. In addition, the relative polarization and attenuation of the pump and probe were carefully chosen for each experiment.

After recombination, the two pulses are focused into the molecular system being studied. The pump initiates the dynamics at time zero (defined as the arrival time of the center of the pump pulse) and the probe interrogates the system at the delay time. A molecular beam apparatus (see section 2.2) was used with detection of the ions produced following probing. In other experiments, a quartz cell with a gas phase sample was used in combination with laser-induced fluorescence (LIF) detection by a monochromator (section 2.3). The detected signal was sent to a boxcar averager (Stanford Research, SR 250) before being transferred to a computer (Apple, Macintosh II) for further analysis. The data acquisition programs were developed by this group and have been extensively documented.[2, 6]

Great care was exercised in ensuring consistent and reproducible experimental conditions, not only for the laser pulses but also for the molecular system and the detection schemes. In each experiment, the laser pulses were characterized temporally via auto- or cross-correlation, and spectrally using the monochromator. To accurately determine time zero in a transient (signal *vs.* time delay), when the peak of the probe coincides with that of the pump, cross-correlations of the pump and probe were performed. Often it proved useful to use an iodine vapor cell and perform a pump-probe experiment with LIF detection to quickly locate time zero (care should be taken in using this observed transient in the exact determination of time zero due to the influence of polarization). Conditions such as temperature, pressure and concentration of the molecules were carefully monitored whenever possible, and attention was paid to avoiding any saturation of the signal intensity by the detection scheme employed.

2.2 Molecular Beam Apparatus

Fig. 2.4 illustrates the operation of our molecular beam apparatus[7] in a fs pump-probe experiment with ion detection. The pump pulse excites the molecules in the focal region and the probe further excites the evolving system and generates the ions. These ions are repelled, accelerated and allowed to drift through the field-free region before being detected by micro-channel plates. Time-of-flight (TOF) mass spectra were taken using either a transient digitizer (LeCroy 8818A) or a 300 MHz digital oscilloscope (LeCroy 9361). The fs transient for a specific mass was obtained using the boxcar integrator (SR 250) and monitoring the selected ion signal as a function of the time delay between the pump and probe laser pulses.

The sample was typically placed externally in a quartz cell with a backing pressure line attached. If necessary, the temperature, and hence the vapor pressure, of the sample was raised by ohmic heating using a wire wrapped around the cell and the stainless steel tubing leading to the pulsed nozzle. By regulating the temperature using the reading from a thermocouple attached to the nozzle, it was possible to ensure increased heating closer to the nozzle and thereby prevent sample condensation in it. The molecules were expanded through a 0.3 mm nozzle orifice (triggered by the "oscillator out" of the Nd:YAG laser) and skimmed (2 mm diameter) before reaching the interaction region 12 cm downstream from the nozzle. The TOF spectrometer was used either in its mass resolution mode or in its kinetic energy resolution mode.[8] For the former case, the first two plates had a large electric field (on the order of 1000 V/cm) between them resulting in sharp peaks in the mass spectrum. The latter mode used a low electric field (<100 V/cm) which resulted in a spread of the signal at each mass position in the TOF spectrum, reflecting a distribution of the arrival time for each mass at the multichannel plates due to an initial velocity distribution. It is this latter mode which is used in the kinetic energy time-of-flight (KETOF) technique to study anisotropy and rotational alignment.

2.3 Fluorescence Detection

The detection of laser-induced fluorescence (LIF) from a pump-probe experiment is illustrated in Fig. 2.5. The two pulses are focused (L1) into a quartz cell containing a gas sample of the molecule under study. The induced fluorescence is collimated (L2) and focused (L3) into a monochromator (SPEX, 0.34 m) and detected by a photomultiplier tube (e.g., Hamamatsu R1527P). A pre-amplifier (Stanford Research, SR 445) was occasionally used before the

boxcar. A short BNC cable length between the photomultiplier tube (PMT) and the pre-amp ensured noise reduction (decreased influence from ambient electromagnetic noise in the laboratory, e.g., from the YAG laser). In addition, triggering the boxcar using a photodiode directed at scattered light from residual 532 nm YAG light, as opposed to using the Sync Out from the YAG as the trigger, gave less electronic noise in the gating region for the boxcar.

Two possibilities for the production of the fluorescence may be exploited in pump-probe experiments. In both cases the pump initiates the reaction at time zero by exciting the (ground state) molecules. If the probe excites the evolving system to a radiative state, a fluorescence signal is observed that is a function of the pump-probe time delay and no signal is seen if the probe is blocked or if it arrives before the pump (negative delay). This will be referred to as a fluorescence detection experiment. The other scenario involves fluorescence emitted directly following the pump excitation. The action of the probe is then to deplete the fluorescence by decreasing the number of radiating molecules. Such a case is termed a fluorescence depletion experiment. It too reveals information about the molecular dynamics initiated by the pump.

2.4 References

1. R. L. Fork, B. I. Greene, C. V. Shank, *Appl. Phys. Lett.* **38**, 671 (1981).
2. M. Dantus, *"Femtosecond Transition-state Spectroscopy of Chemical Reactions," Ph.D. Thesis, California Institute of Technology* (1991).
3. R. R. Alfano, Ed., *The Supercontinuum Laser Source* (Springer-Verlag, New York, 1989).
4. A. Yariv, *Quantum Electronics* (Wiley, New York, ed. 3, 1989).
5. S. Pedersen, L. Bañares, A. H. Zewail, *J. Chem. Phys.* **97**, 8801 (1992).
6. L. W. Peng, *"Reactions in Small Clusters studied by Time-resolved Laser Spectroscopy," Ph.D. Thesis, California Institute of Technology* (1991).
7. M. Dantus, M. H. M. Janssen, A. H. Zewail, *Chem. Phys. Lett.* **181**, 281 (1991).
8. T. Baumert, S. Pedersen, A. H. Zewail, *J. Phys. Chem.* **97**, 12447 (1993).

2.5 Figure Captions and Figures

Fig. 2.1 Colliding pulse mode-locked ring dye laser (CPM) used in the generation of ~60 fs pulses. Two counterpropagating pulses can exist in the cavity if they simultaneously pass through the saturable absorber jet (SAJ). The gain jet (GJ), pumped by the Ar^+ laser, is positioned at a quarter of the cavity length from the SAJ to guarantee that each pulse experiences maximum gain. The output pulses emerge at a repetition rate of 83 MHz, corresponding to a cavity round-trip time of 12 ns. It is important to choose the right dye concentration of the GJ and SAJ along with appropriate pumping power to ensure that only two pulses exist in the cavity. With higher energy available to the cavity, two pairs of pulses may exist ("double pulsing"), leading to a broadening of the pulse widths, and a lowering of the individual pulse energy as energy is now allocated to four and not two pulses.

Fig. 2.2 Schematic of the 20 Hz Nd:YAG-pumped four-stage pulsed dye amplifier (PDA). The incident ~60 fs pulse (output of CPM, shown in Fig. 1) is amplified by six orders of magnitude. The four stages receive 3%, 3%, 24% and 70%, respectively, of the YAG light, with most given to the last stage. The amplified pulse is recompressed to ~60 fs by two prism pairs.

Fig. 2.3 Arrangement for a typical pump-probe experiment. The probe pulse is delayed with respect to the pump pulse by being reflected in a mirror mounted on a computer-controlled actuator. The wavelengths of both the pump and probe arms may be altered before recombination of the two beams. Upon recombination at the dichroic mirror, the pump and probe pulses travel collinearly and are focused onto the molecular system studied.

Fig. 2.4 Experimental apparatus showing the molecular beam, with the time-of-flight mass spectrometer, and the fs pump and probe laser pulses. The TOF spectrometer may be operated either in mass resolution or in kinetic energy resolution mode.

Fig. 2.5 Schematic showing a fs pump-probe experiment with laser-induced fluorescence detection. The fluorescence is collected perpendicular to the direction of the laser beams by a system of two lenses and a monochromator. Detection is performed using a photomultiplier tube attached to the monochromator.

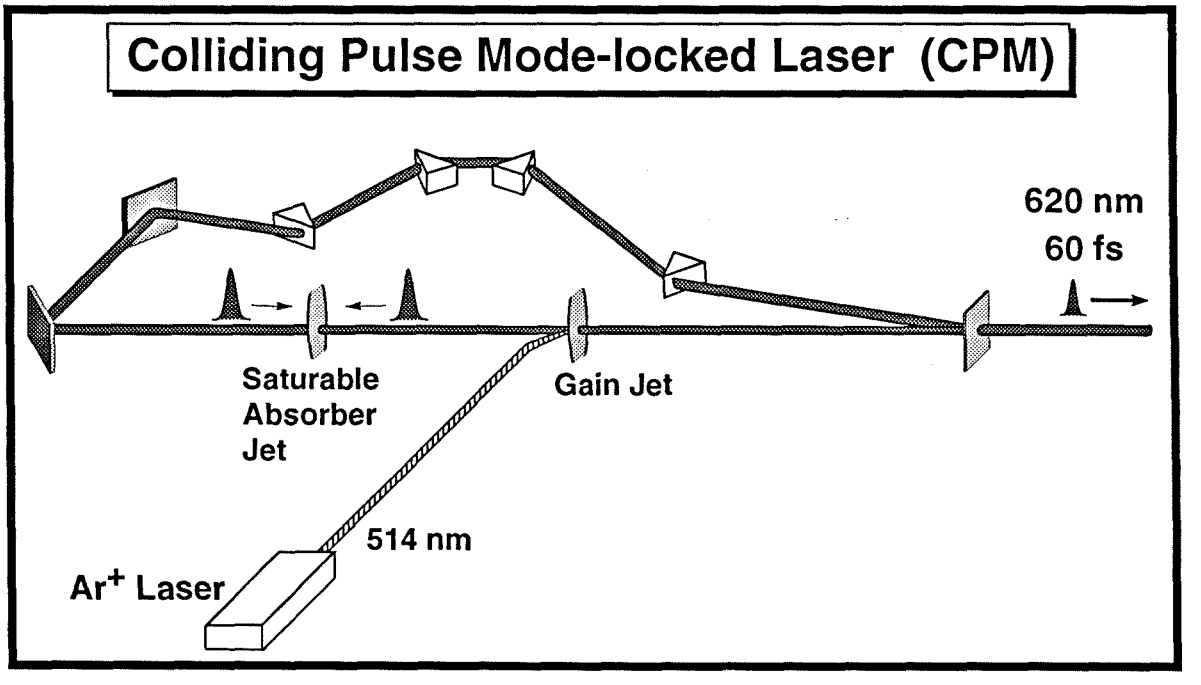
Colliding Pulse Mode-locked Laser (CPM)
620 nm
60 fs
Saturable
Absorber
Jet
Gain Jet
514 nm
Ar+ Laser

Fig. 2.1

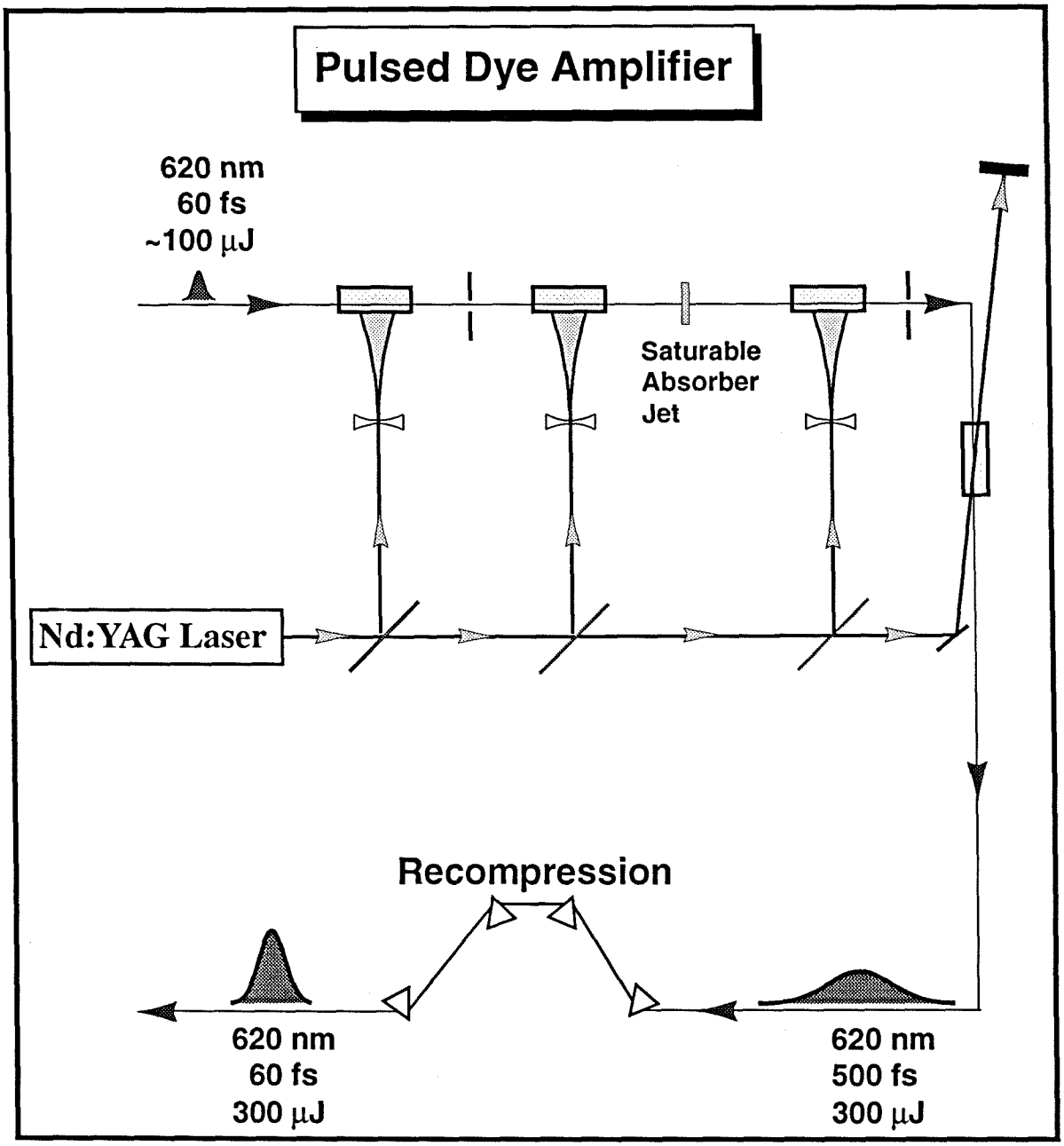
Pulsed Dye Amplifier
620 nm
60 fs
~100 μJ
Saturable
Absorber
Jet
Nd:YAG Laser
Recompression
620 nm
60 fs
300 μJ
620 nm
500 fs
300 μJ

Fig. 2.2

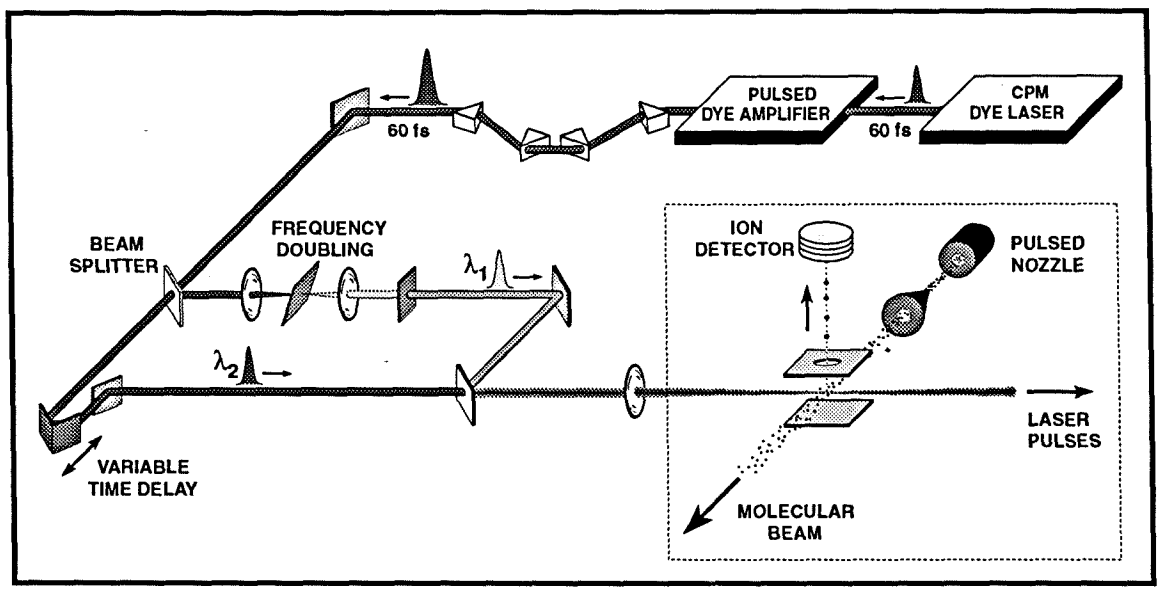
60 fs
PULSED
DYE AMPLIFIER
60 fs
CPM
DYE LASER
BEAM
SPLITTER
FREQUENCY
DOUBLING
λ_1
λ_2
ION
DETECTOR
PULSED
NOZZLE
LASER
PULSES
VARIABLE
TIME DELAY
MOLECULAR
BEAM

Fig. 2.3

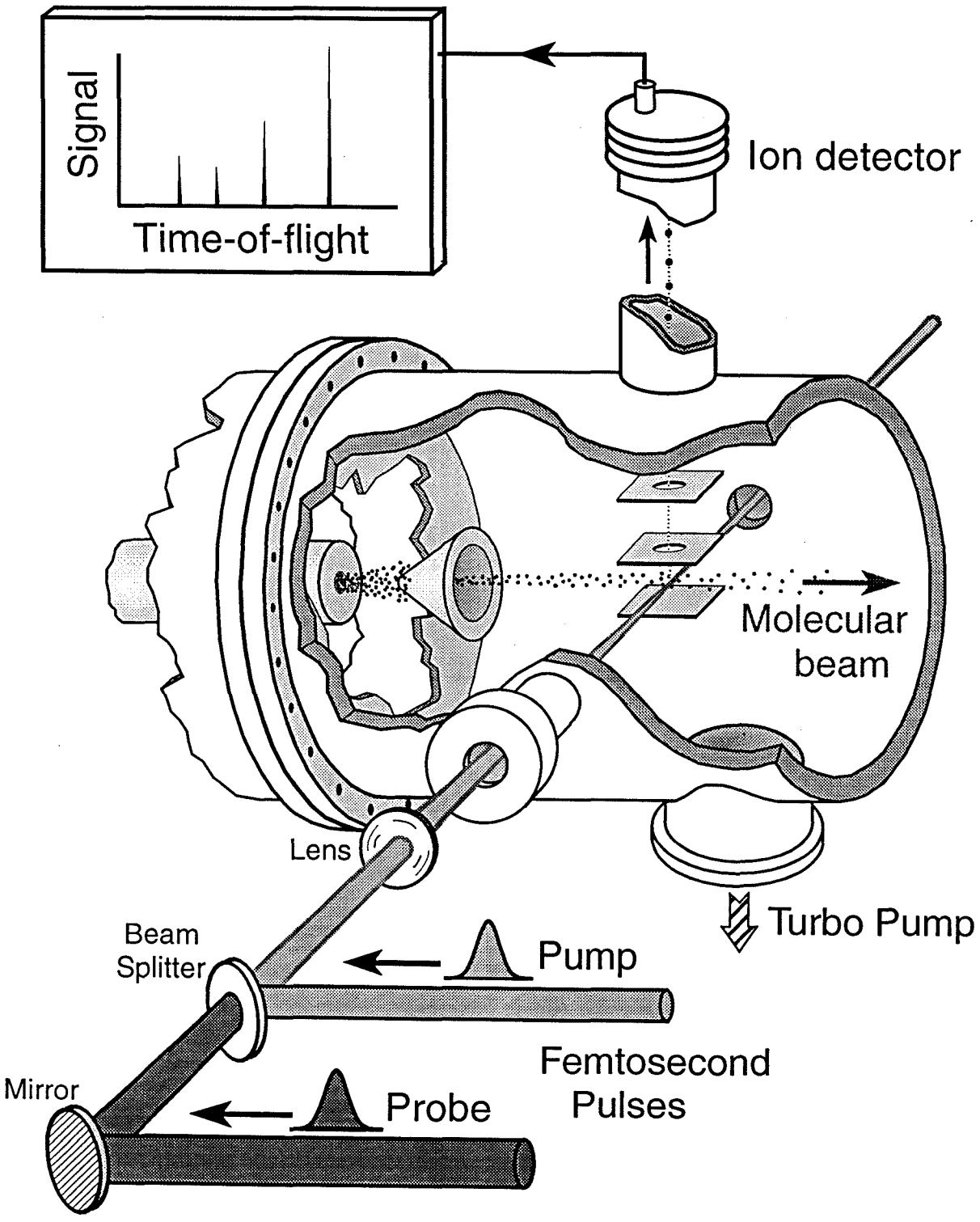
Signal
Time-of-flight
Ion detector
Molecular
beam
Lens
Turbo Pump
Beam
Splitter
Pump
Femtosecond
Pulses
Mirror
Probe

Fig. 2.4

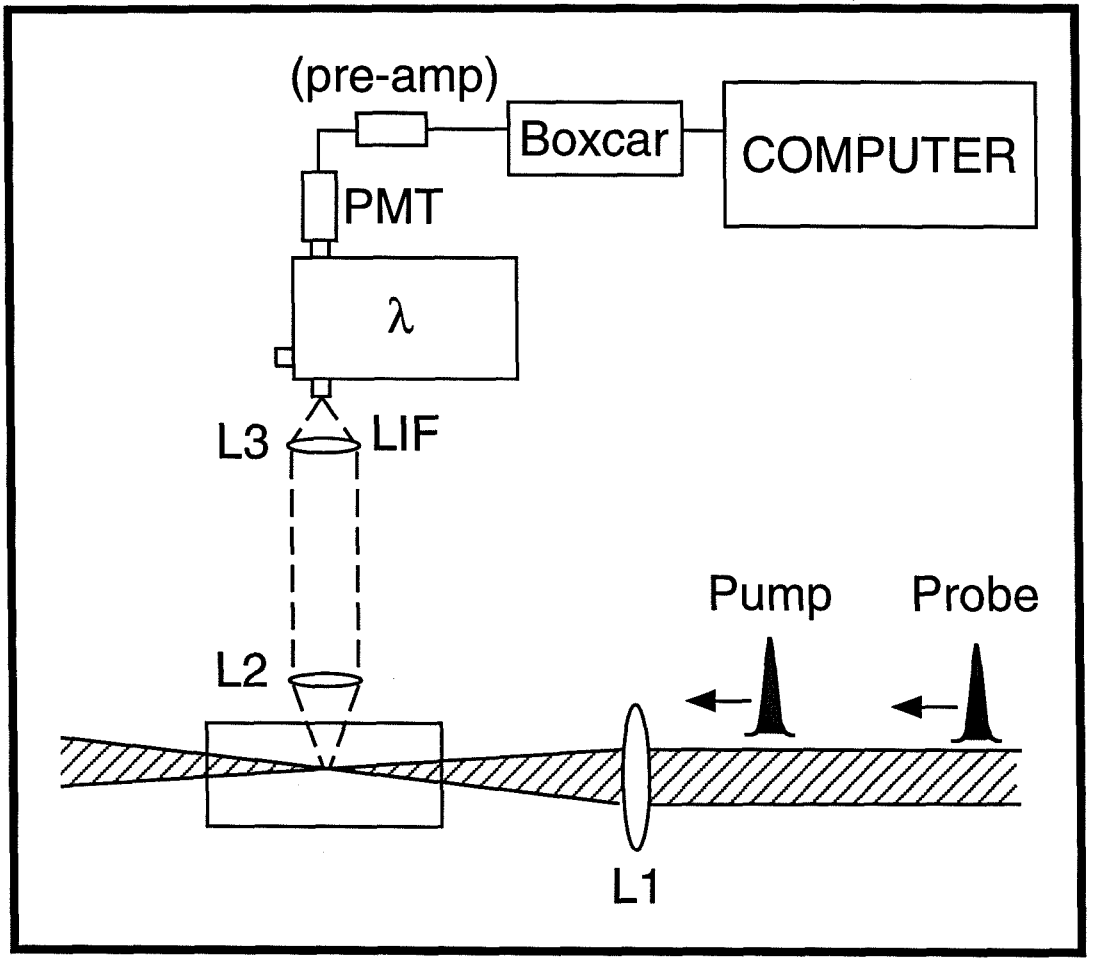

Fig. 2.5

Chapter 3

Theoretical Description of Femtosecond Transition-State Dynamics

3.1 Development of the Kinetic Model

3.1.1 Introduction

In this chapter, a theoretical description of fs transition-state dynamics is developed and numerous examples and limiting cases are provided to illustrate various aspects of the dynamics. A kinetic model is employed in describing typical transients observed in pump-probe experiments. In this model, the continuous nature of transition states is neglected and instead a reaction is depicted by rate determined steps between a discrete number of states. Several effects that influence the transients are discussed, e.g., the relative time scales associated with the rates, the method of detection, the ratio of probing cross sections and the effect of the finite width and shape of the laser pulses. The important influence of pump and probe saturation is covered and detailed analysis of expected results of power dependence studies are provided. Experimental examples are given to show the application of some of the theoretical results. At the end of the chapter, a comparison to classical and quantum mechanical models is made.

3.1.2 Basic Definitions

To describe a molecular system and its evolution, and to explain the effects of the pump and probe laser pulses, it is necessary to begin with some definitions. The instantaneous population of state $|i\rangle$ is $n_i(t^*)$, where t^* is the time; k refers to a rate of transfer from one state to another; f is a fluorescence decay rate; and σ_{ij} is the absorption cross section for the transition between states $|i\rangle$ and $|j\rangle$. Furthermore, a dimensionless parameter, β, may be introduced to describe the

relative ratio of two possible probe absorptions. The initial population of the state accessed by the pump pulse, usually a ground state, is defined by the integer N. This is the number of molecules accessible to the pump in the interaction region. The pump has wavelength λ_{Pu}, total energy E_{Pu}, and is focused to radius R in the interaction region. The total number of pump photons, which impinge on the interaction region, per unit cross-sectional area is then

$$\alpha_{Pu} = \frac{E_{Pu} / (h\nu_{Pu})}{\pi R^2} = \frac{\lambda_{Pu} E_{Pu}}{hc\pi R^2}. \tag{3.1}$$

The cross section, σ_{AB}, is introduced and defined as the probability of absorption of a photon by one molecule in the interaction region, such that the molecule is excited from state |A> to |B>. In section 3.1.4, this cross section is given in terms of the transition dipole moment and the frequency of the transition. If we define

$$F_{Pu} = \frac{\sigma_{AB}\lambda_{Pu}E_{Pu}}{hc\pi R^2} = \sigma_{AB}\alpha_{Pu}, \tag{3.2}$$

where the pump excites from state |A> to |B> say, then in the limit of no saturation, $F_{Pu}N$ of the N molecules in state |A> are excited to state |B>. For example, F_{Pu}=0.001 would imply one in a thousand molecules is excited by the pump laser pulse. If, on the other hand, the pump transition is saturated (F_{Pu} large), then a smaller fraction than F_{Pu} is excited, due to significant stimulated emission from |B> to |A> by the pump pulse. A discussion of saturation and its effects is postponed until section 3.1.5.

The intensity of the pump pulse is given by

$$I_{Pu}(t^*) = \frac{E_{Pu}}{\pi R^2} f_{Pu}(t^*), \tag{3.3a}$$

where $f_i(t^*)$ is a normalized representation of the laser pulse in the sense that

$$\int_{-\infty}^{\infty} f_i(t^*)dt^* = 1. \tag{3.3b}$$

For a Gaussian pulse, f_i is a normalized Gaussian function:

$$f_i(z) = G(z, FWHM_i) = \frac{1}{\sigma_i\sqrt{2\pi}} \exp(-\frac{z^2}{2\sigma_i^2}), \tag{3.4}$$

where the pulse temporal standard deviation is given by

$$\sigma_i = \frac{FWHM_i}{2\sqrt{2\ln 2}}, \tag{3.5}$$

and $FWHM_i$ is the full-width-at-half-maximum. The pump pulse has its maximum intensity at t*=0, also referred to as time zero. The probe pulse arrives at a certain time delay, t, after the pump and its temporal profile is therefore centered at t*=t. The intensity of the probe is thus given by

$$I_{Pr}(t^*-t) = \frac{E_{Pr}}{\pi R^2} f_{Pr}(t^*-t) \tag{3.6}$$

with wavelength λ_{Pr}, total energy E_{Pr}, temporal width $FWHM_{Pr}$, and radius R equal to that of the pump. It is useful to make definitions for the probe that are analogous to those made for the pump. The total number of probe photons per unit area is

$$\alpha_{Pr} \equiv \alpha = \frac{\lambda_{Pr} E_{Pr}}{hc\pi R^2}, \tag{3.7}$$

and

$$F_{Pr} = \frac{\sigma_{ij}\lambda_{Pr}E_{Pr}}{hc\pi R^2} = \sigma_{ij}\alpha \tag{3.8}$$

is (in the unsaturated regime) the fraction of molecules excited by the probe pulse in a probe transition, $|i\rangle \rightarrow |j\rangle$.

In the next section (3.1.3) the pump and probe pulses will be considered instantaneous (to gain insight into the molecular dynamics), and algebraic expressions are obtained for the populations of the states with decay rates appearing explicitly. The calculated signals, which are functions of the time delay between the pump and probe, t, will consequently be molecular response functions, $M_i(t)$. The pump and probe are considered instantaneous in the sense that

$$\lim_{FWHM_i \rightarrow 0} f_i(z) = \delta(z), \tag{3.9}$$

the Dirac-delta function. Hence, the intensities become

$$I_{Pu}(t^*) \rightarrow \frac{E_{Pu}}{\pi R^2}\delta(t^*) \tag{3.10}$$

and

$$I_{Pr}(t^*-t) \rightarrow \frac{E_{Pr}}{\pi R^2}\delta(t^*-t). \tag{3.11}$$

The molecular response functions, $M_i(t)$, when later convoluted with the actual pump and probe temporal intensity line shapes (c.f. equations (3.3) and (3.6)), yield the predicted transients, *i.e.*, signal *vs.* t. This is the convolution approach to the problem. Later, in section 3.1.4, further effects of finite temporal laser pulse widths are discussed, and a treatment is given of the influence of saturation on the signal in section 3.1.5. The advantage of first obtaining the molecular response function is that an algebraic expression is obtained. Limiting cases can therefore be found very easily, providing insight into factors influencing the observed signal, and leading to a better understanding of the dynamics in the molecular system.

3.1.3 Pump-Probe Experiments: Molecular Response Functions

Molecular response functions are found for states in several interesting molecular systems, and the dynamics involved are discussed by analyzing limiting situations. The pump and probe pulses are considered instantaneous as described above. For each system, a level structure is presented, depicting all the states involved, the decay processes linking them, and the optical transitions induced by the pump and probe pulses. Considering the optical transitions as being instantaneous freezes the dynamics during each of the pump and probe excitations. At all other times, the molecular system in question is allowed to evolve freely with the specified decay rates. Where appropriate, a discussion is provided to describe the differences among signals obtained with different detection schemes such as ionization, fluorescence, fluorescence depletion, and absorption.

3.1.3.1 Transient Decay Measurements

(a) Ionization Detection

Consider a reagent molecule, in a state $|A\rangle$ that is excited by a pump pulse (at time $t^*=0$) to a dissociative state $|B\rangle$, as shown in Fig. 3.1(a). This excited state population decays exponentially with a rate k+f, where k and f are the non-radiative and fluorescence decay rates respectively. After a time delay, t, the probe pulse arrives and ionizes part of the population in $|B\rangle$. The experiment is repeatedly performed at different distinct time delays and the resulting signal, *i.e.*, the total number of ions collected, is recorded as a function of the delay time and a so-called transient is obtained. Below, it will be shown that the decay constant, k+f, can be directly extracted from this transient.

Before the pump pulse arrives, all excited states are unpopulated and the ground state, $|A\rangle$, has a population N. At time zero ($t^*=0$), the pump pulse excites a fraction, F_{Pu}, of the ground state molecules to state $|B\rangle$, so : $n_B(0)= F_{Pu}N$. F_{Pu} is given by equation (3.2). After the pump pulse, state $|B\rangle$ decays with time, t^*, at a rate k+f:

$$dn_B/dt^* = -(k+f)n_B , \tag{3.12}$$

and consequently in the absence of probing:

$$n_B(t^*) = 0 , \qquad t^*<0 \tag{3.13a}$$

$$= n_B(0) \exp[-(k+f)t^*], \qquad t^*\geq 0. \tag{3.13b}$$

The probe pulse, arriving at time t, will excite a fraction, F_{Pr}, of the $|B\rangle$ state population at this exact time. With a certain probe delay time, t, the population of $|C\rangle$ will be described in time, t^*, by

$$n_C(t^*,t) = 0 , \qquad t^*<t, \tag{3.14a}$$

$$= F_{Pr}\, n_B(t), \qquad t^*\geq t, \tag{3.14b}$$

where F_{Pr} is given by equation (3.8) with $\sigma_{ij}=\sigma_{BC}$. The total signal ($t^*\rightarrow\infty$), or total number of ions collected, as a function of the time delay, t, is thus given by the following molecular response function:

$$M_C(t) = \lim_{t^* \rightarrow \infty} n_C(t^*,t), \tag{3.15}$$

or writing this explicitly, using (3.13) and (3.14b):

$$M_C(t) = 0, \qquad t<0, \tag{3.16a}$$

$$= F_{Pu}F_{Pr}N \exp[-(k+f)t], \qquad t\geq 0, \tag{3.16b}$$

as $M_C(t=0) = F_{Pr}\, n_B(0) = F_{Pu}F_{Pr}N$.

The resulting signal (see Fig. 3.1(b)) is therefore a pure single exponential decay with rate k+f. The maximum amplitude of the signal, $F_{Pu}F_{Pr}N$, occurring at zero delay of the probe, is a constant depending on the initial ground state population, N, and the pumping and probing fractions, F_{Pu} and F_{Pr} respectively. This initial amplitude is independent of the rates f and k. It is interesting to look at the limit $f<<k$, which occurs, for example, when the fluorescence time, f^{-1}, is in the nanosecond regime, while the non-radiative decay time, k^{-1}, is in the picosecond or femtosecond regime. In this limit, equation (3.16) reduces to:

$$M_C(t) = 0, \qquad t<0, \tag{3.17a}$$

$$= F_{Pu}F_{Pr}N \exp[-kt], \qquad t\geq 0. \tag{3.17b}$$

The exponential decay is now simply with the non-radiative rate, k.

An experimental example[1] (see Appendix D) of probing a dissociative state to ionization is illustrated in Fig. 3.2. An acetone molecule was excited by the pump pulse and this excited parent molecule was probed as it dissociated to an acetyl radical and a methyl radical. By probing to ionization and detecting the parent mass, the temporal behavior of the excited state neutral parent molecule, prepared by the pump pulse, could be observed. The single exponential decay yields the decay time, $k^{-1}=50\pm30$ fs,[1] of the parent. This rate is much faster than

the expected fluorescence rate, so k+f reduces to k in (3.16), resulting in the limiting case described by equation (3.17). The effects that finite pulse widths have on the observed transient will be discussed in section 3.1.4. A good fit to the data was achieved using the molecular response function of equation (3.17), that rises instantaneously at time zero and then exhibits the fast single exponential decay.

(b) Monitoring Fluorescence

Suppose that level $|C\rangle$ is not an ion level but rather a state that fluoresces at a rate f_C, as shown in Fig. 3.3(a). The total number of photons emitted from state $|C\rangle$ then equals the cumulative population of state $|C\rangle$ which is given by (3.16) above. Hence,

$$M_{fluorC}(t) = 0, \qquad t<0, \qquad (3.18a)$$

$$= F_{Pu} F_{Pr} N \exp[-(k+f)t], \qquad t\geq 0. \qquad (3.18b)$$

This molecular response function, shown in Fig. 3.3(b), is identical to that obtained with ionization detection, described in section 3.1.3.1(a) above. If we can impose the limit $f<<k$, then equation (3.18) simplifies and we obtain the following signal, which shows an exponential decay with rate k:

$$M_{fluorC}(t) = 0, \qquad t<0, \qquad (3.19a)$$

$$= F_{Pu} F_{Pr} N \exp[-kt], \qquad t\geq 0. \qquad (3.19b)$$

(c) Monitoring Fluorescence Depletion

Another detection scheme may be employed by utilizing an excited state $|B\rangle$ that fluoresces (see Fig. 3.4(a)). By detecting $|B\rangle$ state fluorescence and depleting it with the probe pulse, the temporal behavior of the system can be

extracted. If the probe were not present, the total fluorescence yield from $|B\rangle$ would be $F_{Pu}Nf/(k+f)$. With the probe present, at the delay time, t, it excites $F_{Pr}n_B(t)$ molecules from $|B\rangle$ to $|C\rangle$ and consequently the signal will be reduced by an amount $F_{Pr}n_B(t)f/(k+f)$. Hence, the fluorescence signal (see Fig. 3.4(b)) from state $|B\rangle$ becomes

$$M_{fluorB}(t) = F_{Pu}N\frac{f}{k+f}, \qquad t<0, \qquad (3.20a)$$

$$= F_{Pu}N\frac{f}{k+f}(1-F_{Pr}\exp[-(k+f)t]), \qquad t\geq 0. \qquad (3.20b)$$

Again, a function containing a single exponential with rate k+f is obtained. The minus sign in (3.20b) indicates that the fluorescence is depleted or reduced at positive times. The depletion is most severe near zero time delay when the probe can deplete the most of the excited $|B\rangle$ state population before this population has had time to decay away. At much longer times, *i.e.*, $t>>(k+f)^{-1}$, the $|B\rangle$ state has had time to lose almost all its population, so the probing of the small population which is still in $|B\rangle$ will only lead to an insignificant depletion of the total fluorescence yield. Hence, at long delay time, the fluorescence gathered before the probe arrives is then already close to the total yield. It should be noted that as we are working in the non-saturated regime, F_{Pr} and F_{Pu} <<1 (see section 3.1.5 on saturation). Equation (3.20) shows that the ratio of the depletion signal to the background fluorescence level (at t<0) is F_{Pr} : 1, and, for an unsaturated probe transition, this puts a restriction on the permitted noise level in the detected signal if the depletion is to be observed clearly in such an experiment. Let us again consider the limiting situation, where the non-radiative decay rate is much faster than the fluorescence rate, *i.e.*, k>>f: equation (3.20) then reduces to:

$$M_{fluorB}(t) = F_{Pu}N\frac{f}{k}, \qquad t<0, \qquad (3.21a)$$

$$= F_{Pu}N\frac{f}{k}(1-F_{Pr}\exp[-kt]), \qquad t\geq 0. \qquad (3.21b)$$

The depletion then simply decays with rate k. It should be noted that, in this limit, the overall fluorescence yield may be low due to the factor f/k appearing in equation (3.21). State $|B\rangle$ has little time (1/k) to fluoresce before it is completely depopulated via the non-radiative channel.

(d) Detection of Absorption

Yet another detection possibility remains, as illustrated in Fig. 3.5(a): monitoring of the absorption of the probe pulse upon passing through the excited molecules. In this case, and again considering single photon unsaturated transitions, the probe pulse (at t*=t) will initially consist of a fixed number, N_{Pr}, of photons. Of these, $M_C(t)$ will be absorbed upon exciting $M_C(t)$ molecules. Hence, the probe pulse emerges attenuated to $N_{Pr} - M_C(t)$ photons. The intensity of a pulse, I, is proportional to the number of photons in the pulse (*vide supra*) and hence the transmitted probe intensity is

$$I_t = I_o\left(1 - \frac{M_C(t)}{N_{Pr}}\right), \tag{3.22}$$

where I_o is the incident probe intensity. The absorption signal is then $M_{abs} = I_o M_C(t)/N_{Pr} \propto M_C(t)$, given by (3.16). Therefore, it has the same exponential decay behavior as that obtained upon detecting ions, fluorescence or fluorescence depletion (see Fig. 3.5(b)).

(e) Remark

If $|C\rangle$ is an ion level, the probe step in ionization cannot involve stimulated emission from $|C\rangle$ to $|B\rangle$. The reason is the ion, a molecule in state $|C\rangle$, having lost an electron within the probe pulse, can not become a neutral molecule ($|B\rangle$) within the time span of the rest of the laser pulse. In contrast, if

$|C\rangle$ is a neutral state, saturation of the probe transition may occur, because stimulated emission is then possible. The case of photon depletion[2] will not be discussed here.

3.1.3.2 Transition-State Measurements

Consider the kinetic model shown in Fig. 3.6a. The excited state $|B\rangle$ evolves via a transition state $|C\rangle$ to a final state $|D\rangle$. By probing the transition state and detecting the appropriate signal (ions, fluorescence or absorption), it is possible to find the rates at which the molecules enter (k_1) and leave (k_2) the transition state. Before the pump arrives, the ground state population is $n_A(t^*<0)=N$ and all the other levels are unpopulated. At time zero, the pump excites $F_{Pu}N$ molecules from $|A\rangle$ to $|B\rangle$. Before the probe arrives, *i.e.*, $0<t^*<t$, the system evolves freely according to the following:

$$dn_B/dt^* = -k_1 n_B\,; \quad dn_C/dt^* = k_1 n_B - k_2 n_C\,; \quad dn_D/dt^* = k_2 n_C\,, \qquad (3.23a;b;c)$$

which imply that:

$$n_B(t^*) = 0\,, \qquad t^*<0, \qquad (3.24a)$$

$$= F_{Pu}N\exp[-k_1 t^*], \qquad t^*\geq 0; \qquad (3.24b)$$

$$n_C(t^*) = 0\,, \qquad t^*<0, \qquad (3.25a)$$

$$= F_{Pu}N\frac{k_1}{k_1-k_2}(\exp[-k_2 t^*] - \exp[-k_1 t^*]), \qquad t^*\geq 0; \qquad (3.25b)$$

$$n_D(t^*) = 0\,, \qquad t^*<0, \qquad (3.26a)$$

$$= F_{Pu}N\{1 - \frac{1}{k_1-k_2}(k_1\exp[-k_2 t^*] - k_2\exp[-k_1 t^*])\}, \qquad t^*\geq 0. \qquad (3.26b)$$

When the probe arrives, at $t^*=t$, a fraction, F_{Pr}, of the $|C\rangle$ state population is excited to the $|E\rangle$ state, so that:

$$n_E(t^*,t) = 0\,, \qquad t^*<t, \qquad (3.27a)$$

$$= F_{Pr}n_B(t)\,, \qquad t^*\geq t. \qquad (3.27b)$$

After the probe has arrived (t*>t), the system again evolves according to (3.23) where now the initial conditions are the populations just after probing. However, the population of the state probed to, $|E\rangle$, will be unaffected by this subsequent dynamics. The signal is given by (3.27b) with the limit $t^* \to \infty$ imposed, and the formula is unaffected by taking this limit. The molecular response function (signal as a function of time delay) is therefore given by:

$$M_E(t) = 0, \qquad t<0, \qquad (3.28a)$$

$$= F_{Pu}F_{Pr}N\frac{k_1}{k_1 - k_2}(\exp[-k_2 t] - \exp[-k_1 t]), \qquad t\geq 0. \qquad (3.28b)$$

This is seen to exhibit a bi-exponential behavior with a rise and a decay (see Fig. 3.6b). The faster of k_1 and k_2 will appear in the rise and the slower in the decay. It is therefore not always k_1 that appears in the rise and k_2 in the decay of the signal. Next, consider a limiting case in which $k_2 \to 0$ and the state $|C\rangle$ probed becomes the final state reached. In this case, (3.28) reduces to:

$$M_E(t) = 0, \qquad t<0, \qquad (3.29a)$$

$$= F_{Pu}F_{Pr}N(1 - \exp[-k_1 t]), \qquad t\geq 0, \qquad (3.29b)$$

an exponential rise with rate k_1 to its final asymptotic value, $F_{Pu}F_{Pr}N$.

If ions are detected, the signal is given directly by (3.28) as M_E will be the total number of ions. If the $|E\rangle$ state were a neutral radiating state, then the fluorescence signal would again be given by (3.28) as each of the molecules in $|E\rangle$ would eventually emit a photon that could be detected. If the absorption of the probe is measured then, in analogy with the analysis for section 3.1.3.1(d) above, the absorption signal would be simply proportional to M_E given by (3.28) above. In the absence of saturation, the three detection mechanisms are thus equivalent. If state $|E\rangle$ is not an ion level, then it is possible to saturate the probe transition and in doing so affect the fluorescence and absorption measurements (see section 3.1.5 below).

Fig. 3.7 shows the case of ICN for which the transition state is monitored directly by the probe. Four different transients were obtained with progressively redder probe wavelength (lower transients). The lower transients in Fig. 3.6 correspond to the probe being "off-resonant" in that it is tuned to the transition-state, $|C\rangle$, instead of the final products. These transients show the expected bi-exponential behavior with one component in the rise and the other in the decay. The rise was slower than what could be accounted for by the cross-correlation of the laser pulses alone, and hence the component in the rise of the molecular response function was required to fit the data, in addition to the decay component. With a probe more to the blue (higher transients, Fig. 3.7), there is a contribution to the total fluorescence from probing state $|D\rangle$ in Fig. 3.6, in addition to the probing of the transition state, $|C\rangle$. This leads to the final asymptotic levels in these transients. The model then becomes that of Fig. 9 in ref. 3.

3.1.3.3 Transient Intermediate Detection

(a) Derivation of the Molecular Response Functions

Fig. 3.8 shows a kinetic model which allows for the probe to access the initially excited state, $|B\rangle$, in addition to the transition state, $|C\rangle$. We shall allow states $|B\rangle$ and $|C\rangle$ to decay radiatively at rates f_B and f_C in addition to decaying non-radiatively at rates k_1 and k_2 respectively. To facilitate taking the results to different limits, the probing cross sections are modeled as $\sigma_{BE}=\beta\sigma_O$ and $\sigma_{CF}=(1-\beta)\sigma_O$, where β is a fixed probing parameter in a given experiment and $0\leq\beta\leq1$. With $\beta=1$ the probe only excites state $|B\rangle$, while with $\beta=0$ only the transition state, $|C\rangle$, is probed. For intermediate β, *i.e.*, $0<\beta<1$, both $|B\rangle$ and $|C\rangle$ are

probed. The fraction of molecules probed from $|B\rangle$ will be $F_{PrB}=\beta F_{Pr}$ and that from $|C\rangle$ will be $F_{PrC}=(1-\beta)F_{Pr}$, where $F_{Pr}=\sigma_O E_{Pr}\lambda_{Pr}/(hc\pi R^2)$. At t=0, the pump pulse excites $F_{Pu}N$ of the N ground state molecules to state $|B\rangle$. The system then evolves with the rates k_1, k_2, f_B and f_C until, at time $t^*=t$, the probe excites $F_{PrB}n_B(t^*=t)$ molecules from $|B\rangle$ to $|E\rangle$ and $F_{PrC}n_C(t^*=t)$ molecules from $|C\rangle$ to $|F\rangle$. After this, *i.e.*, for $t^*>t$, the system again continues to evolve with the four rates. Some interesting conclusions can be made at this stage: the population of states $|E\rangle$ and $|F\rangle$ will remain unchanged at the values attained following probing. In particular, probing state $|B\rangle$ will not lead to a depletion of population $|F\rangle$ as the probing of $|B\rangle$ and $|C\rangle$ occur simultaneously while it takes a finite time ($O(1/k_1)$) for the system to decay from $|B\rangle$ to $|C\rangle$ (in practice, considering finite pulse widths, this is true if the temporal width of the probe pulse is much shorter than $1/k_1$). In Appendix A the full solution to this problem is provided, and considerations of the general results are given. Here, we shall take the general formulae from Appendix A and impose the limits $f_B<<k_1$ and $f_C<<k_2$. This is justified if for each of the states, $|B\rangle$ and $|C\rangle$, the fluorescence rate is much slower than the non-radiative rate. The formulae obtained are then much simpler than the general formulae in Appendix A, and offer a lot of insight into the problem:

$$M_E(t) = 0, \qquad t<0, \quad (3.30a)$$

$$= F_{Pu}F_{Pr}N\beta\exp[-k_1 t], \qquad t\geq 0; \quad (3.30b)$$

$$M_F(t) = 0, \qquad t<0, \quad (3.31a)$$

$$= F_{Pu}F_{Pr}N(1-\beta)\frac{k_1}{k_1-k_2}\left(\exp[-k_2 t]-\exp[-k_1 t]\right), \qquad t\geq 0; \quad (3.31b)$$

$$M_G(t) = F_{Pu}N\frac{f_B}{k_1}\begin{cases}1, & t<0, \quad (3.32a)\\ 1-F_{Pr}\beta\exp[-k_1 t], & t\geq 0; \quad (3.32b)\end{cases}$$

$$M_H(t) = F_{Pu}N\frac{f_C}{k_2}\begin{cases}1, & t<0, \quad (3.33a)\\ 1-F_{Pr}\left[\beta\exp[-k_1t]+(1-\beta)\frac{k_1}{k_1-k_2}\left(\exp[-k_2t]-\exp[-k_1t]\right)\right], & t\geq 0; \quad (3.33b)\end{cases}$$

$$M_D(t) = F_{Pu}N\begin{cases}1, & t<0, \quad (3.34a)\\ 1-F_{Pr}\left[\beta\exp[-k_1t]+(1-\beta)\frac{k_1}{k_1-k_2}\left(\exp[-k_2t]-\exp[-k_1t]\right)\right], & t\geq 0; \quad (3.34b)\end{cases}$$

Population M_E is seen to follow a single exponential decay with rate k_1 as would be expected from section 3.1.3.1(a) above. M_F is a bi-exponential, building up with the faster of the two rates, k_1 and k_2, and decaying with the slower. The first minus sign appearing in each of the expressions for M_G, M_H and M_D indicates that depletion is occurring as a result of probing. M_G shows a depletion which decays with rate k_1, and is analogous to the fluorescence depletion discussed in section 3.1.3.1(c) above.

Suppose that $|E\rangle$ and $|F\rangle$ can not be detected separately, but rather their sum is observed experimentally:

$$M_{ions}(t) = M_E(t) + M_F(t), \quad (3.35a)$$

$$M_{ions}(t) = 0, \quad t<0, \quad (3.36a)$$

$$= F_{Pu}F_{Pr}N\left[\beta\exp[-k_1t]+(1-\beta)\frac{k_1}{k_1-k_2}\left(\exp[-k_2t]-\exp[-k_1t]\right)\right], \quad t\geq 0. \quad (3.36b)$$

This expression, (3.36b), has the exact same temporal behavior as the depletion signal in both M_H and M_D. Understanding the temporal behavior of the total ion signal, M_{ions}, will therefore lead to an understanding of the fluorescence depletion signal in M_H and M_D. A comparison of M_{ions} with M_H and M_D for the general case, where f_A and f_B must be considered, is made in Appendix A.1.

In the analysis above, the probing transitions to yield ions were the same that caused the depletion of the fluorescence and in this sense β was the parameter relevant to both types of signal. For certain different yet related experiments, this may not hold and a β' must be used for depletion that is different from the β associated with ionization. For example, if ionization by the probe is accomplished by the absorption of two or more probe photons while depletion of the fluorescence is achieved with just one or more, then β must be used in the expressions for M_E and M_F, whereas β' should be used for M_G and M_H.

(b) Understanding the Shape of the Molecular Response Function

Equation (3.36) expresses the total ion signal as a single exponential decay function added to a bi-exponential, which has a rise and a decay. However, to more easily visualize the shape of this signal, it is convenient to rewrite equation (3.36) in terms of two exponential terms, one with k_1 and the other with k_2:

$$M_{ions}(t) = 0\,, \qquad t<0, \tag{3.37a}$$

$$= F_{Pu}F_{Pr}NM(t), \qquad t\geq 0, \tag{3.37b}$$

where

$$M(t) = a\exp[-k_1 t] + b\exp[-k_2 t], \tag{3.38a}$$

with $$a = \beta - (1-\beta)\frac{k_1}{k_1 - k_2}, \tag{3.38b}$$

and $$b = (1-\beta)\frac{k_1}{k_1 - k_2}, \tag{3.38c}$$

where we still have $0\leq\beta\leq 1$. Notice that $M(0)=\beta$, so that $M_{ions}(0)=F_{Pu}F_{Pr}\beta N = F_{Pu}F_{PrB}N$, is expected, because at time zero there is no population in $|C>$, so ions are only produced by probing the fraction F_{PrB} of the $F_{Pu}N$ molecules in state

$|B\rangle$. To understand the signal, M(t), it is helpful to first look at the two extrema of the probing parameter. If $\beta=1$ then only state $|B\rangle$ is probed and

$$M(t) = \exp[-k_1 t]. \tag{3.39}$$

In contrast, if $\beta=0$, only state $|C\rangle$ is probed and

$$M(t) = \frac{k_1}{k_1 - k_2}\left(\exp[-k_2 t] - \exp[-k_1 t]\right), \tag{3.40}$$

a bi-exponential, rising with the faster of k_1 and k_2 and decaying with the slower. In the following, the full range of β from 0 to 1 will be addressed to illustrate its influence on the observed signal.

In general, the slope, s, of M(t) at t=0 is given by

$$s = -(k_1 a + k_2 b) = k_1(1-2\beta), \tag{3.41}$$

which, for $k_1>0$, implies that at time zero M(t) increases if $0\le\beta<0.5$, decreases if $0.5<\beta\le1$, or is level if $\beta=0.5$. We shall be interested in non-zero values of k_1 for otherwise there would be no dynamics and M(t) would just equal β at all times. The slope at time zero is independent of k_2 but this is only due to the presence in (3.40) of the first factor, which has a ratio of rates. This factor determines the overall amplitude and its sign governs which of the two rates is in the rise and which is in the decay (see Fig. 3.6).

The signal exhibits a maximum if $0\le\beta\le0.5$ which is located at

$$t_{max} = \frac{1}{k_1 - k_2}\ln\left[\frac{\beta + (1-2\beta)k_1 / k_2}{1-\beta}\right]. \tag{3.42}$$

If k_1 equals k_2, the maximum occurs at

$$t_{max}\Big|_{k_1=k_2} = \frac{1}{k_1}\left(\frac{1-2\beta}{1-\beta}\right). \tag{3.43}$$

For $0.5<\beta\le1$, there is no maximum and the signal is a monotonically decreasing function with time.

It is important to understand how the two rates influence the shape of the transient. For example, if there is a maximum, its amplitude and location will be

affected by k_2 in addition to k_1. To illustrate this point, consider the case $\beta=0$, which yields the bi-exponential in (3.40). The maximum occurs at

$$t_{max}\Big|_{\beta=0} = \frac{\ln[k_1 / k_2]}{k_1 - k_2} \tag{3.44}$$

and the maximum signal amplitude is given by

$$M_{max}\Big|_{\beta=0} = (k2 / k1)^{(k2 / (k1 - k2))}, \tag{3.45}$$

which is a monotonically decreasing function with increase in (k_2/k_1), being 1 at $(k_2/k_1)=0$, decreasing to e^{-1} at $(k_2/k_1)=1$, and asymptoting to 0 when $(k_2/k_1)\rightarrow\infty$. Fig (3.9) shows the bi-exponential, given by (3.40), with different values of k_2, and fixed k_1. The slope at time zero remains unchanged at $s=k_1$, but this arises because of the amplitude factor, $k_1/(k_1-k_2)$ in (3.40), and does not reflect the overall shape. For very fast k_2, the maximum is very close to time zero appearing, as is shown below, at a time of order $1/k_2$. As k_2 is decreased, the maximum appears at a later time, and when $k_2=k_1$, the maximum is at $t=1/k_1$. With further decrease in k_2, Fig. 3.9 shows how the maximum moves to longer times, but remains on a time scale of order $1/k_1$, even for very small k_2.

(c) Molecular Response when the Decays are on Different Time Scales

Often one of the two decay processes is on a much faster time scale than the other. This may lead to simplifications in the formulae as discussed in the two cases below. The general cases, for which the decay times, k_1^{-1} and k_2^{-1}, are not necessarily on different time scales, are discussed in Appendix A.2.

Case 1: $k_1 >> k_2$

This case physically corresponds to a situation where |C> is reached very fast and decays slowly. The constants a and b reduce to:

$$a = 2\beta - 1, \tag{3.46}$$

$$b = 1 - \beta. \tag{3.47}$$

For short times, $t \sim O(1/k_1)$, M(t) reduces to:

$$M(t) = a \exp[-k_1 t] + b. \tag{3.48}$$

For longer times, $t \sim O(1/k_2)$, we obtain

$$M(t) = b \exp[-k_2 t]. \tag{3.49}$$

So M(t) initially changes exponentially with rate k_1, on a time scale of order $1/k_1$, from $M(0)=a+b=\beta$ to a value of $b=1-\beta$, and then on a longer time scale it decays exponentially at a rate k_2 to a value of 0. Rate k_2 can only appear in the decay as b is negative. Rate k_1 appears as a rise or a decay, depending on whether a is negative or positive, respectively. If $0.5<\beta<1$, then $a>0$ and $b>0$, and the signal is a bi-exponential, as shown in Fig 3.10 (a), with both k_1 and k_2 in the decay. If $\beta=0.5$ then $a=0$, $b=0.5$, and $M(t)=0.5\exp[-k_2 t]$, a pure single exponential decay with rate k_2, as shown in Fig. 3.10 (b). For $0 \leq \beta < 0.5$, Fig. 3.10 (c) illustrates the signal obtained. A maximum is reached at a time given by (3.42), which becomes

$$t_{max}\Big|_{k_1 >> k_2} = \frac{1}{k_1} \ln\left[\frac{1-2\beta}{1-\beta} \cdot \frac{k_1}{k_2}\right]. \tag{3.50}$$

This is typically of order $1/k_1$, as expected. The maximum signal height becomes

$$M_{max}\Big|_{k_1 >> k_2} = 1 - \beta. \tag{3.51}$$

Case 2: $k_2 >> k_1$

This happens when the intermediate decays at a rate that is much faster than the rate at which it is populated. The constants a and b become

$$a = \beta + (1-\beta)k_1/k_2, \tag{3.52}$$

$$b = -(1-\beta)k_1/k_2. \tag{3.53}$$

For short times, $t \sim O(1/k_2)$, the signal changes exponentially with rate k_2 from a value (a+b) to a value a:

$$M(t) = a + b \exp[-k_2 t]. \tag{3.54}$$

For longer times, $t \sim O(1/k_1)$, the signal drops exponentially to 0 with rate k_1:

$$M(t) = a \exp[-k_1 t]. \tag{3.55}$$

Rate k_1 is always in the decay of the signal as a is positive. As b is negative, the rate k_2 appears as a rise at early time, but the contribution to the overall signal amplitude is small (unless $\beta=0$) since $|b| << a$.

If $\beta=1$ then a=1, b=0 and the signal, shown in Fig. 11(a), becomes

$$M(t)=\exp[-k_1 t]. \tag{3.56}$$

If $0<\beta<1$ then $a=\beta$, $b=-(1-\beta)k_1/k_2$ and the signal (Fig. 11(b)) is

$$M(t)=\beta \exp[-k_1 t] - (1-\beta)k_1/k_2 \quad (\approx \beta \exp[-k_1 t]). \tag{3.57}$$

If $0<\beta\leq 0.5$ (see Fig. 11(b), insert), a maximum, derived from (3.42), exists at

$$t_{max}\Big|_{k_1 >> k_2} = \frac{1}{k_2} \ln\left[\frac{1-\beta}{\beta}\right], \tag{3.58}$$

which is typically of order $1/k_2$, as expected for the rise time. Because $|b| << a$ this maximum has a very small amplitude and may be difficult to distinguish from the overall shape which just looks like $\beta \exp[-k_1 t]$.

If $\beta=0$ then $a=k_1/k_2$ and $b=-k_1/k_2=-a$, yielding

$$M(t) = \frac{k_1}{k_2}\left(\exp[-k_1 t] - \exp[-k_2 t]\right), \tag{3.59}$$

a bi-exponential with k_2 in the rise and k_1 in the decay (Fig. 11(c)). The amplitude of the signal, determined by the factor (k_1/k_2), may be quite low when $k_2>>k_1$.

(d) Experimental Examples of Transient Intermediate Measurements

(d.i) Detection by Ionization

Fig. 3.12 shows normalized experimental data obtained in a study[4] in which an excited parent molecule, cyclopentanone, decays via decarbonylation to a diradical intermediate, which in turn decays but on a longer time scale (see Appendix C). The probe arrives at a time delay after the pump which excited the parent at time zero. The probe ionizes a fraction of both the parent and the intermediate populations and detection is performed by weighing the masses using time-of-flight (TOF) mass spectrometry. The parent mass (84 amu) could thus be separated from the lighter intermediate (56 amu).

The solid lines in Fig. 3.12 are fits based on the kinetic model depicted in Fig. 3.8, with the fluorescence rates omitted. The parent ($|B>$) is fit with a single exponential, given by equation (3.39), with a decay time of 120±20 fs. The intermediate is fit with a bi-exponential ((3.40)) with a rise time $1/k_1$=150±30 fs, and a decay time $1/k_2$=700±40 fs. The decay of the parent therefore matches the rise of the intermediate. In terms of the probing parameter, β, appearing in the more general equation, (3.38), the parent transient corresponds to β=1 while the intermediate was fit with β=0. The transients in Fig. 3.12 were obtained at low pump and probe intensities. At higher intensities of the probe the transient for the intermediate mass was seen to have a contribution in it corresponding to the shape of the parent transient. This was due to fragmentation of the parent ion by

further absorption of probe photons. This behavior for the intermediate mass could be described by fitting with $\beta>0$.

The approach of using mass resolution to separate intermediate dynamics from that of the parent has proven to be very useful. It has been used to study the α-cleavage reaction of acetone[1] establishing the stepwise nature of the overall process (see Appendix D). The parent acetone decays via α-cleavage to an intermediate, the acetyl radical, which then decays with a different lifetime to the final products. In another study[5], the dynamics of metal-metal and metal-ligand bond cleavage in an organometallic were distinguished by probing to ionization and monitoring the parent and fragment masses (Appendix E).

(d.ii) Detection via Fluorescence Depletion

Fig. 3.13 shows experimental data corresponding to a fluorescence depletion experiment[6] aimed at studying the hydrogen-atom transfer in the molecule methyl salicylate (MS). MS has two different forms: the "blue" and "uv" rotamers (A and B), so-called because of the fluorescence they emit at 440 nm and 330 nm, respectively. Fig. 3.13 shows transients obtained, detecting fluorescence at 440 nm, corresponding to rotamer A, for three different initial excitation energies (λ_{Pu}). The dynamics may be described by the kinetic model in Fig. 3.8. Excited rotamer A* in a $\pi\pi^*$ state, denoted by $|B\rangle$, undergoes hydrogen transfer with rate k_1 to a tautomer T*, denoted by $|C\rangle$. T* decays non-radiatively (k_2) and radiatively (k_1), and the fluorescence at 440 nm, from $|C\rangle$ to $|H\rangle$ in Fig. 3.8, is collected. The probe is allowed to deplete both the initial ($|B\rangle$) and the intermediate ($|C\rangle$) state. The signal is given by $M_H(t)$ in equation (3.33), which may be rewritten in terms of the function M(t) of equation (3.38) as follows:

$$M_H(t) = F_{Pu} N \frac{f_C}{k_2} \begin{cases} 1, & t < 0, \quad (3.60a) \\ 1 - F_{Pr} M(t), & t \geq 0. \quad (3.60b) \end{cases}$$

The minus sign indicates that the fluorescence yield is depleted at positive delay time, t, when the probe arrives after the pump.

The maximum depletion achieved (near time zero) was ≈20%, corresponding to $F_{Pr} \sim 0.2$. The actual detected signal was inverted to give the transient in Fig. 3.13, which therefore should be fit with the positive signal, M(t). Since the hydrogen transfer rate, k_1, is much faster than the non-radiative rate from the intermediate, k_2, the limit $k_1 >> k_2$ was appropriate. The data could be fit well using $\beta=0$ (c.f. equation (3.40) and Fig. 3.10(c)) in which case k_1 is in the rise and k_2 in the decay. The rise time, $1/k_1$, was found to be within 60 fs, and the decay time, $1/k_2$ ($=\tau$ in Fig. 3.13), was on a picosecond to nanosecond time scale, depending on the excess available energy (see Fig. 3.13).

3.1.3.4 Isomerization

Fig. 3.14 shows a kinetic model that may be applied to isomerization reactions. The pump initiates the reaction, exciting the ground state, |A>, of one isomer of the molecule. The excited state, |B>, then decays to the ground state of the other isomer, |D>, via an intermediate state, |C>. The probe, arriving at delay time, t, after the pump, monitors the build-up of the second isomer. The signal is given by the final population, $M_E(t)$, of the state probed to, |E>. Experimentally this may be achieved in different ways, e.g., by monitoring the absorption of the probe, or detecting the total fluorescence from |E> if this state is radiative, or by collecting all ions produced if |E> is an ion level.

State |B> is allowed to fluoresce with rate f, in addition to decaying along the isomerization pathway to |C> with rate k_1. The intermediate, |C>, decays with rate k_2 to the final isomer, |D>, and state |C> also has a decay rate, k_3, back to the initial ground state isomer, |A>. However, since the short pump pulse is

only present at time zero, the partial repopulation at later times of state |A> by rate k_3 does not influence the detected signal, $M_E(t)$. If longer laser pulse widths were used then this repopulation, or feed-back loop, would have to be considered. Here, k_3 will only manifest itself as part of the depopulation rate of state |C>.

Before the pump arrives there are N molecules in ground state |A>. The pump populates state |B> with $F_{Pu}N$ molecules at time zero ($t^*=0$). The system then evolves according to the rates described above and indicated in Fig. 3.14. At a time delay, t, the probe excites a fraction, F_{Pr}, of the population in state |D> to state |E>. By varying t, the signal, M(t), is obtained. The set of differential equations to be solved are:

$$dn_B/dt^* = -(k_1+f)n_B\ ; \tag{3.61}$$

$$dn_C/dt^* = k_1n_B\ - (k_2+k_3)n_C; \tag{3.62}$$

$$dn_D/dt^* = k_2n_C\ , \tag{3.63}$$

with the initial conditions:

$$n_B(0) = F_{Pu}N; \qquad n_C(0) = 0; \qquad n_D(0) = 0. \tag{3.64a-c}$$

Solving (3.61) and (3.62) shows that state |B> decays exponentially with rate k_1+f, while state |C> exhibits a bi-exponential behavior with the faster of (k_1+f) and (k_2+k_3) in the rise, and the slower in the decay:

$$n_B(t^*) = 0, \qquad t^*<0, \tag{3.65a}$$

$$= F_{Pu}N\exp[-(k_1+f)t^*], \qquad t^*\geq 0; \tag{3.65b}$$

$$n_C(t^*) = 0, \qquad t^*<0, \tag{3.66a}$$

$$= F_{Pu}N\frac{k_1}{k_1+f-(k_2+k_3)}\left(\exp[-(k_2+k_3)t^*]-\exp[-(k_1+f)t^*]\right), \qquad t^*\geq 0. \tag{3.66b}$$

The signal, $M_E(t) = F_{Pr}n_D(t^*=t)$, is given by

$$M_E(t) = 0, \qquad t^*<0, \tag{3.67a}$$

$$= F_{Pu}F_{Pr}N\frac{k_1}{k_a}.\frac{k_2}{k_b}M(t), \qquad t^*\geq 0, \tag{3.67b}$$

where $k_a=k_1+f$, $k_b=k_2+k_3$, and

$$M(t) = 1 - \frac{k_a \exp[-k_b t] - k_b \exp[-k_a t]}{k_a - k_b}. \quad (3.68)$$

The signal, $M_E(t)$, rises from 0 at time zero to a final value that is the product of the pump and probe excitation fractions, F_{Pu} and F_{Pr}, and the two ratios $k_1/(k_1+f)$ and $k_2/(k_2+k_3)$. The two ratios of rates express that k_1 competes with f in the decay of $|B\rangle$, and k_2 competes with k_3 in the depopulation of $|C\rangle$.

Fig. 3.15 shows plots of M(t) against time delay for different values of k_b and with k_a fixed. Fig. 3.15(a) illustrates cases in which k_b is faster than or equal to k_a. In the limit that $k_b >> k_a$, the function approaches

$$M(t)\Big|_{k_b >> k_a} = 1 - \exp[-k_a t]. \quad (3.69)$$

The reason is that if k_1+f is very slow then it is the overall rate determining step in the reaction. Even if k_b is only one order of magnitude greater than k_a, the signal is already close to this limit, (3.69). For $k_b=k_a$, (3.68) reduces to

$$M(t)\Big|_{k_b = k_a} = 1 - (1 + k_a t)\exp[-k_a t]. \quad (3.70)$$

For k_b slower than k_a (see Fig. 3.15(b)), k_b becomes the determining rate in the overall reaction: it is now the bottle-neck, so to speak. When $0<k_b<<k_a$, the signal in (3.68) reduces to a single exponential rise with rate k_b:

$$M(t)\Big|_{k_b << k_a} = 1 - \exp[-k_b t]. \quad (3.71)$$

This functional form is almost already attained when k_b is one order of magnitude smaller than k_1, as seen in the bottom part of Fig. 3.15(b). The amplitude of the signal, $M_E(t)$ in (3.67), is not influenced by the magnitude of k_b in relation to k_a but rather by each of the two rate ratios appearing in (3.67): $k_1/(k_1+f)$ and $k_2/(k_2+k_3)$.

3.1.3.5 Stimulated Emission Pumping

A level diagram for a kinetic model of stimulated emission pumping is given in Fig. 3.16(a). Within the pump pulse, state |C> is populated by stimulated emission from state |B> by the pump, which excites population from |A> to |B>. State |C>, prepared in this way, essentially at time zero, decays at a rate k to the final state, |D>. The probe pulse arrives at a delay, t, after the pump and excites a fraction, F_{Pr}, of the |D> state population at this time to a state |E>. Detection may be performed in one of several ways, each of which reveals the temporal behavior: absorption of the probe, or monitoring the total ion signal if |E> is an ion state, or it may be realized by collecting the total fluorescence from |E> if this state radiates.

The temporal pulse widths of the pump will clearly play a role in determining how quickly state |C> is populated. However, by treating the pump and the probe as instantaneous, an overall picture of the process in going from |A> to |D> may be obtained. The influence that finite pulse widths and saturation have on transients is discussed in sections 3.14 and 3.15, respectively. For the approximation that the pump and probe are instantaneous, the description is as follows. At time zero, the pump excites a fraction, F_{Pu}, of the N molecules in state |A> to state |B>. The pump populates state |C> with a fraction, F_{Pu}', of the $F_{Pu}N$ molecules in |B>, resulting in a population $F_{Pu}F_{Pu}'N$ for state |C> at time zero. The pumping fractions, F_{Pu} and F_{Pu}', are approximately given by the expressions of the type in equation (3.2), *i.e.*,

$$F_{Pu} \sim \frac{\sigma_{AB}\lambda_{Pu}E_{Pu}}{hc\pi R^2}; \qquad F_{Pu}' \sim \frac{\sigma_{BC}\lambda_{Pu}E_{Pu}}{hc\pi R^2}. \tag{3.72a,b}$$

After the pump pulse state |C> decays at rate k and its population is therefore given by:

$$n_C(t^*) = 0, \qquad t^*<0, \tag{3.73a}$$

$$= F_{Pu}F_{Pu}'N \exp[-kt^*], \qquad t^*\geq 0. \tag{3.73b}$$

State $|D\rangle$, whose population is given by $dn_D/dt^*=kn_C$ and $n_D(t^*\leq 0)$, shows a build-up with rate k to a final asymptotic value:

$$n_D(t^*) = 0, \qquad t^*<0, \tag{3.74a}$$

$$= F_{Pu}F_{Pu}'N (1-\exp[-kt^*]), \qquad t^*\geq 0. \tag{3.74b}$$

With the probe arriving at delay t, the $|E\rangle$ state population becomes $F_{Pr}n_D(t)$:

$$M_E(t) = 0, \qquad t<0, \tag{3.75a}$$

$$= F_{Pu}F_{Pu}'F_{Pr}N (1-\exp[-kt]), \qquad t\geq 0. \tag{3.75b}$$

This is the single exponential rise with rate k shown in Fig. 3.16(b).

With finite temporal pulse widths, the signal will have the single exponential rise given by (3.75) at time delays much longer than the widths ($FWHM_i$) of the pulses as long as the decay time of $|C\rangle$ is long in the sense that $1/k>>FWHM_i$. At early times, near time zero, the transient is expected to be influenced by the finite laser pulse widths. When the decay (k) is comparable to the pulse widths, $1/k=O(FWHM_i)$, the signal will show a rise of order 1/k to its maximum value, but the shape of the rise will be strongly influenced by the fact that the pulses are not instantaneous. If $|C\rangle$ has a lifetime much shorter than the widths of the pump and probe pulses, then the rise of the signal will occur on a time scale of the pulse widths and not 1/k. In this case, the shape of the transient is greatly affected by the finite pulses.

This is a qualitative description of the effects of finite pulses in the case of the stimulated emission pumping experiment. In the following section (3.1.4), quantitative analysis is presented to describe effects that occur as a result of finite pump and probe temporal pulse widths.

3.1.4 Effects of Finite Temporal Laser Pulse Widths

In the sections above, the pump and probe laser pulses were treated as being instantaneous in the sense of equation (3.9) and an excitation then involved instantaneous transfer of population from one state to another. In this case, the detected signal becomes the molecular response function, M(t). The goal of an experiment is to find the molecular response function as it contains all the dynamical information measurable in the experiment. In practice, the laser pulses are not instantaneous but rather have a finite width and a shape which influence the detected signal. The aim of this section is to describe how observed transients are affected by the characteristics of the laser pulses and to explain how the data should be interpreted to retrieve the molecular response function.

With finite pulses, radiation absorption and emission rates must be considered in an excitation between two levels (lower, $|1\rangle$; upper, $|2\rangle$). When a system is in a region with radiation of energy density per unit frequency, ρ_ν, where ν is the transition frequency, $(E_2-E_1)/h$, the matter-radiation interaction is described as follows.[7, 8, 9, 10, 11, 12] The rate of stimulated absorption per molecule from $|1\rangle$ to $|2\rangle$ is

$$W_{Abs} = B_{12}\,\rho_\nu, \tag{3.76}$$

where B_{12} is the Einstein coefficient of stimulated absorption. The rate of stimulated emission per molecule from $|2\rangle$ to $|1\rangle$ is given by

$$W_{SE} = B_{21}\,\rho_\nu, \tag{3.77}$$

where B_{21} is the Einstein coefficient for stimulated emission. The rate of spontaneous emission (fluorescence) is

$$W_{Sp} = A, \tag{3.78}$$

independent of any radiation present. Einstein showed[7] that for degenerate levels, $|1\rangle$ and $|2\rangle$, the coefficients satisfy (S.I. units used throughout below):

$$A = \frac{8\pi m^3 h\nu^3}{c^3} B_{21} = \frac{8\pi h\nu^3}{c^3} B_{21}, \quad \text{for} \quad n = 1; \tag{3.79}$$

$$B_{12} = B_{21} \quad (\equiv B). \tag{3.80}$$

For electric dipole transitions,[8, 9]

$$A = \frac{16\pi^3 \nu^3}{3\varepsilon_0 hc^3} |\mu_{21}|^2; \tag{3.81}$$

so

$$B = \frac{2\pi^2}{3\varepsilon_0 h^2} |\mu_{21}|^2, \tag{3.82}$$

where μ_{21}=<2 | er | 1> is the transition dipole moment.

Since the Einstein coefficients B_{12} and B_{21} are equal, (3.76) and (3.77) imply that the rate of stimulated absorption, W_{Abs}, equals the rate of stimulated emission, W_{SE}. Calling this common rate, r, the two equations may be combined:

$$r = B \rho_\nu. \tag{3.83}$$

The laser intensity (Watt/m^2) is given by[8]

$$I_\nu = c \rho_\nu / n = c \rho_\nu, \quad \text{for } n=1. \tag{3.84}$$

Therefore, the rate may be written as follows:

$$r = B I_\nu / c. \tag{3.85}$$

The integrated absorption cross section, σ_{12}, is defined as the probability of absorption of a photon by one molecule in the interaction region, from state | 1> to state | 2>. It can be shown to be given by:[11]

$$\sigma_{12} = \frac{2\pi^2 \nu}{3\varepsilon_0 hc} |\mu_{21}|^2, \tag{3.86}$$

where ν is now the average frequency for the absorption band. The oscillator strength, f, is related to this cross section:[11]

$$f = \frac{4 m_e c \varepsilon_0}{e^2} \sigma_{12}, \tag{3.87}$$

where m_e and e are the mass and charge of an electron, respectively. Using (3.85) and (3.86), the rate r may be written as

$$r = \sigma_{12} \frac{\lambda}{hc} I, \tag{3.88}$$

where the frequency index, ν, is dropped on the intensity.

In our experiments, the pump and probe intensities are time dependent. We are therefore interested in finding the pumping and probing rates as a function of time. As (3.88) is valid at any time it may be written as follows:

$$r_i(t) = \sigma_{ij}\frac{\lambda_i}{hc}I_i(t), \tag{3.89}$$

where the subscript i on r, I and λ refers to the pump or the probe, and the cross section, σ_{ij}, is between states $|i\rangle$ and $|j\rangle$. The subscript i on r, I and λ is not to be confused with the subscript i in σ_{ij}. The laser pulses may be expressed in terms of normalized functions, $f_i(t)$, containing information about the shape and width of the pulse:

$$I_i(t) = \frac{E_i}{\pi R^2}f_i(t); \tag{3.90}$$

$$\int_{-\infty}^{\infty} f_i(t)dt = 1, \tag{3.91}$$

$$r_i(t) = F_i f_i(t), \tag{3.92}$$

$$F_i = \frac{\sigma_{ij}\lambda_i E_i}{hc\pi R^2}, \tag{3.93}$$

where E_i is the total energy in the pulse, and R is the common radius for the lasers in the interaction region. The pump and probe are then given by $I_{Pu}(t^*)$ and $I_{Pr}(t^*-t)$, where t^* is time, and t is the delay time between the arrival of the peaks of the two pulses. The delay is positive when the pump arrives first.

Information about the pump and probe pulse shapes is contained in the normalized functions, $f_{Pu}(t^*)$ and $f_{Pr}(t^*-t)$. The effects that these functions have on observed transients is illustrated in the next two sections. Most of these effects may be shown in the unsaturated regime, in which stimulated emission rates may be omitted. In section 3.1.5, stimulated emission will be included to describe saturation effects.

3.1.4.1 Pulse Shape

Effects of the pulse shapes on the observed signal are presented in this section and are shown in several examples.

3.1.4.1.1 Three Level System with no Decay

(a) Pump Only

Consider the three-level system shown in Fig. 3.17. First, the effect of the pump alone is treated. This pump pulse, centered at time zero ($t^*=0$), excites from state $|A\rangle$ to state $|B\rangle$, as shown in Fig. 3.17(a). Only an upward pointing arrow is shown in Fig. 3.17(a) to indicate that the transition is unsaturated. In section 3.1.5, where saturation is considered, the stimulated emission rate becomes crucial and a downward pointing arrow will be added in the diagrams. Neglecting fluorescence (slow), the populations are related by:

$$dn_A/dt^* = - r_{Pu}\, n_A + r_{Pu}\, n_B; \tag{3.94}$$

$$dn_B/dt^* = r_{Pu}\, n_A - r_{Pu}\, n_B, \tag{3.95}$$

with boundary conditions, $n_A(-\infty)=N$, and $n_B(-\infty)=0$. In the unsaturated regime, $n_B(t^*)<<n_A(t^*)$, and then (3.93) reduces to:

$$dn_B/dt^* \approx r_{Pu}\, N, \tag{3.96}$$

leading to

$$n_B(t^*) = N\int_{-\infty}^{t^*} r_{Pu}(t)dt \tag{3.97}$$

$$= NF_{Pu}\bar{f}(t^*), \tag{3.98}$$

where

$$F_{Pu} = \frac{\sigma_{AB}\lambda_{Pu}E_{Pu}}{hc\pi R^2}; \tag{3.99}$$

$$\bar{f}(t^*) = \int_{-\infty}^{t^*} f_{Pu}(t)dt. \tag{3.100}$$

The final population of $|B\rangle$ is then given by $n_B(\infty)=F_{Pu}N$ since $\bar{f}(\infty)=1$. So, in the unsaturated regime, F_{Pu} is the transition probability, referred to in the earlier sections as the fraction excited.

Before introducing the probe pulse (Fig. 3.17(b)), it is necessary to consider the build-up of $|B\rangle$ due to the pump. Equations (3.98) and (3.100) give the number of molecules in $|B\rangle$ as a function of time, t*, and Fig. 3.18(a) shows this growth in the $|B\rangle$ state population for three different pump pulse shapes, $f_{Pu}(t^*)$. If the pump approaches the instantaneous limit of a delta function, then $\bar{f}(t^*)$ vanishes for negative time and equals unity at positive time, yielding the step function (Fig. 3.18(a.i)):

$$n_B(t^*) = 0, \qquad t^*<0, \tag{3.101a}$$

$$= F_{Pu}N, \qquad t^*>0. \tag{3.101b}$$

For a Gaussian pump pulse, with $f_{Pu}(t^*)=G(t^*,FWHM_{Pu})$, given by (3.4) and (3.5) and characterized by the temporal width, $FWHM_{Pu}$, the function $\bar{f}(t^*)$, appearing in (3.98), becomes

$$\bar{f}(t^*) = \int_{-\infty}^{t^*} G(t,FWHM_i)dt \tag{3.102a}$$

$$= \frac{1}{2}(1+\mathrm{erf}[\frac{t^*}{\sigma_i\sqrt{2}}]), \tag{3.102b}$$

where $\sigma_i=\sigma_{Pu}$ is related to $FWHM_i=FWHM_{Pu}$ by (3.5), and the error function is

$$\mathrm{erf}[x] = \frac{2}{\sqrt{\pi}}\int_0^x \exp[-s^2]ds. \tag{3.103}$$

The normalized build-up of $|B\rangle$ for a Gaussian pump pulse is shown in Fig. 3.18(a.ii). If instead the pump pulse is square (Fig. 3.18(a.iii)), then

$$f(t^*) = 1/FWHM_{Pu}, \qquad |t| \le FWHM_{Pu}/2, \tag{3.104}$$

which leads to

$$\bar{f}(t^*) = 0, \qquad t^* < -FWHM_{Pu}/2, \tag{3.105}$$

$$= (t^*+FWHM_{Pu}/2)/FWHM_{Pu}, \qquad |t^*| \leq FWHM_{Pu}/2, \tag{3.106}$$

$$= 1, \qquad t^* > FWHM_{Pu}/2. \tag{3.107}$$

The rise of $|B\rangle$ is linear as shown in Fig. 3.18(a.iii).

(b) Pump and Probe

Next, the probe is introduced at a time delay t after the pump, as shown in Fig. 3.17(b). In the unsaturated regime, $n_C(t^*)<<n_B(t^*)<<n_A(t^*)$, and the $|C\rangle$ state probed to is given by $n(-\infty)=0$, and

$$dn_C/dt^* = r_{Pr}n_B. \tag{3.108}$$

The $|B\rangle$ state is almost unaffected by the probing and the expression(s) derived for n_B above may be used. The population of $|C\rangle$ is therefore given by

$$n_C(t^*,t) = F_{Pr}\int_{-\infty}^{t^*} f_{Pr}(t_2-t)n_B(t_2)dt_2 \tag{3.109}$$

$$= NF_{Pu}F_{Pr}\int_{-\infty}^{t^*} f_{Pr}(t_2-t)\int_{-\infty}^{t_2} f_{Pu}(t_1)dt_1dt_2. \tag{3.110}$$

The measured signal, $S_C(t)$ or simply $S(t)$, is the final ($t^*\rightarrow\infty$) population of $|C\rangle$, which then becomes a function of just the time delay:

$$S(t) = n_C(\infty,t) \tag{3.111}$$

$$= NF_{Pu}F_{Pr}\int_{-\infty}^{\infty}\int_{-\infty}^{t_2} f_{Pu}(t_1)f_{Pr}(t_2-t)dt_1dt_2 \tag{3.112}$$

$$= \int_{-\infty}^{\infty}\int_{-\infty}^{t_2} f_{Pu}(t_1)M(t_2-t_1)f_{Pr}(t_2-t)dt_1dt_2, \tag{3.113}$$

where $M(t)$ is the molecular response function:

$$M(t) = M_C(t) = 0, \qquad t<0, \tag{3.114a}$$

$$= F_{Pu}F_{Pr}N, \quad t\geq 0. \tag{3.114b}$$

A change of variable, $s=t_1-t_2+t$, then leads to

$$S(t) = \int_{-\infty}^{t}\int_{-\infty}^{\infty} f_{Pu}(t_1)f_{Pr}(t_1-s)M(t-s)dt_1ds. \tag{3.115}$$

The laser system response, R(t), defined as the signal if M(t) is set equal to the Dirac-delta function, is easily recognized as the cross-correlation of the two pulses f_{Pu} and f_{Pr}:

$$R(t) = \int_{-\infty}^{\infty} f_{Pu}(t_1) f_{Pr}(t_1 - t)dt_1. \tag{3.116}$$

The observed transient may then be written as

$$S(t) = \int_{-\infty}^{t} R(s)M(t-s)ds, \tag{3.117}$$

which has the form of a convolution of the cross-correlation with the molecular response function.

Fig. 3.18(b) shows the normalized signal, $S(t)/(F_{Pu}F_{Pr}N)$, observed for three different cases. In each case, the probe is assumed to have the same shape as the pump. If the pulses are Dirac-delta functions (c.f. equation (3.9)), then their cross-correlation, (3.116), reduces to:

$$R(t) = \int_{-\infty}^{\infty} \delta(t_1)\delta(t_1 - t)dt_1 \tag{3.118}$$

$$= \delta(t). \tag{3.119}$$

The observed signal becomes

$$S(t) = \int_{-\infty}^{t} \delta(s)M(t-s)ds \tag{3.120}$$

$$= \int_{0}^{\infty} \delta(y-t)M(y)dy \tag{3.121}$$

$$= \begin{cases} 0, & t < 0 \\ M(t), & t \geq 0 \end{cases} \tag{3.122a,b}$$

$$= M(t), \tag{3.122}$$

which is just the molecular response function (see Fig. 3.18(b.i)), as expected for instantaneous transitions.

If instead, the pump and probe are Gaussian functions ((3.4) and (3.5)), then the cross-correlation of the two pulses becomes

$$R(t) = \int_{-\infty}^{\infty} G(t_1, FWHM_{Pu})\, G(t_1 - t, FWHM_{Pr})dt_1 \tag{3.123}$$

$$= G(t, FWHM_{CC}), \tag{3.124}$$

also a Gaussian, whose width is given by

$$FWHM_{CC} = (FWHM_{Pu}^2 + FWHM_{Pr}^2)^{1/2}. \quad (3.125)$$

The signal, given by (3.117), is then

$$S(t) = \int_{-\infty}^{t} G(s, FWHM_{CC})\, M(t-s)ds \quad (3.126)$$

$$= F_{Pu}F_{Pr}N \int_{-\infty}^{t} G(s, FWHM_{CC})ds \quad (3.127)$$

$$= F_{Pu}F_{Pr}N \frac{1}{2}\left(1 + \mathrm{erf}\left[\frac{t^*}{\sigma_{CC}\sqrt{2}}\right]\right), \quad (3.128)$$

where

$$\sigma_{CC} = \frac{FWHM_{CC}}{2\sqrt{2\ln 2}}. \quad (3.129)$$

This signal, shown in Fig. 3.18(b.ii), reaches half its maximum value at time zero. In this figure the pump and probe widths are chosen to equal the same value, FWHM, and the cross-correlation then has a width equal to $\sqrt{2}$·FWHM.

Consider next the case of square laser pulses that have the same width, FWHM. The cross-correlation becomes a triangle whose full width at half maximum is also FWHM:

$$R(t) = \frac{FWHM - |t|}{FWHM^2}, \qquad |t| \le FWHM; \quad (3.130a)$$

$$= 0, \qquad |t| > FWHM. \quad (3.130b)$$

The signal is then

$$S(t) = 0, \qquad t < -FWHM; \quad (3.131a)$$

$$= (1+t/FWHM)^2/2, \qquad -FWHM < t < 0; \quad (3.131b)$$

$$= 1 - (1-t/FWHM)^2/2, \qquad 0 \le t < FWHM; \quad (3.131c)$$

$$= 1, \qquad t > FWHM. \quad (3.131d)$$

This signal (Fig. 3.18(b.iii)) reaches half its maximum height when the probe is at time zero (t=0), and exhibits quadratic behavior in the rise on either side of time zero. Although less realistic physically than Gaussian pulses, square pulses may sometimes reduce the complexity of the mathematics, especially for more involved kinetic models (more rates and levels). The shape of the signal obtained

is usually quite similar to that calculated using Gaussian pulses, as can be seen for the three level model with no decay, by comparing Fig. 3.18(b.ii) and Fig. 3.18(b.iii).

3.1.4.1.2 Three Level System with Decay

The level diagram considered is that of Fig. 3.1(a) with no fluorescence (f=0), and with the nature of $|C\rangle$ not yet specified. The $|B\rangle$ state decays with rate k. The full rate equations are:

$$dn_A/dt^* = - r_{Pu}\, n_A + r_{Pu}\, n_B; \tag{3.132}$$

$$dn_B/dt^* = r_{Pu}\, n_A - (r_{Pu}+k+r_{Pr})\, n_B + r_{Pr}\, n_C; \tag{3.133}$$

$$dn_C/dt^* = r_{Pr}\, n_B - r_{Pr}\, n_C, \tag{3.134}$$

with $n_A(t^*\rightarrow-\infty)=N$, $n_B(t^*\rightarrow-\infty)=n_C(t^*\rightarrow-\infty)=0$, $r_{Pu}=r_{Pu}(t^*)$ and $r_{Pr}=r_{Pr}(t^*-t)$, where t is the time delay. In the unsaturated regime, $n_B=n_B(t^*)$ and $n_C=n_C(t^*,t)$, and the rate equations reduce to

$$n_A \approx N; \tag{3.135}$$

$$dn_B/dt^* = r_{Pu}(t^*)\, N - k\, n_B; \tag{3.136}$$

$$dn_C/dt^* = r_{Pr}(t^*-t)\, n_B. \tag{3.137}$$

Equation (3.136) may be solved using the integrating factor,[13] $\exp[kt^*]$, yielding

$$n_B(t^*) = N\int_{-\infty}^{t^*} \exp[-k(t^*-x)]\, r_{Pu}(x)dx. \tag{3.138}$$

The pulses are assumed to be Gaussian in which case (see (3.92)) $r_{Pu}(x)=F_{Pu}G(x,FWHM_{Pu})$, with G given by (3.4). When carried out, the integration in (3.138) gives

$$n_B(t^*) = F_{Pu}N \exp[-kt^*] \exp\left[\frac{(\sigma_{Pu}k)^2}{2}\right] \frac{1}{2}\left(1+\operatorname{erf}\left[\frac{1}{\sqrt{2}}\left\{\frac{t^*}{\sigma_{Pu}}-\sigma_{Pu}k\right\}\right]\right), \tag{3.139}$$

where σ_{Pu} is given by (3.5). In the limit $k\rightarrow 0$, this reduces to (3.98) with $\bar{f}(t^*)$ given by (3.102b).

Integration of (3.137) leads to an expression for $n_C(t^*,t)$ and, by substituting in n_B from (3.138) and taking $t^* \rightarrow \infty$, the signal as a function of time delay is obtained:

$$S(t) = \int_{-\infty}^{\infty} r_{Pr}(t^* - t) \int_{-\infty}^{t^*} N \exp[-k(t^* - x)]\, r_{Pu}(x) dx dt^*. \tag{3.140}$$

This may be written in the form of (3.117) with cross-correlation, R(t), given by (3.124) and with molecular response function:

$$M(t) = 0, \qquad t<0, \tag{3.141a}$$

$$= F_{Pu}F_{Pr}N \exp[-kt], \qquad t \geq 0. \tag{3.141b}$$

Performing the integration yields

$$S(t) = F_{Pu}F_{Pr}N \exp[-kt] \exp\left[\frac{(\sigma_{CC}k)^2}{2}\right] \frac{1}{2}\left(1 + \mathrm{erf}\left[\frac{1}{\sqrt{2}}\left\{\frac{t}{\sigma_{CC}} - \sigma_{CC}k\right\}\right]\right), \tag{3.142a}$$

where σ_{CC} is the temporal standard deviation of the Gaussian cross-correlation:

$$\sigma_{CC} = \frac{FWHM_{CC}}{2\sqrt{2\ln 2}}, \tag{3.142b}$$

with $FWHM_{CC}$ given by (3.125). Equation (3.142) has a very similar form to (3.139) because each expression was derived from a convolution of a Gaussian ($FWHM_{CC}$ vs. $FWHM_{Pu}$, respectively) with the same molecular response function (except for a factor of F_{Pr} less in (3.139)).

Fig. 3.19 shows the normalized signal, $S(t)/S_{max}$, obtained for different extremes or ranges of k. With δ-function pulses the signal is the molecular response function, given by (3.141). With a Gaussian cross-correlation, the transients (using S(t) from (3.142)) in Fig. 3.19(ii) are obtained. For k=0, the smooth rise in the normalized signal reaches 0.5 at time zero. As k is increased, the value at time zero increases monotonically from 0.5, finally reaching a value of 1 as $k \rightarrow \infty$ (*i.e.*, when $\sigma_{CC}k >> 1$). When k is large, the molecular response function (see Fig. 3.19a.i) starts to resemble a δ-function, although it still has a finite height. The convolution in (3.117) then yields a signal that is proportional to the cross-correlation function, R(t). With square pulses the cross-correlation, R(t), is a

triangle with $FWHM_{CC}$ equal to that of each pulse, FWHM (see (3.130)). The signal, given by 3.140, may be put in the form of a convolution (see(3.117)) of this cross-correlation with the molecular response function of equation (3.141). The signal then becomes

$$S(t) = 0, \qquad t \le -FWHM, \qquad (3.143a)$$

$$= F_{Pu}F_{Pr}N \exp[-kt] \int_{-FWHM}^{t} \frac{(FWHM-|s|)}{FWHM^2} \exp[ks]\, ds, \qquad |t| \le FWHM, \qquad (3.143b)$$

$$= F_{Pu}F_{Pr}N \exp[-kt] \int_{-FWHM}^{FWHM} \frac{(FWHM-|s|)}{FWHM^2} \exp[ks]\, ds, \qquad t \ge FWHM, \qquad (3.143c)$$

and is shown in Fig. 3.19(iii), normalized to 1 at the maximum signal. For k=0, half the maximum value is reached at time zero. When k is increased the value at time zero increases continuously, reaching 1 for large k ($FWHM_{CC}k>>1$). For large k, the signal shape again approaches that of the cross-correlation.

3.1.4.2 n-Level Kinetic Model in the Unsaturated Regime: Convolution

Consider a kinetic model, with any number of levels and decay rates, in which the rates are constants, independent of the populations of the levels. The molecular response function of interest is M(t). The signal, S(t), may be detected by any means, e.g., ionization, fluorescence, fluorescence depletion, and absorption. The probe is allowed to access more than one level:

$$M(t) = \sum_{i=1}^{m} M_i(t), \qquad m \ge 1. \qquad (3.144)$$

The pump arrives with its peak (or center of its shape) at time zero ($t^*=0$) and the peak of the probe comes later at a time $t^*=t$, the delay time.

Consider the pump and probe temporal intensity profiles, f_{Pu} and f_{Pr}, as being made up of infinitesimally narrow square pulses, as shown in Fig. 3.20.

Suppose just one such slice, at $t^*=t_A$, were present in pump and one in the probe, at $t^*=t+t_B$; these are the two highlighted slices in Fig. 3.20. What will be the observed signal? The pump slice initiates the dynamics at $t^*=t_A$, and the probe slice is delayed by a time $t+t_B-t_A$ with respect to the pump slice. This delay must be non-negative to yield a signal, *i.e.*,

$$t+t_B-t_A \geq 0. \tag{3.145}$$

The intensity of the pump slice is

$$I_{Pu}(t^*, t_A) = \frac{E_{Pu}}{\pi R^2} f_{Pu}(t_A), \qquad t_A \leq t^* \leq t_A + \Delta t_A, \tag{3.146a}$$

$$= 0, \qquad \text{otherwise}, \tag{3.146b}$$

and that of the probe slice is

$$I_{Pr}(t^*-t, t_B) = \frac{E_{Pr}}{\pi R^2} f_{Pr}(t_B), \qquad t_B \leq t^*-t \leq t_B + \Delta t_B, \tag{3.147a}$$

$$= 0, \qquad \text{otherwise}. \tag{3.147b}$$

If Δt_A and Δt_B are infinitesimal, then the intensities approach δ-functions:

$$I_{Pu}(t^*, t_A) = \frac{E_{Pu}}{\pi R^2} f_{Pu}(t_A)\Delta t_A\, \delta(t^*-t_A); \tag{3.148}$$

$$I_{Pr}(t^*-t, t_B) = \frac{E_{Pr}}{\pi R^2} f_{Pr}(t_B)\Delta t_B\, \delta(t^*-t-t_B). \tag{3.149}$$

Since the molecular response function, $M_i(t)$, is by definition the signal obtained with the following δ-function pulses:

$$I_{Pu}(t^*) = \frac{E_{Pu}}{\pi R^2} \delta(t^*); \tag{3.150}$$

$$I_{Pr}(t^*-t) = \frac{E_{Pr}}{\pi R^2} \delta(t^*-t), \tag{3.151}$$

the signal obtained with the intensities in (3.148) and (3.149) becomes

$$\Delta S_i(t,t_A,t_B) = f_{Pu}(t_A)\, \Delta t_A\, f_{Pr}(t_B)\, \Delta t_B\, M_i(t+t_B-t_A). \tag{3.152}$$

So far only one pump slice and one probe slice were considered. If we restrict the discussion to the unsaturated regime, then the total signal will be the sum of the contribution from all such pump-probe slice pairs that satisfy (3.145), *i.e.*, for which the probe slice arrives after the pump slice or at the same time as it. For infinitesimal slices, this summation becomes an integration with t_B running

from $-\infty$ to ∞, and t_A from $-\infty$ to $t+t_B$. The signal, a function of just the time delay, t, is therefore given by

$$S_i(t) = \int_{-\infty}^{\infty} \int_{-\infty}^{t+t_B} f_{Pu}(t_A)\, f_{Pr}(t_B)\, M_i(t + t_B - t_A)\, dt_A\, dt_B. \tag{3.153}$$

If more than one level is detected, then the total signal, S(t), is a sum of the $S_i(t)$, where the summation may then be taken inside the integral sign and equation (3.144) may be used. The total signal may therefore be written as

$$S(t) = \int_{-\infty}^{\infty} \int_{-\infty}^{t+t_B} f_{Pu}(t_A)\, f_{Pr}(t_B)\, M(t + t_B - t_A)\, dt_A\, dt_B. \tag{3.154}$$

If we let $s=t_A-t_B$ and let t_A and s be the dummy variables, then if t_A is allowed to run from $-\infty$ to ∞, condition (3.145) restricts t_B to lie in the range (t_A-t) to ∞, and so s must run from t to $-\infty$ (which becomes $-\infty$ to t, using the minus from $ds=-dt_B$). With this change of variable, the signal becomes

$$S(t) = \int_{-\infty}^{t} \int_{-\infty}^{\infty} f_{Pu}(t_A)\, f_{Pr}(t_A - s)\, M(t - s)\, dt_A\, ds \tag{3.155}$$

$$= \int_{-\infty}^{t} R(s)\, M(t - s)\, ds, \tag{3.156}$$

where

$$R(t) = \int_{-\infty}^{\infty} f_{Pu}(t_A)\, f_{Pr}(t_A - t)\, dt_A. \tag{3.157}$$

Therefore, in the unsaturated regime, any kinetic model has a signal that is a convolution of the molecular response function, M(t), with the cross-correlation, R(t), of the laser pulses. Unsaturated here strictly means that the contribution to the total signal from any pair of pump-probe slices must be given by (3.152). In other words, the contribution of a pair must not be altered by any cumulative effect of other pump or probe slices. The pump and probe intensities, as well as the absorption cross sections, determine if a system is unsaturated, or saturated to some extent. Other factors such as the time scale of decay rates compared to the pulse widths, and whether a state (e.g., ion state) cannot be stimulated to emit, also contribute to whether a system is unsaturated or not. These effects are discussed in section 3.1.5.

As an example of applying (3.156), consider an unsaturated system that has a molecular response function given by

$$M(t) = 0, \qquad t<0, \tag{3.158a}$$

$$= A + B\exp[-k_1 t] + C\exp[-k_2 t], \qquad t\geq 0, \tag{3.158b}$$

where A, B and C are constant. If the pump and probe laser pulses are Gaussian, then the cross-correlation, R(t), is Gaussian (see equation (3.4) and (3.5)): $G(t,FWHM_{CC})$. Equation (3.142) shows the result of integration of a single exponential response function with a Gaussian cross-correlation. If we define $S(k,FWHM_{CC},t)$ as the signal obtained by convoluting M=exp[-kt] with the Gaussian, $G(t,FWHM_{CC})$, then

$$S(k,FWHM_{CC},t) = \exp[-kt]\exp\left[\frac{(\sigma_{CC}k)^2}{2}\right]\frac{1}{2}\left(1+\operatorname{erf}\left[\frac{1}{\sqrt{2}}\left\{\frac{t}{\sigma_{CC}}-\sigma_{CC}k\right\}\right]\right). \tag{3.159}$$

The signal obtained by convoluting M(t) of (3.158) with $G(t,FWHM_{CC})$ is then

$S(t) = A + B\,S(k_1,FWHM_{CC},t) + C\,S(k_2,FWHM_{CC},t)$.

Experimental data may be fit using a chosen form of the molecular response function. For example, a single exponential decay uses B>0 and C=0. A single exponential rise has B<0, C=0. A bi-exponential with both rates in the decay would use B>0 and C>0. A bi-exponential, starting at the baseline (A) and rising with k_1 and decaying with k_2 back to the baseline, would use $k_1>k_2$ and B=-C<0.

3.1.4.3 Pulse Width

In the unsaturated regime, the signal was shown in section 3.1.4.2 above to be a convolution (see equation (3.156)) of the cross-correlation, R(t), given by (3.157), of the laser pulses with the molecular response function, M(t). Suppose the cross-correlation has a width $FWHM_{CC}$. If $FWHM_{CC}\rightarrow 0$ then R(t) becomes a delta function and S(t) equals M(t). If, however, $FWHM_{CC}>0$, as is the case with

physical pulses, the signal will be a smeared-out molecular response function, where the degree of smearing, dictated by the convolution in equation (3.156), increases with increase in $FWHM_{CC}$.

With short pulses the condition, $FWHM_{CC} << 1/k_i$, holds, where k_i is the dominant rate in a region of M(t), and the signal in this region will be similar to the shape of M(t), changing on a time scale, τ, of order $1/k_i$. For relatively fast pulses, $FWHM_{CC} \leq O(1/k_i)$, it is possible to retrieve M(t) by accurately measuring the cross-correlation, R(t), leaving M(t) as the only unknown in equation (3.156). For long pulses, $FWHM_{CC} >> 1/k_i$, the signal will only change on a time scale of order $1/FWHM_{CC}$. It may therefore be difficult to accurately retrieve the much faster changing molecular response function as the uncertainty ($\Delta FWHM_{CC}$) in the measured cross-correlation may be on the time scale of the dynamics.

The effect the pulse widths have on the maximum signal, S_{max}, is of interest. For example, how will the signal amplitude change in going from 100 fs pulses to 1 ps or even 1 ns pulses? To answer this question it is necessary to know if M(t) attains its maximum asymptotically at long time (case (i) below) or if M(t) has a local maximum at a finite delay time, case (ii). Using the substitution, y=t-s, equation (3.156) may be written

$$S(t) = \int_0^\infty R(t-y)\, M(y)\, dy . \qquad (3.160)$$

Case (i) **M(t) attains an Asymptotic Maximum**

Here $M_{max} = M(t >> \text{any } 1/k_i) = M(\infty)$. Consider a time delay given by

$$t >> \text{Max}(1/FWHM_{CC}, 1/k_i), \qquad (3.161)$$

then in the region where R is non-zero, $M(t) = M_{max}$. At this long time delay, the signal, S(t), has reached its maximum value, S_{max}, and (3.160) becomes

$$S_{max} = M_{max} \int_0^{\infty} R(t-y)\, dy \tag{3.162}$$

$$= M_{max}, \tag{3.163}$$

as R is a normalized function centered at t-y=0, *i.e.*, y=t, and equation (3.161) ensures the integration covers all non-zero values of R, yielding unity. So for a molecular response function that has an asymptotic maximum, M_{max}, the signal reaches its maximum value at time delays given by (3.161) and this maximum is simply equal to M_{max}.

Case (ii) M(t) has a Local Maximum

The molecular response function exhibits a rise to a maximum, $M_{max}=M(t_{max})$, followed by a decay. The region of time in which M(t) is of order M_{max} will be $\tau=O(1/k_i)$, where k_i is a dominating rate in the region. Consider broad pulses in the sense that $FWHM_{CC}>>\tau$. Then the convolution in (3.160) approaches the following:

$$S(t) \approx \int_0^{\infty} R(t-y)\, M_{max}\, \tau\, \delta(t_{max}-y)\, dy \tag{3.164}$$

$$= M_{max}\, \tau\, R(t-t_{max}). \tag{3.165}$$

R(t) has its maximum at the origin, and since R(t) is a normalized function and has a width $FWHM_{CC}$, its maximum is $R(0) = O(1/FWHM_{CC})$. Hence,

$$S_{max} \approx M_{max}\, \tau\, R(0). \tag{3.166a}$$

$$= M_{max}\, O(1/k_i)\, O(1/FWHM_{CC}), \tag{3.166b}$$

which leads to

$$S_{max} \propto M_{max} / (k_i\, FWHM_{CC}), \tag{3.167}$$

and this may also be written

$$S_{max} \propto M_{max} \frac{\tau}{\tau_P}, \tag{3.168}$$

where $\tau=O(1/k_i)$ is the dominant decay time in the region of the maximum signal and τ_P is a pulse width (e.g., of one of the lasers pulses) that is proportional to the width of the cross-correlation, $FWHM_{CC}$.

Consider then an experiment in which dynamics on a time scale (τ) of say 20 fs is measured, and this may be done with pulses of width τ_P=100 fs (e.g., $FWHM_{Pu}=FWHM_{Pr}$=100 fs), or τ_P=1 ps, or with τ_P=1 ns. The energy in the pump pulse is restricted to the same value, E_{Pu}, and that of the probe to a value E_{Pr}, in each experiment, so that the amplitude of the molecular response function remains the same. The cross-correlation, R(t), is normalized by definition. If the maximum signal, S_{max}, is 1 for 100 fs pulses, then according to equation (3.168) it will be 0.1 (=100 fs/(1 ps)) using 1 ps pulses, and 0.0001 (=100 fs/(1 ns)) using 1 ns pulses.

For a single exponential molecular response function, $M(t)=M_{max}\exp[-kt]$, the maximum signal in the case of Gaussian pulses, each of FWHM much longer than 1/k, may be shown, using equation (3.142), to be

$$S_{max} \approx a\, M_{max} / (k\, FWHM), \tag{3.169}$$

$$= a\, F_{Pu}F_{Pr}N / (k\, FWHM), \tag{3.170}$$

with $a=(\pi^{-1}\, 2\, \ln 2)^{1/2}$. It holds for $FWHM>>(8\ln 2)/k$, but is also reasonable in the region where FWHM~k. The cross-correlation has $FWHM_{CC}=2^{1/2}\,FWHM$.

Consider next the case of the bi-exponential molecular response function, M(t), corresponding to the case of a transition-state measurement (see Fig. 3.6), such as in the femtosecond pump-probe experiment with ICN.[3] Fig. 3.21 (see also ref. 14) shows the signal, S(t), obtained using the parameters of ref. 3. The pump and probe each have the same half-width at half maximum, HWHM, and the signal is shown for four different values of this HWHM. The parameters used (S.I. units) are the following:

k_{23} = $1/(50\text{x}10^{-15}\ \text{s})$; (=$k_1$ in Fig. 3.6) (3.171)

k_{35} = $1/(100\text{x}10^{-15}\ \text{s})$; (=$k_2$ in Fig. 3.6) (3.172)

σ_{12} = $4\text{x}10^{-24}\ \text{m}^2$; (=$\sigma_{AB}$ in Fig. 3.6) (3.173)

σ_{34} = $5\text{x}10^{-21}\ \text{m}^2$; (=$\sigma_{CE}$ in Fig. 3.6) (3.174)

E_{Pu} = $150\text{x}10^{-9}$ J; (3.175)

E_{Pr} = $50\text{x}10^{-9}$ J; (3.176)

R = $40\text{x}10^{-6}$ m; (3.177)

λ_{Pu} = $306\text{x}10^{-9}$ m; (3.178)

λ_{Pr} = $391.4\text{x}10^{-9}$ m; (3.179)

h = 6.626x10-34 Js; (3.180)

c = $2.99792458\text{x}10^{8}\ \text{ms}^{-1}$. (3.181)

The values of F_{Pu} and F_{Pr} (see equation (3.93)) are then 0.000184 and 0.0980, respectively. The factor, F_{Pr}, is quite large (close to 10% excitation probability), but because the transition state is so short lived ($1/k_{35}$=100 fs < FWHM) there is not appreciable saturation (see section 3.1.5). Even though the signal is expected to lie in the unsaturated regime, stimulated emission in both the pump and probe transitions was accounted for in finding the signal in Fig. 3.21, by solving the full set of rate equations which included the stimulated emission rates. In going from HWHM=5 ns to 750 fs, the signal maximum increases by a factor of $6.58\text{x}10^3$ (see caption to Fig. 3.21 for peak signals), very close to the predicted ratio 5 ns/(750 fs)=$6.67\text{x}10^3$ from equation (3.168). In narrowing the HWHM from 750 fs to 250 fs, the peak signal increases by a factor of 2.81, quite close to what equation (3.168) predicts: 750 fs/(250 fs)=3.00. The values are starting to differ slightly at shorter HWHM because the pulses are no longer broad in the sense of $\text{FWHM}_{CC} >> \tau \sim O(1/k_1)$ or $O(1/k_2)$=50 - 100 fs. Thus the condition used in deriving (3.168) is not satisfied completely with pulses that are on the time scale of the dynamics. Nevertheless, the agreement is still good.

When the change is made from 250 fs to 75 fs, the peak signal grows by a factor of 2.39, and the increase predicted by equation (3.168) is 250 fs/(75 fs)=3.33, still a very good estimate even though the condition under which the equation was derived is not strictly satisfied.

3.1.5 Saturation

A signal is saturated by the pump (probe) if the power dependence of the signal differs from that at very low pump (probe) intensity. In a very small range of the intensity centered at intensity I_i, of the peak of the laser pulse ($I_i=I_{Pu}(0)$ or $I_{Pr}(0)$), the signal at a fixed time delay, t, is given by:

$$S(t) = c(t)\ I_i^{m_i(t)}, \tag{3.182}$$

where the power dependence in this range is $m_i(t)$, and c(t) is independent of the intensity of interest. Hence, the power dependence is the slope of a plot of lnS(t) against $\ln I_i$ at the intensity I_i:

$$m_i(t) = \frac{d\ \ln S(t)}{d\ \ln I_i}. \tag{3.183}$$

The fact that the power dependence may be a function of the time delay implies that the shape of a transient may be distorted from its unsaturated form. We shall see that this distortion does not lead to additional features such as changing the underlying nature of the transient (e.g., bi-exponential with a rise and decay). The idea of plotting an experimentally determined intensity dependence, $m_i(t)$, against the time delay was introduced in ref. 15. Here, theoretically predicted plots of the pump and probe dependence will be presented for certain cases.

Saturation is not synonymous with just high laser intensity. The signal S(t) also depends on the absorption cross sections, σ_{ij}, and decay rates, k_i, in the system and these may consequently appear in $m_i(t)$ when the differentiation in (3.183) is carried out. The peak intensity, I_i, is proportional to the factor F_i (see

(3.90) and (3.93)), and it is therefore possible (and very useful) to write the power dependence in terms of this quantity:

$$m_i(t) = \frac{d\ \ln S(t)}{d\ \ln F_i}. \qquad (3.184)$$

Below, several cases are treated to see the effects of pump and probe saturation on different systems. The influence of saturation on transients is illustrated and the power dependence is discussed as a function of time delay in different regimes of the laser intensity and the decay rates.

3.1.5.1 Two Level System with No Decay

We first consider the two-level problem (with no spontaneous relaxation), as shown in Fig. 3.22, with just one laser pulse (pump) present. Using equation (3.92), the appropriate rate equations are:

$$dn_A/dt^* = -F_{Pu}f_{Pu}(t^*)n_A + F_{Pu}f_{Pu}(t^*)n_B; \qquad (3.185)$$

$$dn_B/dt^* = F_{Pu}f_{Pu}(t^*)n_A - F_{Pu}f_{Pu}(t^*)n_B. \qquad (3.186)$$

Substituting $n_B=N-n_A$ (conservation of population) in (3.185) and rearranging terms leads to

$$dn_A/dt^* + 2\,F_{Pu}f_{Pu}(t^*)n_A = F_{Pu}f_{Pu}(t^*)N. \qquad (3.187)$$

Using $\exp[2\,F_{Pu}\bar{f}_{Pu}(t^*)]$ as the integrating factor,[13] where $\bar{f}_{Pu}(t^*)$ is given by equation (3.100), and invoking the boundary conditions, $n_A(-\infty)=N$ and $n_B(-\infty)=0$, equation (3.187) reduces to

$$n_A(t^*) = 0.5\,N\,(1 + \exp[-2F_{Pu}\bar{f}_{Pu}(t^*)]). \qquad (3.188)$$

The population of $|B\rangle$ then follows from population conservation:

$$n_B(t^*) = 0.5\,N\,(1 - \exp[-2F_{Pu}\bar{f}_{Pu}(t^*)]). \qquad (3.189)$$

The final population of $|B\rangle$ is then

$$n_B(\infty) = 0.5\,N\,(1 - \exp[-2F_{Pu}]). \qquad (3.190)$$

In the limit of very high intensity, F_{Pu} is large and $n_B(\infty)$ approaches $n_A(\infty)=0.5N$.

The transition probability is given by

$$P = n_B(\infty)/N = 0.5\,(1 - \exp[-2F_{Pu}]). \qquad (3.191)$$

For low intensity, F_{Pu} is small and $P \approx 0.5\,(1-(1-2F_{Pu})) = F_{Pu}$. The final signal, $S(\infty)$, or total population transferred, $n_B(\infty)$, is then $F_{Pu}N$ in the unsaturated regime. From equation (3.184) we see that the (pump) power dependence is 1, *i.e.*, the signal is linearly proportional to the pump intensity.

Fig. 3.22 illustrates the signal, or $|B\rangle$ state population, in the unsaturated regime ($F_{Pu}<<1$) and in the saturated regime. A Gaussian pump pulse is used as described by equations (3.4) and (3.102b). The signal shifts to earlier times as the transition becomes more saturated. This is because at higher intensities the early part of the laser pulse is already intense enough to significantly populate the upper level, and the amount of stimulated emission then increases, making the rest of the pulse less effective in further increasing the upper population.

3.1.5.2 Three Level System with Decay

This system was treated in section 3.1.4.1.2 in the unsaturated regime in which $n_C<<n_B<<n_A$. Here we lift this restriction, keeping the full set of rate equations:

$$dn_A/dt^* = -r_{Pu}\,n_A + r_{Pu}\,n_B; \qquad (3.192)$$

$$dn_B/dt^* = r_{Pu}\,n_A - (r_{Pu}+k+r_{Pr})\,n_B + r_{Pr}\,n_C; \qquad (3.193)$$

$$dn_C/dt^* = r_{Pr}\,n_B - r_{Pr}\,n_C, \qquad (3.194)$$

with $n_A(t^*\rightarrow -\infty)=N$, $n_B(t^*\rightarrow -\infty)=0=n_C(t^*\rightarrow -\infty)$. The populations n_A, n_B and n_C are functions of the time, t^*, and the time delay, t, as is the probing rate, $r_{Pr}(t^*-t)$. The pumping rate, $r_{Pu}(t^*)$ is independent of the probe arrival time, t. The quantities associated with the pump transition from $|A\rangle$ to $|B\rangle$, $r_{Pu}(t^*)$, $I_{Pu}(t^*)$, $f_{Pu}(t^*)$, F_{Pu}, σ_{AB}, λ_{Pu} and R, are related by equations (3.89) through (3.93). The

equivalent quantities associated with the probe transition (|B> to |C>) obey the same set of relationships.

Unless analytical expressions are derived for limiting situations of equation (3.192) through (3.194), these equations are solved using Runge-Kutta integration techniques inherent in the numerical solution package for differential equations (NDSolve) in the Mathematica programming language.[16] Adaptive stepsize, crucial to problems with different time scales involved, is incorporated in the integration technique and it surpasses approaches such as the modified Euler method.

3.1.5.2.1 Pump Saturation

Fig. 3.23 shows transients and power dependence curves for the signal obtained, detecting the final ($t^* \rightarrow \infty$) population of |C>. The probe transition is kept unsaturated, while the pump is chosen to be either (i) saturated or (ii) unsaturated. Since the probe is unsaturated, the same signal will be seen by detection of any of the following: absorption of the probe, total fluorescence (slow) yield from |C> if it radiates, or total ions if |C> is an ionized state. The transient is shifted to earlier time as the pump transition becomes saturated. This shift decreases as the decay rate grows (see caption of Fig. 3.23). The pump power dependence plots were calculated using (3.184) in the form:

$$m_{Pu}(t) = \frac{\ln S(t, F_{Pu} + \Delta F_{Pu}) - \ln S(t, F_{Pu})}{\ln(F_{Pu} + \Delta F_{Pu}) - \ln F_{Pu}}, \qquad (3.195)$$

and ΔF_{Pu} was chosen to be 1% of F_{Pu} to ensure the power dependence was calculated in the neighborhood of the intensity (or F_{Pu}) used. With $F_{Pu}=10^{-4}$, $m_{Pu}(t)\approx 1$ for all times, but with $F_{Pu}=1$[17] the power dependence changes with time. At very early time, much before time zero when the peak of the pump

arrives, the dependence is linear as the intensity of the early part of the leading edge of the pump pulse is still low. At time zero the power dependence is just above 0.5, and it decreases further to an asymptotic value at longer time.

When k is increased (and F_{Pu}=1) the saturation becomes less severe at early time as |B> starts to decay (k) faster than it is populated (~r_{Pu}), thus reducing the stimulated emission. For example, at time zero the power dependence goes from 0.522 to 0.530 to 0.559 in Fig. 3.23. At long time the power dependence is almost independent of k if k is slow compared with the pulse width (0.311 for k=0 and 0.310 for k=0.5/FWHM). However, when k is very fast (k>>1/FWHM) and the pump transition is saturated (e.g., F_{Pu}=1) the |B> state has no chance to build up before it decays. Stimulated emission is then almost absent, yet the intense pump keeps depleting the ground state, |A>, until it is almost empty by the time the trailing edge of the pulse encounters the molecules.

At any given time the population just excited to state |B> only lingers in this state for a time of order 1/k. Consequently, in a time window of order 1/k the contribution to the signal must be due to what the pump excites in this time span and the number of these molecules the probe can excite to |C> in the same time. Therefore, with a long time delay, *i.e.*, separation of the peaks of the pump and probe pulses, the signal must be due to an overlap of the trailing edge of the pump and the leading edge of the probe pulse. If the whole pump pulse is intense then by the time its trailing edge arrives, there is very little population left in the ground state. Increasing pump intensity will only decrease the ground state population further and this can not be balanced by the added intensity in the trailing edge of the pump. Hence, there is severe saturation of the signal for long time delays: e.g., for k=10/FWHM and F_{Pu}=1 the pump dependence is 0.124 at t=5 FWHM (see Fig. 3.23, bottom right).

3.1.5.2.2 Probe Saturation

(a) Ionization Detection

Fig. 3.24 shows a three level kinetic model where the probe excites state |B> to an ion state |C>. State |B>, excited to by the pump (unsaturated) decays with rate k. The probe transition does not involve stimulated emission as |C> is an ion and |B> is a neutral, but this does not prevent saturation from occurring. The rate equations, (3.192) through (3.194), become

$$n_A \approx N; \tag{3.196}$$

$$dn_B/dt^* = r_{Pu}(t^*)\, N - (k + r_{Pr}(t^*-t))\, n_B; \tag{3.197}$$

$$dn_C/dt^* = r_{Pr}(t^*-t)\, n_B, \tag{3.198}$$

with the same boundary conditions as before. Equation (3.197) may be solved using the following integration factor:

$$\exp\left[kt^* + \int_{-\infty}^{t^*} r_{Pr}(s-t)ds\right] = \exp[kt^* + F_{Pr}\bar{f}_{Pr}(t^*-t)], \tag{3.199}$$

where $\bar{f}_{Pr}(t)$ is given by equation (3.102b) for a Gaussian pulse. The solution to (3.197) is then

$$n_B(t^*,t) = N \exp[-kt^* - F_{Pr}\bar{f}_{Pr}(t^*-t)] \int_{-\infty}^{t^*} F_{Pu} f_{Pu}(s) \exp[ks + F_{Pr}\bar{f}_{Pr}(s-t)]\, ds, \tag{3.200}$$

where $f_{Pu}(t)$ is given by equation (3.4) for a Gaussian pulse. The signal is the final ($t^* \rightarrow \infty$) population of |C>, obtained by solving (3.198):

$$S(t) = F_{Pr} \int_{-\infty}^{\infty} f_{Pr}(s-t)\, n_B(s,t)\, ds. \tag{3.201}$$

It is the appearance of F_{Pr} in n_B of equation (3.200) that can make the signal deviate from the otherwise linear dependence that (3.201) would give.

Fig. 3.24 shows transients and probe intensity dependence plots for different decay rates and probing intensities using an unsaturated pump transition. The transients follow a single exponential decay (k) with a smoothing

out due to the finite pulse widths. With $F_{Pr}=10^{-4}$ (<<1) all transients are unsaturated and have a linear power dependence. For $F_{Pr}=1$ and with slow (k=0.1/FWHM) or intermediate (k=0.5/FWHM) decays, the transients exhibit saturation effects. For slow decay the saturation is greatest as the intense probe has time to depopulate |B> significantly, leading to a less than linear increase in the signal with further increase in probe intensity. At early time and near time zero, the trailing edge of the probe always sees the highest population of |B> and it will contribute significantly to the total signal. The central part of the probe has higher intensity (higher saturation) but does not contribute significantly until it is near or later than time zero, and contributes most when it arrives at a delay long enough that the pump has populated |B> as much as it can. The saturation will therefore be at its most severe value at delays longer than where the maximum of the transient is reached, *i.e.*, longer than $t\sim0.5(FWHM_{Pu}+FWHM_{Pr})$.

With very fast decay rate (k=10/FWHM) the transients approach the cross-correlation, even in the case of $F_{Pr}=1$. The saturation is not very severe, even at high intensity, and the probe dependence is linear at all time delays, except for a dip (slight saturation) near time zero when the peak of the probe pulse encounters the highest population and is most effective. Overall, the dependence is close to 1 because $r_{Pr}/(r_{Pr}+k)$, the fraction of molecules probed from |B>, is much less than 1, and approaches r_{Pr}/k when $r_{Pr}<<k$. For given time delay, $r_{Pr}\propto F_{Pr}$ and hence the signal approaches a linear power dependence. The slight dip below 1 in the intensity dependence near time zero can be explained as follows. The |B> state decays so fast (O(1/k) that any population present in |B> must be probed in a time of order 1/k before it is gone. If the time delay is not near time zero, then the peak region of the probe becomes ineffective in contributing to the signal; instead the trailing edge of the probe is effective if $t < \sim(-FWHM)$ and the leading edge if

t> ~FWHM. Near time zero (~ -FWHM < t < ~FWHM) the peak region of the probe contributes most to the signal and since the intensity is high, appreciable depopulation of |B> may still occur, leading to saturation of the signal and the dip in the intensity dependence plot.

If the pump transition were a two-photon transition via a virtual state, then the effective pump pulse would be narrower. If the virtual state is considered as having zero lifetime, then the effective pump would approach a squared Gaussian, and the rise in the transients would be sharper but still have the same time zero position. If the virtual state has a very short but finite lifetime, then the second pump photon may be absorbed any time within the pump pulse after the first photon, leading to an effective repositioning of time zero at a time later (on the order of 20-40 fs for 100 fs pulses) than that measured in a cross-correlation of the pump with the probe, and this time shift equals the average time (Δt) between the absorption of the first and the second pump photon. In this case, the effective delay to the arrival of the probe is shortened and for a fixed probe delay the transient will have a signal that resembles what it would be at a shorter delay with a one photon pump transition. With time zero fixed using a cross-correlation to be when the peaks of the probe and pump pulses arrive simultaneously, the transient for a virtual state with an ultrashort but finite lifetime will then be shifted to later time (by Δt) from that obtained in a single photon experiment. It is assumed that the decay k of the state pumped to, |B>, and the probing intensity are the same.

(b) Fluorescence Detection

Fig. 3.25 illustrates a three level model with fluorescence detection. The fluorescence rate is assumed slow and the rate equations become

$$n_A \approx N; \tag{3.202}$$

$$dn_B/dt^* = r_{Pu}(t^*)\,N - (k + r_{Pr}(t^*-t))\,n_B + r_{Pr}(t^*-t)\,n_C; \tag{3.203}$$

$$dn_C/dt^* = r_{Pr}(t^*-t)\,n_B - r_{Pr}(t^*-t)\,n_C \tag{3.204}$$

with the boundary conditions, $n_B(t^*\rightarrow -\infty)=n_C(t^*\rightarrow -\infty)=0$. The signal is the final ($t^*\rightarrow\infty$) population of $|C\rangle$. The transients show a shift to earlier time with saturation (F_{Pr} increased), and the saturation, as evidenced by the probe dependence plots, is most severe for large k when significant depopulation of $|B\rangle$ due to k occurs even within the duration time of the probe pulse. After the pump pulse is gone, state $|B\rangle$ just decays and the rising edge of the probe is thus more effective than the rest of this pulse which as a consequence leads to large saturation. At early times when the pump is still present and the population of $|B\rangle$ is rising, the peak and trailing edge regions of the probe are more effective as they encounter a growing population, leading to less overall saturation by the probe pulse.

A comparison of Fig. 3.25 with Fig. 3.23 shows that the transients are identical (comparing the common cases k=0.5/FWHM and k=10/FWHM). Therefore, if the pulses have the same width and if F_{Pu} and F_{Pr} are switched, e.g., so that the pump instead of the probe transition becomes saturated, then the same signal and power dependence (of the saturating pulse) as a function of time delay are obtained. The reason for this is that with this molecular response function, M(t), the signal can be shown[18] to be a convolution of M(t) with a laser response, R(t), that is unchanged by an interchange of F_{Pu} and F_{Pr}. The response, R(t), becomes the cross-correlation in the unsaturated regime (as it must: see section 3.1.4.2). In the saturated regime R(t) is an asymmetric function, showing a steep rise to an early maximum followed by a slower decrease. This early steep behavior translates into the shift and sharpening of the slope at early time in the transients.

(c) Fluorescence Depletion

Fig. 3.26 illustrates two models, (a) and (b), that yield the same fluorescence depletion signal except for a difference in amplitude. Often it may be difficult numerically to solve these models if processes (f and k) are on time scales that differ by more than an order of magnitude. However, if it is possible to treat the problem in the limit that f<<k, then the fluorescence yield in Fig. 3.26(a) is just f/k of the final population of the state |D> that builds up with rate k (assuming it does not further decay). The problem may therefore be solved by omitting f from the set of rate equations and just solving for the final |D> population. This population also equals the fluorescence yield for case (b) in Fig. 3.26. The transients shown are inverted (and normalized) to show the positive depletion signal.

The relevant rate equations are the same as in case (b) above (fluorescence detection) with the addition of

$$dn_D/dt^* = k\, n_B, \tag{3.205}$$

with the boundary condition $n_D(t^* \rightarrow -\infty)=0$. The depletion signal follows the same qualitative behavior as the fluorescence signal discussed in (b) above. The shift of the signal to earlier time is greatest for slow decay rate. Power dependence plots are not calculated because with depletion experiments these may be difficult to measure, and it is easier to establish the presence of saturation by the magnitude of the shift in the transient signal to earlier time with increase in laser power.

3.1.5.3 Four Level System

In this section, a four level model is described in which the pump or the probe transition may be saturated. Stimulated emission is allowed for in both transitions. The pump pulse, centered at time zero ($t^*=0$), excites the ground state, $|A\rangle$, to state $|B\rangle$ which decays with rate k to state $|C\rangle$. The probe pulse arrives later with its peak at a delay t after time zero, and excites from $|C\rangle$ to $|D\rangle$. The signal is the final ($t^*\rightarrow\infty$) population of $|D\rangle$ as measured, for example, by collection of the total fluorescence from this state on a time scale (O(1/f)) much longer than the dynamics (1/k) and the laser pulses (FWHM). The molecular response function, M(t), is as shown in Fig. 3.9 (with $k_2=0$), *i.e.*, a single exponential rise with rate k to a final asymptotic value. In the unsaturated regime the signal would be just M(t) convoluted with the cross-correlation (see section 3.1.4.2). The effect of saturation is to distort the signal further from its unsaturated shape as described below. The approach is again to solve the set of relevant rate equations (using a Runge-Kutta routine).

3.1.5.3.1 Pump Saturation

In Fig. 3.27 the level diagram shows the possibility for a saturated pump transition, and the unsaturated probing. The relevant equations are

$$dn_A/dt^* = - r_{Pu}(t^*)\, n_A + r_{Pu}(t^*)\, n_B; \quad (3.206)$$

$$dn_B/dt^* = r_{Pu}(t^*)\, n_A - (r_{Pu}(t^*)+k)\, n_B\,; \quad (3.207)$$

$$dn_C/dt^* = k\, n_B - r_{Pr}(t^*-t)\, n_C; \quad (3.208)$$

$$dn_D/dt^* = r_{Pr}(t^*-t)\, n_C, \quad (3.209)$$

with boundary conditions, $n_A(t^*\rightarrow -\infty)=N$, $n_B(t^*\rightarrow -\infty)=n_C(t^*\rightarrow -\infty)=n_D(t^*\rightarrow -\infty)=0$.

With a decay time twice as long as the pulse widths (k=0.5/FWHM), the

saturated (F_{Pu}=1) transient is shifted only slightly earlier than the unsaturated ($F_{Pu}=10^{-4}$) transient. The pump dependence is linear for the unsaturated case whereas it exhibits a decrease with time delay in the case of saturation. With fast decay (k=10/FWHM) the transients show a fast rise in a time mainly bounded by the pulse widths. Saturation shifts the transient to earlier time: by 0.12 FWHM at time zero in going from $F_{Pu}=10^{-4}$ to 1.

Unlike the case in section 3.1.5.2.1 in which the probe accessed the state pumped to, the pump dependence in the four level model here shows less saturation with faster decay. The probe is monitoring the accumulating population of state |C> and the signal is thus affected by the averaged saturation effect for the whole pump pulse as opposed to the localized saturation occurring for the tail of the pump in the case in section 3.1.5.2.1. The leading edge and peak of the pump pulse meet a ground state (|A>) population that is not yet depleted fully and in addition encounter little stimulated emission because of the fast non-radiative depopulation of |B>. The trailing edge of the pump sees less population in |A> and is saturated more, but the overall effect is dominated by the less saturated, yet larger, contribution to the signal from the early part of the pump pulse. Hence, it can be said for this model: the faster the decay, the less the saturation: e.g., $m_{Pu}(0)$=0.657 for k=0.5/FWHM and 0.705 with k=10/FWHM; m_{Pu}(5 FWHM)=0.395 for k=0.5/FWHM and 0.561 for k=10/FWHM.

3.1.5.3.2 Probe Saturation

The same level diagram is considered as in section 3.1.5.3.1 above, but now with unsaturated pumping and a saturated probe transition as shown in Fig. 3.28 and given by the following equations:

$$n_A \approx N; \tag{3.210}$$

$$dn_B/dt^* = r_{Pu}(t^*)\, N - k\, n_B; \tag{3.211}$$

$$dn_C/dt^* = k\, n_B - r_{Pr}(t^*-t)\, n_C + r_{Pr}(t^*-t)\, n_D; \tag{3.212}$$

$$dn_D/dt^* = r_{Pr}(t^*-t)\, n_C - r_{Pr}(t^*-t)\, n_D, \tag{3.213}$$

with boundary conditions as above. The effects of saturation are more severe here for the probe transition than they were for the pump transition in the case presented in section 3.1.5.3.1. The reason is the decay rate, k, reduces stimulated emission in the pump transition but does not alter it for the probe transition which depends on the cumulative population of state $|C\rangle$. As a consequence, the transients in Fig. 3.28 exhibit a greater shift to earlier time with saturation of the probe transition: e.g., for k=10/FWHM, 0.5 is reached at 0.095 FWHM for $F_{Pr}= 10^{-4}$ but at 0.23 FWHM earlier than this with $F_{Pr}=1$.

At long delay times (t>>1/k), state $|C\rangle$ is fully populated and the probe dependence is expected to be independent of the decay rate, k. With t=5 FWHM the intensity dependence for k=10/FWHM is 0.311, the asymptotic value, and for k=0.5/FWHM the value is 0.320, almost the asymptotic value of 0.311 that is also reached at longer times for this rate. Near time zero the saturation is more severe for faster decay: $m_{Pr}(0)=0.632$ for k=0.5/FWHM and 0.549 for k=10/FWHM. With a very fast decay the $|C\rangle$ state builds up quickly and if the probe arrives almost at the same time as the pump, the peak region (most saturating) of the probe pulse still sees a large population and can contribute significantly to the signal. With a slow decay and the probe delay near zero, mainly the trailing edge of the probe is effective in yielding signal. Because the trailing edge is less intense than the peak region of the probe, there is less stimulated emission and less saturation of the probe transition near time zero for a slow than for a fast decay rate, k.

3.2 Classical and Quantum Mechanical Models

In considering classical and quantum mechanical models, the nature of the potential energy surface (PES) as a function of internuclear separation must be known, in contrast to the kinetic model for which this is not required. Being able to invert observed fs transition-state transients to a PES is an important aspect of ultrafast studies of molecular dynamics.

3.2.1 Classical Model

A classical mechanical model was developed by Bersohn and Zewail[19] who considered the process of bond breaking as a classical motion of the two fragments on the PES. The effect of the finite laser pulse widths is incorporated by first considering the pulses as instantaneous and later convoluting the calculated signal with the cross-correlation. This is similar to the treatment that may be performed for the kinetic model in the unsaturated regime (see section 3.1.4.2) and in this sense the classical model would have to be modified in order to describe saturation effects.

The key steps in describing a signal that depends on the pump-probe delay are the following.[3, 19] Suppose the probe wavelength is centered at an internuclear separation R=R*. Usually the spectral profile of a fs pulse exceeds the intrinsic linewidth of the transition and consequently the probe absorption at arbitrary R is given by

$$A(R) = C/\{\gamma^2 + [\Delta V(R) - \Delta V(R^*)]^2\}, \qquad (3.214)$$

where γ is the half-width (in the energy domain) of the optical pulse, $\Delta V(R) \equiv V_2(R) - V_1(R)$, and C is a constant. Here, the absorption is assumed to be Lorentzian in shape, but similar expressions may be obtained for a Gaussian or

other shapes. The probe absorption as a function of the delay time, A(t), is directly proportional to the measured signal in an FTS experiment:

$$S(t) \propto A(t) = C/\{\gamma^2 + [\Delta V(t) - \Delta V(t^*)]^2\}, \quad (3.215)$$

where t^* is given by $R(t=t^*)=R^*$. If the upper excited state potential (V_2) is much flatter than the lower (V_1), then (3.125) reduces to

$$S(t) \propto A(t) = C/\{\gamma^2 + [V_1(t) - V_1(t^*)]^2\}. \quad (3.216)$$

For a given form of $V_1(R)$, the equation of motion can be integrated to yield the internuclear distance as a function of time, R(t). Combining the expressions for V(R) and R(t) yields the potential of the reaction as a function of time, V(t), so that the absorption expected to be observed in the FTS experiment is known explicitly as a function of time. Conversely, knowing A(t) implies V(t) and V(R) can be deduced. The example of a single exponential repulsive potential, $V_1(R)$, is given in ref. 3. The form of the predicted transients, A(t), are derived in general and using parameters relevant to the dissociation of ICN, transients very similar to those predicted by the kinetic model are obtained.

3.2.2 Quantum Mechanical Model

In a kinetic model, the off-diagonal terms in the Hamiltonian and the density matrix equations are not considered and coherence effects can not be described. In this sense the kinetic model describes a statistical decay averaged over the whole ensemble of molecules and the state-to-state rates of a unimolecular dissociation process are simply measures of the coupling strength of an approximate molecular state to each continuum channel.[20]

A quantum mechanical model takes into account the full Hamiltonian and allows for coherence effects and the creation of a wave packet. The time dependent Schrödinger equation can be solved numerically. For example, the

wave packet approach of Heller[21] was applied to the dissociation of ICN by Williams and Imre.[22] The only internuclear distance considered as a parameter was the separation of CN and I. The potentials, $V_1(R)$ and $V_2(R)$, were assumed to be single exponentials. The spreading of the wave packet on $V_1(R)$ with time was observed. This is an aspect of the molecular dynamics that can not be described by the kinetic model. For a comparison of aspects of a kinetic and a quantum mechanical model in multilevel systems, see also ref. 23.

The three models are therefore similar in some ways but not in others. The classical and quantum mechanical models require a knowledge of the PES and predict wave packet dynamics. Coherence effects are only fully described by the quantum mechanical model. A kinetic model is easy to apply to problems where no prior knowledge of the PES is required. Effects of saturation are allowed for in both the kinetic and quantum mechanical models, but not in the classical model. Of course, a full quantum mechanical treatment is preferable whenever possible. It is interesting to note that on the fs time scale, the degree of localization is on the atomic scale of distance and the classical description is completely illustrative of the dynamics.

3.3 References

1. S. K. Kim, S. Pedersen, A. H. Zewail, *J. Chem. Phys.* **103**, 477 (1995).
2. A. Materny, J. L. Herek, P. Cong, A. H. Zewail, *J. Phys. Chem.* **98**, 3352 (1994).
3. M. J. Rosker, M. Dantus, A. H. Zewail, *J. Chem. Phys.* **89**, 6113 (1988).
4. S. Pedersen, J. L. Herek, A. H. Zewail, *Science* **266**, 1359 (1994).
5. S. K. Kim, S. Pedersen, A. H. Zewail, *Chem. Phys. Lett.* **233**, 500 (1995).
6. J. L. Herek, S. Pedersen, L. Bañares, A. H. Zewail, *J. Chem. Phys.* **97**, 9046 (1992).
7. A. Einstein, *Physik* Z. **18**, 121 (1917).
8. A. Yariv, *Quantum Electronics* (Wiley, New York, ed. 3, 1989).
9. S. Svanberg, *Atomic and Molecular Spectroscopy* (Springer Verlag, New York, ed. 2, 1992).
10. J. I. Steinfeld, *Molecules and Radiation* (MIT Press, Cambridge, ed. 2, 1985).
11. R. A. Alberty, *Physical Chemistry* (Wiley, New York, ed. 7, 1987).
12. e.g., a more accurate description would be obtained by using the optical Bloch equations or the complete Rabi solutions as derived in the reference, L. Allen, J.H. Eberly, *Optical Resonance and Two-Level Atoms* (Wiley, New York, 1975). This will not be pursued further as the objective here is a simple description of the problem.
13. J. Mathews, R. L. Walker, *Mathematical Methods of Physics* (Addison-Wesley, New York, ed. 2, 1970).
14. A. H. Zewail, in *Femtosecond Chemistry* J. Manz, L. Wöste, Eds. (VCH Verlagsgesellschaft mbH, Weinheim (Germany), 1995) pp. 109.
15. S. Pedersen, T. Baumert, A. H. Zewail, *J. Phys. Chem.* **97**, 12460 (1993).

16. S. Wolfram, *Mathematica: a System of Doing Mathematics by Computer* (Addison-Wesley, Redwood City, California, ed. 2, 1991).

17. This corresponds to a strong transition. For a discussion of the validity of the kinetic model for very strong transitions see, e.g., S. Feneuille, *Rep. Prog. in Phys.* **40**, 1257 (1977).

18. L. R. Khundkar, *Ph.D. Thesis, California Institute of Technology* (1988).

19. R. Bersohn, A. H. Zewail, *Ber. Bunsenges. Phys. Chem.* **92**, 373 (1988).

20. L. R. Khundkar, J. L. Knee, A. H. Zewail, *J. Chem. Phys.* **87**, 77 (1987); and references therein.

21. E. J. Heller, *Acc. Chem. Res.* **14**, 368 (1981).

22. S. O. Williams, D. G. Imre, *J. Phys. Chem.* **92**, 6648 (1988).

23. F. Lahmani, A. Tramer, C. Tric, *J. Chem. Phys.* **60**, 4431 (1974).

3.4 Figure Captions and Figures

Fig. 3.1 (a) Kinetic model showing a dissociative state $|B\rangle$ that is accessed by the pump pulse from the ground state $|A\rangle$. State $|B\rangle$ decays non-radiatively and radiatively at rates k and f, respectively. Detection is by means of probing to an ion level, $|C\rangle$, and monitoring all ions produced. The probe comes at a time delay, t, after the pump, which arrives at time zero. (b) Transient, or signal vs. time delay, t, obtained upon monitoring state $|C\rangle$. At negative t, the probe arrives before the pump and no ions are produced as no molecules are in $|B\rangle$ at the time of arrival of the probe. At positive t, the pump comes first, populating $|B\rangle$ before the probe arrives. The population of $|B\rangle$ decays exponentially at a rate k+f from its maximum value, $F_{Pu}N$, at time zero. The probe excites a fraction, F_{Pr}, of the molecules in $|B\rangle$ to $|C\rangle$, and hence $|C\rangle$ decays at the rate k+f with t from an initial maximum of $M_C(t=0)=F_{Pu}F_{Pr}N$ at t=0.

Fig. 3.2 Transient obtained in an experiment in which a deuterated acetone molecule, $(CD_3)_2CO$, is excited at time zero by a pump pulse and probed to ionization at a time delay t after the pump. The total ion signal was monitored as a function of the delay. The solid line is the fit to the data. It consists of a molecular response function, M, that has been convoluted with the cross-correlation (here, $HWHM_{cc}$~90 fs) of the pump and probe laser pulses. M has an instantaneous rise at t=0 and then decays exponentially with rate k. The value for k^{-1} obtained using several such data sets was 50±30 fs.

Fig. 3.3 (a) State $|B\rangle$, populated with $F_{Pu}N$ molecules at time zero by the pump, decays with rates k and f. The probe arrives at a delay time, t, after the pump, exciting a fraction, F_{Pr}, of the $|B\rangle$ population to the neutral level $|C\rangle$.

The $|B\rangle$ state dynamics is revealed through the collection of the total fluorescence, $M_{FluorC}(t)$, from $|C\rangle$ at discrete values of the delay, t. (b) Transient showing the molecular response function, $M_{FluorC}(t)$, *vs.* t. The fluorescence yield is maximum ($M_{FluorC}(0)=F_{Pu}F_{Pr}N$) at time zero and decays exponentially at the rate k+f.

Fig. 3.4 (a) The total fluorescence from state $|B\rangle$ is measured for different values of the pump-probe delay time, t. The probe depletes this fluorescence yield by exciting a fraction, F_{Pr}, of the molecules in $|B\rangle$ to $|C\rangle$ at time t. (b) Transient showing the total fluorescence from $|B\rangle$ as a function of t. The fluorescence yield, normalized to 1 at negative delay in this figure, is depleted at positive delay, when the probe arrives after the pump pulse. The depletion is most severe when $|B\rangle$ is most populated, which occurs at time zero. The magnitude of the depletion decays exponentially with the rate k+f.

Fig. 3.5 (a) The absorption of the probe is monitored in this experiment as a function of the pump-probe delay time. (b) The absorption follows the $|B\rangle$ state population, which decays exponentially at a rate k+f from its maximum value at time zero, when $|B\rangle$ is excited by the pump.

Fig. 3.6 (a) Level diagram for a kinetic model to study transition-state dynamics. The pump excites the reagent molecule to a state $|B\rangle$, which subsequently decays at a rate k_1 to the transition state, $|C\rangle$, which in turn decays at a rate k_2. The probe monitors this transition state at a time delay, t, after the pump. (b) The molecular response function of the state probed to, $|E\rangle$, from the transition state. This directly reflects the population of the transition state, $|C\rangle$.

The signal exhibits bi-exponential behavior, with the faster of the two rates, k_1 and k_2, in the rise, and the slower in the decay.

Fig. 3.7 Transient showing data obtained by probing the transition state in the dissociation of ICN.[3] The transients show a bi-exponential behavior with one component in the rise and the other in the decay. Key: solid squares: λ_{Pr}=389.7 nm; solid diamonds: λ_{Pr}=389.8 nm; open squares: λ_{Pr}=390.4 nm; open diamonds: λ_{Pr}=391.4 nm. Time zero was determined separately for each data set using the DEA-MPI technique.[3] The solid lines and arrows are guides to the eye, showing the approximate peak position for each data set. By tuning off-resonant to the red, the probe excites the transition state more, and is less sensitive to the build-up of the final products, seen with on-resonant probing.

Fig. 3.8 Kinetic Model for transient intermediate measurements. The probe can excite not only from the initial state, $|B\rangle$, excited to by the pump, but also from the transient intermediate, $|C\rangle$. The cross sections for the two probe transitions depend on the parameter, β, as shown. With β=1, only $|B\rangle$ is probed, while if β=0 then only $|C\rangle$ is probed. For intermediate values, $0<\beta<1$, both states are probed. The probe arrives at a delay time, t, after the pump. By varying this delay and monitoring one or more of the states $|E\rangle$, $|F\rangle$, $|G\rangle$, $|H\rangle$ and $|D\rangle$, the dynamics of the system (k_1, k_2, f_B, f_C) can be observed.

Fig. 3.9 Bi-exponential signal, corresponding to β=0, the case where only the intermediate, $|C\rangle$, is probed. Transients are shown for a fixed rate k_1, and for five different values for the rate k_2. If k_2 could be increased in an experiment, then the signal amplitude would drop and the maximum would move closer to time zero. The rise time, the location of the maximum signal, is given by

$\ln[k_1/k_2]/(k_1-k_2)$ (see text). If $k_2>k_1$ (e.g., the two lowest curves), then in general terms the shape is such that the rise is dominated by k_2 and the decay by k_1 (=1 unit). For the opposite case, $k_2<k_1$ (e.g., the two highest curves), the rise is with k_1 and the decay is with k_2.

Fig. 3.10 Signal obtained for a transient intermediate experiment in which the decay (k_2) of the intermediate state, $|C\rangle$, is much slower than the rate at which it is populated (k_1) from $|B\rangle$, *i.e.*, $k_1>>k_2$. (a) $0.5<\beta\leq1$: the initial state, $|B\rangle$, has a higher probe absorption cross section than the intermediate, $|C\rangle$. The signal is a bi-exponential with both rates in the decay. (b) $\beta=0.5$: both states ($|B\rangle$ and $|C\rangle$) are probed to the same extent. The transient is independent of k_1, showing a pure exponential decay with k_2. (c) $0\leq\beta<0.5$: the intermediate has the larger probing cross section. The signal has an initial step at time zero, followed by a rise with k_1 and a decay with k_2.

Fig. 3.11 Signal for transient intermediate measurements in which the intermediate, $|C\rangle$, decays (k_2) much faster than the rate at which it is populated (k_1) from $|B\rangle$, *i.e.*, $k_2>>k_1$. (a) $\beta=1$: only the initial state, $|B\rangle$, is probed and the signal is a single exponential decay with rate k_1. (b) $0<\beta<1$: both the initial state, $|B\rangle$, and the intermediate state, $|C\rangle$, are probed. The long time behavior is described by a single exponential decay with k_1. The short time behavior shows a small amplitude maximum if $0<\beta<0.5$; if $0.5\leq\beta<1$ then there is no maximum at positive time: the signal decreases monotonically and does so slower than rate k_1 at early time. (c) $\beta=0$: only the intermediate state, $|C\rangle$, is probed, leading to a bi-exponential signal. Since $k_2>>k_1$, k_2 appears in the rise and k_1 in the decay. The maximum amplitude of the signal equals k_1/k_2 when $k_2>>k_1$, and the amplitude may consequently be small.

Fig. 3.12 Femtosecond transients showing the detected ion signal of a given mass as a function of the delay time between the pump and the probe laser pulses.[4] The parent cyclopentanone (84 amu) exhibits a single exponential decay with a lifetime of 120±20 fs. The intermediate (56 amu), the tetramethylene diradical, shows a bi-exponential behavior with a rise ($\tau_1=1/k_1=150\pm30$ fs) to a maximum followed by a slower decay ($\tau_2=1/k_2=700\pm40$ fs).

Fig. 3.13 Depletion transients observed[6] for the 440 nm emission of methyl salicylate as a function of excitation energy (pump wavelength, λ_{Pu}; excess vibrational energy, E_v). The solid lines are least-squares fits to the data, yielding the time constants as shown for the non-radiative lifetime. This is the long time behavior of the signal. The short time behavior, not shown with the time scale chosen in this figure, has a very fast (<60 fs) rise component with the rate of the hydrogen transfer.

Fig. 3.14 Level diagram for a kinetic model of isomerization. The ground state, $|A\rangle$, of one isomer is excited by the pump to state $|B\rangle$ at time zero. $|B\rangle$ decays radiatively (f), and non-radiatively (k) along the isomerization pathway to $|C\rangle$, which in turn has a finite lifetime due to the rates k_2 and k_3. The other isomer, $|D\rangle$, in the system is populated at a rate k_2 from $|C\rangle$. The probe, arriving at a delay after time zero, excites a fraction of the $|D\rangle$ state population to the state $|E\rangle$, the population of which constitutes the signal.

Fig. 3.15 Molecular response function, M(t), showing the build-up of the final state reached in an isomerization reaction (kinetic model of Fig. 3.14). The rate $k_a=k_1+f$ is the total decay rate of the initial excited state, $|B\rangle$, and $k_b=k_2+k_3$ is the

total decay rate of the intermediate, $|C\rangle$, which populates the final isomer, $|D\rangle$, at rate k_2. When k_1 and k_2 are non-zero, a signal may be detected, and the normalized signal, M(t), asymptotes to 1 at long time delays. (a) Signal for different values of $k_b/k_a \geq 1$. In the limit $k_b >> k_a$, M(t) becomes a single exponential rise with rate k_a. (b) Signal with distinct values of $k_b/k_a \leq 1$. When $0 < k_b << k_a$, M(t) approaches a single exponential rise with rate k_b. If $k_b = 0$ then M(t)=0 at all times.

Fig. 3.16 Kinetic model for stimulated emission pumping. The pump pulse (t=0) excites from the ground state, $|A\rangle$, to an excited state, $|B\rangle$, and then stimulates emission to a state $|C\rangle$. State $|C\rangle$, thus populated by the pump, decays with rate k to a final state, $|D\rangle$. This final state is probed at a time delay, t, after the pump, resulting in an excitation to state, $|E\rangle$, whose population after the probe pulse constitutes the signal.

Fig. 3.17 Three level kinetic model in which the influence of the shapes of the laser pulses is considered. There is no decay in the system. (a) Pump present only, with its center at time zero ($t^*=0$). The build-up of $|B\rangle$ is of interest. (b) Pump and probe both present. The pump arrives at time zero, and the probe at a time delay, t, later. The detected signal is the final ($t^* \rightarrow \infty$) population of $|C\rangle$.

Fig. 3.18 The effect of the shape of the laser pulses in the unsaturated regime. The three-level model with no decay is considered (see Fig. 3.17). The pump and probe are considered to have the same shape and width, as given by f(t). (i) For δ-function pulses, the $|B\rangle$ state (see (a.i)) is populated instantaneously at time zero ($t^*=0$), and the signal observed by detecting the final ($t^* \rightarrow \infty$) population of $|C\rangle$ as a function of the time delay, t, is also a step function (see (b.i)). This signal

equals the molecular response function. (ii) For Gaussian pulses, the |B> population rises during the presence of the pump, reaching half its maximum value at time zero (see (a.ii)). The signal in (b.ii) shows the effect of both the pump and the probe in the rise. Half the maximum population is reached at zero delay (t=0), the point at which the center of the probe coincides with that of the pump (t*=0). (iii) A square pump pulse gives a linear rise of level |B> as seen in (a.iii). With the square probe pulse present, the |C> state signal detected (b.iii) shows a smoother rise (see text).

Fig. 3.19 The effect of the shape of the laser pulses in the unsaturated regime. The three-level model with a decay (k) of the middle state (|B>) is considered. The probe excites from |B> to |C> at a time delay t after the pump arrives (t*=0). The signal is the final ($t^* \rightarrow \infty$) population of |C>, and is a function of t. The signal is considered for three different types of cross-correlation, and, in each case, for three different values or ranges of k. (i) With δ-function pulses, the cross-correlation is also a δ-function and the signal becomes the molecular response function: a single exponential decay with rate k. (ii) Gaussian pump and probe pulses, each of width FWHM (= separation of small ticks), yield a Gaussian cross-correlation with $FWHM_{CC}=2^{1/2}FWHM$ (larger ticks). The signal is a convolution (see text) of the cross-correlation and the molecular response function. Note the signal value at t=0. (iii) Square laser pulses (each FWHM) give a triangular cross-correlation ($FWHM_{CC}=FWHM$), which when convoluted with the molecular response function yields the detected signal shown. The shapes of the signals are quite similar to those obtained with the Gaussian cross-correlation.

Fig. 3.20 The pump (peak at t*=0) and probe (peak at t*=t) are considered as being made up of infinitesimal square pulses or slices. A slice of width Δt_A at

$t^*=t_A$ in the pump pulse and a slice of width Δt_B at $t^*=t+t_B$ in the probe will contribute an amount $\Delta S(t, t_A, t_B)$ to the total signal, S(t), if the probe slice has a positive delay with respect to the pump, *i.e.*, $t+t_B-t_A \geq 0$. In the unsaturated regime, the total signal S(t) is the sum (or integration) of the contributions from all such pump-probe slice pairs. The signal then becomes a convolution of the pump-probe cross-correlation with the molecular response function (see text).

Fig. 3.21 Predicted transients for a transition state measurement. The molecular response function is a bi-exponential with a rise ($1/k_1$=50 fs) and decay ($1/k_2$=100 fs). Due to the finite pulse widths, the detected signal is that shown. The pump and probe pulse each has the same HWHM, and transients are shown for different values of this common width. Note the change in the signal height as the pulses become longer. For 75 fs, the peak height is 5.22×10^6; for 250 fs, 2.18×10^6; for 750 fs, 7.77×10^5; and for 5 ns, 1.18×10^2. The parameters used in this simulation are similar to those in ref. 3, except for the pulse widths.

Fig. 3.22 A Gaussian pump pulse (top) is used to excite a transition from $|A\rangle$ to $|B\rangle$ (inset). In the unsaturated regime (bottom), $F_{Pu} \ll 1$ and the final population of $|B\rangle$ is $F_{Pu}N$. The signal in the unsaturated regime reaches half its final value at time zero ($t^*=0$). When F_{Pu} is increased (e.g., by increasing the pump intensity, or if the absorption cross section is higher) to such an extent that $F_{Pu} \ll 1$ is no longer valid, then the transition is saturated (middle). The signal with F_{Pu}=0.2 grows to a final population of 0.165N (not 0.2N) and half this value is reached before time zero, at t^*=-0.0530 FWHM. The signal with F_{Pu}=1 reaches an asymptotic value of 0.432N, and half this value is attained already at t^*=-0.244 FWHM. The rise also becomes steeper with increase in F_{Pu}, *i.e.*, as the transition

becomes more saturated. In the limit of very severe saturation ($F_{Pu} >> 1$), the final value of n_B approaches 0.5N.

Fig. 3.23 (Top) Three level kinetic model with a decay (k) of the middle state, |B>, and detection of the uppermost state, |C>. Gaussian pulses are used. The probe transition is unsaturated ($F_{Pr}=10^{-4}<<1$). Two values are considered for the pump: (i) $F_{Pu}=1$ (saturation) and (ii) $F_{Pu}=10^{-4}$ (unsaturated). (Bottom) Normalized transients (left) for different decay rates, and pump power dependence (right) corresponding to each transient. (a) For k=0 with case (i), 0.5 is reached at time zero, and the whole transient is unsaturated, showing a linear power dependence, $M_{Pu}(t)=1$. For k=0 with case (ii), 0.5 is at t=-0.235 FWHM, and the rise is steeper. The signal is saturated even at negative time. Note the decrease in the power dependence: e.g., $m_{Pu}(0)=0.522$ and $m_{Pu}(5\ \text{FWHM})=0.311$. (b) For k=0.5/FWHM, (i) shows a transient with 0.5 at -0.214 FWHM, and (ii) is 0.195 FWHM earlier. The peaks are separated by 0.202 FWHM and for (i) the peak is at 0.763 FWHM. The power dependence is linear for (i), but not for (ii): 0.530 at t=0, 0.310 at 5 FWHM. (c) With k=10/FWHM, half maximum is at -0.618 FWHM for (i), and 0.123 FWHM earlier for (ii). The peaks are at (i) 0.097 FWHM and (ii) -0.033 FWHM. Case (i) shows a linear pump dependence. Case (ii) has less saturation than for (b) above at early times (e.g., $m_{Pu}(0)=0.559$) since fast k means low |B> population and hence low stimulated emission. However, there is more saturation later ($m_{Pu}(5\ \text{FWHM})=0.124$) as state |A> becomes depopulated.

Fig. 3.24 (Top) Three level kinetic model with ion detection. No stimulated emission from the ion, |C>, to the neutral state, |B>, exists, and it is possible to deplete |B> severely with an intense probe if the decay, k, is slow. The pump is

kept in the unsaturated regime. (Bottom) Normalized transients (left), and probe intensity dependence plots (right) for three values of k and with one of two values for the probe intensity: $F_{Pr}=10^{-4}$ (unsaturated) and 1 (saturated). Saturation shifts the rise of the transients to earlier time and steepens its slope. When the rise is 0.5, the shift here is 0.12 FWHM at k=0.1/FWHM, 0.09 FWHM at k=0.5/FWHM, and 0.01 FWHM at k=10/FWHM. At the peak, the shift changes from 0.10 to 0.08 to 0.004 x FWHM. The probe dependence plots show that for low and intermediate k, the saturation increases with time delay to a final value. For k=0, $m_{Pr}(0)=0.72$ and $m_{Pr}(5\ FWHM)=0.59$. For k=0.5/FWHM, $m_{Pr}(0)=0.75$ and $m_{Pr}(5\ FWHM)=0.64$. For a very fast decay there is very little saturation at all times (except some near time zero) as k competes effectively against the probing rate. The slight saturation near t=0 ($m_{Pr}(0)=0.93$ for $F_{Pr}=1$) occurs because this is when the probe is most effective.

Fig. 3.25 Three level kinetic model showing the effect of probe saturation on fluorescence detection. The pump transition is unsaturated. The pump and probe laser pulses have the same width, FWHM. Three different decay rates, k, are considered: slow (0.1/FWHM), intermediate (0.5/FWHM) and fast (10/FWHM). In each case transients are shown for (i) a saturated and (ii) an unsaturated probe transition. For the slow decay in the unsaturated regime, 0.5 is reached at -0.07 FWHM, and the peak at 1.21 FWHM. For the saturated transition these positions are each 0.23 FWHM earlier. The probe dependence is 1 in the unsaturated case, (ii), while it decreases in the saturated case, (i) ($m_{Pr}(0)=0.524$, $m_{Pr}(5\ FWHM)=0.311$). For the decay with intermediate rate, transient (ii) has 0.5 at -0.21 FWHM and the peak at 0.76 FWHM. The saturated transient, (i), is earlier by 0.20 FWHM at both 0.5 and the peak. For fast k, (ii) reaches 0.5 at -0.62 FWHM and 1 at 0.10 FWHM; for (i) these are 0.12 FWHM earlier. The probe dependence

plots for the unsaturated probe, (ii), show a linear dependence for all delays, independent of k. With saturation, (i), the intensity dependence decreases with time until a constant value is reached when the entire probe pulse arrives after the whole pump pulse. The saturation increases with faster k: $m_{Pr}(0)$ changes from 0.524 to 0.530 to 0.559, and m_{Pr}(5 FWHM) from 0.311 to 0.310 to 0.124.

Fig. 3.26 Kinetic model demonstrating the effect of probe saturation on fluorescence depletion experiments. The pump transition is kept unsaturated and it is assumed that the fluorescence rate, f, is slow. Both (a) and (b) yield the same depletion signal as a function of time delay, except in (a) the overall fluorescence yield is f/k of that in (b). Transients are shown for slow (k=0.5/FWHM) and fast (k=10/FWHM) decay rates and for unsaturated ($F_{Pr}=10^{-4}$) and saturated ($F_{Pr}=1$) probing. The pump and probe laser pulses have the same width, FWHM. For slow decay the shift in the saturated case is 0.20 FWHM to earlier time from the unsaturated position (0.5 at -0.21 FWHM). For the fast decay the shift is 0.12 to earlier time from the unsaturated transient which has 0.5 at -0.62 FWHM. The peak of the unsaturated transients are at 0.76 FWHM (slow) and 0.10 FWHM (fast). In the saturated case they are at 0.56 FWHM (slow) and -0.03 FWHM.

Fig. 3.27 Effect of pump saturation on a four level model. State $|B\rangle$, accessed by the pump, decays (k) to state $|C\rangle$ which is probed. The probe is kept unsaturated. The transients show a slight shift to earlier time with increased pump intensity. For k=10/FWHM the time at which 0.5 is reached is 0.10 FWHM with $F_{Pu}=10^{-4}$ and -0.02 FWHM with $F_{Pu}=1$. The pump intensity dependence, $m_{Pu}(t)$, plots show a linear response in the unsaturated regime ($F_{Pu}=10^{-4}$). With $F_{Pu}=1$, $m_{Pu}(t)$ decreases from 1 at very early delays to a final asymptotic value below 1 at long times. With k=0.5/FWHM, $m_{Pu}(0)=0.657$ and m_{Pu}(5

FWHM)=0.395; with k=10/FWHM these values become 0.705 and 0.561, respectively.

Fig. 3.28 The effect of probe saturation for a four level model with a decay (k) from the state excited to by the pump, |B>, to the state probed from, |C>. Significant shift of the transients to earlier time is seen as the probe intensity is raised. In going to F_{Pr}=1, for k=10/FWHM, the shift at 0.5 is 0.23 FWHM from a position of 0.095 FWHM with $F_{Pr}=10^{-4}$. With $F_{Pr}=10^{-4}$ the probe dependence plots yield constant straight lines: $m_{Pr}(t)=1$, reflecting the unsaturated regime. With F_{Pr}=1 severe saturation occurs: the asymptotic long time dependence is 0.311 in both cases (for k=0.5/FWHM this value is not yet reached at t=5 FWHM, where it is 0.320); at time zero, $m_{Pr}(0)$=0.632 for k=0.5/FWHM and 0.549 for k=10/FWHM (see text).

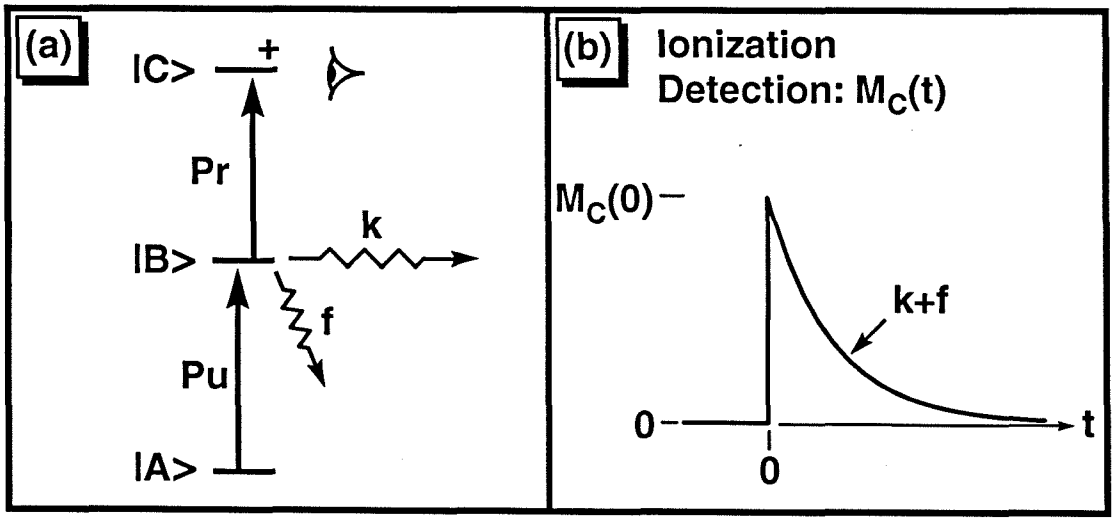

Fig. 3.1

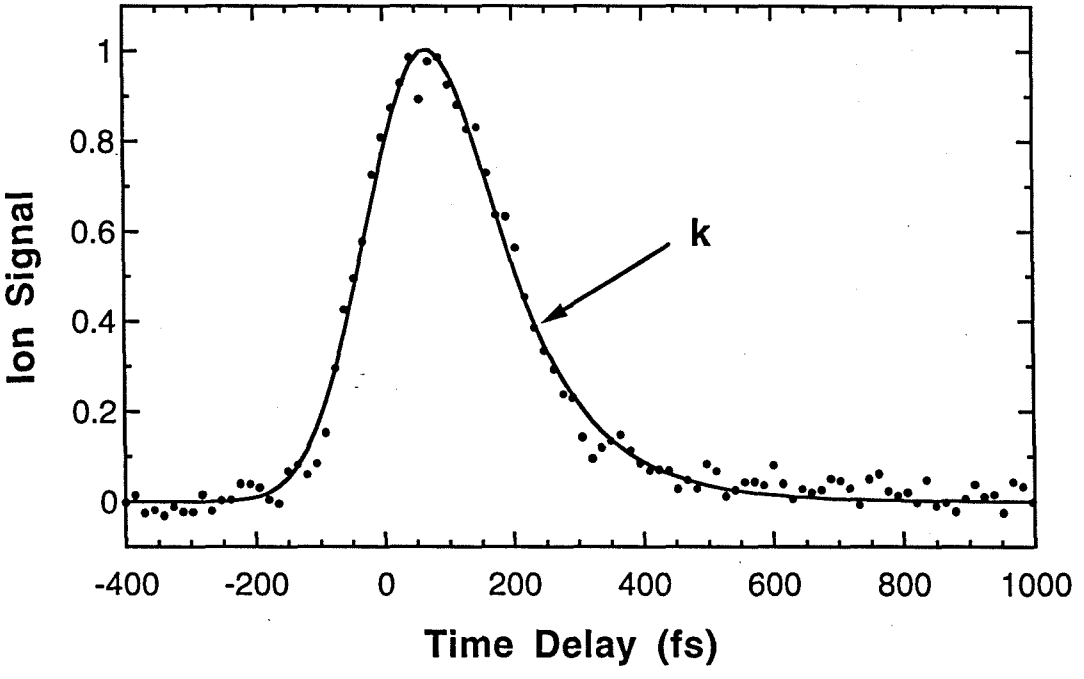
Ion Signal
1
0.8
0.6
0.4
0.2
0
k
-400
-200
0
200
400
600
800
1000
Time Delay (fs)

Fig. 3.2

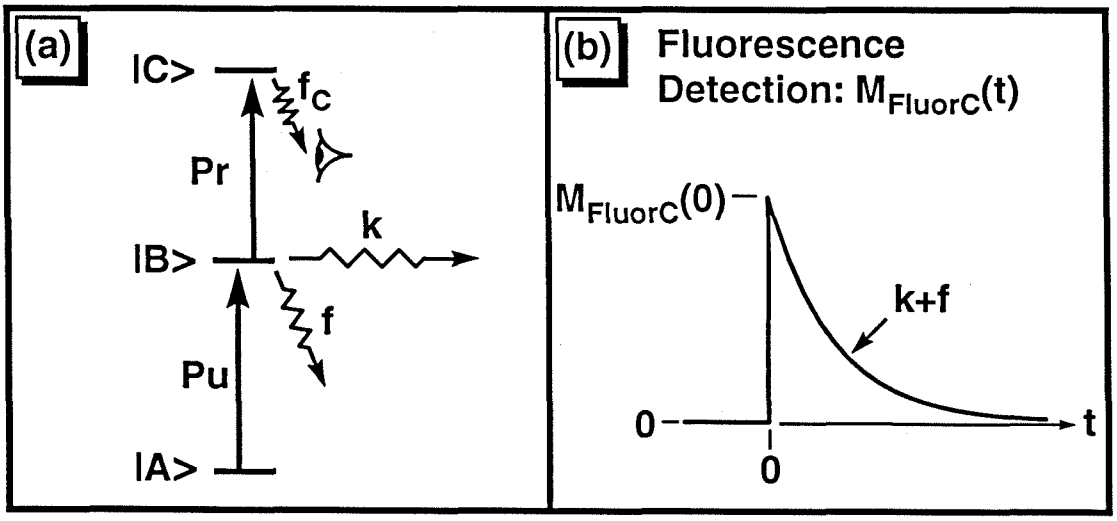
(a)
|C>
f_C
Pr
k
|B>
f
Pu
|A>
(b)
Fluorescence
Detection: $M_{FluorC}(t)$
$M_{FluorC}(0)$
k+f
0
t
0

Fig. 3.3

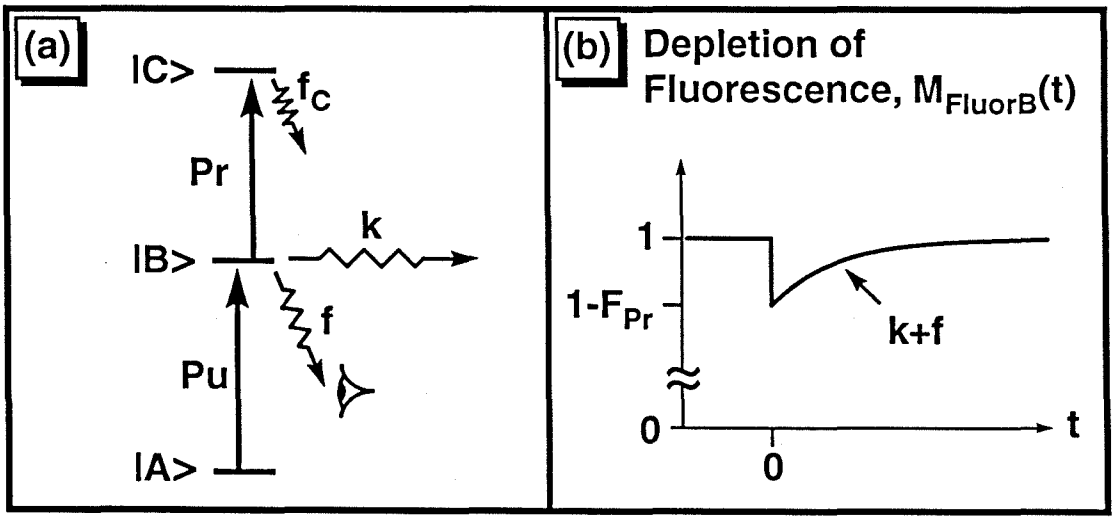
(a)
IC>
f_C
Pr
k
IB>
f
Pu
IA>
(b)
Depletion of
Fluorescence, $M_{FluorB}(t)$
1
$1-F_{Pr}$
k+f
0
t
0

Fig. 3.4

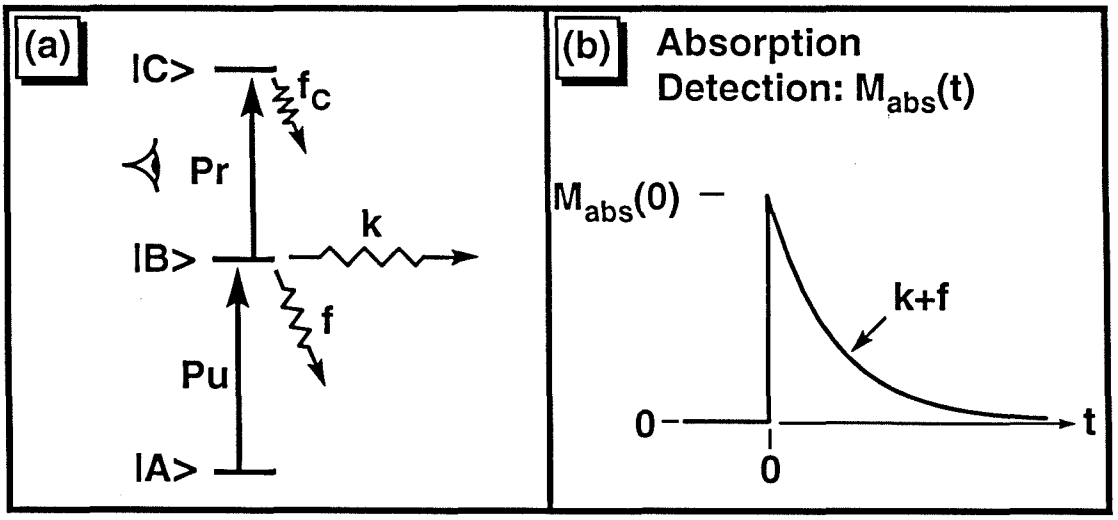

Fig. 3.5

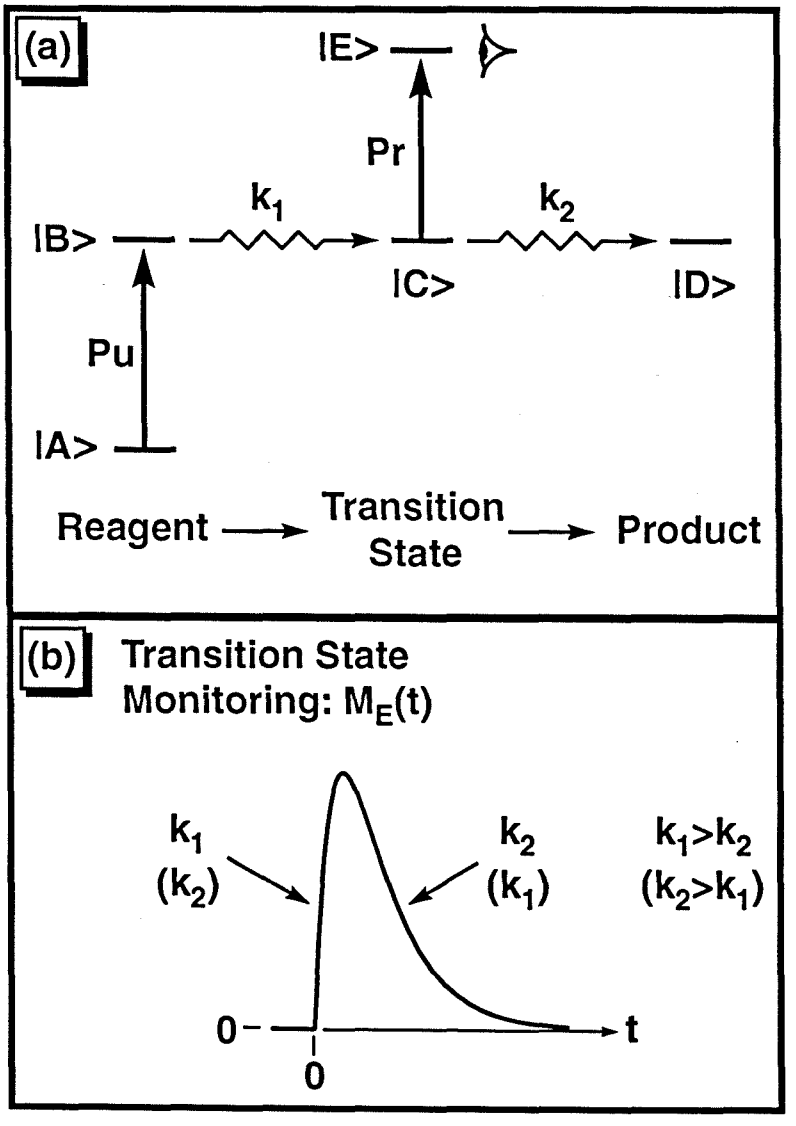
(a)
|E>
Pr
k1
k2
|B>
|C>
|D>
Pu
|A>
Reagent
Transition State
Product
(b)
Transition State Monitoring: ME(t)
k1 (k2)
k2 (k1)
k1>k2 (k2>k1)
0
t
0

Fig. 3.6

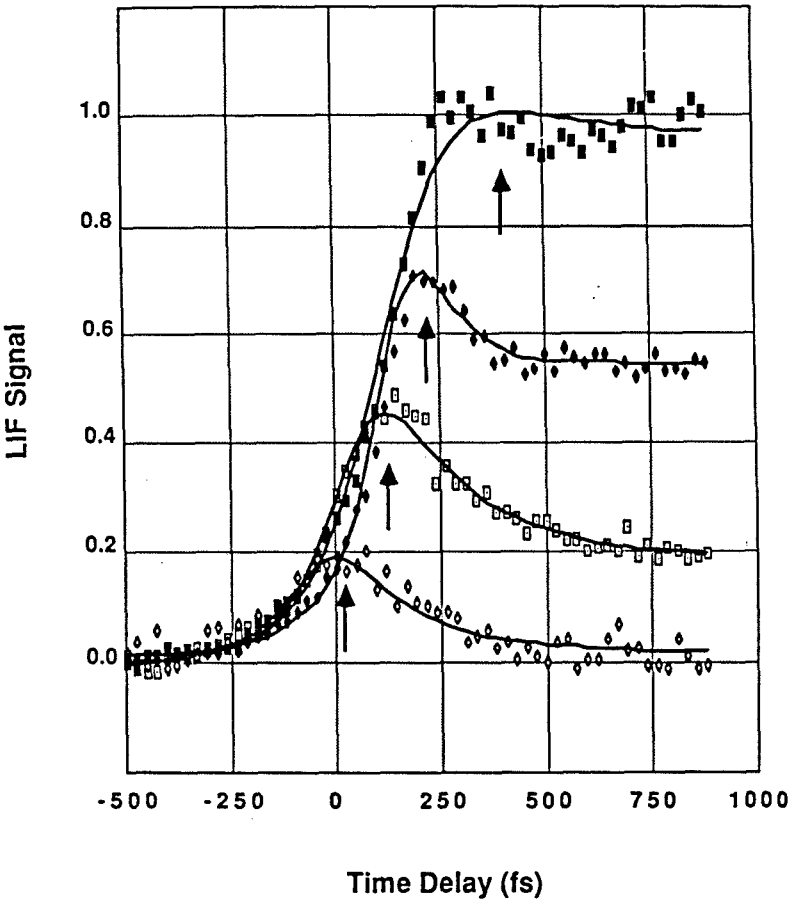
LIF Signal
1.0
0.8
0.6
0.4
0.2
0.0
-500
-250
0
250
500
750
1000
Time Delay (fs)

Fig. 3.7

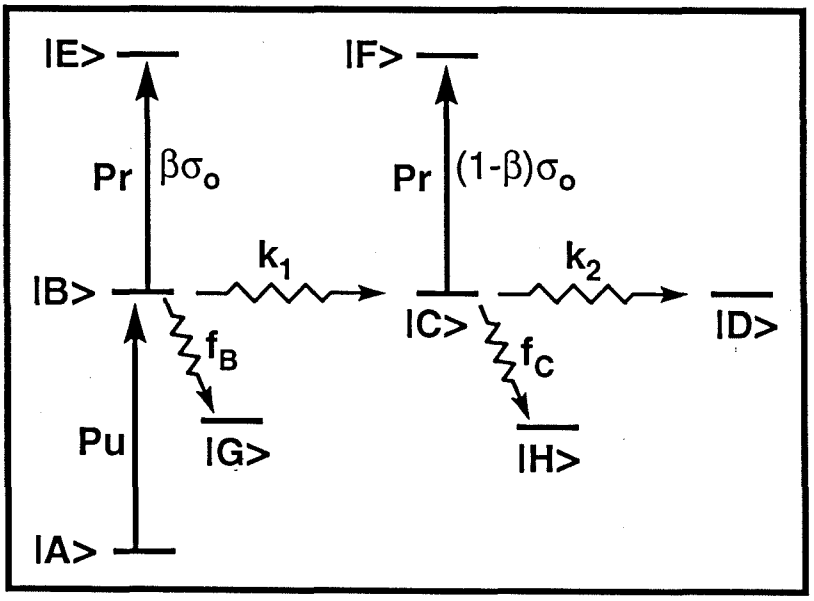

Fig. 3.8

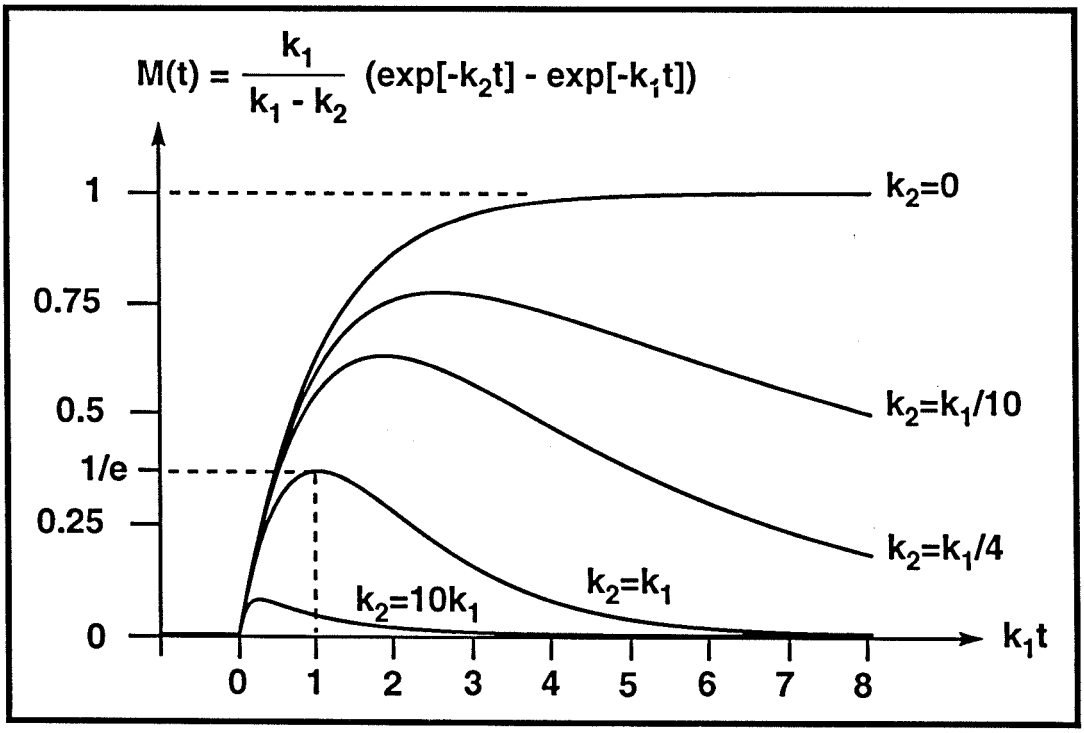
M(t) = k1 / (k1 - k2) (exp[-k2t] - exp[-k1t])
1
0.75
0.5
1/e
0.25
0
k2=0
k2=k1/10
k2=k1/4
k2=k1
k2=10k1
k1t
0 1 2 3 4 5 6 7 8

Fig. 3.9

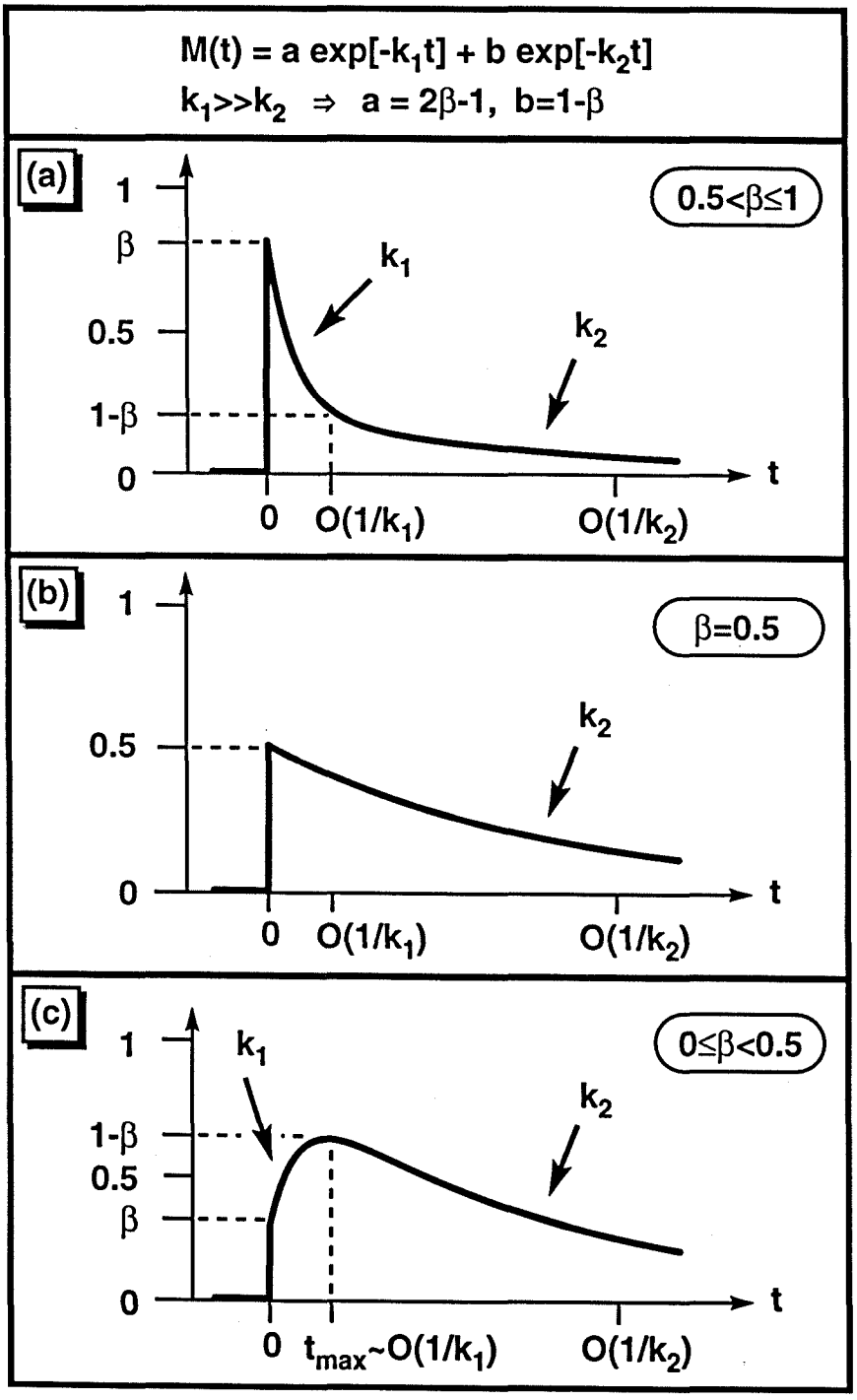
M(t) = a exp[-k1t] + b exp[-k2t]
k1>>k2 ⇒ a = 2β-1, b=1-β
(a)
0.5<β≤1
1
β
0.5
1-β
0
k1
k2
t
0
O(1/k1)
O(1/k2)
(b)
β=0.5
1
0.5
0
k2
t
0
O(1/k1)
O(1/k2)
(c)
0≤β<0.5
1
k1
k2
1-β
0.5
β
0
t
0
tmax~O(1/k1)
O(1/k2)

Fig. 3.10

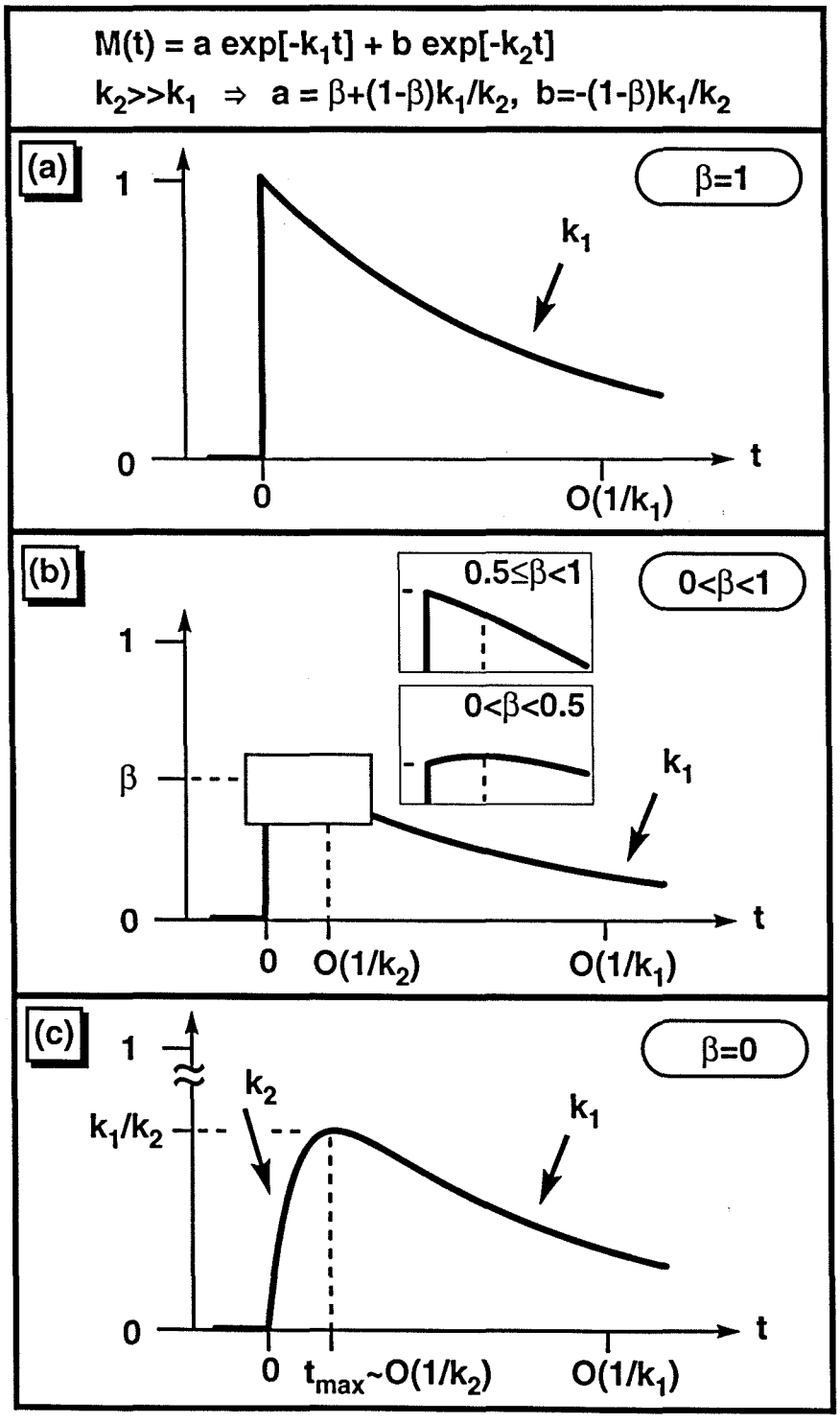
M(t) = a exp[-k1t] + b exp[-k2t]
k2>>k1 ⇒ a = β+(1-β)k1/k2, b=-(1-β)k1/k2
(a)
β=1
1
k1
0
t
0
O(1/k1)
(b)
0<β<1
0.5≤β<1
0<β<0.5
1
β
k1
0
t
0
O(1/k2)
O(1/k1)
(c)
β=0
1
k2
k1
k1/k2
0
t
0
tmax~O(1/k2)
O(1/k1)

Fig. 3.11

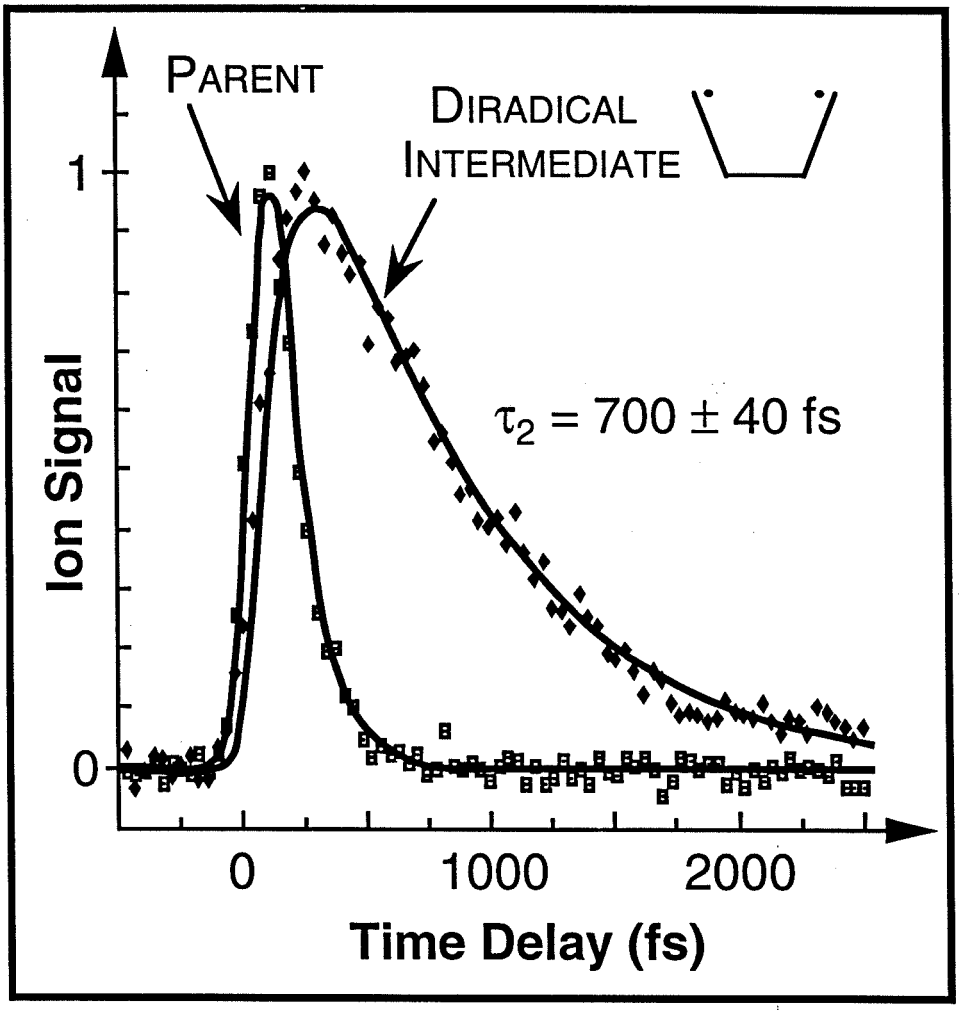
PARENT
DIRADICAL
INTERMEDIATE
$\tau_2 = 700 \pm 40$ fs
Ion Signal
1
0
0
1000
2000
Time Delay (fs)

Fig. 3.12

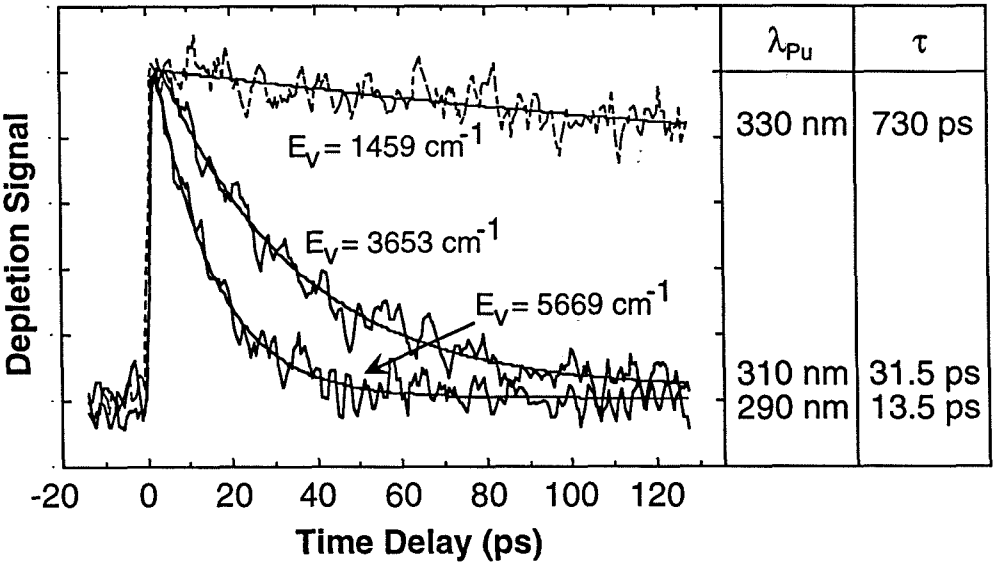
Depletion Signal
-20
0
20
40
60
80
100
120
Time Delay (ps)
E_V = 1459 cm^{-1}
E_V = 3653 cm^{-1}
E_V = 5669 cm^{-1}
λ_{Pu}
τ
330 nm
730 ps
310 nm
31.5 ps
290 nm
13.5 ps

Fig. 3.13

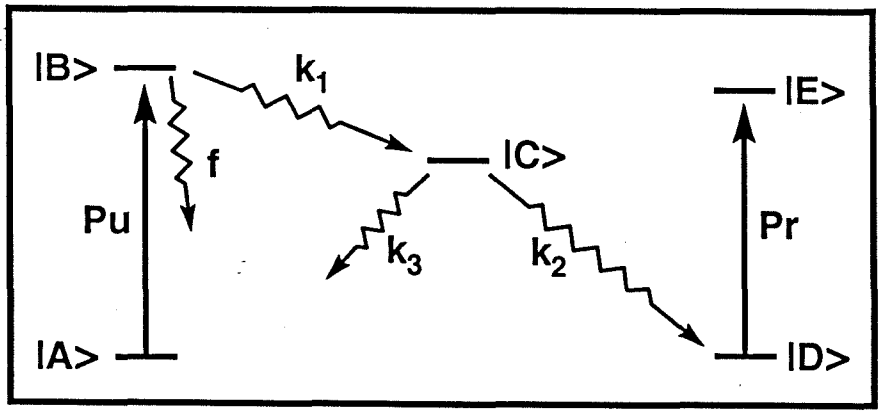

Fig. 3.14

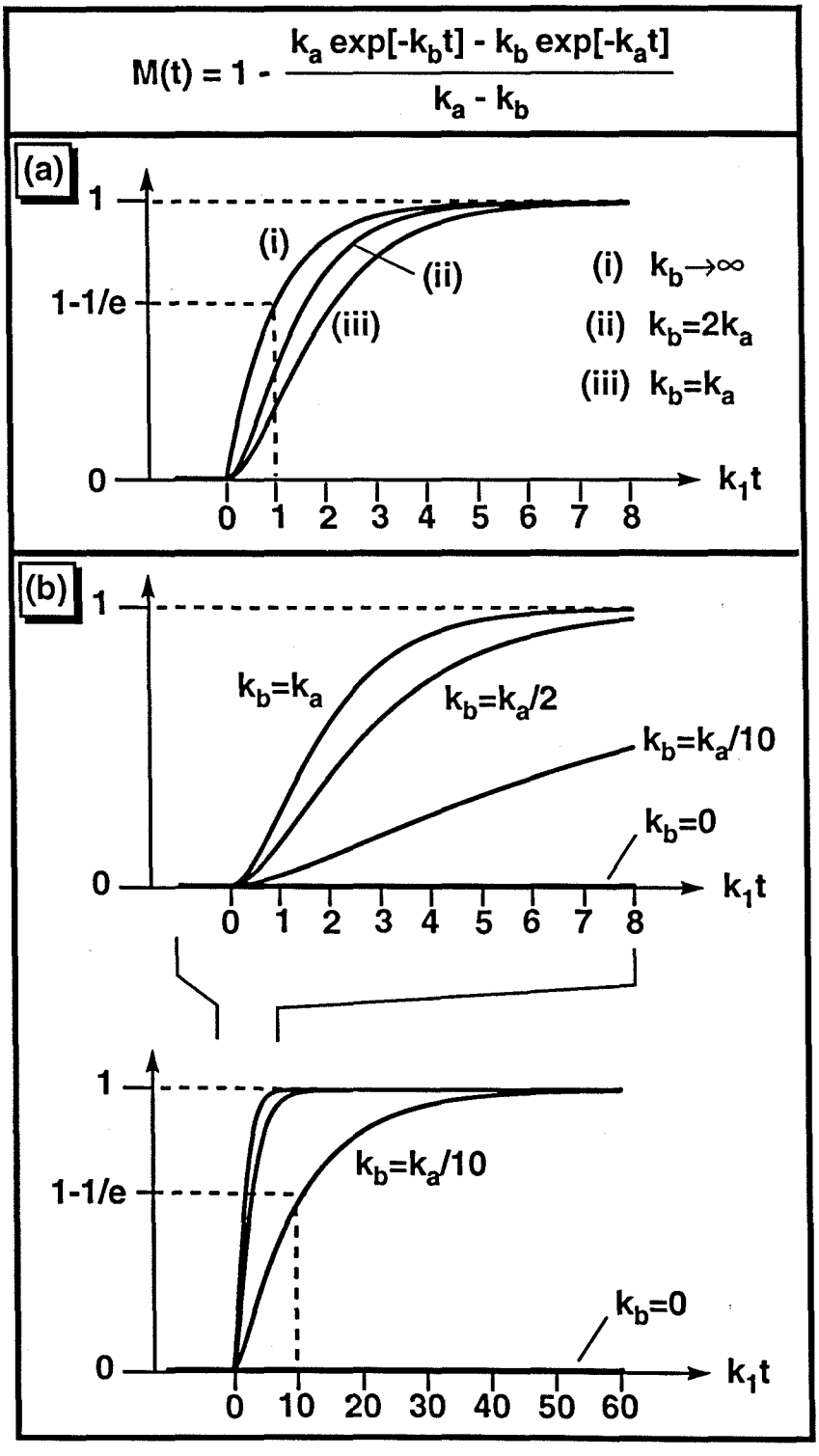
M(t) = 1 - (k_a exp[-k_b t] - k_b exp[-k_a t]) / (k_a - k_b)
(a)
1
1-1/e
0
(i)
(ii)
(iii)
(i) k_b→∞
(ii) k_b=2k_a
(iii) k_b=k_a
k_1t
0 1 2 3 4 5 6 7 8
(b)
1
0
k_b=k_a
k_b=k_a/2
k_b=k_a/10
k_b=0
k_1t
0 1 2 3 4 5 6 7 8
1
1-1/e
0
k_b=k_a/10
k_b=0
k_1t
0 10 20 30 40 50 60

Fig. 3.15

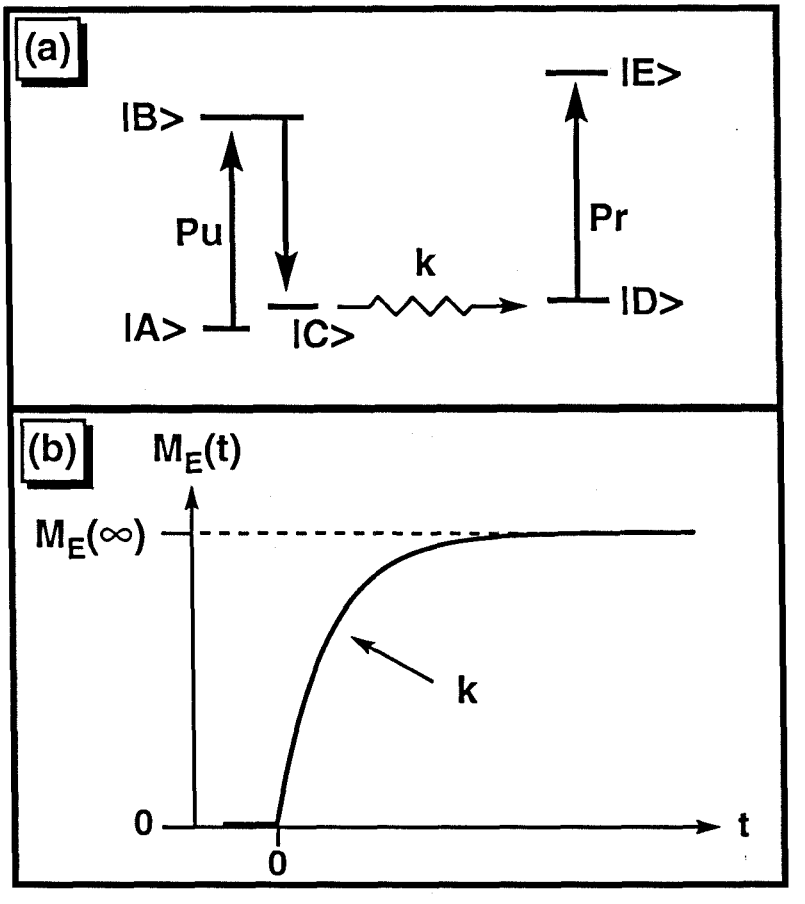

Fig. 3.16

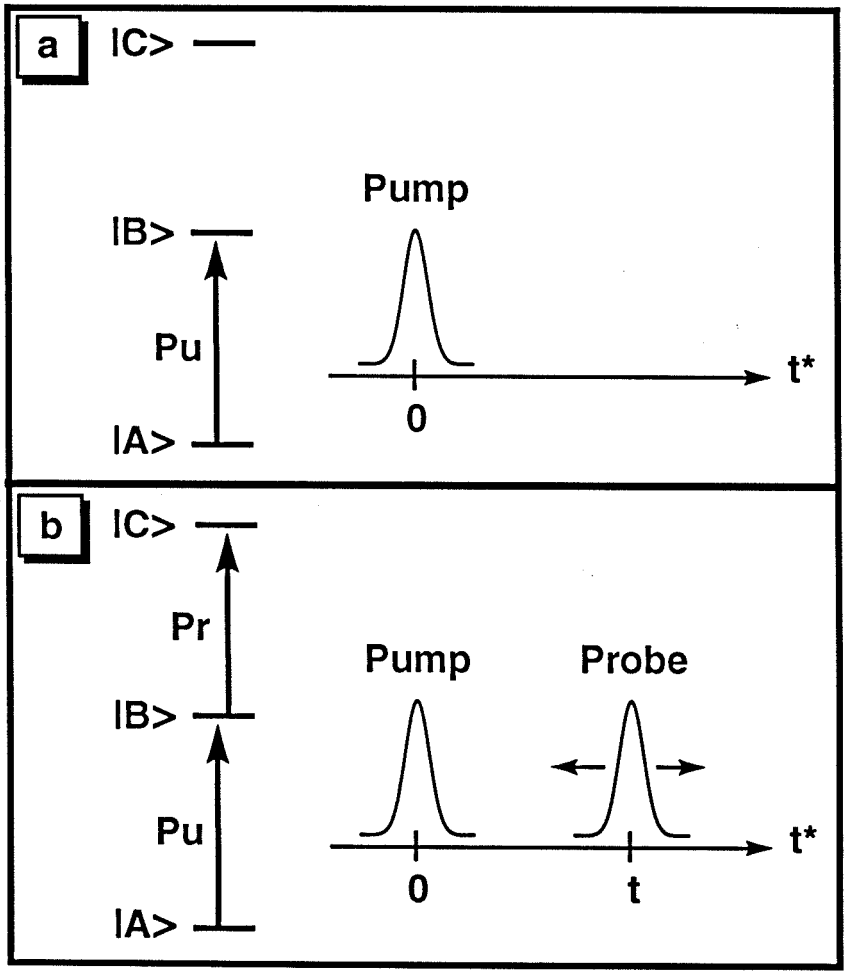

Fig. 3.17

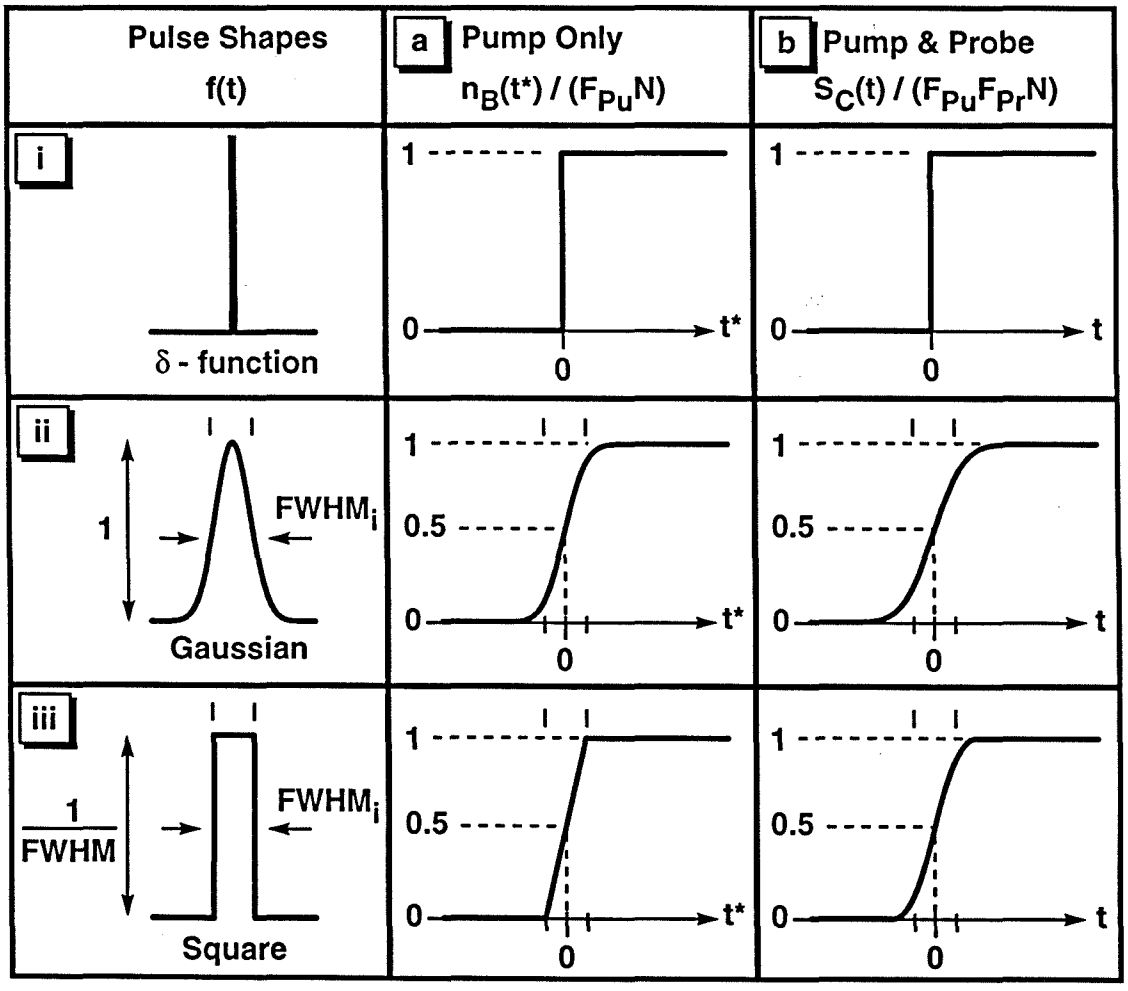
Pulse Shapes
f(t)
a Pump Only
$n_B(t^*) / (F_{Pu}N)$
b Pump & Probe
$S_C(t) / (F_{Pu}F_{Pr}N)$
i
δ - function
ii
1
FWHM$_i$
Gaussian
iii
$\frac{1}{FWHM}$
FWHM$_i$
Square
1
0.5
0
t*
t
0

Fig. 3.18

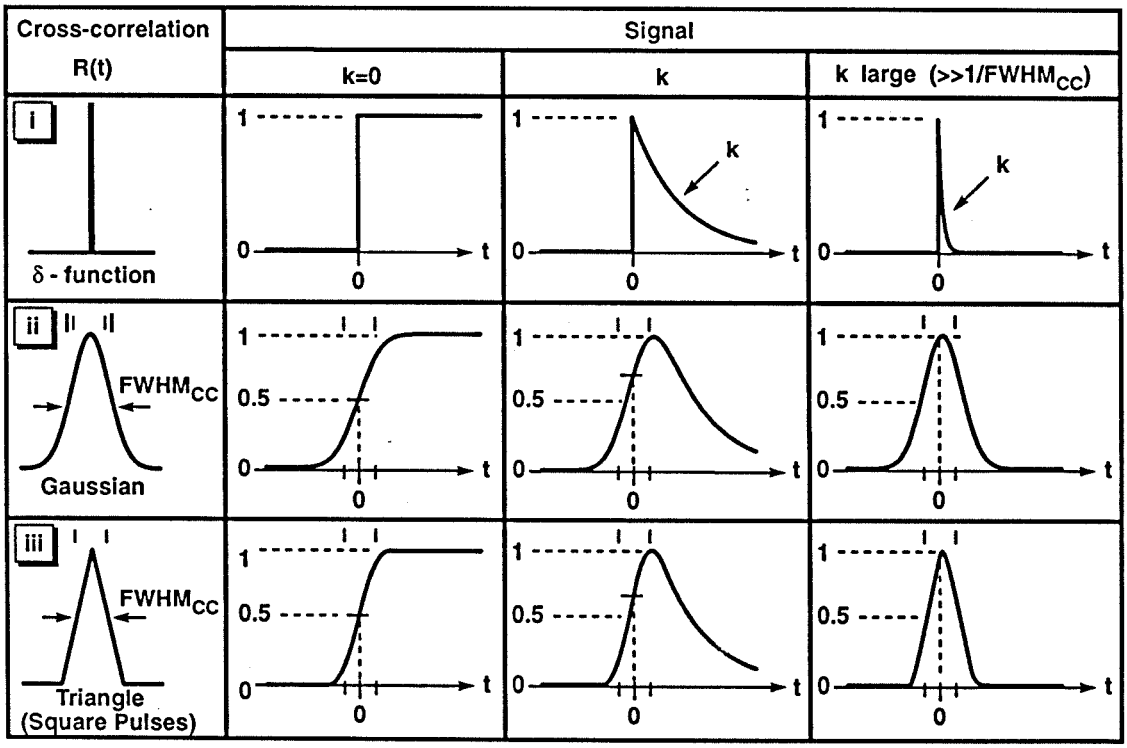
Cross-correlation R(t)
Signal
k=0
k
k large (>>1/FWHMCC)
i
δ - function
ii
FWHMCC
Gaussian
iii
FWHMCC
Triangle (Square Pulses)
1
0.5
0
t
k

Fig. 3.19

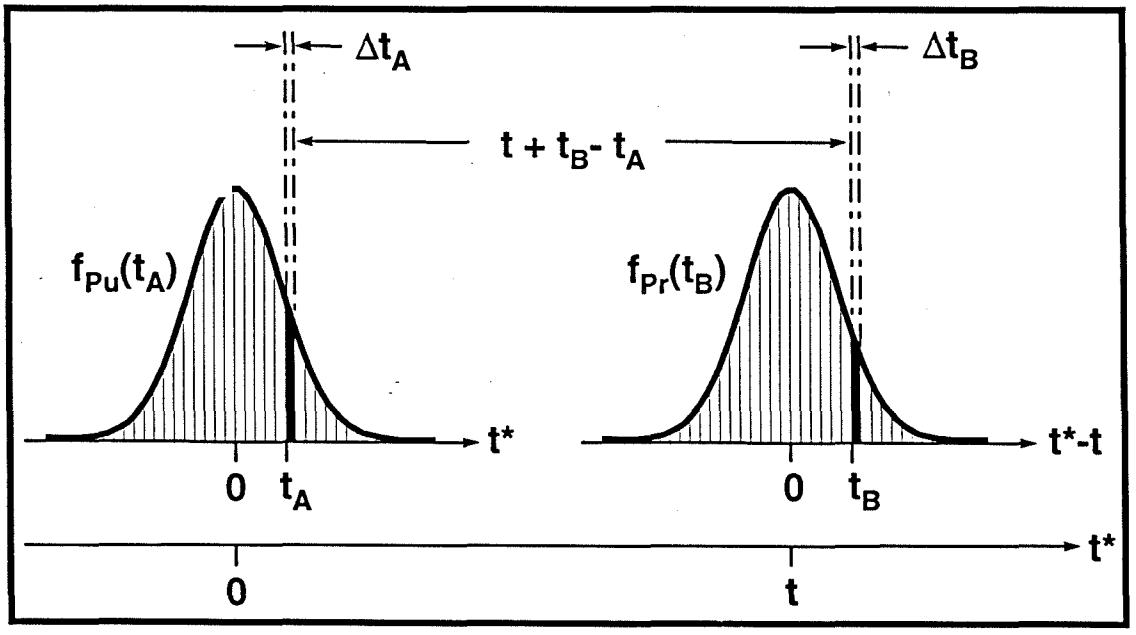

Fig. 3.20

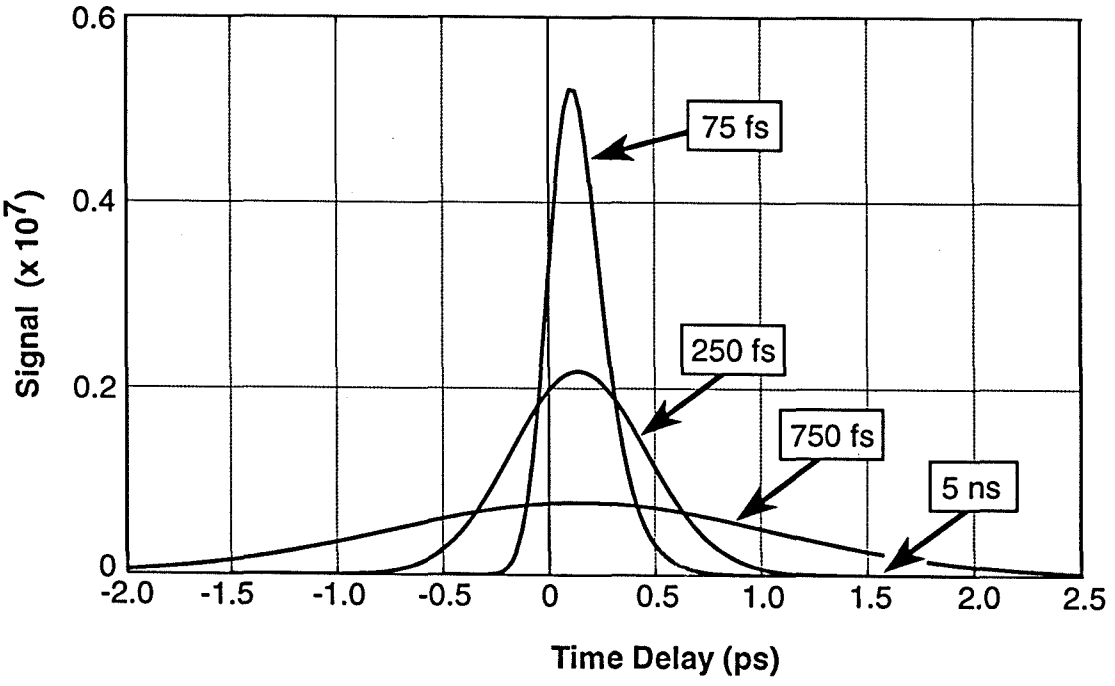
0.6
0.4
0.2
0
Signal (x 10^7)
75 fs
250 fs
750 fs
5 ns
-2.0
-1.5
-1.0
-0.5
0
0.5
1.0
1.5
2.0
2.5
Time Delay (ps)

Fig. 3.21

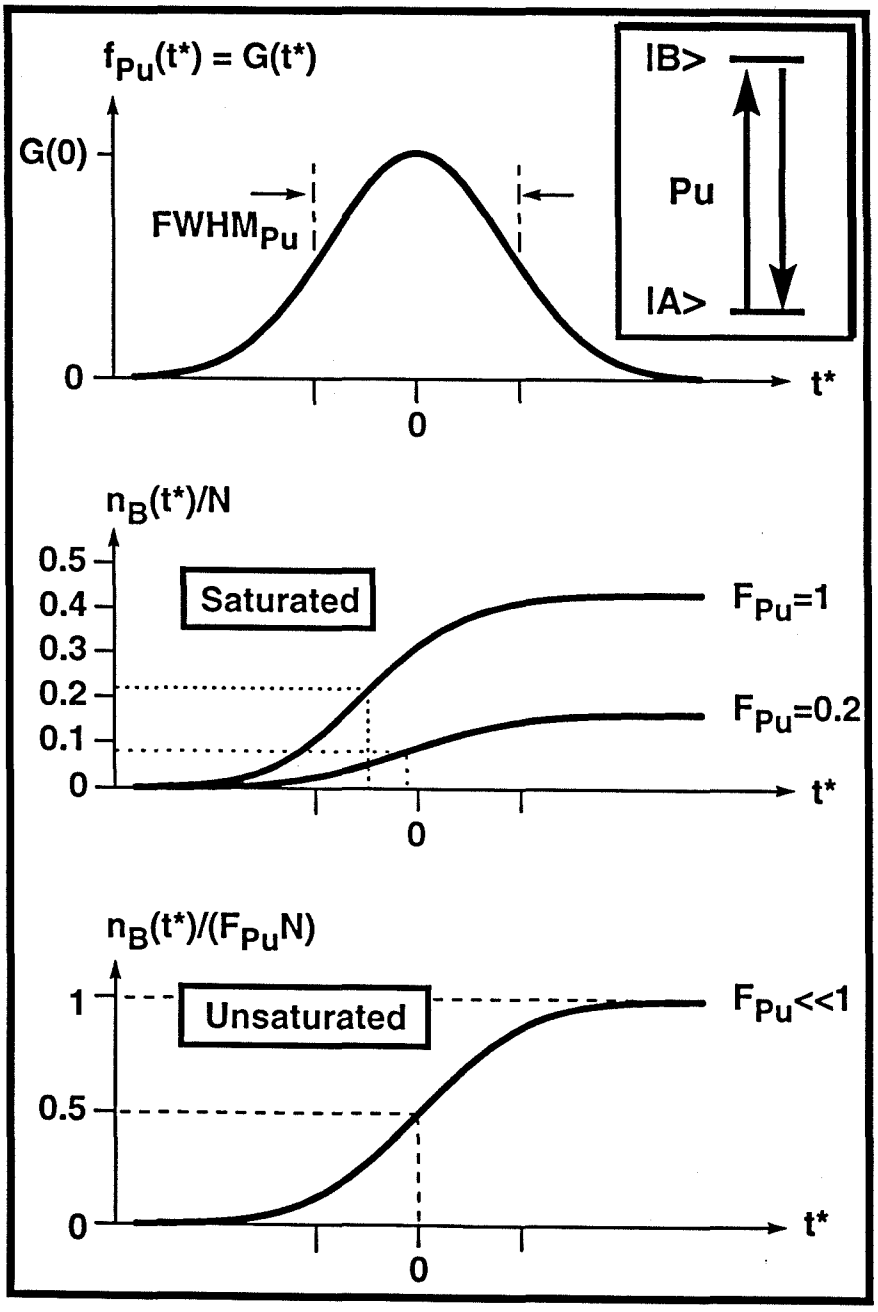
$f_{Pu}(t^*) = G(t^*)$
G(0)
0
$FWHM_{Pu}$
0
t*
|B>
Pu
|A>
$n_B(t^*)/N$
0.5
0.4
0.3
0.2
0.1
0
Saturated
F_{Pu}=1
F_{Pu}=0.2
0
t*
$n_B(t^*)/(F_{Pu}N)$
1
0.5
0
Unsaturated
F_{Pu}<<1
0
t*

Fig. 3.22

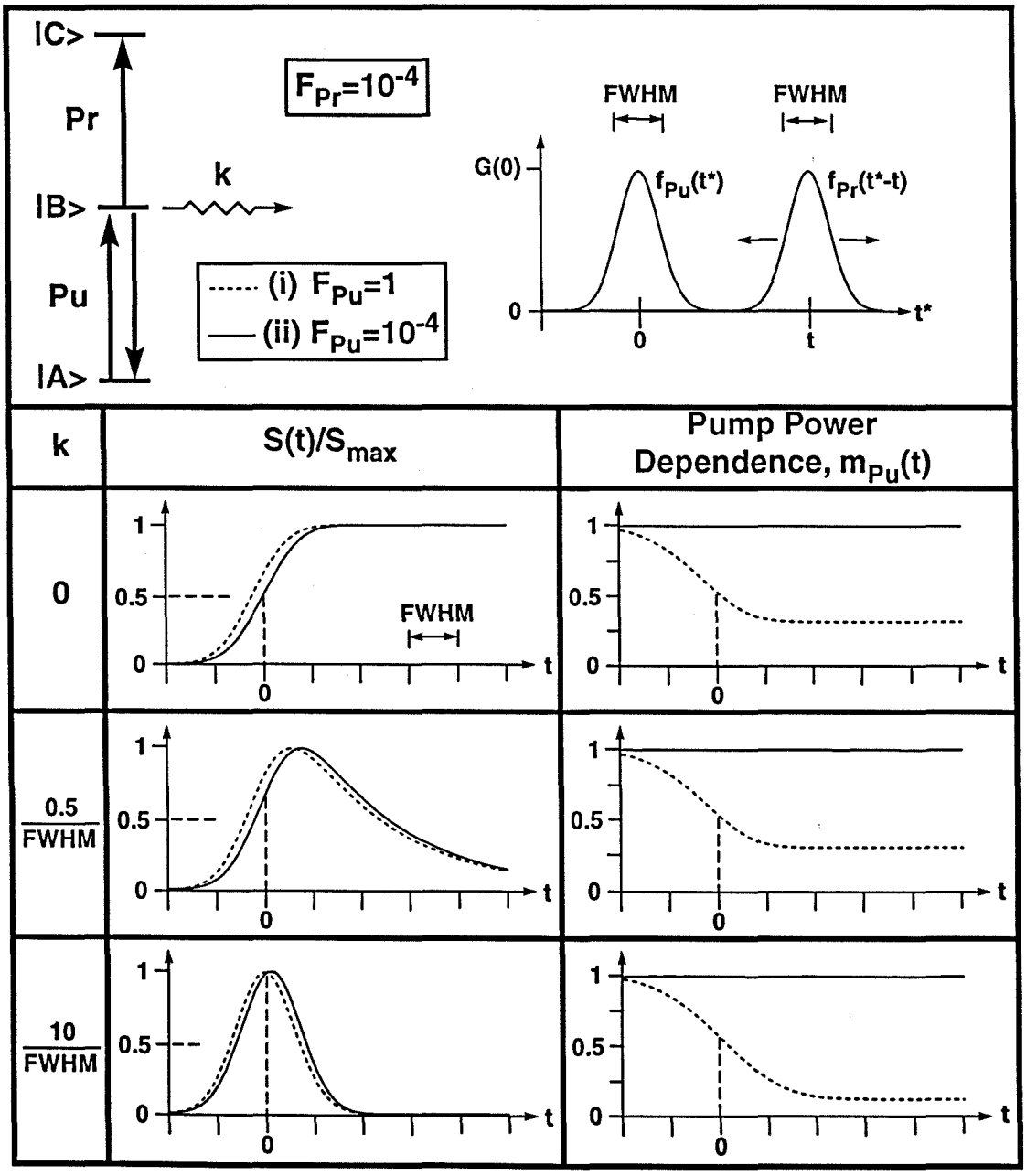
|C>
Pr
|B>
Pu
|A>
k
$F_{Pr}=10^{-4}$
(i) $F_{Pu}=1$
(ii) $F_{Pu}=10^{-4}$
FWHM
FWHM
G(0)
$f_{Pu}(t^*)$
$f_{Pr}(t^*-t)$
0
t*
0
t
k
$S(t)/S_{max}$
Pump Power Dependence, $m_{Pu}(t)$
0
0.5 FWHM
10 FWHM
1
0.5
0
t

Fig. 3.23

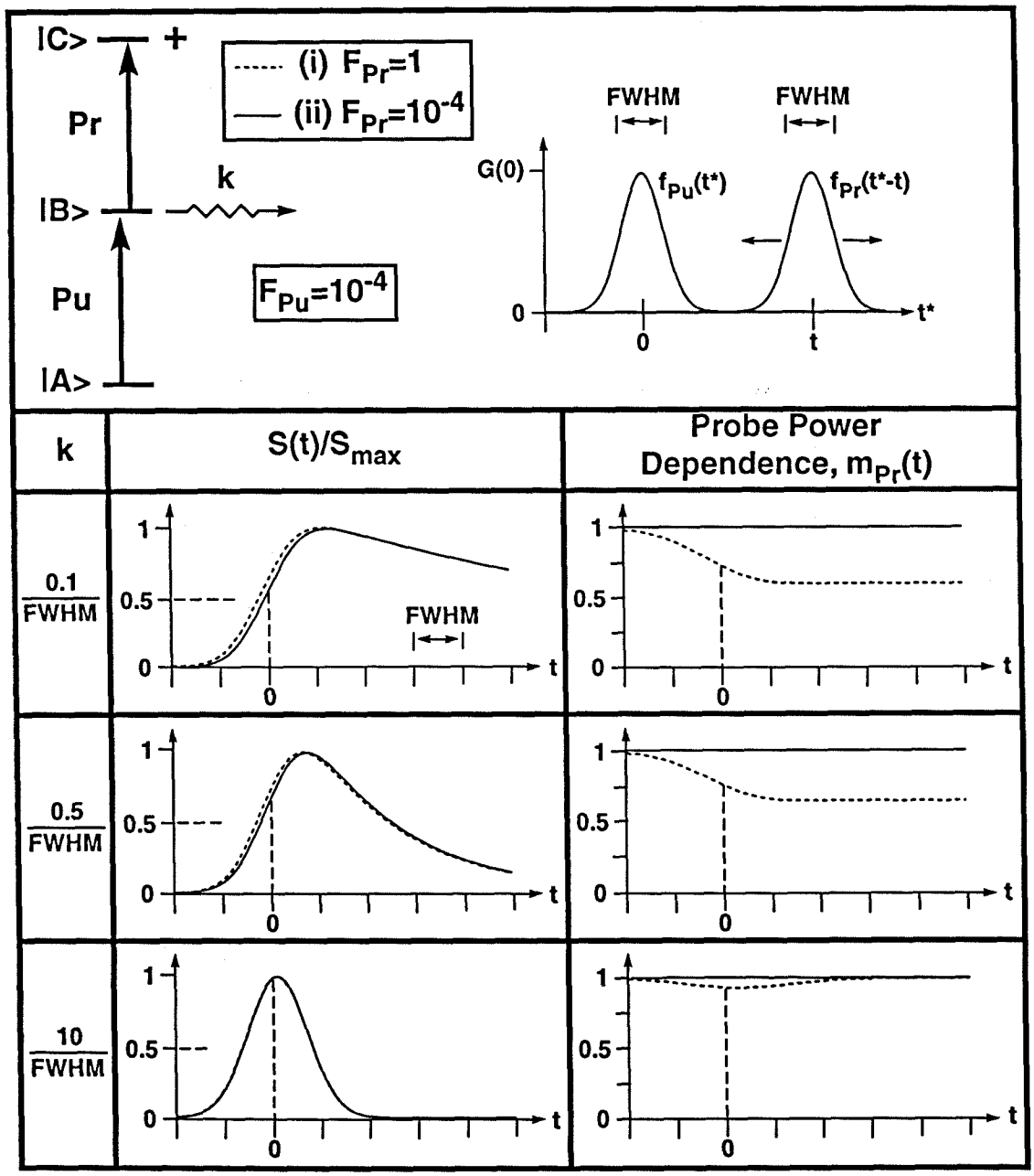
|C>
+
Pr
|B>
Pu
|A>
k
(i) F_{Pr}=1
(ii) F_{Pr}=10^{-4}
F_{Pu}=10^{-4}
FWHM
FWHM
G(0)
$f_{Pu}(t^*)$
$f_{Pr}(t^*-t)$
0
t*
0
t
k
S(t)/S_{max}
Probe Power Dependence, $m_{Pr}(t)$
0.1/FWHM
0.5/FWHM
10/FWHM
1
0.5
0
t
FWHM

Fig. 3.24

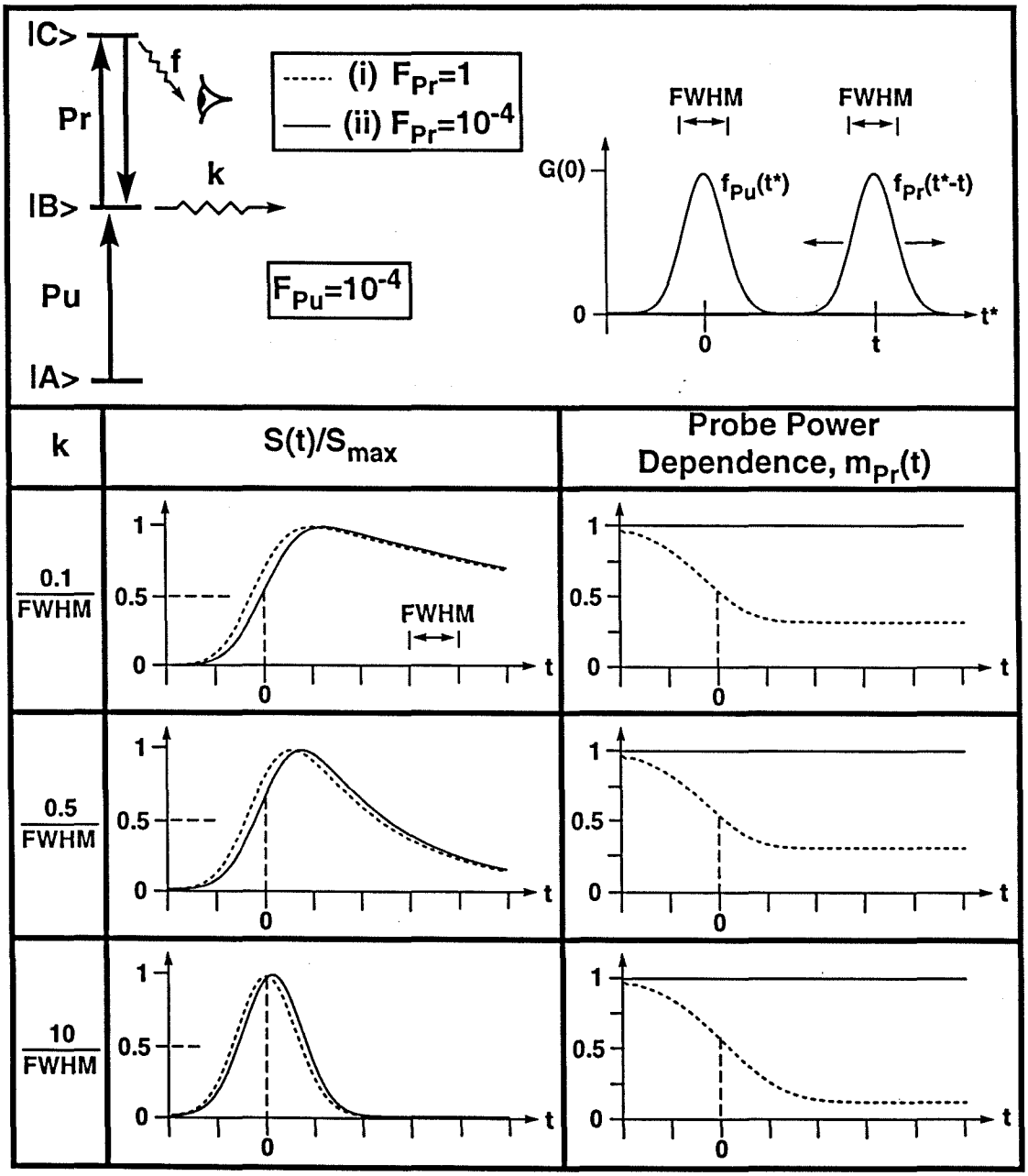
|C>
f
Pr
|B>
k
Pu
|A>
(i) F_{Pr}=1
(ii) F_{Pr}=10^{-4}
F_{Pu}=10^{-4}
FWHM
FWHM
G(0)
$f_{Pu}(t^*)$
$f_{Pr}(t^*-t)$
0
t*
0
t
k
S(t)/S_{max}
Probe Power Dependence, $m_{Pr}(t)$
0.1 / FWHM
0.5 / FWHM
10 / FWHM
1
0.5
0
t
FWHM
0

Fig. 3.25

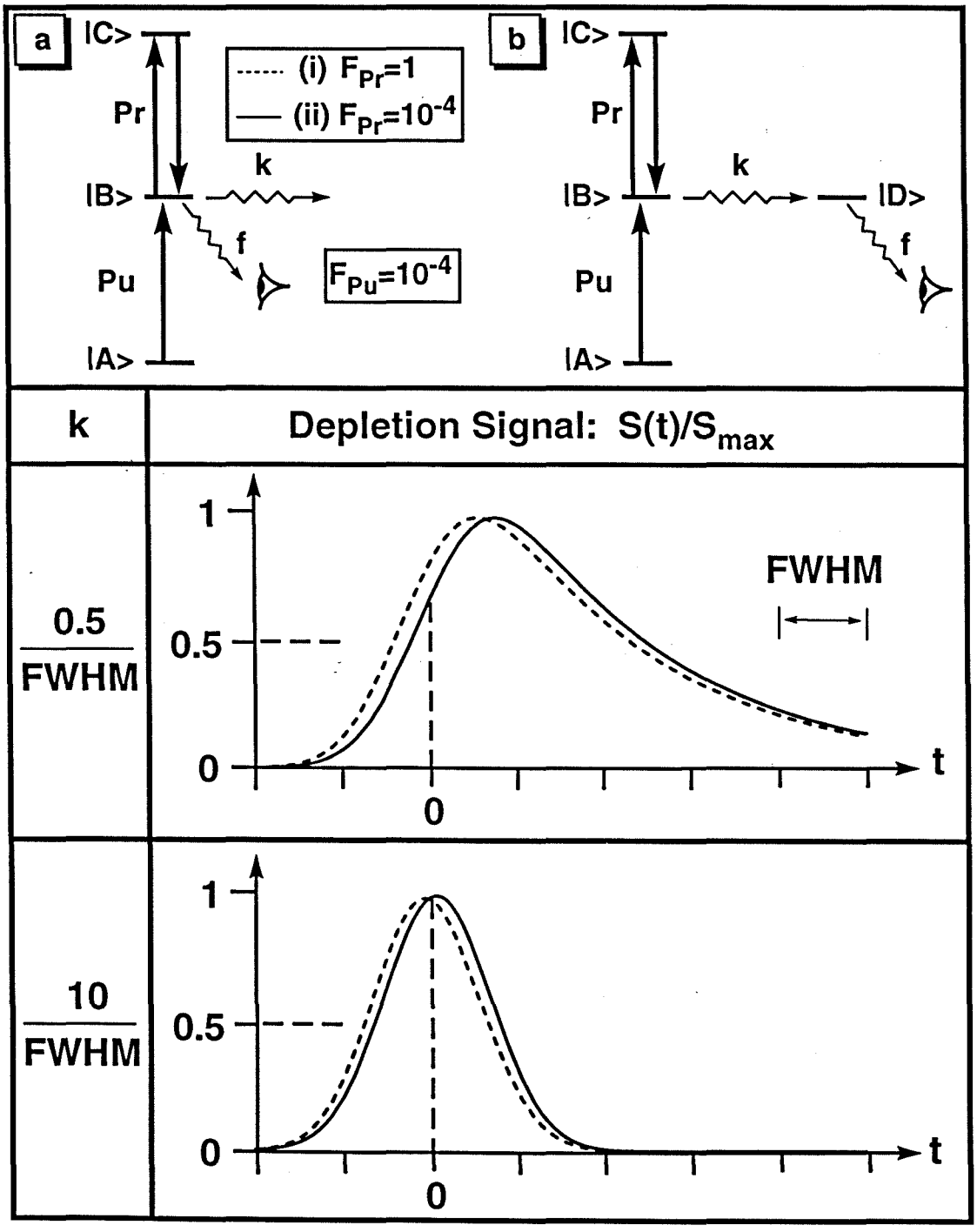
a
|C>
Pr
|B>
Pu
|A>
k
f
(i) F_{Pr}=1
(ii) F_{Pr}=10^{-4}
F_{Pu}=10^{-4}
b
|C>
Pr
|B>
Pu
|A>
k
|D>
f
k
Depletion Signal: $S(t)/S_{max}$
0.5 / FWHM
1
0.5
0
0
t
FWHM
10 / FWHM
1
0.5
0
0
t

Fig. 3.26

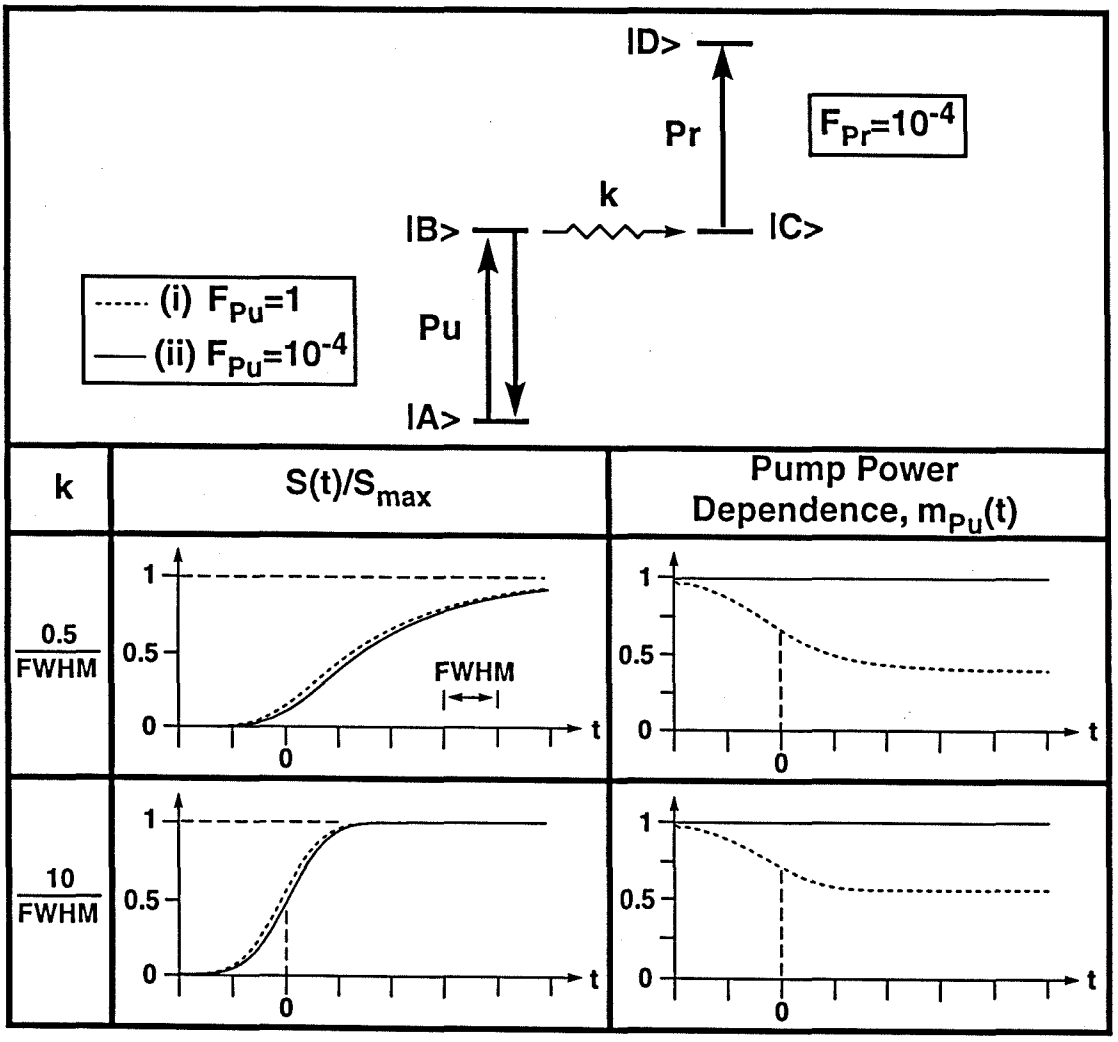
|D>
Pr
$F_{Pr}=10^{-4}$
k
|B>
|C>
Pu
|A>
(i) $F_{Pu}=1$
(ii) $F_{Pu}=10^{-4}$
k
$S(t)/S_{max}$
Pump Power Dependence, $m_{Pu}(t)$
0.5/FWHM
10/FWHM
FWHM
1
0.5
0
t
0

Fig. 3.27

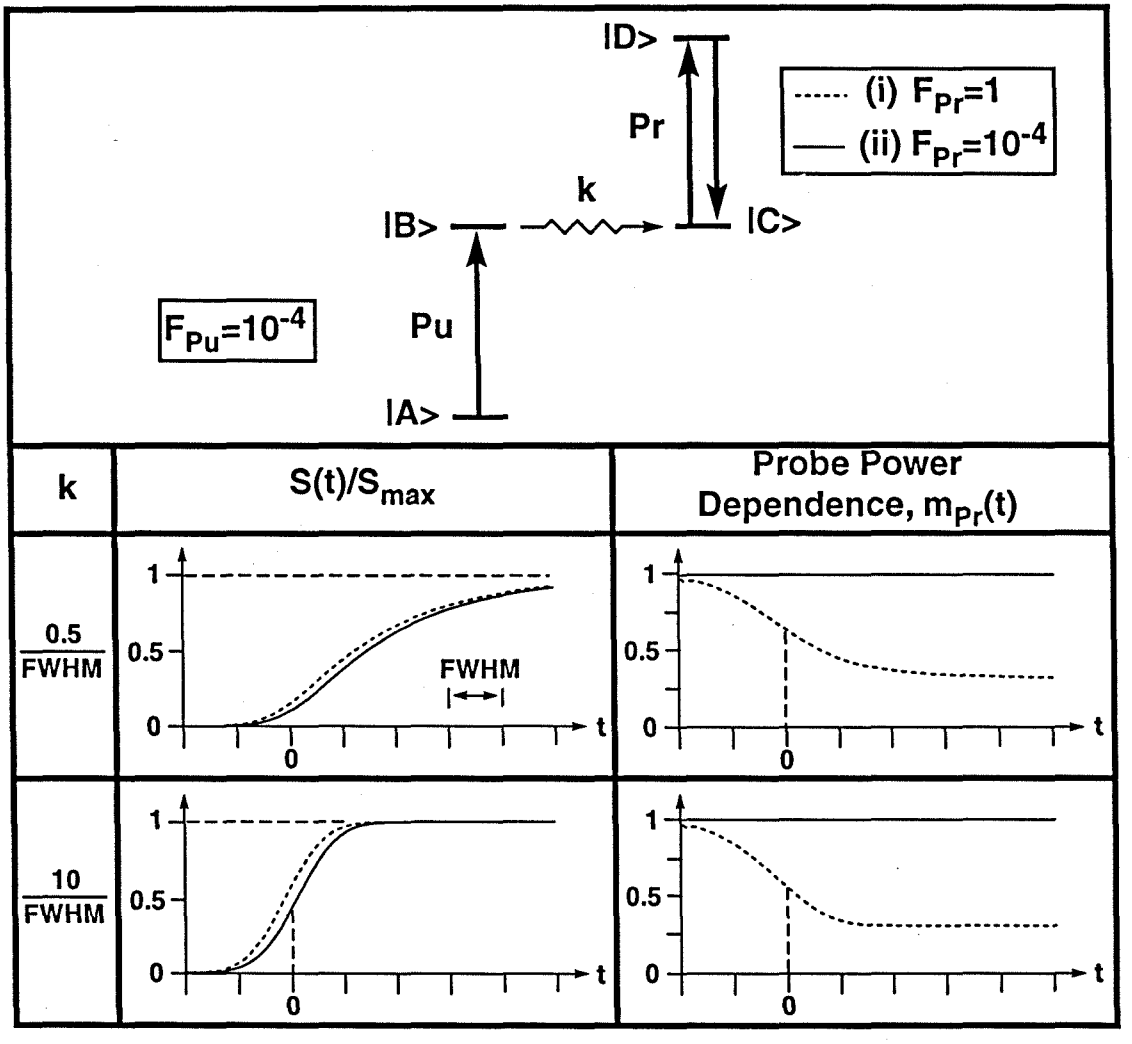
|D>
Pr
(i) F_{Pr}=1
(ii) F_{Pr}=10^{-4}
k
|B>
|C>
F_{Pu}=10^{-4}
Pu
|A>
k
S(t)/S_{max}
Probe Power Dependence, m_{Pr}(t)
0.5/FWHM
10/FWHM
FWHM
1
0.5
0
t

Fig. 3.28

Chapter 4

Investigating Ultrafast Dynamics via Multiphoton Ionization (MPI)

Molecular beam chemistry[1, 2, 3] and photofragment spectroscopy[4, 5, 6, 7] have contributed significantly to the observation of chemical reactions.[8, 9] In femtosecond transition-state spectroscopy (FTS), several detection schemes may be used: LIF,[10, 11, 12, 13] absorption,[14] mass spectrometry with MPI-TOF detection,[15, 16, 17, 18] photoelectron[19, 20] kinetic energy[21] and ZEKE spectroscopy,[22, 23] stimulated emission pumping,[24] and fs degenerate four wave-mixing (DFWM) (see chapter six). The use of supersonic beams in our group has been particularly fruitful (see p. 6 of ref. 15). The emphasis of this chapter is on mass spectrometry with MPI-TOF detection and how it can be used in femtosecond experiments. A comparison to LIF detection is also provided.

4.1 Mass Spectrometry and Time-of-Flight (TOF)

4.1.1 Experimental Considerations and Basic TOF Formulae

A good account of the early development and history of mass spectrometry is given in ref. 25, and sources of technical descriptions of molecular beams and mass spectrometry are refs. 26, 27, 28. Fig. 4.1 shows a simple TOF mass spectrometer. Ions are generated in an acceleration region. Many different ion sources exist,[29, 30] but the interest here is the generation of ions using fs lasers in pump-probe type experiments. Much of the discussion here holds for other sources as well. The initial part of this section deals with the motion of ions in the TOF tube. Later, effects of their generation and initial conditions are described. In a pump-probe experiment where the probe produces the ions, the zero position in the TOF spectrum corresponds to the time of arrival of the probe laser pulse.

Assuming the ions are initially at rest, all ions are accelerated to the same final kinetic energy (given by the work done by the constant electric field: force x distance),

$$U_1 = q\,E\,x_1, \tag{4.1}$$

before leaving the acceleration region and entering the field-free drift region (see Fig. 4.1). As $U_1=\frac{1}{2}mv^2$, the velocity of an ion of mass m in the field-free region is

$$v = \sqrt{\frac{2U_1}{m}}. \tag{4.2}$$

The time spent in this region at this constant velocity is therefore

$$t_2 = x_2/v = x_2\sqrt{\frac{m}{2U_1}}. \tag{4.3}$$

The time spent in the acceleration region (a=F/m = qE/m) is given by

$$t_1 = v/a \tag{4.4a}$$

$$= \frac{\sqrt{2mU_1}}{qE} \tag{4.4b}$$

$$= x_1\sqrt{\frac{2m}{U_1}}. \tag{4.4c}$$

The total time-of-flight is then

$$T = t_1 + t_2 \tag{4.5a}$$

$$= \left(x_1\sqrt{\frac{2}{U_1}} + x_2\sqrt{\frac{1}{2U_1}}\right)\sqrt{m} \tag{4.5b}$$

$$\propto \sqrt{m}, \tag{4.5c}$$

i.e., it is proportional to the square root of the mass of the ion. Heavier ions will therefore be more closely spaced in the TOF spectrum.

The capability of a mass spectrometer to differentiate masses is usually given in terms of its resolution defined by

$$R = \frac{m}{\Delta m} \tag{4.6}$$

where Δm is the mass difference between two adjacent peaks in the TOF spectrum that are just resolved and m is the mass corresponding to the first of the

two peaks (sometimes the mean mass of the two peaks is used instead). Two peaks are considered to be separated if the valley between them is no more than some percentage of their height (often 10%). For example, a spectrometer with a resolution of 5000 would resolve peaks occurring at m/q=500.0 and 500.1 (or 50.00 and 50.01). Commercial spectrometers usually vary from R=500 to 50000 and typical TOF times are 1 to ~1000 μs.

The mass resolution, R, is determined by:

(i) Definition of T=0 (ion formation):

- pulsed electron impact ionization: ms - μs;
- flash lamp ionization: ms - ns;
- ns laser ionization: 1 ns - 20 ns;
- ps and fs laser ionization: ps and fs, respectively.

For our fs laser pulses this is an almost negligible uncertainty in the time-of-flight, T. Even though the TOF display is not triggered by the probe, the fs - ps pump-probe delay times do not influence the definition of T=0.

(ii) Initial spatial distribution:

This effect, discussed later in section 4.1.2, is governed by the radius of the region ionized, e.g., for the focal region of our lasers it may be 40 μm.

(iii) Initial velocity (kinetic energy) distribution along TOF direction.

- thermal distribution of the neutrals: a cold molecular beam is better than an effusive source from a high temperature oven;
- kinetic energy release from neutral and/or ion fragmentation. The anisotropic velocity distribution created by the pump pulse and affected by the relative polarization of the probe is covered in detail in chapter five and ref. 16 (see Appendix F). The experimental effects and opportunities this offers are explained briefly in sections 4.1.3 and 4.2.2. The effect of ion fragmentation is discussed later in section 4.1.4.

- space charge effect. The (positive) ions repel each other when close together. This is a problem also encountered in the generation of ultrashort electron pulses where it leads to a broadening of the pulse duration over time[31] and a trade-off between temporal resolution and electron pulse density.[32]

4.1.2 Correction for Initial Spatial Distribution

The limitations due to electronics, ion detector response and space charge effects will not be expanded upon here. The effect of (ii) is to give the ions that are initially further away from the exit of the acceleration region more kinetic energy when they enter the field-free drift region (see Fig. 4.2). This figure illustrates how at some point in the drift region (the space focus) they (b) will catch up with and overtake the ions (a) of the same mass that started above them. It would therefore be best to place the detector at this point. The condition for space focusing is

$$\frac{dT}{dx_1} = 0, \tag{4.7}$$

i.e.,

$$\frac{d}{dx_1}(t_1 + t_2) = 0 \tag{4.8}$$

and using (4.3) and (4.4c) this reduces to

$$\frac{x_2}{x_1} = 2, \tag{4.9}$$

which is independent of m and E. However, it means the free drift region becomes too short to separate different masses. This led to the introduction of the two-stage time-of-flight mass spectrometer of Wiley and McLaren[33] shown in Fig. 4.3. This is the type used in our experiments as illustrated in Fig. 2.4 and shown very detailed on p. 8 of ref. 15. The idea is that a second acceleration stage is introduced between the first stage and the field-free drift region and with an appropriate choice of x_1, x_2, x_3 and the ratio of the electric fields, E_2/E_1, (see Fig.

4.3) it is possible to position the space focus exactly at the detector. The initial spatial distribution may thus be counterbalanced and the finite laser diameter will not influence the arrival time, which is still proportional to $\sqrt{m}$. Detailed calculations and numerical examples using typical parameters are provided in ref. 33. In the discussion below it will be assumed the ions are initially at rest when produced and the calculations simplify.

The time to travel from the initial position to the end of the first acceleration stage is

$$t_1 = x_1\sqrt{2m}\left(\frac{1}{\sqrt{U_1}}\right), \tag{4.10}$$

i.e., the same as (4.4c) and U_1 is given by (4.1). The time taken to pass through the second stage is

$$t_2 = x_2\sqrt{2m}\left(\frac{\sqrt{U}-\sqrt{U_1}}{U_2}\right) \tag{4.11}$$

where

$$U = U_1+U_2 \tag{4.12}$$

and $$U_2 = q\,x_2\,E_2. \tag{4.13}$$

To cross the field-free region requires a time, t_3, where

$$t_3 = x_3\sqrt{\frac{m}{2}}\left(\frac{1}{\sqrt{U}}\right), \tag{4.14}$$

which of course is of the same form as equation (4.3).

The total time is therefore given by

$$T = t_1 + t_2 + t_3 \tag{4.15}$$

$$\propto \sqrt{m}. \tag{4.16}$$

Space focusing occurs where (4.7) is satisfied. The following are required and derived using the definitions above:

$$\frac{dt_1}{dx_1} = \sqrt{\frac{m}{2qE_1}}\frac{1}{\sqrt{x_1}}; \tag{4.17}$$

$$\frac{dt_2}{dx_1} = -\sqrt{\frac{m}{2qE_1}}\left(\frac{E_2}{E_1}\right)^{-1}\left[\frac{1}{\sqrt{x_1}} - \frac{1}{\sqrt{x_1 + x_2(E_2/E_1)}}\right]; \tag{4.18}$$

$$\frac{dt_3}{dx_1} = -\sqrt{\frac{m}{2qE_1}}\left[\frac{x_3}{2(x_1 + x_2(E_2/E_1))^{3/2}}\right]. \tag{4.19}$$

Hence (4.15) implies

$$\frac{dT}{dx_1} = \sqrt{\frac{m}{2qE_1}}\, f(x_1, x_2, x_3, \frac{E_2}{E_1}) \tag{4.20}$$

where

$$f(x_1, x_2, x_3, \frac{E_2}{E_1}) = \frac{1}{\sqrt{x_1}} - \left(\frac{E_2}{E_1}\right)^{-1}\left[\frac{1}{\sqrt{x_1}} - \frac{1}{\sqrt{x_1 + x_2(E_2/E_1)}}\right] - \left[\frac{x_3}{2(x_1 + x_2(E_2/E_1))^{3/2}}\right]. \tag{4.21}$$

Space focusing then occurs when

$$f(x_1, x_2, x_3, \frac{E_2}{E_1}) = 0. \tag{4.22}$$

For our TOF tube, x_2=1.27 cm, x_3=26.7 cm, and positioning the lasers at the center of the first acceleration stage gives x_1=0.635 cm. The space focus then occurs at our detector when

$$E_2/E_1 = 3.822. \tag{4.23}$$

Our plates in the two stages are equally spaced ($d=x_2=2x_1$) and condition (4.23) may be expressed in terms of the applied (positive) voltages (see Fig. 4.3):

$$\frac{(V_2 - 0)/d}{(V_1 - V_2)/d} = 3.822, \tag{4.24a}$$

i.e.,

$$\frac{V_2}{V_1 - V_2} = 3.822, \tag{4.24b}$$

or

$$V_1/V_2 = 1.262. \tag{4.24c}$$

This is the required voltage ratio that should be used at all times. So, for example: V_2=1000 V and V_1=1262 V would satisfy the space focusing condition for our TOF tube. It is the fact that our drift-free region (x_3) is quite short that gives the low ratio in (4.23). If this region had been 1 m long then the ratio would have been 9.24. This is closer to what a lot of systems have (10 - 30). The advantage of a

short tube is that the X-Y deflection plate voltages (see p. 8 of ref. 15) may be kept low or are even not needed if the focus of the lasers is slightly displaced horizontally to the left in Fig. 4.3 to balance the horizontal velocity of the molecular beam.

4.1.3 Effect of Initial Fragment Velocity Distribution

The distribution in initial velocity may be corrected for using a reflectron TOF mass spectrometer, first introduced by Mamyrin *et al.*[34, 35] The idea is to compensate for the difference in times-of-flight by using a system of electrostatic fields which result in focusing of the ion packets in space and time at the detector entrance plane. Ions of higher velocity will require a longer turn-around time as they penetrate further into this system of electrostatic fields before reversing and traveling to the detector. For a certain ratio setting of the electric field strengths, the time-of-flight is independent of the initial velocity, v_i, for the detection of a particular mass:

$$\frac{dT}{dv_i} = 0. \tag{4.25}$$

As we have a Wiley-McLaren TOF mass spectrometer and not a reflectron, an initial velocity distribution will lead to a spread in the arrival time at a mass peak in our TOF spectrum. However, this may be used to great advantage. Fig. 4.4 illustrates how the width of the profile in the TOF can be used to determine the kinetic energy of the most energetic ions released along (up and down) the TOF direction. The formulae are derived in section 5.4 and in ref. 16. Fig. 4.5 gives an idea of how the TOF profile (or equivalently, the velocity projection onto the TOF axis) is affected by the initial anisotropic velocity distribution. The TOF spectrum shows a splitting or two peaks for one mass corresponding to these ions initially traveling straight up (1) and arriving early, or straight down (2) and

trailing behind at the detector by the turn-around time in the first acceleration stage. If instead the ions were initially confined to traveling mainly horizontally before swinging up, they would arrive centered about a peak time and any width of the profile would be due to some initial vertical velocity component. The width only reflects the kinetic energy associated with the maximum initial vertical velocity. However, the extremes of the distribution almost always correspond to ions that have traveled at maximum speed either straight up or down and therefore the profile width gives the total maximum kinetic energy release possible to this ion mass.

Chapter five gives a full account of how the orientation of the pump and probe laser polarizations, the TOF direction, and the pump and probe dipole moments and transitions (parallel *vs.* perpendicular) influence the velocity (and hence TOF) profile. In that chapter, a discussion is provided of existing theory for the probing of free fragments. For transition-state probing, a new theory is provided that is in agreement with experimental observations.[16] For the latter case, the basic ideas are quite intuitive. Fig. 4.6 shows the relative orientations. Suppose the pump polarization is vertical, just like the TOF direction. For a parallel pump transition, the neutral parts (not yet fragments as they are still part of the transition-state molecule) will separate primarily along the polarization direction, *i.e.*, up and down. Supposing the probe transition is parallel (see chapter five) and choosing the probe polarization to be vertical too, this will enhance the sharpness of the distribution, favoring the excitation of the neutral molecules that exhibit fragmentation along the TOF axis. If the dissociation to form the ion mass is prompt (fs, *i.e.*, no time for rotation), then the ions will travel either up or down, resulting in the splitting indicated in Fig. 4.4 and observed experimentally[16] as shown in Fig. 4.7. If the probe polarization were turned to be

perpendicular to that of the pump, then it would not enhance the distribution created by the pump (see chapter five).

If instead a dissociation channel exists which is accessed via a perpendicular pump transition, then if the pump polarization is still along the TOF direction (vertical), the molecules will dissociate in a horizontal plane. If the probe is polarized vertically (and still assuming a parallel probe transition), it will not generate many ions. By aligning the probe polarization horizontally, the probe will ionize many neutrals and generate a distribution that is more strongly peaked at a central value at the mass position in the TOF. This is illustrated schematically in Fig. 4.5 (bottom right). Fig. 4.8 shows a comparison of the two scenarios, detecting I^+ emerging from the transition-state probing of HgI_2. Two channels are present: one with a parallel pump transition, the other perpendicular. It is therefore a very powerful technique in that it allows the detection of simultaneously accessed channels with the detection of the same mass. A further technique, gating the velocity profile, is covered in section 4.2.2.

4.1.4 Ion Fragmentation

The effects of ion fragmentation in fs pump-probe experiments are indicated in Fig. 4.9. Details of the ion fragmentation mechanisms[36] will not be covered here. What may influence the mass spectrum in our experiments (which aim to detect neutral dissociation dynamics) is the lifetime of the fragmenting ion. Ions AB^+ and B^+ are detected and the latter may come from either a probing of the neutral, B, or from a fragmentation of an excited parent ion, AB^{+*}. In addition to absorption cross sections and the initial number of ions (B^+, AB^+, AB^{+*}) produced by probing at the pump-probe delay time, the features in the TOF

spectrum depend on the lifetime, τ_{ion}, in relation to the time spent in the acceleration region for the fragmenting ion, AB^{+*}.

If the decay of the ion, AB^{+*}, is much faster than the μs time scale for the period spent in the acceleration region, *i.e.*, $\tau_{ion} << t_{acc}$ (case (i) in Fig. 4.9), then fragmentation occurs in a very localized region close to the initial point of ionization. All ions AB^+ (and AB^{+*}) and B^+ then travel independently almost from the start and yield their separate distinct mass peaks. In transients where the AB^+ mass is detected, only AB^* dynamics are observed, but detecting the B^+ mass gives contributions from both the AB^* decay dynamics and the build-up dynamics of B.

If fragmentation occurs during the acceleration time ($\tau_{ion} \sim t_{acc}$, case (ii) in Fig. 4.9), then different flight times arise for B^+ ions generated in this way because of their different starting conditions: they will be born with the velocity of the AB^{+*} ion at the time and place of fragmentation. A kinetic energy release in the ion fragmentation will lead to a further smearing out. As the fragmentation occurs in the acceleration region, the B^+ generated will move ahead of all the AB^+ (and AB^{+*}) ions present but will never catch up with the B^+ ions originally generated in the interaction region. The result is a decaying distribution in the TOF spectrum (see, e.g., ref. 37). Should a sharp peak at the B^+ mass position occur, in addition to the distribution, then this peak corresponds to the probing of the neutral B. In a fs pump-probe experiment, monitoring the AB^+ mass will give the dynamics of the neutral AB^*, while detecting the B^+ mass will give contributions from both the decay of AB^* and the rise of B.

The third region to be considered (case (iii) in Fig. 4.9) is that of slow ion fragmentation: $\tau_{ion} << t_{acc}$. Here there is little fragmentation in the acceleration region. The fragmentation of AB^{+*} that occurs on the longer time scale spent in the field-free drift region gives A and B^+, but the center of mass of these two

fragments travels at the same constant velocity as the AB^{+*} ion, and if there is little kinetic energy release in this ion dissociation, then the B^+ from this reaction will arrive at the detector at the same time as the AB^+ and AB^{+*} ions, and hence contributes to the peak at the parent mass. The peak at the B^+ mass is from probing of the neutral B. Detecting the AB^+ mass and scanning the pump-probe delay will still only give the neutral AB* dynamics since the B^+ contribution to this mass peak came from AB^{+*} ions generated from the probing of the neutral AB* and not from the neutral B. Monitoring the B^+ mass peak will just give the neutral dynamics of the build-up of B.

4.2 Femtosecond Transients

4.2.1 Parent and Fragment Dynamics

By pumping a parent molecule and probing with MPI at a time delay after the pump, it is possible to see both the parent and intermediate (fragment) dynamics by virtue of their difference in mass and the ultrashort time resolution of the fs laser pulses. By fixing the time delay, a mass spectrum may be taken, revealing the parent and fragment masses at this time. If, instead, the gate of the boxcar is set to a specific mass peak and the delay is varied, a transient corresponding to the gated mass species is obtained.

Numerous cases and considerations for such transient intermediate measurements were provided in section 3.1.3.3 using the kinetic model description. An experimental example[38] was presented (see Fig. 3.12), displaying transients obtained for a parent (cyclopentanone) and the intermediate (tetramethylene diradical) reached. Appendix C contains the full report of this experiment. In addition, appendices D and E provide further examples of the

attractiveness and versatility of the combination of MPI probing, mass spectrometry and fs pulses.

To illustrate the connection between the mass spectra at different time delays and the transients for different masses, the case of the diradical intermediate (Appendix C, ref. 38) will be used (later an alternate way of presenting mass spectra is offered using data from Appendix D). Fig. 4.10 shows the relevant pump and probe schemes. The parent molecule is excited to the Rydberg region from which decarbonylation leads to the birth (τ_1) of the diradical intermediate. This intermediate has a lifetime (τ_2) which is much longer than τ_1.[38] Both the parent and the intermediate are ionized by the probe. For low probe powers, fragmentation of the parent ion by further absorption of probe photons was eliminated. This was confirmed, at low probe intensity, by the absence in the transient for the intermediate mass (56 amu) of any contribution resembling the transient for the parent (84 amu) (see part (d.i) of section 3.1.3.3).

Mass spectra for different femtosecond delay times are shown in Fig. 3 of Appendix C. The parent signal is seen to appear at time zero and subsequently decays. The tetramethylene diradical intermediate exhibits a completely different behavior. It is almost absent in the mass spectrum at time zero, and rises (τ_1=150±30 fs) with increase in the delay time, peaking at 300±50 fs, and then decays very slowly (τ_2=700±40 fs). The small amount of detected signal present at t=0 can be accounted for by the finite laser pulse widths (see section 3.1.4). By tuning the pump wavelength it was possible to give the parent, and in turn the intermediate, more excess internal energy, decreasing τ_1 and τ_2 (see Appendix C).

To further illustrate the connection between mass spectra at different time delay, and transients for different masses, it is useful also to view a figure, such as the one just described, with the axes turned. This was done with the data from a different experiment[39] in which the dissociation process initiated by the Norrish

Type-I α-cleavage reaction of acetone was monitored (see Appendix D). Fig. 4.11 shows mass spectra *vs.* time delay where the time axis is now presented horizontally as is done for transients. As the area under each mass peak is proportional to its height and also to the observed signal in a transient (boxcar gate set to detect full peak area) for this mass, it is possible to draw the (fits to the) observed transient above the mass peaks as a function of time delay, as shown in Fig. 4.11. The fits correspond to the observed transients of Fig. 3(b) in Appendix D. The temporal parent (acetone) signal corresponds to a single exponential decay (τ=50±30 fs) convoluted (see section 3.1.4.2) with the cross-correlation of the laser pulses ($FWHM_{CC}$=150±30 fs). The signal for the intermediate produced, the acetyl radical, CH_3CO, was fit with a bi-exponential with $\tau_1=\tau$ in the rise and τ_2 in the decay. For the data shown, λ_{Pu}=307 nm, and τ_2=500±100 fs. The lifetime (τ_2) of the intermediate was found to decrease with increase in excess internal energy (see Appendix D).

4.2.2 Gating the Velocity Distribution of a Fragment

The effect of an initial fragment (m) velocity distribution is to cause a finite width of the profile centered at the mass m in the TOF spectrum. This profile is also referred to as the kinetic-energy time-of-flight (KETOF) spectrum.[16] The position relative to the central time, T, in the TOF spectrum corresponding to an initial velocity component, $v_{\parallel}$, along the TOF direction is given by[16]

$$t = -\frac{mv_{\parallel}}{qE}. \qquad (4.26)$$

Without loss of generality, the TOF direction may be taken as vertical (gravity is negligible). The fragments with zero initial vertical velocity then arrive at time T while those with an initial upward velocity component reach the detector earlier, and those traveling down at the start are detected later. The fast fragments that

travel along the TOF axis initially will contribute to the wings of the TOF profile as indicated in Fig. 4.12 (top). In contrast, initially slow fragments (strictly speaking, slow here means small initial vertical velocity component) arrive near the central time T. This suggests gating the velocity distribution and detecting either fast or slow fragments. By gating in this way and scanning the pump-probe delay line, transients may be obtained corresponding to fast or slow neutral dynamics. This may be an easy way of discriminating two possible reaction channels if one has a high and the other a low kinetic energy release to the fragment detected. For example, by gating very early or very late in the TOF profile, the transient obtained reflects the dynamics corresponding only to the channel associated with a high kinetic energy release.

This technique was used in ref. 16 to distinguish between different channels in the dissociation of HgI_2, each of which contributed to the same mass peak (I^+ ion). Transients are shown in Fig. 4.12 (bottom) corresponding to three different gating conditions. When the total profile is gated, both channels contribute to the signal, whereas by choosing a narrower boxcar gate and selecting either fast or slow ions, the dynamics of the two channels may be clearly distinguished.

Therefore, in addition to yielding substantial anisotropy information in the profile shape (see chapter five), the full impact of the femtosecond-KETOF method also introduces a means of channel selectivity in fs transient measurements. The profile shape depends on the relative alignment of the pump and probe laser polarizations and the TOF direction. By carefully choosing these orientations and using an appropriate gating of the profile in transient measurements, detailed information about the dynamics may be extracted, and otherwise indistinguishable reaction pathways may be resolved.

4.3 Comparison of MPI and Laser-Induced Fluorescence (LIF) Detection

MPI and LIF offer two unique ways of measuring transients in addition to other methods mentioned at the start of this chapter. They each have particular advantages that may be completely different. For example, in the detection of ions produced via MPI probing, the KETOF method explained above may be employed, placing emphasis on the anisotropic velocity distribution of the fragments in the dissociation. For LIF, wavelength tunability in the detection may play a key role in determining the vibrational content of an emitting product species. The dissociation of HgI_2 is a case in point. This reaction was studied in separate experiments using the unique aspects of LIF[12, 40] and MPI[16, 41] to reveal different details about the molecular dynamics.

Even when such unique approaches are not employed, the transients obtained for MPI and LIF may differ and yield complementary information about the dynamics. This is best illustrated by an example. In section 3.1.3.3 transient intermediate detection was discussed in terms of the kinetic model developed in chapter three and formulae were obtained for ion and fluorescence signals. Fig. 3.8 shows the relevant model. The fluorescence to $|G\rangle$ is given by (3.32) and that to $|H\rangle$ is determined by (3.33). These differ significantly in temporal behavior (and amplitude) from the signal obtained detecting ions separately from either $|E\rangle$ or $|F\rangle$ (equations (3.30) and (3.31), respectively), with the exception of the ion signal, M_E, and the fluorescence signal, M_G, having the same decay behavior (although inverted). If ions from $|E\rangle$ and $|F\rangle$ are not distinguishable to the detector, then it was shown that the combined ion signal had the same temporal form as the depletion observed in the fluorescence to $|H\rangle$ under the condition that $f_B << k_1$ (see section 3.1.3.3 and Appendix A.1). They could still differ, however, if the effective probing cross section parameter (β *vs.* β') were different

for MPI and LIF. This is usually the case as a depletion requires just one probe photon while two or more are usually needed to probe to ionization. These differences between the two methods, even for such a simple model, are a great advantage in retrieving information in ultrafast real-time studies of chemical reactions.

4.4 References

1. D. Herschbach, *Angew. Chem. Int. Ed.* **26**, 1221 (1987).
2. Y. T. Lee, *Angew. Chem. Int. Ed.* **26**, 939 (1987).
3. J. C. Polanyi, *Angew. Chem. Int. Ed.* **26**, 952, 1298 (1987).
4. R. N. Zare, D. R. Herschbach, *IEEE* **51**, 173 (1963).
5. S. J. Riley, K. R. Wilson, *Faraday Discuss. Chem. Soc.* **53**, 132 (1972).
6. G. E. Busch, K. R. Wilson, *J. Chem. Phys.* **56**, 3626 (1972).
7. M. J. Dzvonik, *J. Chem. Phys.* **61**, 4408 (1974).
8. R. D. Levine, R. B. Bernstein, *Molecular Reaction Dynamics* (Oxford University Press, New York, ed. 2, 1987).
9. R. B. Bernstein, *Chemical Dynamics via Molecular Beam and Laser Techniques* (Clarendon Press, Oxford, 1982).
10. A. H. Zewail, *Faraday Discuss. Chem. Soc.* **91**, 207 (1991); *J. Chem. Soc. Faraday Trans. 2* **85**, 1221 (1989).
11. M. J. Rosker, M. Dantus, A. H. Zewail, *J. Chem. Phys.* **89**, 6113 (1988).
12. M. Dantus, R. M. Bowman, M. Gruebele, A. H. Zewail, *J. Chem. Phys.* **91**, 7437 (1989).
13. J. L. Herek, S. Pedersen, L. Bañares, A. H. Zewail, *J. Chem. Phys.* **97**, 9046 (1992).
14. J. H. Glownia, *et al.*, in *Femtosecond Chemistry* J. Manz, L. Wöste, Eds. (VCH Verlagsgesellschaft mbH, Weinheim (Germany), 1995) pp. 131, and references therein.
15. A. H. Zewail, *Femtochemistry - ultrafast dynamics of the chemical bond* (World Scientific, Singapore, 1994), vol. I & II.
16. T. Baumert, S. Pedersen, A. H. Zewail, *J. Phys. Chem.* **97**, 12447 (1993).

17. T. Baumert, R. Thalweiser, V. Weiss, G. Gerber, in *Femtosecond Chemistry* J. Manz, L. Wöste, Eds. (VCH Verlagsgesellschaft mbH, Weinheim (Germany), 1995) pp. 403, and references therein.

18. J. L. Knee, L. R. Khundkar, A. H. Zewail, *J. Chem. Phys.* **82**, 4715 (1985).

19. T. Baumert, R. Thalweiser, G. Gerber, *Chem. Phys. Lett.* **209**, 29 (1993).

20. T. Baumert, *et al.*, *Phys. Rev. Lett.* **69**, 1512 (1992).

21. J. L. Knee, in *Femtosecond Chemistry* J. Manz, L. Wöste, Eds. (VCH Verlagsgesellschaft mbH, Weinheim (Germany), 1995) pp. 167.

22. I. Fischer, D. M. Villeneuve, M. J. J. Vrakking, A. Stolow, *J. Chem. Phys.* **102**, 5566 (1995).

23. K. Mueller-Dethlefs, M. Sander, E. W. Schlag, *Z. Naturforsch.* **39 A**, 1089 (1984); *Annu. Rev. Phys. Chem.* **42**, 109 (1991).

24. L. Hunziker, *et al.*, in *Molecular Dynamics and Spectroscopy by Stimulated Emission Pumping* H. Dai, R. W. Field, Eds. (World Scientific, Singapore, 1995), vol. 4, pp. 73.

25. A. O. Nier, in *Encyclopedia of Physics* R. G. Lerner, G. L. Trigg, Eds. (VCH, New York, 1991) pp. 703.

26. G. Scoles, Ed., *Atomic and Molecular Beam Methods* (Oxford University Press, New York, 1988), vol. 1

27. D. A. Skoog, J. L. Leary, *Principles of Instrumental Analysis* (Sanders HBJ, Fort Worth, 1992).

28. J. H. Moore, C. C. Davis, M. A. Coplan, *Building Scientific Apparatus - a Practical Guide to Design and Construction* (Addison-Wesley, Redwood City, ed. 2, 1989).

29. B. W. Rossiter, J. F. Hamilton, Eds., *Physical Methods of Chemistry* (Wiley Interscience, New York, 1987), vol. III A.

30. U. Boesl, R. Weinkauf, C. Weickhardt, E. W. Schlag, *Int. J. Spectrometry Ion Processes* **131**, 87 (1994).

31. M. Dantus, S. B. Kim, J. C. Williamson, A. H. Zewail, *J. Phys. Chem.* **98**, 2782 (1994).

32. H. Niu, W. Sibbett, *Rev. Sci. Instrum.* **52**, 1830 (1981).

33. W. C. Wiley, I. H. McLaren, *Rev. Sci. Instrum.* **26**, 1150 (1955).

34. B. A. Mamyrin, V. I. Karataev, D. V. Shmikk, V. A. Zagulin, *Sov. Phys. JETP* **37**, 45 (1973).

35. B. A. Mamyrin, D. V. Shmikk, *Sov. Phys. JETP* **49**, 762 (1979).

36. F. W. McLafferty, *Interpretation of Mass Spectra* (W.A. Benjamin, London, ed. 2, 1973).

37. H. Kühlewind, A. Kiermeier, H. J. Neusser, *J. Chem. Phys.* **85**, 4427 (1986).

38. S. Pedersen, J. L. Herek, A. H. Zewail, *Science* **266**, 1359 (1994).

39. S. K. Kim, S. Pedersen, A. H. Zewail, *J. Chem. Phys.* **103**, 477 (1995).

40. R. M. Bowman, M. Dantus, A. H. Zewail, *Chem. Phys. Lett.* **156**, 131 (1989).

41. S. Pedersen, T. Baumert, A. H. Zewail, *J. Phys. Chem.* **97**, 12460 (1993).

4.5 Figure Captions and Figures

Fig. 4.1 Basic TOF tube with the ions produced in the acceleration region and each accelerated to the same kinetic energy ($U_1=\frac{1}{2}mv^2$) before entering the field-free drift region. The heavier masses will have a smaller velocity and arrive last at the detector, as indicated in the TOF spectrum. The overall flight time is proportional to $\sqrt{m}$ (see text).

Fig. 4.2 The idea of space focusing due to an initial spatial distribution caused by the finite laser cross section. Ions a and b have the same mass. Ion b overtakes a at the space focus because it gains more kinetic energy before entering the field-free drift region. This suggests placing the detector at the space focus. However, this would lead to a short drift region and low mass resolution.

Fig. 4.3 Wiley-McLaren TOF mass spectrometer. [33] Two acceleration stages are used, and with appropriate choices of x_1, x_2, x_3 and E_2/E_1, it is possible to position the space focus at the detector even for a long field-free drift region (x_3).

Fig. 4.4 Schematic illustrating the relationship between the width, Δt, of the TOF profile and the maximum kinetic energy release, E_{kinA}, to an ion, A^+, of mass m_A and charge q, when an electric field E is used between the first two plates. An ion that follows case 2 will return to the initial position of excitation with the same speed, v_0, as it was originally kicked downwards with, because the electrostatic field is conservative. After this it travels under the same conditions as case 1, and therefore the overall flight time will be slower by an amount equaling the turn-around time, Δt. A consequence of energy and momentum conservation in the

dissociation/fragmentation process is that the total kinetic energy release, E_t, may be deduced from E_{kinA} and the ratio m_A/m_B.

Fig. 4.5 Principle of how an initial anisotropic velocity distribution of a detected ion species determines the shape of the profile in the TOF spectrum at the position of the mass of this ion. The detected profile is sensitive to the probability distribution of the initial vertical velocity component. If initially the ions travel straight up or down, a splitting results, while ions traveling sideways arrive at a central time, yielding less ions collected early and late (c.f. "inverted parabola" shape). In order to simplify the figure, the third plate, which is part of the second acceleration stage, is not shown.

Fig. 4.6 Figure showing the perpendicular intersection of the molecular beam, the fs pump and probe pulses, and the TOF direction. The pump polarization is aligned vertically along the TOF direction. The probe polarization is chosen either parallel or perpendicular to that of the pump in order to influence the initial velocity distribution and, in turn, the profile in the TOF spectrum.

Fig. 4.7 Full TOF spectrum experimentally obtained[16] at a fixed pump-probe delay of 90 fs (transition-state probing) in the dissociation of HgI_2. The iodine mass peak shows a clear splitting when the probe polarization is aligned vertically, parallel to the pump polarization and the TOF direction.

Fig. 4.8 Effect of changing the probe polarization while keeping the pump polarization fixed parallel to the TOF axis. The left-hand side shows a splitting for a parallel probe polarization (see also Fig. 4.8), while a distribution peaked at the center is seen for a perpendicular polarization of the probe (right).

Fig. 4.9 Effects of ion fragmentation on the TOF mass spectrum. Consequences for pump-probe experiments are discussed in the text. (i) Fast ion dissociation, occurring close to the initial excitation position. (ii) Ion dissociation on the time scale of the period (~μs) spent in the acceleration region for the dissociating ion species, AB^{+*}. (iii) Slow ion dissociation, leading to little dissociation during the flight time, and any dissociation occurring will primarily be in the field-free drift region (see text).

Fig. 4.10 Femtosecond pump-probe experiment[38] indicating the two-photon pump excitation at time zero to the Rydberg region and REMPI probing, at a time delay later, of the parent (cyclopentanone) and intermediate (tetramethylene diradical).

Fig. 4.11 Femtosecond mass spectra for the dissociation of acetone, taken at discrete time delays.[39] The parent acetone molecule (58 amu) appears at time zero and decays exponentially (τ=50±30 fs). The acetyl intermediate (43 amu) formed shows a rise of $\tau_1=\tau$ and a decay of τ_2=500±100 fs for a pump wavelength of 307 nm. The dashed and solid lines are fits to the transients in ref. 39, using a single exponential for the parent (τ) and a bi-exponential (τ_1, τ_2) for the intermediate with the stated values. Note the expected good agreement between the transient fits and the peaks of the mass spectra (see text).

Fig. 4.12 (Top) Gating of the velocity profile for the I^+ ion mass in the TOF spectrum obtained in the fs study of the HgI_2 dissociation. Fast or slow fragments (I mass) may be detected separately by gating in the wing or at the center, respectively. A broad gate covering the full profile yields the combined signal

from fast and slow fragments and is therefore not sensitive to the kinetic energy release. (Bottom) Transients obtained for the three different gating positions.[16] Note the drastic difference in the transients corresponding to the detection of fast *vs.* slow fragments. This may be used in distinguishing (neutral) dynamics from two channels that have different kinetic energy release to the detected fragment.

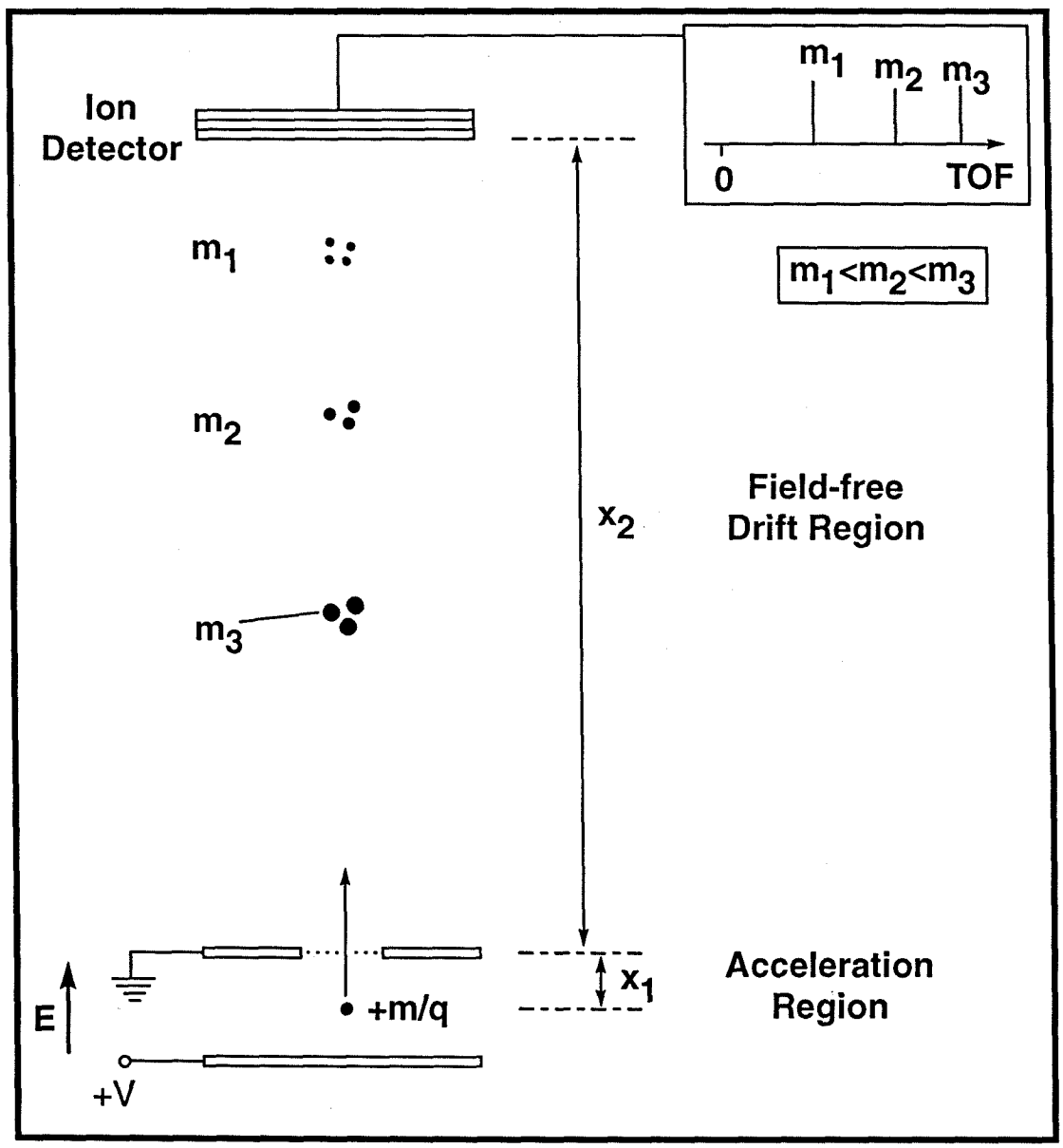
Ion
Detector
m1
m2
m3
0
TOF
m1<m2<m3
x2
Field-free
Drift Region
x1
Acceleration
Region
E
+m/q
+V

Fig. 4.1

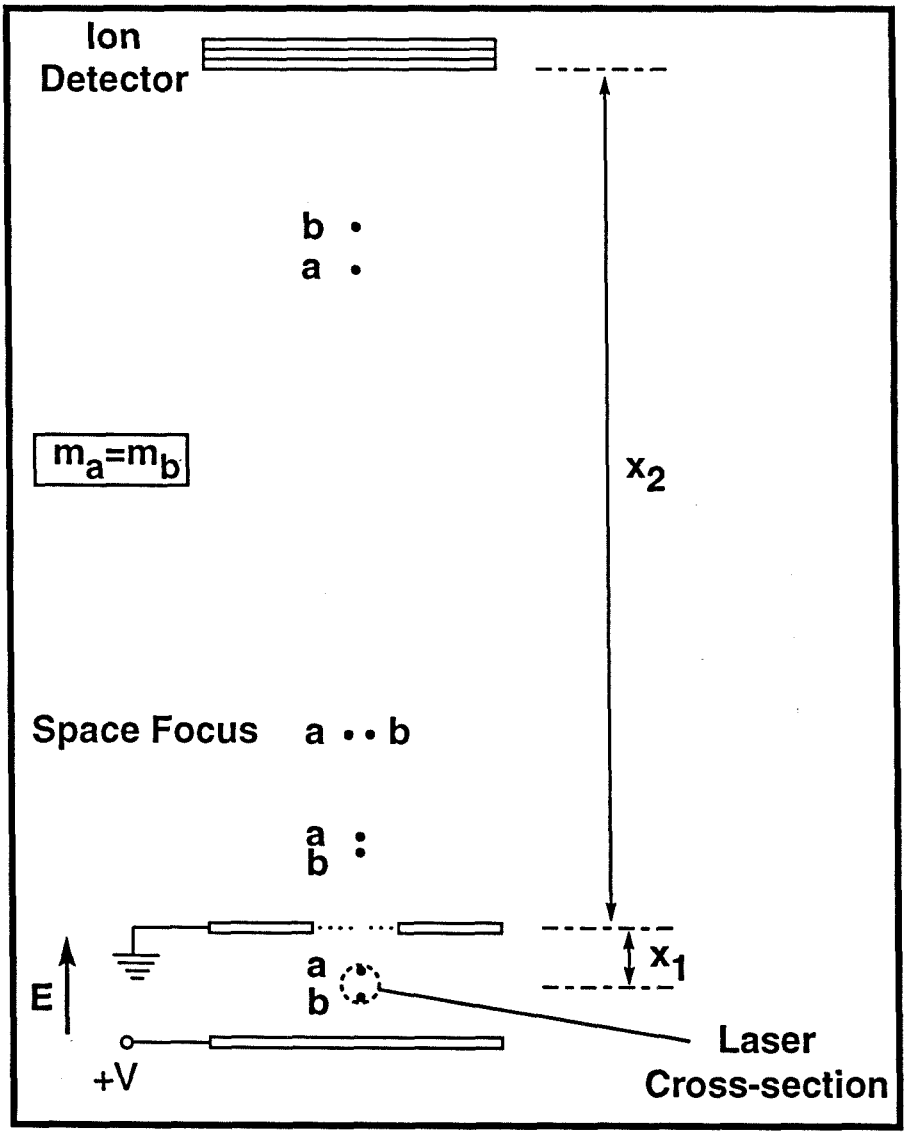
Ion
Detector
b
a
$m_a=m_b$
x_2
Space Focus
a b
a
b
E
a
b
x_1
+V
Laser
Cross-section

Fig. 4.2

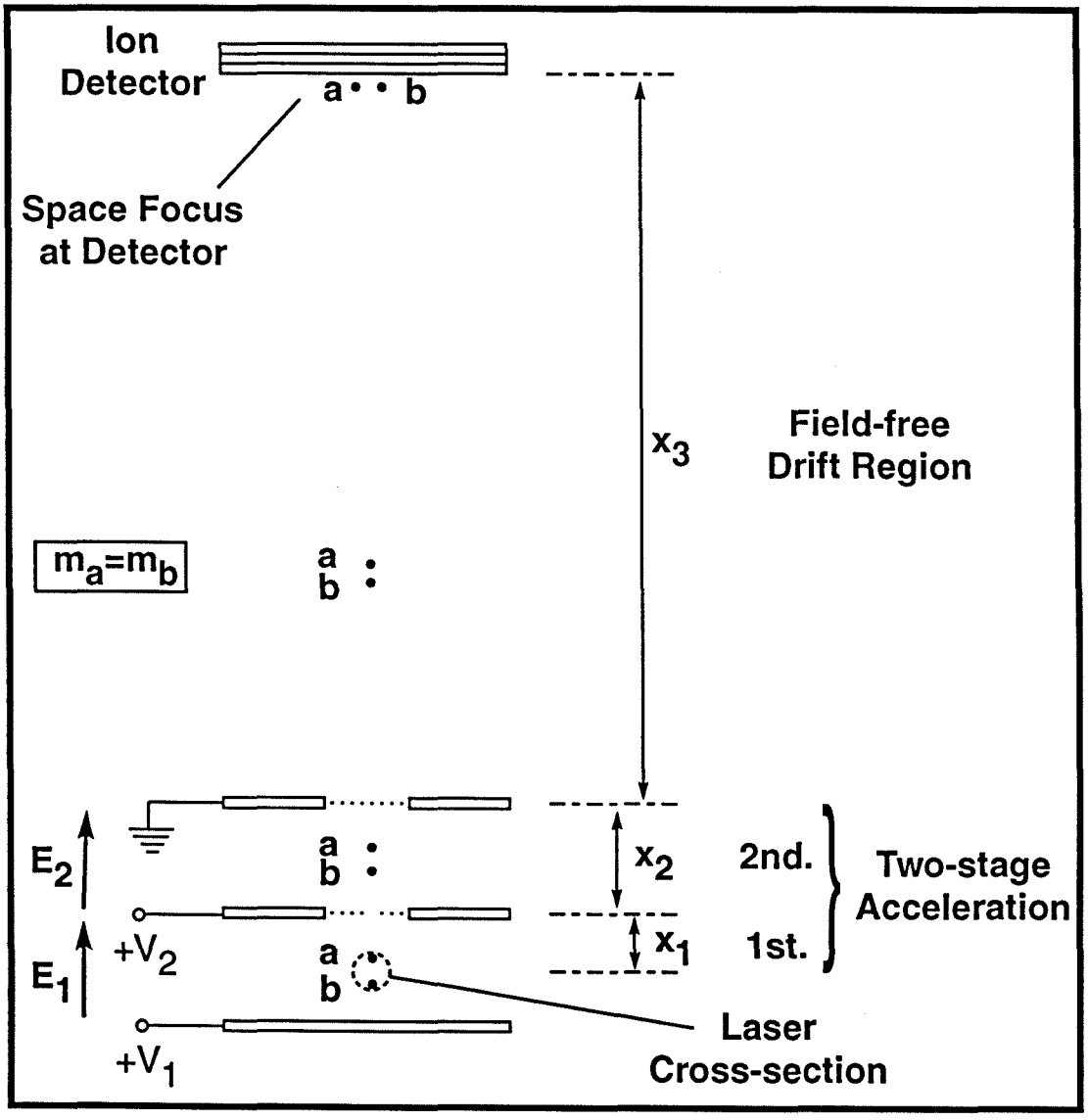
Ion
Detector
a • • b
Space Focus
at Detector
x3
Field-free
Drift Region
ma=mb
a
b
E2
a
b
x2
2nd.
Two-stage
Acceleration
E1
+V2
a
b
x1
1st.
Laser
Cross-section
+V1

Fig. 4.3

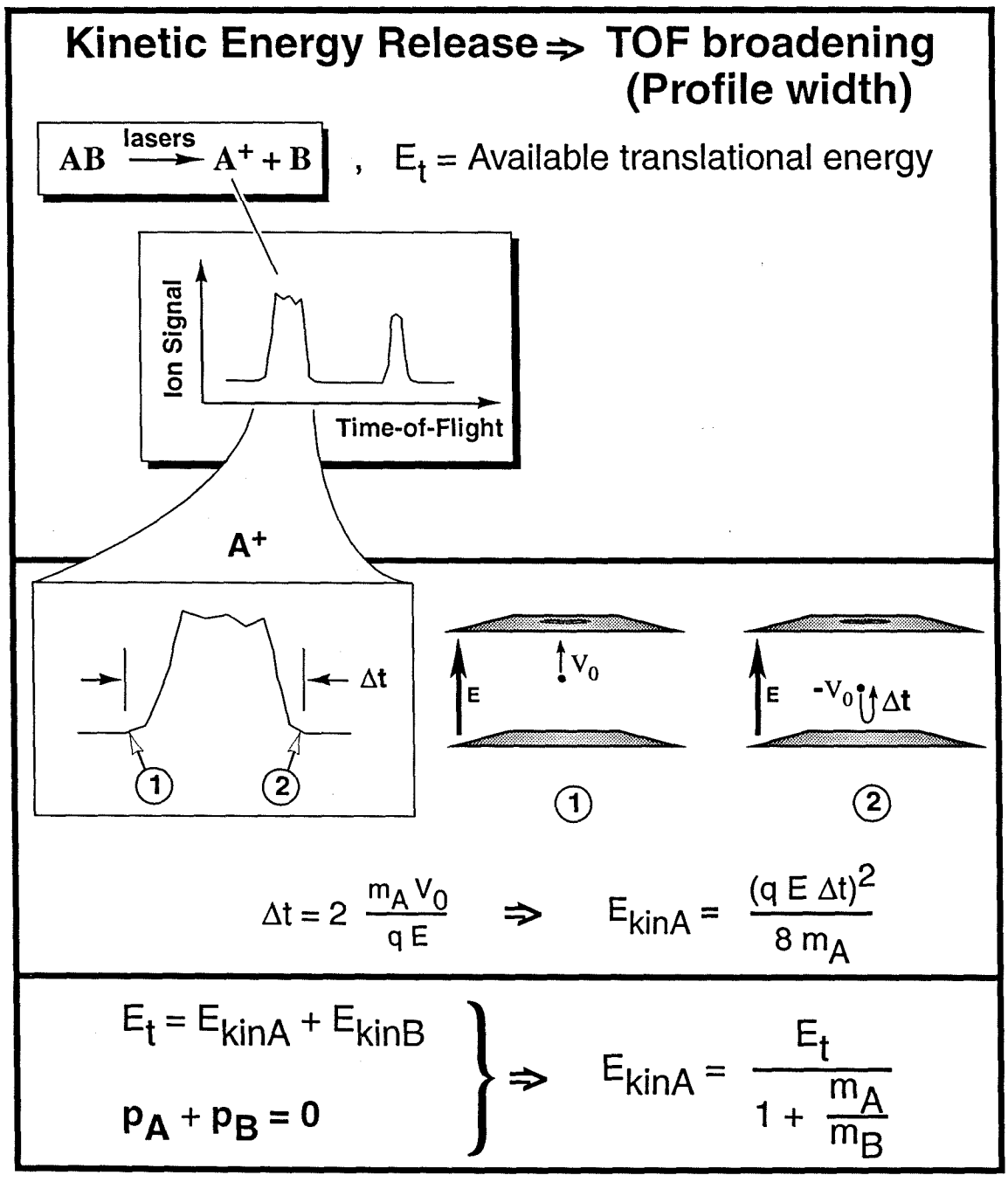
Kinetic Energy Release ⇒ TOF broadening
(Profile width)
AB lasers A+ + B , Et = Available translational energy
Ion Signal
Time-of-Flight
A+
Δt
1
2
E
v0
E
-v0
Δt
1
2
Δt = 2 mA V0 / q E ⇒ EkinA = (q E Δt)2 / 8 mA
Et = EkinA + EkinB
pA + pB = 0
⇒ EkinA = Et / (1 + mA / mB)

Fig. 4.4

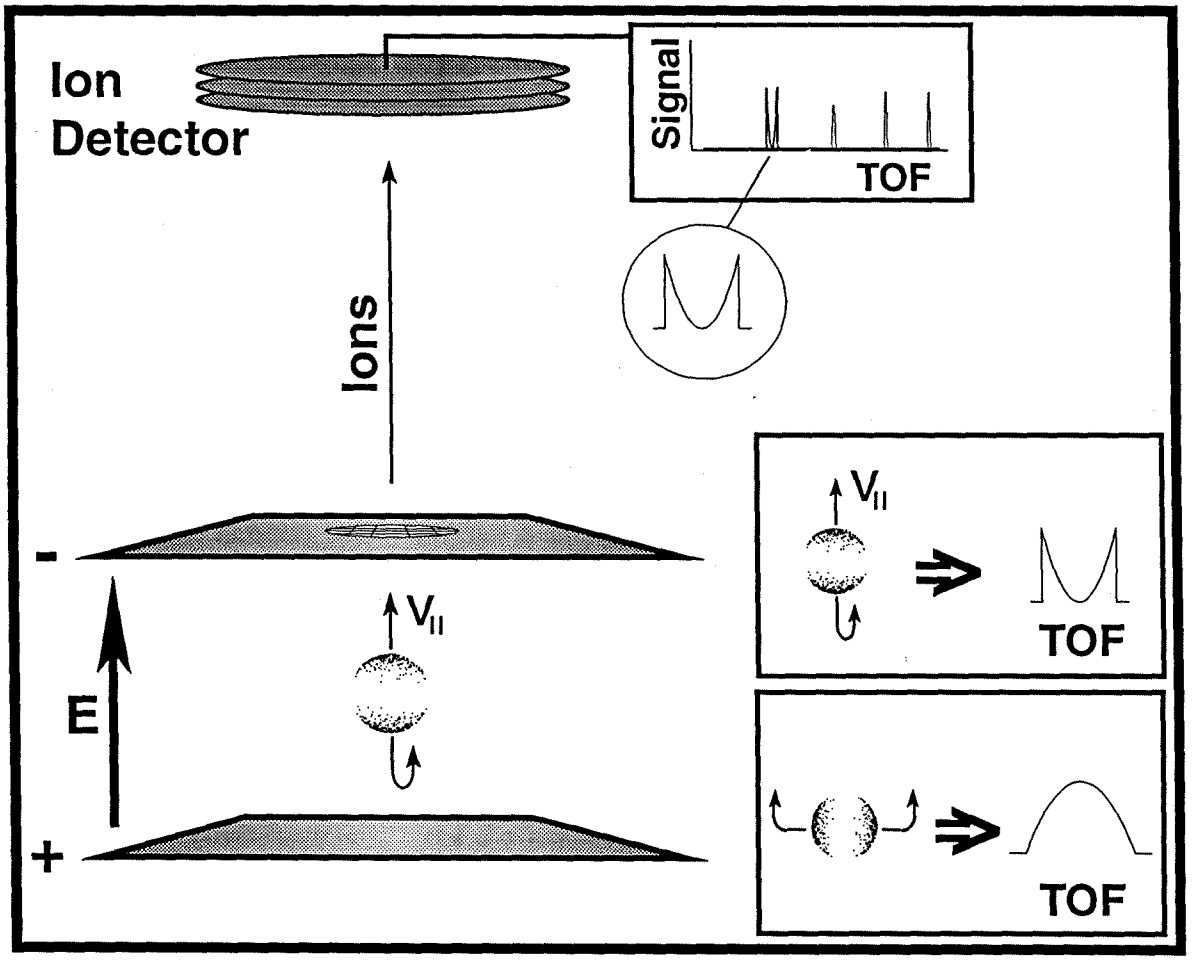

Fig. 4.5

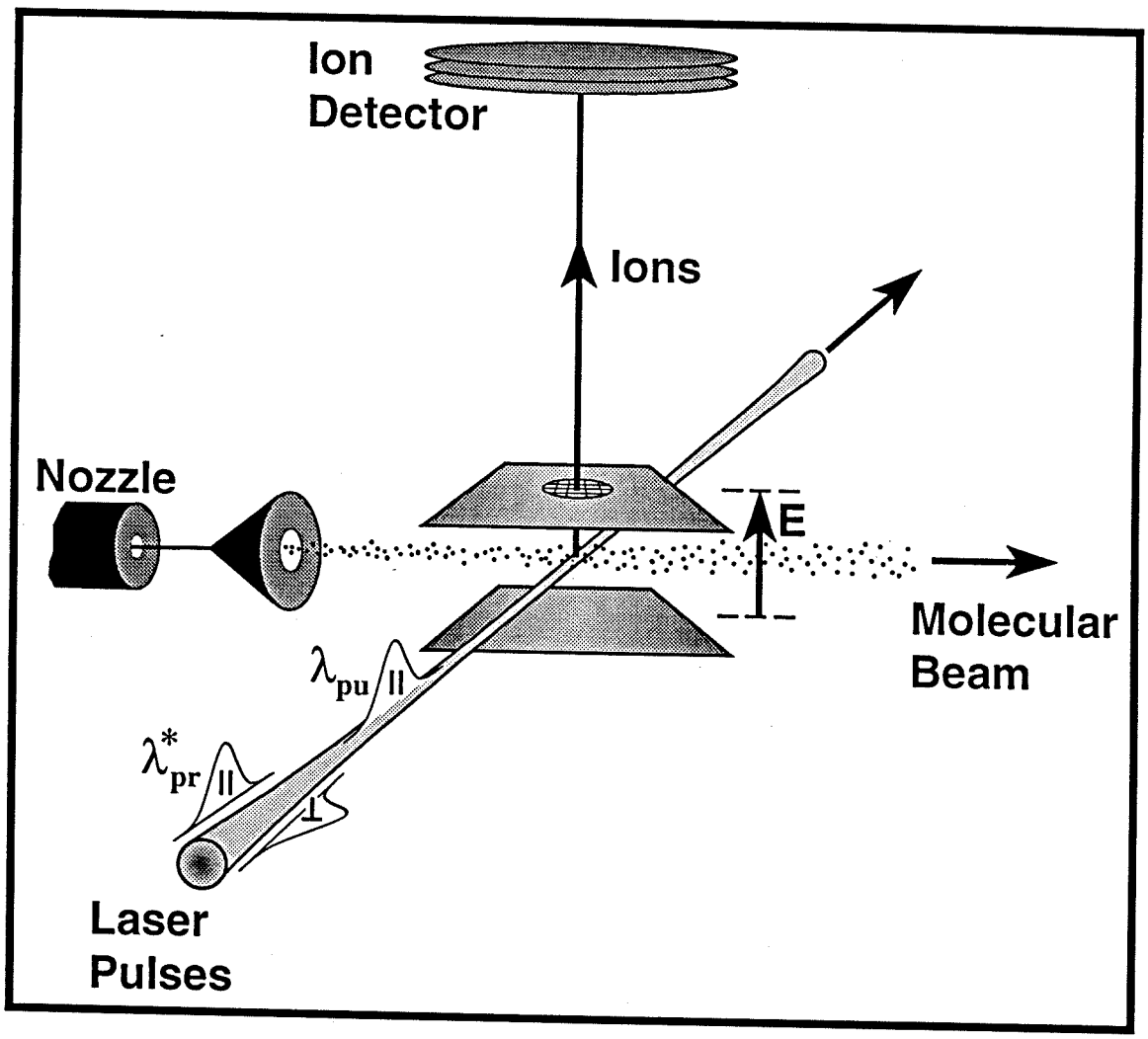
Ion
Detector
Ions
Nozzle
E
Molecular
Beam
λ_{pu} ||
λ^*_{pr} ||
⊥
Laser
Pulses

Fig. 4.6

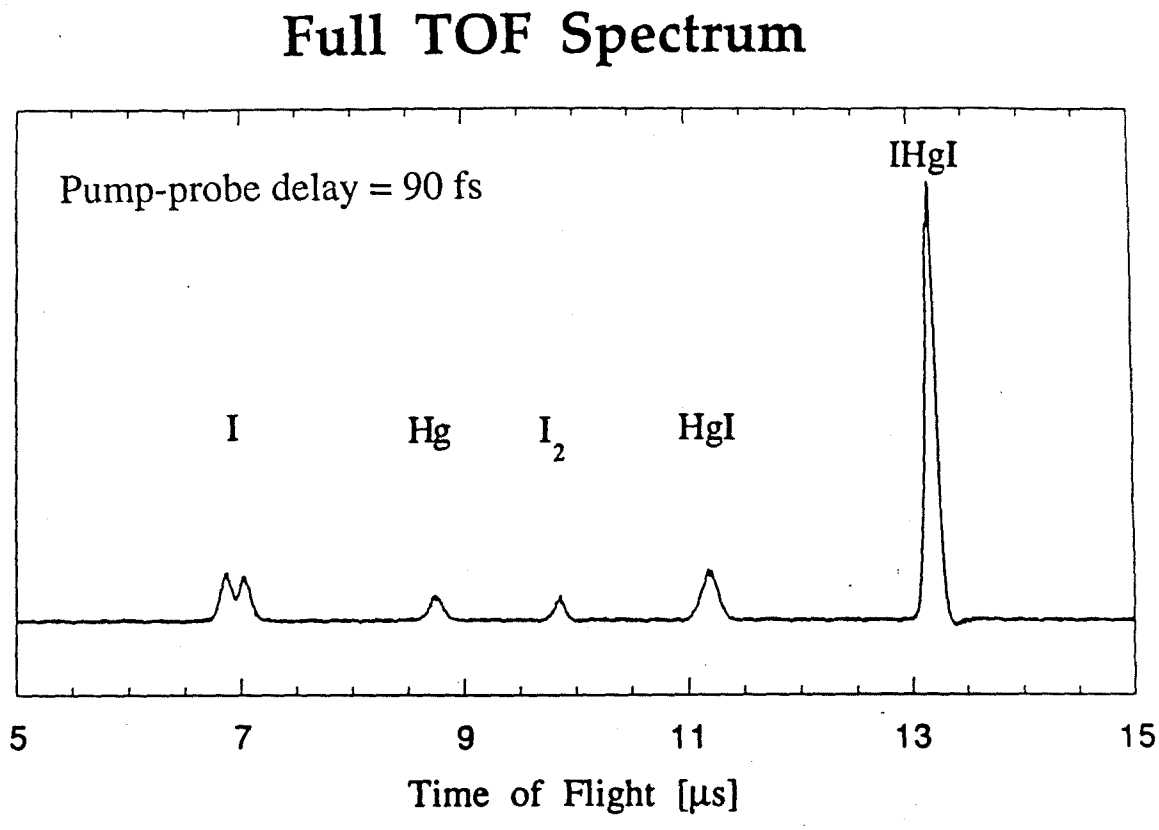
Full TOF Spectrum
Pump-probe delay = 90 fs
IHgI
I
Hg
I_2
HgI
5
7
9
11
13
15
Time of Flight [μs]

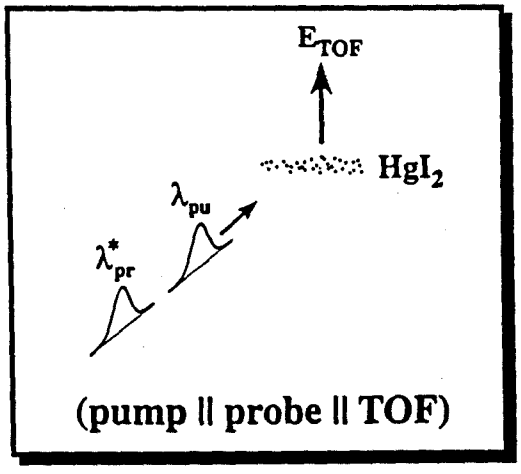
E_{TOF}
HgI_2
λ_{pu}
λ^*_{pr}
(pump || probe || TOF)

Fig. 4.7

Probe Polarization Dependence: I^+ TOF

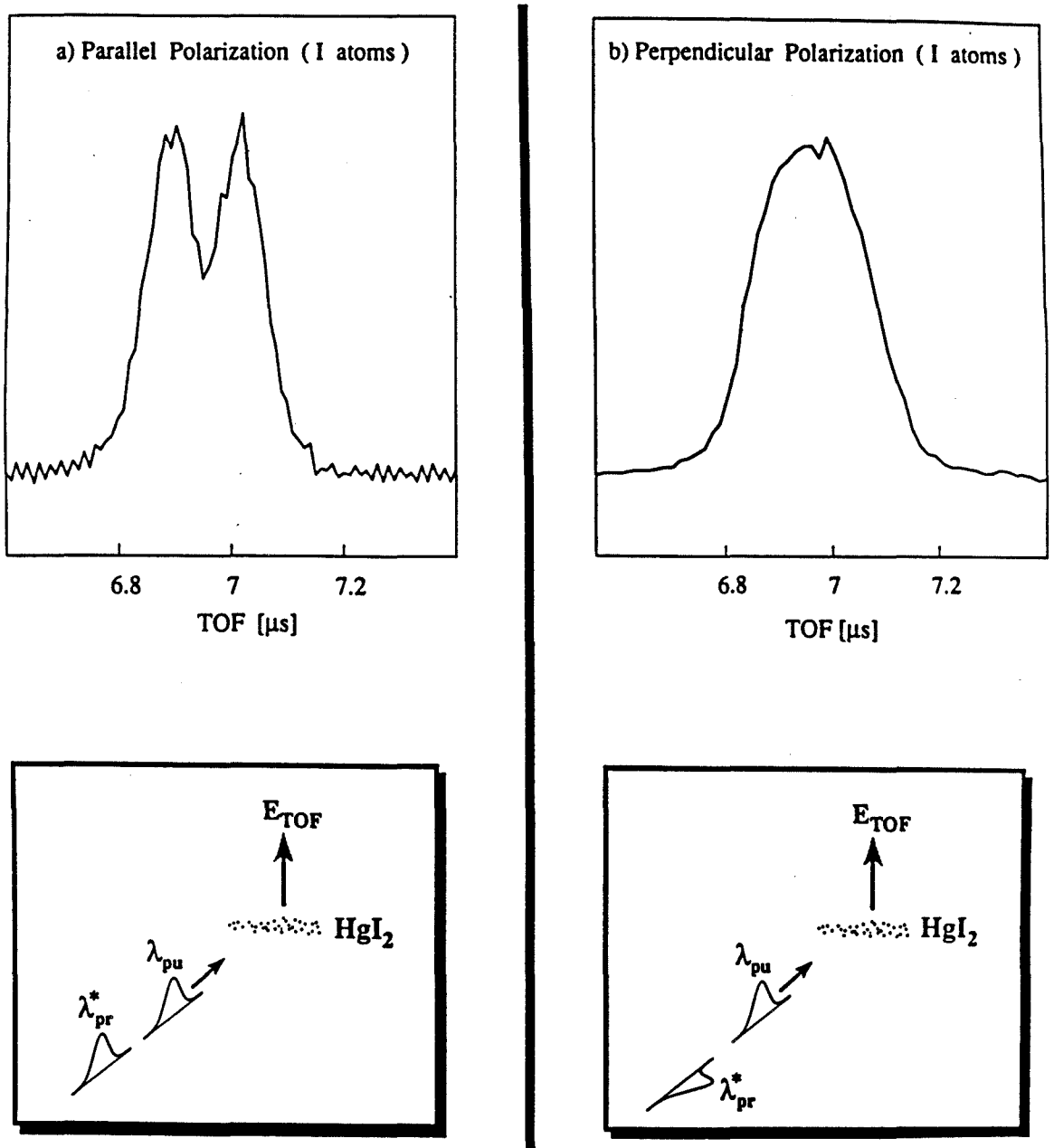

Fig. 4.8

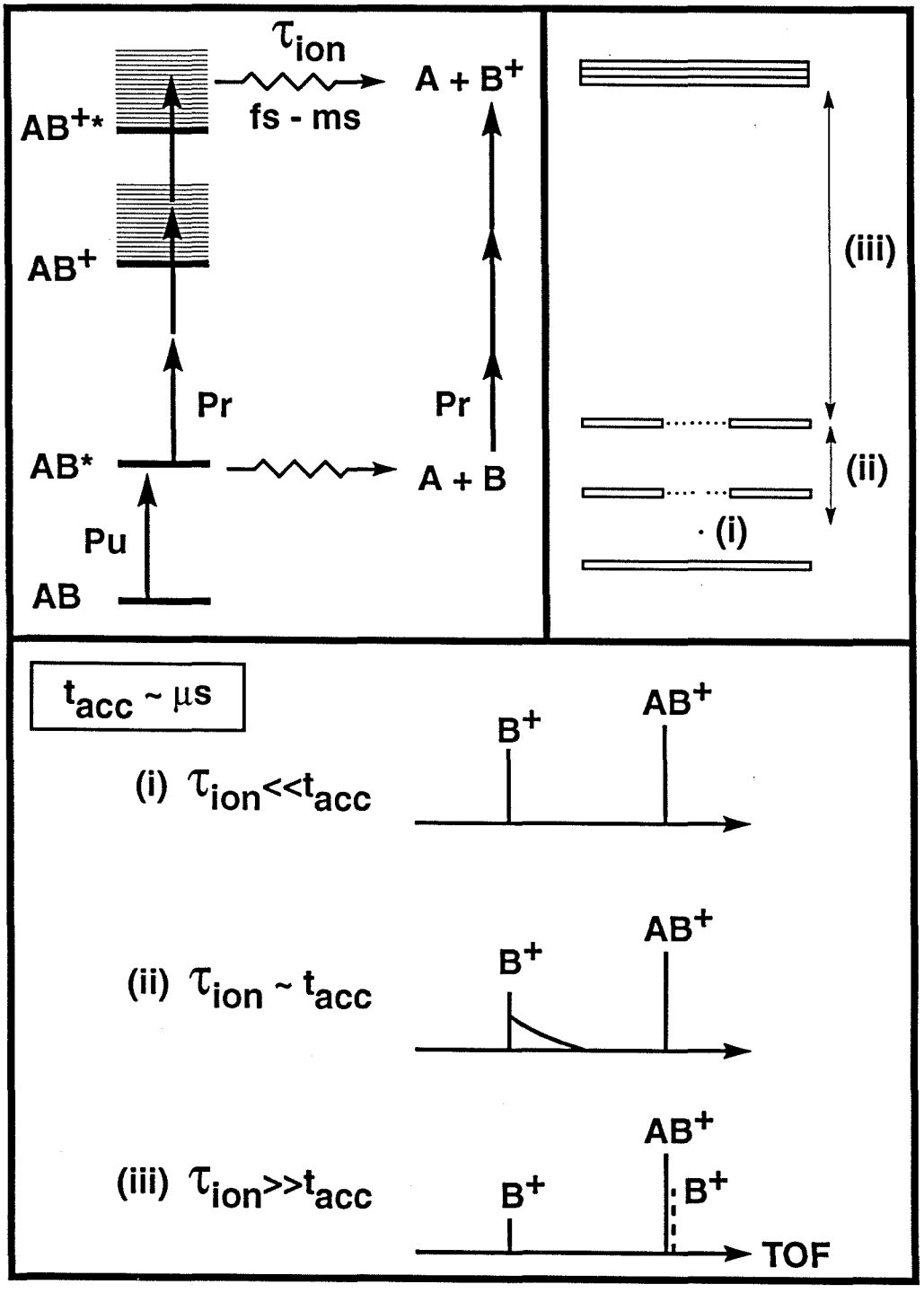
τion
fs - ms
AB+*
AB+
Pr
AB*
Pu
AB
A + B+
Pr
A + B
(iii)
(ii)
(i)
tacc ~ μs
(i) τion<<tacc
B+
AB+
(ii) τion ~ tacc
B+
AB+
(iii) τion>>tacc
B+
AB+
B+
TOF

Fig. 4.9

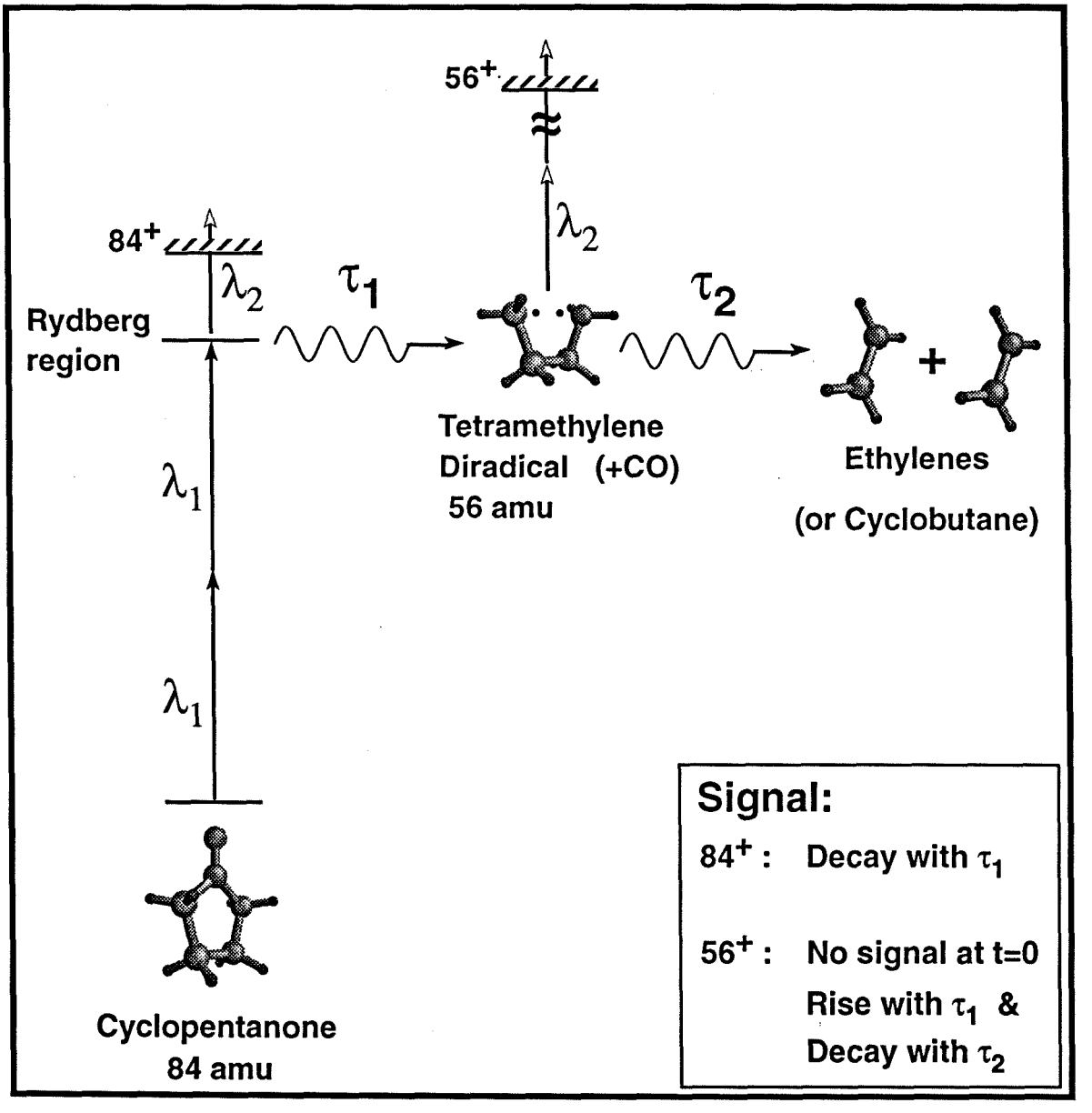
56+
λ2
84+
λ2
τ1
τ2
Rydberg
region
Tetramethylene
Diradical (+CO)
56 amu
Ethylenes
(or Cyclobutane)
λ1
λ1
Signal:
84+ : Decay with τ1
56+ : No signal at t=0
Rise with τ1 &
Decay with τ2
Cyclopentanone
84 amu

Fig. 4.10

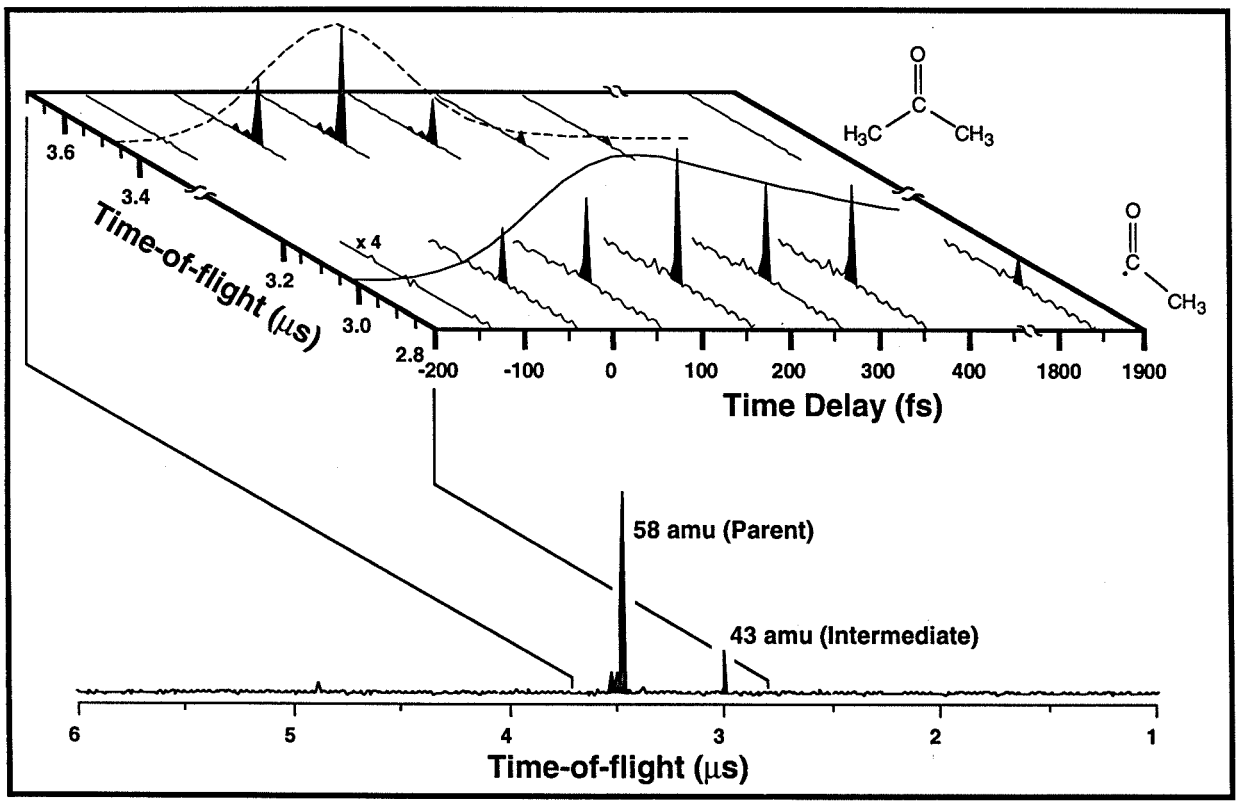
3.6
3.4
3.2
3.0
2.8
Time-of-flight (μs)
x 4
-200
-100
0
100
200
300
400
1800
1900
Time Delay (fs)
58 amu (Parent)
43 amu (Intermediate)
6
5
4
3
2
1
Time-of-flight (μs)

Fig. 4.11

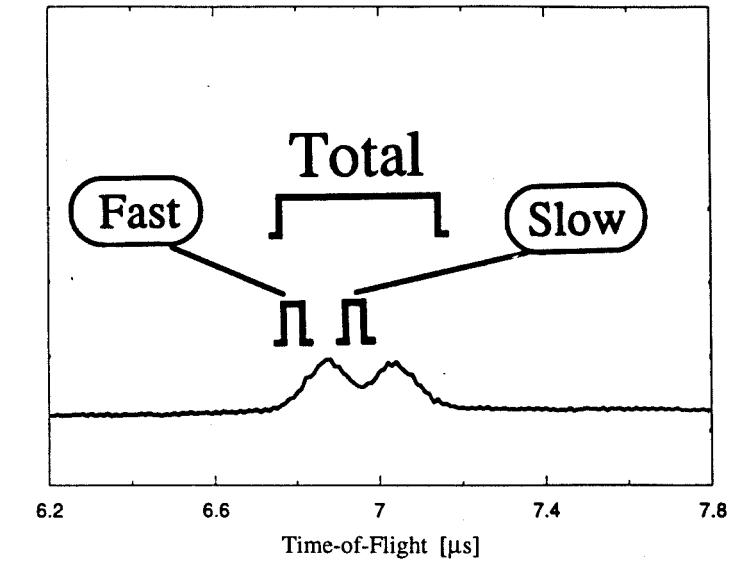
Total
Fast
Slow
6.2
6.6
7
7.4
7.8
Time-of-Flight [μs]

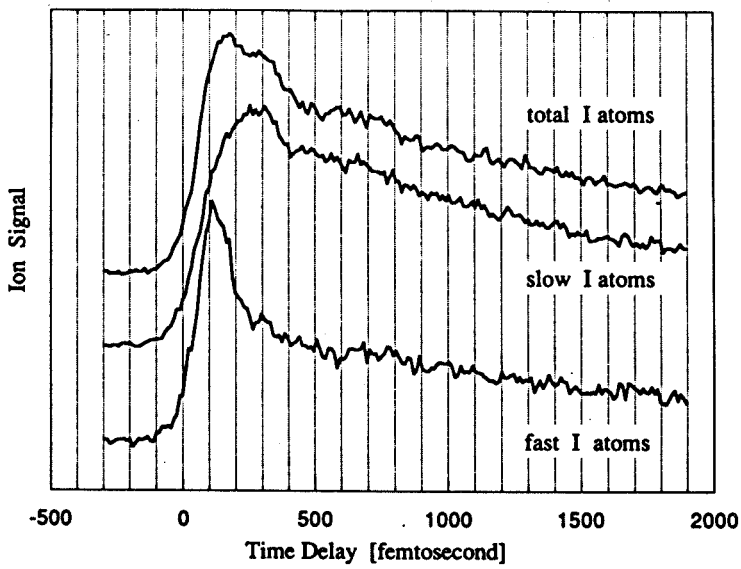
total I atoms
slow I atoms
fast I atoms
Ion Signal
-500
0
500
1000
1500
2000
Time Delay [femtosecond]

Fig. 4.12

Chapter 5

Kinetic-Energy Time-of-Flight (KETOF) Method: Anisotropy and Rotational Alignment in Pump-Probe Experiments

5.1 Introduction

When a molecule is excited by a pump laser, the optical transition dipole moment, μ, is preferentially aligned along the pump polarization direction, ε_{pu}. If the parent subsequently dissociates, then the resulting fragments will be characterized by their velocity, **v**, and angular momentum, **J**. Because of the alignment of the parent transition moment (μ), the fragments will be described by a recoil anisotropy (μ-**v** correlation[1, 2, 3, 4, 5, 6, 7]) and will have a rotational alignment (μ-**J** correlation[8, 9, 10, 11, 12, 13, 14]). In addition to **v** and **J** of the fragment being correlated with μ of the parent, they must also be correlated with each other.[15, 16, 17, 18, 19, 20, 21, 22] The theory for the angular distributions and correlations has been developed thoroughly (see the excellent review by Hall and Houston[23]). Both LIF (Doppler profile; see refs. 14, 23, 24, 11, 22, 25, 26) and MPI detection (see refs. 14, 23, 24, 27, 28, 29, 30, 31, 32, 33) have been used to measure the correlations and to extract information such as the nature of the parent transition and estimate of the lifetime of the dissociating parent molecule. While LIF Doppler spectroscopy relies on very narrow line widths to detect anisotropic profiles, the resonance-enhanced multiphoton ionization (REMPI) detection methods do not need such narrow line widths and have instead to ensure that the spectral width of the probe laser used covers the entire Doppler profile.

First we shall consider the μ-**v** correlations, which describe the fragment velocity recoil anisotropy. After this, the effect of REMPI probing and detection of the resulting fragment velocity profile along the TOF axis will be explained in detail. Next, the effect of probing the transition state as opposed to the free

fragments will be discussed. Finally, a section dealing with the energetics is presented.

5.2 Angular Distribution Created by the Pump Pulse

Consider an electric dipole transition in which a single photon excites a target that subsequently breaks up into two fragments. Using Fermi's Golden Rule, the probability of transition is given by:

$$P \propto \left|\varepsilon_{pu} \cdot \mu\right|^2, \tag{5.1}$$

where ε_{pu} is the pump polarization, the direction of the E field of the pump laser, and μ is the transition dipole moment of the parent molecule ($\mu = \mu_{fi} = \langle f | \mu | i \rangle$). Hence, if γ is the angle between ε_{pu} and μ, then the normalized transition probability is

$$P = \frac{3}{4\pi}\cos^2\gamma. \tag{5.2a}$$

The probability of a transition for a dipole, μ, lying in a solid angle $d\Omega$ and at angle γ to ε_{pu} is $Pd\Omega$ and the normalization is such that

$$\int_{(4\pi)} Pd\Omega = 1. \tag{5.2b}$$

The probability distribution can be expressed in terms of the second degree Legendre polynomial:

$$P = \frac{1}{4\pi}[1 + 2P_2(\cos\gamma)], \tag{5.3a}$$

where $P_2(x) = \frac{1}{2}(3x^2 - 1)$. (5.3b)

5.2.1 No Rotational Effects

If all fragments recoil such that there is a fixed angle χ_0 between μ and the direction of dissociation (given by the final recoil velocity, **v**, since no rotation is assumed here) of the fragment of interest, then the center of mass (CM) angular distribution for the fragment recoil is given by:[1, 4, 5, 34]

$$P(\theta) = \frac{1}{4\pi}\left[1+\beta\ P_2(\cos\theta)\right], \tag{5.4a}$$

where θ is the angle between **v** and ε_{pu}, and β is the anisotropy parameter:

$$\beta = 2\ P_2(\cos\chi_0). \tag{5.4b}$$

This can be seen[2] from Fig. 5.1 and noting that

$$P(\theta) = \frac{1}{4\pi}\int_{\Omega} P \sin\gamma\ d\gamma\ d\phi, \tag{5.5}$$

where P is given by (5.2). We can express the $\cos^2\gamma$ in P in terms of ϕ since:

$$\cos\gamma = \cos\theta\cos\chi_0 + \sin\theta\sin\chi_0\cos\phi. \tag{5.6}$$

Hence,

$$P(\theta) = \frac{1}{4\pi}\int_0^{\pi}\sin\gamma\ d\gamma \int_0^{2\pi} P\ d\phi \tag{5.7a}$$

$$= \frac{1}{4\pi}\left[1+2\ P_2(\cos\chi_0)\ P_2(\cos\theta)\right], \tag{5.7b}$$

which is just (5.4). We can generalize to give the CM angular distribution for an arbitrary recoil distribution $P(\chi)$ by averaging over this $P(\chi)$:

$$P(\theta) = \int_0^{\pi} \frac{1}{4\pi}\left[1+2\ P_2(\cos\chi)\ P_2(\cos\theta)\right]\ P(\chi)\ d\chi \tag{5.8}$$

$$= \frac{1}{4\pi}\left[1+\beta\ P_2(\cos\theta)\right] \tag{5.9a}$$

with $$\beta = 2\int_0^{\pi} P_2(\cos\chi)\ P(\chi)\ d\chi. \tag{5.9b}$$

The anisotropy parameter, β, being the average of $P_2(\cos\chi)$ over the probability distribution of χ, must lie between the maximum and minimum values of $P_2(\cos\chi)$, *i.e.*, $-1 \le \beta \le 2$.

In certain experiments, the "axis of detection," e.g., TOF axis, is well defined in the laboratory. If the pump pulse is parallel to this axis and the fragments can be detected along this axis, then equation (5.4a) can be expressed in terms of the projection of the fragment velocity parallel to this axis, $v_\parallel$:

$$P(v_\parallel) = \frac{1}{2v_0}\left[1+\beta\, P_2\left(\frac{v_\parallel}{v_0}\right)\right], \qquad (5.4c)$$

which is a parabola or "inverted parabola" depending on the value of β (see Fig. 5.2, and section 5.5). For LIF detection, an equation of the same parabolic form is obtained.[22]

Let us return to the case of $P(\chi) = \delta(\chi - \chi_0)$, and look at three cases. If the excitation involves a parallel transition moment ($\mu \parallel v$), then $\chi_0 = 0$ and $\beta = 2$, implying that $P(\theta) = \frac{3}{4\pi}\cos^2\theta$, *i.e.*, a dumbbell shaped angular distribution with respect to the ε_{pu} direction. In this case, the fragment is therefore most likely to travel along (collinear or anticollinear) the ε_{pu} direction (Fig. 5.2(a)). This can also be seen from the velocity profile, which is given by: $P(v_\parallel) = \frac{3}{2v_0}\left(\frac{v_\parallel}{v_0}\right)^2 \propto \left(\frac{v_\parallel}{v_0}\right)^2$, *i.e.*, a parabolic probability distribution with maximum probability at $\pm v_0$. On the other hand, with a perpendicular transition moment ($\chi_0 = 90°$), we obtain $\beta = -1$ and $P(\theta) = \frac{3}{8\pi}\sin^2\theta$, a probability distribution that is shaped like a torus with respect to the ε_{pu} direction (Fig. 5.2(b)). In this case, the fragment has maximum probability to travel at right angles to ε_{pu}. The velocity profile is $P(v_\parallel) = \frac{3}{4v_0}\left[1-\left(\frac{v_\parallel}{v_0}\right)^2\right] \propto 1-\left(\frac{v_\parallel}{v_0}\right)^2$, which is

an "inverted parabola" with maximum probability at $v_{\|}=0$, and zero probability at $\pm v_0$. In the very unlikely case that χ_0 happens to be 54.7°, we would obtain an isotropic distribution (Fig. 5.2(c)): $P(\theta)=\frac{1}{4\pi}$, and $P(v_{\|})=\frac{1}{2v_0}$, *i.e.*, a constant.

Let us briefly present some commonly used terminology, just to tie it in with the present work. For a linear molecule in the classical limit, the transition dipole moment, μ, can point in either of two directions: along the angular momentum vector of the molecule, **J**, for a Q branch ($\Delta J = 0$), or in the plane of rotation for a P or R branch ($\Delta J = \mp 1$). For parallel transitions (Σ-Σ, Π-Π, etc.) only P and R branches have intensities in the classical limit, while for perpendicular transitions (Σ-Π, Π-Σ, etc.) all branches are present. Later, when discussing the effect that probing has on the pump generated fragment distribution, the alignment of μ with respect to the angular momentum of one of the fragments will be described. Then the symbol **J** will be used to refer to the angular momentum of the nascent fragment.

5.2.2 Effects of Rotation

There are two rotational effects to be dealt with. First of all, the excited parent complex may not fragment instantaneously, but rather have a finite, non-vanishing average lifetime, T_0, before dissociating. Secondly, when the excited state does dissociate, the nascent fragment will have a tangential velocity component, $\mathbf{v_t}$, that is perpendicular to the "radial" velocity component $\mathbf{v_0}$ (called **v** above), yielding a final recoil velocity $\mathbf{v} = \mathbf{v_0}+\mathbf{v_t}$. For a diatomic molecule, $\mathbf{v_0}$ lies along the internuclear axis. The tangential velocity component is a result of

the finite angular momentum of the parent excited state, which possesses a finite rotational energy.

These two effects, the finite lifetime and the tangential velocity component, have been discussed by various authors. Busch and Wilson[5] first analyze the case of an instantaneous fragmentation ($T_0 = 0$, $\mathbf{v_t} \neq 0$), but then generalize to the case of a finite lifetime ($T_0 \neq 0$, $\mathbf{v_t} \neq 0$), treating the two effects simultaneously. Yang and Bersohn,[6] while also using the results of Jonah,[3] first consider the case of finite lifetime, ignoring the effect of the tangential velocity ($T_0 \neq 0$, $\mathbf{v_t} = 0$). Next, they treat the effect of tangential velocity as a separate factor in β, concluding that this factor typically reduces the magnitude of β by 5 - 10%. A derivation of the angular distribution of rotating excited molecules of arbitrary shape was performed by Yang and Bersohn,[6] using the methods of St. Pierre and Steele;[35] this derivation will not be described here except to say that very general expressions for β were found for cases such as linear molecules, symmetric tops, and an accidentally spherical top.

Let us first follow the treatment of Busch and Wilson who used a pseudodiatomic model for polyatomic molecules in which each of the two fragments is treated as a point mass located on the bond axis to be broken (their model describes a diatomic in the limit that each of the two fragment masses is just an atom). To begin with, consider the case of instantaneous dissociation, where the lifetime of the complex vanishes: $T_0 = 0$. There is still a tangential velocity, $\mathbf{v_t}$, due to the finite angular velocity ω of the excited parent: $\mathbf{v_t} = \omega \times \mathbf{r}$, where $\mathbf{r}$ is the radial vector from the center of mass to the fragment part. The final recoil velocity is then $\mathbf{v} = \mathbf{v_0}+\mathbf{v_t}$, in which $\mathbf{v_0}$ is the radial velocity along the $\mathbf{r}$ direction. This is illustrated in Fig. 5.3. The angle θ is defined as the angle between the polarization direction of the pump laser, $\boldsymbol{\varepsilon}_{\mathbf{pu}}$, and the final recoil

velocity, **v**. The angle between **v** and $\mathbf{v_0}$ is fixed: $\alpha = \sin^{-1}(v_t / v)$. The angle between $\mathbf{v_0}$ and μ is still fixed at χ_0. In a manner similar to how (5.4) was derived, we find:

$$P(\theta) = \frac{1}{4\pi}\left[1 + 2\ P_2(\cos\alpha)\ P_2(\cos\chi_0)\ P_2(\cos\theta)\right]. \tag{5.10}$$

This reduces to (5.4), of course, in the limit of $\alpha = 0$.

Next we let the excited state have a finite lifetime before breaking up. If the molecule lives for a time τ and is rotating with an angular velocity ω, then it will rotate through an angle $\psi = \omega\tau$ before fragmenting. We now follow a path similar to Jonah's classical route.[3] Assuming the molecule dissociates with a first order decay, then the distribution of lifetimes is: $P(\tau) = \frac{1}{T_0}\exp\left[-\frac{\tau}{T_0}\right]$, where T_0 is the average lifetime. This distribution, $P(\tau)$, is the probability that the molecule has not dissociated in a time τ. The total angle at which the fragment recoils is now $\eta = \psi + \alpha$ (see Fig. 5.4), with respect to the orientation that this fragment part had in the molecule in the initially excited configuration (gray lines in Fig. 5.4). The angles α and ψ are both about the same axis along which the total angular momentum of the parent complex lies. We assume that when the lifetime τ is over, the molecule dissociates rapidly with respect to rotation. Then we have (again the derivation is similar to that of (5.4)):

$$P(\theta) = \frac{1}{4\pi}\left[1 + 2\ P_2(\cos\eta)\ P_2(\cos\chi_0)\ P_2(\cos\theta)\right], \tag{5.11a}$$

i.e.,
$$\beta = 2\ P_2(\cos\eta)\ P_2(\cos\chi_0). \tag{5.11b}$$

But there is a distribution of η due to the distribution of lifetimes, and this must be taken into account. We have $P(\eta)\,d\eta = P(\tau)\,d\tau$, which leads to:

$$P(\eta) = \frac{1}{\omega T_0}\exp\left[\frac{\alpha - \eta}{\omega T_0}\right]. \tag{5.12}$$

Hence $$\beta = 2\left(\int_{\alpha}^{\infty} P_2(\cos\eta)\ P(\eta)\ d\eta\right) P_2(\cos\chi_0) \qquad (5.13)$$

$$\Rightarrow \qquad \beta = 2\left\{\frac{P_2(\cos\alpha) + (\omega T_0)^2 - 3\ (\omega T_0)\ \sin\alpha\ \cos\alpha}{1 + 4\ (\omega T_0)^2}\right\} P_2(\cos\chi_0), \qquad (5.14)$$

and so writing it out in full, the fragment angular probability distribution is given by:

$$P(\theta) = \frac{1}{4\pi}\left[1 + 2\frac{P_2(\cos\alpha) + (\omega T_0)^2 - 3\ (\omega T_0)\ \sin\alpha\ \cos\alpha}{1 + 4\ (\omega T_0)^2} P_2(\cos\chi_0)\ P_2(\cos\theta)\right]. \qquad (5.15)$$

This is the general expression derived by Busch and Wilson to describe the two effects of rotation: (a) the finite average lifetime, T_0, of the excited parent complex which rotates with angular velocity ω, and (b) the presence of a tangential velocity component yielding a resultant fragment recoil velocity that lies at an angle, α, to the main, radial, velocity component. Equation (5.15) was used by Busch and Wilson to set an upper bound of 0.23 ps on the lifetime of excited NO_2 reached by absorption at 28810 cm^{-1}. If we set T_0 to zero we return to (5.10), which describes instantaneous fragmentation, but still takes into account the tangential velocity effect. If we further decide to omit this tangential velocity effect, by setting $\alpha = 0$, we get back to (5.4). Let us look at (5.15) in a different limit: let us see what happens if we retain the finite lifetime T_0, but assume that $\alpha = 0$. In this limit, the angular distribution for fragment recoil becomes

$$P(\theta) = \frac{1}{4\pi}\left[1 + 2\frac{1 + (\omega T_0)^2}{1 + 4\ (\omega T_0)^2} P_2(\cos\chi_0)\ P_2(\cos\theta)\right], \qquad (5.16a)$$

i.e., $$\beta = 2\frac{1 + (\omega T_0)^2}{1 + 4\ (\omega T_0)^2} P_2(\cos\chi_0). \qquad (5.16b)$$

This formula neglects the effect of the contribution from the tangential velocity of the fragment as this fragment finally breaks free from the rotating complex. This

assumption is justified if $\omega T_0 >> \alpha$ and α is very small, *i.e.*, the assumption holds well if the complex does not dissociate instantaneously ($T_0 \neq 0$) but ω is still small (note that $\alpha \approx \frac{\omega r}{v_0}$ if the rotational energy of the complex is much smaller than the translational energy available to the fragment). Equation (5.16) has been used to determine an upper bound for the lifetime, T_0, of the excited state. For instance, an upper bound of 0.4 ps was found[36] for the lifetime of 350 nm excited methyl nitrite (CH_3ONO), which dissociates to the two neutral fragments CH_3O and NO.

Let us turn our attention now to the approach of Yang and Bersohn[6] and Jonah.[3] These references discuss the effect of a finite lifetime of the excited complex. This predissociation, with an average lifetime T_0, is found to yield an expression for β that is given exactly by (5.16b). In the limit of very slow dissociation ($\omega T_0 >> 1$), the anisotropy is reduced by a factor of 4. If the form of β given by (5.16b) is averaged over the Boltzmann distribution, then one finds

$$\beta = \frac{1}{2}\left(1 + 3\,\gamma' e^{\gamma'} \int_{\gamma'}^{\infty} x^{-1} e^{-x} dx\right) P_2(\cos\chi_0), \tag{5.17a}$$

where $\gamma' = \frac{I}{8kT\,T_0}$, and I is the parent moment of inertia. (5.17b)

Next, the effect of the presence of a small tangential velocity of the fragments during rotation when treated as a separate effect, is seen to reduce β by a factor of:[3, 6]

$$1 - \frac{3}{2}\sqrt{2}\ kT/E_{rel} + O\left[(kT/E_{rel})^2\right], \tag{5.18}$$

where E_{rel} is the energy of relative motion of the fragments. Equation (5.18) was derived for a diatomic molecule. Let us see how this description compares with that of Busch and Wilson. In particular, consider the presence of the $P_2(\cos\alpha)$ in

(5.10). If $v_t << v_0$ then $\alpha = \sin^{-1}\frac{v_t}{v_0} \approx \frac{\omega\, r}{v}$, and hence $P_2(\cos\alpha) \approx 1 - \frac{3}{2}\frac{\omega^2 r^2}{v^2}$. But $\frac{\omega^2 r^2}{v^2} \propto \frac{\langle E_{rot}\rangle}{E_{rel}} \propto \frac{kT}{E_{rel}}$ and so it follows that the two approaches show the same dependence on the ratio of the rotational energy to the translational energy. Yang and Bersohn state that application of (5.18) to typical cases causes a reduction of β by 5 - 10%. Busch and Wilson apply their general formula, (5.15), to the problem of the photodissociation of NO_2 (at 28810 cm^{-1}) and find $\langle\omega\rangle = \left(\frac{\pi k T}{2 I}\right)^{1/2} = 3.5 \times 10^{12}\ s^{-1}$, $v_t \sim 400 - 500\ ms^{-1}$ and $\alpha \sim 13° - 24°$, which implies that $P_2(\cos\alpha) \sim 0.92 \rightarrow 0.75$, corresponding to a reduction in the magnitude of β on the order of 8 to 25%.

5.3 Probing to Ionization and KETOF Detection

When the pump pulse encountered the ground state parent molecules, it found these with an isotropic distribution of dipole moments because these molecules were randomly oriented (in the molecular beam). This is the assumption used in (5.5): any orientation of the parent transition dipole moment, μ, is equally probable. Upon excitation, these parent molecules began to dissociate, with a finite average excited state lifetime, T_0, before breaking apart into two fragments. The CM velocity angular distribution of one of these fragment types was found to be, in general, anisotropic (with the rare exception of χ_0 = magic angle = 54.7°) and is given by (5.4):

$$P(\theta) = \frac{1}{4\pi}\left[1 + \beta\, P_2(\cos\theta)\right], \quad \text{(fragment distribution due to pump)} \qquad (5.19)$$

where θ is the angle between the pump laser polarization, ε_{pu}, and the final direction of recoil given by the final recoil velocity, **v**. The anisotropy parameter, β, characterizing this distribution, was described in detail already.

When the probe pulse arrives (at a time delay, t, after the pump) it sees an anisotropic fragment recoil velocity angular distribution, characterized by β. It also encounters an anisotropic fragment rotational distribution. This is different from the case of the pump excitation, because when the pump arrived the rotational distribution of the parent molecules was isotropic. It is therefore necessary to know the fragment rotational distribution as well. In order to eliminate the effect of molecular alignment, one may be able, with a specific detection scheme, to use the magic angle ($\nu = 54.7°$) between the pump (ε_{pu}) and probe (ε_{pr}) beam polarization vectors. This may be done for both LIF measurements[8, 15] and for REMPI TOF. We shall concentrate on TOF detection here and discuss the velocity profiles obtained for arbitrary orientations of ε_{pu}, ε_{pr} and the TOF axis. The description of the translational and rotational anisotropies for the situation in which the probe pulse arrives after the excited molecules have completely dissociated ($t >> T_0$) has been treated in the literature. After presenting results and references pertaining to this situation, we shall proceed to discuss the case in which the transition state of the dissociating complex is probed. The sections on free fragment probing and on transition-state probing may be read in reverse order as the necessary concepts are very different and are described in each section from the beginning.

5.3.1 Free Fragment Probing

Let us first introduce and develop the formalism required to describe the physical state of the molecular system. Mons and Dimicoli[33] have described very clearly the case of a pump initiated dissociation for which the resulting free fragments are probed by REMPI. They have related the TOF distribution to the angular correlation between the fragment velocity, angular momentum, the pump and probe orientations, the parent transition moment, and the direction of the TOF axis. In general,[21] the intensity, I, of any optical process acting on a set of rotating molecules, characterized by its moments or multipoles, ${}^{(R)}A_Q^K$, is given by:

$$I = \sum_{K,Q} q_Q^K \, {}^{(R)}A_Q^K, \tag{5.20}$$

where the q_Q^K coefficients depend on the physics of the optical process, R(Ox,Oy,Oz) is a fixed axis system, and K and Q are integers with $-K \le Q \le K$.[33] The moments are defined in such a way that the ${}^{(R)}A_{Q\neq 0}^K$ moments vanish if the angular distribution of the angular momentum, **J**, is invariant under rotation about the Oz axis. The ${}^{(R)}A_0^K$ moments with odd K vanish if the rotational distribution of **J** is invariant under inversion of the Oz axis. The summation in (5.20) only has even K with Q=0 if the optical process exhibits invariance under rotation around an Oz' axis (axis system R') and invariance under inversion of this axis. The highest value of K in the sum is twice the maximum tensorial order appearing in the operator responsible for the optical process.[21] Rotational and inversion invariance with respect to an Oz' axis is satisfied by a REMPI process induced by a linearly polarized probe laser. The Oz' axis here is parallel to the probe polarization axis, ε_{pr}. Hence, the probe intensity for each rotational level is given by:

$$I = \sum_{K\ even} q_K\ {}^{(R')}A_0^K, \tag{5.21}$$

where the q_K are real and determined by the probed quantum state of the fragment. The same treatment applies to LIF in which linearly polarized light is used. However, for invariance under rotation, the fluorescence must be detected in a direction parallel to the laser polarization. The q_2 coefficient for LIF detection has been calculated for one[37] and two[15] photon excitation.

For REMPI detection little is known about the rotational selection rules for the ionization step.[38] This difficulty is removed if the last step is a very high probability (near 1 and hence isotropic) ionization step, in which case the anisotropy of the whole process only depends on the preceding steps made by the probe: e.g., in a 2+1 REMPI probing of the fragments, the anisotropy would depend on the two photon step if the final step has very high probability. The highest K value appearing is then 4 (if there is strong saturation present in the first two steps, then the REMPI process may become very weakly sensitive to even higher moments[38]). The intensity dependence for a linearly polarized probe (ε_{pr} along Oz') then reduces to:

$$I = I_0 \left(1 + q_2\ {}^{(R')}A_0^2 + q_4\ {}^{(R')}A_0^4\right), \tag{5.22}$$

where the q_K are assumed to be known and the A_0^K are mean values of combinations of the angular momentum operators, **J**, of the fragment that resulted from the pump process:[8, 33]

$$A_0^0 = 1, \tag{5.23a}$$

$$A_0^2 = \left\langle \frac{3\ J_z^2 - J^2}{J^2} \right\rangle = 2 \left\langle P_2(\hat{\mathbf{J}}.\hat{\mathbf{z}}) \right\rangle, \tag{5.23b}$$

$$A_0^4 = \left\langle \frac{3\ J^4 - 6J^2 - 30J_z^2J^2 + 25J_z^2 + 35J_z^4}{8J^4} \right\rangle, \tag{5.23c}$$

In the limit $J_i \rightarrow \infty$ for the fragment state $|J_i>$, we get: $A_0^4 = \left\langle P_4(\hat{j}.\hat{z}) \right\rangle$. In general, $-1 \leq A_0^2 \leq 2$ and $-\frac{3}{7} \leq A_0^4 \leq 1$. If the alignment is created by a pump excitation (with ε_{pu} along Oz), then we have ${}^{(R)}A_0^4 = 0$ and $-1 \leq {}^{(R)}A_0^2 \leq \frac{4}{5}$, and for high J_i this becomes: $-\frac{2}{5} \leq {}^{(R)}A_0^2 \leq \frac{4}{5}$. In this case, since ${}^{(Oz')}A_0^2 = {}^{(Oz)}A_0^2 \, P_2(\cos\nu)$, the intensity of a symmetrical probe process (ε_{pr} along Oz') is given by:

$$I(\nu) = I_0 \left(1 + q_2 \; {}^{Oz}A_0^2 \; P_2(\cos\nu)\right), \tag{5.24}$$

where ν is the angle between the pump and the probe laser polarizations. Hence, the fragment rotational alignment A_0^2 can be deduced from measurements of line intensities for different relative orientations of the pump and probe polarization vectors, e.g., using $\nu = 0°$ (parallel) and $\nu = 90°$ (perpendicular):[15, 39]

$$A_0^2 = \frac{2[I(0^0) - I(90^0)]}{\left[I(0^0) + 2\; I(90^0)\right] q_2} \propto \frac{I_{par} - I_{perp}}{I_{par} + 2\; I_{perp}}, \tag{5.25}$$

which is the signal polarization anisotropy, where $I_{par} = I(0°)$ and $I_{perp} = I(90°)$. Equation (5.24) also shows that at $\nu = 54.7°$, the intensity becomes equal to I_0.

However, if a projection of the velocity distribution along an axis Oz'' is detected, then the fragment distribution can not in general be considered as invariant under rotation about the polarization direction ε_{pu} (the Oz axis), unless of course the Oz and Oz'' axes coincide. The general expression, (5.21), should then be used. For instance, in the case of a two photon unsaturated probe process (such as in a 2+1 REMPI, with a saturated final ionization step), we need to use (5.22).

5.3.1.1 Fragment Angular Correlations

First we need to refine the definitions of the angular correlations. Mons and Dimicoli[33] applied a semiclassical model similar to that of Dixon.[22] The correlation between the velocity (**v**) and the angular momentum (**J**) of the probed fragment are described by an angular distribution $P(\omega_t,\omega_r)$ expressed as an expansion on a basis consisting of the bipolar (**v**-**J**) harmonics $B_{KQ}(k_1,k_2,\omega_t,\omega_r)$:

$$P(\omega_t,\omega_r)=\sum_K\sum_Q\sum_{k_1}\sum_{k_2}\frac{\sqrt{2k_1+1}\sqrt{2k_2+1}}{16\pi^2}\,b_Q^K(k_1,k_2)\;B_{KQ}(k_1,k_2,\omega_t,\omega_r), \qquad (5.26)$$

where ω_t and ω_r are the CM angular coordinates of **v** and **J** with respect to μ, the transition moment of the parent molecule. The $b_Q^K(k_1,k_2)$ are called the bipolar moments,[33] and they describe mean values of different types of angular correlations involving μ, **v**, and **J**. The integers k_1 and k_2 are the orders at which the translational and rotational motions are involved, respectively. The $b_0^0(k,k)$ coefficients describe **v** - **J** correlations that are independent of μ. One such coefficient of relevance here is:

$$C=\langle P_2(\cos\omega_{tr})\rangle \qquad (=\sqrt{5}\;b_0^0(2,2)\;), \qquad (5.27)$$

where ω_{tr} is the angle between the CM quantities **v** and **J**. The $b_0^2(k_1,k_2)$ coefficients describe correlations of **v** and/or **J** relative to μ. Another relevant coefficient is the previously encountered anisotropy parameter, $\beta = 2b_0^2(2,0)$, describing the correlation between μ and **v** and it is given by one of the formulas from the preceding section, such as (5.15). Another parameter, which has also been discussed, describes the second order μ - **J** correlation:

$$A=A_0^2(\mathbf{J})=\frac{4}{5}\langle P_2(\cos\theta_r)\rangle \qquad (=\frac{4}{5}\,b_0^2(0,2)\;), \qquad (5.28)$$

where θ_r is the angle between μ and $\mathbf{J}$. Another coefficient will be of importance here: $C' = \sqrt{\frac{7}{2}}\, b_0^2(2,2)$, which describes a μ-**v**-**J** correlation. The quantities C, $\frac{1}{2}\beta$, $\frac{5}{4}$A and C' all lie in the range $-\frac{1}{2}$ to 1.

5.3.1.2 Velocity Profiles of Resonance-Enhanced Multiphoton Ionization (REMPI) Ionized Fragments

Having described the center of mass angular properties of the fragment, the laboratory fragment velocity profile must be found. The following assumptions are made:

- the linear pump polarization, ε_{pu}, lies along an Oz axis.

- dissociation leads to a final single fragment recoil speed, v_0.

- the linear probe polarization, ε_{pr}, lies along an Oz' axis, and the probing process exhibits invariance about this axis and is invariant under inversion of this axis. The q_2 coefficients of this REMPI process are assumed known.

- the velocity profiles of the ionized fragments are detected along an Oz" axis in this KETOF method.

As explained previously, because we perform a velocity projection, we will start with (5.22). The ${}^{(R')}A_Q^K$ moments must be expressed explicitly in terms of the velocity component $v_{\parallel}$ along the Oz" axis. Mons and Dimicoli[33] use the procedure reported by Dixon[22] to arrive at the appropriate expressions. By inserting these ${}^{(R')}A_Q^K$ moments into (5.22), the velocity profile, $g(v_{\parallel})$, of the ionized fragment along the TOF axis (Oz") is obtained ($g(v_{\parallel})$ is used in ref. 22 and here we use $P(v_{\parallel})$). This profile contains not only $P_0(x)$ and $P_2(x)$ like the neutral

fragment profile (5.19), but also terms in $P_4(x)$ and $P_6(x)$. However, the high order Legendre polynomial contributions are difficult to evidence experimentally. According to Mons and Dimicoli, if, in addition, no strong angular correlations are expected, it seems reasonable to neglect these higher order terms and to focus our attention on the first coefficients: β, A, C, and C'. Under these assumptions, the experimental profiles can be expressed in the form:[33]

$$g(v_{\parallel}) = \frac{1}{2v_0}\left(g_0 + g_2 P_2\left(\frac{v_{\parallel}}{v_0}\right)\right)$$

$$\Rightarrow \qquad g(v_{\parallel}) \propto 1 + \beta_{eff}\, P_2\left(\frac{v_{\parallel}}{v_0}\right), \tag{5.29a}$$

where β_{eff} is an effective anisotropy parameter defined by:

$$\beta_{eff} = \frac{g_2}{g_0}, \tag{5.29b}$$

where $\quad g_0 = 1 + q_2\, A\, P_2(\cos\nu), \tag{5.30a}$

and

$$\begin{aligned} g_2 = {} & \beta P_2(\cos\xi) \\ & + q_2 C\left\{2P_2(\cos\xi)\, P_2(\cos\nu) + 6\cos\xi \sin\xi \sin\nu \cos\nu \cos\phi + \frac{3}{2}\sin^2\xi \sin^2\nu \cos 2\phi\right\} \\ & - \frac{2}{7} q_2 C'\left\{4P_2(\cos\xi)\, P_2(\cos\nu) + 6\cos\xi \sin\xi \sin\nu \cos\nu \cos\phi - 3\sin^2\xi \sin^2\nu \cos 2\phi\right\} \end{aligned} \tag{5.30b}$$

in which ξ is the angle between the pump polarization direction, ε_{pu}, and the TOF axis, **S**, and ν is the angle between ε_{pu} and ε_{pr}. The angle φ is given by Fig. 5.5. The dynamical range of the q_2 coefficient is typically $[-\frac{1}{2}, \frac{1}{2}]$.[15] The second degree Legendre polynomial, $P_2\left(\frac{v_{\parallel}}{v_0}\right) = \frac{1}{2}\left[3\left(\frac{v_{\parallel}}{v_0}\right)^2 - 1\right]$, in (5.29a), expresses the fact that the velocity profile is parabolic, where $v_{\parallel}$ lies in the range $-v_0 \le v_{\parallel} \le v_0$. The

limits $v_{\parallel} = \pm v_0$ describe fragments whose final recoil velocity was aligned either directly up along and parallel to the TOF axis or directly down, anticollinear with the TOF axis. The point $v_{\parallel}=0$ corresponds to fragments whose final recoil velocity was perpendicular to the TOF axis. The velocity profile is shown in Fig. 5.6 for different values of β_{eff}.

The most commonly used method detects the REMPI ionized fragments through a TOF system in which an electric field, **E**, is responsible for velocity discrimination. Here, the TOF for the ionized fragments is a linear function of their velocity projection onto the TOF axis at the ionization time[33] (see section 5.4 for derivation) and hence the TOF spectra obtained can be considered as good images of the velocity profile. Mons and Dimicoli consider various specific pump-probe geometries (see ref. 33 for diagrams with specific values of the correlation coefficients). Here, these cases are given along with a few more. If the pump and probe lasers propagate collinearly and the TOF axis is perpendicular to this propagation direction, then $\phi = 0°$ or 180°, depending on our choice. However, let us look at some geometries that are even more restrictive than this, but which serve as special cases of this set-up:

(1) Pump ∥ Probe ∥ TOF axis, *i.e.*, $\varepsilon_{pu} \parallel \varepsilon_{pr} \parallel \mathbf{S}$ ($\xi = 0, \nu = 0, \phi$ undefined)

$$\beta_{eff} = \frac{\beta + 2\, q_2 \left[C - \frac{4}{7}C'\right]}{1 + q_2 A} \tag{5.31}$$

Here β_{eff} is not just the anisotropy parameter, β, describing the μ-**v** correlation. It is distorted by the alignment parameter A (μ-**J** correlation) and **v**-**J** (C parameter) and μ-**v**-**J** (C' parameter) correlations. The error arising from their omission can reach $\frac{1}{2}$. They therefore have a significant effect.

(2) Pump ∥ TOF axis, probe at magic angle (ξ =0, ν=54.7°, ϕ undefined)

$$\beta_{eff} = \beta \tag{5.32}$$

This experimental geometry directly yields the exact anisotropy of the neutral fragments created by the pump pulse.

(3) Pump ∥ TOF axis, pump ⊥ probe (ξ =0, ν=90°, ϕ undefined)

$$\beta_{eff} = \frac{\beta - q_2\left[C - \frac{4}{7}C'\right]}{1 - \frac{1}{2}q_2 A} \tag{5.33}$$

(4) Probe ∥ TOF axis, pump ⊥ probe (ξ =90°, ν=90°, ϕ= 0)

$$\beta_{eff} = \frac{-\frac{1}{2}\beta + 2\,q_2\left[C + \frac{2}{7}C'\right]}{1 - \frac{1}{2}q_2 A} \tag{5.34}$$

(5) Probe ∥ TOF axis, pump at magic angle (ξ =54.7°, ν=54.7°, ϕ=0)

$$\beta = 2q_2 C \tag{5.35}$$

This doubly magic geometry leaves only the contribution of the **v-J** correlation, and causes the contribution of the second order angular coefficients related to μ: A, β, C', to vanish.

(6) Pump ∥ probe, pump at magic angle to TOF (ξ =54.7°, ν=0, ϕ undefined)

$$\beta_{eff} = 0 \tag{5.36}$$

The experimental profiles are isotropic to the order of the approximation used. This geometry would test the presence of any higher order terms like $q_2\beta_2 P_4\left(\frac{v''}{v_0}\right)$ or $q_4 A_2 P_2\left(\frac{v''}{v_0}\right)$, where $\beta_2 = \sqrt{\frac{7}{2}} b_0^2(4,2)$ is a higher order μ-**v** correlation, and $A_2 = \sqrt{\frac{7}{2}} b_0^2(2,4)$ is a higher order μ-**J** correlation.

(7) Pump $\perp$ TOF, probe at magic angle to pump (ξ=90°, ν=54.7°, ϕ=0)

$$\beta_{eff} = -\frac{1}{2}\beta + q_2\left[C + \frac{4}{7}C'\right] \tag{5.37}$$

(8) Probe $\perp$ TOF, pump at magic angle to probe (ξ=90°-54.7°, ν=54.7°, ϕ =180°)

$$\beta_{eff} = \frac{1}{2}\beta - q_2\left[C - \frac{4}{7}C'\right] \tag{5.38}$$

Using the result of an experiment of type (7) above together with this, one can find the product $q_2 C'$. Alternatively, one can derive $q_2 C'$ using β from (5.32) and $q_2 C$ from (5.35) and combining this with (5.37) or (5.38). The alignment parameter, A, can then be found from (5.31), (5.33), or (5.34).

5.3.2 Probing the Transition-State Region

If femtosecond pump and probe pulses are used, the time delay can be varied on a time scale that is comparable to the average lifetime, T_0, of the excited complex. For short enough settings of the time delay, $t \leq T_0$, the transition state of the complex can be probed. In this case there are, of course, no free fragments and we cannot speak of a fixed fragment velocity or fixed fragment angular momentum.

Let us define $\mu_2(t)$ to be the probing transition moment at time t after the arrival of the pump pulse. Following the pump excitation, the probability of finding the complex with $\mu_2(\theta,\phi)$ in a solid angle $d\Omega$ (= $\sin\theta\ d\theta\ d\phi$) is given, in analogy with equation (5.4), by:

$$P(\theta)\ d\Omega = \frac{1}{4\pi}\left[1+\beta(t)\ P_2(\cos\theta)\right] d\Omega, \tag{5.39a}$$

where θ is the angle between $\mu_2(t)$ and ε_{pu}, and $\beta(t)$ is the anisotropy parameter given, in general, by:

$$\beta = 2\ \left\langle P_2(\hat{\mu}\ .\ \hat{\mu}_2(t))\right\rangle \tag{5.39b}$$

$$= 2\ \left\langle P_2(\cos\zeta(t))\right\rangle, \tag{5.39c}$$

where $\zeta(t)$ is the angle between the parent transition dipole moment, μ, and the probing moment, $\mu_2(t)$ (see Fig. 5.7a). The ensemble averaging in (5.39) accounts for effects such as those described in (5.9b), as well as accounting for rotational averaging. If, after probing, the velocity of the nascent fragment, **v**, lies along the same direction as $\mu_2(t)$, then $\zeta(t)$ will be the angle between μ and **v** (see Fig. 5.7). The effect of rotation is incorporated into this angle since β describes these effects (see (5.14)). In particular, if rotational effects are negligible, then $\zeta(t) = \chi_0$ (see (5.4b) and (5.39c)).

The probability of probing one of the excited complexes is given by:

$$P_{pr}(\Theta) \propto \cos^2\Theta, \tag{5.40}$$

where Θ is the angle between ε_{pr} and $\mu_2(t)$ (see Fig. 5.7b). The probability of finding a probed molecule, whose orientation at the time of probing, t (=time delay), was given by $\mu_2(\theta,\phi)$, is then:

$$P(\theta,\phi)\ d\Omega \propto \left[1+\beta(t)\ P_2(\cos\theta)\right] \cos^2\Theta\ d\Omega. \tag{5.41}$$

If rotational effects are negligible, and the final velocity, $\mathbf{v}$, is parallel to μ, then $P(\theta,\phi)d\Omega$ is the probability of finding a fragment from the probed molecule traveling in a solid angle $d\Omega$ in the direction given by the velocity of this fragment, $\mathbf{v}(\theta,\phi)$.

First, let us digress and ask the question: what is the total absorption of the probe laser? This question is relevant to an experiment in which the intensity of the transmitted probe laser is measured.[40] The probe absorption coefficient at time t is given by:

$$\alpha(t) \propto \int P(\theta,\phi)d\Omega, \tag{5.42}$$

where the integration is performed over all solid angle (4π). The transmitted intensity is given by the Beer-Lambert law:[41]

$$i(t) = i_0 e^{-\alpha(t)\, l}, \tag{5.43}$$

where i(t) is the probe pulse intensity after the sample, i_0 is the intensity before the sample, and l is the sample length. Using the identity:

$$\cos\Theta = \sin\theta\,\sin\phi\,\sin\nu + \cos\theta\,\cos\nu, \tag{5.44}$$

obtained by looking at the dot product, $\mu_2(t) \cdot \varepsilon_{pr}$, in Fig. 5.7b, we find that

$$\alpha(t) \propto \int \left[1+\beta(t)\, P_2(\cos\theta)\right] \cos^2\Theta\, \sin\theta\, d\theta\, d\phi \tag{5.45a}$$

$$\Rightarrow \quad \alpha(t) \propto \frac{4\pi}{3}\left[1+\frac{2}{5}\beta(t)\, P_2(\cos\nu)\right] \tag{5.45b}$$

$$\propto 1+\frac{2}{5}\beta(t)\, P_2(\cos\nu) \tag{5.45c}$$

$$\Rightarrow \quad \alpha(t) \propto 1+ 2\, r(t)\, P_2(\cos\nu), \tag{5.45d}$$

where $r(t) \equiv \dfrac{\beta(t)}{5} = \dfrac{2}{5}\left\langle P_2(\hat{\mu} \cdot \hat{\mu}_2(t))\right\rangle = \dfrac{2}{5}\left\langle P_2(\cos\zeta(t))\right\rangle$ is the so called reduced anisotropy. The proportionality constant in (5.45d) is $\sigma_{pr}\sigma_{pu}\alpha_{pu}n$, where σ_{pu} and σ_{pr} are the absorption cross-sections for the pump and probe transitions

respectively, α_{pu} is the total number of photons in the pump pulse per unit area (given by equation (3.1)), and n is the total density of molecules in the region of overlap of the pump and probe (in Millar's thesis,[40] the same cross-section is involved: $\sigma_{pu} = \sigma_{pr}$ $(= \sigma)$). The quantity, $\sigma_{pu}\alpha_{pu}n$, is the concentration or density of molecules excited by the (unsaturated) pump pulse (see section 3.1.2). The absorption coefficient thus depends on the angle, v, between the probe and pump polarizations. If the probe is parallel to the pump ($\varepsilon_{pr} \parallel \varepsilon_{pu}$), then we get:

$$\alpha_{\parallel}(t) \propto 1 + 2\, r(t), \tag{5.46}$$

while for perpendicular polarizations we have:

$$\alpha_{\perp}(t) \propto 1 - r(t). \tag{5.47}$$

This implies that,

$$r(t) = \frac{\alpha_{\parallel}(t) - \alpha_{\perp}(t)}{\alpha_{\parallel}(t) + 2\ \alpha_{\perp}(t)}. \tag{5.48}$$

It was assumed above that the pump and probe processes were essentially instantaneous. The effect of the pulse shapes on $\alpha(t)$ is described by convoluting $\alpha(t)$ calculated assuming δ-function pulses (equation (5.45d)) with the cross-correlation of the pump and probe pulses (see ref. 40). This ends the short digression.

We shall now proceed to discuss what happens when we detect the ions along a TOF direction. We shall restrict the discussion to the case in which the final recoil velocity, **v**, is along the direction of the probing transition moment, $\mu_2(t)$, *i.e.*, we have a parallel probe transition. In general, the velocity profile along the TOF axis involves an integration around this axis, adding up the probability that an ion is traveling with a velocity whose projection along the TOF axis is $v_{\parallel}$ (an analogous treatment, but for free fragments and expressing the distribution as a function of a Doppler shift, can be found in the Appendix of ref.

22). The most general case, in which ε_{pu}, ε_{pr}, and the TOF axis are oriented in arbitrary directions, is presented in section 5.5. Here, we will present the case in which the pump polarization, ε_{pu}, is along the TOF axis. Using $v_{\parallel}=v_0 \cos\theta$, it follows that $d\Omega = \sin\theta\, d\theta\, d\phi = -\frac{dv_{\parallel}}{v_0} d\phi$. The angle θ lies in the range $0 \le \theta \le \pi$, corresponding to $v_0 \ge v_{\parallel} \ge -v_0$. We can therefore write,

$$P(v_{\parallel})\, dv_{\parallel} \propto \Big[\int_{\theta \text{ fixed}} P(\theta,\phi)\, d\phi \Big]\, dv_{\parallel}. \tag{5.49}$$

Making use of (5.44), and carrying out the integration yields,

$$P(v_{\parallel})\, dv_{\parallel} \propto \left[1+\beta\, P_2\left(\frac{v_{\parallel}}{v_0}\right)\right]\left[1+2\, P_2(\cos\nu)\, P_2\left(\frac{v_{\parallel}}{v_0}\right)\right] dv_{\parallel}, \tag{5.50}$$

where ν is the angle between ε_{pu} and ε_{pr}, and the TOF axis is along ε_{pu}. Equation (5.50) describes the velocity profile obtained in a process involving one pump photon, and one probe transition from the transition state (if additional steps are made by the probe, then (5.40) must be altered).

If the neutral fragments following pump excitation could be detected, then the observed velocity profile would be given by $1+ \beta\ P_2(v_{\parallel}/v_0)$. The effect of probing the transition-state is to introduce the second factor, $1+ 2\ P_2(\cos\nu)\ P_2(v_{\parallel}/v_0)$, in (5.50). If the polarization of the probe is oriented at the magic angle to that of the pump ($\nu = 54.7°$), then this second factor reduces to unity and the velocity profile is unaltered by the probing.

Let us consider the two distinct cases of a parallel ($\beta = 2$) and a perpendicular pump transition ($\beta = -1$), and in each case investigate the effect of probing with a polarization that is either parallel or perpendicular to the pump polarization. These cases are illustrated in Fig. 5.8 in which both the spatial distributions and the velocity profiles are shown.

(i) Parallel pump transition: $\beta = 2$.

The spatial distribution generated by the pump *only* is $\frac{3}{4\pi}\cos^2\theta$, and the corresponding velocity profile is proportional to $(v_{\parallel}/v_0)^2$, *i.e.*, parabolic and peaking at $\pm v_0$. Probing the transition state alters this profile in a way that depends on the orientation of the probe polarization:

(a) TOF ∥ pump ∥ probe ($\nu = 0°$)

In this case, the resulting spatial distribution, $P(\theta,\phi)$, is proportional to $\cos^2\theta\cos^2\theta$, *i.e.*, $\cos^4\theta$, and the velocity profile is given by:

$$P(v_{\parallel}) \propto (v_{\parallel}/v_0)^2 (v_{\parallel}/v_0)^2 = (v_{\parallel}/v_0)^4. \qquad (5.51)$$

The velocity profile is thus enhanced and sharpened near the limits $\pm v_0$.

(b) TOF ∥ pump ⊥ probe ($\nu = 90°$)

$$P(\theta,\phi) \propto \cos^2\theta \sin^2\theta \sin^2\phi;$$

$$P(v_{\parallel}) \propto (v_{\parallel}/v_0)^2 [1-(v_{\parallel}/v_0)^2]. \qquad (5.52)$$

The velocity profile is greatly altered and the yield of ions is less than for case (a) above.

(ii) Perpendicular pump transition: $\beta = -1$.

The spatial distribution generated by the pump only is $\frac{3}{8\pi}\sin^2\theta$ and so the velocity profile is proportional to $1-(v_{\parallel}/v_0)^2$, *i.e.*, parabolic and peaking at $v_{\parallel}=0$, corresponding to a preference for fragmentation in the plane perpendicular to the pump polarization. This profile is also altered upon probing the transition state:

(a) TOF ∥ pump ∥ probe ($\nu = 0°$)

The resulting distribution here is given by:

$$P(\theta,\phi) \propto \sin^2\theta\cos^2\theta;$$

$$P(v_{\parallel}) \propto [1-(v_{\parallel}/v_0)^2]\,(v_{\parallel}/v_0)^2. \qquad (5.53)$$

The velocity profile is thus changed and the yield is lower than for case (b) below.

(b) TOF ∥ pump ⊥ probe ($\nu = 90°$)

$$P(\theta,\phi) \propto \sin^2\theta \sin^2\theta \sin^2\phi = (\sin^2\theta)^2 \sin^2\phi;$$

$$P(v_{\parallel}) \propto [1-(v_{\parallel}/v_0)^2]\,[1-(v_{\parallel}/v_0)^2] = [1-(v_{\parallel}/v_0)^2]^2. \qquad (5.54)$$

The velocity profile is enhanced about $v_{\parallel}=0$ due to the probing.

5.4 Kinematics and Energetics

Here we will derive some of the basic equations related to the KETOF method. First it will be shown that the time-of-flight for the ionized fragments is a linear function of their velocity projection, $v_{\parallel}$, onto the TOF axis. It is convenient to consider two identical ions formed at the same initial spatial position $\mathbf{r}_1$ with equal but oppositely directed speeds along the (vertical) TOF axis (ion 1, say, travels vertically upwards). Ion 2 is decelerated by the electric field **E** of the extraction region until it stops at a position $\mathbf{r}_2$ directly below $\mathbf{r}_1$. It is then accelerated, and returns to $\mathbf{r}_1$ with its original speed, and in the same time it took to decelerate from $\mathbf{r}_1$ to $\mathbf{r}_2$. Subsequently, the motion of ion 2 is identical to that of ion 1, which it will now continue to lag by the "turn-around" time. Let us look at ion 2 (which has a charge q): it has a vertical acceleration:

$$a = qE/m, \qquad (5.55)$$

since the force acting on it is given by: F = ma = qE. The time, T_1, taken to stop when moving downward is given by (using v = u + at):

$$T_1 = \frac{mv_{\parallel}}{qE}. \tag{5.56}$$

The ion then accelerates back, passing through the initial position. As it is a conservative field, the speed at the return to the initial position will be the same as the initial speed (just directed in the opposite direction), hence the time to accelerate back to the initial position is given by:

$$T_2 = T_1 = \frac{mv_{\parallel}}{qE}. \tag{5.57}$$

The total turn-around time is then given by:

$$2\,T_1 = 2\frac{mv_{\parallel}}{qE}. \tag{5.58}$$

Hence, t, the position relative to the central time T (note: $T \propto \sqrt{m}$) in the TOF spectrum corresponding to $v_{\parallel}$ is given by:

$$t = -\frac{mv_{\parallel}}{qE}. \tag{5.59}$$

Therefore, the total time-of-flight, $T+t$, is a linear function of the velocity projection, $v_{\parallel}$. In an experiment, the maximum time spread for a particular fragment ion, Δt, resulting from an initial fixed translational energy release (fixed initial fragment speed v_0) is the "turn-around" time of an ion of this type, whose initial velocity lies directly downwards, parallel to the TOF axis. We therefore have:

$$\Delta t = 2\frac{mv_0}{qE}. \tag{5.60}$$

The kinetic energy of the ion is $E_{kin} = \frac{1}{2}mv_0^2$, which can then be written:

$$E_{kin} = \frac{q^2E^2(\Delta t)^2}{8m}. \tag{5.61}$$

Because of the excitation distribution, determined by the pump polarization and the direction of the transition moment, there is a distribution in t, as discussed

below. It should be mentioned that alternative methods of determining the kinetic energy release have been used: one such uses a pulsed-acceleration TOF mass spectrometer.[42] They will not be discussed further here.

In the type of experiment considered, two fragments (1 and 2) are formed in the dissociation of the pump excited molecule. Let us define the ground state of the parent as the zero of potential energy. If the pump accesses the potential energy surface $V_1(R)$, then, because of conservation of energy in the CM frame, we have:[43]

$$E_{avl} = V_1(R_{pu}) - V_1(\infty) = E_{int} + E_t, \tag{5.62}$$

where E_{avl} is the energy available to be partitioned among internal and translational degrees of freedom of the recoiling fragments, $V_1(R_{pu}) = E^P_{int} + h\nu_{pu}$, $V_1(\infty) = D^0_0$, E^P_{int} is the thermal internal energy of the parent molecule, $h\nu_{pu}$ is the pump energy, D^0_0 is the dissociation energy from the ground state parent to the ground state fragments, E_{int} is the total internal excitation energy of the two neutral fragments and E_t is the total CM translational energy of both fragments.

In the CM frame ($\mathbf{p_1} = -\mathbf{p_2}$; $p_1 = p_2 \equiv p$) the total available translational energy is shared between the two fragments:

$$E_t = E_{kin1} + E_{kin2}, \tag{5.63}$$

where $E_{kin1} = \frac{p^2}{2m_1}$, and $E_{kin2} = \frac{p^2}{2m_2}$. Hence we have the relationships:

$$E_{kin1} = \frac{E_t}{1+\frac{m_1}{m_2}}$$

and $$E_{kin2} = \frac{E_t}{1+\frac{m_2}{m_1}} = \frac{m_1}{m_2}E_{kin1}. \tag{5.64}$$

5.4.1 Free Fragment Probing

Consider the probing of a free fragment. Conservation of energy in the frame in which the fragment is at rest (the frequency shift in the probe in going from the laboratory frame to this frame is negligible as $v/c \ll 1$) is given by:

$$E_{int1} + h\nu_{pr} = \frac{p_e^2}{2m_e} + \frac{p_1'^2}{2m_1} + E_{int1}', \tag{5.65}$$

where, in this frame, $\mathbf{p_e}$ is the momentum of the emitted electron, $\mathbf{p_1}'$ is the momentum of the resulting ionized fragment, E_{int1} is the internal energy of the free fragment before it is ionized, E_{int1}' is the internal energy of the ionized fragment and $h\nu_{pr}$ is the energy of the probe photon. Conservation of momentum in this frame implies that

$$\mathbf{p}_\gamma = \mathbf{p_1}' + \mathbf{p_e}, \tag{5.66}$$

where $\mathbf{p}_\gamma$ is the photon momentum. Let us consider some of the magnitudes involved here. From (5.65) we obtain a very rough order of magnitude estimate for the momentum of the ion in this frame (see later for better estimate):

$$p_1' \sim \sqrt{2m_1 h\upsilon_{pr}} \sim 5 \times 10^{-22} \text{ kg m s}^{-1}, \tag{5.67}$$

for a fragment ion of mass ~ 100 amu and for a probe wavelength ~ 300 nm. In contrast,

$$p_\gamma = \frac{h}{\lambda} \sim 2 \times 10^{-27} \text{ kg m s}^{-1}. \tag{5.68}$$

Therefore, (5.66) becomes:

$$\mathbf{p_1}' + \mathbf{p_e} = 0, \quad \text{or} \quad v_1' = \frac{m_e}{m_1} v_e \tag{5.69}$$

For example, if $m_1 = 100$ amu then $v_1' \approx \frac{1}{100}\frac{m_e}{m_p}v_e \approx \frac{1}{100}x\frac{1}{1836}v_e \sim 5 \times 10^{-6}\, v_e$.

Equation (5.64) implies that the kinetic energy of the ionized fragment in this frame is

$$E_{kin1}' = \frac{p_1'^2}{2m_1} = \frac{m_e}{m_1}\frac{p_e^2}{2m_e} = \frac{m_e}{m_1}E_{e\ kin}. \tag{5.70}$$

Hence the estimate made in (5.67) was instead a good estimate for p_e and not for p_1' which should instead be estimated at:

$$p_1' \sim \sqrt{\frac{m_e}{m_1}}\sqrt{2m_1 h\upsilon_{pr}} \sim 1 \times 10^{-24}\ \text{kg m s}^{-1}, \tag{5.71}$$

which, although it is three orders of magnitude smaller than the momentum of the emitted electron, is still three orders of magnitude larger than the momentum of the probe photon. The additional velocity imparted to a 100 amu fragment is then ~ 6 m s^{-1}, *i.e.*, of order 10 m s^{-1}. This is negligible in comparison with the velocity that the fragment has in the CM frame (or that it has in the laboratory frame): typically of order 10^3 to 10^4 m s^{-1} (in the dissociation initiated by the pump pulse the two nascent fragments were of comparable mass, thus sharing the available translational energy more evenly).

5.4.2 Probing the Transition-State Region

On the other hand, if the pump-probe delay time is small enough ($t \leq T_0$) that the transition state is probed, then the picture is different. In the transition state, the available energy, partitioned among internal and translational degrees of freedom, is given by:

$$E_{avl}^{TS}(R) = V_1(R_{pu}) - V_1(R) = E_{int}(R) + E_t(R). \tag{5.72}$$

When the transition state is probed to a dissociative state above the ionization level, the excess energy above the asymptotic level (free ion and free fragment) can be shared by the two nascent parts as well as by the ejected electron. The kinetic energy of the resulting ion thus depends on the probe wavelength or excess energy probed to. Immediately after probing, the velocity, $\mathbf{v}(t)$, is unchanged. However, the subsequent evolution is on a new potential energy surface, $V_2(R)$, with a different total available energy. If the kinetic energy, E_e, of the photoelectron is measured, then the difference potential may be determined. It should be noted that if the potential energy, V_1, has dropped significantly (*i.e.*, dropped from $V_1(R_{pu})$ to $V_1(R_{pr})$, where $V_1(R_{pr}) - V_1(\infty) << V_1(R_{pu}) - V_1(\infty)$), then the ionization process is characteristic of the asymptotic limit (free fragment probing) and the kinetic energy release is similar to that of the neutrals on V_1.

5.5 Velocity Profile for Arbitrary TOF and Polarization Directions

In section 5.3.2 of the text, the velocity profile of the ions, resulting from a probing of the transition-state region, was derived for the case in which the TOF axis was parallel to the pump polarization, $\boldsymbol{\varepsilon_{pu}}$. Here we shall treat the same experiment (one pump, and one probe transition), but generalize to the case where the TOF axis is also allowed to be in an arbitrary direction. The angles defining the orientations of $\boldsymbol{\varepsilon_{pu}}$, $\boldsymbol{\varepsilon_{pr}}$, the TOF axis, and the (ionized) fragment velocity, $\mathbf{v}$, are shown in Fig. 5.9. The spatial distribution, $P(\theta,\phi)$, is, of course, independent of the direction of the TOF axis, and is still given by (5.41). However, we now have $v_{\|} = v_0 \cos\eta$, where η is the angle between $\mathbf{v}$ and the TOF axis (see Fig. 5.9), and ϕ is the azimuthal angle about the TOF axis (see Fig. 5.9). Therefore, we write:

$$P(v_{\parallel})\ dv_{\parallel} \propto \left[\int_{\eta \text{ fixed}} P(\theta,\phi)\ d\phi \right] dv_{\parallel}, \tag{5.73}$$

where θ is expressed in terms of η and ϕ. By looking at the dot product, $\mathbf{v} \cdot \varepsilon_{pu}$, we find (see Fig. 5.9):

$$\cos\theta = \sin\eta \cos\phi \sin\xi + \cos\eta \cos\xi, \tag{5.74}$$

where ξ is the angle between ε_{pu} and the TOF axis. Looking at the scalar product, $\mathbf{v} \cdot \varepsilon_{pr}$, shows that:

$$\cos\Theta = \sin\eta \cos\phi \sin\psi \cos\Phi + \sin\eta \sin\phi \sin\psi \sin\Phi + \cos\eta \cos\psi, \tag{5.75}$$

where ψ is the angle between ε_{pr} and the TOF axis, and Φ is the angle between the plane that ε_{pu} and the TOF axis lie in and the plane containing ε_{pr} and the TOF axis.

Carrying out the integration in (5.73) and making use of simplifying identities such as:

$$\cos^2\psi \cos^2\eta + \frac{1}{2}\sin^2\psi \sin^2\eta = \frac{1}{3}\left[1 + 2\ P_2(\cos\psi)\ P_2(\cos\eta)\right] \tag{5.76}$$

leads to

$$\begin{aligned} P(v_{\parallel}) \propto & \left[1 + \beta\ P_2\left(\frac{v_{\parallel}}{v_0}\cos\xi\right)\right]\left[1 + 2\ P_2(\cos\psi)\ P_2\left(\frac{v_{\parallel}}{v_0}\right)\right] \\ & + 9\beta\left[1 - \left(\frac{v_{\parallel}}{v_0}\right)^2\right] \sin\xi \left\{ \left(\frac{v_{\parallel}}{v_0}\right)^2 \cos\xi \cos\psi \sin\psi \right. \\ & \left. + \frac{1}{16}\sin\xi \left(4\left(\frac{v_{\parallel}}{v_0}\right)^2 \cos^2\psi + \left[1 - \left(\frac{v_{\parallel}}{v_0}\right)^2\right] (1 + 2\cos^2\Phi) \sin^2\psi \right) \right\}. \end{aligned} \tag{5.77}$$

This is the velocity profile for arbitrary orientations of ε_{pu}, ε_{pr} and the TOF axis (see Fig. 5.9). If the TOF axis is parallel to the pump polarization, ε_{pu}, then $\xi = 0$, and (5.77) simplifies to (5.50):

$$P(v_{\parallel}) \propto \left[1+\beta P_2\left(\frac{v_{\parallel}}{v_0}\right)\right]\left[1+2 P_2(\cos\nu) P_2\left(\frac{v_{\parallel}}{v_0}\right)\right], \tag{5.78}$$

in that the angle ν between ε_{pu} and ε_{pr} becomes identical to the angle ψ.

Let us consider a new case in which the TOF axis is parallel to the probe laser polarization: $\psi = 0$ in Fig. 5.9. In this case, (5.77) reduces to (omitting an overall factor of 3):

$$P(v_{\parallel}) \propto \left\{1+\beta P_2\left(\frac{v_{\parallel}}{v_0}\cos\xi\right) + \frac{3}{4}\beta\left[1-\left(\frac{v_{\parallel}}{v_0}\right)^2\right]\sin^2\xi\right\}\left(\frac{v_{\parallel}}{v_0}\right)^2. \tag{5.79}$$

If we make the further restriction that the pump polarization be perpendicular to the probe polarization, then $\xi = 90°$ and we obtain:

$$P(v_{\parallel}) \propto \left[1-\frac{1}{2}\beta P_2\left(\frac{v_{\parallel}}{v_0}\right)\right]\left(\frac{v_{\parallel}}{v_0}\right)^2. \tag{5.80}$$

If the pump transition is parallel, then $\beta = 2$ and the velocity profile becomes:

$$P(v_{\parallel}) \propto \frac{3}{2}\left[1-(v_{\parallel}/v_0)^2\right](v_{\parallel}/v_0)^2 \qquad \propto \left[1-(v_{\parallel}/v_0)^2\right](v_{\parallel}/v_0)^2. \tag{5.81}$$

On the other hand, if the pump transition is perpendicular, $\beta = -1$, then we have,

$$P(v_{\parallel}) \propto \frac{3}{4}\left[1+(v_{\parallel}/v_0)^2\right](v_{\parallel}/v_0)^2 \qquad \propto \left[1+(v_{\parallel}/v_0)^2\right](v_{\parallel}/v_0)^2. \tag{5.82}$$

The spatial distribution arising from the above geometry (probe polarization along TOF axis; pump polarization perpendicular to this direction) is in fact given by (see (5.41)):

$$P(\theta,\phi) \propto \left[1+\beta P_2(\sin\eta\cos\phi)\right]\cos^2\eta, \tag{5.83}$$

since $\Theta = \eta$ (hence, $\cos\Theta = \cos\eta = v_{\parallel}/v_0$) and $\cos\theta = \sin\eta\cos\phi$. Of course, one arrives at (5.80) by directly inserting (5.83) into (5.73). The way (5.80) was obtained above was to use the derived, general expression for the velocity

profile, (5.77), and then make the simplifications appropriate to the chosen geometry.

5.6 References

1. R. N. Zare, D. R. Herschbach, *Proc. IEEE* **51**, 173 (1963).
2. R. Bersohn, S. H. Lin, *Advan. Chem. Phys.* **16**, 67 (1967).
3. C. Jonah, *J. Chem. Phys.* **55**, 1915 (1971).
4. R. N. Zare, *Mol. Photochem.* **4**, 1 (1972).
5. G. E. Busch, K. R. Wilson, *J. Chem. Phys.* **56**, 3638 (1972).
6. S. Yang, R. Bersohn, *J. Chem. Phys.* **61**, 4400 (1974).
7. R. Schmiedl, H. Dugan, W. Meier, K. H. Welge, *Z. Phys. A.* **304**, 137 (1982).
8. C. H. Greene, R. N. Zare, *J. Chem. Phys.* **78**, 6741 (1983).
9. C. H. Greene, R. N. Zare, *Annu. Rev. Phys. Chem.* **33**, 119 (1982).
10. U. Fano, J. H. Macek, *Rev. Mod. Phys.* **45**, 553 (1973).
11. R. Vasudev, R. N. Zare, R. N. Dixon, *J. Chem. Phys.* **80**, 4863 (1984).
12. G. A. Chamberlain, J. P. Simons, *J. Chem. Soc. Faraday Trans. 2* **71**, 2043 (1975).
13. G. A. Chamberlain, J. P. Simons, *Chem. Phys. Lett.* **32**, 355 (1975).
14. J. P. Simons, *J. Phys. Chem.* **88**, 1287 (1984).
15. M. Dubs, U. Bruehlmann, J. R. Huber, *J. Chem. Phys.* **84**, 3106 (1986).
16. G. E. Hall, N. Sivakumar, P. L. Houston, *Phys. Rev. Lett.* **56**, 1671 (1986).
17. G. E. Hall, N. Sivakumar, D. Chawla, P. L. Houston, I. Burak, *J. Chem. Phys.* **88**, 3682 (1988).
18. M. P. Docker, A. Hodgson, J. P. Simons, *Chem. Phys. Lett.* **128**, 264 (1986).

19. K.-H. Gericke, S. Klee, F. J. Comes, *J. Chem. Phys.* **85**, 4463 (1986).

20. A. U. Grunewald, K.-H. Gericke, F. J. Comes, *Chem. Phys. Lett.* **133**, 501 (1987).

21. D. A. Case, G. M. McClelland, D. R. Herschbach, *Mol. Phys.* **35**, 541 (1978).

22. R. N. Dixon, *J. Chem. Phys.* **85**, 1866 (1986).

23. G. E. Hall, P. L. Houston, *Annu. Rev. Phys. Chem.* **40**, 375 (1989).

24. S.J. Riley, K.R. Wilson, *Faraday Discuss. Chem. Soc.* **53**, 132 (1972); R. Bersohn In *Advances in Gas-phase Photochemistry and Kinetics*, M.N.R. Ashfold, J.E Baggott, Eds.; Royal Society of Chem.: London (1987) p.1; A.M. Wodtke, Y.T. Lee, *ibid.*, p.31; M.P. Docker, A. Hodgson, J.P. Simons, *ibid.*, p.115; M.N.R. Ashfold, I.R. Lambert, D.H. Mordaunt, G.P. Morley, C.M. Western, J. Phys. Chem. **96** , 2938 (1992).

25. I. Nadler, D. Mahgerefteh, H. Reisler, C. Wittig, *J. Chem. Phys.* **82**, 3885 (1985).

26. A.J. Bain, A.J. McCaffery, *J. Chem. Phys.* **80**, 5883 (1984); **83**, 2627, 2632, 2641 (1985).

27. M. Mons, I. Dimicoli, *Chem. Phys. Lett.* **131**, 298 (1986).

28. G. E. Hall, *et al.*, *Faraday Discuss. Chem. Soc.* **82**, 13 (1986).

29. J. F. Black, I. Powis, *Chem. Phys.* **125**, 375 (1988).

30. R. O. Loo, *J. Phys. Chem.* **92**, 5 (1988).

31. M. Kawasaki, *et al.*, *J. Chem. Phys.* **86**, 4431 (1987).

32. H. J. Krautwald, L. Schnieder, K. H. Welge, M. N. R. Ashfold, *Faraday Discuss. Chem. Soc.* **82**, 99 (1986).

33. M. Mons, I. Dimicoli, *J. Chem. Phys.* **90**, 4037 (1989).

34. R. N. Zare, *Ph. D. Thesis, Harvard University.*

35. A.G. St. Pierre, W.A. Steele, *Phys. Rev.* **184**, 172 (1969).

36. B. A. Keller, P. Felder, J. R. Huber, *J. Phys. Chem.* **91**, 1114 (1987).

37. A. C. Kummel, G. O. Sitz, R. N. Zare, *J. Chem. Phys.* **88**, 7357 (1988).

38. D. C. Jacobs, R. N. Zare, *J. Chem. Phys.* **85**, 5457 (1986).

39. M. Dantus, R. M. Bowman, J. S. Baskin, A. H. Zewail, *Chem. Phys. Lett.* **159**, 406 (1989).

40. D.P. Millar, *Ph.D. Thesis, California Institute of Technology (1982).* In our case here, the probe probes the state that was pumped to, whereas in the work of Millar's thesis, the probe probes the ground state just like the pump.

41. H.J. Hwang, M.A. El-Sayed, *Chem. Phys. Lett.* **170**, 161 (1990); J. *Chem. Phys.* **94**, 4877 (1991); *J. Phys. Chem.* **95**, 8044 (1991); *J. Chem. Phys.* **96**, 856 (1992); *J. Phys. Chem.* **96**, 8728 (1992); See also R.O. Loo, G.E. Hall, H.-P. Haerri, P.L. Houston, *J. Phys. Chem.* **92**, 5 (1988).

42. H. J. Hwang, M. A. El-Sayed, *Chem. Phys. Lett.* **170**, 161 (1990).

43. J. H. Ling, K. R. Wilson, *J. Chem. Phys.* **63**, 101 (1975).

5.7 Figure Captions and Figures

Fig. 5.1: Pseudodiatomic model used to derive the functional form of the anisotropy β (see (5.4)). This shows a nonrotating excited parent molecule which dissociates along **r** at an angle χ_0 to μ, the parent transition moment. Since all orientations of **r** about μ are equally probable, the CM fragment recoil velocity **v** will be found in a cone of half-angle χ_0 about μ.

Fig. 5.2: CM angular probability distribution of the fragments for (non-rotating molecule): (a) Parallel transition: fragment recoil direction is along the direction of the parent transition dipole moment ($\mathbf{v} \parallel \mu$, $\chi_0 = 0$, $\beta = 2$), yielding a dumbbell-shaped distribution; (b) Perpendicular transition: fragment recoil direction is perpendicular to the transition moment ($\mathbf{v} \perp \mu$, $\chi_0 = 90°$, $\beta = -1$), yielding a toroidal-like distribution; (c) Magic angle transition: this is a rare case in which the fragment recoil direction happens to be at the magic angle to the transition moment ($\chi_0 = 54.7°$, $\beta = 0$), yielding an isotropic distribution. For a diatomic molecule, only cases (a) and (b) are possible.

Fig. 5.3: As for Fig. 5.1, there is no excited state lifetime, but we allow for an additional deflection of the CM fragment velocity vector, **v**, by an angle α due to rotation of the molecule. The molecule is equally likely to be rotating in any direction, and hence **v** will be found in a cone of half-angle α about the radial velocity vector $\mathbf{v}_0$. See (5.10).

Fig. 5.4: The excited molecule lives for a finite lifetime τ and rotates through $\psi = \omega\tau$ before dissociating. This angle adds to α from Fig. 5.3 so that $\mathbf{v}$ is found in a cone with half angle $\eta = \alpha + \psi$. See (5.15).

Fig. 5.5: Definition of the angles (θ,ν,ϕ), characterizing the relative arrangement of the vectors (ε_{pu}, ε_{pr}, $\mathbf{S}$) involved in the REMPI-KETOF method.

Fig. 5.6: Velocity profiles of monokinetic fragments, detected in a REMPI KETOF experiment. Fragmentation is induced by the linearly polarized pump pulse, ε_{pu}, generating well-defined μ-$\mathbf{v}$-$\mathbf{J}$ correlations, described by β, A, C, and C'. The linearly polarized probe pulse (ε_{pr}) induces a REMPI process on the well-defined ro-vibronic state(s) of the fragments, characterized by the q_2 coefficient. The effective anisotropy parameter, $\beta_{eff} = \beta_{eff}(\beta, A, C, C', q_2, ...)$, describes the velocity profiles. See (5.29).

Fig. 5.7: (a) The orientations of the pump polarization, ε_{pu}, the pump transition moment, μ, and the probe transition moment, $\mu_2(t)$, in the transition state at a time t after the arrival of the pump pulse. (b) The orientations of ε_{pu}, $\mu_2(t)$, and the probe polarization, ε_{pr}.

Fig. 5.8: The pump polarization, ε_{pu}, is chosen to be along the TOF axis (z-axis). The spatial distributions and corresponding velocity profiles (along the TOF axis) are shown for both a parallel and a perpendicular pump transition. Two probing geometries are shown: $\varepsilon_{pr} \parallel \varepsilon_{pu}$, and $\varepsilon_{pr} \perp \varepsilon_{pu}$ (in the latter case, we choose ε_{pr} to be along the y-axis). The effect of probing is to alter the spatial

distribution and velocity profile (See text; the exception, although not shown, is ν = 54.7° for this set-up). Note that different spatial distributions may have the same velocity profile.

Fig. 5.9: The general case of arbitrary orientations of the pump (ε_{pu}) and probe (ε_{pr}) polarizations, the TOF axis, and the velocity, **v**, which is assumed to be parallel to the probing transition moment, $\mu_2(t)$. See section 5.5.

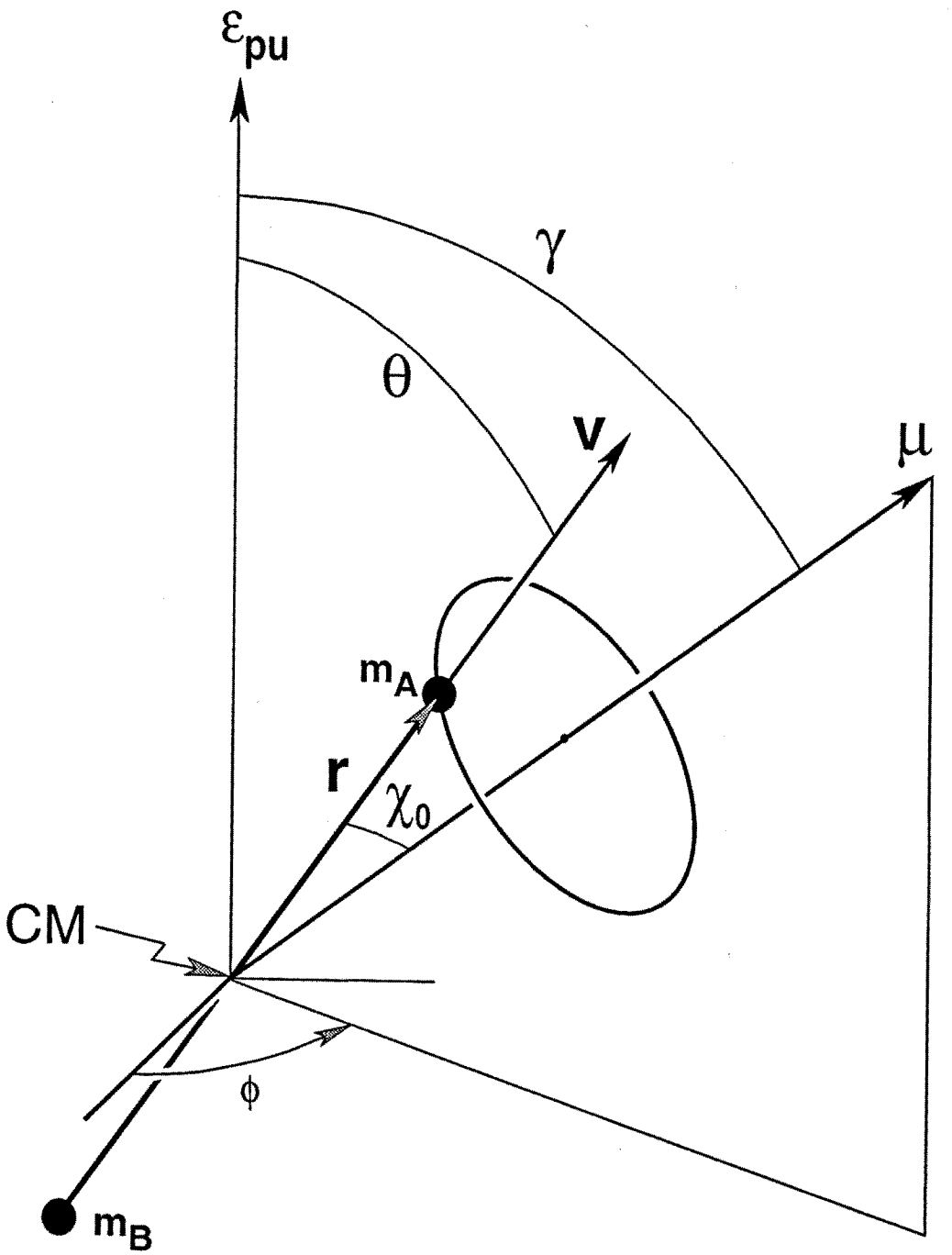
ε_{pu}
γ
θ
$\mathbf{v}$
μ
m_A
$\mathbf{r}$
χ_0
CM
ϕ
m_B

Fig. 5.1

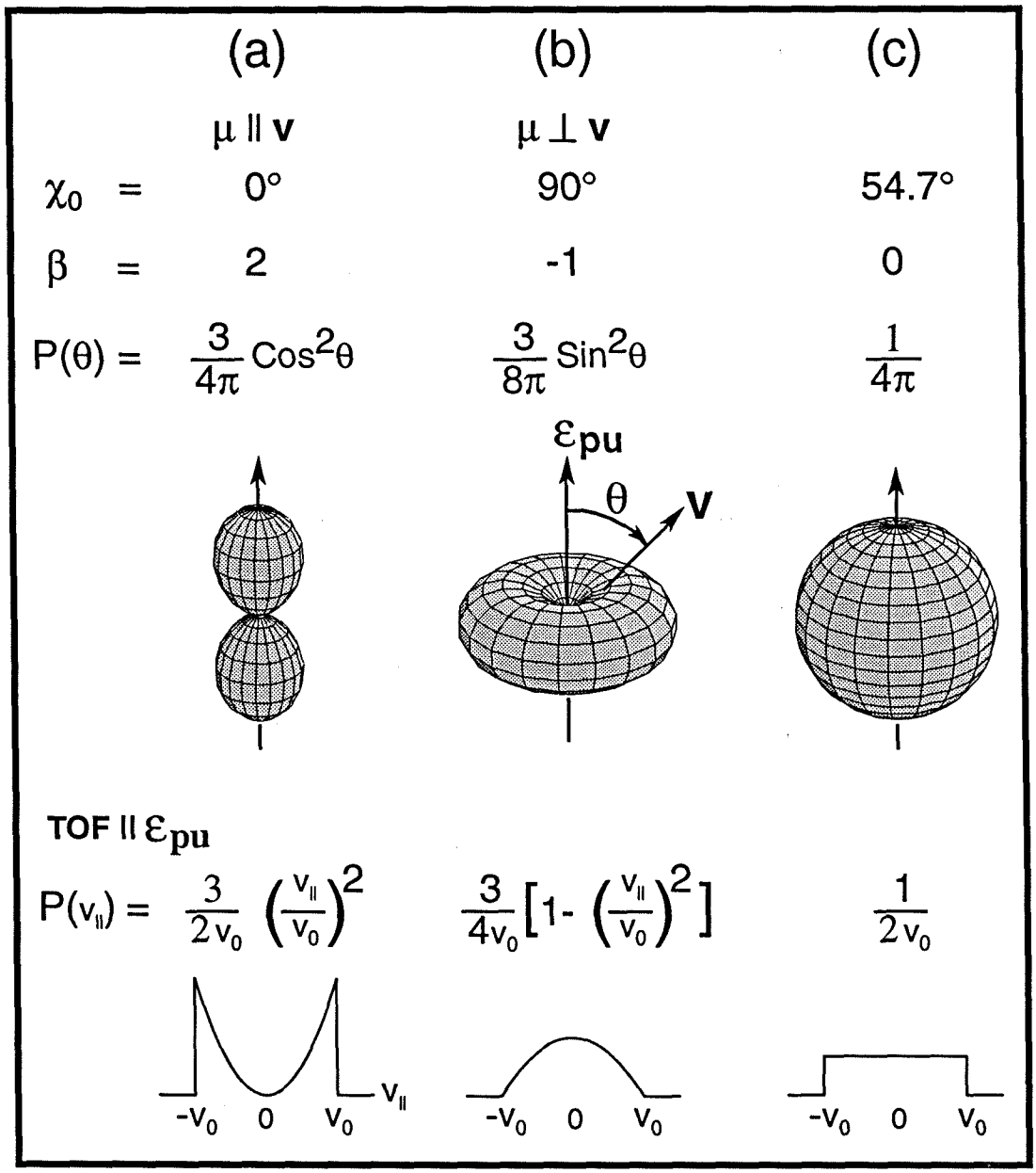
(a)
(b)
(c)
μ ∥ v
μ ⊥ v
χ0 = 0° 90° 54.7°
β = 2 -1 0
P(θ) = 3/4π Cos²θ 3/8π Sin²θ 1/4π
εpu
θ
v
TOF ∥ εpu
P(v∥) = 3/2v0 (v∥/v0)² 3/4v0 [1- (v∥/v0)²] 1/2v0
v∥
-v0 0 v0
-v0 0 v0
-v0 0 v0

Fig. 5.2

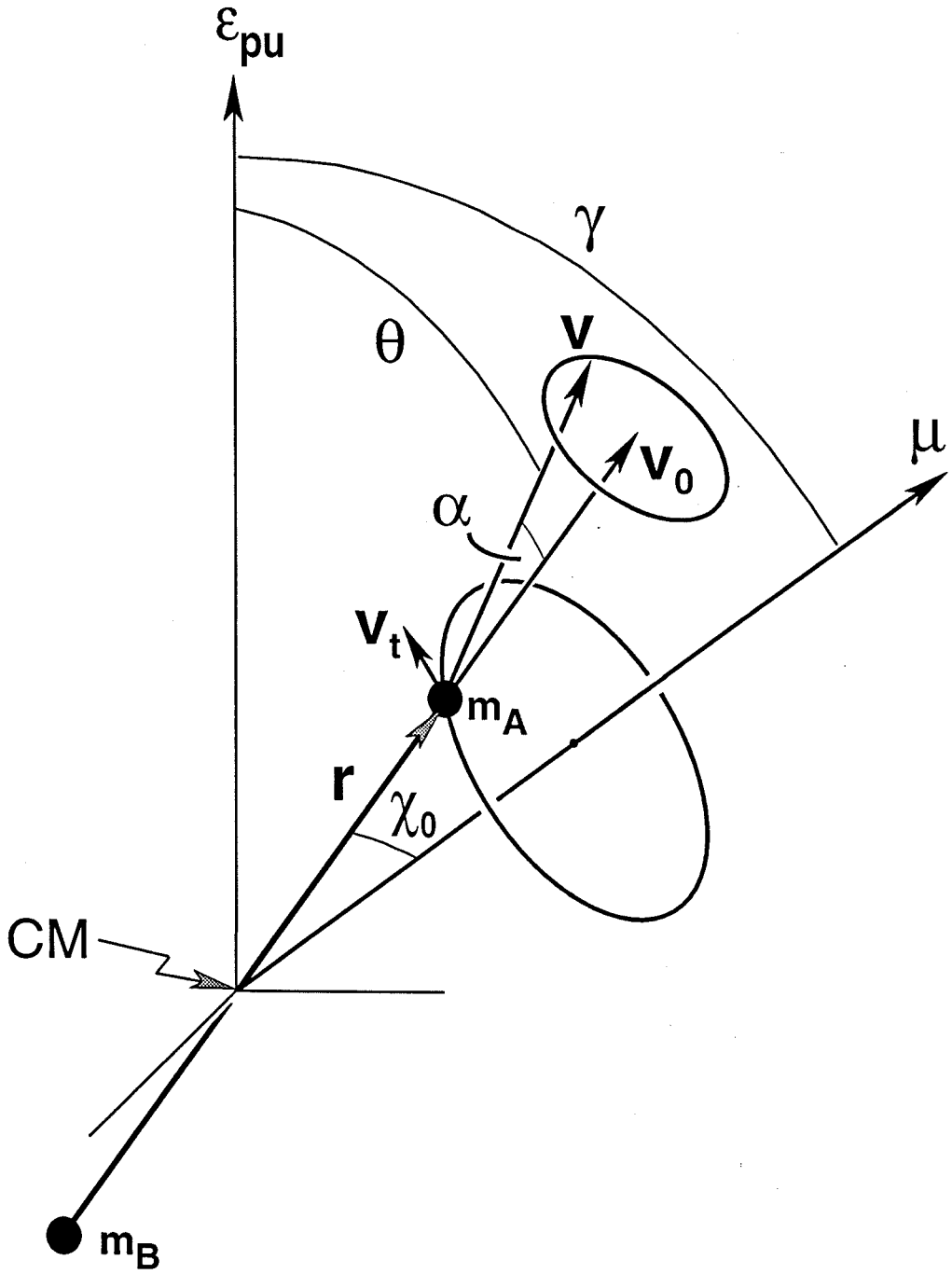
ε_{pu}
γ
θ
$\mathbf{v}$
$\mathbf{v}_0$
μ
α
$\mathbf{v}_t$
m_A
$\mathbf{r}$
χ_0
CM
m_B

Fig. 5.3

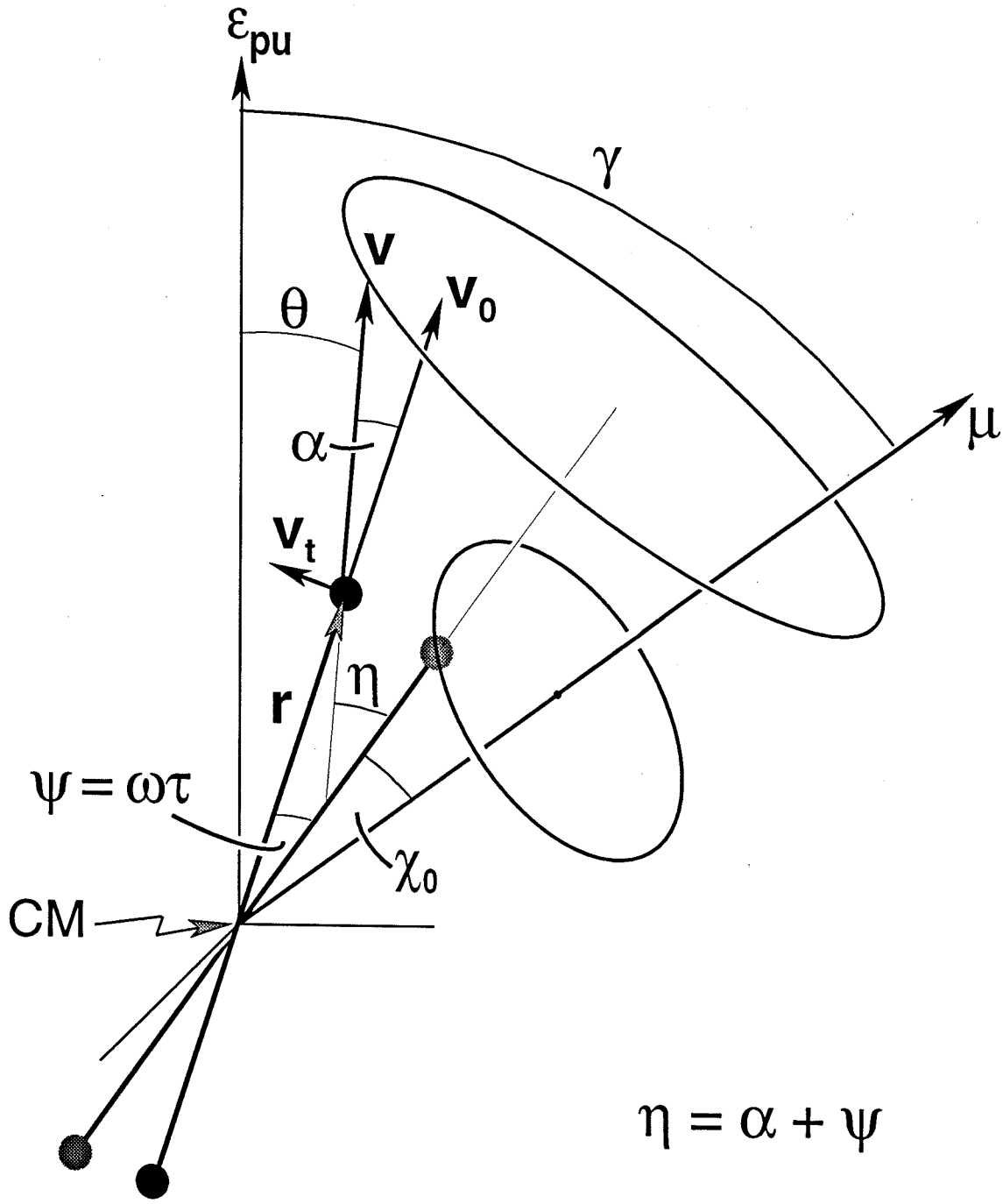
ε_{pu}
γ
$\mathbf{v}$
$\mathbf{v}_0$
θ
α
μ
$\mathbf{v}_t$
η
$\mathbf{r}$
$\psi = \omega\tau$
χ_0
CM
$\eta = \alpha + \psi$

Fig. 5.4

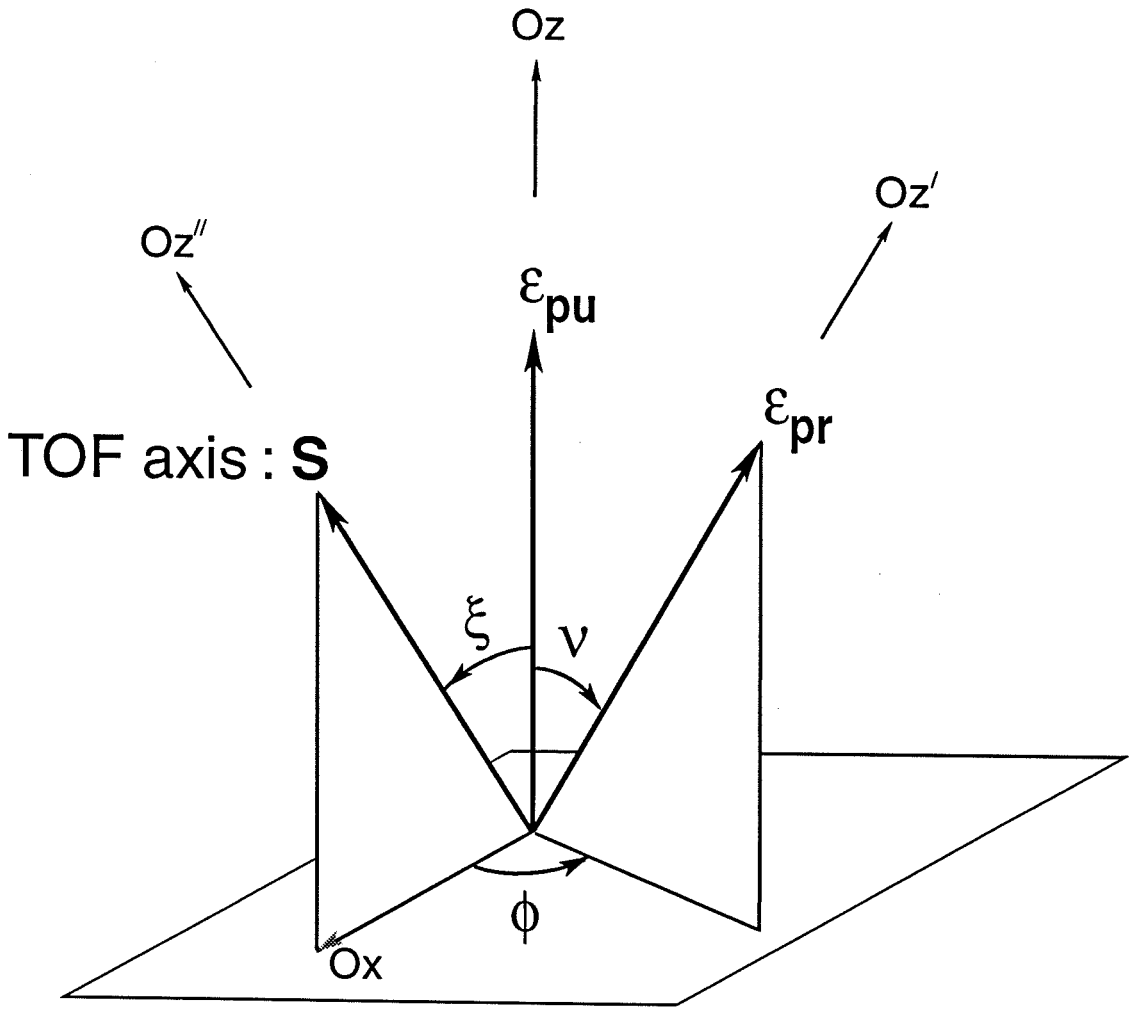

Fig. 5.5

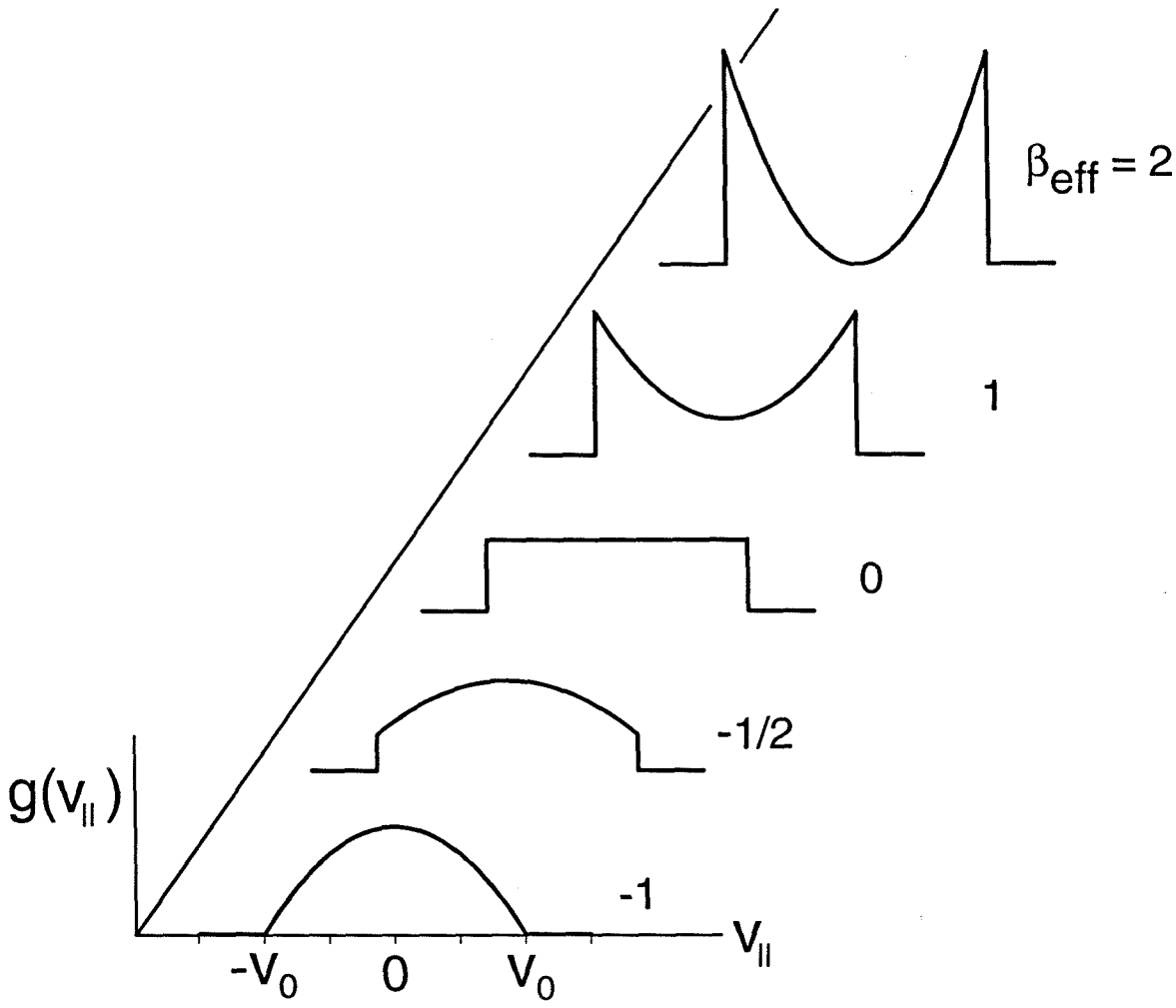

Fig. 5.6

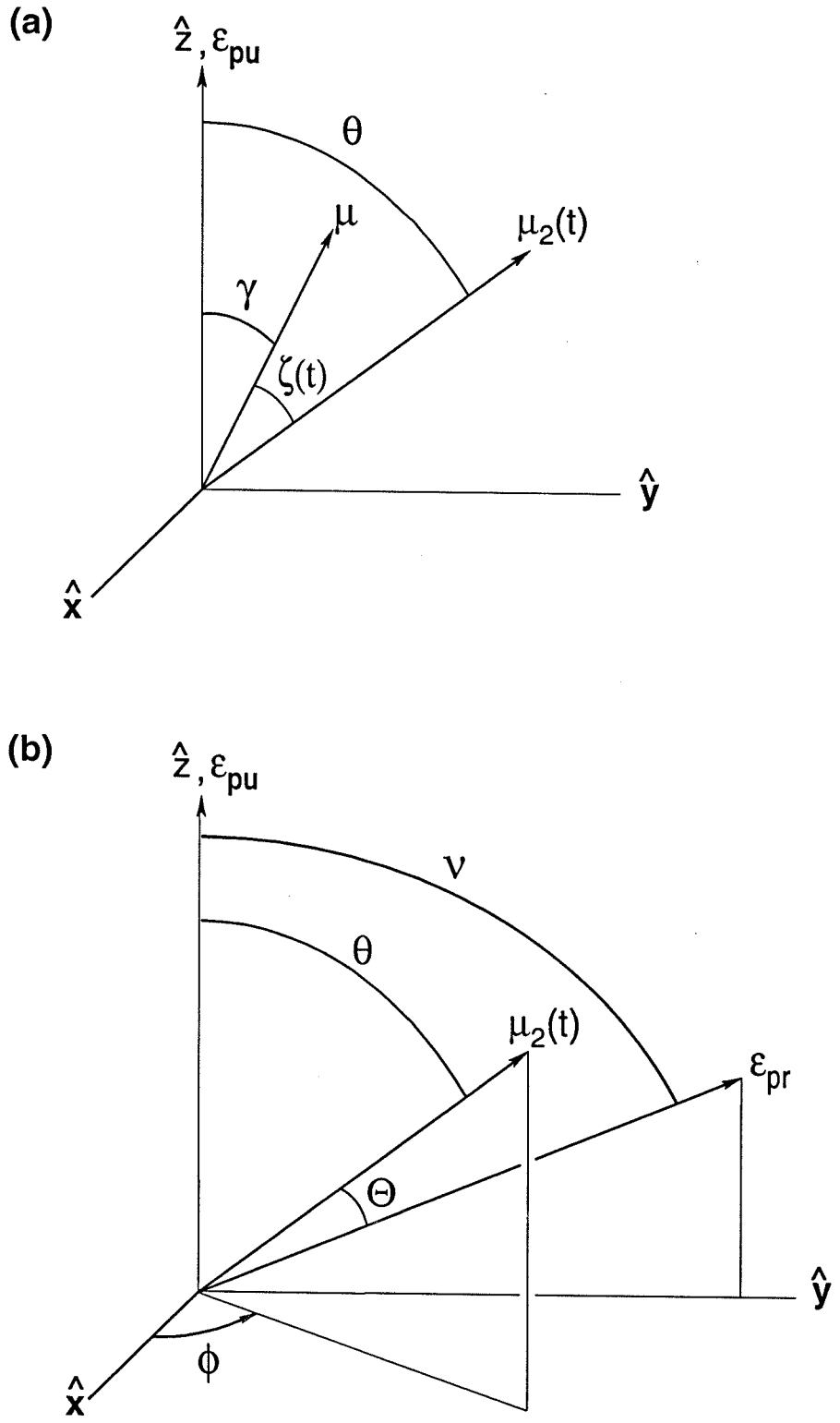
(a)
$\hat{z}$, ε_{pu}
θ
μ
$\mu_2(t)$
γ
ζ(t)
$\hat{y}$
$\hat{x}$
(b)
$\hat{z}$, ε_{pu}
ν
θ
$\mu_2(t)$
ε_{pr}
Θ
$\hat{y}$
ϕ
$\hat{x}$

Fig. 5.7

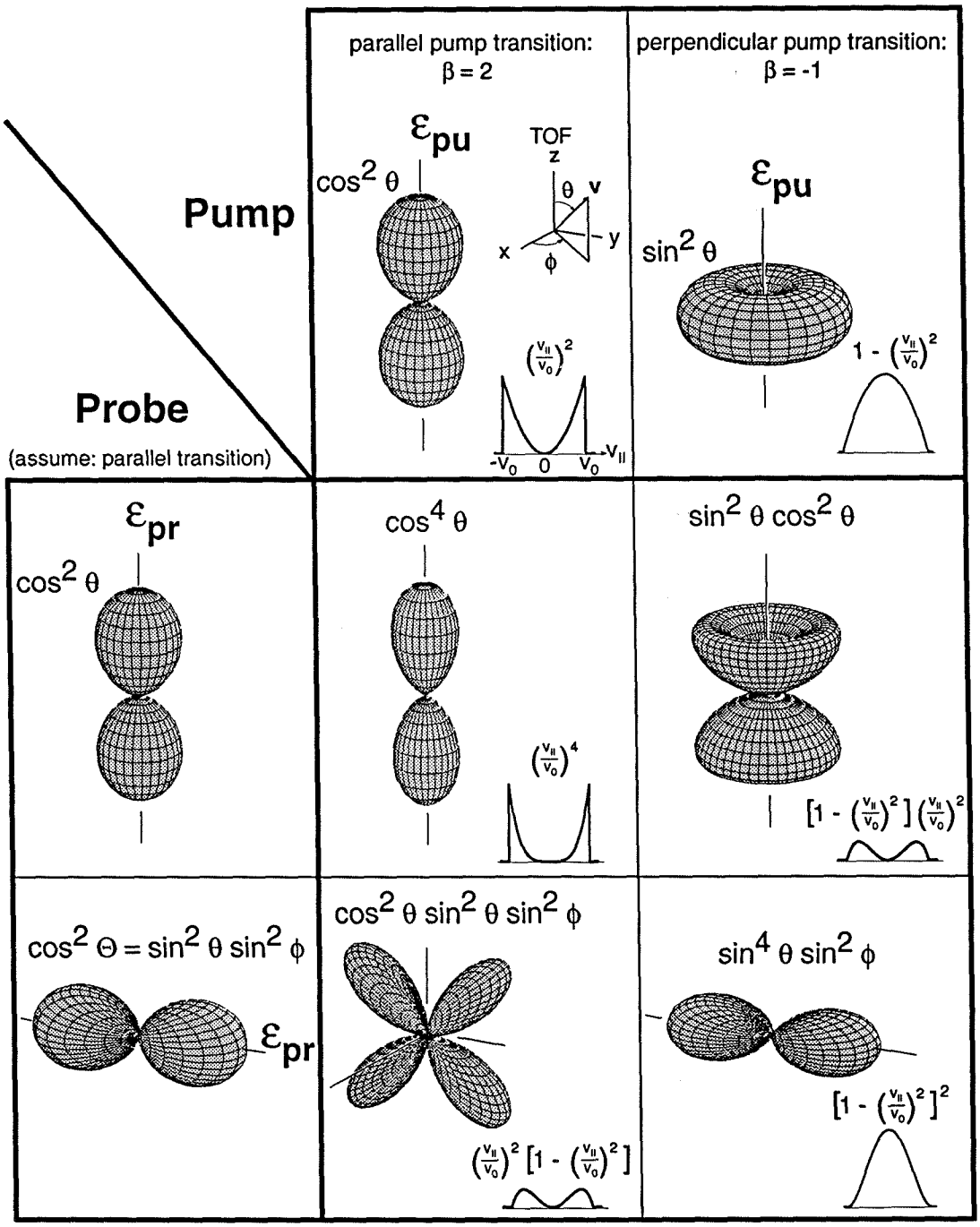
Pump
Probe
(assume: parallel transition)
parallel pump transition:
β = 2
perpendicular pump transition:
β = -1
ε pu
cos² θ
TOF
z
θ v
x
y
φ
(v∥/v0)²
-v0 0 v0 -v∥
ε pu
sin² θ
1 - (v∥/v0)²
ε pr
cos² θ
cos⁴ θ
(v∥/v0)⁴
sin² θ cos² θ
[1 - (v∥/v0)²] (v∥/v0)²
cos² Θ = sin² θ sin² φ
ε pr
cos² θ sin² θ sin² φ
(v∥/v0)² [1 - (v∥/v0)²]
sin⁴ θ sin² φ
[1 - (v∥/v0)²]²

Fig. 5.8

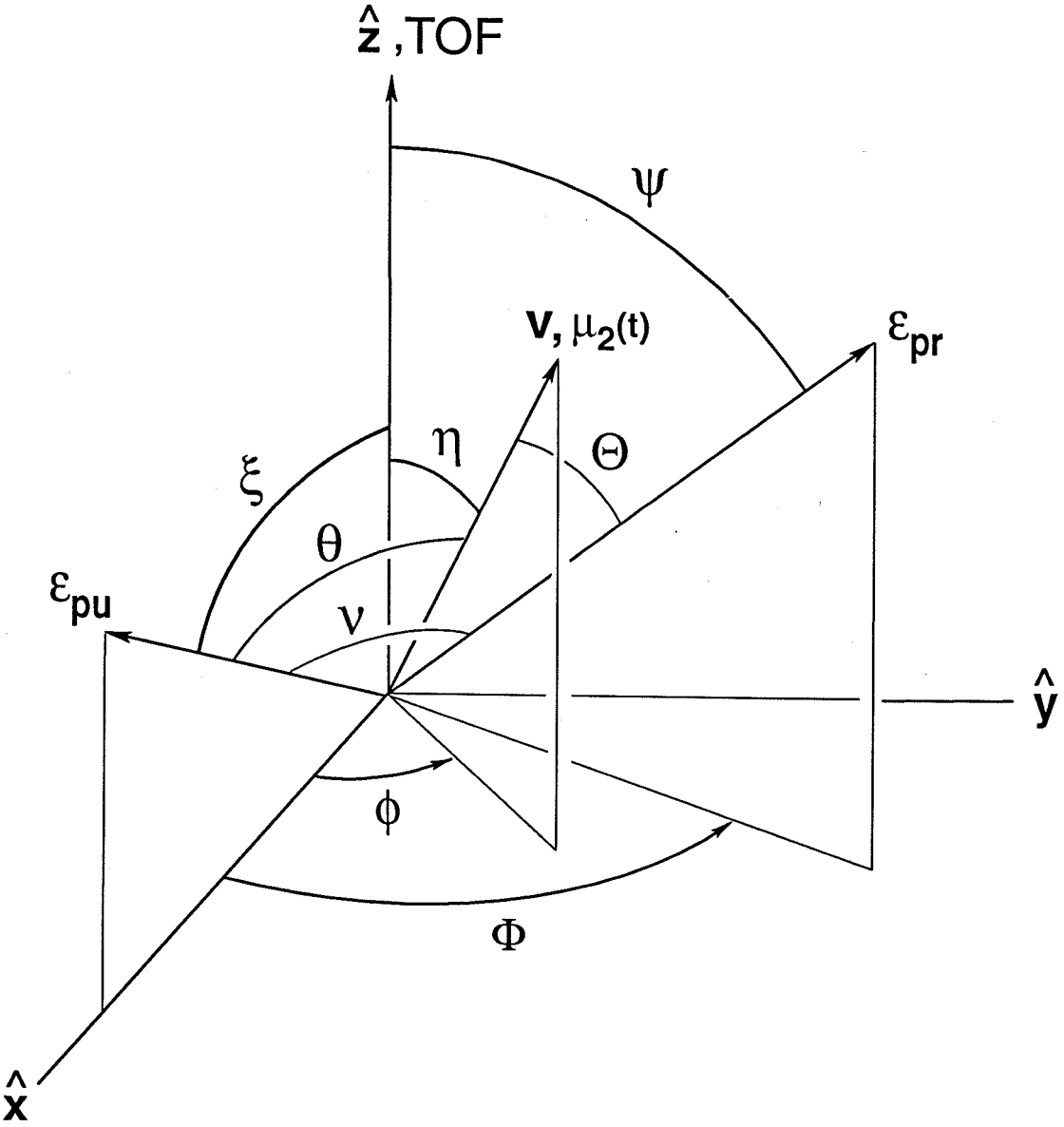
$\hat{z}$,TOF
ψ
V, μ_2(t)
ε_{pr}
η
Θ
ξ
θ
ε_{pu}
ν
$\hat{y}$
ϕ
Φ
$\hat{x}$

Fig. 5.9

Chapter 6

Femtosecond Degenerate Four-Wave-Mixing (DFWM) Techniques: Applications to Gas Phase Dynamics

6.1 Introduction

In previous studies of chemical reaction dynamics on the femtosecond (fs) time scale (see refs. 1, 2, 3, 4 for reviews), the initiation and the probing are made using a linear response to the optical field. Typically, a fs pump pulse initiates the dynamics and establishes the zero of time. A fs probe is introduced, after a time delay, with the wavelength being resonant either with the final product transition or with a particular nuclear separation which corresponds to a transition-state configuration. This way the elementary dynamics are probed in real-time.

The fs probing and signal detection mechanism can be realized in various ways. These include, for probing, the methodology of laser-induced-fluorescence (LIF),[5, 6, 7] absorption,[8] mass spectrometry with multiphoton ionization (MPI),[2, 9, 10, 11] photoelectron kinetic energy[12] and ZEKE[13] and stimulated emission pumping.[14] Non-linear Optical Four-Wave-Mixing (FWM) techniques, like Degenerate FWM (DFWM), provide an additional and significant probing method, especially for generalization of absorption techniques in gas-phase reaction dynamics.

DFWM is a fully resonant process (for excellent reviews see the book by Mukamel[15] and the chapter by Vaccaro[16]), offering high sensitivity with background-free detection of a coherent signal beam. By combining this with fs resolution, a unique and powerful probe/detection scheme is formed. It has already been shown in the studies of liquid and solid systems[17, 18, 19] that DWFM with such resolution provide direct information on the decay rates of fast relaxation processes, the polarization dephasing time, T_2, in an ensemble of two-level systems. In liquid and solid systems, T_2 is in the picosecond (ps) to subpicosecond range and hence the need for DFWM with fs resolution. In the gas phase, however, the dephasing time is much longer, lying in the ps to ns regime.

Only recently have some studies of DFWM in the gas phase been made with picosecond resolution; these studies measured pulse length-induced extra resonances in the time domain,[20] determined Maxwell-Boltzmann velocity distributions[21] and the influence of absorption.[22]

In this paper we develop fs DFWM in the gas phase to study transition-state dynamics of chemical reactions. By using the folded boxcar configuration[23, 24] (see Fig. 6.1) for the fs DFWM laser beams, and by propagating all beams in the forward direction, exact phase matching is achieved throughout the full overlap region. This approach makes it possible to compensate for the low sample density in the gas phase, allowing one to investigate chemical dynamics in a broad range of experimental settings such as in gas-phase cells, in molecular beams and even in flames. With different variant schemes of fs DFWM we apply the methodology to studies of unimolecular and bimolecular reactions.

For unimolecular reactions, we have chosen the well-known NaI system. Extensive fs studies[25, 26, 27, 28, 29, 30] have been performed on this system, and these experiments, using LIF for detection, provide the means for critical comparison with the new results, from fs DFWM, reported here. For this reaction, the wave packet motion of the $[Na\cdots I]^{*\ddagger}$ activated complex was probed (off-resonance detection) in the adiabatic well, which is a consequence of the crossing between the ionic ground state and the covalent first excited state. The free Na atoms escaping through the Landau-Zener coupled[31, 32] region could be monitored by a resonant (to Na) probe pulse. Here, fs DFWM is introduced by replacing the probe pulse with *three degenerate fs beams* and detecting the *fourth* coherent signal. This non-linear technique in the gas phase with fs resolution makes it possible to probe the activated complexes and their coherence. Furthermore, we have incorporated fs DFWM into a control experiment, which illustrates some advantages of this non-linear technique.

For both the unimolecular (NaI) and bimolecular ($Na+H_2$) systems we investigate the fs DFWM of Na as a special case to further help the understanding of the various aspects of the approach, such as sensitivity and coherence. We take advantage of the coherent properties of the fs pulses, which allows for simultaneous access to the two 3p levels of the fine structure (splitting of 17.2 cm^{-1}), to observe the wave packet behavior with the corresponding period. This period had been previously observed in studies[33, 34] exploiting the ultrashort coherence times of *incoherent nanosecond* laser pulses, and in a study[35] using an incident subpicosecond pulse, where the envelope of the transmitted pulse was measured by cross correlation. With the Na system we have also studied the effect of density, which causes pulse-propagation effects. By using different pulse sequences with fs DFWM, we are able to measure the population decay (T_1) and dephasing (T_2) times. Additionally, a fs two-color grating experiment was carried out taking advantage of the 3s, 3d and 5s levels.

The extension of the approach to bimolecular systems involves probing of the coherent signal from the complex system by absorption with fs DFWM. This class of collision systems is different from the unimolecular case: the two reactants collide, form a complex in the transition state, and this complex then decays to the final products. Many of these systems are not accessible to fluorescence detection due to the nature of the reactive potentials, or a low collision cross section, or due to a luminous environment. For the system of interest here, the $Na+H_2$, which serves as a typical example of collisions between excited alkali atoms and simple molecules, extensive experimental research has been carried out in the nanosecond regime.[36, 37, 38, 39, 40, 41, 42, 43, 44] Recently, quantum mechanical calculations have also been performed to describe the dynamics of the collision process.[45, 46, 47] The experimental condition involves the full collision of Na and H_2 (or He), in a heat pipe, and with this arrangement we discuss the approach

and some initial results. Three different experimental realizations which aim at revealing the dynamics on different surfaces are discussed.

This paper is outlined as follows. We first provide in section 6.2 a brief discussion of theory in order to help design the applications of DFWM in the reported fs experiments. Next, the different types of fs DFWM techniques are detailed in a methodology section 6.3. This is followed by a description of the experimental set-up (section 6.4). In the Applications section 6.5, we present the results and discussion for unimolecular and bimolecular systems. After this are the conclusions (section 6.6). Finally, in the Appendix (6.7), a general expression is found for the density of bimolecular collision complexes as a function of the laser pulse width.

6.2 Theory

6.2.1 Phenomenological Description

In the process of DFWM, three input beams of same frequency, ω, interact with a non-linear medium, producing a coherent fourth beam also at the frequency ω. Fig. 6.2(a) shows the energy diagram corresponding to this process for a simple two-level system. The configuration of the momenta of the three input beams and the generated DFWM signal beam is shown in Fig. 6.2(b), and as part of the experimental set-up in Fig. 6.1. This is a so-called 3-dimensional forward geometry, or folded boxcar arrangement, for which the beams converge at small angular separation. The overlap of the three incident beams defines the interaction volume. The non-linearity of the sample medium couples the beams: the absorption of two photons from two incident beams leads to amplification of the third beam by stimulated emission and to generation of a signal photon

(ω_{DFWM}, $\mathbf{k}_{DFWM}$) in the fourth direction. The direction of the signal beam follows from the phase matching or momentum conservation condition:[48]

$$\mathbf{k}_{DFWM} = \mathbf{k}_1 - \mathbf{k}_2 + \mathbf{k}_3. \tag{6.1}$$

Similarly, energy conservation restricts the frequency of the emerging signal:

$$\omega_{DFWM} = \omega_1 - \omega_2 + \omega_3. \tag{6.2}$$

6.2.2 Source of DFWM Process

The local response of the medium to the incident electromagnetic radiation can be described by the induced macroscopic electric polarization, $\mathbf{P}$. Linear processes such as absorption, and Rayleigh and spontaneous Raman scattering arise from polarizations proportional to the first power of the electric field strength, $\underline{E}$. Non-linear optical interactions are introduced via higher order terms in the electric field, yielding, in a Taylor expansion:[48, 49, 50]

$$\mathbf{P} = \mathbf{P}^{(1)} + \mathbf{P}^{(2)} + \mathbf{P}^{(3)} + \ldots \tag{6.3a}$$

$$= \varepsilon_0 \cdot (\chi^{(1)} \cdot \mathbf{E} + \chi^{(2)} \cdot \mathbf{E} \cdot \mathbf{E} + \chi^{(3)} \cdot \mathbf{E} \cdot \mathbf{E} \cdot \mathbf{E} + \ldots), \tag{6.3b}$$

where $\chi^{(1)}$ is the linear susceptibility. $\chi^{(2)}$ and $\chi^{(3)}$ are the second- and third-order non-linear optical susceptibilities, representing tensors of rank 3 and 4, respectively. $\chi^{(2)}$ is responsible for three-wave mixing processes like frequency doubling, but vanishes in isotropic media. The third term, with the susceptibility $\chi^{(3)}$, is responsible for four-wave mixing processes like DFWM, Coherent-Anti-Stokes-Raman Scattering (CARS), and third harmonic generation. These processes are not restricted by symmetry reasons, being allowed in non-centrosymmetric as well as centrosymmetric media, and hence constitute the lowest order non-linear effect in gases and liquids. $\chi^{(3)}$ is specific to the medium and describes a distinct frequency dependence, intrinsic to the fundamental

atomic or molecular system constituting the medium. For a chosen wavelength of the DFWM laser pulses, a particular configuration of the system may be accessed.

Depending on the strength of the light-matter interaction, there are different approaches to calculating $\chi^{(3)}$. One such method uses perturbation theory with a density matrix approach. The quantum mechanical equation of motion is solved in a recursive manner,[48, 49] and the procedure converges in the regime where the interaction is weak. On the other hand, for a strong interaction, like a strong resonant transition, the system is approximated by a two-level system and solved via a density matrix approach[15] in a nonperturbative manner.[15, 48, 49] If a temporal sequence of pulses is used, the matrix formalism can be extended in a formal way by simple multiplication of matrices to describe the equations of motion.[51, 52]

6.2.3 FWM Signal Intensity

Once $\chi^{(3)}$ is known, the non-linear macroscopic polarization, $P^{(3)}(\omega)$, may be calculated using equation (6.3). To find the FWM signal intensity, this polarization is incorporated as a source term in the following inhomogeneous Maxwell equation:[48, 49, 50]

$$\left[\nabla^2 + \frac{\omega^2}{c^2}\varepsilon(\omega)\right] E_{FWM} = -\frac{4\pi\omega^2}{c^2}P^{(3)}(\omega). \tag{6.4}$$

To obtain a solution to this differential equation, different approximation methods are usually employed: the slowly-varying-envelope-approximation (SVEA) or the rotating-wave-approximation (RWA).[48, 49] The general expression for the solution, the FWM signal intensity, can be written as:

$$I_{FWM} \propto \left|\chi^{(3)}\right|^2 I_1 I_2 I_3 L^2 \left[\frac{\sin(\frac{1}{2}\Delta k\ L)}{\frac{1}{2}\Delta k\ L}\right], \tag{6.5}$$

where $I_{i=1,2,3}$ are the intensities of the incoming laser beams, L is the interaction length and Δk the phase mismatch. The equation is only fully valid for small intensities and optically thin media and it shows the important dependencies which are involved in this experiment. The square of the absolute value of the susceptibility leads to the dependence of FWM processes on the square of the difference population. Normally the upper state is not populated, as it lies far above the thermal energy, and the ground state is probed. The spectral dependence of $\chi^{(3)}$ makes the FWM signal sensitive to a specific transition. For example, if ns pulses are used, this aspect enables the detection of a distinct ro-vibrational level accessed in an electronic transition for a molecule.[16] In contrast, the use of fs pulses allows interrogation of the molecule at a particular window of internuclear separation, and so it permits accessing of the transition-state region.

The expected cubic intensity dependence of the FWM process is represented by the product of the intensities of the three incident beams. If the frequency of the laser beams are close to an optical resonance, severe absorption and saturation may occur, leading to a more complicated dependence on the intensities. By using fs pulses, a typical consequence is pulse propagation effects.[22] The square dependence of the interaction length, L, suggests making this length as long as possible. The last factor in equation (6.5) is a squared sinc function with argument $\Delta k \cdot L/2$. This factor can be optimized to unity if phase matching, $\Delta k=0$, is achieved. In the case of DFWM, this can be attained with a folded-boxcar arrangement (see Fig. 6.2(b)).

Another way to realize phase matching is with the so-called phase conjugated geometry,[53] where two collinear beams are propagated in opposite directions. The third beam forms the interaction region by crossing the path of the other two, generating a phase conjugated signal (with respect to the third beam) that emerges in the opposite direction to the third beam. This phase

conjugated geometry is typically used in ns experiments.[54] However, in fs studies, to maintain the relative temporal displacement of the pulses, and to optimize the interaction length, all beams are propagated in the forward direction. Hence, the folded-boxcar configuration is used in our fs experiments.

6.2.4 Transient Grating Picture

The origin of FWM can also be explained in terms of a transient grating picture, where the signal is a result of Bragg scattering from an induced grating. For this picture it is convenient to rewrite equation (6.3) in the following form:[55]

$$\mathbf{P}^{(3)} = \varepsilon_0 \chi^{(3)} \mathbf{E}_1 \mathbf{E}_2^* \mathbf{E}_3 \tag{6.6a}$$

$$= A \cdot (\mathbf{E}_1 \mathbf{E}_2^*) \mathbf{E}_3 + B \cdot (\mathbf{E}_3 \mathbf{E}_2^*) \mathbf{E}_1 + C \cdot (\mathbf{E}_1 \mathbf{E}_3) \mathbf{E}_2^*. \tag{6.6b}$$

This FWM polarization, $\mathbf{P}^{(3)}$, is responsible for the DFWM signal in the direction of $\mathbf{k}_{DFWM}$ given by the phase matching condition (equation (6.1)). Each term represents a distinct combination of the incident beams. For the terms with constants A and B, the first two E fields, in brackets, create an interference pattern. This pattern interacts with the medium forming different types of gratings: phase- (or refractive index-) and absorption- (or population-) gratings,[55] with a grating constant, d, given by

$$d = \frac{\lambda}{2\sin\frac{\phi}{2}}, \tag{6.7}$$

where ϕ is the angle between the two grating beams. As shown in Fig. 6.3, the incoming third beam is scattered from the induced grating in a direction given by the Bragg condition. The last term in $\mathbf{P}^{(3)}$ also produces a signal in the same direction, but involves a two-photon step, for which a simple grating picture is not valid. This process proceeds via a virtual state and is therefore comparably weak.

By introducing a temporal sequence for the three incident DFWM laser pulses, it is possible to directly obtain information about the dynamics in the time domain. This information is contained in $\chi^{(3)}$ and hence in the DFWM signal (see equation (6.5)). Many experimental and theoretical FWM studies have been performed using pulse sequences in DFWM[18, 56, 57, 58, 59] and the related[57] echo,[58, 60, 61] and laser-induced grating (LIG)[55, 62, 63, 64, 65, 66, 67, 68, 69] experiments. Here, for our DFWM-type experiments, we shall employ pulse sequences to measure the population decay time, T_1, and dephasing time, T_2. Two grating pulses are made to coincide temporally, and the third pulse is moved relative to them. This scheme is described below in the Methodology section.

6.3 Methodology: Femtosecond Pulse Schemes and Temporal Dynamics

6.3.1 Introduction

DFWM is often used as a way of measuring the dephasing time, T_2, of a system. One of the DFWM beams is moved temporally with respect to the others, creating a time scale (fs-ns) on which T_2 is measured. However, as shown in Fig. 6.4, this is just one of many ways in which DFWM may be employed in fs time-resolved studies. The different techniques offer versatility in retrieving different types of information from among others, atomic, unimolecular and bimolecular systems. In addition to measuring the dephasing time, T_2, the population decay time, T_1, of a species may be monitored. DFWM may also be employed as a probe in its own right in a pump-DFWM type experiment to monitor transition states of chemical reactions.

Fig. 6.4 shows three different types of fs DFWM techniques which we wish to define and explain in terms of temporal pictures and spatial configurations in

the experiments. The left side of Fig. 6.4 shows the temporal sequence of the incoming pulses. The relative temporal displacement of the pulse(s) is indicated by the double arrows. The right-hand side illustrates the relative spatial positions of the incident parallel laser beams. These schematic spatial cuts correlate with the view presented at the bottom of Fig. 6.1. The signal beam spot is traced here along with the incident beams to indicate the relative direction it propagates in, on the output side of the cell. The following describes the different schemes used.

6.3.2 DFWM

In the DFWM-type experiment, sometimes referred to as time-resolved DFWM,[59] there are "only" three incident laser beams involved (see Fig. 6.4, top). If one of the pulses (3) comes before the other two (1,2), then the signal obtained reveals the overall dephasing time, T_2, of the system. The first pulse (3) creates a macroscopic polarization in the medium, and it is this polarization which decays with an overall dephasing time, T_2. At a certain time delay later, the electric field of one of the other two pulses (1, say) interferes with this macroscopic polarization, creating a grating. The trailing edge of the other beam (2), which arrives simultaneously with 1, will then probe this grating, yielding the signal. If, on the other hand, pulse 3 comes after the other two pulses, then it interrogates a grating set up by these two pulses (1,2). In this case, the overall decay of the signal reflects the population decay or T_1 time.

6.3.3 Pump-DFWM

In this scheme (middle section of Fig. 6.4), the three incident fs DFWM beams are made to all arrive simultaneously. A fs pump pulse is introduced to

initiate the dynamics in the gas phase and at a certain time delay later the three DFWM beams arrive and probe the system. The pump beam is located spatially at the center. In contrast to section 6.3.2 above, there is now the added flexibility in wavelength in that the pump and DFWM wavelengths can be different. The DFWM may thus be tuned to probe not only the initially excited species but also the transition states or the final products in a reaction. DFWM, acting here as a probe on the fs time scale, serves as a very useful tool, particularly for systems that may not allow for fluorescence detection.

6.3.4 Pump-Control-DFWM

In a recently developed chemical control experiment,[25] three fs pulses were employed in a pump-control-probe sequence. The control pulse captures the molecular system in the transition state and regulates the outcome of the reaction. Here we utilize an analogous fs pulse sequence: a pump pulse initiates the reaction which is controlled by a different pulse at a certain time delay and monitored at a fixed time delay (after the pump) by a fs DFWM probe (see Fig. 6.4, bottom).

6.4 Experimental Realization

Figure 6.5 shows a schematic of the experimental apparatus: the fs laser system, including wavelength selectivity, and the DFWM set-up with the sample cell and signal detection. The output of an 83 MHz colliding pulse mode-locked laser (CPM) was passed into a four stage Nd:YAG-pumped pulsed dye amplifier (PDA) operating at 20 Hz.[5] The output pulses were recompressed with a prism pair configuration yielding ~60 fs, 150 μJ horizontally polarized pulses at 616 nm.

A beam splitter (BS1), located after the recompression, divided the laser beam into the pump and DFWM arms. A second beam splitter (BS2), placed in the pump arm, diverted a beam into the probe (or control) arm.

Depending on the experiment of interest, different optical configurations were employed in selecting the pump wavelength. The 616 nm beam could be frequency doubled in a 0.5 mm-thick type-I KD*P (99%, 59.3°) crystal as shown, yielding a λ_{Pu}=308 nm, pump pulse which was used in the NaI experiments. Alternatively, a white light continuum could be generated from the 616 nm beam, followed by wavelength selection with a Corion 10 nm bandpass interference filter (F1). To compensate for the loss in laser intensity, the pulse thus generated was subsequently amplified in a dye cell pumped with residual 532 nm Nd:YAG laser light. For example, to pump the Na D-lines, a 589 nm interference filter was used in conjunction with a kiton red/methanol solution as laser dye, the concentration of which was optimized to yield the desired spectral profile.

In the DFWM arm, a continuum generation scheme was built in to gain wavelength tuning flexibility. This scheme was followed by a Corion 10 nm bandpass interference filter (F2) and an amplification cell, pumped by residual 532 nm light from the same Nd:YAG laser. A kiton red/methanol solution was also added to this cell, but with a concentration specific to the chosen wavelength, λ_{DFWM}. The amplified beam was branched by two beam splitters (BS3 and BS4) to produce the three fs DFWM beams (1, 2 and 3). These three beams were aligned parallel to one another and spatially overlapped at the common focus in the cell by lens L1; the angle, ϕ, between the grating beams was then 2°. In order to fulfill the phase-matching condition, we employed the folded boxcar configuration[23, 24] as discussed above (equation (6.1)) and shown in figures 6.1 and 6.2(b). The pump beam was aligned parallel to and spatially separated from

the three DFWM beams (see Fig. 6.1 and Fig. 6.4, right) and passed through the center of lens L1, focusing in the same overlap region as the DFWM beams.

To control the temporal separation of the laser pulses, retroreflecting corner cubes on computer controlled actuators were placed in some of the arms. In all experiments performed here, two of the DFWM grating beams (1,2) were kept temporally overlapped and fixed. In a DFWM-type experiment, to measure a transient, the DFWM probing beam (3) was temporally displaced with respect to the two grating beams. In contrast, for a pump-DFWM-type experiment, beam 3 was fixed to coincide with beams 1 and 2, while the actuator in the pump arm was moved. The determination of the position of temporal overlap (time zero) between different beam pairs was made using a cross correlation set-up with sum or difference frequency mixing in a 0.2 mm-thick type-I KD*P crystal.

The fs DFWM signal pulse generated in the cell travels in a direction determined by the phase matching condition (Fig. 6.2). This direction is different from that of the incident laser beams and the signal could thus be easily separated by a spatial filter (Fig. 6.1). The emerging DFWM signal beam was collimated by a second lens (L2) and traveled over a long path length (~10m) before being focused into a monochromator (SPEX, 0.34m) and detected by a Hamamatsu R1527P photomultiplier tube. In addition, several pinholes were used to reduce stray light from Rayleigh scattering and fluorescence caused by the incident beams in the cell. Before each experiment, the signal beam path and divergence were checked with the aid of a He-Ne laser beam, which was spatially displaced from the incident DFWM laser beams to the signal spot position, indicated in Fig. 6.4, and passed through the overlap region of the lasers in the cell.

For transients, the monochromator was set to detect a fixed bandwidth of the signal. The monochromator could also be used to obtain a spectrum of the signal for a fixed pump-DFWM time delay. This provided a means of detecting

the absorption of the signal beam in the cell. The PMT output was amplified (x25 in SR445 pre-amp) and sent to a boxcar-averager, AD-converter, and was finally stored in a computer for further analysis. For the pump-control-DFWM experiments (see the methodology section) a fixed pump-DFWM time delay was chosen and the pump-control delay time was varied by stepping the actuator in the control arm.

To compare the non-linear fs DFWM gas-phase technique with the conventional pump-probe laser-induced-fluorescence (LIF) technique, LIF collection optics were arranged as shown in Fig. 6.5.[2] For the NaI unimolecular experiments, the same quartz cell arrangement was used as described in refs. 25, 26. The oven temperature was kept at 660°C, giving a vapor pressure in the range of 100 mTorr.

For the DFWM studies of the sodium atom and our investigations of bimolecular reactions, a crossed heat-pipe oven[70] was used. The heat pipe was filled with sodium (99%, Aldrich) and as a buffer gas He was used with a pressure in the range 500-600 mbar for the studies of the Na D-lines. For the bimolecular studies, H_2 gas at 0.5 to 1.5 bar was used. The temperature at the center of the heat pipe was monitored by a thermocouple inside a hollow thin metal rod, introduced into the cell via a fifth vertical arm. The temperature was fixed at 190°C, corresponding to a Na density of 1.6×10^{12} cm^{-3}.[71] The heat pipe was oriented such that the lasers passed through the two arms that did not have heating coils around them. This was done to allow for minimum absorption before and after the interaction region, yet still achieving maximum sample density in the focal region.

6.5 Applications

The fs DFWM techniques, outlined in the methodology section, have a wide range of applicability. Here, we give examples of three different systems to illustrate the versatility of the approach and to consider sensitivity and future directions.

6.5.1 Unimolecular Reactions

One of the most studied unimolecular systems is that of NaI. Its dissociation in real-time (see, e.g., refs. 27, 28, 72, 73) has been studied extensively, both experimentally and theoretically. In contrast to directly dissociative reactions, the NaI reaction,

$$NaI^* \rightarrow [Na\cdots I]^{*\ddagger} \rightarrow Na(^2S_{1/2}) + I(^2P_{3/2}), \qquad (6.8)$$

is governed by the avoided crossing of the ionic ground state ($X^1\Sigma_0^+$) with the lowest excited covalent state, which corresponds asymptotically to $Na(^2S_{1/2})$ + $I(^2P_{3/2})$. The potential energy surfaces relevant to the dynamics are shown in Fig. 6.6. The interaction of the ionic and covalent potentials is quite strong, leading to an adiabatic well with a ~10% probability for the excited wave packet to escape through the Landau-Zener coupled region. Hence, the wave packet prepared by the pump pulse oscillates in the well with a constant fraction of population dissociating each time the outer turning point is reached. The products produced (c.f. equation (6.8)) thus build up in a stepwise manner, where the separation of adjacent steps equals the period of oscillation in the well. Fig. 6.7 (top) shows the pump-DFWM scheme employed to excite (308 nm) the NaI system and resonantly probe the free Na product with fs DFWM (589 nm) in a clocking-type experiment. The resulting transient (top right, Fig. 6.7) clearly shows the stepwise build up of

this final product. This is in excellent agreement with previous fs studies in which LIF was used for detection as described in references 27, 28, 29, 30.

The NaI reaction is interesting not only for studying its dynamics in real time but also as a model system for fs control experiments.[25] The middle part of Fig. 6.7 illustrates the application of fs DFWM in this type of control experiment. As in the on-resonant pump-DFWM clocking experiment (Fig. 6.7, top), the fs pump pulse initiates the excited state dynamics of the NaI system. However, the wave packet is now intercepted at a fixed internuclear separation in the transition-state region by a fs control pulse. This laser pulse arrives after the pump (time zero) at a time delay, which can be varied by stepping the actuator in the control arm (Fig. 6.5) as described in section 6.3.4. The control pulse captures a fraction of the excited state population which is frozen on the fs time scale in the "window" at the short internuclear range accessed by this off-resonant pulse. The captured molecules are thus sent to a second excited state that asymptotes to Na(3p)+I. As a consequence of the control pulse, the final asymptotic population on the first excited surface, Na(3s)+I, is depleted and the ratio of the product yield in the reaction channel is changed. Femtosecond DFWM, tuned resonantly to the Na D-line transition, is introduced at a fixed time delay (19.2 ps) after the pump pulse to monitor the effect of the control pulse on the transition-state dynamics.

The spatial alignment of the pump, control and DFWM beams is depicted in Fig. 6.4, bottom. The fs DFWM transient in the middle of Fig. 6.7 shows the periodic depletion of the signal and the decay in the depletion amplitude with time. This modulated depletion is a direct consequence of the control beam opening up a window in the transition-state region. The temporal behavior is identical, except for the sign, to that observed with LIF detection (Fig. 6.7, bottom) in which a probe is tuned off-resonant. The observed behavior describes the oscillatory motion in the adiabatic well and exhibits an overall decay due to the

fractional escape at the outer turning point. These results establish the applicability of fs DFWM to the study of reactions. It is worth noting that the IBM group has observed the steps (and not the resonance) in the absorption detection approach.[8] Although DFWM is basically an absorption technique, its background-free and sensitivity features are very important for this type of application.

The depletion of the transition-state population may be described by a kinetic model.[26] We shall provide a simplified description to compare the fs pump-control-DFWM technique employed here to a pump-control-probe method with the LIF detection used in ref. 25. The pump pulse excites N molecules from the NaI ground state into the adiabatic well. When the control pulse arrives, at a time delay, t, after the pump, it excites a fraction, $p_1(t)$, of these N molecules. This fraction $p_1(t)$ is of course maximum when the wave packet is located at the control window at the control time t. The oscillatory motion and decay of the population in the well is accounted for by the temporal dependence of $p_1(t)$. The second excited state is thus populated by $p_1(t)N$ molecules, each of which will asymptote to Na(3p)+I. The first excited state is depleted to $(1-p_1(t))N$ molecules that will all become Na(3s)+I. By waiting (ps) for all molecules to dissociate, but not so long (ns) that fluorescence has affected the excited state population, the final asymptotic populations may be monitored with a fs probe pulse (and LIF) or with fs DFWM. What is important is the difference population of the two levels (Na 3s and 3p) involved in the resonant transition. This difference, $(1-2p_1(t))N$, can be monitored as a function of the delay time, t, of the off-resonant control, revealing the first excited state dynamics, described by $p_1(t)$.

Femtosecond DFWM yields a signal (Fig. 6.7, middle) that is directly proportional to the square of the population difference (see section 6.2) and hence serves as a direct monitor of the dynamics:

$$\text{DFWM} \propto (1-2p_1(t))^2 N^2. \tag{6.9}$$

In the other control experiment, pump-control-probe with LIF detection,[25] a single probe pulse monitors the asymptotic populations, exciting a fixed fraction, p_2, of the final difference population to the Na(3p) level. The final Na(3p) population, following probing, is thus given by:

$$A = p_1(t)N + p_2(1-2p_1(t))N. \tag{6.10}$$

This population subsequently decays via fluorescence on a ns time scale, and can be monitored by collecting all the fluorescence.[25] By omitting the final resonant excitation (p_2=0), the resulting conventional two pulse experiment (ref. 25; Fig. 6.7, bottom) yielded a fluorescence signal, $B=p_1(t)N$. By subtraction, the population difference is obtained:

$$A - B = p_2(1-2p_1(t))N \tag{6.11}$$

$$\propto (1-2p_1(t))N. \tag{6.12}$$

We note that with DFWM a single transient sufficed.

6.5.2 Bimolecular Reactions

Above in section 6.5.1 it was shown that fs DFWM is well suited to the study of unimolecular reactions. A natural extension of this approach is to bimolecular systems, especially with the new features of sensitivity and absorption. Such systems involve a broad range of collision processes where not only electronic energy but also vibration, rotation and kinetic energy in different internuclear coordinates must be taken into account. The collision process is of the type,

$$A + BC \rightarrow [ABC]^{\ddagger} \rightarrow AB + C \quad \text{(bimolecular)}, \tag{6.13}$$

where $[ABC]^{\ddagger}$ denotes the collision complex, which forms on the ps to fs time scale and determines the pathway to the final products. Using fs DFWM, a

coherent signal can be produced at the internuclear configuration of interest, revealing the dynamics with temporal resolution only limited by the width of the laser pulses.

Collisions between excited alkali atoms and molecules in the gas phase constitute an important class of such chemical processes. These systems provide a means of studying the reaction dynamics and also the energy transfer from electronic into ro-vibronic and kinetic energy (quenching) degrees of freedom:

$$A^* + BC(v,J) \rightarrow [ABC]^{\ddagger} \rightarrow \begin{cases} A + BC(\tilde{v},\tilde{J}) + \Delta E_{kin} & \text{(quenching)} \\ AB + C & \text{(reaction)} \end{cases} \qquad (6.14)$$

Fig. 6.8(a) illustrates the processes indicated in equation (6.14) in general. On the left-hand side in this figure the collision of A* with BC initiates the processes. After forming the collision complex, $[ABC]^{\ddagger}$, two pathways are possible. The complex may undergo quenching and separate along the same coordinate, A-BC, or it may move on to a repulsive surface along the AB-C coordinate.

Of particular interest here is the well-known collision system, Na(nl)+H_2, which exhibits both reactive and quenching channels. For example, the reactive nature of the Na(4p)+H_2 system (to NaH+H) has been studied experimentally[42, 44, 74, 75] and theoretically.[76, 77] The quenching pathway is exhibited by the system, Na(3p)+H_2, which has received considerable experimental[37, 38, 39] and theoretical[36, 38, 47, 76, 77] attention and represents a prototype system for the study of energy transfer processes. In addition this system also has a reactive behavior to NaH+H if the H_2 molecule possesses sufficient vibrational energy.[78] Quenching processes have remained an active topic of research since the first investigation in 1911 by Wood and Franck.[79]

The schematic in Fig. 6.8(b) shows a cut through the ground (X $^2A_1$) and first electronically excited potential energy surface of the Na+H_2 collision system in C_{2v} symmetry, which favors the quenching process. The horizontal axis represents the distance, R, between the sodium atom and the center of the H_2 molecule.[36, 37] The ground state is purely repulsive, while the excited state shows a potential well (exciplex) at short R. The non-adiabatic crossing of the two potential energy surfaces shown in this plot (6.8b) is responsible for the quenching process. The crossing point lies at an energy below that of the excited state asymptote (2.1 eV),[36, 37] consistent with the experimentally observed high efficiency of the quenching process.[37, 80, 81, 82, 83]

All studies on this system to date have employed nanosecond resolution to examine the asymptotic properties. The nature of the non-adiabatic crossing, which is similar to NaI, and the exciplex have not yet been fully characterized. Recent quantum mechanical calculations have been performed to describe the short-lived vibrational states of the exciplex[36, 45] and the resulting yield following quenching.[46] The metastable states or resonances have a lifetime in the picosecond or subpicosecond range. The motivation here was to take advantage of the high sensitivity (background free laser signal) and time resolution of fs DFWM to measure the dynamics in real-time of the Na+H_2 collision complex. In the following sections we first consider the case of atomic sodium. This system is not only interesting in its own right but also ideal for studying different aspects of fs DFWM and is a necessary precursor to understanding the dynamics of the bimolecular system. Experimental efforts to study this latter system are presented along with future directions aimed at further elucidating the dynamics of this system.

6.5.2.1 Atomic Sodium

These investigations were performed in the gas phase using the heat pipe oven, described in the experimental section. Fig. 6.9 shows a diagram of the lowest energy levels for the Na atom. For the 3p orbital, spin-orbit coupling results in the $3p_{1/2}$ and $3p_{3/2}$ levels, which are separated by 17.2 cm^{-1}.[84] We performed a number of experiments on this system. First we present a pump-DFWM experiment, Fig. 6.10, in which both the pump and DFWM beams were tuned to be resonant with the 3p ← 3s transition. Note that the fs DFWM signal is sensitive to (the square of) the population difference (see Theory), *i.e.*, the ground state (3s) minus the excited state (3p) population.

At negative time delay, the fs DFWM beams arrive first, probing the full ground state population and thus yielding maximum signal. This signal, being a fs pulse that emerges directly after the DFWM, is unaffected by the later arrival of the pump pulse. For positive time, the pump arrives first and can influence the DFWM signal. The pump excites a certain fraction of the ground state atoms into the first excited state. The DFWM signal is consequently depleted since the DFWM beams encounter a reduced population difference. The decay of the depletion is determined by the excited state lifetime, T_1, which is on a nanosecond time scale (see Fig. 6.9), much longer than the range explored here. The sharp dip in the signal at time zero is caused by a coherence coupling of the pump and the DFWM beams.[18, 60, 85, 86]

In Fig. 6.11, we show a different pump-DFWM type experiment, in which an overall exponential decay (~3 ps) is modulated. The period (2 ps) of the oscillations corresponds to the fine structure splitting (17.2 cm^{-1}) of the 3p state. Here, the three beams, which constitute the DFWM probe, no longer have the same wavelength. Instead, two of the beams have a common wavelength of 589

nm, resonant with the 3p ← 3s transition, while the third was tuned to the 5s ← 3p resonance at 616 nm. The monochromator was positioned at 616 nm to select the signal at this wavelength. Strictly speaking, the scheme is not a pure DFWM set-up, but rather the more general case (FWM) of a two-color grating[87] experiment. The choice of wavelength was achieved by using the full continuum generation output, with appropriate interference filters in the three FWM arms. The two 589 nm beams produce a grating off which the third beam (616 nm) is scattered. The grating beams are configured as 1 and 2 in Fig. 6.1, and the 616nm beam as 3. This arrangement produced the scattered beam or signal in the desired direction according to the phase matching condition (equation (6.1)). Alternatively, the grating beams could have been 2 and 3, as was verified in an experiment, not detailed here, which yielded a nearly identical transient.

The inset in Fig. 6.11 shows the pump-FWM scheme used in obtaining the transient. The fs pump, being coherent, excites a superposition of the two energetically separated 3p levels, that evolves in time with a period (see ref. 88; pp. 18 of ref. 1) corresponding to the energy splitting. The oscillatory dynamics of the 3p levels is accessed by the FWM probe at a time delay after the pump. The modulations in Fig. 6.11 are complete in the sense that depending on the delay time, the emerging fs laser signal can be controlled to be completely on or off. This type of control of a laser beam, a control that is based on the coherent superposition of two quantum states, is related to the recently developed techniques of laser without inversion[89] and electromagnetic induced transparency.[90]

The transient in Fig. 6.11 does not exhibit a distinct coherence spike at time zero as was seen in Fig. 6.10. The peaks in Fig. 6.11 are all separated by 2 ps with the exception that the first peak is separated by 1.6 ps from the second. Reasons for this may be the initial phase of the coherent superposition prepared, and the

possibility of a coherent interaction at time zero of the pump and the two grating beams of the FWM which have the same wavelength (589 nm) as the pump.

In Figs. 6.12 and 6.13 we describe the results of a pure DFWM-type experiment, in which no pump beam is used. In this experiment (see section 6.3.2), two of the three incident fs DFWM pulses are kept temporally overlapped, while the time delay of the third is varied. The oscillatory behavior (2 ps) is again observed, with an exponential envelope. Due to the chosen pulse sequence, and the common wavelength of the three DFWM beams (589 nm), a sharp coherence spike is observed at time zero.[18, 55] At negative time delay, the decay time for the signal envelope is 7.4 ps, corresponding to half the polarization dephasing time, $T_2/2$. This T_2 time (14.8 ps) is lower than that expected for a He pressure of 600 mbar using the Na-He collision cross section.[91] We believe our transient may still be influenced by absorption[22] which shortens the decay in the transient as shown below. At positive delay time, an asymptotic signal (on our time scale) is expected, corresponding to a population decay time, T_1,[55] which is on a nanosecond time scale. In addition, a short time behavior, also with a 2 ps modulation, is observed with an exponential decay of ~2.3 ps.

Fig. 6.13 shows the influence of strong absorption leading to pulse propagation effects[22] for the fs pulses. The conditions are the same as for Fig. 6.12, except the heat pipe was turned by 90° to increase the absolute number of Na atoms encountered by the laser beams. According to ref. 22, at high optical density the measured decay rate is mainly influenced by linear absorption and dispersion, and not by the actual polarization decay time, T_2. The transient obtained here (Fig. 6.13) with fs resolution shows a more symmetric behavior (than Fig. 6.12), as was observed in ref. 22, where 2 ps pulses were used.

6.5.2.2 The Na+H_2 System

Elsewhere,[92] an approach was outlined for probing surfaces of full-collision, bimolecular reactions using absorption and stimulated emission to obtain the dynamics of collision complexes. Here, we first discuss our efforts to investigate the Na(3p)+H_2 system and afterwards we give three possible fs DFWM experiments aimed at characterizing the dynamics on any two surfaces involved. The goal of the studies is to reveal the key features of the dynamics: the quenching rate and period of the vibrational motion in the crossing region (exciplex) as a function of excess energy.

All the Na+H_2 experiments were conducted in a heat-pipe environment, as already described in the experimental section, but using H_2 instead of He as a buffer gas.[44, 93] In an earlier experiment[39] a ns laser tuned off-resonant at various points in the red wing of Na to excite the complex and a ns probe laser detected the substantially altered vibrational distribution of the product, $H_2(v)$.

Here we wish to study the real-time dynamics of the collision complex. In these experiments the fs pump pulse was tuned off-resonant and DFWM was introduced at a time delay later as part of a fs pump-DFWM scheme, as described in the methodology section. The pump wavelength (7 nm bandwidth) was tuned in the range 595 - 620 nm, and was typically positioned at 600 nm. The DFWM pulses were tuned in the range 580 - 630 nm, *i.e.*, to both sides of the resonance. The idea was that the pump pulse excites a wave packet at the outer region of the bound NaH_2 exciplex (see Fig. 6.8(b)) and the evolution of the system would be detected by the fs DFWM, revealing the vibrational motion in the well and the time scale for the quenching process. With the DFWM wavelength in the range 580 - 620 nm, only dynamics similar to that of atomic sodium as described above were observed. An increase in the H_2 pressure by one order of magnitude (from

500 mbar) to raise the number of collision complexes by one order of magnitude still did not reveal any bimolecular dynamics (see Fig. 6.14). The increase in pressure also lead to more Rayleigh scattering appearing as straylight noise. In addition, different temperatures were chosen to increase the Na and thereby the NaH_2 concentration. Due to the significant effect of absorption at high temperatures, the chosen range was restricted to 180 - 270°C, corresponding to a Na density range of one and a half orders of magnitude.

Fig. 6.14 (left) shows a set of fs DFWM experiments in the bimolecular Na-H_2 system performed at three distinct H_2 pressures (0.5, 3.6 and 6.8 bar) and at a temperature of about 250°C . The wavelength of the DFWM pulses were tuned off-resonant to 605 nm, more than 15 nm to the red of the Na D-line. The oscillations (2 ps period) corresponding to the D-line splitting are still visible except at the highest pressure. The signal intensity decreases with increasing H_2 pressure, and added pressure leads to a faster decay of the envelope due to a faster dephasing time with higher Na-H_2 collision frequency.

The right-hand side of Fig. 6.14 shows fs DFWM transients (top) for the Na-He system detection at (i) 589 nm and (ii) 616 nm. The He pressure was 0.6 bar and the temperature 190°C. The difference in the peak positions (820 fs) is due to differences in the optical path length as a result of using the full continuum profile (no spectral filters) in each pulse, and due to the difference in the signal generation processes yielding the detected wavelengths. Spectra (Fig. 6.14 right, bottom) of the DFWM signal in the red wing were taken at the two fixed time delays corresponding to the main peaks in the transients as indicated. With the time delay fixed at the peak of transient (i), the main Na-D line is seen with a DFWM signal still existing far away from this resonance in the red wing, indicating the great sensitivity of fs DFWM (see Appendix). The peak at 616 nm appearing when the time delay is set to the other position, (ii), indicates that at

this wavelength, there is a dominance of the two-color grating process (see also Fig. 6.11).

With the pump and DFWM both still in the red wing close to the Na D-line, only the atomic sodium dynamics could be observed. To see the bimolecular dynamics, it is therefore necessary to tune the wavelength of one or both of these very far to the red. With our CPM fs laser system, it was not feasible to realize the tuning further to the red of resonance with sufficient intensity. A higher intensity should overcome the small population of NaH_2 collision complexes frozen on the fs time scale in the off-resonant pump window (see Appendix); more intensity in the DFWM ($\sim I^3$) pulses, maintaining a good beam profile and divergence, should enhance the detection. A Ti:Sapphire fs system provides a means of tuning to the infrared with high intensity and offers a possibility to detect the bimolecular dynamics in a variant scheme of transition-state spectroscopy.[94] It will also allow us to carry out the control experiments described in the article by Polanyi *et al.*[94] In the following we offer three possible fs DFWM approaches which, using higher intensities, promise to yield information about the ground and excited-state dynamics of this bimolecular system.

The top section of Fig. 6.15 shows a fs pump-DFWM type experiment (see section 6.3.3) in which the pump is tuned to be just off-resonant, to the red, of the Na D-line. The pump creates a wave packet on the excited state surface. Due to the kinetic energy of the ground state molecules in the pump window, the total energy of the excited molecules can exceed the asymptotic level, $Na(3p)+H_2$. Therefore, a fraction of the wave packet moves out and is detected via fs DFWM, resonantly tuned to the Na ($4d \leftarrow 3p$) transition. The remaining population of the wave packet, however, moves directly into the well, reaching the non-adiabatic crossing region, where some are quenched. The rest of the wave packet is

reflected and moves back on the excited state surface, reaching the outer turning point where reflection and partial escape occur. As a consequence of this dynamics, a stepwise build-up of the Na(3p) results, and should yield a transient as indicated in the top right of Fig. 6.15. Analogous to the observed stepwise behavior for NaI (Fig. 6.7, top), the period and crossing probability may be extracted.

The middle part of Fig. 6.15 shows a pump-control-DFWM (see section 6.3.4) scheme. Similar to the control experiment performed on NaI, a control pulse is introduced to intercept the wave packet in the transition state. Here, the control depopulates the excited state via stimulated emission to the ground state at a window determined by the control wavelength. By varying the time delay of the control, a depletion-type transient reflects the dynamics, and, by repeating this at several discrete control wavelengths, the potentials can be mapped out.

The bottom section of Fig. 6.15 shows a different pump-DFWM set-up where the DFWM is tuned to the infrared, directly probing the nascent quenched molecules at short internuclear distance. Tuning λ_c to the infrared will eliminate the influence[10] of sodium dimers present[95] because λ_c then lies to the red of the A-X absorption band of the dimers.[96] This clocking experiment yields information, not only about the period, but also about the crossing time and the quenching probability. By varying the pump wavelength it should be possible to map out the outer regions of the potential at which there is appreciable initial ground state population.

Femtosecond DFWM is a method similar to absorption and therefore is capable of monitoring collision complexes directly. Similar to the linear absorption experiments of Brooks and Curl,[97, 98] and the recent experiment of Marvet and Dantus,[99] the laser is tuned off-resonant in order to probe the dynamics of the complex at a particular configuration. As discussed in the

Appendix, the present approach, besides offering the background-free and large sensitivity features, allows one to observe an enhanced density for a given internuclear separation and maintains the correct zero of time without collisional smearing out at long times.

6.6 Conclusions

In this paper, we introduced the technique of degenerate four-wave-mixing (DFWM) as part of the methodology for femtosecond transition-state spectroscopy in the gas phase. This non-linear optical technique of DFWM with this fs time resolution is described and applied to unimolecular and bimolecular systems. Specifically, we examined the transition-state region of the unimolecular NaI and bimolecular $Na+H_2$ systems, and we detailed different aspects of DFWM on atomic Na. A variety of fs pulse-sequenced DFWM schemes were designed to probe different characteristics of the dynamics, and to measure the coherent and population decays of complexes.

A key feature of this fs DFWM approach is that it may be used to detect ultrafast dynamics with high sensitivity in systems where other means of detection, such as LIF or MPI, are not applicable. The fs temporal resolution combined with a background-free, highly collimated coherent signal makes the approach unique for studying the dynamics of reactions, especially under conditions of low concentration in collision systems. The aspect of relative polarization of the laser beams may also be exploited as in other probe methods. In femtochemical studies, the potential of this fs DFWM approach demonstrated here should prove useful for other applications.

6.7 Appendix: Density of Collision Complexes for a given Laser Pulse Width

We wish to compare the number of collision complexes that may be probed using fs *vs.* ns laser pulses. This number, N, is given by

$$N = Vol_{int} \cdot \rho_{complex}(R, \Delta R), \tag{6.15}$$

where Vol_{int} is the total interaction volume of the laser beam and the molecules in the sample:

$$Vol_{int} = \pi \cdot a^2 \cdot L, \tag{6.16}$$

where a is the beam radius and L is the interaction length. The concentration (density) of collision complexes resonant with the laser is $\rho_{complex}(R, \Delta R)$, where R is the internuclear separation corresponding to the resonant wavelength and ΔR is the range resonant with the pulse, corresponding to the spread in wavelength (energy) in the laser pulse.

In a bimolecular collision of A and B, consider one partner A and the number, $N_B(R, \Delta R)$, of B's in the "resonant shell" in the volume, $\Delta V = 4\pi \cdot R^2 \cdot \Delta R$, between R-$\Delta$R/2 and R+$\Delta$R/2:

$$N_B(R, \Delta R) = \rho_B(R) \cdot \Delta V. \tag{6.17}$$

(When ΔR is not small, $\Delta V = \frac{4}{3}\pi\{(R + \Delta R/2)^3 - (R - \Delta R/2)^3\}$ should be used). The concentration of partners, B, in (R,ΔR) is given by

$$\rho_B(R, \Delta R) = \rho_B^0 \cdot \bar{f}(E(R)), \tag{6.18}$$

where the concentration of B with any energy is ρ_B^0 and

$$\bar{f}(E(R)) = \int_{E(R)}^{\infty} f(E) \cdot dE \tag{6.19}$$

is the probability that B has an energy above or equal to the required E(R) to be at position R, and f(E) is the Maxwell-Boltzmann distribution for the thermally equilibrated system:[100]

$$f(E) = \frac{2\pi}{(\pi kT)^{3/2}} \cdot E^{1/2} \cdot \exp\left[-\frac{E}{kT}\right]. \tag{6.20}$$

The function, $\bar{f}(E(R))$, becomes unity for on-resonance probing where E(R)=0, and for the collision complex the function decreases from 1 toward 0 as the internuclear distance is decreased and the potential energy increases above the thermal energy level.

The concentration of A-B complexes is then the concentration of A's multiplied by $N_B(R,\Delta R)$:

$$\rho_{complex}(R,\Delta R) = \rho_A^0 \cdot \rho_B^0 \cdot 4\pi \cdot R^2 \cdot \Delta R \cdot \bar{f}(E(R)). \tag{6.21}$$

The factors ρ_A^0 and ρ_B^0 are independent of the lasers. The internuclear position R = R(E) and the factor $\bar{f}(E)$ depend only on the central wavelength of the laser and not on the temporal width of the pulse. $\Delta R = \Delta R(E,\Delta E)$ is the only factor that depends on the temporal pulse width as it depends on the window or resonant energy range, ΔE, on the potential energy surface.[101] Therefore, for a given central wavelength of the laser pulse, R is fixed, and using equations (6.15) and (6.21) the following is noticed:

$$N \propto \Delta R = \frac{\Delta E}{m}\ , \tag{6.22}$$

where ΔE is the laser bandwidth and m is the slope of the potential energy surface at R:

$$m = \frac{\Delta E}{\Delta R}\ . \tag{6.23}$$

Due to the broad laser bandwidth of a fs pulse (e.g., $\Delta E \sim 150\ cm^{-1}$ for a 100 fs pulse), the number of molecules excited may be large, compared to the pulse in

the ps to ns range where the bandwidth is typically much smaller and only a small shell volume is accessed. However, the discussion above is based on the assumption that there are no collisions during the pulse duration. For ns lasers this no longer holds true and the frequency with which collision partners move into the shell volume during the pulse, increasing the number of accessible complexes, must be considered. Nevertheless, by using laser pulses with longer duration a direct observation of the dynamics is not possible anymore.

Figure 6.16 (lower part) shows a plot of $\rho_{complex}$ *vs.* R for two different laser bandwidths: $\Delta E=1.8\cdot10^{-2}$ eV, corresponding to a 100 fs transform limited pulse, and $\Delta E=1.8\cdot10^{-7}$ eV, the width for a 10 ns transform limited pulse. A set of typical conditions for a gas phase cell experiment are chosen: $\rho_A^0=1\cdot10^{14}$ cm^{-3}, $\rho_B^0=1\cdot10^{19}$ cm^{-3} and T=250°C. The curves in this figure indicate the decreasing concentration at shorter R where the potential rises above the thermal energy level. The potential used in the calculations of these density curves is shown in the upper part of Fig. 6.16 and is a single exponential decay:

$$V = V_0 \cdot \exp\left[-\frac{R-R_0}{L}\right], \tag{6.24}$$

where V_0= 3 eV, R_0=1 Å, and L=1 Å.

The internuclear separation at which the laser bandwidth becomes comparable to the energy above the asymptotic value of the potential signifies the transition between the existence of a complex (off-resonant probing) and the presence of free collision partners (on-resonant probing). Equation (6.21) is valid for internuclear separations shorter than this upper bound for the existence of a complex. For a larger bandwidth, this position occurs at smaller R and is the point at which the curve for the concentration of the complexes must be terminated. This is shown in the case of a 100 fs pulse in the lower part of Fig.

6.16, where the curve ends at R~6.5 Å. For a discussion of the position used in distinguishing between off- and on-resonant probing see ref. 102.

6.7.1 Application to Na+H_2 Collision System

In the case of the bimolecular Na+H_2 system, the concentration of collision complexes is calculated using equation (6.21) and the following parameters: T=250°C, p_{H2} = 1 bar, λ_{Pu}= 595 nm (and so R= 4.5 Å), $\Delta\lambda$= 5.5 nm (implies ΔR= 0.7 Å). At the temperature of 250°C the Na vapor pressure has a concentration of $\rho^{0}_{Na} = 3.1\cdot 10^{13}\,cm^{-3}$. An H_2 pressure of 1 bar implies a density of $\rho^{0}_{H_2} = 1.4\cdot 10^{19}\,cm^{-3}$. The T and R specify that $\bar{f}(E(R)) = 0.92$. Hence $\rho_{complex}(Na-H_2) \approx 7\cdot 10^{10}\,cm^{-3}$. This is to be compared with on-resonant probing where the relevant concentration is simply $\rho^{0}_{Na} = 3.1\cdot 10^{13}\,cm^{-3}$. The concentration of the complex at the given condition is then 450 times smaller. However, by using a 10 ns (transform limited) pulse, the density of collision complexes decreases to an amount of about $\rho_{complex}(Na-H_2) \approx 1.3\cdot 10^{6}\,cm^{-3}$, which is 54000 times smaller than the density obtained in the complex using a 100 fs pulse. Note that at this pressure of 1 bar, the average collision time is ~ 50 ps, using a van der Waals cross section of 51 Å^2.

6.8 References

1. J. Manz, L. Wöste, Eds., *Femtosecond Chemistry* (VCH Verlagsgesellschaft mbH, Weinheim (Germany), ed. 1, 1995).
2. A. H. Zewail, *Femtochemistry - ultrafast dynamics of the chemical bond* (World Scientific, Singapore, 1994), vol. I & II.
3. M. Chergui, Ed.;, Femtochemistry - The Lausanne Conference 1995, Femtosecond Chemistry, the Lausanne Conference (World Scientific, Singapore, 1996, 1995).
4. J. Manz, A. W. Castleman, Jr., Eds., "Femtosecond Chemistry," J. Phys. Chem., 97, no. 48 (1993).
5. M. J. Rosker, M. Dantus, A. H. Zewail, *J. Chem. Phys.* **89**, 6113 (1988).
6. M. Dantus, R. M. Bowman, M. Gruebele, A. H. Zewail, *J. Chem. Phys.* **91**, 7434 (1989).
7. J. L. Herek, S. Pedersen, L. Bañares, A. H. Zewail, *J. Chem. Phys.* **97**, 9046 (1992).
8. J. H. Glownia, *et al.*, in *Femtosecond Chemistry* J. Manz, L. Wöste, Eds. (VCH Verlagsgesellschaft mbH, Weinheim (Germany), 1995) pp. 131, and references therein.
9. T. Baumert, S. Pedersen, A. H. Zewail, *J. Phys. Chem.* **97**, 12447 (1993).
10. T. Baumert, R. Thalweiser, V. Weiss, G. Gerber, in *Femtosecond Chemistry* J. L. Manz, E. Wöste, Eds. (VCH Verlagsgesellschaft mbH, Weinheim (Germany), 1995) pp. 403, and references therein.
11. J. L. Knee, L. R. Khundkar, A. H. Zewail, *J. Chem. Phys.* **82**, 4715 (1985).
12. J. L. Knee, in *Femtosecond Chemistry* J. Manz, L. Wöste, Eds. (VCH Verlagsgesellschaft mbH, Weinheim (Germany), 1995) pp. 167.

13. I. Fischer, D. M. Villeneuve, M. J. J. Vrakking, A. Stolow, *J. Chem. Phys.* **102**, 5566 (1995).

14. L. Hunziker, *et al.*, in *Molecular Dynamics and Spectroscopy by Stimulated Emission Pumping* H. Dai, R. W. Field, Eds. (World Scientific, Singapore, 1995), vol. 4, pp. 73.

15. S. Mukamel, *Nonlinear Optical Spectroscopy* (University Press, Oxford, 1995).

16. P. H. Vaccaro, in *Molecular Dynamics and Spectroscopy by Stimulated Emission Pumping* H. Dai, R. W. Field, Eds. (World Scientific, Singapore, 1995), vol. 4, pp. 1.

17. T. Höfer, P. Kruck, W. Kaiser, *Chem. Phys. Lett.* **224**, 411 (1994).

18. W. Kaiser, Ed.;, *Ultrafast Laser Pulses - Generation and Applications* (Springer-Verlag, Berlin, ed. 2nd, 1993).

19. P. F. Barbara, W. H. Knox, G. A. Mourou, A.H. Zewail, Eds., Proceedings of the 9th IC, Ultrafast Phenomena IX, Dana Point, California (Springer-Verlag: Berlin, New York, 1994).

20. J. T. Fourkas, R. Trebino, M. A. Dugan, M. D. Fayer, *Opt. Lett.* **18**, 781 (1993).

21. T. R. Brewer, J. T. Fourkas, M. D. Fayer, *Chem. Phys. Lett.* **203**, 344 (1993).

22. O. Kinrot, Y. Prior, *Phys. Rev. A* **50**, 1999 (1994).

23. Y. Prior, *Appl. Opt.* **19**, 1741 (1980).

24. J. A. Shirley, R. J. Hall, A. C. Eckbreth, *Opt. Lett.* **5**, 380 (1980).

25. J. L. Herek, A. Materny, A. H. Zewail, *Chem. Phys. Lett.* **228**, 15; and references therein (1994).

26. A. Materny, J. L. Herek, P. Cong, A. H. Zewail, *J. Phys. Chem.* **98**, 3352 (1994).

27. T. S. Rose, M. J. Rosker, A. H. Zewail, *J. Chem. Phys.* **88**, 6672 (1988).

28. M. J. Rosker, T. S. Rose, A. H. Zewail, *Chem. Phys. Lett.* **146**, 175 (1988).

29. T. S. Rose, M. J. Rosker, A. H. Zewail, *J. Chem. Phys.* **91**, 7415 (1989).

30. A. Mokhtari, P. Cong, J. L. Herek, A. H. Zewail, *Nature* **348**, 225 (1990).

31. J. L. Magee, *J. Chem. Phys.* **8**, 687 (1940).

32. J. W. Gadzuk, *Comments At. Mol. Phys.* **16**, 219 (1985).

33. R. Beach, D. DeBeer, S. R. Hartmann, *Phys. Rev. A* **32**, 3467 (1985).

34. J. E. Golub, T. W. Mossberg, *J. Opt. Soc. Am. B* **3**, 554 (1986).

35. J. E. Rothenberg, D. Grischkowsky, *Opt. Lett.* **10**, 22 (1985).

36. R. de Vivie-Riedle, P. Hering, K. L. Kompa, *Z. Phys. D* **17**, 299 (1990).

37. P. Botschwina, W. Meyer, I. V. Hertel, W. Reiland, *J. Chem. Phys.* **75**, 5438 (1981).

38. I. V. Hertel, in *Dynamics of the Excited State* K. P. Lawley, Ed. (J. Wiley and Sons Ltd., New York, 1982) pp. 475.

39. P. Hering, S. L. Cunha, K. L. Kompa, *J. Phys. Chem.* **91**, 5459 (1987).

40. G. Pichler, *et al.*, *Nuov Cim D* **14**, 1065 (1992).

41. R. R. B. Correira, *et al.*, *Chem. Phys. Lett.* **186**, 531 (1991).

42. M. Motzkus, G. Pichler, K. L. Kompa, P. Hering, *to be published.*

43. P. D. Kleiber, T. H. Wong, S. Bililign, *J. Chem. Phys.* **98**, 1101 (1993).

44. S. Bililign, P. D. Kleiber, W. P. Kearney, K. M. Sando, *J. Chem. Phys.* **96**, 218 (1992).

45. S. L. Mielke, G. J. Tawa, D. G. Truhlar, *J. Am. Chem. Soc.* **115**, 6436 (1993).

46. D. W. Schwenke, *et al.*, *Chem. Phys. Lett.* **203**, 565 (1993).

47. G. J. Tawa, S. L. Mielke, D. G. Truhlar, D. W. Schwenke, *J. Chem. Phys.* **100**, 5751 (1994).

48. Y. R. Shen, *The Principles of Nonlinear Optics* (John Wiley and Sons, New York, 1984).

49. R. W. Boyd, *Nonlinear Optics* (Academic Press, San Diego, 1992).

50. A. Yariv, *Quantum Electronics* (Wiley, New York, ed. 3rd, 1989).

51. W. Zinth, W. Kaiser, in *Ultrafast Laser Pulses - Generation and Applications* W. Kaiser, Ed. (Springer-Verlag, Berlin, 1993) pp. 235.

52. W. H. Hesselink, D. A. Wiersma, *J. Chem. Phys.* **73**, 648 (1980).

53. R. W. Hellworth, *J. Opt. Soc. Am.* **67**, 1 (1977).

54. R. L. Farrow, D. J. Rakestraw, *Science* **257**, 1894 (1992).

55. H. J. Eichler, P. Gunter, D. W. Pohl, *Laser-Induced Dynamic Gratings*. T. Tamir, Ed. (Springer-Verlag, Berlin, 1986, and references therein).

56. T. Yajima, Y. Taira, *J. Phys. Soc. Jpn.* **47**, 1620 (1979).

57. P. Ye, Y. R. Shen, *Phys. Rev. A* **25**, 2183 (1982).

58. K. Duppen, D. A. Wiersma, *J. Opt. Soc. Am. B* **3**, 614 (1986).

59. T. Joo, A. C. Albrecht, *Chem. Phys.* **176**, 233 (1993).

60. A. M. Weiner, S. DeSilvestri, E. P. Ippen, *J. Opt. Soc. Am. B* **2**, 654 (1985).

61. C. V. Shank, R. W. Schoenlein, C. J. Bardeen, D. M. Mittleman, in *Femtosecond Reaction Dynamics* D. A. Wiersma, Ed. (North-Holland, Amsterdam, 1994).

62. K. A. Nelson, D. R. Lutz, M. D. Fayer, *Phys. Rev. B* **24**, 3261 (1981); R. J. D. Miller, R. Casalegno, K. A. Nelson, M. D. Fayer, *Chem. Phys.* **72**, 371 (1982); T. S. Rose, M. D. Fayer, *Chem. Phys. Lett.* **117**, 12 (1985).

63. D. W. Phillion, D. J. Kuizenga, A. E. Siegman, *Appl. Phys. Lett.* **27**, 85 (1975).

64. T. J. Butenhoff, E. A. Rohlfing, *J. Chem. Phys.* **98**, 5460 (1993); T. J. Butenhoff, E. A. Rohlfing, *J. Chem. Phys.* **98**, 5469 (1993); J. R. Dunlop, E. A. Rohlfing, *J. Chem. Phys.* **100**, 856 (1994).

65. T. S. Rose, W. L. Wilson, G. Wäckerle, M. D. Fayer, *J. Chem. Phys.* **86**, 5370 (1987).

66. J. Gray, J. E. M. Goldsmith, R. Trebino, *Otics Lett.* **18**, 444 (1993).

67. E. F. McCormack, S. T. Pratt, P. M. Dehmer, J. L. Dehmer, *Chem. Phys. Lett.* **211**, 147 (1993).

68. M. D. Wheeler, I. R. Lambert, M. N. R. Ashfold, *Chem. Phys. Lett.* **211**, 381 (1993).

69. M. A. Buntine, D. W. Chandler, C. C. Hayden, *J. Chem. Phys.* **102**, 2718 (1995).

70. P. D. Kleiber, A. M. Lyyra, K. M. Sando, V. Zafiropulos, W. C. Stwalley, *J. Chem. Phys.* **85**, 5493 (1986).

71. A. N. Nesmeyanov, *Vapor Pressure of the Chemical Elements* (Academic Press, New York, 1963, pp. 132-135).

72. V. Engel, H. Metiu, R. Ameida, R. A. Marcus, A. H. Zewail, *Chem. Phys. Lett.* **152**, 1 (1988).

73. V. Engel, H. Metiu, *J. Chem. Phys.* **90**, 6116 (1989).

74. S. Bililign, P. D. Kleiber, *J. Chem. Phys.* **96**, 213 (1992).

75. S. Bililign, P. D. Kleiber, *Phys. Rev. A* **42**, 6938 (1990).

76. A. Sevin, P. Chaquin, *Chem. Phys.* **93**, 49 (1985).

77. F. Rossi, J. Pascale, *Phys. Rev. A* **32**, 2657 (1985).

78. M. Motzkus, *Ph.D. Thesis, Max-Planck-Institut für Quantenoptik, Garching, MPQ-Report 196* (1994).

79. J. Franck, R. W. Wood, *Verh. Dtsch. Phys. Ges.* **13**, 78 (1911).

80. P. McGuire, J. Bellum, *J. Chem. Phys.* **71**, 1975 (1979).

81. B. K. Kipple, G. Copley, L. Krause, *Phys. Rev.* **159**, 11 (1967).

82. C. W. Eaker, *J. Chem. Phys.* **87**, 4532 (1987).

83. J. R. Barker, R. E. Weston Jr., *J. Chem. Phys.* **65**, 1427 (1976).

84. A. Lindgard, S. E. Nielsen, *Atomic Data and Nuclear Data Tables* **19**, 571 (1977).

85. S. L. Palfrey, T. F. Heinz, *J. Opt. Soc. Am. B* **2**, 674 (1985).

86. C. C. Hayden, R. Trebino, *Appl. Phys. B* **51**, 350 (1990).

87. M. A. Buntine, D. W. Chandler, C. C. Hayden, *J. Chem. Phys.* **97**, 707 (1992).

88. C. Cohen-Tannoudji, B. Diu, F. Laloë, in *Quantum Mechanics*. (Wiley-Interscience, New York, 1977), vol. 1, Chap. IV,C.

89. M. O. Scully, M. Fleischhauer, *Science* **263**, 337; and references therein (1994).

90. J. Marangos, *Nature* **374**, 679 (1995).

91. T. Mossberg, A. Flusberg, R. Kachru, S. R. Hartmann, *Phys. Rev. Lett.* **42**, 1665; and references therein (1979).

92. A. H. Zewail, in *Ultrafast Phenomena 8* J. L. Martin, A. Migus, G. Mourou, A. H. Zewail, Eds. (Springer Verlag, Berlin, 1993) pp. 43.

93. M. Motzkus, M. Dillmann, G. Pichler, K. L. Kompa, P. Hering, *Appl. Phys. B* **57**, 261 (1993).

94. J. C. Polanyi, A. H. Zewail, *Acc Chem Re* **28**, 119 (1995).

95. in *Gmelins Handbuch der Anorganischen Chemie.* (Verlag Chemie GmbH, Weinheim, Germany, 1965), vol. 21, pp. 505.

96. G. Gerber, R. Möller, *Chem. Phys. Lett.* **113**, 546 (1985).

97. M. D. Barnes, P. R. Brooks, R. F. Curl, P. W. Harland, B. R. Johnson, *J. Chem. Phys.* **96**, 3559 (1992).

98. P. Hering, P. R. Brooks, R. F. Curl, *Phys. Rev. Lett.* **44**, 687 (1980).

99. U. Marvet, M. Dantus, *Chem. Phys. Lett.* **245**, 393 (1995).

100. T. L. Hill, *An Introduction to Statistical Thermodynamics* (Dover, New York, 1986).

101. R. B. Bernstein, A. H. Zewail, *J. Chem. Phys.* **90**, 829 (1989).

102. Liu, Q.; Zewail, A. H. *J. Phys Chem.* **97**, 2209 (1993).

6.9 Figure Captions and Figures

Fig. 6.1 Schematic showing the configuration of the incident pump beam and the three DFWM laser beams. A lens focuses the femtosecond pulses into the sample cell (quartz cell in oven, or heat-pipe oven), generating the femtosecond DFWM signal beam, which is spatially selected and subsequently collimated.

Fig. 6.2 (a). Three monochromatic laser beams, resonant between two energy levels, generate a degenerate four-wave-mixing beam (ω_{DFWM}) of the same frequency. (b). Wave vectors of the three incident beams ($\mathbf{k}_1$, $\mathbf{k}_2$, $\mathbf{k}_3$) and the emerging signal beam ($\mathbf{k}_{DFWM}$) oriented in the folded boxcar configuration. This produces exact phase matching throughout the (gas) sample in addition to a spatially separable signal beam.

Fig. 6.3 Femtosecond DFWM process illustrated in terms of a transient grating picture. (a) The electric fields, $\mathbf{E}_1$ and $\mathbf{E}_2$, of two incident fs pulses set up an interference pattern that writes a grating into the medium. The grating has a spatial periodicity or grating constant, d, that depends on the common wavelength, λ_{DFWM}, and the crossing angle, ϕ, for the intersecting beams. (b) The third incident fs pulse encounters this transient grating and undergoes Bragg scattering, creating the fourth pulse indicated, the fs DFWM signal pulse, which travels in a direction consistent with the phase matching condition.

Fig. 6.4 Three different techniques involving femtosecond DFWM and used to probe the ultrafast dynamics of gas phase atomic or molecular systems. The temporal pulse sequence is presented with its corresponding spatial beam configuration for each technique (see Methodology section).

Fig. 6.5 Experimental setup showing the femtosecond pulse production, the generated pump, control and three DFWM beams (1, 2, 3), the sample cell and the detection of the emerging femtosecond DFWM laser signal beam. Computer-controlled actuators were used to vary the relative arrival time of the femtosecond pulses. Only one actuator was moved in an experiment to obtain a transient.

Fig. 6.6 Potential energy surfaces relevant to the dissociation of excited NaI. A pump pulse excites the molecule which then vibrates with a fixed period in the adiabatic well, formed by the crossing of the ionic ground state and the lowest excited covalent state. A constant fraction of the excited wave packet escapes out at the outer turning point of the motion, yielding a stepwise build-up of neutral Na and I products.

Fig. 6.7 Three distinct femtosecond experiments performed on gaseous NaI. *Top* A pump pulse (308 nm) initiates the excited state dynamics which is probed by fs DFWM at a certain time delay later at the resonant wavelength of the Na D-line (589 nm). The DFWM signal data show the expected stepwise accumulation of the product. *Middle* The fs DFWM beams are now kept at a fixed time delay (19.2 ps) after the pump pulse. A fs control pulse (616 nm) is introduced at a time delay after the pump. It further excites part of the wave packet from the transition state to a second excited state which asymptotes to Na(3p)+I. As DFWM is sensitive to population difference, periodic depletion of the signal results with the frequency of the oscillatory motion in the well. *Bottom* A fs pump(308 nm)-probe(616 nm) experiment with LIF(589 nm) detection. The data show the same oscillatory behavior observed with DFWM detection above.

Fig. 6.8 (a) Shown are the two possible channels for a general bimolecular system as described by equation (6.14): the quenching process where the separation is along the same coordinate, A···BC, and the reactive channel along the AB···C coordinate. (b) Sketch of the ground state and first excited state (exciplex) of the Na+H_2 system in C_{2v} geometry. The ground state is purely repulsive while the excited state has a well at short separation. The excited state collision complex is quenched by a non-adiabatic crossing of the two surfaces at short internuclear separation. The ground state has a thermal population which restricts its distribution of complexes, inhibiting population at short separations.

Fig. 6.9 Energy diagram of sodium atomic energy levels and wavelengths associated with allowed transitions. The natural radiative lifetime is presented below each level.[84] The fine structure splitting of the 3p level is indicated.

Fig. 6.10 Transient obtained in a pump-DFWM-type experiment with the Na (600 mbar He) atomic system. The pump wavelength was 589 nm as was the wavelength for the three DFWM beams. The pump and probe laser bandwidth was 10 nm (FWHM). A 0.7 nm bandwidth at 595 nm was selected from the DFWM signal spectrum by the monochromator. The resulting signal exhibits depletion at positive time delay, *i.e.*, when the DFWM beams arrive (together) after the pump pulse (see text).

Fig. 6.11 Femtosecond transient showing coherent oscillations with a 2 ps period corresponding to the fine structure splitting of the Na 3p level. A femtosecond pump pulse (589±5 nm) prepares a coherent superposition of the two levels that evolves in time. The oscillating wavefunction is probed at a time delay later by means of femtosecond four-wave-mixing (589/589/616) yielding a

616 nm femtosecond laser signal pulse. The femtosecond FWM probing method used in this particular experiment constitutes a two-color grating scheme. A He buffer pressure of 500 mbar was used.

Fig. 6.12 Femtosecond transient showing the DFWM signal obtained for the Na (600 mbar He) atomic system. The technique is as per Fig. 6.4 (top) with a common wavelength for the three beams of 589±5 nm. The oscillations (2 ps period) match the difference frequency in the Na 3p fine structure splitting (17.2 cm^{-1}). The exponential decay time of the signal envelope is discussed in the text.

Fig. 6.13 Femtosecond transient obtained in a DFWM-type experiment. Two of the three incident pulses (1,2) arrive simultaneously and the third (3), also of the same wavelength (589 nm), comes at a time delay later. The Na crossed heat-pipe oven was turned 90° from its normal orientation, to have the lasers now pass through the arms with the heating coils. The substantial absorption in this setup causes a pulse propagation effect, leading to a more symmetric transient with signal mainly near time zero (see text).

Fig. 6.14 (Left) Fs DFWM transients obtained in the Na-H_2 system by detecting in the red wing at 605 nm. at three different H_2 pressures. Full continuum is used for each of the three incident DFWM pulses and the detection is selected using the monochromator (7.2 nm bandwidth). Good signal-to-noise ratio is achieved even this far in the red wing. (Right) The top part shows fs DFWM transients detecting at (i) 589 nm and (ii) 616 nm for Na with He at a pressure of 0.6 bar. The spectra at the bottom are taken at the peaks of transients (i) (a and b) and transient (ii) (c). Spectrum (b) was performed by removing a

neutral density filter, increasing the intensity admitted to the monochromator by a factor of 1000. The peak in (c) is centered at 616 nm.

Fig. 6.15 Three schemes relevant to the study of the bimolecular collision complex system, $Na+H_2$. *Top* A pump pulse excites ground state complexes in a just "off-resonant" transition. The excited wave packet, with initial kinetic energy, similar to that on the ground state, will oscillate in the well, being quenched at short separations and escaping out at the outer turning point. Femtosecond DFWM (569 nm) is used to resonantly probe the stepwise build-up of free Na (3p). *Middle* A fs control pulse is introduced to deplete the excited state population at $Na-H_2$ separations shorter than that accessed by the pump. The aim is to deduce the ground and excited state potential energy surfaces. *Bottom* A clocking fs pump-DFWM experiment with the DFWM tuned to the infrared (e.g., with fs Ti:Sapphire laser) to detect the quenched $Na+H_2$ complex as it arrives on the ground state surface. The pump wavelength may be tuned to map out the potential energy surfaces at large $Na-H_2$ separations.

Fig. 6.16 (Top) Potential energy surface showing a typical repulsive ground state for a bimolecular collision, together with the Maxwell-Boltzmann distribution, revealing the fraction of particles of sufficient energy, relevant to equation (6.19). The bandwidth of the laser pulse defines an energy range, ΔE, corresponding to a window, ΔR, centered at an internuclear separation, R. (Bottom) Density of collision complexes as a function of R for two different laser bandwidths corresponding to transform limited pulses of FWHM = 100 fs and 10 ns. The densities of the collision partners, A and B, are set to $\rho_A^0 = 1 \cdot 10^{14}$ cm^{-3} and $\rho_B^0 = 1 \cdot 10^{19}$ cm^{-3}. A typical temperature of T=250°C is chosen and this governs the Maxwell-Boltzmann energy distribution, f(E), indicated in the top right corner.

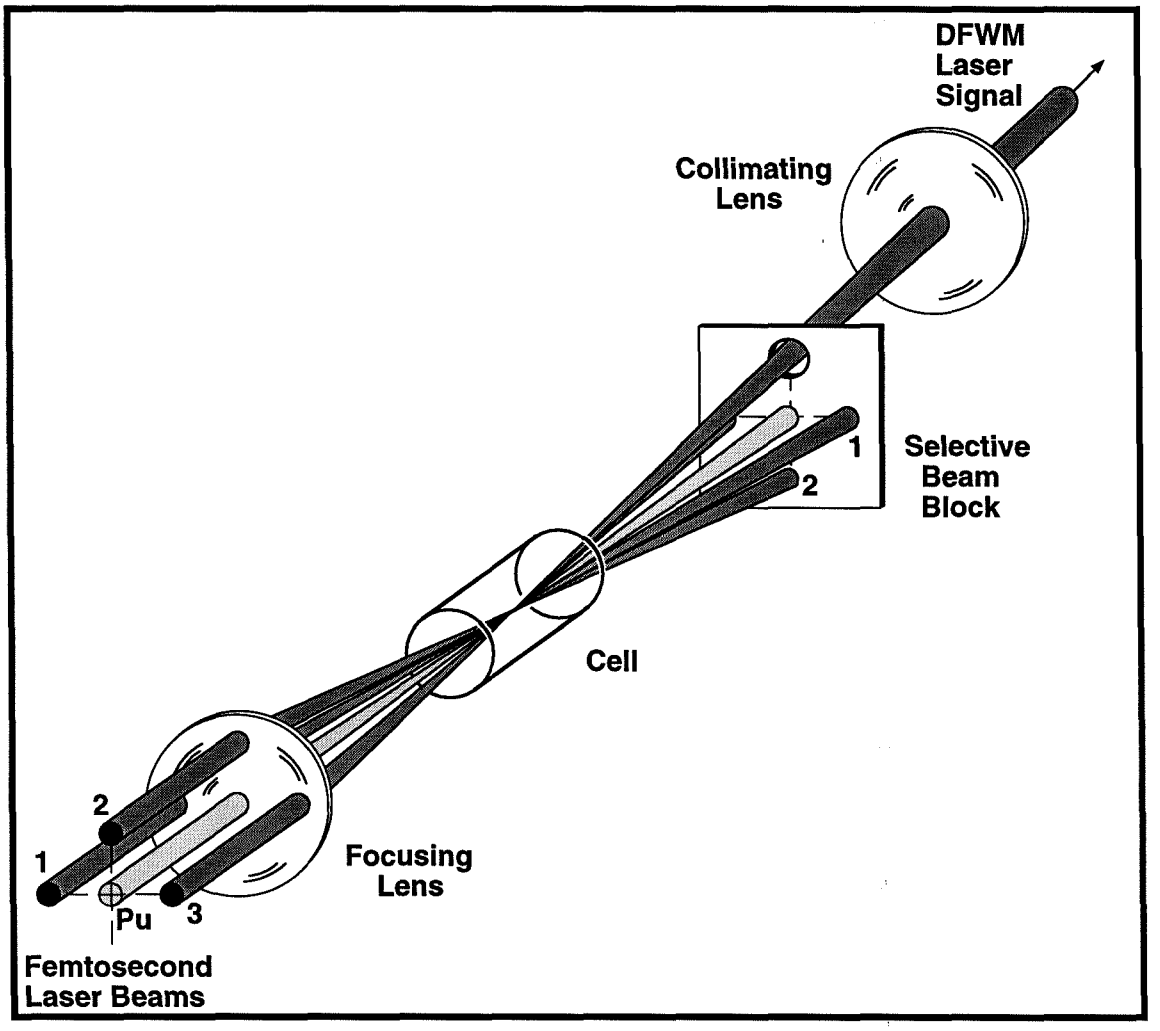
DFWM
Laser
Signal
Collimating
Lens
1
2
Selective
Beam
Block
Cell
2
1
Pu
3
Focusing
Lens
Femtosecond
Laser Beams

Fig. 6.1

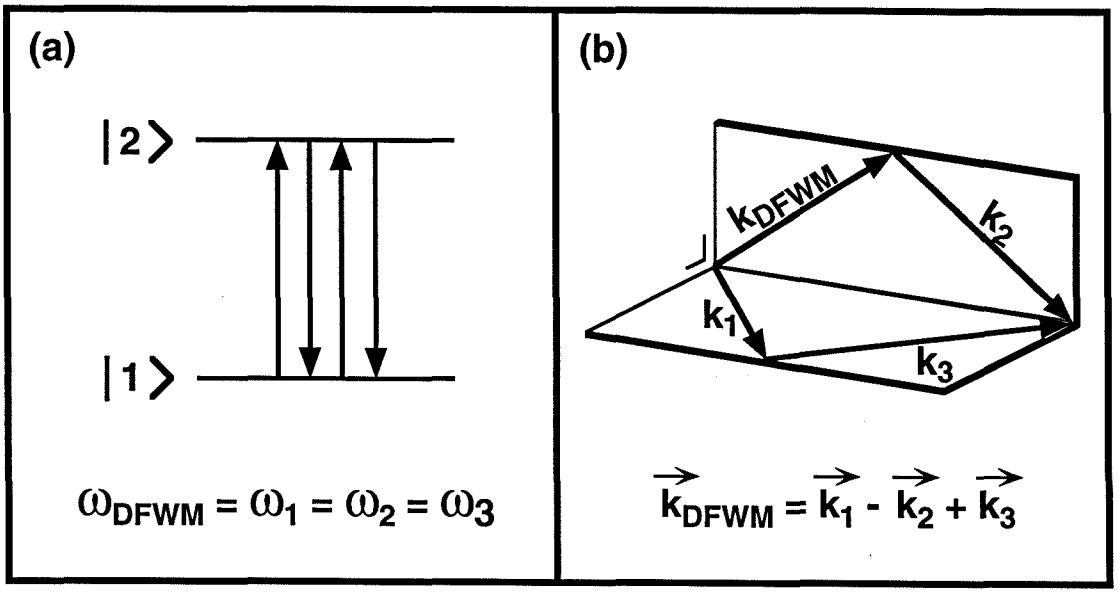
(a)
|2>
|1>
$\omega_{DFWM} = \omega_1 = \omega_2 = \omega_3$
(b)
k_{DFWM}
k_2
k_1
k_3
$\vec{k}_{DFWM} = \vec{k}_1 - \vec{k}_2 + \vec{k}_3$

Fig. 6.2

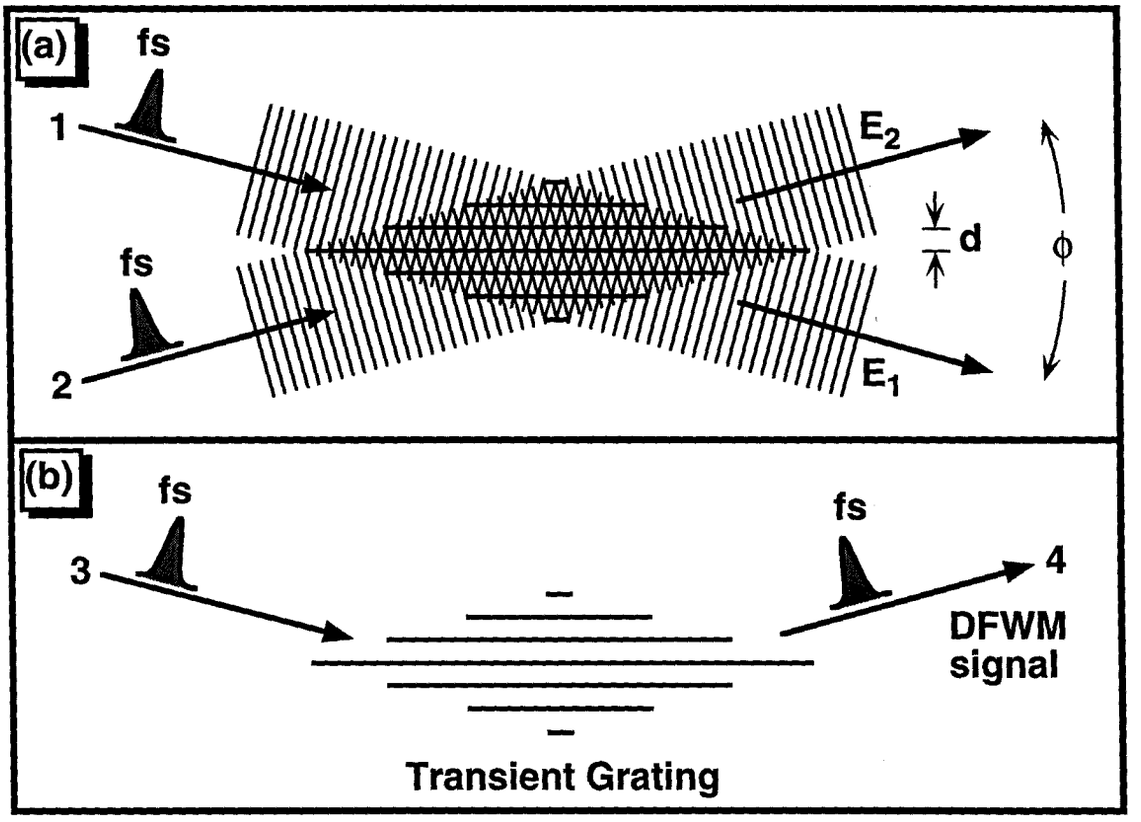

Fig. 6.3

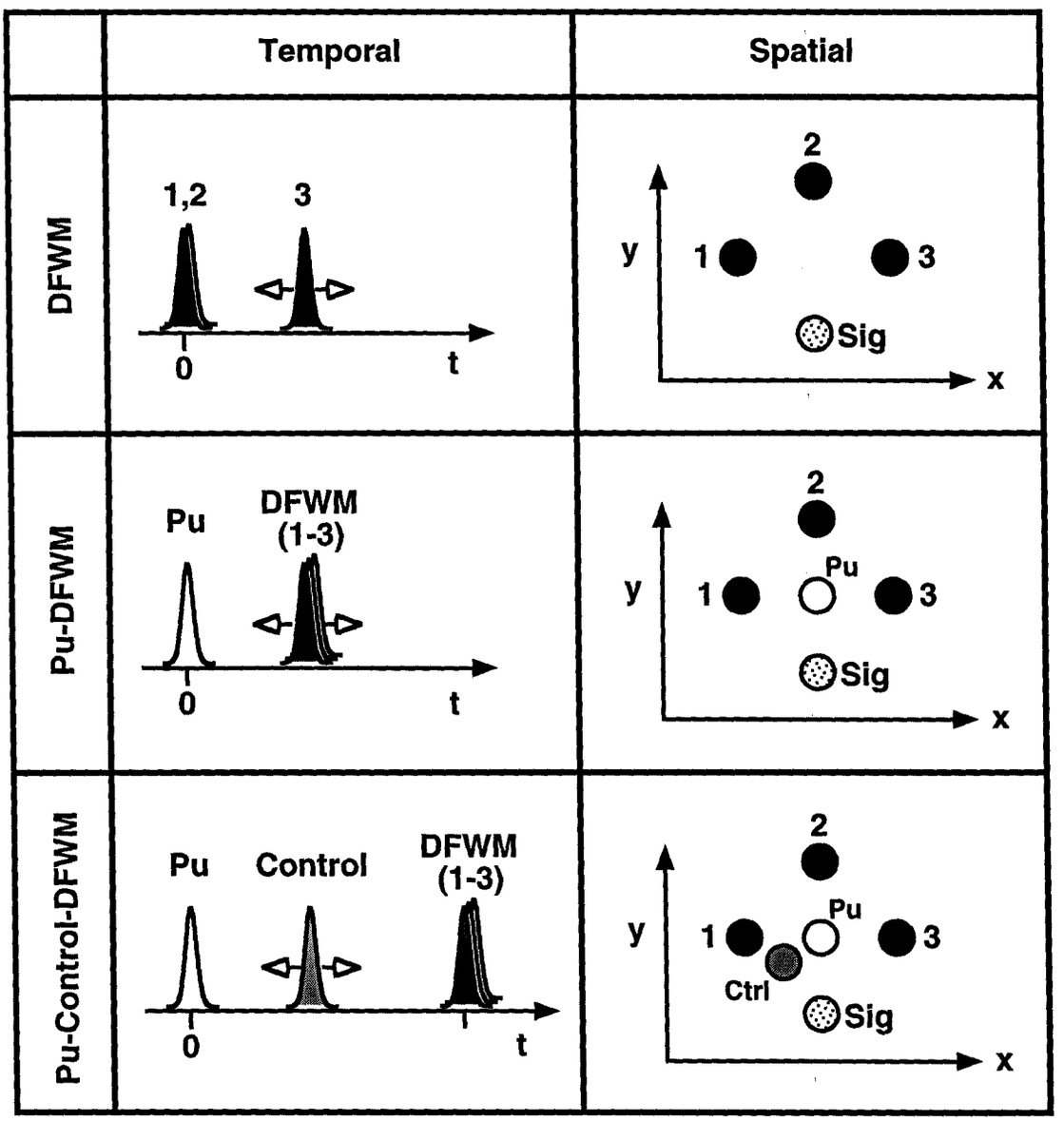
Temporal
Spatial
DFWM
1,2
3
0
t
2
y
1
3
Sig
x
Pu-DFWM
Pu
DFWM
(1-3)
0
t
2
y
1
Pu
3
Sig
x
Pu-Control-DFWM
Pu
Control
DFWM
(1-3)
0
t
2
y
1
Pu
3
Ctrl
Sig
x

Fig. 6.4

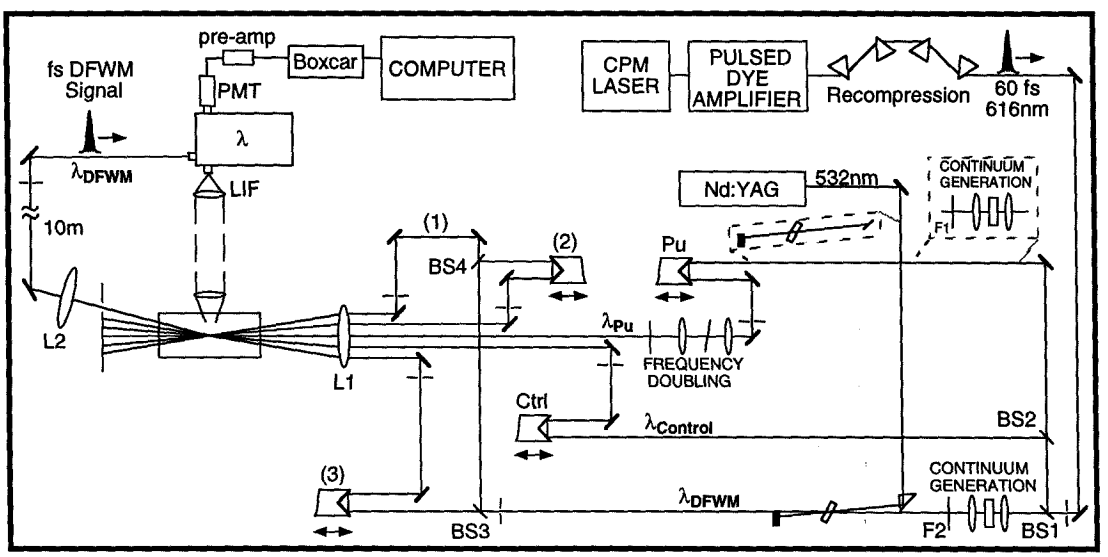
pre-amp
Boxcar
COMPUTER
fs DFWM
Signal
PMT
λ
λDFWM
LIF
10m
L2
L1
(1)
BS4
(2)
Pu
λPu
FREQUENCY
DOUBLING
CPM
LASER
PULSED
DYE
AMPLIFIER
Recompression
60 fs
616nm
Nd:YAG
532nm
CONTINUUM
GENERATION
F1
Ctrl
λControl
BS2
(3)
BS3
λDFWM
CONTINUUM
GENERATION
F2
BS1

Fig. 6.5

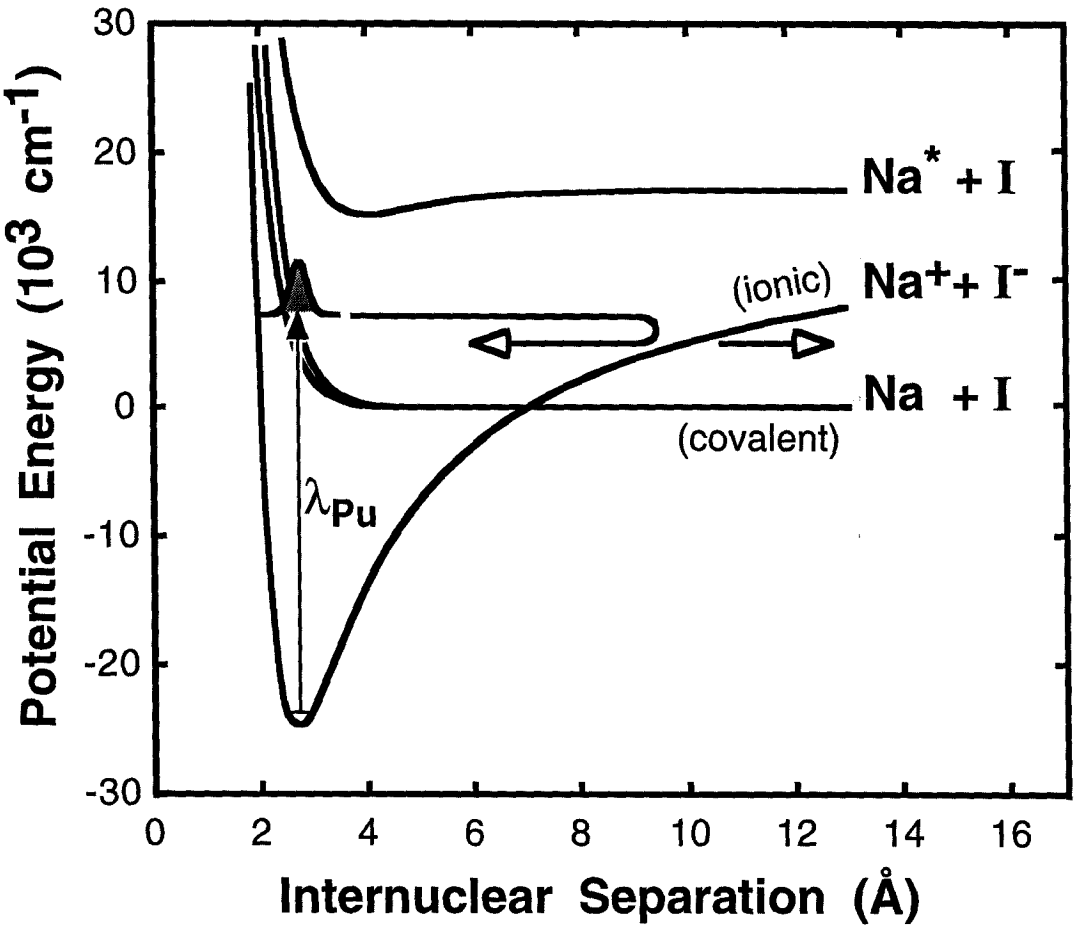
Potential Energy (10^3 cm^{-1})
30
20
10
0
-10
-20
-30
0
2
4
6
8
10
12
14
16
Internuclear Separation (Å)
Na* + I
(ionic) Na+ + I-
Na + I
(covalent)
λPu

Fig. 6.6

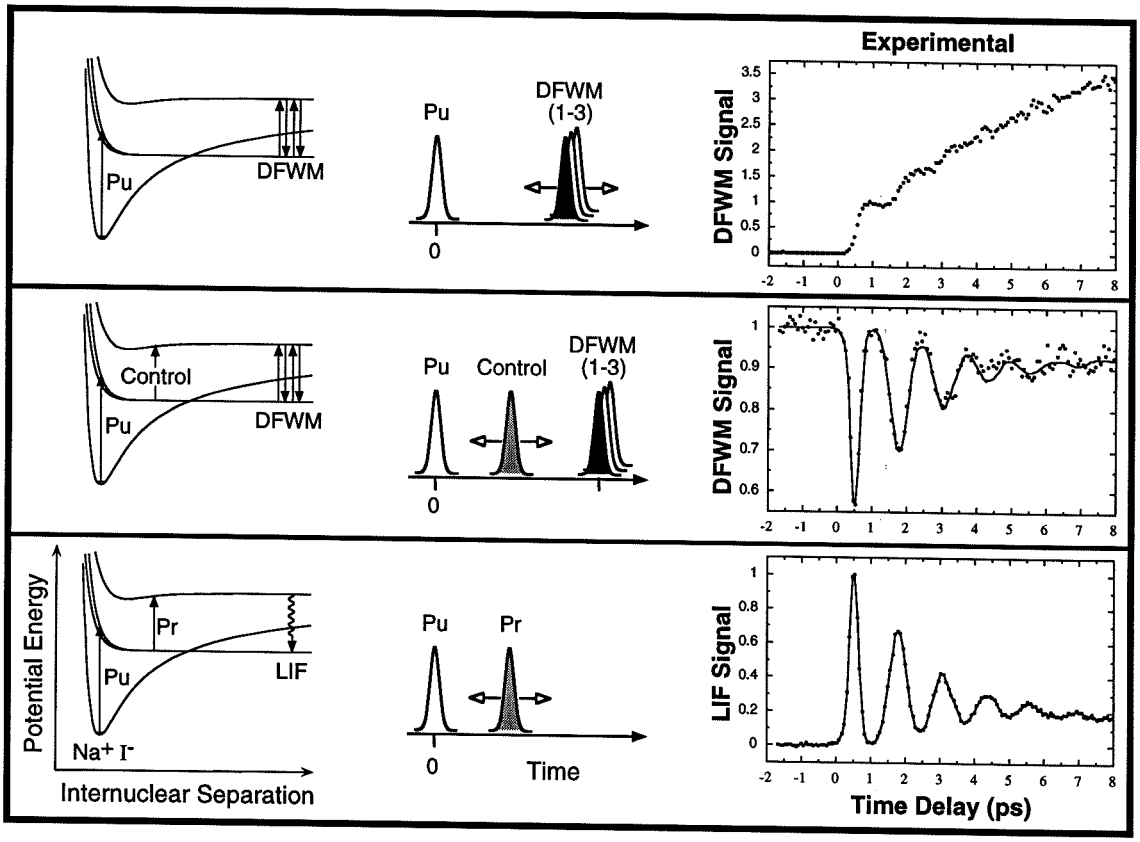
Experimental
Pu
DFWM
DFWM (1-3)
0
DFWM Signal
Control
Pu
DFWM
Pu
Control
DFWM (1-3)
0
DFWM Signal
Potential Energy
Pr
Pu
LIF
Na+ I-
Internuclear Separation
Pu
Pr
0
Time
LIF Signal
Time Delay (ps)

Fig. 6.7

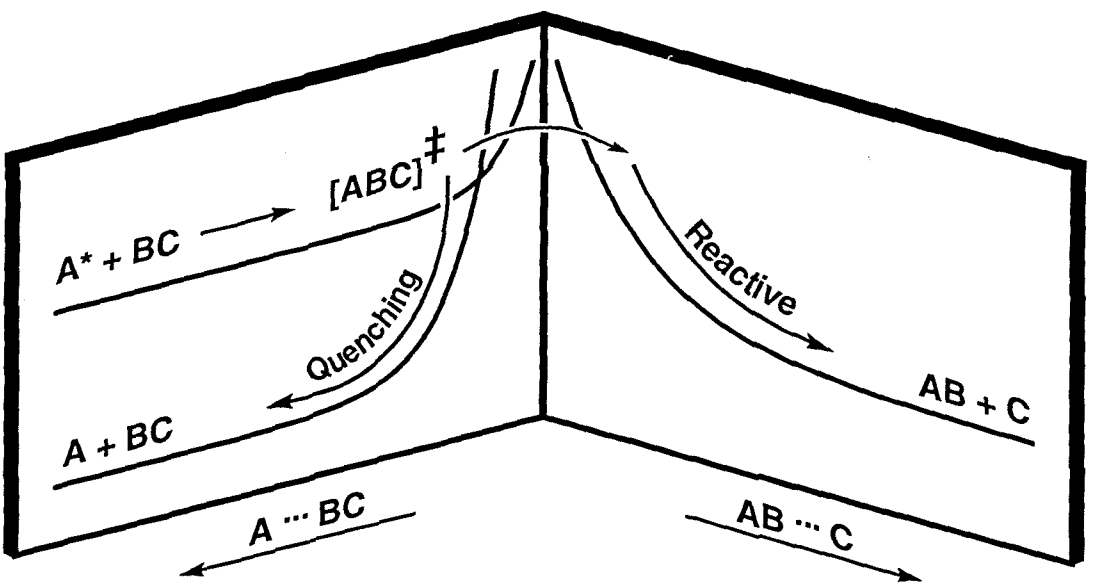

Fig. 6.8a

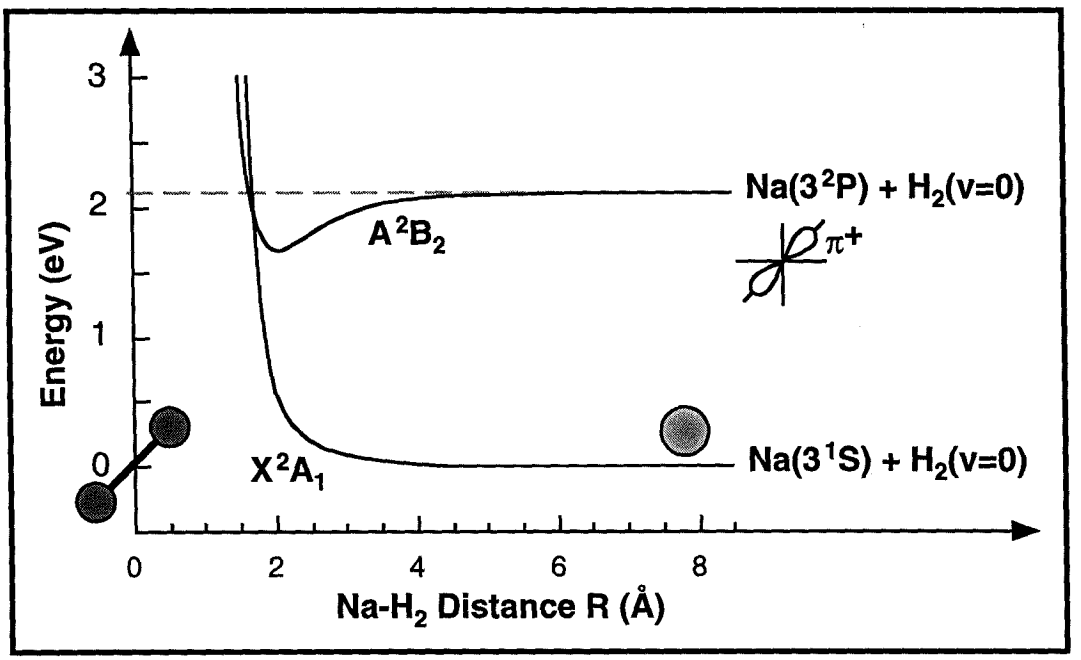
3
2
1
0
Energy (eV)
A^2B_2
X^2A_1
$Na(3^2P) + H_2(v=0)$
π^+
$Na(3^1S) + H_2(v=0)$
0
2
4
6
8
Na-H_2 Distance R (Å)

Fig. 6.8b

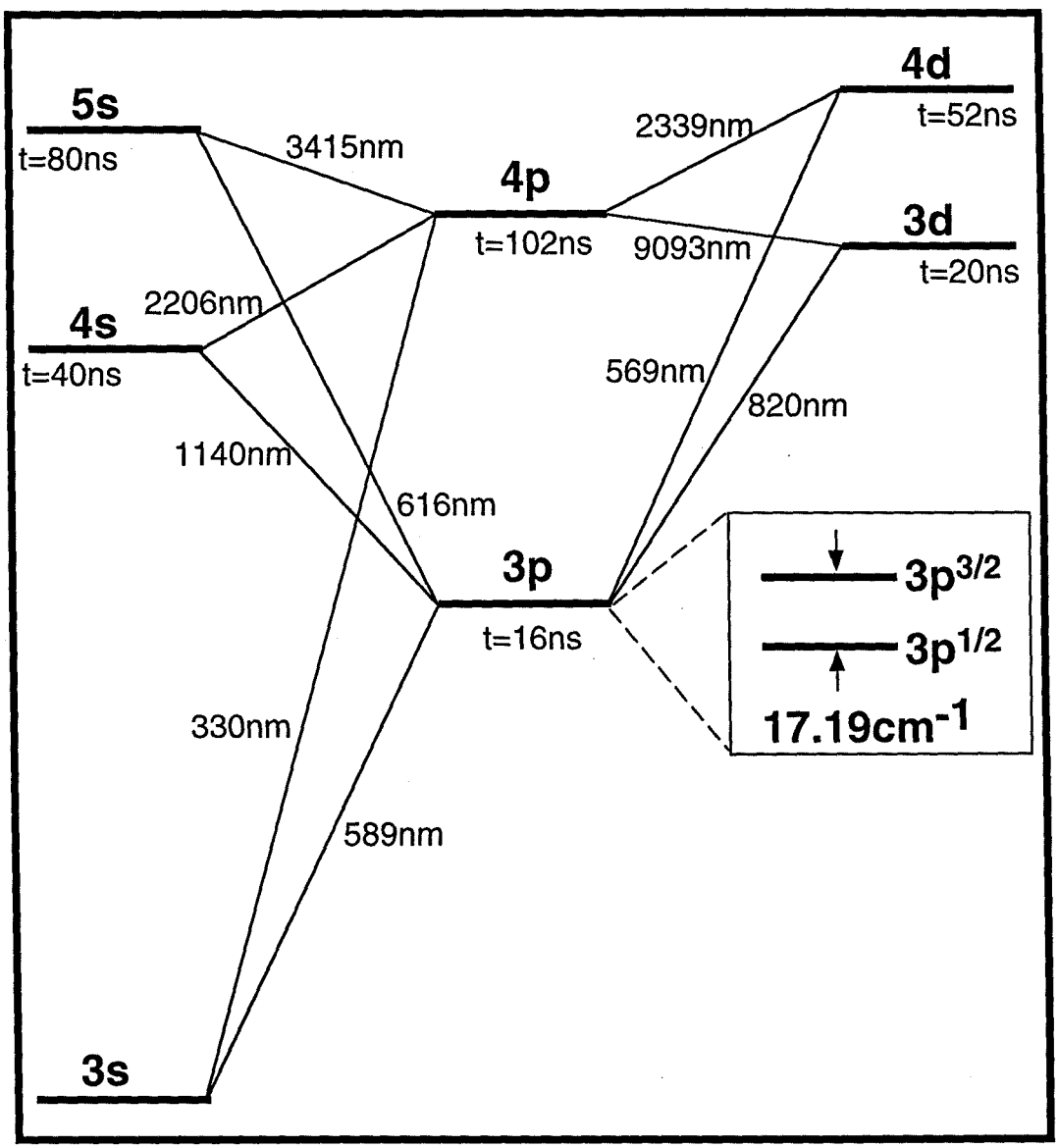
5s
t=80ns
3415nm
4p
t=102ns
2339nm
4d
t=52ns
9093nm
3d
t=20ns
2206nm
4s
t=40ns
569nm
820nm
1140nm
616nm
3p
t=16ns
3p3/2
3p1/2
17.19cm-1
330nm
589nm
3s

Fig. 6.9

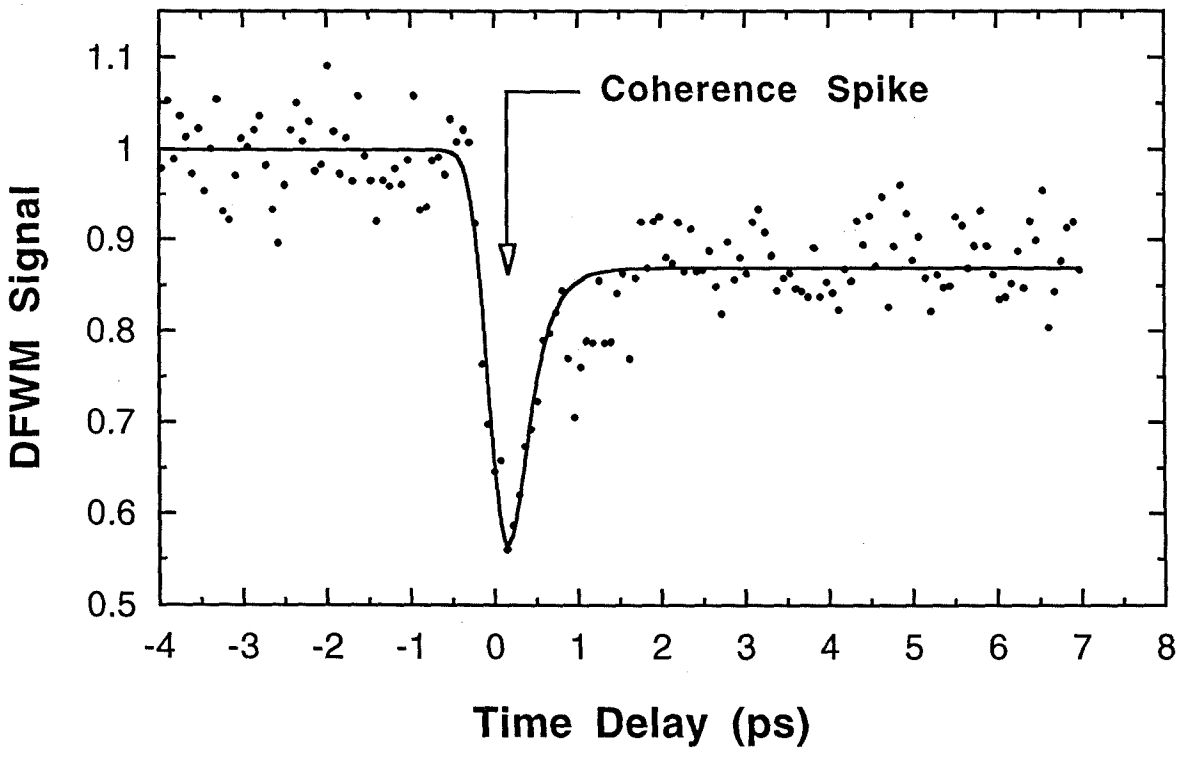
Coherence Spike
DFWM Signal
Time Delay (ps)
1.1
1
0.9
0.8
0.7
0.6
0.5
-4
-3
-2
-1
0
1
2
3
4
5
6
7
8

Fig. 6.10

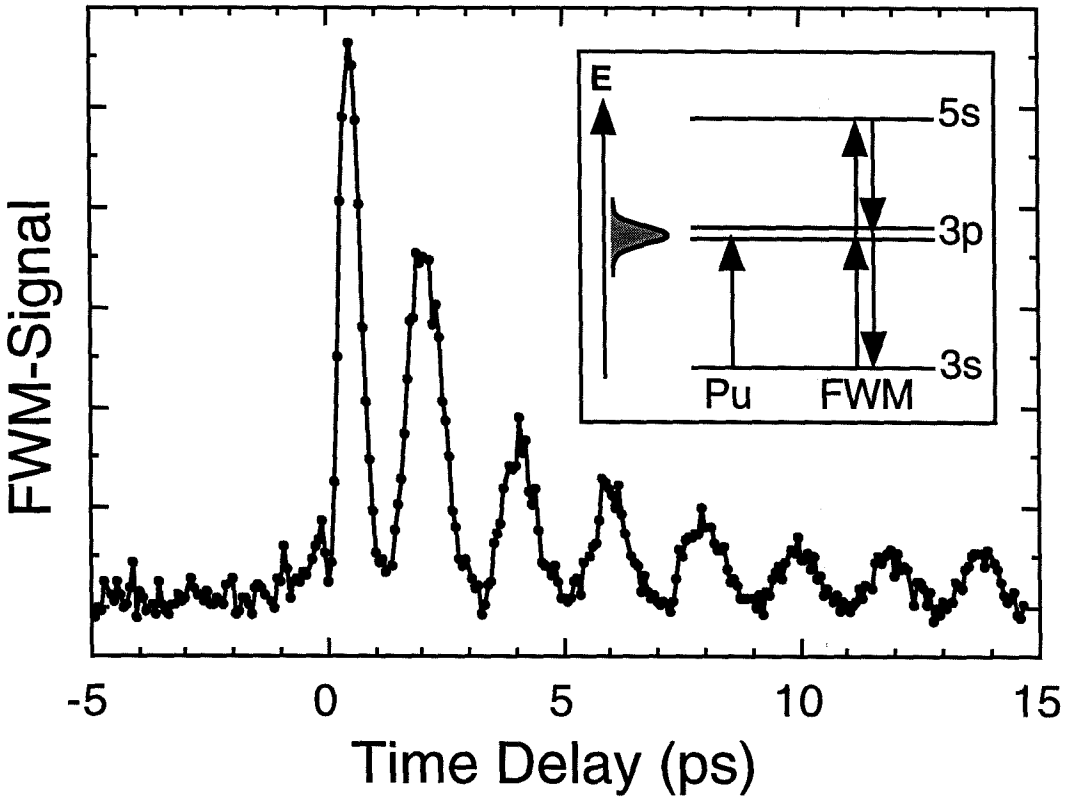

Fig. 6.11

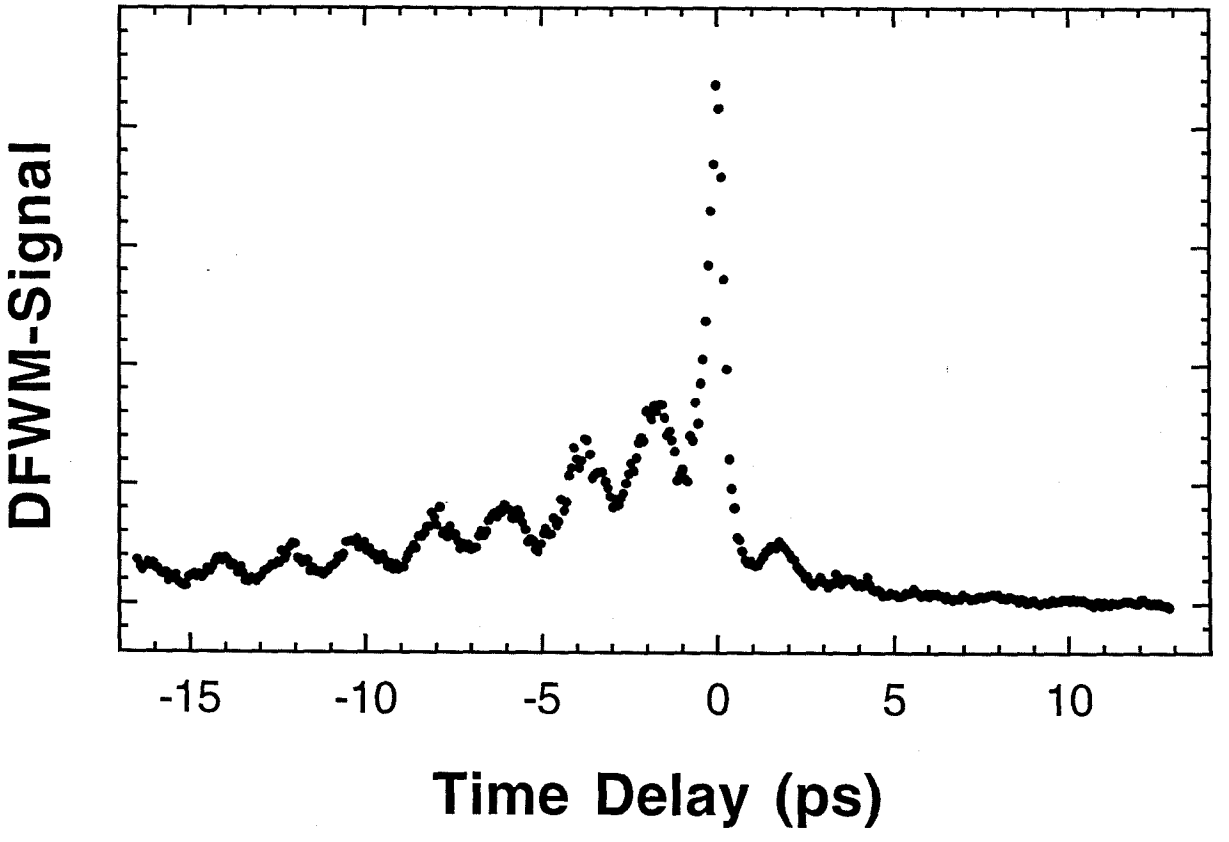

Fig. 6.12

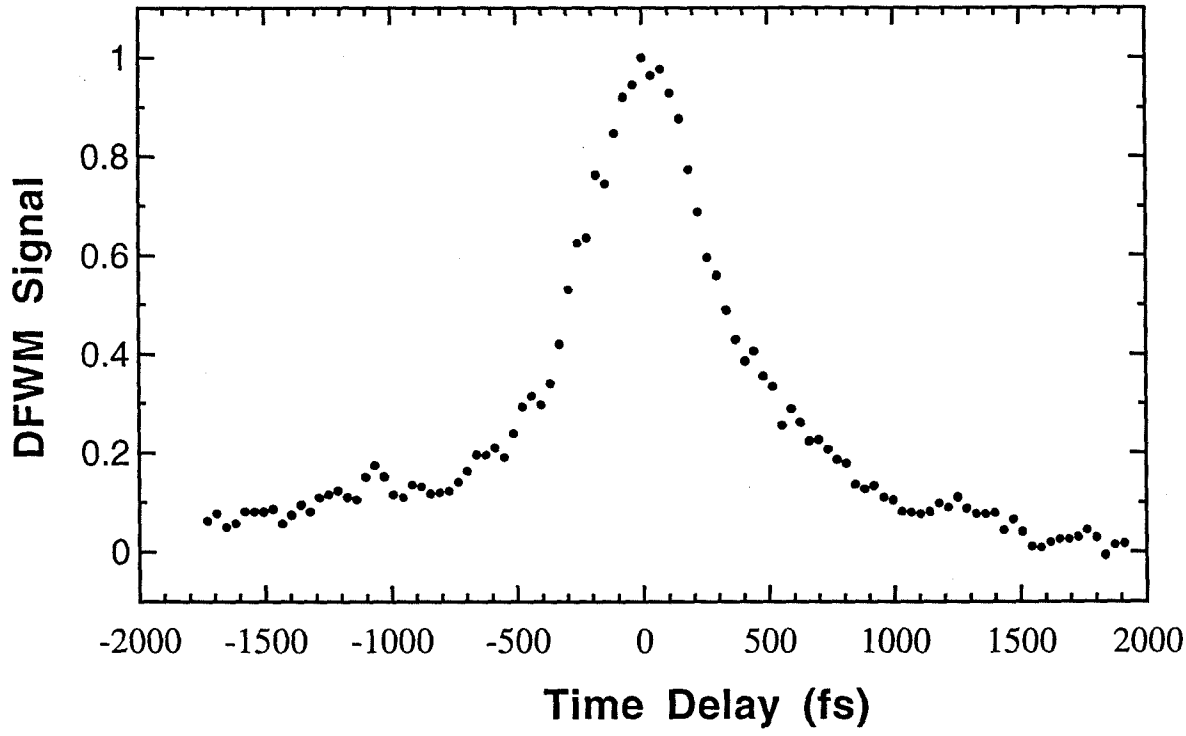
DFWM Signal
1
0.8
0.6
0.4
0.2
0
-2000
-1500
-1000
-500
0
500
1000
1500
2000
Time Delay (fs)

Fig. 6.13

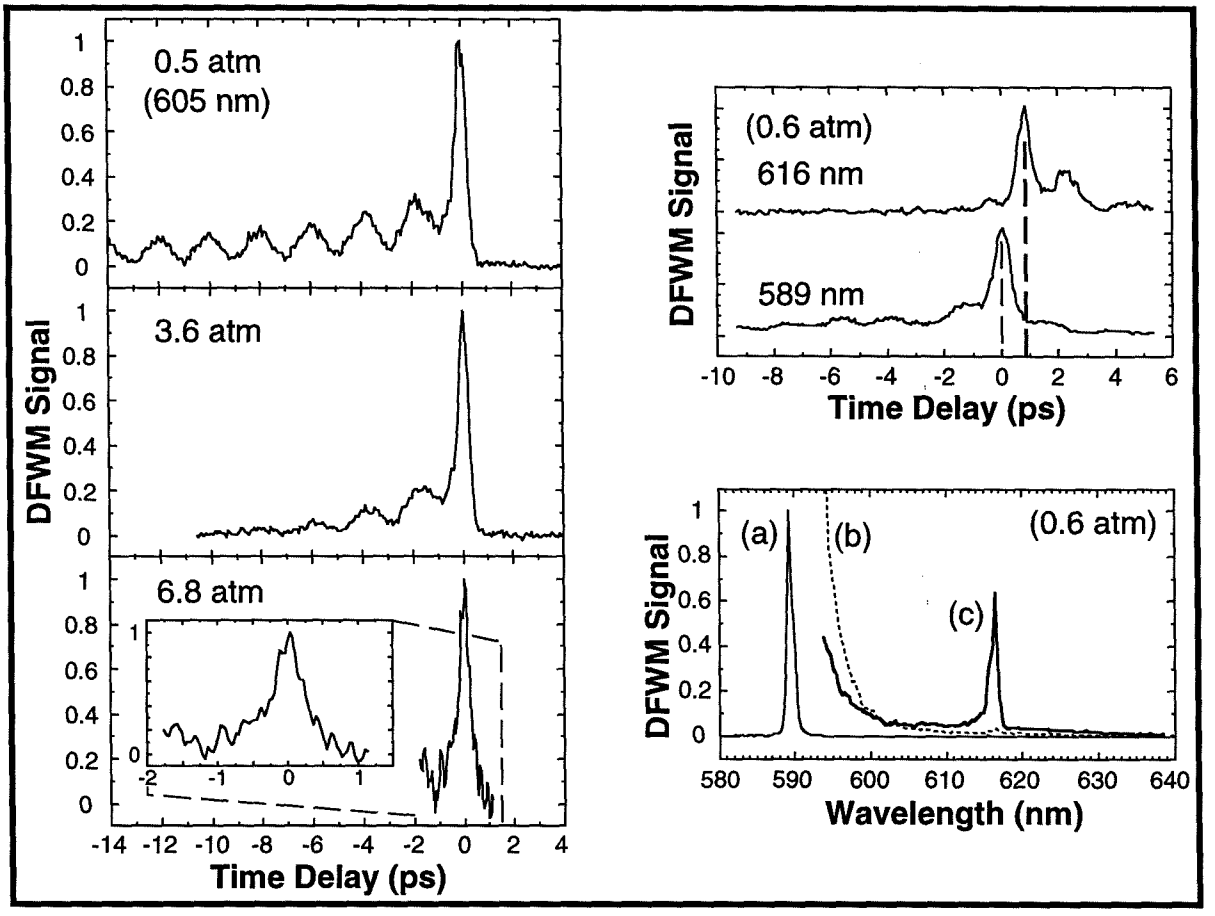
0.5 atm
(605 nm)
3.6 atm
6.8 atm
DFWM Signal
Time Delay (ps)
(0.6 atm)
616 nm
589 nm
DFWM Signal
Time Delay (ps)
(a)
(b)
(c)
(0.6 atm)
DFWM Signal
Wavelength (nm)

Fig. 6.14

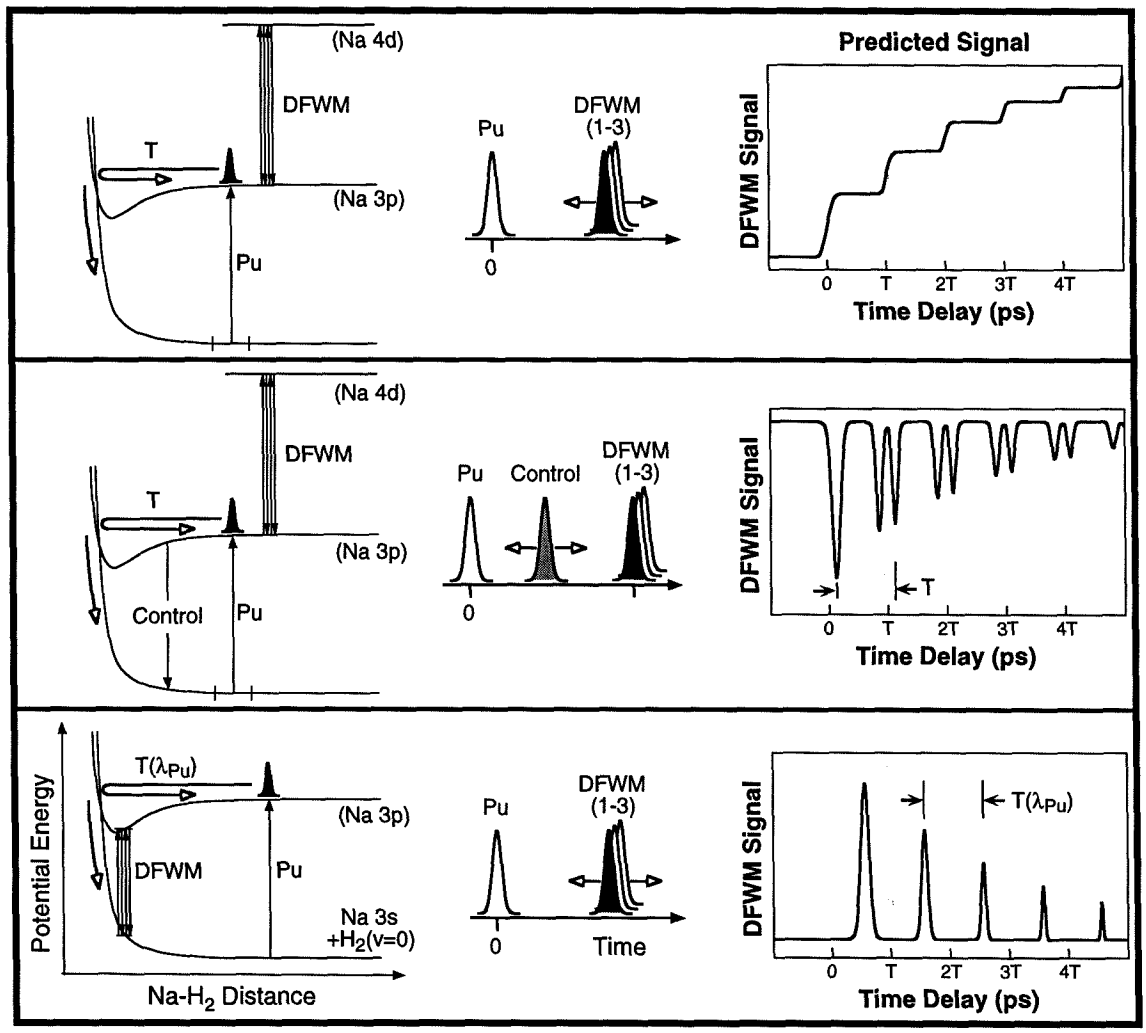
(Na 4d)
DFWM
T
(Na 3p)
Pu
Pu
DFWM
(1-3)
0
Predicted Signal
DFWM Signal
0
T
2T
3T
4T
Time Delay (ps)
(Na 4d)
DFWM
T
(Na 3p)
Control
Pu
Pu
Control
DFWM
(1-3)
0
DFWM Signal
T
0
T
2T
3T
4T
Time Delay (ps)
Potential Energy
T(λPu)
(Na 3p)
DFWM
Pu
Na 3s
+H2(v=0)
Na-H2 Distance
Pu
DFWM
(1-3)
0
Time
DFWM Signal
T(λPu)
0
T
2T
3T
4T
Time Delay (ps)

Fig. 6.15

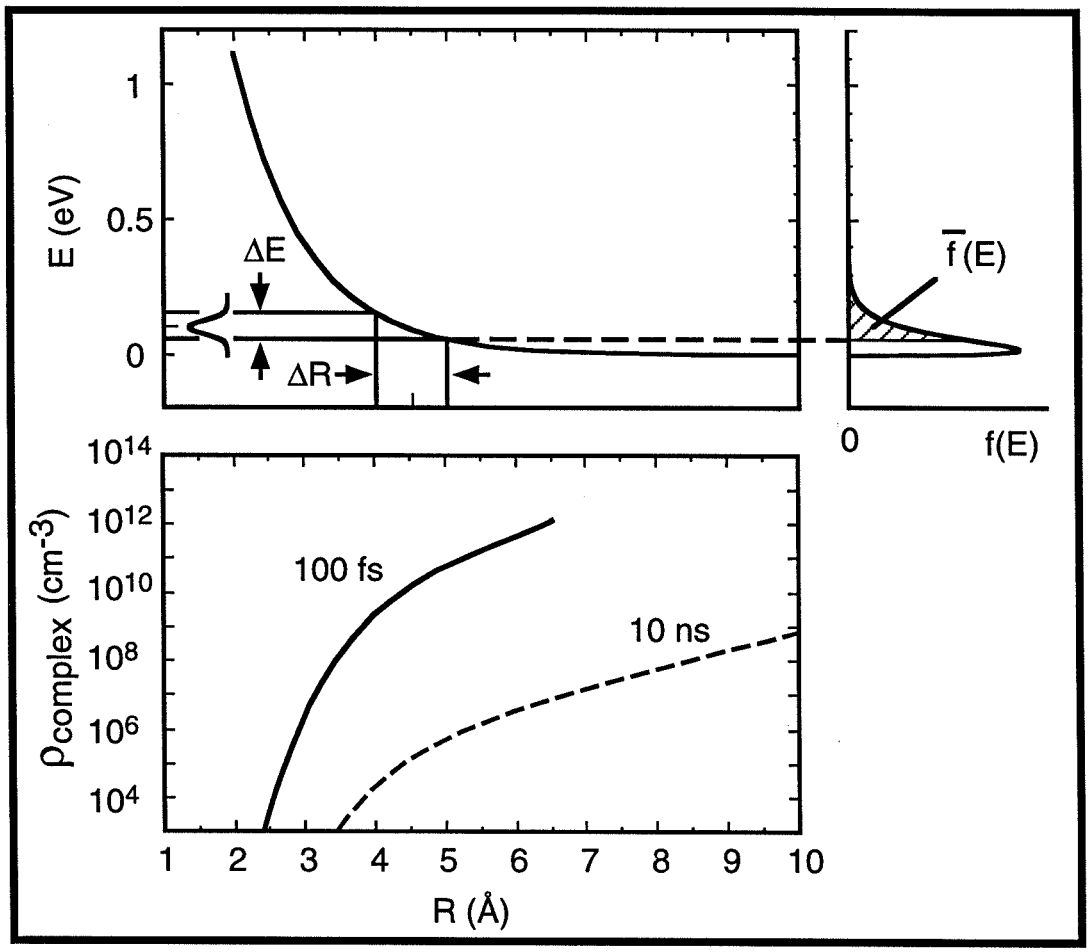
1
0.5
0
E (eV)
ΔE
ΔR
$\overline{f}$(E)
0
f(E)
10^{14}
10^{12}
10^{10}
10^{8}
10^{6}
10^{4}
$\rho_{complex}$ (cm^{-3})
100 fs
10 ns
1 2 3 4 5 6 7 8 9 10
R (Å)

Fig. 6.16

Chapter 7

Appendices

Appendix A

Kinetic Model: General Formulae and Derivations

A.1 General Formulae for Transient Intermediate Measurements

Fig. 3.8 shows the level diagram for the kinetic model relevant to transient intermediate detection. The scheme was introduced in section 3.1.3.3 and the general solution is presented here. At all times when the pump ($t^*=0$) and probe ($t^*=t$) are not present, the system evolves with the rates k_1, k_2, f_B and f_C:

$$dn_B/dt^* = -(k_1+f_B)n_B\,; \tag{A.1a}$$

$$dn_C/dt^* = k_1n_B - (k_2+f_C)n_C; \tag{A.1b}$$

$$dn_D/dt^* = k_2n_C\,; \tag{A.1c}$$

$$dn_G/dt^* = f_Bn_B\,; \tag{A.1d}$$

$$dn_H/dt^* = f_Cn_C\,. \tag{A.1e}$$

Before the pump arrives ($t^*<0$) state $|A\rangle$ with N molecules is the only populated state. The pump excites $F_{Pu}N$ molecules to $|B\rangle$ at $t^*=0$. The system then evolves according to equations (A.1) until the probe arrives at $t^*=t$. The probe excites $\beta F_{Pr}n_B(t^*=t)$ molecules from $|B\rangle$ to $|E\rangle$, and $(1-\beta)F_{Pr}n_C(t^*=t)$ from $|C\rangle$ to $|F\rangle$, where $F_{Pr}=\sigma_O E_{Pr}\lambda_{Pr}/(hc\pi R^2)$. For $t^*>t$, the system again evolves according to (A.1), but now with initial conditions being the populations, $n_i(t^*=t^+)$, just after the probe has transferred molecules from $|B\rangle$ to $|E\rangle$ and from $|C\rangle$ to $|F\rangle$. As explained in section 3.1.3.3, the evolution for $t^*>t$ does not influence the populations of states $|E\rangle$ and $|F\rangle$. The molecular response functions for the detected levels ($|E\rangle$, $|F\rangle$, $|G\rangle$, $|H\rangle$ and $|D\rangle$) are the final ($t^*\rightarrow\infty$) populations, each a function of the pump-probe time delay, t. The limit $t^*\rightarrow\infty$ must therefore be imposed on the solutions to the differential equations and when this is done the following molecular response functions are obtained:

$$M_E(t) = 0\,, \qquad t<0, \tag{A.2a}$$

$$= F_{Pu}F_{Pr}N\beta\exp[-(k_1+f_B)t]\,, \qquad t\geq 0; \tag{A.2b}$$

$$M_F(t) = 0, \qquad t<0, \qquad \text{(A.3a)}$$

$$= F_{Pu}F_{Pr}N(1-\beta)\frac{k_1}{k_1+f_B-(k_2+f_C)}\left(\exp[-(k_2+f_C)t]-\exp[-(k_1+f_B)t]\right), \qquad t\geq 0; \qquad \text{(A.3b)}$$

$$M_G(t) = F_{Pu}N\frac{f_B}{k_1+f_B}\begin{cases}1, & t<0, \quad \text{(A.4a)}\\ 1-F_{Pr}\beta\exp[-(k_1+f_B)t], & t\geq 0; \quad \text{(A.4b)}\end{cases}$$

$$M_H(t) = F_{Pu}N\frac{k_1}{k_1+f_B}\frac{f_C}{k_2+f_C}\left\{\begin{array}{ll}1, & t<0, \quad \text{(A.5a)}\\ 1-F_{Pr}\Big[\beta\exp[-(k_1+f_B)t] & \\ +(1-b)\dfrac{k_1+f_B}{k_1+f_B-(k_2+f_C)}\left(\exp[-(k_2+f_C)t]-\exp[-(k_1+f_B)t]\right)\Big], & t\geq 0; \quad \text{(A.5b)}\end{array}\right.$$

$$M_D(t) = F_{Pu}N\frac{k_1}{k_1+f_B}\frac{k_2}{k_2+f_C}\left\{\begin{array}{ll}1, & t<0, \quad \text{(A.6a)}\\ 1-F_{Pr}\Big[\beta\exp[-(k_1+f_B)t] & \\ +(1-b)\dfrac{k_1+f_B}{k_1+f_B-(k_2+f_C)}\left(\exp[-(k_2+f_C)t]-\exp[-(k_1+f_B)t]\right)\Big], & t\geq 0; \quad \text{(A.6b)}\end{array}\right.$$

Population M_E is seen to follow a single exponential decay with rate k_1+f_B as would be expected from section 3.1.3.1(a). M_F is a bi-exponential, building up with the faster of the two rates (k_1+f_B) and (k_2+f_C) and decaying with the slower. The first minus sign appearing in each of the expressions for M_G, M_H and M_D indicates that depletion is occurring as a result of probing. The depletion of $|G\rangle$, a depletion which shows a decay with rate k_1+f_B, is analogous to the fluorescence depletion discussed in section 3.1.3.1(c). M_D is obtained from M_H by an interchange of k_2 and f_C in the expression for M_H.

Suppose that $|E\rangle$ and $|F\rangle$ can not be detected separately, but rather their sum is what is experimentally observed:

$$M_{ions}(t) = M_E(t) + M_F(t), \qquad \text{(A.7)}$$

$$M_{ions}(t) = 0\,, \qquad t<0, \quad \text{(A.8a)}$$

$$= F_{Pu}F_{Pr}N\left[\beta\exp[-(k_1+f_B)t] + (1-\beta)\frac{k_1}{k_1+f_B-(k_2+f_C)}\left(\exp[-(k_2+f_C)t]-\exp[-(k_1+f_B)t]\right)\right], \quad t\geq 0. \quad \text{(A.8b)}$$

This expression is quite similar to that for M_H (and M_D). One noticeable difference is in the term containing (1-β): in M_{ions} there is a k_1 whereas in M_H there is a k_1+f_B. If we consider the case where $f_B<<k_1$, as would be the case, for example, if f_B were on a nanosecond time scale and k_1 were in the picosecond or femtosecond regime, we obtain:

$$M_H(t) =$$

$$F_{Pu}N\frac{f_C}{k_2+f_C}\begin{cases}1, & t<0, \quad \text{(A.9a)}\\ 1-F_{Pr}\left[\beta\exp[-k_1t]+(1-\beta)\frac{k_1}{k_1-k_2-f_C}\left(\exp[-(k_2+f_C)t]-\exp[-k_1t]\right)\right], & t\geq 0; \quad \text{(A.9b)}\end{cases}$$

$$M_{ions}(t) = 0\,, \qquad t<0, \quad \text{(A.10a)}$$

$$= F_{Pu}F_{Pr}N\left[\beta\exp[-k_1t]+(1-\beta)\frac{k_1}{k_1-k_2-f_C}\left(\exp[-(k_2+f_C)t]-\exp[-k_1t]\right)\right], \quad t\geq 0. \quad \text{(A.10b)}$$

The temporal behavior of the fluorescence depletion signal and the ion signal are now seen to be identical, the signals differing only in their overall magnitude: the depletion signal is smaller by the factor $f_C/(k_2+f_C)$.

In analogy with the explanations in section 3.1.3.1(d), the signal obtained in an absorption measurement as a function of the pump-probe delay time will be proportional to M_{ions} as given by (A.8) above, or (A.10) when the restriction $f_B<<k$ applies.

A.2 Transient Intermediate Measurements with Rates Faster than Fluorescence

Fig. 3.8 shows the kinetic model considered for transient intermediate measurements, and the discussion here is restricted to the region where $f_B << k_1$, and $f_C << k_2$. In this region, the signal considered, M(t), is that given by equation (3.38). First, the special case $k_1 = k_2$ is discussed and in the second section a methodical analysis is carried out to describe the shape of the signal for all possible values of the rates, k_1 and k_2, and the probing parameter, β.

Case $k_1 = k_2$

Here the case is considered where the rate, k_1, at which the intermediate state, $|C\rangle$, is populated from $|B\rangle$ equals the rate, k_2, at which the intermediate decays. When $k_1 = k_2$, the resulting signal can be found by applying the limit $k_2 \rightarrow k_1$ to equation (3.38) and using L'Hôpital's rule, yielding:

$$M(t) = [\beta + (1-\beta)k_1 t] \exp[-k_1 t]. \qquad (A.2.1)$$

If $0 \leq \beta < 0.5$ this signal will increase, from a value of β at t=0, to a maximum value of $(1-\beta)\exp[-(1-2\beta)/(1-\beta)]$ at $t = k_1^{-1}(1-2\beta)/(1-\beta)$, before decreasing towards an asymptotic value of 0 at long times. To the eye, the overall shape resembles that of a bi-exponential with a rise and a decay, and with an initial value (β) at time zero. If, however, $0.5 \leq \beta \leq 1$ then M(t) is a monotonically decreasing function, starting off at a value of β at time zero and approaching the asymptotic value of 0 at long time. The shape resembles that of a single exponential decay.

A.2.1 General Description of the Molecular Response Function

Having presented these special cases we will now proceed to understand, in detail, the shape of the signal, M(t), given by (3.38). This signal can be understood by considering a and b, and whether each of these is positive, negative or zero. The three different cases for b are considered, with subcases for a, if the restriction on b does not already fix the value of a.

Case (i) $b=0$

This occurs if $\beta=1$ or if $k_1=0$. If $\beta=1$ then $a=\beta=1$ and $M(t)=\exp[-k_1 t]$, a single exponential decay with rate k_1. If $k_1=0$ then $a=\beta$ and $M(t)=\beta$, *i.e.*, a constant signal as there is no decay of state $|B\rangle$. In cases (ii) and (iii) below, $0\leq\beta<1$ and $k_1>0$ because if $\beta=1$ or if $k_1=0$, then $b=0$, which is case (i).

Case (ii) $b>0$

From (3.38c), the condition $b>0$ is equivalent to $k_2<k_1$ as $\beta\neq1$, and so

$$0 \leq k_2/k_1 <1. \qquad \text{(A.2.2)}$$

Subcase (ii.1) $b>0, a>0$

With both a and b positive, the molecular response function, (3.38a), is a bi-exponential with both rates k_1 and k_2 in the decay, as shown in Fig. A.2.1. The condition $a>0$ is equivalent to

$$\beta > (2-k_2/k_1)^{-1}. \qquad \text{(A.2.3)}$$

Combining (A.2.2) and (A.2.3) yields:

$$0.5 \leq (2-k_2/k_1)^{-1} < \beta < 1. \qquad \text{(A.2.4)}$$

Therefore, the signal, M(t), will have both rates in its decay (and none in the rise), as shown in Fig. A.2.1, if and only if k_2 is slower than k_1 (c.f. (A.2.2)) and β satisfies (A.2.4).

The two rates are indicated in Fig. A.2.1 as being distinguishable. This is the case if k_2 is not close to k_1, and of course in the limit $k_2 >> k_1$, the two rates are easily distinguished, as shown in Fig. 3.10(a), as they are essentially on different time scales. If k_2 ($>k_1$) approaches k_1, then the shape of the transient may at first sight not seem to be a bi-exponential, even though both rates are in the decay. In the limit $k_2 \rightarrow k_1$ (discussed at the start of this appendix) and with $0.5<\beta<1$, the transient resembles a single exponential decay (although it is not).

If β is very close to 0.5 (low amplitude for k_1 component) or to 1 (low amplitude for k_2 component), then it may also be difficult experimentally to see that the transient is truly a bi-exponential.

Subcase (ii.2) $b>0, a<0$

With b positive, k_2 must be in the decay. With a being negative, k_1 contributes with a term that increases with time. Using (3.38b), the condition $a<0$ is equivalent to $\beta=0$ or $0<\beta<(2-k_2/k_1)^{-1}$. Combining these with (A.2.2) yields

$$0 \le \beta < (2-k_2/k_1)^{-1} < 1. \qquad \text{(A.2.5)}$$

As discussed in section 3.1.3.3, the signal exhibits a maximum at a time given by (3.42), if $0 \le \beta < 0.5$, but if $0.5<\beta<1$, the signal has no maximum and is a monotonically decreasing function with time. Fig. A.2.2 (a) and (b) shows these two cases.

Subcase (ii.3) $b>0, a=0$

In this case (3.38) implies that the signal reduces to $M(t)=b \exp[-k_2 t]$. The condition that a vanishes implies

$$\beta = (1-\beta)k_1/(k_1-k_2), \qquad (A.2.6)$$

and hence $b=\beta$, leading to $M(t)=\beta \exp[-k_2 t]$, as shown in Fig. A.2.3. The condition $b>0$ and equation (A.2.6) prevent β from being 0 or 1. Therefore, $k_1>0$, and (A.2.6) may be rearranged to give $\beta=(2-k_2/k_1)^{-1}$. Combining this with (A.2.2) yields

$$0.5 \le \beta = (2-k_2/k_1)^{-1} < 1. \qquad (A.2.7)$$

The molecular response function will consequently exhibit a pure exponential decay with k_2, as shown in Fig. A.2.3, if and only if conditions (A.2.2) and (A.2.7) are met, *i.e.*, k_2 is slower than k_1 and β happens to be exactly $(2-k_2/k_1)^{-1}$. In section 3.1.3.3, the limit $k_1>>k_2$ was considered. In this regime, β approaches 0.5 and Fig. A.2.3 becomes Fig. 3.10(b).

Case (ii) $b<0$

From (3.38c) this case leads to $0\le\beta<1$ and $k_2>k_1>0$ or

$$0 < k_1/k_2 < 1. \qquad (A.2.8)$$

The case $\beta=0$ was illustrated in section 3.1.3.3, and in the subcases it is then relevant to consider the following range for the probing parameter:

$$0 < \beta < 1. \qquad (A.2.9)$$

Subcase (ii.1) $b<0, a>0$

For positive a, k_1 must be in the decay. With b being negative, k_2 contributes with a term that increases with time. How this affects the shape of the transient depends on β as described below. Since $k_1-k_2<0$, the condition $a>0$ is seen from (3.38b) to be equivalent to

$$1/\beta > 2-k_2/k_1. \qquad (A.2.10)$$

If $k_1<k_2<2k_1$ then this equation leads to $\beta<1<(2-k_2/k_1)^{-1}$. If $2k_1\le k_2$ then equation (A.2.10) leads to $1/\beta>0$ which implies $\beta>0$. If $2k_1=k_2$ then $a=1$ and $b=-(1-\beta)$, and

so the condition $b<0$ prevents β from being 1. Therefore, the values of k_1 and k_2 do not introduce any restriction on β beyond (A.2.9).

The condition for the existence of a maximum was covered in section 3.1.3.3 and, with the range of β restricted by (A.2.9), this condition takes the following form: if $0.5<\beta<1$ there is no maximum, but if $0<\beta\leq 0.5$ there exists a maximum at a time delay given by equation (3.42). The shape of the transient is as indicated in Fig. A.2.4, (a) and (b).

Subcase (ii.2) $b<0, a<0$

This condition is impossible as $a=\beta-b$ and β is non-negative. Physically, M(t), given by (3.38), represents population(s) and can not be negative.

Subcase (ii.3) $b<0, a=0$

Again, this condition is not physically possible for the same reason as was given in the subcase above.

A.2.2 Figure Captions and Figures

Fig. A.2.1 Molecular response function, M(t), for the transient intermediate measurements in which two conditions hold: (i) the rate of decay of the intermediate, k_2, is slower than the rate, k_1, at which it is populated, and (ii) the probing parameter lies in the range $0.5 \leq (2-k_2/k_1)^{-1} < \beta < 1$.

Fig. A.2.2 Signal, M(t), for transient intermediate measurements in which k_2 is slower than k_1 and the probing parameter, β, lies in the range $0 \leq \beta < (2-k_2/k_1)^{-1} < 1$. (a) The case where $0.5 \leq \beta$. The signal is a monotonically decreasing function with time delay, t. The rate k_1 makes the early part of the transient decay less slowly than at long time, where the decay approaches a single exponential with k_2 since $k_2 < k_1$. (b) The case $0 \leq \beta < 0.5$, showing the existence of a maximum reached at a delay time, t_{max}, which is of order $1/k_1$. The rate k_2 is in the decay.

Fig. A.2.3 Signal for transient intermediate measurements in which the probing parameter, β, is such that the signal is a pure single exponential decay with rate k_2. This unique case occurs if β happens to equal $(2-k_2/k_1)^{-1}$, and at the same time $k_2 < k_1$ must be satisfied. For example, if k_2 were close to k_1, this would occur if β were close to 0.5.

Fig. A.2.4 Molecular response function, M(t), for transient intermediate measurements in which the rate of decay of the intermediate, k_2, is faster than the rate at which it is populated, k_1, *i.e.*, $k_2 > k_1$. (a) For $0.5 \leq \beta < 1$, the signal decreases monotonically with the pump-probe delay, t. At long time the decay is mainly with k_1. At early time, $O(1/k_2)$, the decay is not as fast due to the contribution of the term with k_2 in M(t). (b) For $0 \leq \beta < 0.5$, the signal rises to a maximum located

at a delay, t_{max}, that is of order $1/k_2$. At longer time the signal decays and does so mainly with k_1.

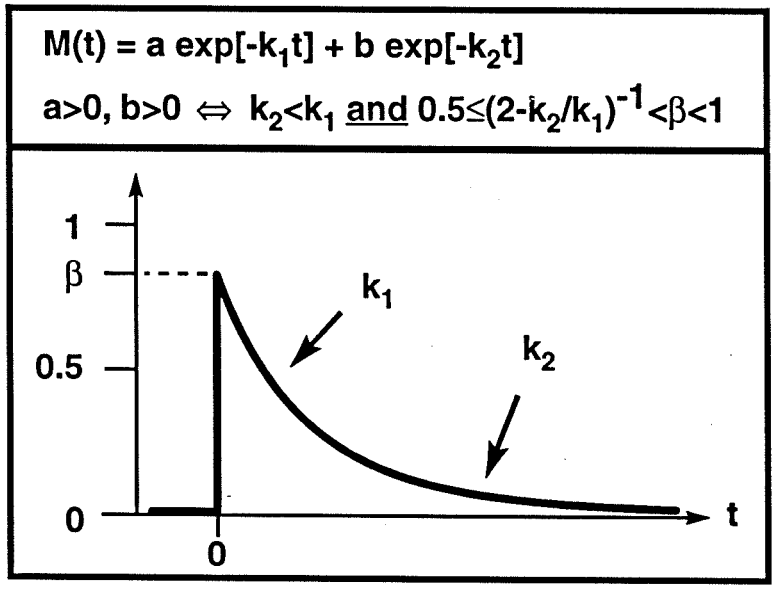

Fig. A.2.1

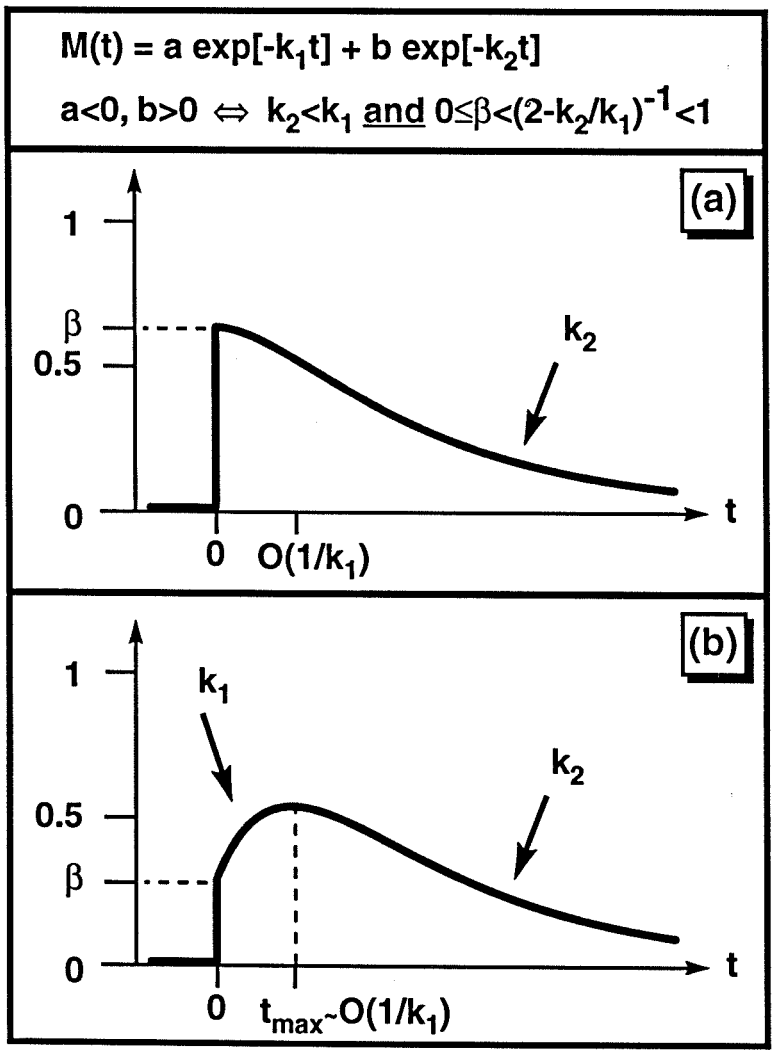
M(t) = a exp[-k1t] + b exp[-k2t]
a<0, b>0 ⇔ k2<k1 and 0≤β<(2-k2/k1)^-1<1
(a)
1
β
0.5
0
k2
t
0
O(1/k1)
(b)
1
k1
k2
0.5
β
0
t
0
tmax~O(1/k1)

Fig. A.2.2

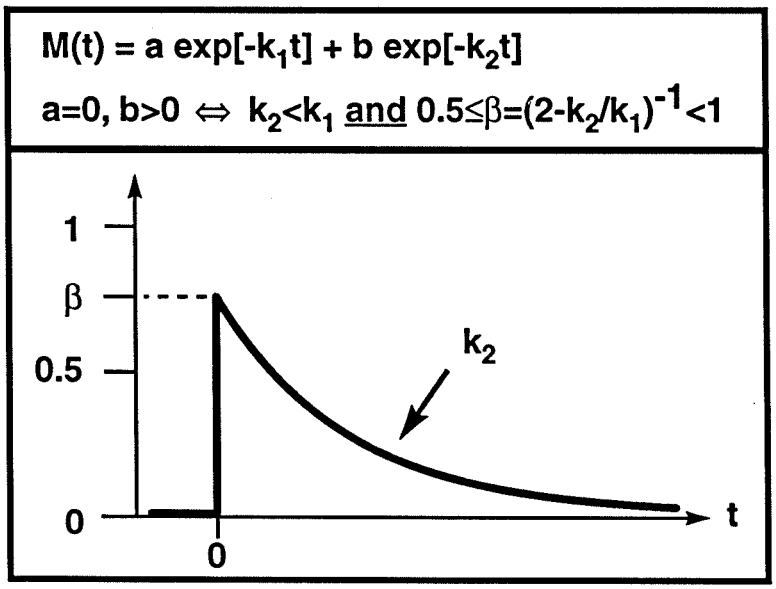

Fig. A.2.3

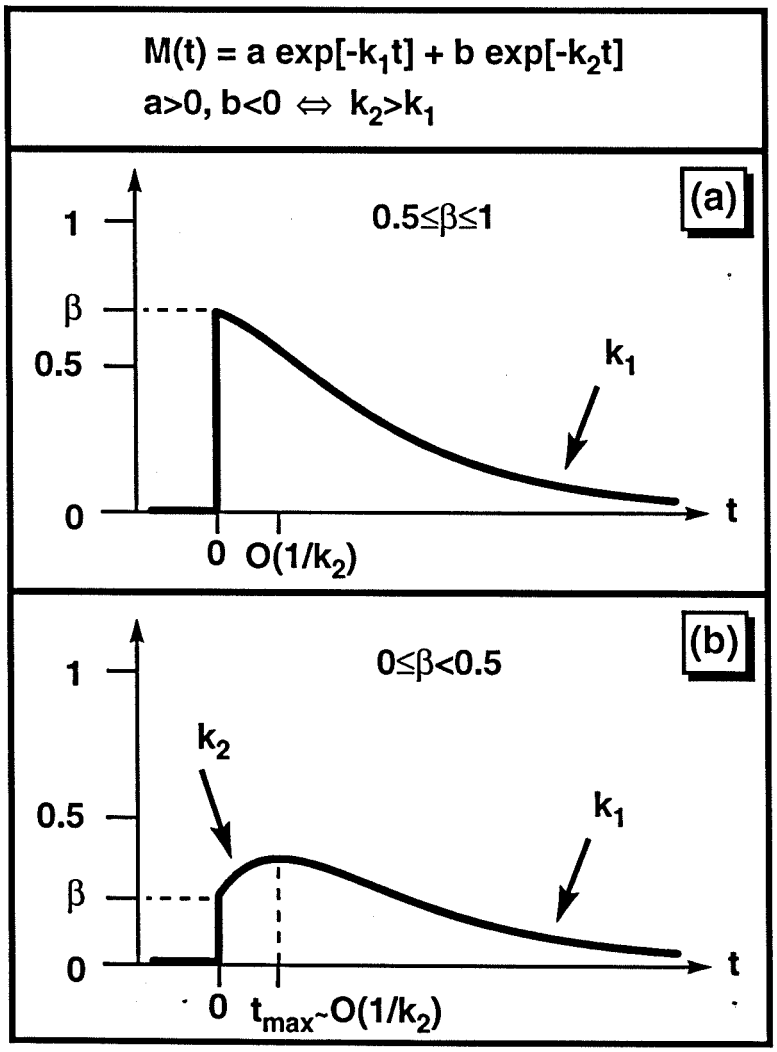
M(t) = a exp[-k1t] + b exp[-k2t]
a>0, b<0 ⇔ k2>k1
(a)
0.5≤β≤1
1
β
0.5
0
k1
t
0
O(1/k2)
(b)
0≤β<0.5
1
k2
0.5
k1
β
0
t
0
tmax~O(1/k2)

Fig. A.2.4

Appendix B

Femtosecond Vibrational Transition-State Dynamics in a Chemical Reaction

Femtosecond vibrational transition-state dynamics in a chemical reaction

S. Pedersen, L. Bañares,[a] and A. H. Zewail
Arthur Amos Noyes Laboratory of Chemical Physics,[b] California Institute of Technology, Pasadena, California 91125

(Received 27 August 1992; accepted 30 September 1992)

When excited directly, complexes in transition states undergo nuclear motions characteristic of bound, quasibound, or unbound dynamics. In elementary reactions, the motions are on the femtosecond time scale and depend on the dimensionality of the potential.[1] For example, in the reaction $ABA^{*\dagger} \rightarrow A+BA$, there are two relevant coordinates that describe the motion of the triatomic transition state species, $ABA^{*\dagger}$: the symmetric and antisymmetric stretch modes, in addition to the bend. Near the saddle point, the motion is bound in the symmetric stretch and unbound in the antisymmetric stretch (reaction coordinate), and the complex could exhibit vibrational motion in the symmetric coordinate, perpendicular to the reaction coordinate. This quantized and bound motion is expected to remain at infinity (i.e., final products) with well defined coherence, as observed experimentally[1] and studied theoretically.[1,2]

The behavior perpendicular to the reaction coordinate is different from the Feshbach-type resonance along the reaction coordinate. For this type of resonance, popular in reactive scattering (cross section vs energy), the motion is quasibound along the reaction coordinate and the complex is trapped (finite lifetime), but has no bound motion at infinity.[3] Transition state (TS) vibrational dynamics, which are important to the understanding of the nature of the potential in the TS region,[4-7] are particularly relevant to studies which directly or indirectly probe the TS. These include emission[4] and Raman scattering during dissociation,[5] temporal dynamics,[1] photodetachment spectra,[6] peaks in the continuum spectra of dissociation reactions, [8] and structure (steps) in the rate constants vs energy.[9]

For systems with a large number of degrees of freedom (N), the situation is more complex. First, the one coordinate, perpendicular to the reaction coordinate, is now replaced by the N-1 of TS theory.[10] Despite the large N, quantum localization may occur on a dynamic potential.[11] Second, the wave packet motion may suffer fast spreading as its structure is now made of a large number of modes. The isomerization of diphenylethylene (stilbene) is an example of such a complex reaction with 72 modes; the reaction coordinate is described by a single motion about the double bond (torsional angle θ).[12] The molecule at the *cis* configuration is unbound (or quasibound) in the θ coordinate, but, in principle, is bound along all the other coordinates: a saddle point TS in its strict definition.

In this communication, we report the observation of the femtosecond dynamics of the TS in the isomerization reaction of *cis*-stilbene under collisionless conditions. An isolated coherent motion that lasts for several hundred femtoseconds and depends on the total excess vibrational energy has been observed. Such motion correlates with the topology of the potential energy surface (PES) and represents a nonstatistical behavior. The experimental results are compared with calculations on a model PES for the reaction.

As shown in Fig. 1, the wave packet is initially prepared by a UV femtosecond laser pulse. The temporal evolution of the wave packet is then probed by resonance MPI in a pump–probe scheme.[13] As in *trans*-stilbene, the ionization efficiency[14] of *cis*-stilbene is high due to the existence of resonant intermediate states, studied theoretically[15] and experimentally.[16] The PES in Fig. 1 illustrates the methodology.

The experimental apparatus has been described in detail elsewhere.[17] Here, the two beams (pump and probe pulses, ~80 fs) were collinearly recombined and focused into the ionization chamber, evacuated to $\sim 10^{-5}$ Torr. The *cis*-stilbene used in these experiments was of very high purity (99.98%), courtesy of the Saltiel group who have used it in careful studies in solutions.[18]

Figure 2(b) shows the measured transient for $\lambda_{\text{pump}} = 306$ nm, $\lambda_{\text{probe}} = 2 \times 612$ nm. The decay curve is nonexponential and shows a peak at a time delay of ~0.5 ps. The transient has an exponential decay (lifetime) and the oscillatory pattern in Fig. 2(a) [see Eq. (1)]. The single-exponential fit was obtained using a nonlinear least-squares method where the finite and measured response function was included. We have used the following molecular response function to describe the population and coherence decays:[19]

$$M(t) = \exp(-\gamma t) \cdot \{a + b \cos[\omega(t) \cdot t]\}, \qquad (1)$$

where γ is the decay rate and a,b are constants. The time-dependent frequency is $\omega(t) = 2\pi/(T_0 + kt)$, where T_0 is the initial period (Fig. 1) and k gives its change with time. The single-exponential fit of the transient gives $\gamma^{-1} = 307$ fs and $a = 1.37$. For the data in Fig. 2(a), $a = 0$, and we obtained $b = 0.25$, $T_0 = 360$ fs, and $k = 0.42$. The oscillatory behavior was found to be independent of the relative polarization[20] and intensity (linear regime) of the pump and probe pulses.

Greene and Farrow[22] were the first to measure the initial decay of *cis*-stilbene in the gas phase. They reported a single exponential decay with a long lifetime component attributed to some *trans* impurity. As discussed above, the decay is observed to be nonexponential with a peak structure. This behavior is lost when wider pulses are used. In their case, the decay was reported to be 320±20 fs and the

 0021-9606/92/238801-04$006.00

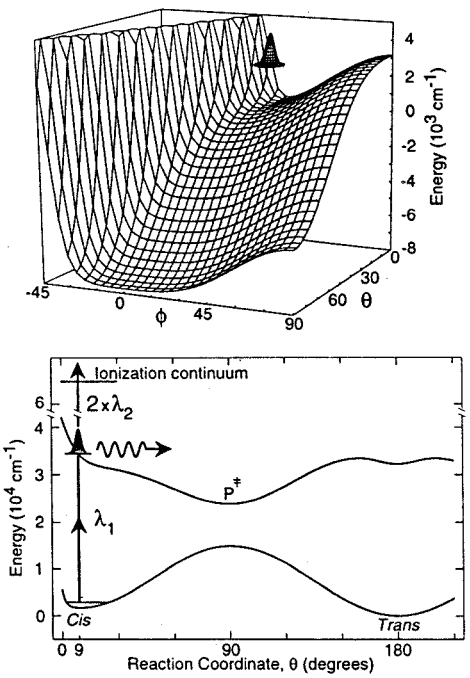

FIG. 1. The potential energy surface describing the isomerization reaction along the θ and ϕ coordinates, maintaining all other degrees of freedom fixed (see text). The cut at the bottom showing the potential energy vs θ represents the twisting about the double bond. $P^{\dagger}$ is the perpendicular state with minimum energy along θ. The initial preparation of the wave packet is by λ_1 and the probing is by $2\times\lambda_2$ (through ionization). Note that the zero of energy is different in the two figures. The initial wave packet is at a nonequilibrium configuration, as determined by λ_1.

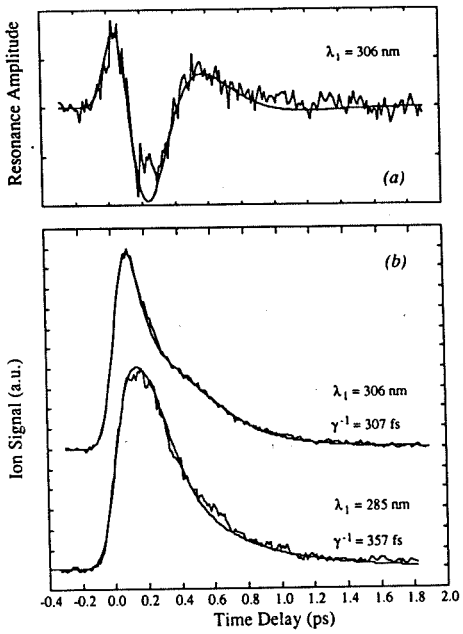

FIG. 2. Femtosecond transients obtained from the $\lambda_1=306$ nm and 285 nm experiments. (a) The vibrational resonance [cosine term of (1)] amplitude for $\lambda_1=306$ nm was obtained from (b) after subtracting the overall decay component of Eq. (1) (see text). The smooth line is the best fit using Eq. (1) (setting $a=0$) with the parameters listed in the text. The same parameters (with $a=1.37$) reproduce the solid line fit in (b). Also shown in (b) is the femtosecond transient obtained from the $\lambda_1=285$ nm experiments. The smooth line is the result of the fit using Eq. (1) and similar methodology to the $\lambda_1=306$ nm data treatment. A single exponential does not fit the data well, particularly at early times.

laser pulse widths were 250 fs. Here, our pulses are shorter by a factor of ~ 3, and the peak is clearly visible. Also, there is no long decay component (*trans* impurity) in our transients. Figure 2(b) shows the same set of data, but now for a higher pump energy; note the shape near the $t=0$ region. The total vibrational energy was changed from ~ 4300 cm^{-1} (at 306 nm) to ~ 6700 cm^{-1} (at 285 nm).[23]

In the isomerization region there are at least three angular coordinates, out of the 72 modes, directly involved: the C_e–C_e torsional angle, θ (reaction coordinate), the C_e–C_e–C_{Ph} in-plane bending angle, α, and the C_e–C_{Ph} torsional angle, ϕ (Fig. 3). Myers and Mathies[28] estimated that the torsional angle θ increases from 9° to 34° during the first 20 fs (*vide infra*).

Petek *et al.*[25,29] have addressed the issue of the dimensionality of the PES. They concluded that the ϕ and α coordinates must be considered not only in the isomerization but also in the photocyclation.[30] We have modified the Frederick *et al.* PES[29] to include a complete θ dependence[33] for the system to reach large θ's, up to $\pi/2$ and π (Fig. 1). To obtain the dynamics we have considered the wave packet centered at the equilibrium configuration ($\theta=9°$, $\phi=26.8°$, $\alpha=124°$) at $t=0$. The time evolution in each coordinate was obtained by solving the equation of motion for $\dot{\theta}(t)$, $\dot{\alpha}(t)$, or $\dot{\phi}(t)$, knowing the total energy and the derived PES.

At the total energy of interest ~ 2600 cm^{-1} (*vide infra*), the wave packet motion in the θ coordinate takes ~ 210 fs to end at $\theta=90°$. Along ϕ, half the vibrational period is ~ 340 fs, comparable to the decay time along θ. According to the results of Fig. 2, the wave packet displays not only a decay but also a significant spreading and a change of the period. This is consistent with the motion being along the θ valley which "opens up" with time; the period changes by *kx* time. The changes in the PES are shown in Fig. 3, together with the representation of the correlated motions at different θ's.

There are several points to be made here. First, the absorption spectrum of *cis*-stilbene is unstructured,[34] and the results reported here indicate that this simply reflects the steep slope of the potential in the Franck–Condon region; there are two time scales involved: one for the initial dephasing and the other for the nuclear dynamics.[1,5,35] Second, the localization of motion is consistent with a Born–

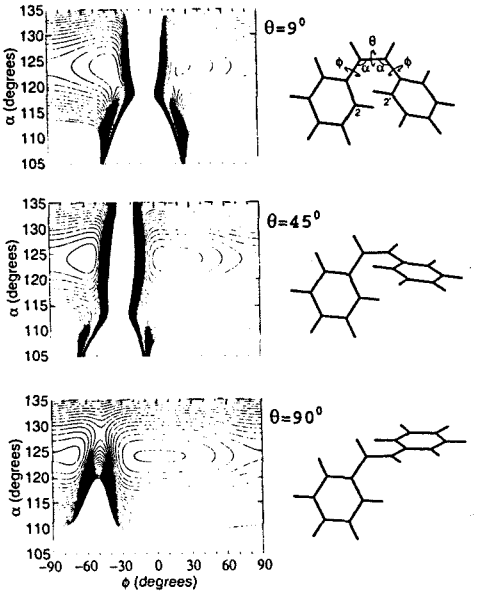

FIG. 3. Calculated PES for the *cis*-stilbene system as outlined in the text. The angles of interest are defined in one of the structures. Notice that at low θ there are two minima in the α–ϕ surface corresponding to *cis*-stilbene and DHP separated by a barrier, of height $\sim 535\ cm^{-1}$, above the *cis* minimum (see Ref. 29). As θ is increased, the DHP configuration becomes more unstable and the stilbene well more stable and wider. At $\theta=90°$, the only stable configuration is twisted stilbene (*phantom* state). We made the θ dependence to include the change in the potential energy given in the text and in Fig. 1. This change in θ is a modification of the PES in Ref. 29. The contour lines in all three plots are separated by 1000 cm^{-1}. The lowest and highest contour lines for the different plots are (a) $\theta=9°$, $-8600\ cm^{-1}$, and $15\,400\ cm^{-1}$, (b) $\theta=45°$, $-1600\ cm^{-1}$, and $22\,400\ cm^{-1}$; and (c) $\theta=90°$, $-7600\ cm^{-1}$, and $16\,400\ cm^{-1}$.

Oppenheimer dynamical separation[11] of vibrational frequencies.

Third, the deduction of the slope of the potential at the Franck–Condon region, obtained from resonance Raman studies,[28] is consistent with the time scale that we have calculated for the θ motion. However, our calculated time is much longer than that deduced using the approximation made in Ref. 28 for relating θ to time.[36] If we consider the θ motion, the time scale depends on how far the system is twisted.[37] For example, from $\theta=9°$ to 20° and back to 9°, the motion takes only ~ 80 fs (energy, $\sim 2600\ cm^{-1}$), much shorter than the resonance period. But if the packet moves on beyond $\theta=20°$, there is a well at the phantom configuration ($\theta=90°$) and IVR to other available modes will produce a very long "return time," back to the $\theta<20°$ region. At $\theta=90°$, if the energy is lowered (by IVR) below that of the *cis* configuration, the wave packet becomes bound. We have assumed that $\sim 60\%$ of the total energy goes to the mode of interest, but if more energy is allocated to other modes, slower dynamics will be observed. The fraction of energy in each mode is not known without further experiments.

As the total energy was increased (285 nm excitation), the results in Fig. 2(b) were observed: the decay gets longer and near the $t=0$ region the transient does not fit a single exponential. At this energy, the motion is above the barrier in the ϕ coordinate (free phenyl rotation), and we expect a significant spreading of the wave packet. Moreover, bath modes may exchange energy with the relevant isomerization modes and this may result in a nonexponential behavior, in analogy with "diffusive" motions. The overall decay of the wave packet is slower than that at lower excess energy, indicating a nonstatistical behavior. In view of the time scales involved, this reaction represents a case where there is not enough time for conventional IVR[38] and it is not clear that TS theory is appropriate for rate constants.

There are further studies to be made and these include: (a) calculation of the dynamics on the multidimensional PES, and including the bath modes;[40] (b) studies at lower internal energy in supersonic beams; and (c) identification of the Franck–Condon modes and their fractional energies. In our full account [41] we plan to complete these studies for this and related reactions.

Note added in proof. We have recently obtained the fs transients in a molecular beam with helium and argon as the expanding gases. The isolated molecules and the cluster dynamics are currently under examination. In a recent paper by the Hochstrasser group [J. Chem. Phys. **97**, 5239 (1992)], they concluded that complete IVR in solution is not observed. Troe's group [J. Chem. Phys. **97**, 4827 (1992)] has shown, from temperature and viscosity dependences, the need of a bottleneck in explaining the dynamics in solutions. The nonstatistical behavior reported here should be relevant to these new studies in solutions.

We wish to thank Professor J. Saltiel for helpful discussions and for providing us with the ultrapure sample. We also wish to acknowledge stimulating discussions with Professor W. Miller, Professor R. Marcus, and Professor D. Neumark. This work was supported by a grant from the US AFOSR and by the NSF.

[a] Fulbright/M.E.C. of Spain Postdoctoral Fellow.

[b] Contribution No. 8712.

[1] For a recent review, see A. H. Zewail, Faraday Discuss. Chem. Soc. **91**, 207 (1991), and references therein.

[2] For a recent study, see J. Manz, B. Reischl, T. Schröder, F. Seyl, and B. Warmuth, Chem. Phys. Lett. (*in press*, 1992).

[3] (a) See the papers in the recent volume Faraday Discuss. Chem. Soc. **91**, (1991); (b) W. H. Miller, Annu. Rev. Phys. Chem. **41**, 245 (1991).

[4] H.-J. Foth, J. C. Polanyi, and H. H. Telle, J. Phys. Chem. **86**, 5027 (1982).

[5] D. Imre, J. L. Kinsey, A. Sinha, and J. Krenos, J. Phys. Chem. **88**, 3956 (1984).

[6] D. M. Neumark, Annu. Rev. Phys. Chem. **43**, (1992). See, also, the author's papers in Ref. 3.

[7] (a) P. R. Brooks, Chem. Rev. **88**, 407 (1988); (b) M. D. Barnes, P. R. Brooks, R. F. Curl, and P. W. Harland, J. Chem. Phys. **94**, 5245 (1991); (c) M. D. Barnes, P. R. Brooks, R. F. Curl, P. W. Harland, and B. R. Johnson, *ibid.* **96**, 3559 (1992).

[8] See, for example, (a) C. Jouvet, M. Boivineau, M. C. Duval, and B. Soep, J. Phys. Chem. **91**, 5416 (1987); W. H. Breckenridge, C. Jouvet, and B. Soep, J. Chem. Phys. **84**, 1443 (1986); (b) P. D. Kleiber, A. M. Lyyra, K. M. Sando, S. P. Heneghan, and W. C. Stwalley, Phys. Rev.

Lett. **54**, 2003 (1985); (c) L. J. Butler, Chem. Phys. Lett. **182**, 393 (1991).

[9] (a) E. R. Lovejoy, S. K. Kim, and C. B. Moore, Science **256**, 1541 (1992); (b) G. A. Brucker, S. I. Ionov, Y. Chen, and C. Wittig, Chem. Phys. Lett. **194**, 301 (1992); (c) L. R. Khundkar, J. L. Knee, and A. H. Zewail, J. Chem. Phys. **87**, 77 (1987).

[10] See (a) R. A. Marcus, Science **256**, 1523 (1992); (b) M. M. Kreevoy and D. G. Truhlar, in *Investigations of Rates and Mechanism of Reactions*, edited by C. F. Bernasconi (Wiley, New York, 1986), Vol. 6, Part 1, p. 13; (c) P. Pechukas, Annu. Rev. Phys. Chem. **32**, 159 (1981); (d) See, also, Ref. 3.

[11] (a) G. Hose, H. S. Taylor, and Y. Y. Bai, J. Chem. Phys. **80**, 4363 (1984); (b) B. Hartke, J. Manz, and J. Mathis, Chem. Phys. **139**, 123 (1989).

[12] For reviews see (a) R. M. Hochstrasser, Pure Appl. Chem. **52**, 2683 (1980); (b) J. Saltiel and Y.-P. Sun. *Photochroism-Molecules and Systems*, edited by H. Durr and H. Bouas-Laurent (Elsevier, Amsterdam, 1990), p. 64.

[13] L. R. Khundkar and A. H. Zewail, Annu. Rev. Phys. Chem. **41**, 15 (1990), and references therein.

[14] (a) J. W. Perry, N. F. Scherer, and A. H. Zewail, Chem. Phys. Lett. **103**, 1 (1983); (b) N. F. Scherer, L. R. Khundkar, T. S. Rose, and A. H. Zewail, J. Phys. Chem. **91**, 6478 (1987).

[15] (a) G. Orlandi, P. Palmieri, and G. Poggi, J. Am. Chem. Soc. **101**, 3492 (1979); (b) G. Olbrich, Ber. Bunsenges. Phys. Chem. **86**, 209 (1982); (c) G. Hohlneicher and B. Dick, J. Photochem. **27**, 215 (1984).

[16] (a) B. I. Greene and T. W. Scott, Chem. Phys. Lett. **106**, 399 (1984); (b) F. E. Doany, R. M. Hochstrasser, B. I. Greene, and R. R. Millard, *ibid.* **118**, 1 (1985); (c) S. H. Courtney, S. K. Kim, S. Canonica, and G. R. Fleming, J. Chem. Soc., Faraday Trans. 2 **82**, 2065 (1986); (d) S. Abrash, S. Repinec, and R. M. Hochstrasser, J. Chem. Phys. **93**, 1041 (1990); (e) J. K. Rice and A. P. Baronavski, J. Phys. Chem. **96**, 3359 (1992).

[17] M. J. Rosker, M. Dantus, and A. H. Zewail, J. Chem. Phys. **89**, 6113 (1988).

[18] J. Saltiel, A. Waller, Y.-P. Sun, and D. F. Sears, Jr., J. Am. Chem. Soc. **112**, 4580 (1990).

[19] A. H. Zewail, M. Dantus, R. M. Bowman, and A. Mokhtari, J. Photochem. Photobiol. A Chem. **62**, 301 (1992), and references therein.

[20] Measurements were made for parallel, perpendicular, and magic angle polarizations and the anisotropy was obtained as described elsewhere (Ref. 21). The oscillation was found to be the same in all polarizations and only the magnitude of the signal was affected.

[21] (a) P. M. Felker and A. H. Zewail, J. Chem. Phys. **86**, 2460 (1987); (b) J. S. Baskin and A. H. Zewail, J. Phys. Chem. **93**, 5701 (1989).

[22] B. I. Greene and R. C. Farrow, J. Chem. Phys. **78**, 3336 (1983).

[23] The excess vibrational energies were calculated knowing the difference in energy between the *trans* and *cis* isomers in the ground (1605 cm^{-1}) (Ref. 24) and excited (set at $\sim 500\ cm^{-1}$) (Ref. 25) state. The thermal energy for *cis*-stilbene was calculated as described in a previous paper (Ref. 26) using the S_0 vibrational frequencies calculated by Warshel (Ref. 27). A thermal energy of $\sim 1740\ cm^{-1}$ was obtained for a temperature of 25 °C.

[24] J. Saltiel, S. Ganapathy, and C. Werking, J. Phys. Chem. **91**, 2755 (1987).

[25] H. Petek, Y. Yoshihara, Y. Fujiwara, Z. Lin, J. H. Penn, and J. H. Frederick, J. Phys. Chem. **94**, 7539 (1990).

[26] J. L. Herek, S. Pedersen, L. Bañares, and A. H. Zewail, J. Chem. Phys. **98** (1992).

[27] A. Warshel, J. Chem. Phys. **62**, 214 (1975).

[28] A. B. Myers and R. M. Mathies, J. Chem. Phys. **81**, 1552 (1984).

[29] J. H. Frederick, Y. Fujiwara, J. H. Penn, K. Yoshihara, and H. Petek, J. Phys. Chem. **95**, 2845 (1991).

[30] Photocyclation to dihydrophenanthrene (DHP) is another open channel for excited *cis*-stilbene. Former investigations in solution (Ref. 31) gave quantum yields of 35% and 10% for *cis*-to-*trans* and *cis*-to-DHP reactions, respectively. However, recently it was suggested that as much as 30% of excited *cis*-stilbene may undergo photocyclation to form excited DHP (Refs. 25 and 29). The dynamics toward DHP have been studied also in solution (Ref. 32) and ground-state DHP was found to be formed in 1.7 ps in hexadecane.

[31] (a) K. A. Muszkat and E. Fischer, J. Chem. Soc. B **662**, (1967); (b) T. Wismonski-Knittel, G. Fischer, and E. Fischer, J. Chem. Soc. Perkin Trans. **1**, 1930 (1974); (c) S. Sharafy and K. A. Muszkat, J. Am. Chem. Soc. **93**, 4119 (1971); (d) K. A. Muszkat, Top. Curr. Chem. **88**, 89 (1980).

[32] S. T. Repinec, R. J. Sension, A. A. Szarka, and R. M. Hochstrasser, J. Phys. Chem. **95**, 10380 (1991).

[33] The θ dependence has been empirically introduced by considering a truncated Fourier series in the torsional angle θ of the form $V_{tor} = V_2 \sin^2\theta + V_4 \sin^2 2\theta$. V_2 determines the height of the barrier to torsion about the double bond and has been taken to be $-7850\ cm^{-1}$, as deduced from the slope of the potential estimated by Myers and Mathies (Ref. 28). V_4, which determines the flatness (shape) of the potential to torsion, was set at $1528\ cm^{-1}$, maintaining the same V_2/V_4 ratio as for the conjugation potential of Ref. 29.

[34] H. Petek, Y. Fujiwara, D. Kim, and K. Yoshihara, J. Am. Chem. Soc. **110**, 6269 (1988), and references therein.

[35] J. A. Beswick and J. Jortner, Chem. Phys. Lett. **168**, 246 (1990).

[36] In Ref. 41 we will discuss these methods of calculation.

[37] The probe pulse can be in resonance on different parts of the PES, either along the reaction coordinate or perpendicular to it. In fact, one may assign the peak in Fig. 2 as a delayed probe along the θ coordinate with an induction period (Refs. 1 and 17). However, the resonance has a well defined phase change (cosine type), and also the time scale is not consistent with the potential characteristics as discussed in the text. As shown in Fig. 1, the probe is close to the the initial motion of the wave packet because of λ_1 promotion. Also, the twisting along θ takes the system away from resonance [Ref. 16(a)] due to large conformational changes in S_1.

[38] At $\theta = 180°$, it is known that the *trans* form has a barrier of 3.3 ± 0.2 kcal/mol to isomerization under collisionless conditions (Ref. 39). We have also studied the femtosecond dynamics of the *trans* configuration to compare with the *cis*. Unlike the *cis*,, IVR is evident and we observe biexponential decay behavior which we shall detail in Ref. 41.

[39] L. Bañares. A. A. Heikal, and A. H. Zewail, J. Phys. Chem. **96**, 4127 (1992), and references therein.

[40] (a) T. Carrington and W. H. Miller, J. Chem. Phys. **84**, 4364 (1986); (b) S. Fischer and M. Karplus, Chem. Phys. Lett. **194**, 252 (1992).

[41] L. Bañares, S. Pedersen, and A. H. Zewail (in preparation).

Appendix C

The Validity of the Diradical Hypothesis:
Direct Femtosecond Studies of the Transition-State Structures

The Validity of the "Diradical" Hypothesis: Direct Femtosecond Studies of the Transition-State Structures

S. Pedersen, J. L. Herek, A. H. Zewail*

Direct studies of diradicals, the molecular species hypothesized to be archetypal of chemical bond transformations in many classes of reactions, have been made using femtosecond laser techniques with mass spectrometry in a molecular beam. These studies are aimed at "freezing" the diradicals in time and in the course of the reaction. The passage of these species through the transition-state region was observed and the effect of total energy and alkyl substitution on the rates of bond closure and cleavage was examined. The results establish the nature of these intermediates and define their existence during reactions.

For the past 60 years, the concept of diradicals as intermediates has been hypothesized to be archetypal of chemical bond transformations in many classes of thermally activated as well as photochemical reactions. Since the development of extended Hückel theory, Woodward-Hoffmann rules, and frontier-orbital descriptions of bonding (*1*), diradicals have become central to the understanding of reaction mechanisms as well as to the predictability of reaction products, rates, and stereochemistry. One of the most well-studied reactions, both theoretically and experimentally, is the ring opening of cyclobutane to yield ethylene or the reverse addition of two ethylene molecules to form cyclobutane:

Scheme 1.

Such a reaction is a classic case study for a Woodward-Hoffmann description of concerted reactions. The reaction may pro-

Arthur Amos Noyes Laboratory of Chemical Physics, California Institute of Technology, Pasadena, CA 91125, USA.

*To whom correspondence should be addressed.

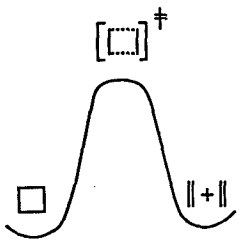

Scheme 2. Transition-state mechanism.

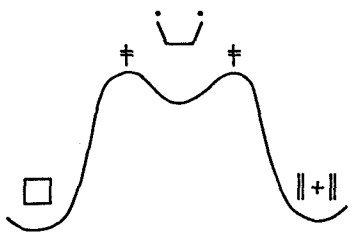

Scheme 3. Diradical mechanism

ceed directly through a transition state at the saddle region of an activation barrier. Alternatively, it could proceed by a two-step mechanism, beginning with the breakage of one σ-bond to produce tetramethylene as a diradical intermediate, which in turn passes through a transition state before yielding final products. These two extreme cases are illustrated in Schemes 2 and 3 with a potential-energy curve along the reaction coordinate.

The concept, therefore, besides being important to the definition of diradicals as stable species, is crucial to the fundamental nature of the reaction dynamics: a concerted one-step process versus a two-step process with an intermediate. Such intermediates are expected to exist in a potential well at internuclear configurations between reactants and products. Accordingly, they are expected to be longer lived than transition states, such that the dynamics of their nuclear motions (vibration and rotation), unlike a concerted motion (translation), determine the outcome of the reaction; that is, product channels, product-energy distributions, and stereochemistry.

Experimental and theoretical studies have long focused on the possible existence of diradicals and on the role they play in affecting the processes of cleavage, closure, and rotation. A large number of studies have been reviewed in books and articles [see, for example, (2–5)], and we mention only the general approaches used. The experimental approach is based primarily on studies of the stereochemistry of reactants and products, chemical kinetics, and the effect of different precursors on the generation of diradicals. The time "clock" for rates is internal, inferred from the rotation of a single bond, and is used to account for any retention of stereochemistry from reactants to products. Berson, Bergman, Dervan, Baldwin, and others (see below) have shown the value of this approach in studies of reaction mechanisms. Theoretical approaches basically fall into two categories, those involving thermodynamical analysis of the energetics (enthalpic criterion) and those concerned with semiempirical or ab initio quantum calculations of the potential energy surface (PES) describing the motion of the nuclei in the reaction [see (6, 7)].

Hoffmann and co-workers (8), using extended Hückel theory, have provided a PES for reaction 1 and concluded the absence of the tetramethylene diradical as a stable intermediate; they suggested that the top of the potential along the reaction coordinate is "flat," favoring Scheme 2. This flatness was important to allow the nuclei to spend some time in the region, thereby explaining the lack of stereochemical retention. Such a region, termed "twixtyl," was suggested as a possible common feature of nonconcerted reactions. Benson (9), on the other hand, estimated the enthalpy of tetramethylene to lie at least 4 kcal/mol below the experimental activation energy (62.5 kcal/mol), favoring Scheme 3. This last finding was supported by ab initio calculations by Segal (10), but more recent studies by Doubleday, Bernardi *et al.*, Borden *et al.*, and others have found shallow minima that survive or disappear, depending on the correction for the zero-point energy (11). In contrast, for the analogous reaction of cyclopropane, Benson's calculation (9), which assumed no cooperative effects, indicated that the trimethylene 1,3-diradical is also thermodynamically stable, whereas the ab initio calculations by Salem, Borden, Davidson, Schaefer, Doubleday, and others showed no significant stability (5, 12, 13). Recent considerations (7) of the heats of formation of relevant species have addressed some of these discrepancies. An ab initio calculation must account for the large dimensionality of the PES (see below), as the intermediate has 30 vibrational degrees of freedom. Doubleday's recent theoretical work on tetramethylene (11) suggests a definite intermediate with a free energy barrier on the minimum energy reaction path.

Experimental studies of the mechanisms involving 1,3- and 1,4-diradicals are similarly numerous and cannot be fully detailed here. Since the seminal work by Rabinovitch, Schlag, and Wiberg in 1958 (14), which suggested the involvement of a diradical in the isomerization of cyclopropane, many groups have examined the

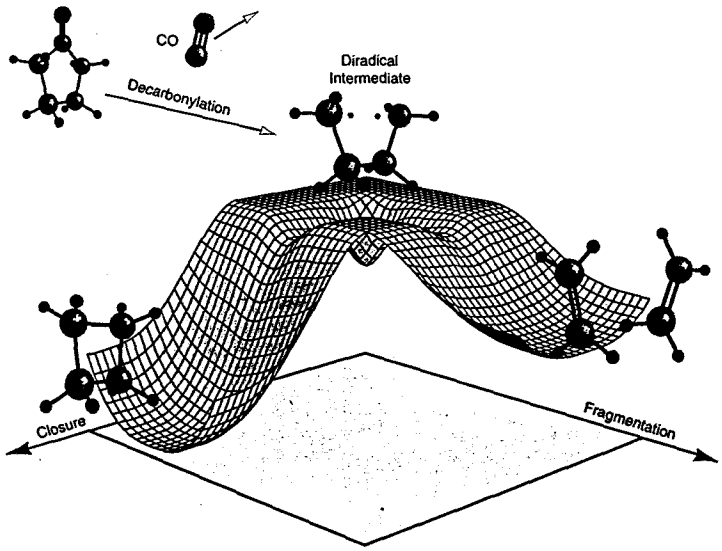

Fig. 1. The diradical reaction on a schematic potential energy surface. Extrusion of the carbon monoxide group from the parent molecule creates the diradical (tetramethylene) intermediate with a well-defined energy. Shown are the two channels for product formation, closure to cyclobutane or fragmentation to two ethylene molecules.

mechanistic routes of relevant systems, from different precursors for photochemical reactions or thermal processes similar to Scheme 1. To formulate the presence (or absence) of such diradicals, stereochemical and kinetics studies were advanced by several groups [see (2–5)]. For tetramethylene, measurements of the relative rates of rotation, cleavage, and closure by Dervan and co-workers (*15*) provided evidence for the 1,4-diradical as a common intermediate formed by different precursors. Earlier, Brauman and Stephenson (*16*) suggested that the method of generation of diradicals may be the key to their difference in behavior. For trimethylene (*2, 3, 7, 17*), the experiments suggested that the 1,3-diradical is not stable but some of its derivatives are.

The key to the above issues is the time scale for the passage of the nuclei through the transition-state region. It was suggested that an intermediate may have a lifetime on the order of a nanosecond whereas an activated complex should exist for no more than a picosecond (*18*). This disparity is not cardinal as it depends, of course, on the total internal energy and on the nature of the force governing the transformation. It appears, therefore, that real-time studies of these reactions should allow one to examine the nature of the transformation and to elucidate the fundamentals of the dynamics and the concept of diradicals.

We report direct studies of the femtosecond dynamics which are aimed at "freezing" the diradicals in time and in the course of the reaction. We use precursors (cyclopentanone, cyclobutanone, and their derivatives) to generate the diradicals and to monitor the formation and the decay dynamics of the reaction intermediate or intermediates. We identify the parent or the intermediate species using time-of-flight (TOF) mass spectrometry. The concept behind the experiment is illustrated in Fig. 1 with the PES, and a schematic of the apparatus is presented in Fig. 2. To avoid collisional deactivation and other perturbations, the reaction is carried out in a skimmed molecular beam.

In the molecular beam apparatus, which is equipped with the TOF mass spectrometer, an initial femtosecond pulse decarbonylates the precursor and establishes the zero of time. The second femtosecond pulse, delayed in time, probes the dynamics of a given mass species by ionization. We could either select a specific mass and study the femtosecond temporal evolution corresponding to this species, or, for a given femtosecond delay, monitor the entire mass distribution of the reaction. As with other femtochemical studies (*19*), the zero of time can be established in situ when the ion signal is recorded while the two pulses overlap in time. Accordingly, the femtosecond delay of the appearance of a given intermediate fragment can be accurately determined and its decay can be followed at longer times. By changing the pump energy, we have examined the energy dependence of the dynamics. Also, we have studied polarization and power dependencies, and, for the effect of initial geometry, substitution influence on the rates.

The experimental apparatus has been described in detail elsewhere (*19*). Briefly, a colliding pulse mode-locked ring dye laser generated the femtosecond pulses around 620 nm. These pulses were amplified by a Nd:YAG (neodymium:yttrium-aluminum-garnet)–pumped four-stage dye amplifier. The output pulses were temporally recompressed to 60 fs in a sequence of four high refractive-index glass prisms. The 310-nm initiation ("pump") pulse was generated by frequency doubling a part of the output in a 0.5-mm KD*P (potassium dihydrogen phosphate) crystal. For the 620-nm probe, we used the remaining part of the output. Pump tuning experiments (334 to 280 nm) were performed by selecting a part from a white-light continuum followed by further amplification and frequency doubling. The pump and probe beams were delayed in time relative to one another in a Michelson interferometer and were then recombined collinearly and focused onto the molecular beam. The output of the TOF mass spectrometer was monitored while scanning the interferometer, which was driven in steps by a computer-controlled actuator.

The mass spectra obtained at different femtosecond time delays are shown in Fig. 3. At negative times, that is, when the probe arrives before the pump pulse, there is no signal present. At time zero, the parent mass (84 amu) of the precursor cyclopentanone is observed, while the fragment mass of 56 amu is not apparent. As the time delay increases, we observe the decrease of the 84 mass signal, and, for the 56 (or 55, corresponding to the species of interest minus one hydrogen) mass, first the increase and then decrease of the signal. The 56 mass corresponds to the parent minus the mass of CO. In addition to cyclopentanone, other precursors were studied similarly, including cyclobutanone, methyl-substituted cyclopentanones (2,2,5,5-tetramethyl, 2-methyl, and 2,2-dimethyl), and 2-cyclopenten-1-one.

Figure 4 shows time-resolved transients in which the different masses of the parent and intermediate species of three systems are detected. For the 56 mass species, the buildup time is $\tau_1 = 150 \pm 30$ fs, whereas the decay time is $\tau_2 = 700 \pm 40$ fs. The precursor cyclopentanone decays with $\tau = 120 \pm 20$ fs, and the peak of the 56 mass signal is shifted from the parent signal by $\Delta t = 300 \pm 50$ fs. These experiments were done at a total energy $E = 82$ kcal/mol (see below). When the total energy was decreased by ~5 kcal/mol, slower dynamics

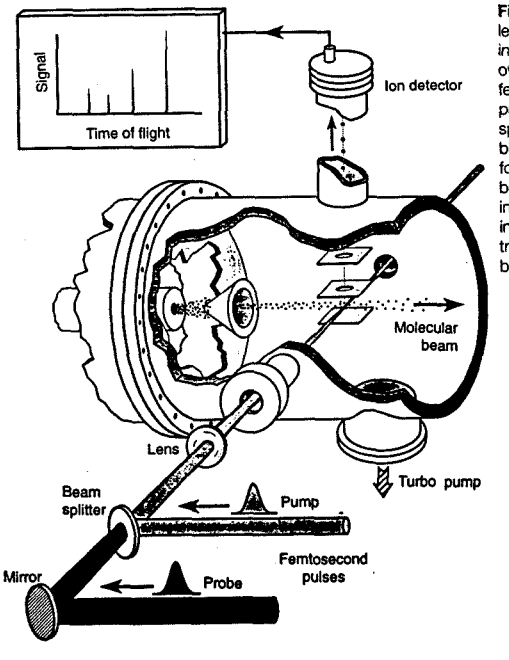

Fig. 2. The femtosecond molecular beam apparatus illustrating the mass selection and the overlap of the three beams. The femtosecond pump and probe pulses, delayed in time with respect to one another, are combined collinearly before being focused onto the molecular beam. The ions produced in the interaction region are detected in a time-of-flight mass spectrometer which can distinguish between different masses.

were observed: $\tau_1 = 240 \pm 30$ fs, $\tau_2 = 840 \pm 50$ fs ($\Delta t = 400 \pm 50$ fs), and $\tau = 120 \pm 20$ fs. On the other hand, increasing the total energy by 18 kcal/mol, faster dynamics were observed: $\tau_1 = 100 \pm 30$ fs, $\tau_2 = 340 \pm 30$ fs ($\Delta t = 150 \pm 40$ fs), and $\tau = 120 \pm 20$ fs. At the same total energy E, substitution of methyl groups at the 2 and 5 positions leads to a drastic change: $\tau_1 = 0.9 \pm 0.2$ ps and $\tau_2 = 1.4 \pm 0.2$ ps, for the 112 mass, whereas $\tau = 0.5 \pm 0.1$ ps for the 140 mass. For cyclobutanone, we carried out similar experiments and observed both the decay of the parent and the buildup and decay of the intermediate: At the total energy E, the dynamics is much faster with τ_1, τ_2, and $\tau \approx 100$ fs.

The reaction of carbonyls is well known to proceed through a Norrish-type α-cleavage (*20*), which in this case leads to the C–C bond breakage and decarbonylation. The PES involves a reaction coordinate along the C–C bonds adjacent to the CO (*21*). Since the 1942 work by Benson and Kistiakowsky, the gas-phase photolysis of cyclopentanone is known to yield primarily ethylene, cyclobutane, and carbon monoxide; at a wavelength similar to our excitation energy, the yield of this channel is ~90% (*22*, *23*). Therefore, the reaction path is a clear decarbonylation with the formation of tetramethylene, as discussed by Scala and Ballan (*23*) and others. The tetramethylene diradical forms cyclobutane (by closure) and two ethylene molecules (by fragmentation) (see Fig. 1). The time scale for this decarbonylation depends on the state excited. In our case, it is observed to be 100 to 200 fs (Fig. 4), and this clearly indicates its promptness; as will be detailed elsewhere, this is because we prepare a high-energy state (~150 nm) that correlates adiabatically to products of CO and tetramethylene. This situation is different from other cases studied at low energies (first excited $n\pi^*$ state) and where the correlation is absent and the decarbonylation takes place by a slower internal conversion or intersystem crossing, as discussed by Butler and co-workers for related systems (*24*). The spectrum of cyclopentanone at our energies of excitation is known (*25*), and indeed it exhibits broad bands of Rydberg and valence states, consistent with our time scale (*26*). The spectra, of course, do not have signatures of any of the subsequent dynamics of the diradical intermediate.

In our experiments, we typically use two photons (320, 310, or 280 nm) from the femtosecond pump pulse to induce the α-cleavage. At time zero in Fig. 3, we note that there is *no* signal for the 56 mass (at these low power levels). This result indicates that there is no fragmentation in the ion channels and that we are only observing the dynamics of the neutral diradical, which is then probed by ionization (*27*). Such separation of fragmentation from ionization is one powerful feature of the femtosecond time resolution, as shown previously by several groups (*19*, *28*). From the wavelength dependence of τ and τ_1, and the power dependence, we can conclude that the tetramethylene is formed in a nonconcerted manner (*29*). It is therefore possible, from the dynamics of the parent and the intermediates, to separate the two steps responsible for the formation of the diradical and to provide directly the hitherto unknown time scale for an elementary Norrish process, as will be detailed elsewhere. Here, we shall focus attention on the dynamics of the diradicals and their intrinsic lifetimes (τ_2).

From the data in Fig. 4, the tetramethylene and methyl-substituted tetramethylene diradicals are observed to be substantially different. Moreover, in tetramethylene, as we increased the total energy from the lowest value we studied by 5 kcal/mol to the value E (*30*, *31*) and then by an additional 18 kcal/mol, τ_2 decreased from 840 to 700 and then to 340 fs, respectively. Considering the dynamics (*19*) of the nuclei at the top of the barrier, it is impossible at these velocities to obtain such time scales if a wave packet is moving translationally on a flat surface. For example, over a distance of 0.5 Å, which is significantly large on a bond scale, the time in the transition-state region will be ~40 fs. To explain the reported (sub)picosecond times, other nuclear degrees of freedom must be involved.

The diradical in a "basin" defines a multidimensional PES with the involvement of many degrees of freedom. At the energies of interest, the total energy E available to the diradical is greater than the barrier height (E_o). If we use our energy-dependent rates ($1/\tau_2$) and invoking RRK (Ramsperger-Rice-Kassel) theory, we obtain a barrier height of $E_o \approx 4$ kcal/mol, taking the frequency (150 cm^{-1} or 1/220 fs) of the reaction coordinate from the PES calculation (*11*); note that per mode the energy is less than E_o and that the calculations are microcanonical, $k(E)$, and not $k(T)$ [further analysis will require Rice-Ramsperger-Kassel-Marcus theory (RRKM); calculations in progress]. Doubleday's calculation (*11*) indicates that tetramethylene is trapped on the free energy surface, and he estimates that the total rate for closure and fragmentation should correspond to 0.4 ps at 693 K and 0.3 ps at 1130 K. If we assume that Doubleday's temperature is equivalent to a microcanonical distribution, the corresponding total internal energy is then ~70 kcal/mol, similar in range to our E values. Moreover, he found that the lifetime is relatively insensitive to the temperature change in this range. As noted above, when we varied the internal energy by changing the energy of the initiation pulse, the change in the lifetime is not drastic, a feature reflecting the involvement of many modes in a bound state of the diradical.

Additional support for the intermediacy

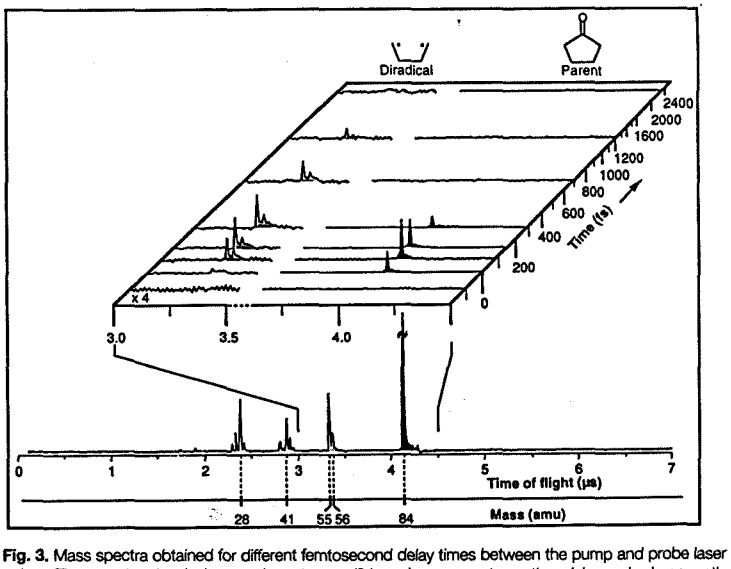

Fig. 3. Mass spectra obtained for different femtosecond delay times between the pump and probe laser pulses. The parent molecule, here cyclopentanone (84 amu), appears at zero time delay and subsequently decays. In contrast, the tetramethylene diradical intermediate (56 amu) appears later, growing in and peaking at ~300 fs, and then decays very slowly ($\tau_2 = 700$ fs); see text. The masses at 28 and 41 amu are due to ion fragmentation and their studies will be reported elsewhere.

of tetramethylene came from substitution effects on the observed femtosecond dynamics. Substituting the hydrogens at the active sites (where the two electrons reside) with methyl groups increases the lifetime of the diradical from the subpicosecond to the picosecond regime (see Fig. 4). The extra stability of the diradical is the result of delocalization of electron density (hyperconjugation) and possible steric repulsion (barrier) due to alkyl substitution. Studies of such effects in these systems goes back to the 1961 work by Gerberich and Walters (*32*) on the thermal decomposition of methyl-substituted cyclobutanes. Finally, the results have a direct impact on product-channel distributions. With methyl substitution, the internal rotation slows down with respect to fragmentation (*33*), thus altering the stereospecificity.

The results in Fig. 4 show that the 42 mass for the trimethylene system exhibits much faster dynamics, 120 fs. This observation indicates that trimethylene is shorter lived than tetramethylene and that a wavepacket concerted motion is appropriate to describe the reaction. It is also interesting that the parent cyclobutanone decays on a comparable time scale of 105 ± 10 fs, indicating that the decarbonylation and the diradical rearrangement all involve minimum nuclear motions in degrees of freedom other than the reaction coordinate. Further studies of this system are required in order to establish the intermediates involved; cyclobutanone, unlike cyclopentanone, can give the so-called C_2 channel in which there is no direct CO elimination. Because product-state distributions are known from the work of Houston and co-workers (*31*), we should be able to examine the dynamics of the different channels.

With different precursors and polarizations, the entrance channel of the global PES (*34*) and internal rotations could also be studied. Clearly further work is needed. For example, the nature of the different configurations (gauche, trans, and so forth) should be studied. Also, the initiation of the reaction from different precursors and from cyclobutane will help the mapping of the PES and identify the dynamical routes.

These studies of reaction intermediates involving diradicals provide a real-time picture of the nuclear motions and structural changes during the reaction. The observations establish the diradical, frozen on the femtosecond time scale, as a distinct molecular species. The discovery of their time scales and elementary dynamics defines the mechanistic concept crucial to the understanding of the nature of chemical-bond changes. There is a wealth of studies awaiting these and other classes of reactions, and the approach should be general for the examination of other reactive intermediates.

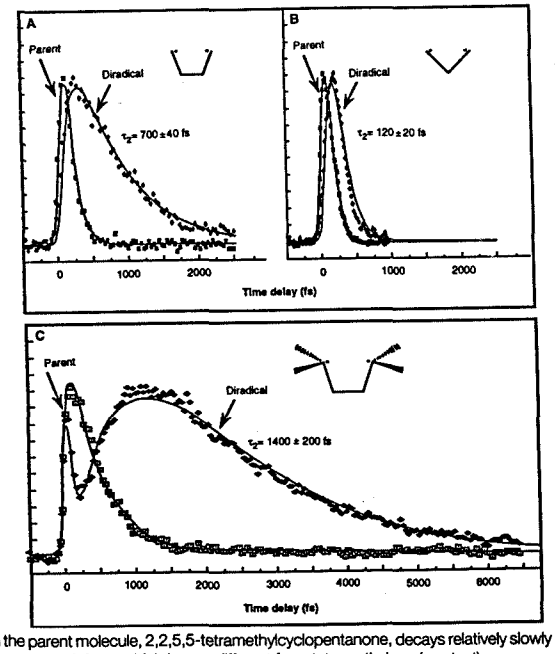

Fig. 4. (**A**) Femtosecond transients showing the detected ion signal of a given mass as a function of the time delay between the pump and probe laser pulses. The parent cyclopentanone (84 amu) signal simply decreases with an exponential decay time of 120 ± 20 fs. The diradical shows a biexponential behavior, building up to a maximum (τ_1 = 150 ± 30 fs) followed by a relatively slow decay (τ_2 = 700 ± 40 fs). (**B**) The buildup and decay characteristics for the 42 mass obtained from the precursor cyclobutanone; τ_1 and τ_2 = 120 ± 20 fs. As noted, in this case the fit to an exponential rise and decay is not as good, consistent with a wave packet motion. (**C**) Substituent effect on the time scales of the dynamics, examined with the same pump and probe lasers. The 1,4-diradical formed from the parent molecule, 2,2,5,5-tetramethylcyclopentanone, decays relatively slowly with a decay constant: τ_2 = 1.4 ± 0.2 ps, which is very different from tetramethylene (see text).

REFERENCES AND NOTES

1. See R. B. Woodward and R. Hoffmann, *The Conservation of Orbital Symmetry* (Academic Press, New York, 1970); L. Salem, *Electrons in Chemical Reactions* (Wiley, New York, 1982).
2. J. A. Berson, *Annu. Rev. Phys. Chem.* **28**, 111 (1977); in *Rearrangements in Ground and Excited States*, P. de Mayo, Ed. (Academic Press, New York, 1980), vol. 1, pp. 311–390.
3. R. G. Bergman, in *Free Radicals*, J. K. Kochi, Ed. (Wiley, New York, 1973), pp. 191–237.
4. P. D. Bartlett, *Q. Rev. Chem. Soc.* **24**, 473 (1970).
5. P. B. Dervan and D. A. Dougherty, in *Diradicals*, W. T. Borden, Ed. (Wiley, New York, 1982), pp. 107–149; W. T. Borden, in *ibid.*, pp. 1–72.
6. L. Salem and C. Rowland, *Angew. Chem. Int. Ed. Engl.* **11**, 92 (1972).
7. W. von E. Doering, *Proc. Natl. Acad. Sci. U.S.A.* **78**, 5279 (1981).
8. R. Hoffmann, S. Swaminathan, B. G. Odell, R. Gleiter, *J. Am. Chem. Soc.* **92**, 7091 (1970).
9. S. W. Benson, *Thermochemical Kinetics* (Wiley, New York, ed. 2, 1976), and references therein.
10. G. A. Segal, *J. Am. Chem. Soc.* **96**, 7892 (1974).
11. C. Doubleday Jr., *ibid.* **115**, 11968 (1993), and references therein.
12. C. Doubleday Jr., J. W. McIver Jr., M. Page, *J. Phys. Chem.* **92**, 4367 (1988), and references therein.
13. Y. Yamaguchi, H. F. Schaefer III, J. E. Baldwin, *Chem. Phys. Lett.* **185**, 143 (1991), and references therein.
14. B. S. Rabinovitch, E. W. Schlag, K. B. Wiberg, *J. Chem. Phys.* **28**, 504 (1958).
15. P. B. Dervan, T. Uyehara, D. S. Santilli, *J. Am. Chem. Soc.* **101**, 2069 (1979); *ibid.* **102**, 3863 (1980).
16. L. M. Stephenson and J. I. Brauman, *ibid.* **93**, 1988 (1971).
17. J. E. Baldwin, A. H. Andrist, R. K. Pinschmidt Jr., *Acc. Chem. Res.* **5**, 402 (1972); J. E. Baldwin, Y. Yamaguchi, H. F. Schaefer III, *J. Phys. Chem.* **98**, 7513 (1994).
18. G. Jones II, *J. Chem. Ed.* **51**, 175 (1974).
19. A. H. Zewail, *Femtochemistry: Ultrafast Dynamics of the Chemical Bond* (World Scientific, Singapore, 1994), and references therein.
20. See N. J. Turro, *Modern Molecular Photochemistry* (Benjamin/Cummings, Menlo Park, CA, 1978).
21. J. Michl and V. Bonačić-Koutecký, *Electronic Aspects of Organic Photochemistry* (Wiley, New York, 1990).
22. S. W. Benson and G. B. Kistiakowsky, *J. Am. Chem. Soc.* **64**, 80 (1942); see (*23*); R. Becerra and H. M. Frey, *J. Chem. Soc. Faraday Trans. 2* **84**, 1941 (1988), and references therein.
23. A. A. Scala and D. G. Ballan, *Can. J. Chem.* **50**, 3938 (1972).
24. M. D. Person, P. W. Kash, L. J. Butler, *J. Chem. Phys.* **97**, 355 (1992).
25. L. O'Toole, P. Brint, C. Kosmidis, G. Boulakis, P. Tsekeris, *J. Chem. Soc. Faraday Trans.* **87**, 3343 (1991); see also *ibid.*, p. 2891.
26. For cyclopentanone and cyclobutanone, the lifetimes of the lowest $n\pi^*$ states are nanoseconds and the yields from these states vary with energy; see R. G. Shortridge Jr., C. F. Rusbult, E. K. C. Lee, *J. Am. Chem. Soc.* **93**, 1863 (1971); J. C. Hemminger, C. F. Rusbult, E. K. C. Lee, *ibid.*, p. 1867.
27. M. Baba, H. Shinohara, N. Nishi, N. Hirota, *Chem. Phys.* **83**, 221 (1984); P. Jungwirth and T. Bally, *J. Am. Chem. Soc.* **115**, 5783 (1993), and references therein.
28. T. Baumert, M. Grosser, R. Thalweiser, G. Gerber, *Phys. Rev. Lett.* **67**, 3753 (1991); S. Wei, J. Purnell, S. A. Buzza, R. J. Stanley, A. W. Castleman Jr., *J. Chem. Phys.* **97**, 9480 (1992).
29. A. T. Blades, *Can. J. Chem.* **48**, 2269 (1970).
30. Two pump photons at 310 nm correspond to a total energy of 184 kcal/mol. The available energy is 99 kcal/mol, which corresponds to the value of 184 kcal/mol minus the bond energies. The internal energy in the diradical is E^* ~ 82 kcal/mol because of the translational and the energy disposal in the CO (*31*).
31. K. A. Trentelman, D. B. Moss, S. H. Kable, P. L. Houston, *J. Phys. Chem.* **94**, 3031 (1990); R. Jimen-

ez *et al.*, *ibid.* **96**, 4188 (1992).
32. H. R. Gerberich and W. D. Walters, *J. Am. Chem. Soc.* **83**, 4884 (1961).
33. See (*2*), (*5*), and J. A. Berson, L. D. Pedersen, B. K. Carpenter, *ibid.* **98**, 122 (1976).
34. B. K. Carpenter, *Acc. Chem. Res.* **25**, 520 (1992).
35. Supported by a grant from the Air Force Office of Scientific Research and by the National Science Foundation. We are grateful to P. B. Dervan, D. A. Dougherty, M. Okumura, J. D. Roberts, and W. von. E. Doering for the helpful discussions. We thank J. A. Berson and B. K. Carpenter for their helpful suggestions and penetrating questions, C. Doubleday Jr. for his interest in this work and for communicating unpublished results, K. Anderson for the preparation of 2,2,5,5-tetramethylcyclopentanone, and L. Bañares for his help in the preliminary work (bulb studies) in this group. Contribution no. 8970 from the Arthur Amos Noyes Laboratory of Chemical Physics.

26 August 1994; accepted 23 September 1994

Appendix D

Direct Femtosecond Observation of the Transient Intermediate in the α-cleavage Reaction of $(CH_3)_2CO$ To $2CH_3+CO$: Resolving the Issue of Concertedness

Direct femtosecond observation of the transient intermediate in the α-cleavage reaction of $(CH_3)_2CO$ to $2CH_3+CO$: Resolving the issue of concertedness

Sang Kyu Kim, Soren Pedersen, and Ahmed H. Zewail
Arthur Amos Noyes Laboratory of Chemical Physics,[a] California Institute of Technology, Pasadena, California 91125

(Received 17 April 1995; accepted 2 May 1995)

When a reaction involving two equivalent bonds has sufficient energy to break both of them, it can proceed by either a *concerted* or a *stepwise* mechanism. For Norrish type-I and other reactions, this issue has been controversial since direct time resolution of the individual C–C cleavage events was not possible. Here, for the elementary α-cleavage of acetone, we report on the femtosecond resolution of the intermediates using mass spectrometry. The results show the nonconcertedness of the reaction, provide the times for the primary and secondary C–C breakage, and indicate the role of electronic structure (σ^*, antibonding impulse) and the vibrational motions involved. © *1995 American Institute of Physics.*

I. INTRODUCTION

For a chemical reaction with multiple-bond breaking or bond making, one of the most fundamental questions has been whether or not the events occur in a *concerted* or in a *stepwise* manner. Many experimental and theoretical studies (see, e.g., Refs. 1–3) have been devoted to answer such a question, and the issue in different reactions (pericyclic, S_N2, elimination, etc.) has been controversial. However, several *operational* concepts have been invoked.

A commonly used criterion between the concerted and stepwise mechanisms involves the kinetic time scale. A concerted reaction is defined as one that takes place in a single kinetic step without necessarily being synchronous.[2] In contrast, a stepwise reaction involves two kinetically distinct steps via a stable intermediate. Houston and co-workers[3] used the calculated molecular rotational time scale (~ps) of the intermediate as a dividing line between a concerted and a stepwise mechanism, defining concertedness when the intermediate lifetime becomes shorter than its rotational period.

The difference between a stepwise and a concerted process obviously rests with the direct detection of the intermediate species. What is critical is the nature of the transition-state region, e.g., a saddle-point concerted structure, an energy minimum describing an intermediate along the reaction coordinate, or a global potential energy surface with many degrees of freedom involved. Consequently, the dynamics of the nuclear motion on the femtosecond (fs) time scale must be established in order to conclusively define concertedness as a useful general concept.

In this contribution, we report direct femtosecond (fs) studies of the elementary processes in the three-body dissociation of $(CH_3)_2CO$ to CO and two CH_3 radicals. This two-bond (C–C) breakage is an ideal example for addressing the issue of concertedness and belongs to the general class of α-cleavage processes known as Norrish type-I reactions.[4,5] Our focus is on the fragmentation at excitation energies high enough for both bonds to, in principle, dissociate with a quantum yield for $2CH_3+CO$ close to unity.[6] We use the fs mass spectrometry approach[7] to identify the parent and transient intermediates, and to examine the energy and isotope effects on the dynamics.

The mechanism of α-cleavage in acetone has been investigated through spectroscopic, kinetic, and product-state studies (see, e.g., Refs. 8–12). For example, Baba *et al.* inferred from a nanosecond power dependence of the MPI signal of acetone and acetyl in the mass spectrum that neutral CH_3CO exist in a one-photon dissociation at 193 nm.[10] Vaida and co-workers, from the absorption spectra, suggested a predissociative mechanism for the photolysis of acetone at around 193 nm.[11] Leone and co-workers[12] found that the CO (at 193 nm excitation) is highly rotationally excited, and interpreted this as evidence for a stepwise mechanism. Houston and co-workers[3] measured the translational energy of the CH_3 fragments and did not observe a bimodal distribution (for two methyls) which they gave as evidence for a concerted dissociation. They also measured the internal energy of the methyl fragments to be very small, leading them to conclude that the dissociation of each C–C bond occurs prior to complete randomization of the available energy by a concerted mechanism.[3]

Later, Strauss and Houston[3] examined the same system with the information-theoretic approach to investigate the correlation of velocity vectors of two methyl fragments and concluded that the fragmentation at 193 nm proceeds in an intermediate way between the stepwise and concerted mechanisms. Subsequently, Hall *et al.*[13] removed an approximation in the information-theoretic analysis[3] and found that there is no correlation between the recoil directions of the two methyl radicals. They suggested that the lifetime of the reaction intermediate is long relative to the time of randomization.

Very recently, Lee and co-workers[14] carefully measured the fragments translational energy at two different wavelengths, 248 and 193 nm. From the fit of the distributions for CH_3 and CO, they provided evidence for a stepwise mechanism at 193 nm. The product-state distributions give valuable information on the energy changes in the exit channel, as discussed below.

 0021-9606/95/103(1)/477/4/$6.00

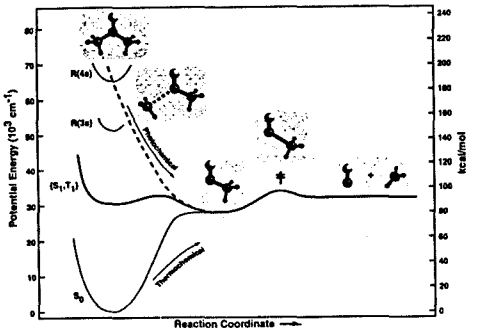

FIG. 1. A cut of the potential energy surface along the reaction coordinate illustrating the concerted vs stepwise mechanism of the reaction: $(CH_3)_2CO \rightarrow 2CH_3+CO$, or $(CH_3)_2CO \rightarrow CH_3CO+CO \rightarrow 2CH_3+CO$. Photochemical and thermochemical pathways are denoted by arrows, and the structures are shown only for five configurations. Energies are given in two units, and the states are labeled with R denoting Rydberg, S singlet and T triplet, and S_0 the ground state.

In our fs studies of this reaction, as with pericyclic[15] and elimination[16] reactions, we initiate the motion with a fs laser pulse and detect with probe fs pulses, using multiphoton ionization/time-of-flight mass spectrometry. By probing a specific mass, parent acetone or intermediate acetyl, as a function of time, the real-time dynamics can be directly observed; see Fig. 1. We observe a buildup (50 fs) and decay (500 fs) of the transient intermediate, and the dynamical time scale for the secondary bond cleavage is found to be isotope and energy dependent (106 and 124 kcal/mol above dissociation). These results establish the nonconcertedness and the mechanism of the reaction, and are directly related to the electronic structure and vibrational motions.

II. EXPERIMENT

Figure 2 depicts a schematic of the experimental apparatus which combines a (skimmed) molecular beam and a fs laser system.[7] Two modes of detection were employed. In one mode, the evolution of all mass species was monitored at different time delays, while in the other mode, the transient for a specific mass was recorded. The latter was obtained by gating the mass signal as a function of the delay time between the first and second fs laser pulses.

The helium carrier gas was bubbled through the sample, acetone-h_6 (Mallinckrodt, 99.5%) or acetone-d_6 (CIL), 99.9% D, at ice or room temperature with a typical backing pressure of 20 psi. To reduce cluster formation, the pulsed nozzle was heated to 100 °C. The pressure in the TOF chamber was 3×10^{-6} Torr when the nozzle (0.3 mm diameter) was opened. The data were recorded, using a transient digitizer or a boxcar integrator, collected, and analyzed with a computer.

III. RESULTS AND DISCUSSION

The TOF mass spectra at different reaction times are shown in Fig. 3. The signals due to the parent $[(CH_3)_2CO^+$; 58 amu] and the reaction intermediate $[(CH_3CO^+$; 43 amu)] are both identified, but their evolution on the fs time scale is entirely different. The parent signal is strong at time zero and it completely disappears within a few hundred fs of the reaction time. Meanwhile, the intermediate signal increases in the first few hundred fs as the parent signal decreases, and then it decreases more slowly with increasing reaction time. This behavior indicates the presence of the intermediate, CH_3CO^+, following the first α-cleavage of the C–C bond. From the observed power dependence of ~1.4 (two photons through intermediate), we can obtain the available energy of the reaction, as discussed below.

The transients of the parent and intermediate are shown in Fig. 3 together with the theoretical fits. The decay of the parent signal gives the lifetime (τ) of 50±30 fs when the transient was fit to a single exponential decay including a convolution of the laser pulse width;[7] the cross-correlation HWHM was 75±15 fs. The buildup and decay of the transient intermediate was also fit giving the τ_1 (buildup time) and τ_2 (decay time); τ_1 was found to correspond to the decay of the parent (50 fs), but τ_2 is much longer and depends on the total energy and isotopic composition.

For the 307 nm experiments (186 kcal/mol), $\tau_2=500\pm100$ fs for CH_3CO^+ while for CD_3CO^+ (see Fig. 3), $\tau_2=750\pm100$ fs. While the buildup time τ_1 is similar for both isotopic species, the decay time of CD_3CO^+ is ~1.5 times longer than that of CH_3CO^+. Moreover, the transients show a significant energy dependence in τ_2 of the acetyl intermediate. For the 280 nm experiments (204 kcal/mol), $\tau_2=180\pm50$ fs for the protonated species and $\tau_2=280\pm50$ fs for the deu-

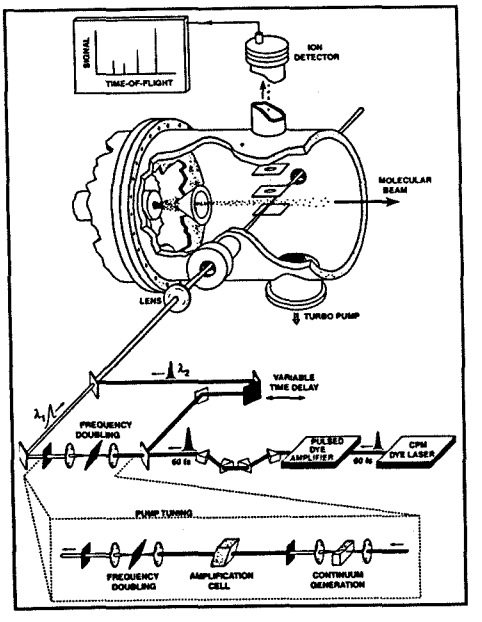

FIG. 2. Experimental apparatus showing the molecular beam, with the mass spectrometer, and the fs laser system. The white light generation for the 280 nm experiment is outlined in the dotted box.

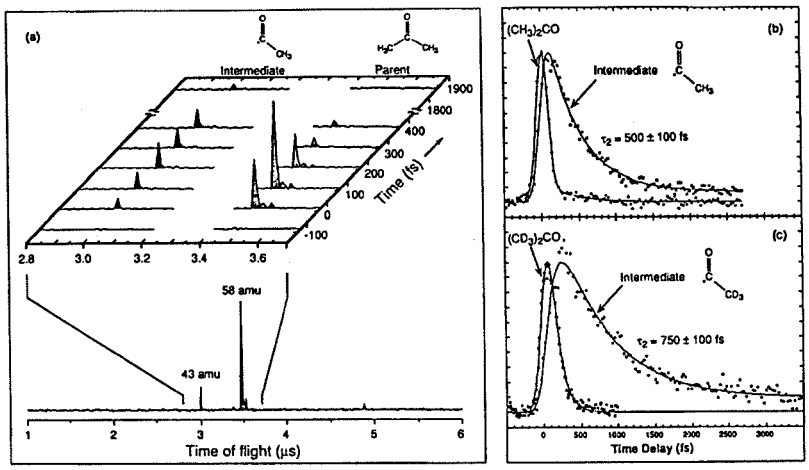

FIG. 3. Femtosecond mass spectra and transients for $(CH_3)_2CO$ and $(CD_3)_2CO$ reactions. (a) Time-of-flight mass spectra at different time delays. Notice the evolution of the parent signal (58 amu) and the longer decay of the intermediate (43 amu). Transients of (b) acetone and acetyl; (c) deuterated acetone and acetyl obtained at $\lambda_{pump}=307$ nm and $\lambda_{probe}=615$ nm. The theoretical fits are presented as solid lines (see the text for values). A less than 10% background, observed in the acetyl transient might be due to a small contribution from acetone dimers possible in the molecular beam (Ref. 11). Note that near time zero in (a) the signal is primarily that of the parent, indicating that the probed intermediate is ionized following neutral parent fragmentation. This is a key feature of the fs time resolution (Refs. 7 and 15).

terated species, both shorter than the values obtained in the 307 nm experiments.

The above results demonstrate that the reaction of acetone is nonconcerted and dynamically involves two steps. The first α-cleavage (50 fs) occurs on a time scale less or comparable to the vibrational period (essentially frozen nuclei), and the second cleavage involves the vibrational degrees of freedom, as evident by its longer time scale, isotope effect, and the energy dependence. These primary and secondary bond breakages must, therefore, be considered differently.

The fact that the primary C–C bond cleavage at these high energies is found to occur on a time scale shorter than 100 fs suggests that the potential energy surface is antibonding, repulsive along the reaction coordinate. The vibrational period of the C–C bond[17] is ~43 fs and accordingly the σ^* promotion is prompted before any significant energy redistribution. This is consistent with the insignificant H/D isotope effect observed in the primary cleavage, and with the nature of the initial state. The excitation by two-photon absorption at 307 or 280 nm reaches the n-4s Rydberg state which is broadened (~200 cm^{-1}, ~30 fs)[18] by interaction with valence states. The *ab initio* calculation by the Bonn group[19] clearly identifies the states, and we have made symmetry correlations[20] for the reaction path which indicate σ^* repulsion in the C–C bond. This correlation is also consistent with Butler's analysis of nonadiabatic interactions in the dissociation of ketones studied by her group.[21]

The secondary C–C bond breakage is from the nascent hot acetyl intermediate. The breakage proceeds with a reaction barrier of 17 kcal/mol.[22,23] Because of this barrier, we consider the global PES and compare our results with the rate constants we calculate from the RRKM theory. The vibrational frequencies of CH_3CO, calculated by Hess and colleagues,[24] were used; for those of CD_3CO, a scaling, based on the ratios of vibrational frequencies of h_6 and d_6, was invoked. The rate constant is not strongly dependent on the angular momentum (J) for a reaction with a barrier, and the calculations were carried out for $J=0$ as a function of energy.

The available energy can be obtained from knowledge of the total deposited energy and product-state distributions. As discussed above, the primary α-cleavage occurs in 50 fs and this indicates that there is not enough time for the available energy to be redistributed among vibrational degrees of freedom, other than the motion along the reaction coordinate. An impulsive model (see Refs. 3 and 14), where all of the energy is in the C–C bond repulsion, predicts that 54% of the available energy goes into translational energy, 10% into the internal energy of CH_3, and 36% into the internal energy of CH_3CO. At 307 or 280 nm, the available energy to the CH_3CO and CH_3 products is (186−80)=106 or (204−80) =124 kcal/mol, respectively, since the bond energy is ~80 kcal/mol (see Fig. 1).[25] Hence, the impulsive model predicts an internal energy of 38 or 45 kcal/mol for the acetyl intermediate at the two energies studied. The rotational energy of CH_3CO is taken to be ~1 kcal/mol.[14]

For $E=37$ kcal/mol, our RRKM calculations give $\tau_2=375$ and 460 fs for $CH_3CO^{\dagger}$ and $CD_3CO^{\dagger}$, respectively. For $E=44$ kcal/mol, these values are $\tau_2=175$ and 200 fs. The theoretical values match well with the experimental results, not only qualitatively but also quantitatively in terms of the H/D isotope effect and energy dependence. However, it is questionable that one of the basic assumptions of a statistical rate theory, i.e., a complete randomization of the energy prior to reaction, will be satisfied for such a femtosecond reaction.

It seems that the first impulse of primary α-cleavage creates the needed vibrational distribution even on this short time scale. It is interesting to note that the translational energy distribution measured at 193 nm is broad and has a FWHM of ~15 kcal/mol.[14] Not all modes of the phase space have to be involved, and the large isotope effect and energy dependence may have its origin in the dynamical motion of the wave packet on the PES, as observed before in the dissociation of methyl iodide.[26] Molecular dynamics will be part of our future work to unravel the extent of the vibrational motion in the secondary step.

IV. CONCLUSIONS

The elementary dynamics of the Norrish reaction in acetone were studied in real time. The primary and secondary C–C bond cleavage occur *nonconcertedly* on time scales one order of magnitude different. The intermediate lifetime at the energy studied here is shorter than its rotational period, which would mean a concerted mechanism if the internal molecular clock is used as the dividing line between the stepwise and concerted mechanisms, a criterion widely used. Therefore, the use of the rotational period of the intermediate or the rotation about a single bond is not indicative of true concertedness. Rather, the concertedness of the reaction should be judged from the comparison of the intermediate lifetime to the vibrational period along the reaction coordinate. Such a definition directly reflects concertedness and synchronicity, and describes the actual nuclear motions in the transition states.[27]

ACKNOWLEDGMENTS

This research was supported by a grant from the Air Force Office of Scientific Research and by the National Science Foundation. We wish to thank Professor Y. T. Lee for providing us with a preprint of their recent work, Jennifer Herek for the helpful discussion, and Dr. W. P. Hess for communicating the *ab initio* results.

[a]Contribution No. 9086.

[1] W. T. Borden, R. J. Loncharich, and K. N. Houk, Annu. Rev. Phys. Chem. **39**, 213 (1988), and references therein.
[2] M. J. S. Dewar, J. Am. Chem. Soc. **106**, 209 (1984).
[3] C. E. M. Strauss and P. L. Houston, J. Phys. Chem. **94**, 8751 (1990); K. A. Trentelman, S. H. Kable, D. B. Moss, and P. L. Houston, J. Chem. Phys. **91**, 7498 (1989).
[4] R. G. W. Norrish, Trans. Faraday Soc. **30**, 103 (1934); *Photochemistry and Reaction Kinetics*, edited by P. G. Ashmore, F. S. Dainton, and T. M. Sugden (Cambridge University, Cambridge, 1967).
[5] N. J. Turro, *Modern Molecular Photochemistry* (Benjamin/Cummings; Menlo Park, CA, 1978); E. K. C. Lee and R. S. Lewis, Adv. Photochem. **12**, 1 (1980).
[6] P. D. Lightfoot, S. P. Kirwan, and M. J. Pilling, J. Phys. Chem. **92**, 4938 (1988).
[7] A. H. Zewail, *Femtochemistry: Ultrafast Dynamics of the Chemical Bond* (World Scientific, Singapore, 1994), and references therein.
[8] M. A. Khan, R. G. W. Norrish, and G. Porter, Proc. R. Soc. London Ser. A **219**, 312 (1953).
[9] A. Shilman and R. A. Marcus, Bull. Soc. Chem. Belg. **71**, 653 (1962).
[10] M. Baba, H. Shinohara, N. Nishi, and N. Hirota, Chem. Phys. **83**, 221 (1984).
[11] G. A. Gaines, D. J. Donaldson, S. J. Strickler, and V. Vaida, J. Phys. Chem. **92**, 2762 (1988); D. J. Donaldson, G. A. Gaines, and V. Vaida, *ibid.* **92**, 2766 (1988).
[12] D. J. Donaldson and S. R. Leone, J. Chem. Phys. **85**, 817 (1986); E. L. Woodbridge, T. R. Fletcher, and S. R. Leone, J. Phys. Chem. **92**, 5387 (1988).
[13] G. E. Hall, D. V. Bout and T. J. Sears, J. Chem. Phys. **94**, 4182 (1991).
[14] S. W. North, D. A. Blank, J. D. Gezelter, C. A. Longfellow, and Y. T. Lee, J. Chem. Phys. **102**, 4447 (1995).
[15] S. Pedersen, J. L. Herek, and A. H. Zewail, Science **266**, 1359 (1994).
[16] L. R. Khundkar and A. H. Zewail, J. Chem. Phys. **92**, 231 (1990).
[17] P. Cossee and J. H. Schachtschneider, J. Chem. Phys. **44**, 97 (1966).
[18] P. Brint, L. O'Toole, S. Couris, and D. Jardine, J. Chem. Soc. Faraday Trans. **87**, 2891 (1991).
[19] B. Hess, P. J. Bruna, R. J. Buenker, and S. D. Peyerimhoff, Chem. Phys. **18**, 267 (1976).
[20] J. Michl and V. Bonačić-Koutecký, *Electronic Aspects of Organic Photochemistry* (Wiley, New York, 1990).
[21] G. C. G. Waschewsky, P. W. Kash, T. L. Myers, D. C. Kitchen, and L. J. Butler, J. Chem. Soc. Faraday Trans. **90**, 1581 (1994), and references therein.
[22] K. W. Watkins and W. W. Word, Int. J. Chem. Kinet. **6**, 855 (1974).
[23] S. North, D. A. Blank, and Y. T. Lee, Chem. Phys. Lett. **224**, 38 (1994).
[24] S. Deshmukh, J. D. Myers, S. S. Xantheas, and W. P. Hess, J. Phys. Chem. **98**, 12535 (1994).
[25] H. Zuckermann, B. Schmitz, and Y. Haas, J. Phys. Chem. **92**, 4835 (1988).
[26] M. H. M. Janssen, M. Dantus, H. Guo, and A. H. Zewail, Chem. Phys. Lett. **214**, 281 (1993); H. Guo and A. H. Zewail, Can. J. Chem. **72**, 947 (1994).
[27] A. H. Zewail (to be published).

Appendix E

Femtochemistry of Organometallics: Dynamics of Metal-Metal and Metal-Ligand Bond Cleavage in $M_2(CO)_{10}$

ELSEVIER

24 February 1995

Chemical Physics Letters 233 (1995) 500–508

CHEMICAL PHYSICS LETTERS

Femtochemistry of organometallics: dynamics of metal–metal and metal–ligand bond cleavage in $M_2(CO)_{10}$

Sang Kyu Kim, Soren Pedersen, Ahmed H. Zewail

Arthur Amos Noyes Chemical Physics Laboratory [1], California Institute of Technology, Pasadena, CA 91125, USA

Received 30 December 1994

Abstract

We report femtochemical studies of the organometallic dimetal decacarbonyl. By the use of mass spectrometry, we obtain the temporal dynamics in the channels for metal–metal and metal–ligand bond cleavage. The time scale observed for cleavage and for structural bridging indicates the nature of the repulsion along the two reaction coordinates and the interplay between the bond order and the femtosecond dynamics.

1. Introduction

Organometallic compounds have unique functions and properties which are totally determined by the dynamics of metal–metal (M–M) and metal–ligand (M–L) bonding [1,2]. The time scales for such cleavage determine the product yield and the selectivity in the product channel. It also establishes the nature of the reactive surface: ground-state versus excited-state chemistry.

One class of reactions which has been the subject of detailed spectroscopic, mechanistic, and theoretical studies is the carbonyl containing metal–metal compounds (for recent reviews, see Refs. [3,4]). For these compounds it is known that both the M–M and M–CO bonds can be broken upon UV excitation. There have been numerous studies aimed at understanding the dissociation mechanism of these metal complexes in solutions as well as in the gas phase. The energetics, spectroscopy, and photochemistry of these metal complexes have also been extensively studied.

For dimetal and related complexes, several aspects of the dissociation mechanism have been addressed, starting with the assignment of the optical transitions [5]. The primary photodissociation channels [6–11] and their time scales for dissociation [8,12–16] have been examined. The bond energies and internal energy distributions of photoproducts [8,17–19], molecular rearrangement and bridging [20–22], and solvent complexation and vibrational relaxation in solutions [13–15,23] have also been studied by many groups.

On the theoretical side, there has been significant progress in understanding the electronic structure of these and related systems [24,25]. The molecular electronic structure [26] and correlation diagrams [27] of the reactive channels have been described. Molecular dynamics studies by the Manz group [28,29] on related systems have determined the elementary time scale for metal–ligand bond breakage

[1] Contribution No. 9032.

SSDI 0009-2614(95)00050-X

and exploited these femtosecond (fs) time scales to control the outcome of reactions.

In this Letter, we report the first studies of the fs dynamics of isolated $Mn_2(CO)_{10}$ in a molecular beam. The goal is to directly obtain the cleavage time for the M–M and M–CO bonds and to examine the mechanism in relation to bonding characteristics. Since these studies are carried out in a molecular beam, complications from solvent caging of ligands and possible cooling by vibrational relaxation can be eliminated. Hence, direct comparison with theory could be made. To date most measurements (see below) have provided an upper limit of a few picoseconds. However, it is important to resolve the elementary motion in order to compare the dynamics in the two channels and to establish whether the dissociation takes place on the excited surface, or on the ground state reached by intramolecular vibrational-energy redistribution (IVR).

In the gas phase, the time scale of dissociation in these and related systems were obtained, as an upper limit, using two different approaches: Measurement of the anisotropy parameter (β) and the fluence dependence of ionization yield. Bersohn's group [8] reported the first collision-free gas-phase photodissociation study for $Mn_2(CO)_{10}$ and $Re_2(CO)_{10}$. From measurement of $\beta \approx 1.9$ (for $Mn_2(CO)_{10}$) they deduced an upper limit of 2–3 ps for the lifetime (from calculation of the rotational period). In this same study, they showed that M–M fragmentation is the primary channel. In a subsequent study, Vaida's group [10] showed that both the M–M and M–CO fragmentation channels are active. Grant's group [12] used the fluence dependence of ionization versus fragmentation in supersonic jets and again deduced an upper limit for the dissociation time (≈ 1 ps) in the case for $Fe(CO)_5$.

Nelson's group studied the M–CO bond cleavage in $M(CO)_6$, where M = Cr, Mo, and W [14], in solution using fs laser pulses, and reported a dissociation time of less than ≈ 500 fs. From their experiments, also in solution, Harris' group obtained an upper limit of the dissociation time (actually referred to as predissociation) of 2–3 ps or less [13]. In a later study the results for the photolysis of $Mn_2(CO)_{10}$ were interpreted in terms of ultrafast geminate recombination which occurs on a ≈ 350 fs time scale, predominantly by a single collision with the surrounding solvent cage [16]. This analysis of the results in solution suggests a shorter time scale for the primary dissociation channel. Recently, the group of Ruhman observed coherent photodissociation, using fs pulses, and provided a simplified molecular orbital scheme for the decarbonylation [15].

The absorption spectrum of $Mn_2(CO)_{10}$ in cyclohexane is very broad and does not give dynamical information. The spectrum shows that the maximum extinction coefficient is at ≈ 345 nm and that the transition can be assigned as $\sigma \rightarrow \sigma^*$ promotion along the Mn–Mn bond, Fig. 1 [5,13]. The $\sigma \rightarrow \sigma^*$ transition removes the bonding character of the Mn–Mn bond and leads to the dissociation into two $\cdot Mn(CO)_5$ products. According to a state-correlation diagram, two $\cdot Mn(CO)_5$ product states correlate with the lower-lying triplet, excited state, which could be directly accessed either by the optical excitation or through intersystem crossing from the excited singlet state [3,27]. The other absorption transitions, peaking near ≈ 260 and ≈ 300 nm, have been assigned to metal-to-ligand charge transfer (MLCT) transitions, which correspond to $d\pi \rightarrow \pi^*(CO)$ and $\sigma \rightarrow \pi^*(CO)$ transitions, respectively [5]. These transitions tend to weaken the metal–ligand bond and could lead to Mn–CO bond breakage. However, the mechanism describing the dynamics of elementary bond dissociation could not be resolved from the spectra.

In this work, we examine the elementary dissociation dynamics of $Mn_2(CO)_{10}$ and provide a direct measurement of the M–M and M–CO bond cleavage, free of the solvent. From these results we describe the mechanism for the reaction in the two channels. The products of $Mn_2(CO)_{10}$ in the molecular beam were detected by time-of-flight (TOF) mass spectrometry with fs time resolution. Two primary channels were distinguished by detecting Mn^+ from $\cdot Mn(CO)_5$ and Mn_2^+ from $Mn_2(CO)_9$ (Fig. 1). On the fs time scale, the primary steps could be isolated, as ionization is observed before fragmentation. The time scale for the cleavage provides a dynamical picture which is correlated with the nature of the M–M and M–CO bond potentials. We also relate the observed long-time behavior of the Mn_2^+ transient to the molecular rearrangement of the $Mn_2(CO)_9$ product to form a 'bridged' complex, a process studied in low-temperature matrices [21,22], and on the basis of

solution-phase studies thought to occur within a picosecond [15].

2. Experimental

The system for the generation of the fs laser pulses has been described in detail elsewhere [30]. Briefly, the 514.5 nm output of an Ar^+ laser (Coherent, 2.8–3.0 W) pumped a colliding-pulse mode-locked (CPM) ring dye laser to generate ultrafast laser pulses at $\lambda_{max} \approx 620$ nm with an 83 MHz repetition rate. The pulses from the CPM laser were amplified by a four-stage pulsed dye amplifier (PDA) pumped by a Nd:YAG laser (Spectra Physics DCR3) with a 20 Hz repetition rate. The amplified pulses were recompressed by prism pairs and split into two pulses for use as clocking pump and probe. The laser pulse for the pump was focused into a KD*P crystal (0.5 mm thick, type I) to generate the frequency-doubled output with a peak at 310 nm. The 620 nm probe was delayed with respect to the pump by a retro-reflector on a computer-controlled actuator. The pulse length of the final output of the laser system was ≈ 85 fs (fwhm) measured by autocorrelation. The spectral width was measured to be ≈ 7 nm for 620 nm. The laser pulses were recombined collinearly by a dichroic mirror and focused into the molecular beam chamber.

The molecular beam chamber had a two-stage pumping system divided by the ≈ 2 mm diameter skimmer, Fig. 2. The sample, $Mn_2(CO)_{10}$ (98% assay, Strem Chemicals), was heated to 45–50°C and seeded in He carrier gas with a typical backing pressure of ≈ 20 psi. The background pressure in the ionization TOF chamber was maintained at $\approx 3 \times 10^{-6}$ Torr when the nozzle (0.3 mm diameter) was open. The nozzle temperature was set at ≈ 5°C higher than the sample holder to prevent condensation inside the nozzle. Diethylaniline (DEA) was purchased from Aldrich (98% assay) and used without further purification.

The products following excitation of $Mn_2(CO)_{10}$ were ionized by the probe fs laser pulse. The ions formed were repelled, accelerated, and allowed to drift through the field-free region before being detected by micro-channel-plates (MCP). The TOF mass spectrum was taken using a transient digitizer

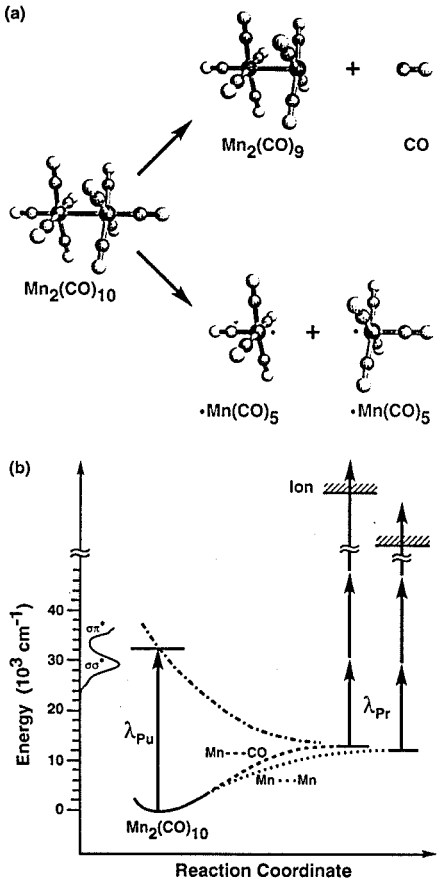

Fig. 1. (a) Molecular structures and bond cleavage in the two channels leading to $Mn_2(CO)_9$ and $\cdot Mn(CO)_5$. (b) Energetics of the scheme for probing the fragmentation dynamics in the two channels along the metal–metal (Mn–Mn) and the metal–ligand (Mn–CO) bond. The absorption spectrum shown here is taken in solution [13] and bond energies are from solution phase studies [13,18,19].

(LeCroy 8818A). The fs transient for a specific mass was obtained using a boxcar integrator (SR250) and monitoring the selected ion signal as a function of the delay time between the pump and probe laser pulses. Each data point was averaged for 3 laser

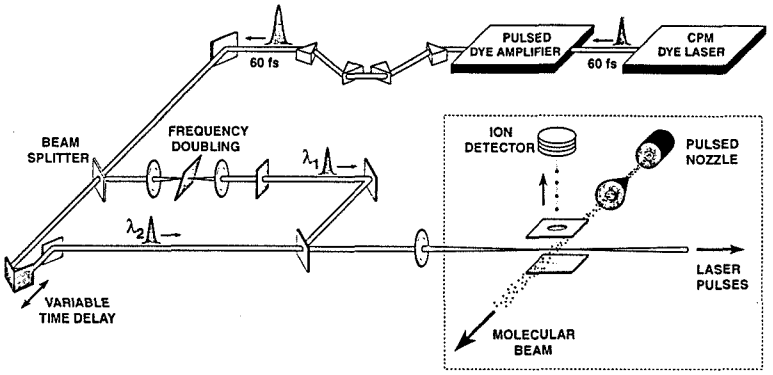

Fig. 2. The experimental setup, showing the generation of femtosecond laser pulses. The probe pulse (λ_2) is delayed with respect to the pump pulse (λ_1) by a computer-controlled actuator. The two pulses were made to travel collinearly and focused onto the molecular beam. Ions are detected in the time-of-flight mass spectrometer.

shots, and the transients were accumulated for over 100–300 scans to achieve a signal-to-noise ratio of at least 10–20.

3. Results and discussion

The TOF mass spectrum of $Mn_2(CO)_{10}$ taken with fs pulses at 310 nm is shown in Fig. 3. Two main peaks, Mn^+ and Mn_2^+, were observed, which are consistent with the mass spectra reported earlier [10,31]. Other species such as $Mn_2(CO)_{10}^+$, $\cdot Mn(CO)_5^+$, and $Mn_2(CO)_4^+$ could also be observed, but with weaker intensities. The distribution of ion fragmentation is known to depend on the wavelength and the intensity of laser pulses [31,32].

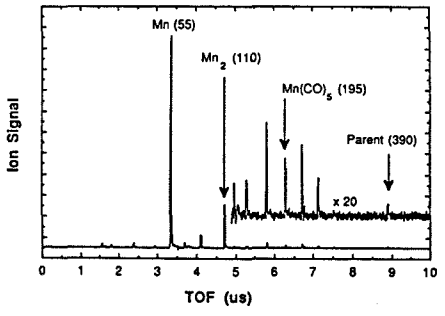

Fig. 3. The time-of-flight (TOF) mass spectrum of $Mn_2(CO)_{10}$ taken with femtosecond laser pulses at 310 nm.

A pump and probe intensity-dependence study was performed on the Mn^+ signal. A log–log plot of the Mn^+ signal versus the laser intensity gave a number close to unity for the pump laser and significantly larger than unity for the probe laser. This indicates that excitation by the pump laser is predominantly a one-photon absorption process, while ionization by the probe laser requires a multiphoton process, consistent with the scheme in Fig. 1. The multiphoton excitation by the probe laser involves dissociation and ionization, and the evaporation of all CO ligands in the process of probing is due to both processes [31,32], depending on the time scale and the fluence.

Transients for $Mn_2(CO)_{10}^+$, Mn_2^+, Mn^+ are shown with the fits in Fig. 4. Here, the pump and probe laser intensities were so weak that there was no ion signal due to either pump or probe laser alone. The Mn^+ and Mn_2^+ transients were taken at the pump intensity where the Mn^+ signal is linear with the pump laser intensity. For the $Mn_2(CO)_{10}^+$ transient, since the signal was so weak, the pump intensity was increased from that used for Mn^+ and Mn_2^+. The pump laser was polarized parallel to the TOF detec-

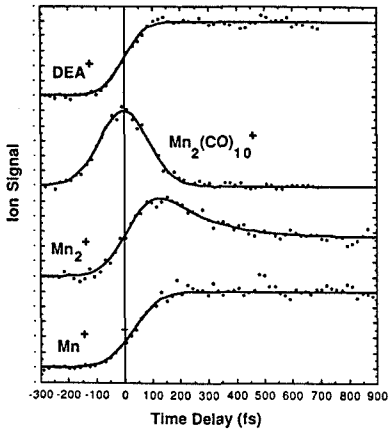

Fig. 4. Femtosecond transients of $Mn_2(CO)_{10}^+$, Mn_2^+, and Mn^+, and for calibration DEA^+. The fits are shown as solid lines. The solid vertical line indicates time-zero at which there is no delay between the pump and probe pulses. The Mn_2^+ transient was fit with a decay time of 160 fs to the asymptote.

tion axis, and the probe laser polarization was at 54.7° to that of the pump. This is not necessarily the magic angle [33]. If this was close to the magic angle, this setup gives transients which are not affected by the rotational motion of the fragment for which the recoil vector was initially aligned by the pump laser polarization [34].

The transient for DEA^+ in the molecular beam was taken with the exact same conditions and displayed in Fig. 4. Time-zero is defined as the middle of the rise of the DEA^+ transient. As expected, this corresponds to the peak of the $Mn_2(CO)_{10}^+$ transient. The transients for $Mn(CO)_5^+$ and $Mn_2(CO)_4^+$ were also recorded, and these are very similar to the $Mn_2(CO)_{10}^+$ transient, indicating their origin from the parent.

The Mn_2^+ transient shows an apparent peak shift of ≈ 100 fs, while the Mn^+ transient shows a shift to a plateau of ≈ 150 fs. More quantitative fits indicate that the initial rise in both Mn^+ and Mn_2^+ transients is similar to the calibration transient of DEA^+. The Mn^+ transient shows the initial rise to the plateau and the signal remains constant for more than ≈ 100 ps. Meanwhile, the Mn_2^+ transient displays the initial rise to the peak and a decay (≈ 160 fs) to an asymptotic level where it then remains constant for more than ≈ 100 ps.

The polarization anisotropy as a function of the delay time, $r(t)$, was also measured for both Mn^+ and Mn_2^+ transients. The $r(0)$ was nearly ≈ 0.4 for both ions, consistent with the initial transition involved being parallel to the molecular axis [34]. The $r(t)$ shows an exponential fit with a characteristic time of ≈ 700 fs for the Mn^+ transient and ≈ 100 fs for the Mn_2^+ transient. This large difference in the $r(t)$ for the two transients provides information about rotations in fragmentation as well as about changes in the transition moment due to rearrangement of the molecular structure, as discussed below.

3.1. Femtosecond mass spectrometry of the two channels

The transients obtained by mass detection of ions reflect the dynamics of the parent $Mn_2(CO)_{10}$ or the nascent $\cdot Mn(CO)_5$ and $Mn_2(CO)_9$ products. Fragmentation in the ion channel does not influence such measurements since fs resolution enables one to observe ionization prior to fragmentation [30]. The $Mn_2(CO)_{10}^+$ transient in Fig. 4 indicates an ultrashort lifetime of the excited parent molecule, which decays completely in less than ≈ 85 fs, our fs pulse width. The Mn^+ and Mn_2^+ transients do not show this fs decay component, and hence represent the dynamics of the nascent products, $\cdot Mn(CO)_5$ and $Mn_2(CO)_9$.

The Mn_2^+ transient arises from $Mn_2(CO)_9$ and not from the $\cdot Mn(CO)_5$ product; note that from the energetics in Fig. 1, the available energy is sufficient to decarbonylate one CO and at most two. The peak of the Mn_2^+ transient is shifted by ≈ 100 fs from the time-zero (Fig. 4), while the Mn^+ transient does not have any corresponding peak, indicating that it represents the dynamics of the other nascent product, $\cdot Mn(CO)_5$. This is consistent with the fragmentation and ionization pathways. First, neutral Mn_2 species, even if fragmented by the probe (or in free flight) to give an Mn^+ species, will display the same fs transient, whether detecting Mn^+ or Mn_2^+. This is not the case in our experiment, indicating that the Mn^+ and Mn_2^+ signals are from two different neutral channels. Second, a secondary pathway for an Mn species is in principle possible from a Mn_2 neutral

species. For example, the nascent vibrationally hot $Mn_2(CO)_9$ may dissociate into $\cdot Mn(CO)_5$ and $\cdot Mn(CO)_4$, and these species could be ionized to give the Mn^+ signal. However, the dissociation of vibrationally hot product requires IVR on the ps time scale. Therefore, the transients presented here reflect the dynamics of the neutral two channels (Fig. 1). This is consistent with previous photofragment spectroscopic studies [8,10].

The preference of Mn_2^+ over Mn^+ in probing the $Mn_2(CO)_9$ product can be understood on the basis of the strengthening of the M–M bond upon CO elimination. The strength of the M–M bond increases with CO elimination, thus reducing the M–M bond cleavage during probing. This also accounts for the formation of the bridged complex in the $Mn_2(CO)_9$ product. The Mn–Mn bond distance in $Mn_2(CO)_{10}$ is relatively long (≈ 3.0 Å) [26], and there is no evidence of bridging in $Mn_2(CO)_{10}$. There is, however, some experimental evidence for the formation of the bridged $Mn_2(CO)_9$ product upon UV excitation [21,22].

Finally, it should be emphasized that the absorption maximum found in solutions is at ≈ 500 nm for $Mn_2(CO)_9$ and ≈ 800 nm for $\cdot Mn(CO)_5$ [9], and accordingly the probe wavelength used here (620 nm) is between absorption maxima of the two fragments. If the probe wavelength is chosen in favor of one of these two absorptions, then the Mn^+/Mn_2^+ transients would also reflect such changes in the dynamics.

3.2. Metal–metal bond cleavage

The $\sigma \rightarrow \sigma^*$ transition of the Mn–Mn bond reduces the bond order to zero and therefore leads to the repulsive dissociation of $Mn_2(CO)_{10}$ along this bond. But the electronic states of $Mn_2(CO)_{10}$ are complex, and the upper electronic states involved in the optical excitation and dissociation are not yet totally certain [3,4]. According to a simple state-correlation diagram, the optically allowed singlet $^1(\sigma\sigma^*)$ state does not correlate to the ground state of two $\cdot Mn(CO)_5$ products. The lower-lying triplet $^3(\sigma\sigma^*)$ state to which an optical transition is spin-forbidden, in a zeroth-order approximation, could make such a correlation [3,27]. Therefore, dissociation along the M–M bond occurs on the $^3(\sigma\sigma^*)$ state accessed either through the intersystem crossing (ISC) from the optically prepared $^1(\sigma\sigma^*)$ state or by the direct excitation due to strong spin–orbit coupling.

The time shift observed for the Mn^+ signal is measured to be ≈ 40 fs halfway up on the rise (Fig. 4). This observation of a fs shift excludes the possibility that the cleavage is due to predissociation. It also excludes ground-state dissociation since the time is too short for internal conversion and IVR to be effective. Because of its impulsive nature, we conclude that the mechanism of the cleavage must involve a dissociative, repulsive potential-energy surface, accessed directly (i.e. $^3\sigma\sigma^*$) or reached by very large non-adiabatic ISC ($^1\sigma\sigma^*/^3\sigma\sigma^*$). It is interesting to note that, in the first quantum simulation [28], Manz and co-workers have shown that direct dissociation of $HCo(CO)_4$ to H and $Co(CO)_4$ takes 20 fs while the indirect ISC takes 50 fs.

For fragmentation on the repulsive surface, the shift represents the time for the two fragments to move beyond their force field of interaction. In analogy with direct dissociation reactions [35], we can deduce the nature of the repulsive potential and its interaction length from knowledge of the bond energy, the available energy and the reduced mass. The Mn–Mn bond energy in the gas phase is still not certain, and different values ranging from 22 to 42 kcal/mol have been reported [17]. Assuming a value of D(Mn–Mn) ≈ 36 kcal/mol [18], which has been determined in solution, the available energy is then ≈ 56 kcal/mol at the pump wavelength of ≈ 310 nm. If all the available energy is transformed to kinetic motion of the fragments, the upper limit for the recoil velocity is ≈ 0.022 Å/fs. Accordingly, for ≈ 40 fs of delay time, the separation between centers of masses of the two $\cdot Mn(CO)_5$ fragments must be ≈ 0.9 Å from the equilibrium distance.

For a one-dimensional repulsive potential, $V(R) = E \exp[-(R - R_0)/L]$, for two fragments at separation (R), the length parameter (L) can be determined from a simple relationship relating the time shift to the recoil velocity and total energy [30]. For the Mn–Mn cleavage we obtained $L \approx 0.2$ Å, indicating a very steep potential for repulsion in the σ^* charge density. From experiments carried out in the gas phase and in solution [3,8], the $\cdot Mn(CO)_5$ product has actually been found to be vibrationally hot,

indicating that L could be even less than 0.2 Å. Furthermore, the reaction coordinate for the Mn–Mn bond cleavage cannot be simply described as the elongation of the distance between two 'frozen' fragments. It should include other vibrational motions (e.g. those involving CO ligands) as the ultrafast repulsion between the metal atoms changes with time. A more accurate determination of the Mn–Mn bond energy along with the information about the time delay and internal energy distributions at different energies would be very helpful for a complete picture of the molecular dynamics. Theoretical studies now should be of interest.

3.3. Metal–ligand bond cleavage

As mentioned above, the transient for Mn_2^+ probing can be simulated with a smaller time shift of ≈ 20 fs and a decay of ≈ 160 fs. This fs and very short delay observed for the Mn_2 species again excludes a predissociative or ground-state reaction mechanism. If the dynamics of this metal–ligand cleavage involves an initial bound $\sigma\sigma^*$ transition, then a non-adiabatic but strong crossing to a Mn–CO repulsive state must be involved. Waldman et al. [15] suggested that following the excitation of the molecule to the $(\sigma\sigma^*)$ state a non-adiabatic coupling to other electronic states will lead to cleavage of the Mn–CO bond. The direct transition to the $\pi^*(CO)$ orbital can also lead to rupture of the Mn–CO bond [13]. Actually, as shown in Fig. 1, at the pump wavelength of 310 nm, the transitions to both σ^* and $\pi^*(CO)$ are optically accessible. The fs appearance of the Mn_2^+ signal supports the mechanism that the Mn–CO bond cleavage *effectively* occurs on a repulsive, dissociative potential energy surface along the Mn–CO reaction coordinate, Fig. 5. It is interesting to note that this type of decarbonylation has been studied theoretically by Manz and co-workers for e.g. in $H_2Fe(CO)_4$ and found to occur in ≈ 100 fs [29].

The Mn–CO cleavage is faster than Mn–Mn cleavage and this is consistent with the kinematics. For the same amount of available energy, the recoil velocity for the Mn–CO bond dissociation is expected to be about 2 times higher than that for the Mn–Mn bond cleavage. This is because the reduced mass for the former is ≈ 4 times smaller than that

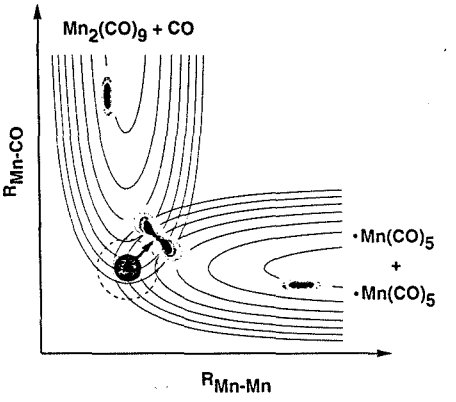

Fig. 5. Proposed scheme for the dynamics of bond cleavage in $Mn_2(CO)_{10}$. The direct excitation to the dissociative potential energy surfaces lead to fs bond ruptures along the M–M and M–L reaction coordinates. Both the diabatic and adiabatic (note the dotted circle) surfaces are shown, along with the wave packet motion along the two coordinates.

for the latter. Hence, a time-shift in the Mn_2^+ transient is expected to be ≈ 2 times less than that in the Mn^+ transient if the dissociative potential energy curves for both channels are of the similar nature. This simple picture is entirely consistent with our findings. In solution the Mn–CO bond energy is estimated to be ≈ 38 kcal/mol [19], which is comparable to the value of ≈ 36 kcal/mol for the Mn–Mn bond energy [18]. For the available energy of ≈ 54 kcal/mol, an upper limit for the recoil velocity is ≈ 0.042 Å/fs for Mn–CO. This is about twice the Mn–Mn bond recoil velocity. This again is consistent with the experimentally measured time shift of ≈ 20 fs for the Mn–CO bond cleavage compared to the ≈ 40 fs for the Mn–Mn bond.

The Mn_2^+ transient shows an initial rise to a maximum and a decay to an asymptote with a characteristic time constant of ≈ 160 fs (see Fig. 4). This decay reflects the change of nascent $Mn_2(CO)_9$ in the first few hundred fs. We now consider two pathways, one of which is the molecular rearrangement to form a bridged $Mn_2(CO)_9$ and the other is a further dissociation of vibrationally hot $Mn_2(CO)_9$

product. Both of these product channels have been studied by transient IR in solutions and matrices [11,21,22]. The dissociation process is less likely though because the time constant is too short for the vibrationally hot $Mn_2(CO)_9$ product to undergo statistical energy redistribution. The other pathway, i.e. the ligand bridging, is consistent with this time scale since molecular rearrangement occurs on a very short time scale, leading to a significant change in the ionization cross section. In this case, our measured decay of 160 fs for bridging is consistent with the recent finding by Ruhman's group that this process occurs on $<$ 1 ps time scale [15].

The fast decay ($\approx$ 100 fs) in the anisotropy $r(t)$ observed for the Mn_2^+ signal is also consistent with the bridging of $Mn_2(CO)_9$. As the molecule rearranges, the cylindrical symmetry is reduced, and this leads to a decrease in the polarization anisotropy with a time constant comparable to that of intramolecular rearrangement. For $r(t)$ of the Mn^+ signal we observed a longer decay ($\approx$ 700 fs) and this could reflect the rotational dynamics of the $\cdot Mn(CO)_5$ fragment. Because these $r(t)$ measurements involve multiphoton ionization [33], these results will be analyzed more quantitatively in further studies.

4. Conclusions

In this contribution, we present our first direct measurement of the dynamics of M–M and M–L bond cleavage using fs time resolution and TOF mass spectrometry. Both bond cleavages in $Mn_2(CO)_{10}$ occur on the fs time scale, indicating that previous estimate of the upper limit (2–3 ps) from measurements of the anisotropy parameter in the gas phase is about two orders of magnitude longer than obtained here. The rotational period is too slow to be used as an internal clock for this heavy molecule!

The fs cleavage dynamics excludes ground state dissociation as the time scale is much shorter than most vibrational motions needed to complete internal conversion and IVR. It represents direct dissociation on repulsive surfaces involving both the M–M and M–L charge distributions. Although the initial transition is assigned as $\sigma\sigma^*$, the dynamics is controlled by the reduction in bond order introduced by the repulsion in these coordinates, surprisingly leading to a slower M–M than M–L bond breakage. We deduce a repulsive length of $\approx$ 0.2 Å (upper limit $\approx$ 0.9 Å).

We account for the disparity in the time scale for M–M and M–L breakage on the basis of simple kinematics. The reduced mass in the Mn–CO cleavage is $\approx$ 4 times smaller than that of the Mn–Mn and, hence, the CO product separates apart $\approx$ 2 times faster than does $\cdot Mn(CO)_5$ product. Unlike the Mn-species, which builds up and live for at least 100 ps, the Mn_2-species decays in $\approx$ 160 fs. We relate this decay to the bridging of the nascent $Mn_2(CO)_9$ product.

There are several implications of these new findings. First, the measurements in solutions, which in many cases showed a longer time scale, must include possible caging by the solvent and/or vibrational cooling on the time scale of the experiment. The M–L may appear slower than M–M dynamics in solutions simply because of the easier kinematics of caging for the former. Second, the potential energy surface is not predissociative, as previously inferred, since we do not observe ps dynamics for the isolated reaction. Finally, while the bonding characteristics in these very interesting systems may involve a simple description (e.g. $\sigma\sigma^*$) of 'bound' states, the dynamics clearly shows the strong repulsive nature of the force. We consider this as evidence of the strong interactions leading to the adiabatic picture in Fig. 5.

Future work will include studies of the energy dependence, the time-dependent anisotropy, the detection of different fragments, and the comparison with other systems. Preliminary studies of $Re_2(CO)_{10}$ and of kinetic energy time-of-flight (KETOF) have been made and will be published later. Molecular dynamics calculations will also be of interest.

Acknowledgements

This work was supported by a grant from the National Science Foundation. We wish to thank Professor J. Manz for stimulating and helpful correspondence, and Professor S. Ruhman for communicating his work.

References

[1] G.L. Geoffroy, M.S. Wrighton, Organometallic photochemistry (Academic Press, New York, 1979).
[2] J. Chaiken, ed., Laser chemistry of organometallics (Am. Chem. Soc., Washington, 1993).
[3] T.J. Meyer and J.V. Caspar, Chem. Rev. 85 (1985) 187, and references therein.
[4] W.E. Hollingsworth and V. Vaida, J. Phys. Chem. 90 (1986) 1235.
[5] R.A. Levenson and H.B. Gray, J. Am. Chem. Soc. 97 (1975) 6042.
[6] M.S. Wrighton and D.S. Ginley, J. Am. Chem. Soc. 97 (1975) 2065.
[7] J.L. Hughey IV, C.R. Bock and T.J. Meyer, J. Am. Chem. Soc. 97 (1975) 4440.
[8] A. Freedman and R. Bersohn, J. Am. Chem. Soc. 100 (1978) 4116.
[9] L.J. Rothberg, N.J. Cooper, K.S. Peters and V. Vaida, J. Am. Chem. Soc. 104 (1982) 3536.
[10] D.G. Leopold and V. Vaida, J. Am. Chem. Soc. 106 (1984) 3720.
[11] T.A. Seder, S.P. Church and E. Weitz, J. Am. Chem. Soc. 108 (1986) 7518.
[12] R.L. Whetten, K.-J. Fu and E.R. Grant, J. Chem. Phys. 79 (1983) 4899.
[13] J.Z. Zhang and C.B. Harris, J. Chem. Phys. 95 (1991) 4024.
[14] A.G. Joly and K.A. Nelson, Chem. Phys. 152 (1991) 69.
[15] A. Waldman, S. Ruhman, S. Shaik and G.N. Sastry, Chem. Phys. Letters 230 (1994) 110.
[16] B.J. Schwartz, J.C. King, J.Z. Zhang and C.B. Harris, Chem. Phys. Letters 203 (1993) 503.
[17] J.A.M. Simões, J.C. Schultz and J.L. Beauchamp, Organometallics 4 (1985) 1238, and references therein.
[18] J.L. Hughey IV, C.P. Anderson and T.J. Meyer, J. Organomet. Chem. 125 (1977) c49.
[19] G.P. Smith, Polyhedron 7 (1988) 1605.
[20] A. Fox and A. Pöe, J. Am. Chem. Soc. 102 (1980) 2497.
[21] A.F. Hepp and M.S. Wrighton, J. Am. Chem. Soc. 105 (1983) 5934.
[22] I.R. Dunkin, P. Härter and C.J. Shields, J. Am. Chem. Soc. 106 (1984) 7248.
[23] J.D. Simon and X. Xie, J. Phys. Chem. 90 (1986) 6751.
[24] B.O. Roos, in: Proceeding of new challenges in computational quantum chemistry, eds. R. Broer, P.J.C. Aerts and P.S. Bagus, Groningen, Holland (1994).
[25] B. Persson, B.O. Roos and K. Pierloot, J. Chem. Phys. 101 (1994) 6810, and references therein.
[26] A. Veillard and M.-M. Rohmer, Intern. J. Quantum Chem. 42 (1992) 965.
[27] A. Veillard and A. Dedieu, Nouveau J. Chimie 7 (1983) 683.
[28] J. Manz, B. Reischl, T. Schröder, F. Seyl and B. Warmuth, Chem. Phys. Letters 198 (1992) 483; C. Daniel, M.-C. Heitz, J. Manz and C. Ribbing, J. Chem. Phys., in press.
[29] C. Daniel, R. de Vivie-Riedle, M.-C. Heitz, J. Manz and P. Saalfrank, Intern. J. Quantum Chem., in press; 52 (1994) 71.
[30] A.H. Zewail, Femtochemistry – ultrafast dynamics of the chemical bond (World Scientific, Singapore, 1994), and references therein.
[31] S. Leutwyler and U. Even, Chem. Phys. Letters 84 (1981) 188.
[32] J. Opitz and D. Bruch, Intern. J. Mass Spectrom. Ion. Processes 124 (1993) 157.
[33] P.M. Felker and A.H. Zewail, in: Jet spectroscopy and molecular dynamics, eds. M. Hollas and D. Phillips (Chapman and Hall/Blackie, London/London, 1994).
[34] A.H. Zewail, J. Chem. Soc. Faraday Trans. II 85 (1989) 1221.
[35] M.J. Rosker, M. Dantus and A.H. Zewail, J. Chem. Phys. 89 (1988) 6113.

Appendix F

Femtosecond Real-Time Probing of Reactions. XII. Vectorial Dynamics of Transition States

Femtosecond Real-Time Probing of Reactions. 12. Vectorial Dynamics of Transition States

T. Baumert,† S. Pedersen, and A. H. Zewail*

Arthur Amos Noyes Laboratory of Chemical Physics,‡ California Institute of Technology, Pasadena, California 91125

Received: September 9, 1993•

Femtosecond time-resolved techniques with KETOF (kinetic energy time-of-flight) detection in a molecular beam are developed for studies of the vectorial dynamics of transition states. Application to the dissociation reaction of IHgI is presented. For this system, the complex $[I\cdots Hg\cdots I]^{\ddagger *}$ is unstable and, through the symmetric and asymmetric stretch motions, yields different product fragments: $[I\cdots Hg\cdots I]^{\ddagger *} \rightarrow HgI(X^2\Sigma^+) + I(^2P_{3/2})$ [or $I^*(^2P_{1/2})$] (1a); $[I\cdots Hg\cdots I]^{\ddagger *} \rightarrow Hg(^1S_0) + I(^2P_{3/2}) + I(^2P_{3/2})$ [or $I^*(^2P_{1/2})$] (1b), lead to different kinetic energy distributions in the products. It is shown that the motion of the wave packet in the transition-state region can be observed by MPI mass detection; the transient time ranges from 120 to 300 fs depending on the available energy. With polarized pulses, the vectorial properties (transition moments alignment relative to recoil direction) are studied for fragment separations on the femtosecond time scale. The results indicate the nature of the structure (symmetry properties) and the correlation to final products. For 311-nm excitation, no evidence of crossing between the I and I* potentials is found at the internuclear separations studied. (Results for 287-nm excitation are also presented.) Molecular dynamics simulations and studies by laser-induced fluorescence support these findings.

I. Introduction

With polarized femtosecond excitation and analyzed femtosecond detection, using laser-induced fluorescence (LIF) or multiphoton ionization mass spectrometry (MPI-MS), one gains the ability to examine the vectorial properties of molecular dynamics in real time.[1,2] For nonreactive systems, the change in the time-dependent alignment gives the molecular structure.[3,4] For reactive systems, it provides new information on the evolution[1,2,5-7] of the angular momenta and the anisotropic decay of the fragment orientation.

In this paper, in the series, we develop kinetic energy time-of-flight (KETOF) as a method for obtaining the vectorial properties of transition states on the femtosecond time scale. As with time-of-flight photofragment translation spectroscopy, we examine the polarization properties (see Appendix for original references and also refs 8–10 for reviews) of the velocity distribution anisotropy, but now at femtosecond resolution of the dynamics. The mass selectivity enables the separate observation of parent and fragment dynamics. In general, ionization of the initial parent is not observed in the mass spectrum if the reaction time is ultrashort and competition of dissociation with ionization is efficient. This problem is circumvented by femtosecond pulses as the system can be "frozen out" prior to fragmentation, and the ladder switching[11] to product ionization at long times can be controlled. Examples can be found in the studies of elementary reactions (e.g., Na_2,[12] CH_3I,[13] and OClO[14]) and of clusters (e.g., Na_n[15] and $(NH_3)_n$[16]). A single-pulse femtosecond experiment on a molecular beam with KETOF detection, studying MPI-induced fragmentation processes in Na_2,[17] was reported, but no femtosecond time-resolved KETOF experiments have been reported up to now.

The application made here of the femtosecond/KETOF method involves a study of the dissociation reaction of IHgI:

$$IHgI + h\nu \rightarrow [I\cdots Hg\cdots I]^{\ddagger *} \rightarrow HgI(X^2\Sigma^+) + I(^2P_{3/2}) \quad (2a)$$

For this product channel the wave packet motion ultimately involves the asymmetric stretch mode of the complex. Both products are in their ground state. Energetically, at the wavelengths used, the iodine atoms can also be formed in the excited state

$$IHgI + h\nu \rightarrow [I\cdots Hg\cdots I]^{\ddagger *} \rightarrow HgI(X^2\Sigma^+) + I^*(^2P_{1/2}) \quad (2b)$$

and this channel also involves the asymmetric stretch motion. The two surfaces leading to the I and I* asymptotes are separated by the spin–orbit splitting of free iodine atoms (7600 cm^{-1}) at long internuclear distances; the splitting is less at the complex geometry near the Franck–Condon region, as discussed below. One important question addressed here is the nature of the two surfaces and the crossing (or lack thereof) between them.

If the complex is prepared above the limit of total dissociation, then it is possible to produce the three atomic fragments:

$$IHgI + h\nu \rightarrow [I\cdots Hg\cdots I]^{\ddagger *} \rightarrow I(^2P_{3/2}) + Hg(^1S_0) + I(^2P_{3/2}) \quad (2c)$$

The nuclear motions in this case involve the symmetric stretch mode.

In these channels described above the fragment atom (or diatom) has a different kinetic energy in each case, and resolution of the kinetic energy in the velocity distribution anisotropy gives the vectorial correlation corresponding to the channel of interest. The scalar part (kinetic energy release) of the dissociation is studied here with the transient time measured as the wave packet leaves the transition-state region of the complex. The vectorial part (transition moment correlation with fragmentation) of the dissociation process is examined by the change in the velocity distributions at times between 0 and 500 fs. The approach adds a useful dimension to femtosecond transition-state spectroscopy (FTS) and may be applied to the different detection schemes of

† Deutsche Forschungsgemeinschaft (DFG) postdoctoral fellow.
‡ Contribution No. 8847.
• Abstract published in *Advance ACS Abstracts*, November 1, 1993.

0022-3654/93/2097-12447$04.00/0

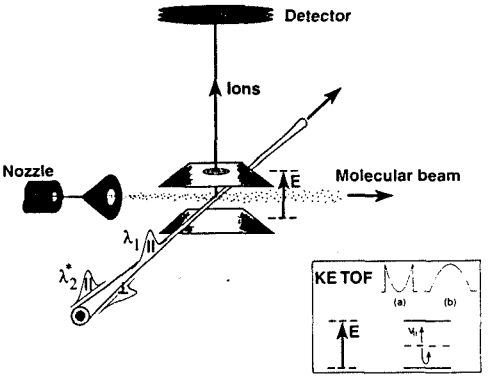

Figure 1. Schematic of the experimental approach utilizing two polarized femtosecond pulses and a TOF mass spectrometer. The femtosecond lasers, the molecular beam, and the TOF axis are mutually perpendicular. The TOF axis is defined by the electric field E. For the experiments described here, the pump laser (λ_1) polarization was kept parallel to the TOF axis, whereas the probe laser (λ_2^*) polarization was either parallel or perpendicular with respect to the pump. On the left (a) a distribution resulting from a pure parallel transition is indicated, whereas the distribution to the right (b) resembles a pure perpendicular transition (see text), if the pump laser polarization is parallel to the TOF axis.

LIF,[2] absorption,[18] MPI-TOF,[12,13,16] photoelectron detection[15] using ZEKE photoelectron spectroscopy,[19] and stimulated emission pumping.[20]

The outline of the paper is as follows: In section II, a discussion of the approach is given. The experimental description is given in section III, followed by the results in section IV. The discussion in section V focuses on the femtosecond dynamics and the reaction path, with reference to other findings from molecular dynamics and laser-induced fluorescence studies. The conclusions are given in section VI, followed by an Appendix detailing anisotropy and rotational alignment in pump–probe experiments.

II. Femtosecond/KETOF Method

In the studies of reaction dynamics on the femtosecond time scale, the two attributes of TOF,[21] the mass selectivity and the possibility of measuring fragment energies, add a unique dimension. Not only can the decay of the parent complex be monitored directly, but also the delay of the fragments. By measuring the temporal evolution of fragments with different kinetic energy, different fragmentation channels leading to the same fragment can, in principle, be distinguished. As the TOF axis is well-defined, rotating the pump laser polarization, with respect to the TOF axis, and analyzing the resulting KETOF spectra gives the vectorial properties, such as the alignment of a transition moment with respect to the excitation polarization. Rotating the probe laser polarization with respect to the pump laser polarization can then finally deliver information on the alignment of the fragment transition moment in a particular dissociation process. In the following, we will briefly describe the basic idea and relate its application to the case under study.

In this application of a TOF spectrometer, ions are created by MPI with femtosecond laser pulses. The interaction region is in the electric field of a parallel plate capacitor with a ringlike aperture in the direction of the detector; the aperture is covered with a mesh in order to ensure a homogeneous electric field in the interaction region. The direction of this electric field thus defines our TOF axis (Figure 1). After leaving this extraction region, the ions are further accelerated and are detected with a set of multichannel plates after they have passed the field-free drift region. Solving the classical equations of motion yields the result that the flight time T (for all three regions) is proportional to the square root of the mass m of the ionized particles.[21]

In terms of mass resolution, a well-defined initial spatial position and a well-defined time zero for creating the ions is important. The starting spatial distribution is determined by the diameter of the focused laser beam (on the order of 50–100 μm), whereas the starting time is determined by the time duration of the laser pulse. Using femtosecond laser pulses, and femtosecond or picosecond pump–probe delay times, the TOF broadening due to poorly defined starting times is negligible, as the flight time is on the order of microseconds. The mass resolution of our TOF spectrometer is about 1:150.

The velocity distribution due to fragmentation causes a spread around the central time-of-flight, T. The spread in the time-of-flight for the ionized fragments is a linear function of their velocity projection, $v_\parallel$, onto the TOF axis (see below). Consider two identical ions formed at the same initial position r_1 with equal but oppositely directed velocities ($\pm v_\parallel$) along the TOF axis (ion 1 travels up). Ion 2 is decelerated by the electric field E of the extraction region, stopping at a position r_2 directly below r_1. It is then accelerated, returning to r_1 with its original speed, in the same time it took to decelerate to r_2. Subsequently, the motion of ion 2 is identical to that of ion 1, which it now continues to lag by the "turn-around" time. Hence, t, the position relative to the central time T in the TOF spectrum corresponding to $v_\parallel$ is given by (from $F = ma = qE$)

$$t = -(mv_\parallel/qE) \tag{3}$$

The total time-of-flight, $T + t$, is a linear function of the velocity projection, $v_\parallel$. For a fixed translational energy release (recoil speed v_0) the maximum time spread for a fragment ion becomes

$$\Delta t = 2(mv_0/qE) \tag{4}$$

Therefore, the kinetic energy of the ion ($^1/_2mv_0^2$) can be written as

$$E_{kin} = q^2E^2(\Delta t)^2/8m \tag{5}$$

In the type of experiment considered, two fragments are formed in the dissociation of the pump excited molecule. Because of the excitation distribution, determined by the pump polarization and the direction of the transition moment, there is a distribution in t, as discussed below.

The total energy in the center-of-mass frame (CM) is conserved, implying that[22]

$$E_{avl} = E_{int}^P + h\nu_{pu} - D_0^0 = E_{int} + E_t \tag{6}$$

where E_{avl} is the energy available to be partitioned among internal and translational degrees of freedom of the recoiling fragments, E_{int}^P is the thermal internal energy of the parent molecule, $h\nu_{pu}$ is the pump energy, D_0^0 is the dissociation energy from the ground-state parent to the ground-state fragments, E_{int} is the total internal excitation energy of the two fragments, and E_t is the CM translational energy. In the CM frame, the two fragments share the total available translational energy, which means that

$$E_{kin1} = \frac{m_2}{m_1}E_{kin2} = E_t\left[1 + \frac{m_1}{m_2}\right]^{-1} \tag{7}$$

Consider the probing of a *free* fragment. Due to the small photon momentum, the translational energy available to the ion and ejected electron is shared unequally in a manner similar to eq 7. If, for example, a 100 amu fragment is ionized, leaving 5000 cm^{-1} available as translational energy, then the change in the fragment velocity is <3 m s^{-1}, while the electron velocity is $\sim 5 \times 10^5$ m s^{-1}. As the neutral fragment velocity in the CM frame is typically of order 10^3 m s^{-1}, it is practically unaltered by probing to ionization. Hence, the translational energy, E_t, of the parent dissociation can be deduced from the velocity profiles of the probe ionized fragments.

In the transition state a probe transition moment, $\mu_2(t)$, may

be defined. The orientation of this transition moment depends on the anisotropic distribution created by the pump pulse as well as the subsequent evolution of the excited complex in the transition state. Using different orientations of the pump (ϵ_{pu}) and probe (ϵ_{pr}) polarizations with respect to the TOF axis, different velocity profiles result, each of which characterizes distinct features (correlations) of the anisotropic distribution in the transition state. From this, one may deduce the nature of the pump transition (parallel *vs* perpendicular) and of the probe transition in the evolution of the transition state. In addition, it is possible to calculate the translational energy release. In the Appendix, we discuss these issues with focus on the anisotropic fragment distribution involved in pump–probe experiments. The velocity profile for free fragment probing is parabolic, characterized by an effective anisotropy parameter, β_{eff} (eq A11), which may differ from the anisotropy parameter, β, associated with the pump alone process (eq A3).

For illustration, we consider a specific example (see Figure 12). Suppose the pump pulse excites molecules that dissociate fast with respect to rotation and the parent transition is parallel, *i.e.*, the transition moment is parallel to the internuclear axis. In this case, we have $\chi_0(t) = 0°$ (see Appendix) and the pump creates a $\cos^2\theta$, dumbbell-shaped distribution. For the case when, in the transition state, the transition moment for probing is aligned along the direction of the internuclear axis of the complex $\mu_2 \| \mathbf{r}(t)$ (the direction $\mathbf{r}(t)$ is along the final recoil direction for a nonrotating molecule), the situation is easy to picture. If the probe is parallel to the pump ($\epsilon_{pr} \| \epsilon_{pu}$), then the distribution created by the pump pulse will be enhanced, yielding a maximum probability for the probed fragments to recoil along the pump polarization direction: $\theta = 0°$ or 180°. If, on the other hand, the probe is perpendicular to the pump ($\epsilon_{pr} \perp \epsilon_{pu}$), then the distribution is greatly reduced in magnitude and also altered. Consider next a different process in which the parent transition is perpendicular (see Figure 12). Here $\chi_0(t) = 90°$ and the pump excitation yields a $\sin^2\theta$, toroidal angular distribution of the fragments. Let us suppose that the transition moment, μ_2, in the transition state is still along the fragment recoil direction. If the probe is now parallel to the pump, then few fragments will be ionized by the probe, while if the probe is perpendicular to the pump, the velocity distribution created by the pump will be enhanced and carried over to the ionized fragments (ion fragmentation is faster than rotation). These distributions which change in shape with polarization thus reflect the correlation and symmetry; they are discussed in the Appendix.

III. Experimental Section

The femtosecond laser apparatus has been described in detail previously[23] and is discussed only briefly here. Femtosecond pulses were generated from a colliding pulse mode-locked ring dye laser (CPM) and amplified by a Nd:YAG-pumped pulsed dye amplifier (PDA). The recompressed output pulses had an (unattenuated) energy of 0.2–0.3 mJ at a repetition rate of 20 Hz. The 311 nm (fwhm = 5 nm) pump wavelength was generated by frequency-doubling a part of the PDA output in a 0.2-mm-thick KDP crystal. The 287-nm pump was generated by frequency mixing part of the PDA output at 622 nm with a residual part of the Nd:YAG output at 532 nm in a 0.5-mm-thick KD*P crystal. For the probe MPI we used the remaining output of the PDA (622 nm, fwhm = 13 nm).

The pump and probe beams, with proper attenuation and parallel or perpendicular polarization, were delayed in time relative to one another in a Michelson interferometer and were then recombined collinearly and focused onto the IHgI molecular beam. Before entering the molecular beam, we routinely recorded autocorrelations of the probe (fwhm ~ 60 fs sech^2). Cross-correlations were derived by convoluting a Gaussian cross-correlation (100 fs) with the molecular response function of I_2 in a 622-nm excitation and 311-nm probe experiment, where the fluorescence at 340 nm was recorded as a function of the pump–probe delay time.[24]

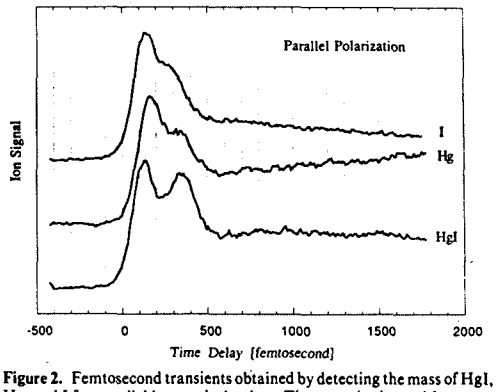

Figure 2. Femtosecond transients obtained by detecting the mass of HgI, Hg, and I for parallel laser polarization. Time zero is given with respect to half the rise of the parent IHgI.

The molecular beam consisted of an oven with a nozzle diameter of 0.3 mm. The oven was heated to 445 K (measured at the nozzle). MPI femtosecond experiments on the skimmed molecular beam were carried out in a differentially-pumped ionization chamber about 12 cm downstream from the nozzle. The TOF spectrometer was used either in its mass resolution mode or in its kinetic energy resolution mode. The molecular beam, the lasers, and the TOF detection axes were mutually perpendicular. For the set of experiments described here, the pump laser polarization was kept fixed and parallel to the TOF axis. A sketch of the experimental setup is shown in Figure 1.

The sample was 99.999% HgI_2 (Aldrich) containing the natural isotope distribution of Hg (196–204 amu). This resulted in a time-of-flight broadening on the HgI_2 parent and the HgI and Hg fragments. Therefore, the KETOF technique was applied to the iodine mass; for the other masses isotopically pure samples are needed.

Two types of data collection were used: For the transients, a boxcar gate was set to the mass under investigation, and the (femtosecond) delay line was scanned until a satisfactory signal-to-noise level on the transients was achieved. The KETOF transients on the fragment iodine atom were taken by setting the boxcar gate to different parts of the kinetic energy distribution. The TOF spectra were obtained by setting the pump–probe delay at different fixed positions and averaging the mass spectra over 1500 laser shots with a transient digitizer (10-ns channel resolution).

IV. Results

In Figure 2 the femtosecond transients for the HgI, Hg, and I are shown for parallel polarization of pump (λ_1) and probe (λ_2*) lasers. Time zero for each of these transients is shown with respect to half of the rise time of the HgI_2 parent. The parent mass gives a multiexponential decay which will be discussed in another publication[25] that carefully considers the complete decay (linear and nonlinear behavior) at long times. The measured time shifts, with respect to half the rise of the parent, when monitoring the transition state on different mass fragments are 47 ± 15 fs for HgI, 61 ± 15 fs for I, and 75 ± 15 fs for Hg. (The influence of saturation on the rise time of transients will also be discussed in ref 25.) The time shifts indicate that the initial motion of the wave packet to the transition state from the Franck–Condon region takes ~50 fs. This is consistent with the measured decay on the parent ion signal, as discussed below.

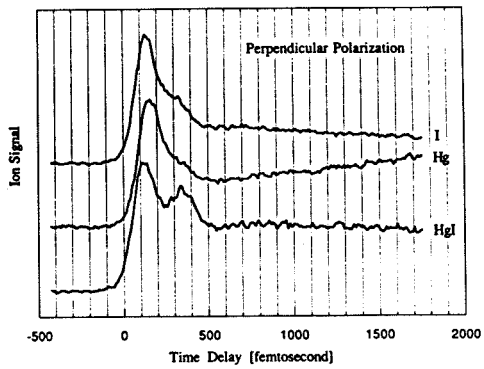

Figure 3. Femtosecond transients obtained by detecting the mass of HgI, Hg, and I for perpendicular polarization. Note the decrease of the second component around 350 fs with respect to the first component, in comparison to parallel laser polarization (Figure 2).

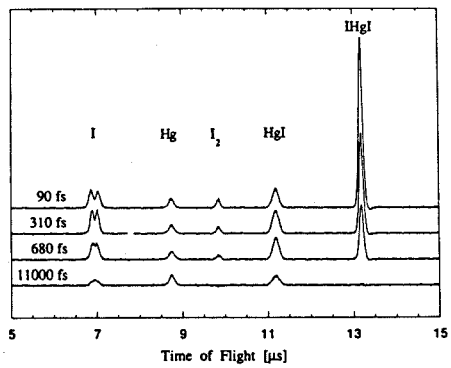

Figure 4. Complete TOF mass spectrum at different time delays, showing the parent IHgI and the nascent fragments.

The transients on all three fragment masses show a double-peak structure within the first 500 fs. We checked the asymptotic behavior of these three transients up to 100 ps: the I transient and HgI transients reach a constant asymptotic value, while the Hg transient increases over several picoseconds. In order to obtain more insight into this behavior discussed in ref 25, we performed careful pump and probe intensity studies on all masses. After 500 fs, the transients in Figure 2 are dominated by multiphoton dynamics. The early time behavior is the one-photon excitation dynamics to the repulsive surface leading to reactions 1 and 2, and our focus here is on these one-photon dynamics to the repulsive continuum (we shall refer to it as the A-continuum). Of particular interest is the early-time behavior of the fragments, their alignment, and their kinetic energy release.

For comparison, in Figure 3 transients on the same masses are shown but now with perpendicular polarization of probe (λ_2*) versus pump (λ_1). Note that the pump polarization for all experiments described here was kept fixed and parallel to the TOF axis. Special care was taken to ensure the same energies in the pump and probe lasers for the two polarizations used. The difference to notice here is that for all transients the second peak structure in the early-time behavior is enhanced for parallel polarization (Figure 2) in comparison to perpendicular polarization (Figure 3).

In Figure 4, TOF spectra are shown for different λ_1–λ_2* delay times: 90 fs is close to the first structure of the transients in Figure 2 and 310 fs is close to the second structure, whereas 680 and 11 000 fs belong to the asymptotic part of the transients. The

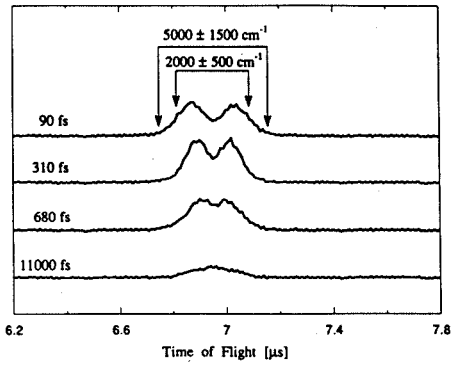

Figure 5. KETOF distribution of I at different time delays. The arrows indicate the kinetic energy release of I associated with the width of the distribution.

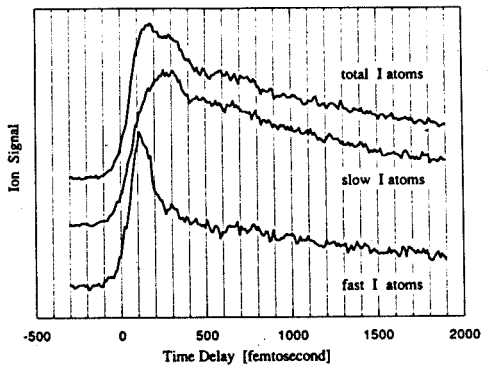

Figure 6. Femtosecond transients detected on the I mass, but with different kinetic energies.

TOF spectra are not normalized; only the time-independent background was subtracted. The decay of the HgI_2 parent and of the I_2 fragment as well as the asymptotic values for the HgI, Hg, and I fragments is clear. An interesting change in the KETOF distribution, with respect to the time delay between pump and probe pulses, is observed on the I fragment.

Figure 5 shows the I portion of Figure 4. In this figure, the TOF spectrum is shown for $E = 63$ V/cm. The experiment was also performed at other low settings of the electric field to find an average value of the kinetic energy of the I fragment using formula 5. The onset of the KETOF distribution at 90 fs corresponds to a kinetic energy of the I fragment of 5000 ± 1500 cm^{-1}, whereas the 50% value corresponds to 2000 ± 500 cm^{-1}. Formula 7 then gives the total available translational energy (the fragments being I and HgI): using the onset value, it is $E_t = 7000$ ± 2000 cm^{-1}, while the 50% value yields 2700 ± 700 cm^{-1}.

In order to gain deeper insight into the kinetic energy distribution of I with respect to the pump–probe delay time, transients at different kinetic energies were taken: The transient at the bottom of Figure 6 was recorded with a gate position of our boxcar that monitors only fast fragments with a kinetic energy >2000 cm^{-1} (see Figure 5). We will refer to this transient as the fast I transient. The transient in the middle of Figure 6 was taken by setting the gate to that part of the KETOF distribution that mainly contains energies in the range from 0 to 500 cm^{-1}. Note that such a gate position will also accumulate some of the faster fragments, because only the projection of the dissociation distribution along the TOF axis can be monitored by this technique. This transient is referred to as the slow I transient.

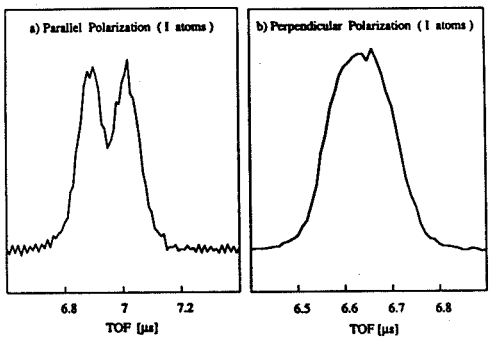

Figure 7. KETOF distribution of I at comparable delay times: (a) parallel laser polarization; (b) perpendicular laser polarization. The difference in flight time is due to different extraction conditions.

The top transient in Figure 6 was obtained by setting the gate to average over the complete KETOF distribution. We will refer to this transient as the total I transient. From the gating experiments, one assigns the first structure in the total I transient to the contribution of the wave packet leading to fast I fragments, whereas the second structure in this transient is due to the wave packet leading to the slow I fragments.

Figure 7 gives an insight into the alignment of the transition moment of the I fragments. In Figure 7a, the KETOF distribution for I is shown at a pump–probe delay time of 310 fs for parallel polarization of the lasers (same as in Figure 6). In Figure 7b, the KETOF spectrum of I for perpendicular polarization is shown at 207-fs delay time. (The difference in flight time is due to different extraction conditions of our TOF spectrometer for these two experiments.) While in the parallel case a splitting in the KETOF distribution is observed, this splitting is not seen in the perpendicular case. This effect is due to the probe laser polarization, since the polarization of the pump was kept parallel to the TOF axis for all the data presented here, as discussed in the following section. (Experiments involving rotation of the pump with respect to the TOF axis are in preparation.)

V. Femtosecond Dynamics and the Reaction Pathway

Figure 8 shows the potential and snapshots of the wave packet for the $[I\cdots Hg\cdots I]^{\ddagger *}$ complex fragmentation along the symmetric and asymmetric stretch coordinates. Parts A and B of Figure 8 correspond to an excitation (310 nm) to 1350 and 8950 cm^{-1}, respectively, above the threshold for total dissociation on surfaces (a) and (b).[2,26] Figure 8A represents the simplest picture of I* channel dissociation with products HgI + I*, I* + HgI, and I* + Hg + I, while Figure 8B represents the simplest picture of I channel dissociation with products HgI + I, I + HgI, and I + Hg + I. The two different excess energies simulate the spin–orbit splitting of 7600 cm^{-1}.

Figure 9 shows the energetics of our λ_1, λ_2* scheme, based on the available spectroscopic information of IHgI and its fragments (see references in figure caption). The 311-nm λ_1 photon initiates the dissociation, whereas the 622-nm probe ionizes either the parent molecule or the transition state in a MPI process. The lowest ionization potential for the parent molecule is 9.5088 ± 0.0022 eV.[27,28] Exciting the ground-state parent molecule, HgI_2, the energy required to produce HgI^+ (+ I + e) is 10.88 ± 0.05 eV,[27,29] and to produce I^+ (+ HgI + e) it is 13.12 ± 0.04 eV.[27,29] The ionization energies of the neutral fragments are 8.23 ± 0.07 eV for HgI,[27] 10.451 eV for I,[30] and 10.437 eV for Hg.[30] If the transition state is probed, it takes at least three probe photons to ionize the parent in a REMPI process, while four probe photons are required to produce HgI^+ and five to yield I^+. On the other hand, five probe photons are needed to ionize the free HgI out

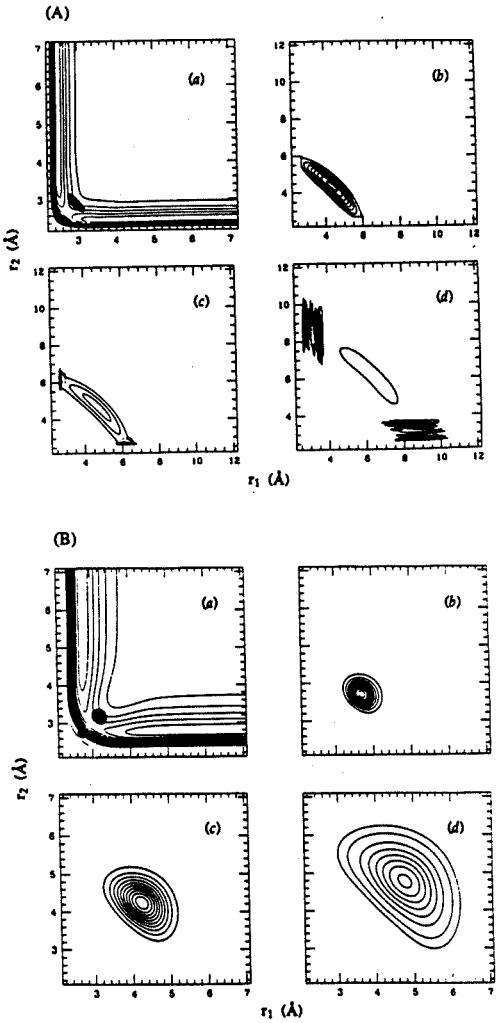

Figure 8. (A) Snapshots of HgI_2 dissociation at 1350 cm^{-1} with respect to total dissociation on surface a.[2,26] This corresponds to I* channel dissociation. The wave packet is shown at different times: (a) 160, (b) 320, (c) 400, (d) 800 fs. (B) The dynamics on surface b at 8950 cm^{-1}, corresponding to I channel dissociation, and at times: (a) 58, (b) 116, (c) 175, (d) 233 fs.

of its ground state in a 1 + 4 REMPI process. Ionizing free $I(^2P_{3/2})$ is a 4 + 2 REMPI process and a 4 + 1 REMPI for free $I^*(^2P_{1/2})$.[30] Free $Hg(^1S_0)$ is also ionized by a 4 + 2 REMPI process.[30] At this wavelength of 622 nm, probing from the transition-state region is consistent with the FTS studies made on this system by LIF detection.[31]

From the energetics, it is clear that reaction channels 1 and 2 are, in principle, open following the creation of the complex. If the complex is bent and/or undergoes bending motion, one additional channel is possible

$$\left[I \cdots Hg \cdots I \right]^{\ddagger *} \longrightarrow Hg(^1S_0) + I_2 \qquad (8)$$

with molecular iodine elimination. We detect the I_2 mass, but before considering its origin let us examine the potentials.

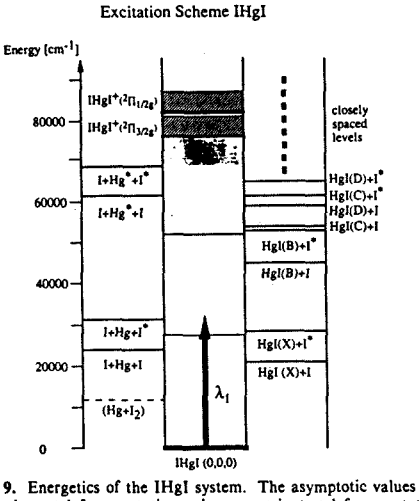

Figure 9. Energetics of the IHgI system. The asymptotic values for symmetric stretch fragmentation and asymmetric stretch fragmentation are shown. Spectroscopic data are taken from ref 30 for the atoms from refs 41 and 77 for IHgI and from refs 41, 78, and 79 for HgI. Ground-state data on IHgI can be found in refs 80 and 81. The lighter shaded excitation area indicates the absorption bands observed by Maya,[77] whereas the darker shaded regions corresponds to higher absorption structures. The excitation wavelength is indicated by λ_1. (I = $^2P_{3/2}$, I* = $^2P_{1/2}$, Hg = $^1S_0$, Hg* = $^3P_0$, HgI(X) = $^2\Sigma^+$, HgI(B) = $^2\Sigma^+$, HgI(C) = $^2\Pi_{1/2}$, HgI(D) = $^2\Pi_{3/2}$).

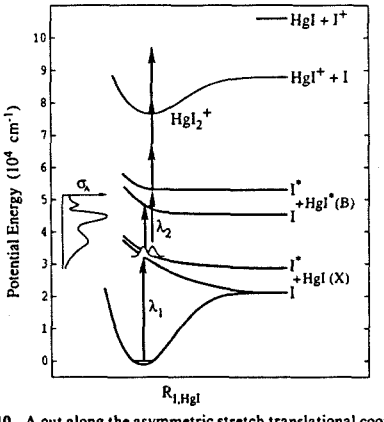

Figure 10. A cut along the asymmetric stretch translational coordinate, together with the absorption cross section,[32] showing the idea for detecting the fragments in the transition state (620 nm) or detecting the free HgI fragments at 390 nm.

The first absorption band of HgI_2 peaks at 265 nm and extends to 350 nm (see Figure 11).[32,33] Leone's group determined the quantum yield of iodine in both spin–orbit states.[32] Production of $I^*(^2P_{1/2})$ was found to be favored for excitation at wavelengths shorter than 295 nm, while at 310 nm the production of $I^*(^2P_{1/2})$ is ~20%. Formation of the two spin–orbit states of iodine is assumed to arise from the two potential energy surfaces of HgI_2, which are separately excited at 310 nm (see Figure 10). In the isoelectronic system, CdI_2, the angular distribution of the fragments was measured by Bersohn's group.[34] They found that a perpendicular excitation leads to $I(^2P_{3/2})$, whereas the parallel excitation leads to dissociation into the $I^*(^2P_{1/2})$ framents.

While the ground state of HgI_2 is linear, relativistic *ab initio* calculations on $HgCl_2$ by Wadt[35] predict that the $^1\Sigma_u^+$ state of

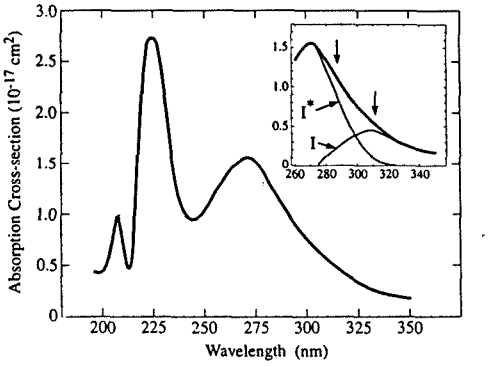

Figure 11. Total absorption cross section for HgI_2.[32] Insert: total HgI_2 absorption cross section and fractional components leading to excited $I(5^2P_{1/2})$ and ground state $I(5^2P_{3/2})$ atoms upon photodissociation of HgI_2.

this latter molecule is bent by ~80–120°. An analogous nonlinear $^1\Sigma_u^+$ state is expected for HgI_2. Using a simple ligand-to-metal charge-transfer model, including spin–orbit coupling, together with magnetic circular dichroism spectra, Mason[33] concluded that the initial absorption has $\Sigma_u^+(1)$ and Π_u character (total spin–orbit states) with the singlet character $^1\Sigma_u^+$ and $^1\Pi_u$ about 20%, with a linear geometry description. The coupling of bending motion to fragment rotation occurs on a time scale of picoseconds and is therefore relatively insignificant on the time scale of the bond-breaking process near the transition state. This type of rotational dephasing and bending motion has been discussed in detail in refs 1 and 2.

Recent femtosecond studies (using LIF)[2,31] and classical[31] and quantum mechanical calculations[26] from this group revealed the coherent motion from the transition state to final products. This striking type of coherence propagation along the reaction path has now been observed even in solutions[36–38] and examined theoretically[39,40] to determine the forces governing the motion. For our purpose here it is sufficient to connect the LIF findings with those of the MPI-TOF. In the LIF studies, ground-state HgI_2 was excited in a cell by a femtosecond pump pulse at 310 nm. As the HgI molecules from channel 1 separate, they were probed independently by a second femtosecond pulse at either 620 or 390 nm. At short interfragment distances, the separation between the potential energy surfaces of the $HgI(X^2\Sigma^+)$ state and the $HgI(B^2\Sigma^+)$ state is smaller than in the asymptotic limit (see Figure 10). Correspondingly, with 620-nm probe, with detection of fluorescence using a monochromator at various detection wavelengths, a double-peak structure was observed and attributed to the slow and fast motions resulting from the two different HgI fragmentation channels 1a. With 390-nm probe, the vibrational product distribution was determined. In the I* channel, relatively little energy is available for vibrational and translational excitation of the HgI X state ($v'' = 7 \pm 1$), whereas in the I channel highly-vibrationally excited HgI X products are formed ($v'' = 29 \pm 2$). Trajectory calculations showed that 60% of the products are formed via process 1b, with Hg + I + I, and 4% via process 1b, with Hg + I + I*.[31] At these energies, the symmetric stretch fragmentation is thus more likely than the asymmetric stretch fragmentation, as is also confirmed by the wave packet calculations.[26]

In the present molecular beam studies, we may deduce the fragmentation energy belonging to the different dissociation channels (see Figures 1 and 12). Taking the spectroscopic data of Wieland[41] for $w_e = 125$ cm^{-1} and $w_e x_e = 1.0$ for $v'' \leq 7$ and $w_e x_e = 1.5$ for $v'' \geq 7$ for the HgI X state, the fragmentation energies can be calculated. The dissociation energy of HgI_2 is 21 000 cm^{-1}.[31] Using formula 7 (*vide supra*) for the transfor-

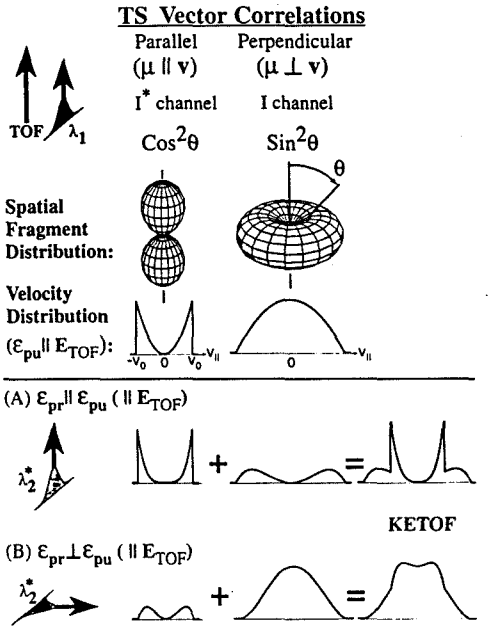

Figure 12. Illustration of the different contributions to our observed KETOF distributions. The top half illustrates the fragment angular distribution and the velocity profiles generated by the pump. The bottom half shows the fragment velocity profiles after probing the transition state. It is assumed that the probing transition moment in the transition state is along the fragmentation direction. The velocity, v, is parallel to the internuclear axis in this case. The complete width of the I channel distribution is greater than that of the I* channel because of the difference in available energy.

mation from total available translational energy to an individual fragment kinetic energy in a collinear two-particle breakup, the kinetic energy of the I atom is calculated and listed below (in the collinear three-particle breakup, the Hg atom will remain at rest):

$$[I\cdots Hg\cdots I]^{\ddagger *} \rightarrow HgI(X^2\Sigma^+) + I(^2P_{3/2}) \quad 6400\ cm^{-1} \quad (9)$$

$$[I\cdots Hg\cdots I^*]^{\ddagger *} \rightarrow HgI(X^2\Sigma^+) + I^*(^2P_{1/2}) \quad 2000\ cm^{-1} \quad (10)$$

$$[I\cdots Hg\cdots I]^{\ddagger *} \rightarrow Hg(^1S_0) + I(^2P_{3/2}) + I(^2P_{3/2}) \quad 4200\ cm^{-1} \quad (11)$$

$$[I\cdots Hg\cdots I^*]^{\ddagger *} \rightarrow Hg(^1S_0) + I(^2P_{3/2}) + I^*(^2P_{1/2}) \quad 400\ cm^{-1} \quad (12)$$

We now turn to the different pathways. Before considering the specific cases, we should mention the Hg + I_2 case. If all energy in this fragmentation channel is transformed into translational energy, we would expect a maximum kinetic energy of the I_2 fragment of 9000 cm^{-1}. (The total fragmentation energy is 1.45 eV.[31]) However, we observe only a maximum kinetic energy of 800 cm^{-1} for the I_2 product in the KETOF experiment. As the symmetric stretch fragmentation into the I* channel is only 4% in comparison to 60% for the I channel, we will also exclude this channel in our further considerations. Now we focus on the alignment and the kinetic energy release due to the different primary dissociation processes (channels 9–11).

A. HgI Product Channel. In the one-photon excitation regime, channels 9 and 10 are open to produce HgI via the asymmetric

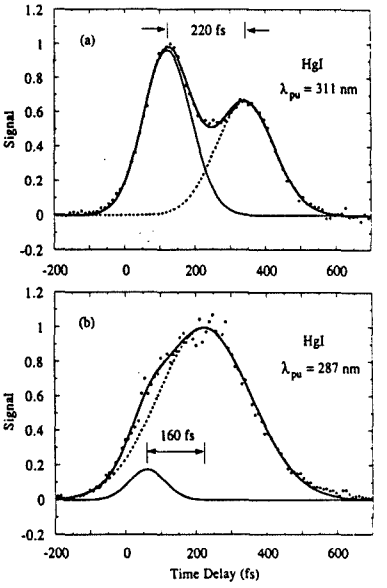

Figure 13. HgI transients for parallel polarization at different pump wavelengths: (a) 311 nm and (b) 287 nm. The long-time component (rise with $\tau \approx 250$ fs; amplitude = 0.46 and 0.042, respectively) convoluted with the Gaussian cross-correlation is removed, leaving the early-time behavior. (a) The first peak (channel 9), at 121 fs, has a fwhm of 159 fs, and its area is 54.4% of the total. The second peak (channel 10), at 341 fs, has a 194 fs fwhm. (b) The peak at 61 fs has a 121 fs fwhm and its area is 6.4%. The peak at 223 fs has a 310 fs fwhm. Deconvoluting the above fwhm widths, F, using the known Gaussian cross-correlation (fwhm $F_c \approx 100$ fs) yields the fwhm values $(F^2 - F_c^2)^{1/2}$.

stretch coordinate. The time shift of half the rise of the HgI transients (Figures 2 and 3) with respect to the half rise time of the parent reflects the time the system needs to enter the transition-state region where the probe photons are resonant with the complex transition, as sketched in Figure 10. The structure and the two peak positions are very similar to that found in the transients obtained in the LIF experiments.[2,31] The first peak is related to channel 9 (high kinetic energy release) whereas the second peak is related to channel 10 (low kinetic energy release). Note that this is not a pure one-dimensional motion, as there is also an oscillatory motion perpendicular to the fragmentation coordinate (Figure 8); this is the motion which leads to coherent excitation in the products.[2,31] In Figure 13a, the HgI transient of Figure 2 is shown, but with the long-time behavior subtracted. Two Gaussians were fitted to the residual, early-time signal. The peaks widths and positions indicate the transient time in the transition state for the two channels (see figure caption, Figure 13).

As the I channel 9 is accessed by a perpendicular transition, the products will predominantly fragment perpendicular to the pump laser polarization. The first probe photon has to make the HgI B ← X ($\Sigma \leftarrow \Sigma$) transition (*i.e.*, a parallel transition). Therefore, the alignment of the HgI transition moment will preferentially be in the plane perpendicular to the pump polarization. If the probe laser polarization is perpendicular to that of the pump, it will lie in this plane. On the other hand, if the probe polarization is parallel to that of the pump, then it will be primarily perpendicular to the HgI transition moment. There is therefore an enhanced REMPI HgI^+ signal of the I channel for perpendicular laser polarization and a reduced REMPI HgI^+ signal for parallel polarization. For the REMPI HgI^+ signal due to the I* channel 10, the argument is reversed as this channel is

accessed by a parallel transition. The HgI transition moment will be preferentially aligned parallel to the pump polarization, and so the probe polarization will be predominantly parallel or perpendicular to this transition moment if it is parallel or perpendicular, respectively, to the pump polarization. This explains the experimental observation that for parallel laser polarization the second component of the HgI transient in Figure 2 is enhanced in comparison to the HgI transient taken with perpendicular polarization, Figure 3. The behavior, also seen in fluorescence,[2] indicates that the excitation process involves a preparation of wave packets on the two different potentials leading to two different fragmentation channels. If the pump were to access only one state, then the system would have to evolve through a conical intersection in order to release I and I*, and a distinct polarization dependence would not be expected.

B. I Product Channel. Atomic iodine can be produced in this one-photon excitation regime along the symmetric stretch coordinate (channel 11) or via the asymmetric stretch coordinate (channels 9 and 10). In Figure 5 it is shown that the onset of the kinetic energy distribution contains I fragments with kinetic energies of about 5000 ± 1500 cm^{-1}. As the I channel 9 is accessed by a perpendicular transition and the pump laser is parallel to the TOF axis, a broad I distribution is expected for this dissociation channel, where the onset of the distribution should reflect the kinetic energy release of the process as described above. The parallel transition leading to the I* channel 10 should deliver a double structure in the kinetic energy distribution. The 50% value of this double structure in Figure 5 corresponds to 2000 ± 500 cm^{-1}. Both values are in reasonable agreement with the calculated values given above (see Appendix).

Assuming the 5p orbital (singly occupied) of I is aligned along the fragmentation axis in an asymptotic limit, and therefore gives rise to a parallel type transition in the REMPI probing of the transition state, a similar behavior with respect to pump–probe laser polarization is expected for the I transients: enhanced I$^+$ REMPI signal from the I* channel for parallel probing and reduced I$^+$ REMPI signal from the same channel for perpendicular probing. This behavior is most obvious in the two KETOF spectra of Figure 7 where the KETOF distribution for parallel pump–probe laser polarization shows the splitting for the I* channel, whereas for perpendicular laser polarization the distribution is the broad one. The latter is typical of a perpendicular pump transition when the pump laser polarization is parallel to the TOF axis, as explained above and in the Appendix and also illustrated in Figure 12 (assuming direct collinear fragmentation and negligible influence of molecular rotation justified by the short time scale we observe the two different distributions). According to the trajectory calculations, 60% of the complexes fragment along the symmetric stretch coordinate, leading to calculated kinetic energies of ~4200 cm^{-1}. We conclude that this dissociation pathway is also accessed by the perpendicular pump transition. (We would have expected a double structure in the KETOF distribution resembling the 4200-cm^{-1} splitting if this fragmentation would be induced by a parallel type transition.) As the REMPI probing of I* need not necessarily occur at the same internuclear distance as the HgI REMPI probing (in the transition-state region), and as there is a contribution to the I fragments from the dissociation along the symmetric stretch coordinate, the double-peak structure in the I transient (Figure 2) is not as pronounced as in the HgI transients.

The final proof that the double structure is due to iodine atoms coming from different dissociation channels is demonstrated in Figure 6. The fast iodine atoms from the asymmetric stretch fragmentation along the HgI + I coordinate and from the symmetric stretch fragmentation contribute mainly to the first peak of the total transient, whereas the second peak is due to the slow iodine atoms originating from a fragmentation along the HgI + I* coordinate. It is therefore concluded that at these internuclear separations of the transition state (within ~50-fs motion) the two potentials (I and I*) are well-defined, and there is not enough mixing to scramble the identity of the anisotropy.

C. Hg Product Channel. According to the one-photon excitation regime, Hg product comes from the dissociation along the symmetric stretch coordinate. The time shift of this transient is again related to the time the system needs to evolve into the transition-state region. In the Hg transient of Figure 2 there is also a double structure seen in the early-time behavior. This double structure is not attributed to a dynamical resonance as a strong polarization dependence is observed. Note that the symmetric motion is bound for low-excitation energies (see Figure 8), and at moderate energies above dissociation partial reflection of the wave packet is possible. The second peak in the Hg transient is suppressed for perpendicular laser polarization and enhanced for parallel laser polarization (Figures 2 and 3). We therefore suggest that the second peak in the Hg transient is due to the HgI + I* dissociation monitored through the fragmentation of HgI$^+$ to Hg$^+$ and I. As discussed above, the HgI$^+$ REMPI signal is enhanced for parallel laser polarization and decreased for perpendicular laser polarization. The observation that the second peak in the Hg transient has nearly the same position as the second peak in the HgI transient (Figure 2) supports this explanation.

D. Effect of Total Energy Change. Results were also obtained at $\lambda_1 = 287$ nm and $\lambda_2^* = 622$ nm. A typical transient on HgI for parallel laser polarization is shown in Figure 13b. The low-amplitude, long-time component has been suppressed (see figure caption). The double-peak structure, seen clearly at $\lambda_1 = 311$ nm (Figure 2 and Figure 13a), is not as conspicuous here. At 311 nm the first peak (channel 9) constitutes 54.4% of the signal, while the second peak (channel 10) contributes 45.6%. In contrast, at 287-nm excitation the first peak (I channel) accounted for only 6.4%. The transient is time-shifted by about 80 fs with respect to the time zero of the parent. The fwhm of the second peak alone is 310 fs and that of the whole transient is 330 fs, much broader than the cross-correlation. The I and the Hg transients do not show a double-peak structure at this pump wavelength, but they too are time-shifted with respect to the parent transient. KETOF transients on "fast" and "slow" I fragments were similar, to within statistical error, to the total transient obtained detecting I fragments at all velocities along the TOF axis.

These results are in agreement with the separation of the I and I* potentials at short times and in accord with the yield ratios at long times (ref 32 and Figure 11). At 311-nm excitation, ~20% of the total iodine atom yield is in the form of I*, while at 287 nm about 80% of the total iodine atom yield is in its spin–orbit excited state (ignoring the small thermal energy difference: in ref 32 a cell at 453 K was used, while here the sample was at 445 K, followed by an expansion through the nozzle with no backing pressure). As discussed above, the yield of HgI originating from the I* channel is enhanced for parallel λ_2^* laser polarization. Thus, the double structure due to the different fragmentation channels should be dominated by the I* channel peak at high (287-nm) excitation energy. It is interesting to note, from the molecular dynamics simulations (see Figure 8 and refs 2 and 26), that at higher energies the packet spreads more and faster into the symmetric stretch coordinate, but the leaking into the asymmetric coordinate becomes slower.

VI. Conclusions

This contribution develops femtosecond kinetic energy time-of-flight (KETOF) as a method of probing the vectorial dynamics of transition states. Studies of the [I···Hg···I]^{I*} transition-state complex in a molecular beam are reported and used to illustrate the approach. The reaction was initiated by a femtosecond laser pulse at 311 nm (or 287 nm) and followed by a time-delayed

probe laser (622 nm) that ionizes the complex and the fragments in a TOF mass spectrometer. This REMPI ionization enabled us to follow the initial dynamics of the wave packet along the symmetric and asymmetric coordinates, resolving the early, less than 50-fs motions. The time for the system to enter the transition state was obtained by measuring time delays in the rise time of the fragments in comparison to the rise of the parent molecule. The transient time of the complex in the transition state ranges from 120 to 300 fs, depending on the available energy. Product fragment masses (Hg, I, HgI) are also studied.

Different dissociation channels yielding the same fragment mass (I) were resolved in two ways: by the nature of the parent transition moment and by the kinetic energy release to the fragment. The channels giving rise to HgI + I and I + Hg + I were both accessed via a perpendicular transition and due to the high kinetic energy release they yielded fast atomic iodine fragments. However, the HgI + I* channel, having less translational energy available, produces slow iodine fragments. This channel is accessed via a parallel transition. The femtosecond resolution of the fragment anisotropy identifies the alignment of the transition moment with respect to fragmentation. As the spectrometer axis is well-defined, rotating the pump and probe laser polarization with respect to the TOF axis gives insight into the vectorial properties, but now during the transition state.

The approach, outlined in Figure 12, promises applications in relation to vector correlations of the dynamics, with the addition of the time resolution to probe early internuclear separations. The same concept should be extended to bimolecular reactions and to other detection schemes.[2,12,13,15,16,18,20] Improvement in time-of-flight resolution can also be made using pulsed acceleration TOF mass spectrometry.[42] There are theoretical and experimental extensions of this work. Theoretically, the treatment of correlations and anisotropy during the transition state needs improvement: in the course of angular momentum evolution maybe a hindered rotation picture would be appropriate. On the experimental side, we plan further experiments aimed at resolving the photoelectrons, using ZEKE,[19] and this should help us map out the kinetic energy change with time.

Acknowledgment. This work was supported by a grant from the Air Force Office of Scientific Research and by the National Science Foundation.

Appendix: Anisotropy and Rotational Alignment in Pump-Probe Experiments

When a molecule is excited by a pump laser, the optical transition dipole moment, μ, is preferentially aligned along the pump polarization direction, ϵ_{pu}. If the parent subsequently dissociates, then the resulting fragments will be characterized by their velocity, v, and angular momentum, J. Because of the alignment of the parent transition moment (μ), the fragments will be described by a recoil anisotropy (μ–v correlation[43–49]) and will have a rotational alignment (μ–J correlation[10,50–53]). In addition to v and J of the fragment being correlated with μ of the parent, they must also be correlated with each other.[54–60] The theory for the angular distributions and correlations has been developed thoroughly (see the excellent review by Hall and Houston[8]). Both LIF (Doppler profiles; see refs 8–10 and 60–63) and MPI detection (see refs 8–10 and 64–70) have been used to measure the correlations and to extract information such as the nature of the parent transition and an estimate of the lifetime of the dissociating parent molecule.

Relevant to the approach presented here, we shall consider the μ–v correlations first, followed by the effect of REMPI probing with detection along a TOF axis. All correlations will be incorporated in order to examine the velocity profile and the time scales. The consequences of probing in the transition-state region are also considered.

1. Angular Distribution Created by the Pump Pulse. For an electric dipole transition in which a single photon excites a parent molecule the transition probability is expressed by

$$P \propto |\epsilon_{pu} \cdot \mu|^2 \tag{A1}$$

where ϵ_{pu} is the pump polarization direction and μ is the transition dipole moment of the parent molecule ($\mu = \mu_{fi} = \langle f|\mu|i\rangle$). Hence, if γ is the angle between ϵ_{pu} and μ, then the normalized transition probability is

$$P = \frac{3}{4\pi}\cos^2\gamma = \frac{1}{4\pi}[1 + 2P_2(\cos\gamma)] \tag{A2}$$

where $P_2(x) = {}^1/_2(3x^2 - 1)$ is the second-degree Legendre polynomial. This relationship, expressed as $P(\theta)$, the angular recoil velocity distribution, may in general be written as

$$P(\theta) = \frac{1}{4\pi}[1 + \beta P_2(\cos\theta)] \tag{A3a}$$

where θ is the angle between the final recoil velocity, v, and the pump polarization vector, ϵ_{pu}, and β is the anisotropy parameter (μ–v correlation).[43–48]

In certain experiments, the "axis of detection", e.g. TOF axis, is well-defined in the laboratory. If the pump pulse is parallel to this axis (see Figure 16) and the fragments can be detected along this axis, then eq A3a can be expressed in terms of the projection of the fragment velocity parallel to this axis, $v_\parallel$:

$$P(v_\parallel) = \frac{1}{2v_0}\left[1 + \beta P_2\left(\frac{v_\parallel}{v_0}\right)\right] \tag{A3b}$$

which is a parabola or "inverted parabola" depending on the value of β (see section 2B of this appendix and Figure 15). For LIF detection, an equation of the same parabolic form is obtained.[60] Let us now consider first the effect of no rotation and next take rotational effects into account.

A. No Rotational Effects (of the Parent). If the molecule dissociates instantaneously on absorption of the light and if the kinetic energy of dissociation is very large compared to the rotational energy of the molecule, then β is given simply by

$$\beta = 2P_2(\cos\chi_0) \tag{A4}$$

where χ_0 is a fixed angle between the parent transition moment, μ, and the direction of dissociation (given by the final recoil velocity, v, for negligible rotation).[44,46] For a diatomic molecule the direction of dissociation is the internuclear axis and thus $\chi_0 = 0°$ or 90°. For a polyatomic molecule χ is less restricted. It can be generalized to describe an arbitrary recoil distribution $P(\chi)$[47]

$$\beta = 2\int_0^\pi P_2(\cos\chi)P(\chi)\,d\chi \tag{A5}$$

The anisotropy parameter, being the average of $P_2(\cos\chi)$ over the probability distribution of χ, must lie between the maximum and minimum values of $P_2(\cos\chi)$, *i.e.*, $-1 \le \beta \le 2$.

Let us return to the case of $P(\chi) = \delta(\chi - \chi_0)$ and consider three cases. If the excitation involves a parallel transition moment ($\mu \| v$), then $\chi_0 = 0$, $\beta = 2$, and $P(\theta) = (3/4\pi)\cos^2\theta$, *i.e.*, a dumbbell-shaped angular distribution with respect to the ϵ_{pu} direction. In this case, the fragment is most likely to travel along (collinear or anticollinear) the direction of ϵ_{pu} (Figure 12). On the other hand, with a perpendicular transition moment ($\chi_0 = 90°$), we obtain $\beta = -1$ and $P(\theta) = (3/8\pi)\sin^2\theta$, a toroidal probability distribution with respect to the ϵ_{pu} direction (Figure 12). In this case, the fragment has maximum probability to travel at right angles to ϵ_{pu}. In the very unlikely case that χ_0 happens to be 54.7° ($\beta = 0$), we would obtain an isotropic distribution: $P(\theta) = 1/4\pi$.

B. Effects of Rotation. If the parent molecule rotates with angular velocity ω there are two rotational effects to be considered,

even for a diatomic molecule, both of which reduce the magnitude of β. First, if the excited molecule lives for an average lifetime, T_0, before dissociating, then[45,48]

$$\beta = 2P_2(\cos\chi_0)\frac{1+(\omega T_0)^2}{1+4(\omega T_0)^2} \tag{A6}$$

where the probability that the molecule has not dissociated in a time t is given by the distribution

$$P(t) = \frac{1}{T_0}\exp\left[-\frac{t}{T_0}\right] \tag{A7}$$

Second, when the molecule finally does dissociate, the nascent fragments will have a tangential velocity due to the rotation of the molecule in addition to the radial velocity of recoil. This effect is significant if the rotational energy of the molecule is not negligible compared to the kinetic energy release in the fragmentation. The effect has been treated for a diatomic molecule, yielding[47]

$$\beta = 2P_2(\cos\chi_0)\left\{\frac{P_2(\cos\alpha)+(\omega T_0)^2-3(\omega T_0)\sin\alpha\cos\alpha}{1+4(\omega T_0)^2}\right\} \tag{A8a}$$

$$\tan\alpha = v_t/v_0 \tag{A8b}$$

where α is the angle between the asymptotic recoil velocity, v, and v_0, the fragment radial recoil velocity. This tangential velocity effect has also been treated separately from the finite lifetime effect. For a small rotation angle, α, the effect is to reduce β, given by (A6), by a factor of[45,48]

$$1 - {}^3/_2\sqrt{2}kT/E_{rel} + O((kT/E_{rel})^2) \tag{A9}$$

where E_{rel} is the energy of relative motion of the fragments. This is compatible with the more general expression (A8) of Busch and Wilson:[47] the tangential velocity effect (if considered as (A8a) with $\omega T_0 = 0$) reduces the magnitude of β by $P_2(\cos\alpha)$. For small α, $\alpha \approx \omega r/v_0$ and $P_2(\cos\alpha) = 1 - (3/2)(w^2r^2/v^2)$, where r is the distance from the CM to the fragment. The two approaches then agree in the limit of small α because $\omega^2r^2/v^2 \propto \langle E_{rot}\rangle/E_{rel} \propto kT/E_{rel}$.

2. Probing to Ionization with KETOF Detection. *A. Free Fragment Probing.* When the probe pulse arrives (at time delay, t_D, after the pump), it sees an anisotropic fragment angular recoil distribution, characterized by β. Unlike the pump, the probe also encounters an anisotropic rotational distribution. Here first we consider the anisotropies for free fragment probing ($t_D \gg T_0$).

In general,[59] the intensity of any optical process acting on a set of rotating molecules, characterized by its moments or multipoles, ${}^{(R)}A_Q^K$, is given by

$$I = \sum_{K,Q} q_Q^K\, {}^{(R)}A_Q^K \tag{A10}$$

where the q_Q^K coefficients depend on the physics of the optical process, $R(Ox,Oy,Oz)$ is a fixed axis system, and K and Q are integers with $-K \le Q \le K$.[70] For REMPI detection details of the rotational selection rules for the ionization step are needed.[71] This difficulty is removed if the last step is a very high probability (near 1) isotropic ionization step (saturation), in which case the anisotropy of the whole process only depends on the preceding steps made by the probe.

In a typical experiment, a projection of the velocities along the TOF axis is detected, giving rise to a velocity profile. The following conditions are considered: (i) The linear pump polarization, ϵ_{pu}, lies along an Oz axis. (ii) Dissociation leads to a final single fragment recoil speed, v_0. (iii) The linear probe polarization, ϵ_{pr}, lies along an Oz′ axis, and the probing process exhibits rotational

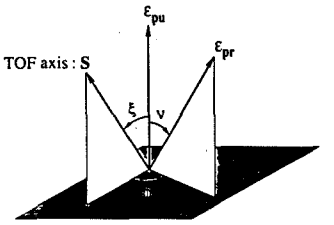

Figure 14. Definition of the angles (θ,ν,ϕ), characterizing the relative arrangement of the vectors $(\epsilon_{pu},\epsilon_{pr},S)$ involved in the REMPI KETOF method.

and inversion invariance with respect to this axis. The q_2 coefficients (see later) of this REMPI process are assumed known. (iv) The velocity profiles of the ionized fragments are detected along an Oz″ axis (TOF axis) in this REMPI TOF method.

The ${}^{(R)}A_Q^K$ moments in (A10) must be expressed explicitly in terms of the velocity component $v_\parallel$ along the TOF axis to obtain the velocity profile, $g(v_\parallel)$, of the ionized fragment ($g(v_\parallel)$ is used in ref 70, and here we use $P(v_\parallel)$). Mons and Dimicoli[70] used the procedure reported by Dixon[60] to arrive at the appropriate expressions. The moments are expressed in terms of the bipolar moments, $b_Q^K(k_1,k_2)$, containing all the angular information of the system: the μ–v–J correlations; k_1 and k_2 are respectively the orders at which translational and rotational motions are involved. The velocity profile contains not only $P_0(x)$ and $P_2(x)$ like the neutral fragment profile (A3) but also terms in $P_4(x)$ and $P_6(x)$, where $x = v_\parallel/v_0$. However, the high-order Legendre polynomial contributions are difficult to evidence experimentally. According to Mons and Dimicoli, if, in addition, no strong angular correlations are expected, it seems reasonable to neglect these higher-order terms and to focus on the first coefficients: β, A, C, and C'. Here $\beta = 2b_0^2(2,0)$ is the previously encountered μ–v anisotropy parameter of eq A3, $A = A_0^2(J) = {}^4/_5 b_0^2(0,2)$ is the alignment parameter,[50,54,70,72,73] $C = \sqrt{5}b_0^0(2,2)$ is the first-order v–J correlation coefficient, and $C' = \sqrt{{}^7/_2}b_0^2(2,2)$ is the first μ–v–J correlation coefficient. Under these assumptions, the experimental velocity profiles can be expressed in the form[70]

$$g(v_\parallel) \propto 1 + \beta_{eff}P_2(v_\parallel/v_0) \tag{A11a}$$

where β_{eff} is an effective anisotropy, and the equation has now similarity to the pump-alone case (A3). The β_{eff} parameter is defined by

$$\beta_{eff} = g_2/g_0 \tag{A11b}$$

with

$$g_0 = 1 + q_2AP_2(\cos\nu) \tag{A12a}$$

and

$$g_2 = \beta P_2(\cos\xi) + q_2C\{2P_2(\cos\xi)P_2(\cos\nu) + 6\cos\xi\sin\xi\sin\nu\cos\nu\cos\phi + {}^3/_2\sin^2\xi\sin^2\nu\cos2\phi\} - {}^2/_7 q_2C\{4P_2(\cos\xi)P_2(\cos\nu) + 6\cos\xi\sin\xi\sin\nu\cos\nu\cos\phi - 3\sin^2\xi\sin^2\nu\cos2\phi\} \tag{A12b}$$

in which ξ is the angle between the pump polarization direction, ϵ_{pu}, and the TOF axis, S, and ν is the angle between ϵ_{pu} and ϵ_{pr}. The angle ϕ is the angle between the plane containing ϵ_{pu} and S and the plane containing ϵ_{pu} and ϵ_{pr} (see Figure 14). The real coefficient q_2[54,72,74–76] specifies the probed quantum state, and its dynamical range is typically $[-{}^1/_2, {}^1/_2]$.[54] The second-degree Legendre polynomial, $P_2(v_\parallel/v_0) = (3(v_\parallel/v_0)^2 - 1)/2$, in (A11a), expresses the fact that the velocity profile is parabolic, where $v_\parallel$ lies in the range $-v_0 \le v_\parallel \le v_0$. The limits $v_\parallel = \pm v_0$ describe fragments whose final recoil velocity is aligned either collinear

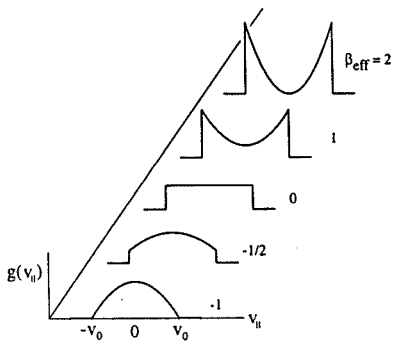

Figure 15. Velocity profiles of monokinetic fragments, detected in a REMPI KETOF experiment. Fragmentation is induced by the linearly polarized pump pulse, ϵ_{pu}, generating well-defined μ–v–J correlations, described by β, A, C, and C'. The linearly polarized probe pulse (ϵ_{pr}) induces a REMPI process on the well-defined rovibronic state(s) of the fragments, characterized by the q_2 coefficient. The effective anisotropy parameter, $\beta_{eff} = \beta_{eff}(\beta,A,C,C',q_2,...)$, describes the velocity profiles. See eq A11.

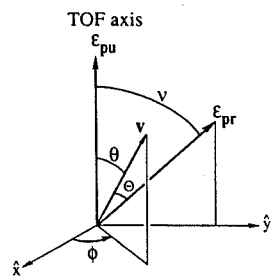

Figure 16. Experimental axis system used: the pump polarization is along the TOF axis, and the probe polarization is at an angle ν to the pump. The direction of recoil is given by the velocity, v.

or anticollinear with the TOF axis. The point $v_{\parallel} = 0$ corresponds to fragments whose final recoil velocity is perpendicular to the TOF axis. The velocity profile is shown in Figure 15 for different values of β_{eff}. Mons and Dimicoli[70] considered some specific pump–probe geometries. Note that if the pump and probe lasers propagate collinearly and the TOF axis is perpendicular to this propagation direction, then $\phi = 0°$ or 180°.

B. Probing the Transition-State Region. In the following section we consider the case when the packet motion is on the femtosecond time scale so that any rotational effects may be neglected both before and after probing. We shall consider the case in which the probe arrives at a short time delay, t_D, after the pump and finds the excited complex in the transition-state region ($t_D \leq T_0$). Let us assume that the probing transition moment, μ_2, is aligned along the recoil velocity, $v(t)$. This velocity is unaltered by the probing, but its magnitude may change in the subsequent evolution of the probed complex leading to two free fragments (one of which is the ion detected). Hence the probe transition is parallel.

Following the pump excitation, the probability of finding the complex with a recoiling velocity $v(\theta,\phi)$ in a solid angle $d\Omega$ (=sin θ $d\theta$ $d\phi$) is given by (A3)

$$P(\theta)\, d\Omega = (1/4\pi)[1 + \beta P_2(\cos\theta)]\, d\Omega \qquad \text{(A13)}$$

where θ is the angle between v and ϵ_{pu} (Figure 16), and β is given by (A4) or (A5). The probability of probing one of the excited complexes is given by

$$P_{pr}(\Theta) \propto \cos^2\Theta \qquad \text{(A14)}$$

where Θ is the angle between $v(\theta,\phi)$ and ϵ_{pr}. The probability of finding a probed molecule in the direction given by $v(\theta,\phi)$ is then given by

$$P(\theta,\phi)\, d\Omega \propto [1 + \beta P_2(\cos\theta)]\cos^2\Theta\, d\Omega \qquad \text{(A15)}$$

In general, the velocity profile along the TOF axis involves an integration around this axis, adding up the probability that an ion is traveling with a velocity whose projection along the TOF axis is $v_{\parallel}$ (an analogous treatment, but for free fragments and expressing the distribution as a function of a Doppler shift, can be found in the Appendix of ref 60). For simplicity, we present the case in which the pump polarization, ϵ_{pu}, is along the TOF axis (see Figure 16). Using $v_{\parallel} = v_0 \cos\theta$, it follows that

$$P(v_{\parallel})\, dv_{\parallel} \propto [\int_{\theta\ \text{fixed}} P(\theta,\phi)\, d\phi]\, dv \qquad \text{(A16)}$$

in which $-v_0 \leq v_{\parallel} \leq v_0$. Making use of the identity

$$\cos\Theta = \sin\theta \sin\phi \sin\nu + \cos\theta\cos\nu \qquad \text{(A17)}$$

and carrying out the integration yields

$$P(v_{\parallel})\, dv_{\parallel} \propto \left[1 + \beta P_2\left(\frac{v_{\parallel}}{v_0}\right)\right]\left[1 + 2P_2(\cos\nu)P_2\left(\frac{v_{\parallel}}{v_0}\right)\right] dv_{\parallel} \qquad \text{(A18)}$$

where ν is the angle between ϵ_{pu} and ϵ_{pr}, and the TOF axis is along ϵ_{pu}. Equation A18 describes the velocity profile obtained in a process involving one pump photon and one probe transition from the transition state. (If additional steps are made by the probe, then (A14) must be altered.)

If the neutral fragments following pump excitation could be detected, then the observed velocity profile would be given by $1 + \beta P_2(v_{\parallel}/v_0)$. The effect of probing the transition state is to introduce the second factor, $1 + 2P_2(\cos\nu)P_2(v_{\parallel}/v_0)$, in (A18). If the polarization of the probe is oriented at the magic angle to that of the pump ($\nu = 54.7°$), then this second factor reduces to unity and the velocity profile is unaltered by the probing.

Let us consider the two distinct cases of a parallel ($\beta = 2$) and a perpendicular pump transition ($\beta = -1$) and in each case investigate the effect of probing with a polarization that is either parallel or perpendicular to the pump polarization. These cases are illustrated in Figure 12.

(i) Parallel pump transition: $\beta = 2$. The velocity profile generated by the pump *only* is proportional to $(v_{\parallel}/v_0)^2$, *i.e.*, parabolic and peaking at $\pm v_0$. Probing the transition state alters this profile in a way that depends on the orientation of the probe polarization:

(a) TOF$\parallel$pump$\parallel$probe ($\nu = 0°$). In this case, the resulting velocity profile is given by

$$P(v_{\parallel}) \propto (v_{\parallel}/v_0)^2(v_{\parallel}/v_0)^2 = (v_{\parallel}/v_0)^4 \qquad \text{(A19)}$$

The velocity profile is thus enhanced and sharpened near the limits $\pm v_0$.

(b) TOF$\parallel$pump$\perp$probe ($\nu = 90°$).

$$P(v_{\parallel}) \propto (v_{\parallel}/v_0)^2\,[1 - (v_{\parallel}/v_0)^2] \qquad \text{(A20)}$$

The velocity profile is greatly altered and the yield of ions is less than case (a) above.

(ii) Perpendicular pump transition: $\beta = -1$. The velocity profile generated by the pump only is proportional to $1 - (v_{\parallel}/v_0)^2$, *i.e.*, parabolic and peaking at $v_{\parallel} = 0$, corresponding to a preference for fragmentation in the plane perpendicular to the pump polarization. This profile is also altered upon probing the transition state.

(a) TOF‖pump‖probe ($\nu = 0°$). The resulting velocity profile here is given by

$$P(v_\parallel) \propto [1 - (v_\parallel/v_0)^2](v_\parallel/v_0)^2 \qquad \text{(A21)}$$

The velocity profile is thus changed and the yield is lower than for case (b) below.

(b) TOF‖pump⊥probe ($\nu = 90°$).

$$P(v_\parallel) \propto [1 - (v_\parallel/v_0)^2][1 - (v_\parallel/v_0)^2] = [1 - (v_\parallel/v_0)^2]^2 \qquad \text{(A22)}$$

The velocity profile is enhanced about $v_\parallel = 0$ due to the probing.

3. Kinetic Energy Release. The velocity profile detected in a KETOF experiment is that of the ion fragments. The width, Δt, of this profile determines the kinetic energy of the ion (see eq 5). These ions may be produced either by probing the neutral fragments or by probing the transition state.

A. Free Fragment Probing. If the internuclear separation is sufficiently large (no potential energy between fragments) that the nascent fragment has acquired its final recoil speed, v_0, then, upon probing to ionization, its velocity will not be altered due to conservation of momentum. Of the translationally available excess energy after probing, the ejected electron carries away a fraction $(1 + m_e/m_{ion})^{-1}$, which is almost unity, leaving the fragment velocity essentially unchanged. Therefore, the fragment velocity is not changed upon probing, and this holds true independent of the excess energy to which the neutral fragment is probed, *i.e.*, independent of the probe wavelength; the electron always carries the excess translational energy of recoil, even if the ion has internal energy. The kinetic energy of the ion (see eq 7) is then governed by the total available translational energy, E_t, in the CM frame after the pump excitation. If we define the ground state of the parent as the zero of potential energy, then if the pump accesses the potential energy surface $V_1(R)$, the available energy (eq 6) may be written

$$E_{avl} = V_1(R_{pu}) - V_1(\infty) = E_{int} + E_t \qquad \text{(A23)}$$

where $V_1(R_{pu}) = E_{int}^P + h\nu_{pu}$, and $V_1(\infty) = D_0^0$.

B. Probing the Transition-State Region. On the other hand, if the pump–probe delay time is small enough ($t_D \leq T_0$) that the transition state is probed, then the picture is different. In the transition state, the available energy, partitioned among internal and translational degrees of freedom, is given by

$$E_{avl}^{TS}(R) = V_1(R_{pu}) - V_1(R) = E_{int}(R) + E_t(R) \qquad \text{(A24)}$$

If the same number of probe photons enter in the probe excitation, then the same total energy will be available to the entire system. However, when the transition state is probed to a dissociative state above the ionization level, the energy excess above the asymptotic level (free ion and free fragment) can be shared by the two nascent parts as well as by the ejected electron. The kinetic energy of the resulting ion thus depends on the probe wavelength or excess energy probed to. Immediately after probing, the velocity, $v(t)$, is unchanged. However, the subsequent evolution is on a new potential energy surface, $V_2(R)$, with a different total available energy. If the kinetic energy, E_e, of the photoelectron is measured, then the difference potential may be determined. It should be noted that if the potential energy, V_1, is dropped significantly, then the ionization process is characteristic of the asymptotic limit (see the discussion in section 3A) and the kinetic energy release is similar to that of the neutrals on V_1. As mentioned in the text, this feature will be utilized in future experiments.

References and Notes

(1) Dantus, M.; Bowman, R. M.; Baskin, J. S.; Zewail, A. H. *Chem. Phys. Lett.* **1989**, *159*, 406.

(2) Zewail, A. H. *Faraday Discuss. Chem. Soc.* **1991**, *91*, 207; *J. Chem. Soc., Faraday Trans. 2* **1989**, *85*, 1221 and references therein.

(3) Felker, P. M.; Zewail, A. H. *J. Chem. Phys.* **1987**, *86*, 2460. Baskin, J. S.; Felker, P. M.; Zewail, A. H. *J. Chem. Phys.* **1987**, *86*, 2483.

(4) Felker, P. M. *J. Phys. Chem.* **1992**, *96*, 7844 and references therein.

(5) Heather, R.; Metiu, H. *Chem. Phys. Lett.* **1989**, *157*, 505.

(6) Benjamin, I.; Wilson, K. R. *J. Chem. Phys.* **1989**, *90*, 4176.

(7) Waldeck, J. R.; Shapiro, M.; Bersohn, R. *J. Chem. Phys.*, to be published.

(8) Hall, G. E.; Houston, P. L. *Annu. Rev. Phys. Chem.* **1989**, *40*, 375.

(9) Riley, S. J.; Wilson, K. R. *Faraday Discuss. Chem. Soc.* **1972**, *53*, 132. Bersohn, R. In *Advances in Gas-Phase Photochemistry and Kinetics*; Ashfold, M. N. R., Baggott, J. E., Eds.; Royal Society of Chemistry: London, 1987; p 1. Wodtke, A. M.; Lee, Y. T. *Ibid*, p 31. Docker, M. P.; Hodgson, A.; Simons, J. P. *Ibid*, p 115. Ashfold, M. N. R.; Lambert, I. R.; Mordaunt, D. H.; Morley, G. P.; Western, C. M. *J. Phys. Chem.* **1992**, *96*, 2938.

(10) Simons, J. P. *J. Phys. Chem.* **1984**, *88*, 1287.

(11) Schlag, E. W.; Neusser, H. *J. Acc. Chem. Res.* **1983**, *16*, 355.

(12) Baumert, T.; Buehler, B.; Grosser, M.; Thalweiser, R.; Weiss, V.; Wiedenmann, E.; Gerber, G. *J. Phys. Chem.* **1991**, *95*, 8103.

(13) Dantus, M.; Janssen, M. H. M.; Zewail, A. H. *Chem. Phys. Lett.* **1991**, *181*, 281. Janssen, M. H. M.; Dantus, M.; Guo, H.; Zewail, A. H. *Chem. Phys. Lett.*, in press.

(14) Baumert, T.; Herek, J. L.; Zewail, A. H. *J. Chem. Phys.*, in press.

(15) Baumert, T.; Thalweiser, R.; Gerber, G. *Chem. Phys. Lett.* **1993**, *209*, 29. Baumert, T.; Roettgermann, C.; Rothenfusser, C.; Thalweiser, R.; Weiss, V.; Gerber, G. *Phys. Rev. Lett.* **1992**, *69*, 1512.

(16) Wei, S.; Purnell, J.; Buzza, S. A.; Stanley, R. J.; Castleman, A. W., Jr. *J. Chem. Phys.* **1992**, *97*, 9480.

(17) Baumert, T.; Buehler, B.; Thalweiser, R.; Gerber, G. *Phys. Rev. Lett.* **1990**, *64*, 734.

(18) Walkup, R. E.; Misewich, J. E.; Glownia, J. H.; Sorokin, P. P. *J. Chem. Phys.* **1991**, *94*, 3389. Glownia, J.; Misewich, J.; Walkup, R.; Kaschke, M. *T. Appl. Phys.* **1992**, *70*, 3.

(19) Mueller-Dethlefs, K.; Sander, M.; Schlag, E. W. *Z. Naturforsch.* **1984**, *39A*, 1089. Mueller-Dethlefs, K.; Sander, M.; Schlag, E. W. *Annu. Rev. Phys. Chem.* **1991**, *42*, 109.

(20) Chen, Y.; Hunziker, L.; Ludowise, P.; Morgen, M. *J. Chem. Phys.* **1992**, *97*, 2149.

(21) Wiley, W. C.; McLaren, I. H. *Rev. Sci. Instrum.* **1955**, *26*, 1150. In this article the energy resolution was discussed and related to the initial fragment kinetic energy.

(22) Ling, J. H.; Wilson, K. R. *J. Chem. Phys.* **1975**, *63*, 101.

(23) Rosker, M. J.; Dantus, M.; Zewail, A. H. *J. Chem. Phys.* **1988**, *89*, 6113.

(24) Bowman, R. M.; Dantus, M.; Zewail, A. H. *Chem. Phys. Lett.* **1989**, *161*, 297. Herek, J. L.; Pedersen, S.; Bañares, L.; Zewail, A. H. *J. Chem. Phys.* **1992**, *97*, 9046.

(25) Pedersen, S.; Baumert, T.; Zewail, A. H. *J. Phys. Chem.*, following paper in this issue.

(26) Gruebele, M.; Roberts, G.; Zewail, A. H. *Philos. Trans R. Soc. London, A* **1990**, *332*, 223.

(27) Linn, S. H.; Tzeng, W.-B.; Brom, J. M., Jr.; Ng, C. Y. *J. Chem. Phys.* **1983**, *78*, 50.

(28) Eland, J. H. D. *Int. J. Mass Spectrom. Ion Phys.* **1970**, *4*, 37.

(29) Rosenstock, J. *Phys. Chem. Ref. Data* **1977**, *6*, 1, 677.

(30) Moore, C. E. *Atomic Energy Levels*; Circular 467; Natl. Bur. Stand.: Washington, DC, 1958; Vol. III.

(31) Dantus, M.; Bowman, R. M.; Gruebele, M.; Zewail, A. H. *J. Chem. Phys.* **1989**, *91*, 7437. Bowman, R. M.; Dantus, M.; Zewail, A. H. *Chem. Phys. Lett.* **1989**, *156*, 131.

(32) Hofmann, H.; Leone, S. R. *J. Chem. Phys.* **1978**, *69*, 3819.

(33) Savas, M. M.; Mason, W. R. *Inorg. Chem.* **1988**, *27*, 658.

(34) Kawasaki, K.; Lee, S. J.; Bersohn, R. *J. Chem. Phys.* **1979**, *71*, 1235.

(35) Wadt, W. R. *J. Chem. Phys.* **1980**, *72*, 2469.

(36) Benjamin, I.; Banin, U.; Ruhman, S. *J. Chem. Phys.* **1993**, *98*, 8337. Banin, U.; Ruhman, S. *J. Chem. Phys.* **1993**, *98*, 4391.

(37) Scherer, N. F.; Ziegler, L. D.; Fleming, G. R. *J. Chem. Phys.* **1992**, *96*, 5544.

(38) Observation of coherent dissociation in solutions of HgI_2 has been made recently: Hochstrasser, R. M. Private communication.

(39) Manz, J.; Reischl, B.; Schroeder, T.; Seyl, F.; Warmuth, B. *Chem. Phys. Lett.* **1992**, *198*, 483.

(40) Ben-Nun, M.; Levine, R. D. *Chem. Phys. Lett.* **1993**, *203*, 450.

(41) Wieland, K. *Z. Elektrochem.* **1960**, *64*, 761.

(42) Hwang, H. J.; El-Sayed, M. A. *Chem. Phys. Lett.* **1990**, *170*, 161; *J. Chem. Phys.* **1991**, *94*, 4877; *J. Phys. Chem.* **1991**, *95*, 8044; *J. Chem. Phys.* **1992**, *96*, 856; *J. Phys. Chem.* **1992**, *96*, 8728. See also: Loo, R. O.; Hall, G. E.; Haerri, H.-P.; Houston, P. L. *J. Phys. Chem.* **1988**, *92*, 5.

(43) Zare, R. N.; Herschbach, D. R. *Proc. IEEE* **1963**, *51*, 173.

(44) Bersohn, R.; Lin, S. H. *Ad. Chem. Phys.* **1967**, *16*, 67.

(45) Jonah, C. *J. Chem. Phys.* **1971**, *55*, 1915.

(46) Zare, R. N. *Mol. Photochem.* **1972**, *4*, 1.

(47) Busch, G. E.; Wilson, K. R. *J. Chem. Phys.* **1972**, *56*, 3638.

(48) Yang, S.; Bersohn, R. *J. Chem. Phys.* **1974**, *61*, 4400.

(49) Scmiedl, R.; Dugan, H.; Meier, W.; Welge, K. H. *Z. Phys. A.* **1982**, *304*, 137.

(50) Greene, C. H.; Zare, R. N. *J. Chem. Phys.* **1983**, *78*, 6741.

(51) Greene, C. H.; Zare, R. N. *Annu. Rev. Phys. Chem.* **1982**, *33*, 119. See also: Fano, U.; Macek, J. H. *Rev. Mod. Phys.* **1973**, *45*, 553 and ref 62.

(52) Chamberlain, G. A.; Simons, J. P. *J. Chem. Soc., Faraday Trans. 2* **1975**, *71*, 2043.

(53) Chamberlain, G. A.; Simons, J. P. *Chem. Phys. Lett.* **1975**, *32*, 355.
(54) Dubs, M.; Bruehlmann, U.; Huber, J. R. *J. Chem. Phys.* **1986**, *84*, 3106.
(55) Hall, G. E.; Sivakumar, N.; Houston, P. L. *Phys. Rev. Lett.* **1986**, *56*, 1671. Hall, G. E.; Sivakumar, N.; Chawla, D.; Houston, P. L.; Burak, I. *J. Chem. Phys.* **1988**, *88*, 3682.
(56) Docker, M. P.; Hodgson, A.; Simons, J. P. *Chem. Phys. Lett.* **1986**, *128*, 264.
(57) Gericke, K.-H.; Klee, S.; Comes, F. J.; Dixon, R. N. *J. Chem. Phys.* **1986**, *85*, 4463.
(58) Grunewald, A. U.; Gericke, K.-H.; Comes, F. J. *Chem. Phys. Lett.* **1987**, *133*, 501.
(59) Case, C. A.; McClelland, G. M.; Herschbach, D. R. *Mol. Phys.* **1978**, *35*, 541.
(60) Dixon, R. N. *J. Chem. Phys.* **1986**, *85*, 1866.
(61) Nadler, I.; Mahgerefteh, D.; Reisler, H.; Wittig, C. *J. Chem. Phys.* **1985**, *82*, 3885.
(62) Vasudev, R.; Zare, R. N.; Dixon, R. N. *J. Chem. Phys.* **1984**, *80*, 4863.
(63) Bain, A. J.; McCaffery, A. J. *J. Chem. Phys.* **1984**, *80*, 5883; **1985**, *83*, 2627, 2632, 2641.
(64) Mons, M.; Dimicoli, I. *Chem. Phys. Lett.* **1986**, *131*, 298.
(65) Hall, G. E.; Sivakumar, N.; Ogorzalek, R.; Chawla, G.; Haerri, H.-P.; Houston, P. L. *Faraday Discuss. Chem. Soc.* **1986**, *82*, 13.
(66) Black, J. F.; Powis, I. *Chem. Phys.* **1988**, *125*, 375.
(67) Loo, R. O.; Hall, G. E.; Haerri, H.-P.; Houston, P. L. *J. Phys. Chem.* **1988**, *92*, 5.
(68) Kawasaki, M.; Sato, H.; Fukuroda, A.; Kikuchi, T.; Kobayashi, S.; Arikawa, T. *J. Chem. Phys.* **1987**, *86*, 4431.
(69) Krautwald, H. J.; Schneider, L.; Welge, K. H.; Ashfold, M. N. R. *Faraday Discuss. Chem. Soc.* **1986**, *82*, 99.
(70) Mons, M.; Dimicoli, I. *J. Chem. Phys.* **1989**, *90*, 4037.
(71) Jacobs, D. C.; Zare, R. N. *J. Chem. Phys.* **1986**, *85*, 5457.
(72) Kummel, A. C.; Sitz, G. O.; Zare, R. N. *J. Chem. Phys.* **1988**, *88*, 7357.
(73) See also ref 1.
(74) Bain, A. J.; McCafferty, A. J. *J. Chem. Phys.* **1985**, *85*, 2627.
(75) Kummel, A. C.; Sitz, G. O.; Zare, R. N. *J. Chem. Phys.* **1986**, *85*, 6874.
(76) Kummel, A. C.; Sitz, G. O.; Zare, R. N. *J. Chem. Phys.* **1988**, *88*, 6707.
(77) Maya, J. *J. Chem. Phys.* **1977**, *67*, 4976.
(78) *Gmelins Handbuch der anorganischen Chemie, Quecksilber, Teil B – Lieferung 2*; Verlag Chemie GmbH: Weinheim, 1967; p 34.
(79) Jordan, K. J.; Lipson, R. H.; Yang, D. S. *J. Chem. Phys.* **1992**, *97*, 9099.
(80) Loewenschuss, A.; Ron, A.; Schnepf, O. *J. Chem. Phys.* **1969**, *50*, 2502.
(81) Bernstein, R. B. *Chemical Dynamics via Molecular Beam and Laser Techniques*; Oxford University Press: Oxford, 1982.

Appendix G

Femtosecond Real-Time Probing of Reactions. XIII. Multiphoton Dynamics of IHgI

12460 J. Phys. Chem. 1993, 97, 12460–12465

Femtosecond Real-Time Probing of Reactions. 13. Multiphoton Dynamics of IHgI

S. Pedersen, T. Baumert,† and A. H. Zewail*

Arthur Amos Noyes Laboratory of Chemical Physics,‡ California Institute of Technology, Pasadena, California 91125

Received: September 9, 1993•

Real-time studies of the dynamics were performed on the reaction of HgI_2 in a molecular beam. Excitation was by either one or multi pump photons (311 nm), leading to two separate sets of dynamics, each of which could be investigated by a time-delayed probe laser (622 nm) that ionized the parent molecule and the fragments by REMPI processes. These dynamics were distinguished by combining the information from transients taken at each mass (HgI_2, HgI, I_2, Hg, and I) with the results of pump (and probe) power dependence studies on each mass. A method of plotting the slope of the intensity dependence against the pump–probe time delay proved essential. In the preceding publication, we detailed the dynamics of the reaction initiated by a one photon excitation to the A-continuum. Here, we present studies of higher-energy states. Multiphoton excitation accesses predissociative states of HgI_2, for which there are crossings into the symmetric and asymmetric stretch coordinates. The dynamics of these channels, which lead to atomic (I or Hg) and diatomic (HgI) fragments, are discussed and related to the nature of the intermediates along the reaction pathway.

I. Introduction

For the reaction of HgI_2, the dynamics were probed in earlier studies using laser-induced fluorescence (LIF) on the femtosecond time scale.[1-4] At a fixed probe wavelength (390 or 620 nm), the fluorescence of HgI, monitored at different wavelengths, was recorded at different delay times. Dispersion of the fluorescence spectrum[5,6] allowed for separation of the different set of trajectories which produce coherence in the final products. There are three coordinates involved in the IHgI reaction, one symmetric stretch, one asymmetric stretch, and one bend, and the molecular dynamics simulations[2,3] revealed the wave packet motion in these coordinates, making comparison with experiments.

In the preceding publication,[7] we reported on the use of the kinetic energy time-of-flight (KETOF) technique in the femtosecond time-resolved study of IHgI fragmentation. With this technique, we were able to measure the scalar part (kinetic energy release) as well as the vectorial part (symmetry and alignment of transition moments) of the dynamics while the system is in the transition-state region. The emphasis was mainly on the early time (up to about 500 fs) behavior, and as will be shown here, this behavior corresponds to one-photon excitation to the A-continuum.

In this paper, mass selectivity is employed in determining the dynamics involved in one- and multi-pump-photon excitation of IHgI. The parent mass (HgI_2^+) and each of the four fragment masses (HgI^+, I_2^+, Hg^+, and I^+) were monitored during the course of the reaction and when final fragments were formed. Pump and probe intensity studies were analyzed with a very simple method, distinguishing and identifying the temporal behavior of the dynamics in the one-photon and multiphoton regimes.

The outline of the paper is as follows: in section II a brief description of the experiment is given. The results are presented in section III and include an analysis of the pump and probe power dependence studies. The discussions are given in section IV, and the summary and conclusions follow in section V.

II. Experimental Section

The femtosecond laser apparatus has been described in detail previously[8] and is discussed only briefly here. Femtosecond pulses were generated from a colliding pulse mode-locked ring dye laser (CPM) and amplified by a Nd:YAG-pumped pulsed dye amplifier (PDA). The recompressed output pulses had an (unattenuated) energy of 0.2–0.3 mJ at a repetition rate of 20 Hz. The pump wavelength was 311 nm (fwhm = 5 nm) and was generated by frequency doubling a part of the PDA output in a 0.2-mm-thick KDP crystal. For the probe MPI we used the remaining output of the PDA (622 nm, fwhm = 13 nm).

The pump and probe beams, with proper attenuation and parallel or perpendicular polarization, were delayed in time relative to one another in a Michelson interferometer and were then recombined collinearly and focused onto the IHgI molecular beam. The temporal pulse characterization was performed following the procedure of ref 7: the probe was found to have a fwhm of 60 fs (sech² fitting), and the pump–probe Gaussian cross correlation had a fwhm of 100 fs.

The molecular beam consisted of an oven with a nozzle diameter of 0.3 mm. The oven was heated to 445 K (measured at the nozzle). MPI pump–probe experiments on the skimmed molecular beam were carried out in a differentially-pumped ionization chamber about 12 cm downstream from the nozzle. The TOF spectrometer was used in its mass-resolution mode; the results obtained using its kinetic energy resolution mode were described in ref 7. The molecular beam, the lasers, and the TOF detection axes were mutually perpendicular. In all experiments described here, the pump laser polarization was kept fixed and parallel to the TOF axis. A sketch of the experimental setup is shown in ref 7.

Pump and probe power dependences were performed on all five masses: HgI_2, HgI, I_2, I, and Hg. For these, the probe polarization was maintained fixed perpendicular to the pump polarization. The intensity of one arm, set using a variable attenuator mounted on a translation stage, was monitored after passing through the molecular beam using a photodiode and appropriate filters to exclude the second wavelength. Meanwhile, the other arm was kept at an intermediate level of intensity. After a set of transients were taken at five different intensities of one arm, the variable attenuator in that arm was repositioned in its original place to confirm laser stability. The MPI background HgI_2 ion signal due to the pump only was reduced to a negligible level (<5% of the maximum signal in the HgI_2 transient at the maximum pump intensity used in the pump intensity dependence).

† Deutsche Forschungsgemeinschaft (DFG) postdoctoral fellow.
‡ Contribution No. 8848.
• Abstract published in *Advance ACS Abstracts*, November 1, 1993.

0022-3654/93/2097-12460$04.00/0

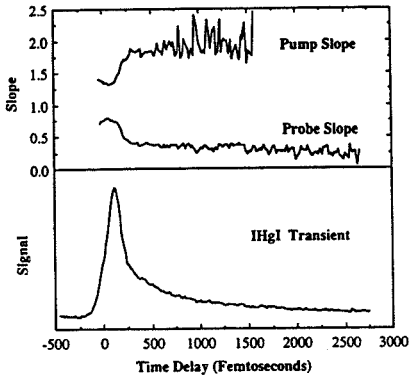

Figure 1. (bottom) The femtosecond HgI_2 transient which shows the multiexponential decay behavior. This transient defines time zero (very close to where the signal has reached half of its maximum value). For this and the other transients shown, excitation is with $\lambda_1 = 311$ nm, and probing is by $\lambda_2 = 622$ nm. (top) The slope of the pump intensity dependence rises from 1.3 ± 0.1 to a constant level of 1.9 ± 0.2 in 200 fs. There is an increasingly stronger probe saturation at long times (slope ~0.4 at 300 fs and 0.25 ± 0.1 at 2.5 ps). Notice that the probe dependence slope mirrors that for the pump (*i.e.*, inverted image) and that there is a temporal correlation between the slope plots and the transient.

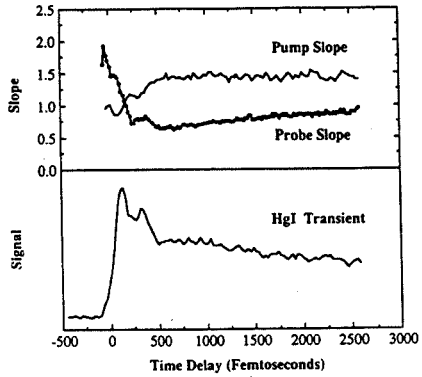

Figure 2. (bottom) The femtosecond HgI transient. Two sharp peaks separated by 220 fs are followed by a broad peak at about 1 ps and by a nonzero asymptote. (top) The pump slope increases from 0.95 ± 0.1 to a constant value of 1.45 ± 0.1 at 500 fs. In the rising part of the pump slope there is a noticeable dip at the position of the second peak in the transient. The probe dependence mirrors the pump dependence: it drops from a slope of more than 1 to a minimum at 500 fs of 0.6 ± 0.1 (some saturation) but then rises again toward 1.

Time zero was defined by the position where the HgI_2 signal reached half of its maximum value. In order to find the position of the signal onset in the transients for each mass relative to time zero, scans over a short pump–probe time delay range were taken, alternating between HgI_2 and one of the other four masses. These time zero shift studies were performed with the probe polarization perpendicular to the pump polarization. For each transient, a boxcar gate was set to the mass under investigation and the pump–probe delay line was scanned until a satisfactory signal-to-noise level was achieved.

The sample was 99.999% HgI_2 (Aldrich) containing the natural isotope distribution of Hg (196–204 amu).

III. Results

A. Parent and Fragment Femtosecond Transients. In Figures 1–5, transients are shown for HgI_2, HgI, I, Hg, and I_2, respectively, for perpendicular polarization of the pump and probe lasers. The time zero shifts are 47 fs for HgI, 61 fs for I, 75 fs for Hg, and 34 fs for I_2. (For each time shift, the uncertainty is ±15 fs.) Hence, each transient has a signal onset that lies later than that of the parent. If the excited wave packet takes some finite time to evolve from the initial region, where probing gives only HgI_2 signal, into a region where a particular fragment mass is obtained upon probing, then this finite time will appear in the time zero shift for the transient of that fragment mass. The time shift is unaffected by the pump or probe intensities if these lie in the unsaturated regime. However, if either the pump or the probe intensity enters the saturation regime, then the onset of the signal will move to earlier times as the intensity is increased. For the HgI_2 transient, the pump is unsaturated and the probe is only weakly saturated. The power dependence for all the other masses is described in the sections that follow.

The HgI_2 transient showed a multiexponential decay behavior. The transient was analyzed as a triple exponential with decay times τ_1, τ_2, and τ_3. To get τ_1, convolution with the pump–probe cross-correlation was required, and a value on the order of 50 fs was obtained. The second component was also fit in the convolution. The third component was most easily obtained from a log plot at long times, yielding a value for τ_3 of about 1 ps. Having determined τ_3, the contribution from this third component

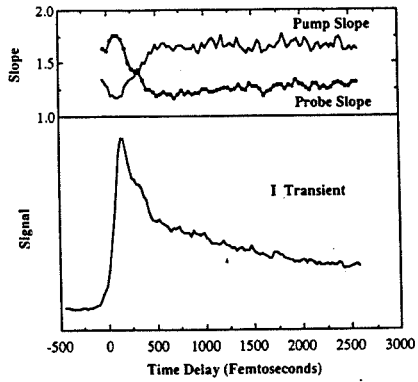

Figure 3. (bottom) The femtosecond transient obtained by detecting the I mass. (top) The slope of the pump intensity dependence rises from 1.3 ± 0.1 to 1.65 ± 0.1 at 500 fs. The slope of the probe intensity dependence shows a mirror image (inverted), decreasing from 1.7 ± 0.1 to below 1.25 (followed by a slight increase again over a picosecond time scale).

($c \exp(-t/\tau_3)$, where c is a constant) was subtracted from the transient, and a log plot of the remainder ($a \exp(-t/\tau_1) + b \exp(-t/\tau_2)$) yielded a value for τ_2 where a linear fit was performed at times much longer than τ_1. Hence, τ_2 was arrived at in two different ways, and in both cases it was found to be on the order of 500 fs.

The I_2 transient (Figure 5) resembles the HgI_2 transient (Figure 1); the signal drops to zero on a time scale of picoseconds, showing that there is no detectable signal from free I_2. The short-time behavior (up to about 500 fs) of HgI, I, and Hg was discussed in detail in ref 7. The emphasis here is on the long-time behavior. In the HgI transient there is an increase (bump) in the signal that is noticeable after 500 fs and peaks around 1 ps (Figure 2). The signal levels off to a nonzero constant value, remaining at this value up to 100 ps (time range checked in the experiment) (Figure 6). The I transient shows a leveling off of the signal after several picoseconds, and as for HgI, this level remains constant up to 100 ps (Figure 6). This asymptotic constant value is, of course, both pump and probe intensity dependent. The Hg transient has a long-time behavior that deviates from that of HgI and I: the

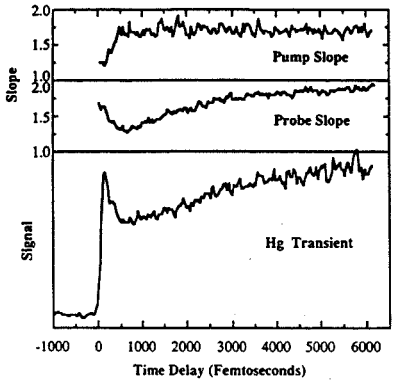

Figure 4. (bottom) The femtosecond transient obtained by detecting the Hg mass (all isotopes). (top) The pump dependence starts off with a slope of 1.25 ± 0.1 up to 100 fs and then rises, reaching an asymptotic value of 1.7 ± 0.1 at 500 fs. The probe dependence slope is initially 1.65 ± 0.1, decreases to a minimum of 1.3 ± 0.1 at 500 fs, and subsequently rises to almost 2 at 2.5 ps.

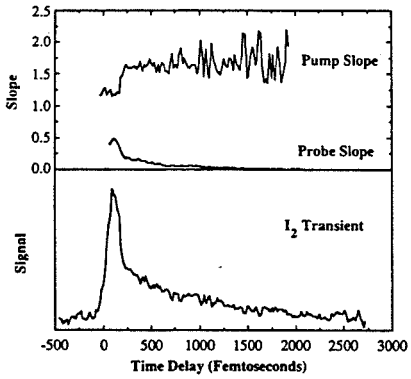

Figure 5. (bottom) The I_2 femtosecond transient which resembles that of HgI_2. (top) The slope of the pump intensity dependence is 1.2 ± 0.1 up to 100 fs, the position of the peak in the transient. The slope then rises in less than 100 fs to an asymptote of 1.65 ± 0.2. The probe slope mirrors the pump slope. There is severe probe saturation after 200 fs.

signal rises at long times, over a range that is on the order of 10 ps (Figures 4 and 6).

The effects of polarization of the pump and probe at early times were described in ref 7. For every mass it was found that at long times there is no significant difference between the transients obtained when the probe was parallel to the pump or perpendicular to the pump. (Note that the pump was always polarized parallel to the TOF axis of the molecular beam and that it was only the probe polarization that was rotated.)

B. Power Dependences. To extract the maximum amount of information from the pump or probe intensity dependence on the transient of each mass, the slope of the power dependence was calculated at each position of the pump–probe time delay. For each value of the time delay, a linear least-squares fit to a graph of ln(signal) *vs* ln(intensity), with data points corresponding to five different laser intensities, was employed to compute the slope corresponding to that time delay. Using this analysis, the slopes of both the pump and probe power dependences could be plotted as a function of the pump–probe time delay, thus tracking and distinguishing between one-photon or multiphoton excitations, the onset of saturation, and the time scales associated with the different processes. Plots of the slopes of the pump and probe

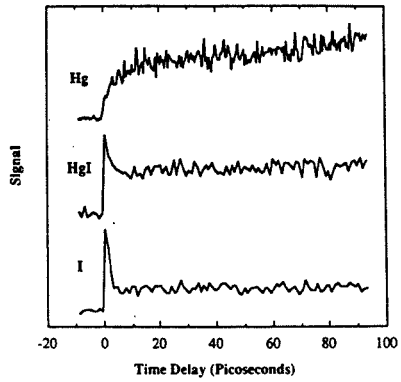

Figure 6. Long-time (up to 100 ps) transients of Hg, HgI, and I. The HgI and I transients show very similar behavior at long times: both have an asymptotic constant signal level (time range limit of experiment). The Hg transient, however, shows a continuous increase in the signal level over tens of picoseconds. Due to the choice of large separation between the data points, the behavior at early times is not well resolved in these transients.

intensity dependences are shown together with the transients for each of the five masses in Figures 1–5. It should be remembered that a slope of less than 1 indicates that a saturated transition contributing to the signal is present. A slope that exceeds 1, having accounted for experimental error, implies that a transition involving more than one photon is present. (Relatively long-lived intermediates may lead to an apparent slope of one, even for a two-photon transition.)

1. Pump Power Dependence. For each mass, five transients were taken over a 1 order of magnitude variation in the pump intensity, keeping the probe fixed. The slope of the intensity dependence was calculated for all values of the pump–probe time delay. The slope plot for every mass is shown together with a transient for that mass. The pump power dependence of the signal can thus be traced as the system evolves. The slope dependence was also performed separately using just the peak values from the five different intensity transients. In the case of HgI_2, for example, this yielded a straight line fit to a plot of ln(signal) *vs* ln(intensity) with a slope of 1.33, consistent with the slope plot value.

The transients for the five different masses show some common features. At early times, in a range up to about 100 fs beyond time zero, the slope of the pump intensity dependence is approximately equal to 1, and then the slope rises to a constant asymptotic value that lies in the range 1.8 ± 0.3. The time taken for the slope to rise is not the same for all five masses. HgI, Hg, and I each have a rise time of about 400 fs; HgI_2 has a slope that rises over a range of 200 fs, while I_2 reaches its asymptotic slope value with a rise time of 100 fs.

2. Probe Power Dependence. The probe intensity was varied in five increments over 1 order of magnitude. The slope of the probe dependence was calculated as a function of the pump–probe time delay for all five masses in the same manner as it was computed for the pump dependence. In general, for each of the five masses, the probe intensity dependence shows a mirror image of the behavior of the pump dependence. For the probe dependence, the slope starts off high and then immediately decays to a lower value. The HgI, I, and Hg slope plots resemble one another. For these three masses, the slope of the probe dependence initially decreases from a value of about 1.5 to a minimum at around 500 fs, and it then increases at longer times. For HgI_2, on the other hand, the slope keeps decreasing at long times, and for I_2 there is severe probe saturation at long times as indicated by the fact that the slope approaches zero.

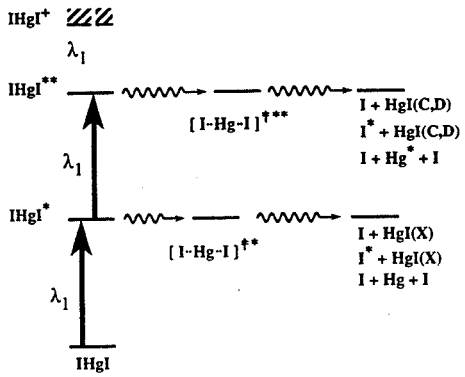

Figure 7. A schematic for the different channels involved in the fragmentation by one photon and multiphoton excitations (see text).

IV. Discussion

From the results of the pump dependence slope plots, it is clear that there is a one-photon excitation process as well as a two-photon process. Three pump photons have sufficient energy to ionize the system, but in the experiment, the MPI background HgI_2 ion signal due to the pump only was reduced to a negligible level.

Consider first the one-pump-photon excitation process (for absorption spectrum see ref 7). This process was detailed in ref 7 and is summarized as follows: After the excitation, the system evolves on the order of 50 fs into the transition state. This explains the time shifts in the rise of the fragment transients with respect to HgI_2. In the transition state, the probing wavelength (622 nm) is resonant (or nearly so), while for the final HgI fragment it is off-resonant (see Figure 9 of ref 2). We observed a double structure on HgI, I, and Hg due to the different fragmentation channels that lead to the final products: I + HgI(X), I* + HgI(X), I + Hg + I (see Figure 7 and ref 7). The transition state, leading to I + HgI(X), is entered at about 50 fs, while the transition state corresponding to the channel with final products, I* + HgI(X), is entered at approximately 270 fs, since a separation of about 220 fs is observed for the two peaks in the HgI transient. HgI originates through an asymmetric stretch, while the I fragment can result from either a symmetric stretch or an asymmetric stretch channel, as discussed in ref 7. The first peak in the Hg transient is attributed to the symmetric stretch motion.

As in the detection of fluorescence from HgI,[1-4] the same double structure was seen here, detecting the HgI ion mass. Both types of experiments yield information on how long the system remains in the transition state. The system, upon leaving the transition state, can no longer be excited to the B state, and hence no fluorescence of HgI was seen after this time of ~500 fs.

Any signal due to the free fragments from a one-pump-photon excitation must be due to MPI nonresonant transitions (4 + 2 for both Hg and I; 4 + 1 for I*; first step is nonresonant for HgI). Any MPI signal, if present, from these final free fragments will result in a small constant background after approximately 500 fs.

Let us turn to the two-pump-photon excitation process. All transients show a pump power dependence with a slope that at very early times is approximately equal to 1 but then rises to a constant asymptotic value that lies in the range 1.8 ± 0.3. An on-resonant two-photon transition (with sufficiently long lifetime) should have a slope near 1, and an off-resonant two-photon transition would result in a slope of 2. The first pump photon excitation ($HgI_2 \rightarrow HgI_2^*$, see Figure 7) is resonant, as a broad absorption feature exists for this transition (see ref 7). The first excited state decays very fast (~50 fs), so that absorption of a second pump photon during this decay period can explain our partly off-resonance behavior in the slope for the two-photon excitation process. From this we conclude that, for every mass, a one-photon pump excitation process is dominant only in the early time regime, giving rise to fast dynamics on the first excited potential energy surface, while a two-photon pump excitation leads to a type of dynamics that dominates and persists at long times.

The time for the rise in the pump dependence slope from a value very near 1 to the asymptotic permanent value of about 1.8 is not the same for all masses. For HgI, Hg, and I, however, this rise time is almost identical (approximately 400 fs). The rise time in the slope for HgI_2 is about 200 fs, which reflects that the decay time away from the one-pump-photon excited initial region of the potential energy surface must be less than 200 fs, consistent with the initial very fast decay time in the HgI_2 transient (Figure 1). (From simulations, the cross-correlation of the pulses broadens the rise time in the slope plot.) Finally, in the case of I_2, the rise for the slope starts at a time delay of about 100 fs and is completed less than 100 fs later. This behavior can be explained as follows: the probe accesses the ion from the one-photon pump excited surface by MPI, causing a slope of 1 in the pump dependence in the first 100 fs. Within the pump pulse duration, the system evolves on the first excited state before a second pump photon further excites the system to the second excited level, which can be probed on a long time scale.

We now consider the long-time behavior. In both of the transients for HgI and I, we see a buildup (bump) in the signal on a time scale on the order of 1 ps, followed by a decay in less than 10 ps to an asymptotic value as discussed before in the Results section (see Figures 2, 3, and 6). This behavior can be explained by an evolution of the system through a transition state to final products. Note that this long buildup time (~1 ps) is not typical of a direct fragmentation but more likely due to an initially excited quasi-bound state in the parent molecule that is crossed by surfaces leading to the final products. The HgI production is promoted by an asymmetric stretch, while the Hg is most probably due to a symmetric stretch mode. For HgI and I, the decay of the transition state reflects the decay in the transient to its asymptotic value which is constant up to 100 ps (limit of experimental range).

Energetically, the B, C, and D states of HgI are accessible as final products. (The B state would be accessed above its dissociation limit, however). These are electronically excited states and hence give rise to a resonant MPI process. This explains the high asymptotic signal level for HgI as resulting from ionization of the electronically excited free fragments. Note that the fluorescence lifetime of these states is on the nanosecond time scale. For example, the B-state lifetime is 23 ± 1 ns.[9]

The I fragment is produced in its ground state ($^2I_{3/2}$) or its spin–orbit excited state ($^2I_{1/2}$), and using the same argument as for the final products formed from one-pump-photon excitation, the off-resonant MPI could contribute to the final value. The pump dependence slope for I at long times is 1.65 ± 0.1, indicating that the contribution to the I signal in the asymptote is due to a two-photon pump process. If the asymptotic signal were due to nonresonant probing (4 + 1 for I*, 4 + 2 for I), then we would have expected more contribution from the one-pump-photon excitation process because it should have a higher yield of free I and I*. This would, in turn, have implied a pump dependence slope of 1 for the asymptotic I signal. We see a steeper slope (1.65 ± 0.1), and hence we must explain the asymptotic I signal by another means. We attribute it to a probe ionization of the electronically excited HgI (that resulted from a two-photon pump process), followed by ionic fragmentation due to further absorption of probe photons. This argument is supported by the following observations. The HgI and I transients show the same long-time

behavior; they both have appreciable signal after 500 fs, which is followed by a decrease in less than 10 ps to an asymptotic constant signal level. The pump dependence slope plot for HgI resembles that for I, and the probe dependence slope plots for the two masses are also very similar in their dynamical features.

The probe dependence slope decreases for HgI and I to a minimum at about 500 fs, followed by an increase in the slope. The decrease reflects a growing contribution to the signal from the transition state of the two-pump-photon excited surface. The increase that follows indicates that the probing cross section decreases upon leaving the transition state and reaching the final products. (For fixed pulse intensity and wavelength, saturation will only depend on the cross section for an excitation.)

The high probe slope in the beginning of the transients does not contradict the fact that the signal is largest at early times. The explanation is that the pump was kept in the unsaturated regime, implying that the one-pump-photon excited surface will be more populated than the two-photon excited surface. Because of the energy difference, the one-pump-photon excited surface requires more probe photons to be ionized, and hence a higher probe dependence slope is associated with the early-time behavior.

The Hg transient is also a superposition of a one- and a two-photon-pump excitation process, as can be seen directly from the pump dependence slope plot (Figure 4). What distinguishes the Hg transient from those of HgI and I is that the Hg transient shows a long time buildup in the signal that persists over tens of picoseconds. We do not attribute this long growth of the Hg signal to be only due to ionic fragmentation of an HgI electronically excited state, as we would then expect a corresponding long-time growth behavior on the I mass. As mentioned earlier, HgI arises from an asymmetric stretch mode, whereas Hg stems from a symmetric stretch mode. If we restrict our discussion to this one-dimensional picture in order to make the general behavior clearer, then this result, the growing of the signal in the transient on a time scale of tens of picoseconds, is analogous to that seen in NaI.[10] It arises from wave packet motion on a bound surface that is crossed by a repulsive surface. Every time the wave packet reaches this crossing region, part of the wave packet leaks out into the asymptote. This behavior is also similar to that of the Rydberg-state dynamics in methyl iodide.[11]

It is the nature of the potentials involved that dictates why buildup of Hg is on the order of tens of picoseconds, whereas the transition-state buildup of HgI is only on the order of 500 fs, and the resulting free fragments of HgI are already formed after less than 10 ps. In order to explain our results, we propose the following: the potential that is reached by a two-pump-photon excitation is bound, but this potential is crossed by two repulsive surfaces accounting for the observed predissociation: (a) One surface has an asymptote to the free HgI(C,D) and I (or I*) products, and the coupling into this surface is promoted by an asymmetric stretch mode. (b) The second surface has an asymptote to the free I + Hg* + I fragments and is coupled to by the symmetric stretch mode.

This second coupling (b) must be weaker than the first one (a) to account for the slow buildup in the Hg channel compared with the fast buildup in the HgI channel. If the initial wave packet were to redistribute quickly into all degrees of freedom, then the parent decay and the product build-up would be dominated by the strongest coupling. As we do see two distinct build-up times on the products, we propose that part of the initial wave packet is not redistributed but rather remains in a defined coordinate leading to symmetric stretch fragmentation with a weak output coupling. So this part of the wave packet is not affected by the strong coupling into the asymmetric stretch coordinate.

The parent decay can now be examined. The different dynamics are reflected in the multiexponential decay of the parent. The one photon pump excitation leads to a fast decay of about 50 fs, as seen in the time shifts of the fragment transients with respect to time zero of HgI_2. The first component in the multiexponential decay in the HgI_2 transient was also found to be on the order of 50 fs, taking the cross-correlation of the pump and probe into account. Both the pump and probe intensity dependence slopes show a drastic change in the first 200 fs. If we take the cross-correlation into account here, as well as the difference in the cross section between the first and second excited state, then we again arrive at a comparable time constant. The HgI_2 transient was analyzed as a triple-exponential decay (*vide supra*). The first, fast component had $\tau_1 \sim 50$ fs. The longer time components were found to be $\tau_2 \sim 500$ fs and $\tau_3 \sim 1$ ps. Components with even longer decay times could not be extracted due to the low signal-to-noise ratio at long time delays, where the signal dropped toward zero. As the long-time behavior, according to the pump dependence slope plot for HgI_2, is associated with two-photon pump excitation, we attribute the long decay times to the lifetimes of the predissociating bound state.

Finally, we come to I_2 (Figure 5). The pump dependence plot shows a very sharp rise in the slope in less than 100 fs, from an initial value of about 1.2 ± 0.1 to a final constant level of 1.65 ± 0.2. Hence, the dynamics of the I_2 production is governed almost entirely by the two pump photon excitation process. The shape of the I_2 transient, for a given pump and probe intensity, is very similar to the HgI_2 transient. In the discussion so far we have shown that the two-photon excitation involves predissociative states of HgI_2. Because of the long (picosecond) lifetimes of these states, there is enough time for the initial linear IHgI molecule to undergo bending motion. This argument is supported by the relativistic *ab initio* calculations of Wadt[12] on the isoelectronic system $HgCl_2$ which shows bound excited states with an equilibrium angle of 70°–100°. When the bend angle is appreciable, corresponding to a triangular configuration of the molecule in the bound state, I_2 elimination is expected. The probe laser can excite this configuration into an ionic fragmentation channel of HgI_2^+ yielding I_2^+.

The probe dependence slope plot shows that initially the I_2 signal has a slope of 0.6 ± 0.2, reflecting some saturation, but this dependence changes to severe saturation at 200 fs (earlier when convolution with cross-correlation is considered). The probe dependence behavior mirrors that of the pump dependence. Thus, the probing transition of I_2, out of the two-pump-photon excited bound state, is a saturated transition, at the probe intensities used. Note that saturation affects transients over a time range of the order of the width of the cross-correlation only, and hence the long-time decay components are relatively unaffected. Saturation also affects the degree of polarization anisotropy, as discussed in ref 7.

V. Summary and Conclusions

Real-time studies of the HgI_2 reaction in a molecular beam are reported here. The reaction was initiated by a femtosecond laser pulse at 311 nm and followed by a time delayed probe laser (622 nm) which ionizes the parent molecule, the reaction intermediates, and final fragments by REMPI processes. Transients were obtained for all masses (HgI_2^+, HgI^+, I_2^+, Hg^+, and I^+), and careful pump and probe intensity dependence studies were performed on each mass. The method of obtaining the slope of the intensity dependence as a function of the pump–probe time delay provides the means of tracking and distinguishing between one-photon or multiphoton excitations, the onset and presence of saturation, and the time scales associated with different dynamical processes.

In the preceding paper,[7] the dynamics on the dissociative A-continuum reached by one-photon excitation were detailed. Here, the two-photon excitation accesses predissociative states of HgI_2, with crossings into the symmetric and asymmetric stretch coordinates. The transition states and the resulting free fragments (HgI(C,D) and Hg*) were probed on the time scale of these

experiments. The analogy with Rydberg-state dynamics is discussed. The time scale for all coordinates, including the bend motion, are the key to final fragmentations into different nascent products (HgI, I, Hg, I_2). Further studies are planned with focus on ionic fragmentation, molecular dynamics simulations, and energy dependences of the observed rates of fragmentation and elimination.

Acknowledgment. This work was supported by a grant from the Air Force Office of Scientific Research and the National Science Foundation.

References and Notes

(1) Bowman, R. M.; Dantus, M.; Zewail, A. H. *Chem. Phys. Lett.* **1989**, *161*, 297.
(2) Dantus, M.; Bowman, R. M.; Gruebele, M.; Zewail, A. H. *J. Chem. Phys.* **1989**, *91*, 7437.
(3) Gruebele, M.; Roberts, G.; Zewail, A. H. *Philos. Trans R. Soc. London, A* **1990**, *332*, 223.
(4) Zewail, A. H. *Faraday Discuss. Chem. Soc.* **1991**, *91*, 207.
(5) McGarvey, J. A., Jr.; Cheung, N. H.; Erlandson, A. C.; Cool, T. A. *J. Chem. Phys.* **1981**, *74*, 5133.
(6) Cheung, N. H.; Cool, T. A. *J. Quantum Spectrosc. Radiat. Transfer* **1979**, *21*, 397.
(7) Baumert, T.; Pedersen, S.; Zewail, A. H. *J. Phys. Chem.*, preceding paper in this issue.
(8) Rosker, M. J.; Dantus, M.; Zewail, A. H. *J. Chem. Phys.* **1988**, *89*, 6113.
(9) Whitehurst, C.; King, T. A. *J. Phys. B: At. Mol. Phys.* **1987**, *20*, 4035.
(10) Rose, T. S.; Rosker, M. J.; Zewail, A. H. *J. Chem. Phys.* **1989**, *91*, 7415
(11) Janssen, M. H. M.; Dantus, M.; Guo, H.; Zewail, A. H. *Chem. Phys. Lett.*, in press.
(12) Wadt, W. R. *J. Chem. Phys.* **1980**, *72*, 2469.